Transactions of the ASME®

Journal of Applied Mechanics

Published Quarterly by The American Society of Mechanical Engineers

VOLUME 57 • NUMBER 1 • MARCH 1990

Transactions of the ASME, Journal of Applied Mechanics (ISSN 0021-8936) is published quarterly (Mar., June, Sept., Dec.) for $120 per year by The American Society of Mechanical Engineers, 345 East 47th Street, New York, NY 10017. Second class postage paid at New York, NY and additional mailing offices. POSTMASTER: Send address changes to Transactions of the ASME, Journal of Applied Mechanics, c/o THE AMERICAN SOCIETY OF MECHANICAL ENGINEERS, 22 Law Drive, Box 2300, Fairfield, NJ 07007-2300.

CHANGES OF ADDRESS must be received at Society headquarters seven weeks before they are to be effective. Please send old label and new address.

PRICES: To members, $29.00, annually; to nonmembers, $120.00. Add $15.00 for postage to countries outside the United States and Canada.

INDEXED by Applied Mechanics Reviews and Engineering Information, Inc.

TECHNICAL PAPERS

1 **A Theory of Fracture Crack Initiation in Solids** (89-WA/APM-37)
T. Mura and Y. Nakasone

7 **Surface Waves for Material Characterization** (89-WA/APM-40)
J. L. Rose, A. Nayfeh, and A. Pilarski

12 **Residual Stress Determination Using Acoustoelasticity**
J. J. Dike and G. C. Johnson

18 **Derivatives of Buckling Loads and Vibration Frequencies With Respect to Stiffness and Initial Strain Parameters** (89-WA/APM-44)
R. T. Haftka, G. A. Cohen, Z. Mróz

25 **A Crystallographic Model for the Tensile and Fatigue Response for René N4 at 982°C**
M. Y. Sheh and D. C. Stouffer

32 **Plane-Strain Shear Dislocations Moving Steadily in Linear Elastic Diffusive Solids** (89-WA/APM-47)
J. W. Rudnicki and E. A. Roeloffs

40 **Plane-Strain Crack-Tip Fields for Pressure-Sensitive Dilatant Materials** (89-WA/APM-48)
F. Z. Li and J. Pan

50 **A Moving Boundary Problem in a Finite Domain**
Z. Dursunkaya and S. Nair

57 **Elastoplastic Finite Element Analysis of Three-Dimensional, Pure Rolling Contact at the Shakedown Limit** (90-WA/APM-2)
S. M. Kulkarni, G. T. Hahn, C. A. Rubin, and V. Bhargava

66 **The Response of an Infinite Railroad Track to a Moving, Vibrating Mass**
D. G. Duffy

74 **Axisymmetric Inclusion in a Half Space**
H. Y. Yu and S. C. Sanday

78 **Stress Distribution in Plane Scarf and Butt Joints**
D. Chen and S. Cheng

84 **Plane Punch Indentation of Anisotropic Elastic Half Space**
J. W. Klintworth and W. J. Stronge

91 **A Crack in a Confocal Elliptic Inhomogeneity Embedded in an Infinite Medium** (89-WA/APM-38)
C. H. Wu and C.-H. Chen

97 **Crack-Path Effect on Material Toughness** (89-WA/APM-43)
A. A. Rubinstein

104 **Fracture Initiation Due to Asymmetric Impact Loading of an Edge Cracked Plate** (89-WA/APM-41)
Y. J. Lee and L. B. Freund

112 **Stress Singularity at the Free Surface of a Dynamically Growing Crack**
P. Gudmudson and S. Ostlund

117 **Dynamic Mixed Mode I-II Crack Kinking Under Oblique Stress Wave Loading in Brittle Solids**
C.-C. Ma

128 **On Membrane and Plate Problems for Which the Linear Theories are Not Admissible**
A. D. Kerr and D. W. Coffin

134 **Elementary Static Beam Theory is as Accurate as You Please** (89-WA/APM-49)
J. M. Duva and J. G. Simmonds

138 **A Mechanical Model for Elastic Fiber Microbuckling**
A. M. Waas, C. D. Babcock, Jr., and W. G. Knauss

150 **Large Axisymmetric Deformation of a Laminated Composite Membrane**
S. P. Joshi and L. M. Murphy

158 **Effective Elastic Moduli of Ribbon-Reinforced Composites**
Y. H. Zhao and G. J. Weng

168 **Effects of Interleaves on Fracture of Laminated Composites: Part I—Analysis** (89-WA/APM-45)
A. K. Kaw and J. G. Goree

175 **Effects of Interleaves on Fracture of Laminated Composites: Part II—Solution and Results** (89-WA/APM-46)
A. K. Kaw and J. G. Goree

182 **Three-Dimensional Solutions for Antisymmetrically Laminated Anisotropic Plates** (89-WA/APM-39)
A. K. Noor and W. S. Burton

189 **Interactive Bending Behavior of Sandwich Beams**
G. W. Hunt and L. S. da Silva

197 **Polynomial Chaos in Stochastic Finite Elements** (89-WA/APM-42)
R. Ghanem and P. D. Spanos

203 **Dynamics of the Elastica With End Mass and Follower Loading**
J. M. Snyder and J. F. Wilson

(Contents continued on Inside Back Cover)

CONTENTS (CONTINUED)

209 **Dynamics of a Weakly Nonlinear System Subjected to Combined Parametric and External Excitation**
K. Yagasaki, M. Sakata, and K. Kumira

218 **Spectral Moments and Pre-Envelope Covariances of Nonseparable Processes**
M. Di Paola and G. Petrucci

225 **The Principle of Asymptotic Proportionality**
H. C. M. Chan

232 **Dynamics and Stability of a Flexible Cylinder in a Narrow Coaxial Cylindrical Duct Subjected to Annular Flow**
M. P. Paidoussis, D. Mateescu, and W.-G. Sim

241 **The Self-Noise From Ordered Structures in a Low Mach Number Jet**
R. R. Mankbadi

BRIEF NOTES

Stress Fields of Interface Dislocations
C.-Y. Hui and D. C. Lagoudas 247

248 Testing Numerical Integrations of Equations of Motion
T. R. Kane and D. A. Levinson

DISCUSSION

250 Discussion on a previously published paper by E. N. Kuznetsov

251 Discussion on a previously published paper by T. M. Cameron and J. H. Griffin

252 Discussion on a previously published paper by M. Ortiz and A. E. Giannakopoulos

BOOK REVIEWS

253 *Mechanics of Machining: An Analytical Approach to Assessing Machinability*, by P. L. B. Oxley
... Reviewed by M. C. Shaw

254 Books Received by the Office of the Technical Editor

255, 256 Worldwide Mechanics Meetings List

49 Addendum to a previously published paper by W. W. King

73 Announcement—I.U.T.A.M. 18th International Congress of Theoretical and Applied Mechanics

103 Call for Papers—International Symposium on Boundary Element Methods: Research Issues

111 Call for Papers—The Second Pan American Congress of Applied Mechanics

188 Change of Address Form

208 Call for Papers—Conference on High Temperature Constitutive Modeling: Theory and Application

217 Call for Papers—22nd Midwestern Mechanics Conference

11, 65, 83, 231, 240 Applied Mechanics Symposium Proceedings

T. Mura
Fellow, ASME

Y. Nakasone

Department of Civil Engineering,
Northwestern University,
Evanston, IL 60208

A Theory of Fatigue Crack Initiation in Solids

Introduction

The Griffith theory (1921) still plays a fundamental role in fracture mechanics. We propose a theory on fatigue crack initiation that is based upon the concept of Gibbs free energy change from a state of dislocation dipole accumulation along a layer (persistent slip band) to a state of crack initiation along the layer. Under some assumptions, when the Gibbs free energy change is plotted against cyclic numbers of loading, it takes a maximum value at a critical value of the cyclic number which is defined as the crack initiation cycle number. This theory is similar to the Griffith theory. In the Griffith theory, the Gibbs free energy change takes a maximum value at a critical size of the crack which becomes unstable for a given load. The present theory predicts a critical cycle number of loading under which the system becomes unstable for a given loading amplitude.

One of the authors and his associates have proposed several theories on fatigue crack initiations (see Tanaka and Mura (1981), Mura and Tanaka (1981), Kato et al. (1984), Hirose and Mura (1985), Lin et al. (1986)). However, none of these theories has taken the present form of nucleation theory, which is similar to the Griffith theory.

In the present paper, an extrusion or a distribution of vacancy dipoles is modeled as a PSB to obtain a crack initiation law. There have been numerous studies which describe intrusions and extrusions observed during fatigue process since the pioneer study of Forsyth (Forsyth (1953)). According to recent experimental observations (see, e.g., Antonopoulos et al. (1976), Mughrabi and Wang (1982)), it seems most likely that the dislocation dipoles of vacancy type play a major role in the formation of a crack or cracks in fatigue. Within the PSB, the accumulation of dislocations may enhance the internal tensile stress more and more with increasing number of loading cycles. The enhancement of the internal stress in the PSB leads to the energetically unstable state of a material considered, and thus the stress is to be released via the formation of an extremely thin flat void, or the initiation of a crack. The critical point, in terms of the number of loading cycles, may be given through the consideration of the balance of the elastic strain energy enhanced by the accumulating dislocations and the energy released via the formation of the crack in the PSB.

The present theory can provide not only the S-N curve for crack initiation but its dependence on material parameters such as yield strength, grain size, etc. The irreversibility of the dislocation motion and the energy dissipation are also taken into consideration, and, via such consideration, more realistic results are obtained.

Dislocation Dipole Model

Consider a cyclic loading as shown in Fig. 1 in terms of shear stress. The loading shear amplitude is $\Delta\tau = \tau_1 - \tau_2$. At the first loading at point 1 in Fig. 1, a slip takes place in the weakest portion of the material. The slip band is denoted by layer I ($-a<x<a$, $y=0$) in Fig. 2 and dislocations are piled up on the layer. Point O is a dislocation source. Point O can be an internal point in the material (Fig. 2(*a*)) or a point on the

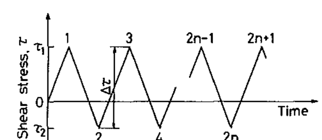

Fig. 1 Applied shear stress pattern

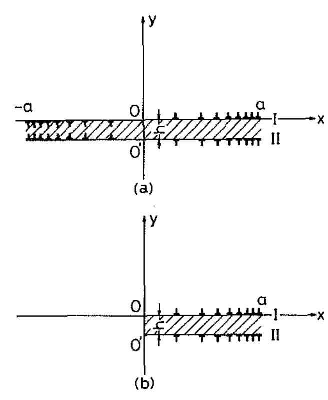

Fig. 2 Vacancy-dislocation-dipole model of the persistent slip band (PSB); (*a*) PSB of length 2a in an infinite body, (*b*) PSB of length a in an infinite half-body ending at the free surface

Contributed by the Applied Mechanics Division of The American Society of Mechanical Engineers for presentation at the Winter Annual Meeting, San Francisco, Calif., December 10-15, 1989.

Discussion on this paper should be addressed to the Editorial Department, ASME, United Engineering Center, 345 East 47th Street, New York, N.Y. 10017, and will be accepted until two months after final publication of the paper itself in the Journal of Applied Mechanics. Manuscript received by the ASME Applied Mechanics Division, March 3, 1988; final revision, March 1, 1989.

Paper No. 89-WA/APM-37.

free surface (Fig. 2(*b*)). When point O is the free surface point, the dislocations on the layer in $x<0$ are fictitious. This is a simplification of calculation. The effect of free surface is complicated in mathematics. It will be published in a separate paper.

The dislocation distribution on the layer I is determined from the equilibrium of Peach-Koehler force on the piled-up dislocations,

$$\tau_1^D+\tau_1-\tau_f=0, \tag{1}$$

when τ_1^D is the dislocation stress and τ_f the frictional stress. When unloaded, the reverse slip takes place on layer II as shown in Fig. 2. There is a good reason why the reverse slip takes place near the layer I. When layer II is close to layer I, the back stress τ_1^D on layer II is almost equal to τ_1^D on layer I and it has the same direction of unloading shear (opposite to τ_1). Namely, τ_1^D stimulates reverse slip on layer II. When layer II is far away from layer I, this stimulation (acceleration) can not be seen. When the layer II is too close to layer I, annihilation of dislocations takes place and no damage of the material is accumulated by the loading and unloading. In order to have fatigue phenomena, layer II is located at a distance h from layer I. The dislocation distribution on layer II at point 2 in Fig. 1 is determined from the equilibrium condition,

$$\tau_2^D+\tau_1^D+\tau_2+\tau_f=0, \tag{2}$$

where τ_2^D is the stress caused by the new dislocations on layer II. When $h/a << 1$, we can assume that τ_1^D in (2) is almost equal to τ_1^D in equation (1). In (2), the frictional force is taken as negative because of the reverse slip. Using (1) we write (2) as

$$\tau_2^D-\Delta\tau+2\tau_f=0, \tag{3}$$

where $\Delta\tau=\tau_1-\tau_2$. The dislocation distribution on layer II is shown in Fig. 2. This can be a model for the extrusion. When layer II is considered at $x_2=h$, it provides a model for the intrusion. For the present theory of crack initiation, it is relevant to consider an extrusion as explained later.

When the specimen is loaded again to point 3 in Fig. 1 slip takes place on layer I by the help of the dislocation stress τ_2^D on layer II. This is the ratcheting effect of damage (dislocation) accumulation. The dislocation distribution on layer I is determined by the equilibrium condition

$$\tau_3^D+\tau_2^D+\tau_1-\tau_f=0, \tag{4}$$

where τ_3^D is the dislocation stress due to the dislocations on layer I. τ_2^D on layer I is assumed to be the same as τ_2^D in layer II. Equation (4) is written from (2) as

$$(\tau_3^D-\tau_1^D)+(\Delta\tau-2\tau_f)=0. \tag{5}$$

Similarly, at point 4 in Fig. 1 the dislocations on layer II is determined from

$$\tau_4^D+\tau_3^D+\tau_2+\tau_f=0 \tag{6}$$

which is written as

$$(\tau_4^D-\tau_2^D)-(\Delta\tau-2\tau_f)=0, \tag{7}$$

where τ_4^D is the stress caused by the dislocations on layer II. Generally, we have

$$(\tau_{2n+1}^D-\tau_{2n-1}^D)+(\Delta\tau-2\tau_f)=0 \tag{8}$$

at the maximum loading τ_1 and

$$(\tau_{2n}^D-\tau_{2n-2}^D)-(\Delta\tau-2\tau_f)=0 \tag{9}$$

at the minimum unloading τ_2.

The shear stress $\tau_n^D(x)$ caused by dislocation distribution $D_n(x)$ is

$$\tau_n^D(x)=A\int_{-a}^{a} D_n(x')/(x-x')\,dx', \tag{10}$$

where $A=\mu b/2\pi(1-\nu)$. b is the Burgers vector, μ the shear modulus, and ν is Poisson's ratio. Equations (8) and (9) are the integral equations for unknown $D_n(x)$ and easily solved,

$$\begin{aligned} D_{2n+1}-D_{2n-1} &= -(D_{2n}-D_{2n-2}) \\ &= (\Delta\tau-2\tau_f)x/\pi A\,(a^2-x^2)^{1/2} \end{aligned} \tag{11}$$

or

$$D_{2n+1}\approx -D_{2n}\approx n(\Delta\tau-2\tau_f)x/\pi A(a^2-x^2)^{1/2} \tag{12}$$

for large cycle number, n. The amount of slip on layer I at point $(2n+1)$ in Fig. 1 is

$$\begin{aligned} [u_1]_I &= b\int_x^a D_{2n+1}(x)dx \\ &= n(\Delta\tau-2\tau_f)(a^2-x^2)^{1/2}b/\pi A \end{aligned} \tag{13}$$

and that on layer II at point $2n$ is

$$[u_1]_{II}=-n(\Delta\tau-2\tau_f)(a^2-x^2)^{1/2}b/\pi A. \tag{14}$$

Energy Calculations

When the dislocation dipoles are piled up as shown in Fig. 2, the elastic strain energy is built up in the material. We evaluate the elastic strain energy W_1 after n cycles of loading (amid point $2n$ and point $(2n+1)$ in Fig. 1),

$$W_1=\frac{1}{2}\int_0^a \sigma_{ij}u_{i,j}d\,D \tag{15}$$

where σ_{ij} is the dislocation stress and $u_{i,j}$ the corresponding elastic distortion. The displacement u_i has multiple values $[u_1]$ = u_1 (upper surface) − u_1 (lower surface) along layer I and also layer II. $[u_1]$ on layer I is denoted by $[u_1]_I$ and it is given by (13). That on layer II, $[u_1]_{II}$, is given by (14). Integrating (15) by parts, considering $\sigma_{ij,j}=0$ in D and $\sigma_{ij}n_j=0$ on $|D|$, we have

$$W_1=-\frac{1}{2}\int_0^a \sigma_{12}\,[u_1]_I dx-\frac{1}{2}\int_0^a \sigma_{12}[u_1]_{II}dx, \tag{16}$$

where I and II indicate the line integrals along layer I and layer II, respectively. σ_{12} is the shear stress due to the dislocations in layers I and II, and $\sigma_{12}=\sigma_{12}^I+\sigma_{12}^{II}$, where σ_{12}^I is the stress caused by the dislocations on layer I and σ_{12}^{II} is the stress caused by the dislocations on layer II. Since $\sigma_{12}^I\,[u_1]_I=\sigma_{12}^{II}\,[u_1]_{II}$, and $\sigma_{12}^I(x,-h)\,[u_1]_{II}=\sigma_{12}^{II}(x,0)\,[u_1]_I$, (16) is written as

$$W_1=-\int_0^a \sigma_{12}^I(x,0)[u_1]_I dx-\int_0^a \sigma_{12}^I(x,-h)[u_1]_{II}dx, \tag{17}$$

where

$$\begin{aligned} \sigma_{12}^I(x,0) &= A\int_{-a}^{a}\frac{D_{2n+1}(x')}{x-x'}dx' \\ \sigma_{12}^I(x,-h) &= A\int_{-a}^{a}\frac{D_{2n+1}(x')(x-x')\{(x-x')^2-h^2\}}{\{(x-x')^2+h^2\}^2}dx'. \end{aligned} \tag{18}$$

Using (12), we get

$$\begin{aligned} \sigma_{12}^I(x,0) &= -n(\Delta\tau-2\tau_f), \\ \sigma_{12}^I(x,-h) &= -n(\Delta\tau-2\tau_f)\{1-(1/R)(-x\sin\theta+h\cos\theta) \\ &\qquad -(a^2h/R^3)\cos 3\theta\}, \end{aligned} \tag{19}$$

where

$$\begin{aligned} R^4 &= \{(a+x)^2+h^2\}\{a-x)^2+h^2\}, \\ \sin\theta &= -\sqrt{2}hx/R(R^2+a^2-x^2+h^2)^{1/2} \\ &= -\mathrm{sgn}(x)(R^2-a^2+x^2-h^2)^{1/2}/\sqrt{2}R, \\ \cos\theta &= (R^2+a^2-x^2+h^2)^{1/2}/\sqrt{2}R. \end{aligned} \tag{20}$$

It is noted that $\sigma_{12}^I(x,0)=\tau_{2n+1}^D$.

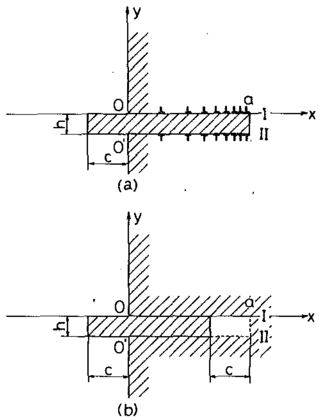

Fig. 3 (a) PSB stretched by the dislocation dipoles enhancing the elastic strain energy; (b) Initiation of a crack of length c in the PSB relaxing the internal stress

Integrals in (17) are completed as

$$\begin{aligned} W_1 &= (1-\nu)(\Delta\tau-2\tau_f)^2 n^2 a^2 (1-k)\ \{3[K(k)-E(k)] \\ &+ kK(k)\}\backslash k\mu, \qquad (21) \\ &\approx (1-\nu)(\Delta\tau-2\tau_f)^2 n^2 a^2 \epsilon^2 [\log(8/\epsilon) \\ &- (3/2)]/\mu, \text{ for small } \epsilon, \end{aligned}$$

where

$$k = \{(4a^2+h^2)^{1/2}-h\}^2/4a^2,$$

$$K(k) = \int_0^1 \frac{d\xi}{(1-\xi^2)^{1/2}(1-k^2\xi^2)^{1/2}}, \qquad (22)$$

$$E(k) = \int_0^1 \frac{(1-k^2\xi^2)^{1/2}}{(1-\xi^2)^{1/2}} d\xi,$$

$$\epsilon = h/a.$$

It is noted that $W_1 = 0$ for $h = 0$ and W_1 becomes the dislocation self energy when $h \to \infty$.

Crack Initiation Law

In order to explain the present crack nucleation theory, the extrusion model Fig. 3(*a*) is used. The extrusion is denoted by *c*. The value *c* is obtained from

$$c = Nb \qquad (23)$$

where N is the total number of positive dislocations on layer I or the total number of negative dislocations on layer II,

$$N = \int_0^a D_{2n+1}\,dx = n(\Delta\tau-2\tau_f)a/\pi A. \qquad (24)$$

b is the Burgers vector.

A crack of length c is nucleated, as shown in Fig. 3(*b*), by the energy release W_1 of the dislocation dipoles in Fig. 3(*a*) and the mechanical energy release W_2, where

$$\begin{aligned} W_2 &\approx \pi(1-\nu)(c/2)^2(\Delta\tau)^2/2\mu \\ &\approx (1-\nu)(\Delta\tau-2\tau_f)^2(\Delta\tau)^2 a^2 b^2 n^2/8\pi A^2\mu. \qquad (25) \end{aligned}$$

Figure 3(*b*) is the dislocation free state or the dislocation stress-free state, but it contains a crack c. The persistent slip band in Fig. 3(*a*) has been stretched by the dislocation dipoles but it is relaxed to Fig. 3(*b*) by the crack nucleation with compensation of the dislocation dipoles.

The Gibbs free-energy change to be considered becomes

$$\begin{aligned} \Delta G &= -W_1 - W_2 + 2c\gamma \\ &= -W_1 - W_2 + 2bn(\Delta\tau-2\tau_f)a\gamma/\pi A \end{aligned} \qquad (26)$$

where γ is the surface energy of the crack.

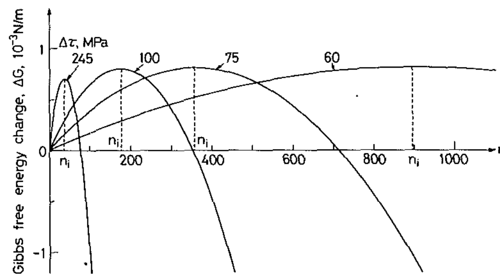

Fig. 4 Variation of the Gibbs free-energy change ΔG with the number of loading cycles showing that the maximum point is retarded by the decrease of the applied stress range $\Delta\tau$

When (26) is plotted against n, Fig. 4 is obtained. ΔG takes a maximum value for $n = n_i$. Similarly to the Griffith theory, the system becomes unstable at n_i. We postulate that n_i is a critical cycle number for fatigue crack initiation under a given applied stress amplitude $\Delta\tau$. This crack initiation cycle number n_i is obtained from

$$\frac{\partial}{\partial n}(\Delta G) = 0 \qquad (27)$$

or

$$\begin{aligned} &-4(1-\nu)(\Delta\tau-2\tau_f)^2 n_i h^2 \log(8/\epsilon)/\epsilon\mu \\ &-2(1-\nu)(\Delta\tau-2\tau_f)^2 n_i (\Delta\tau)^2 a^2 b^2/8\pi A^2\mu \\ &+2b(\Delta\tau-2\tau_f)a\gamma/\pi A = 0. \end{aligned} \qquad (28)$$

Figure 4 illustrates that as $\Delta\tau$ becomes lower, the ΔG versus n curve becomes flatter; in other words, the range of n within which condition (27) can be approximately satisfied becomes wider. Such a tendency may imply wider variation of fatigue life at lower stress ranges.

Equation (28) provides the S-N curves for crack initiation as shown in Figs. 5–9 where the values of the following parameters are varied in order to show their effects on the S-N curves: the frictional stress τ_f, the half length of the persistent slip band a, the surface energy γ, Young's modulus $E = 2(1+\nu)\mu$, and the height of the dislocation dipole h.

In the present theory, the fatigue limit can be regarded as twice the frictional stress as easily seen from (28); i.e., no crack can be initiated at stress ranges lower than $2\tau_f$. Since the frictional stress τ_f is relevant to the yield strength of a material, the dependence of the S-N curve on τ_f as shown in Fig. 5 implies the well-known relationship found between fatigue limit and ultimate tensile strength or yield strength (see, e.g., Hempel (1965)); i.e., the higher the ultimate tensile strength or the yield strength, the higher the fatigue limit.

The present theory also gives the dependence of the crack initiation diagram on the grain size (see, e.g., Taira et al. (1979)), when the length of the persistent slip band $2a$ is regarded as the grain size: The smaller the grain size, the higher the fatigue strength for crack initiation. Figure 6 depicts such dependence.

The dependence of the S-N curve on γ is shown in Fig. 7, in which larger γ gives higher fatigue strength and shifts the knee of the S-N curve rightwards, i.e., to longer n_i region. It is noted that the surface energy of the order of 1N/m (see, e.g., Broek (1982)) gives a more realistic result than the so-called plastic work γ_p does. Namely, the present theory does not require the modification by γ_p which is over 10^3 higher than γ.

Only subtle difference can be seen in Fig. 8; nevertheless, a higher value of Young's modulus E gives a higher value of the fatigue strength, but does not shift the knee of the S-N curve as the case of a (see also Fig. 15 for clearer E-dependence of the curve).

Figure 9 depicts the dependence of the S-N curve on the height of the dislocation dipole h: A smaller value of h gives

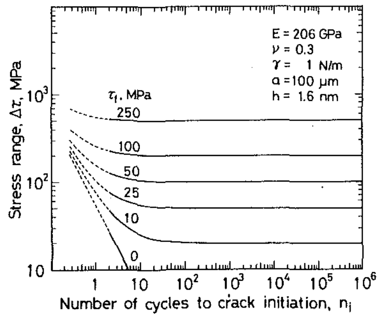

Fig. 5 Effect of the frictional stress τ_f on the S-N curve for crack initiation given by equation (28)

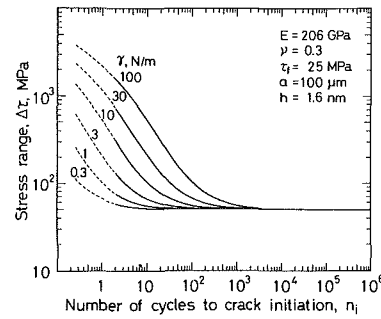

Fig. 7 Effect of the surface energy γ on the S-N curve for crack initiation given by equation (28)

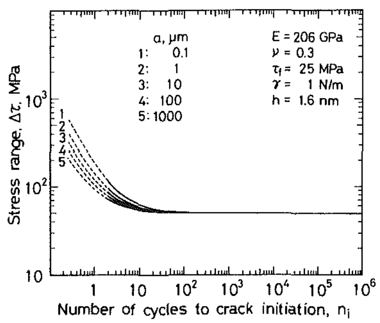

Fig. 6 Effect of the half-length of the PSB *a* on the S-N curve for crack initiation given by equation (28)

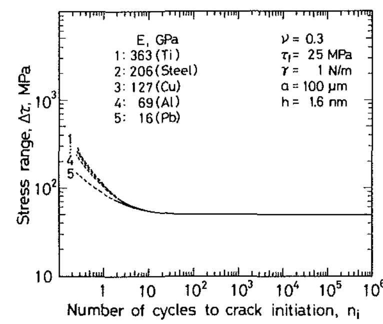

Fig. 8 Effect of Young's modulus *E* on the S-N curve for crack initiation given by equation (28)

a higher value of the fatigue strength and shifts the knee to longer n_i region. The effect of h is saturated for $h < 1.6 \times 10^{-3}$nm in the case of Fig. 9, although the value of h is reportedly in the order of 1.6nm (see, e.g., Antonopoulos et al. (1976), NS Essmann and Mughrabi (1979)) and an h-value lower than 0.3nm (one atomic spacing) is unrealistic.

Reversibility of Dislocations

So far the theory is based upon the assumption that the piled-up dislocations are irreversible. No dislocations accumulated during loading escape or annihilated when unloaded, and no dislocations accumulated during unloading are changed when loaded again. Here this assumption is abandoned.

The equilibrium condition for dislocations on layer I at the first loading is

$$\tau_1^D + \tau_1 - \tau_f = 0 \tag{29}$$

which is the same as (1). When unloaded, the dislocations on layer I are assumed to be reduced by the reversible processes and the corresponding dislocation stress τ_1^D is reduced to $f\tau_1^D$, $0 < f \leq 1$. The equilibrium equation on layer II becomes

$$\tau_2^D + f\tau_1^D + \tau_2 + \tau_f = 0. \tag{30}$$

When loaded again, the stress of the dislocations on layer I is increased by $\Delta\tau_1^D$ and the stress of the dislocations located on layer II is reduced to $f\tau_2^D$. The equilibrium equation on layer I becomes

$$\Delta\tau_1^D + f\tau_1^D + f\tau_2^D + \tau_1 - \tau_f = 0. \tag{31}$$

When unloaded, the increased dislocation stress $\Delta\tau_1^D$ is reduced to $f\Delta\tau_1^D$. The equilibrium equation on layer II becomes

$$\Delta\tau_2^D + f\tau_1^D + f\tau_2^D + f\Delta\tau_1^D + \tau_2 + \tau_f = 0. \tag{32}$$

The same argument holds at points 5 and 6 in Fig. 1 and gives

$$\begin{aligned} &\Delta\tau_1^{2D} + f\tau_1^D + f\tau_2^D + f\Delta\tau_1^D + f\Delta\tau_2^D + \tau_1 - \tau_f = 0, \\ &\Delta\tau_2^{2D} + f\tau_1^D + f\tau_2^D + f\Delta\tau_1^D + f\Delta\tau_2^D + f\Delta\tau_1^{2D} + \tau_2 + \tau_f = 0 \end{aligned} \tag{33}$$

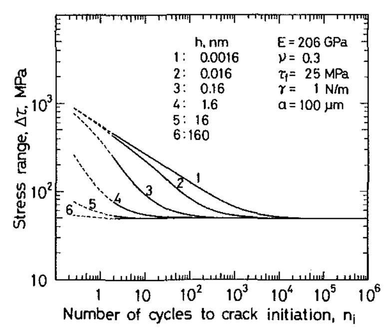

Fig. 9 Effect of the dislocation-dipole height *h* on the S-N curve for crack initiation given by equation (28)

where $\Delta\tau_1^{2D}$ is the stress increment by the increased dislocations on layer I during the third loading, and $\Delta\tau_2^{2D}$ is the stress increment by the increased dislocations on layer II during the third unloading.

Similarly at points $(2n-1)$ and $2n$ in Fig. 1, at the notch loading and unloading, we have

$$\begin{aligned} &\Delta\tau_1{}^{(n-1)D} + f\sum_{j=0}^{n-2}(\Delta\tau_1^{jD} + \Delta\tau_2^{jD}) + \tau_1 - \tau_f = 0, \\ &\Delta\tau_2{}^{(n-1)D} + f\sum_{j=0}^{n-2}(\Delta\tau_1^{jD} + \Delta\tau_2^{jD}) + f\Delta\tau_1^{(n-1)D} + \tau_2 + \tau_f = 0 \end{aligned} \tag{34}$$

where,

$$\Delta\tau_i^{OD} = \tau_i^D \text{ and } \Delta\tau_i^{1D} = \Delta\tau_i^D \ (i = 1,2).$$

These recurrent series give

$$\begin{aligned} &\Delta\tau_1{}^{(n-1)D} = -\frac{1-(1-f)^{2(n-1)}}{2f}(\Delta\tau - 2\tau_f) - (1-f)^{2(n-1)}(\tau_1 - \tau_f) \\ &\Delta\tau_2{}^{(n-1)D} = \frac{1+(1-f)^{2n-1}}{2-f}(\Delta\tau - 2\tau_f) - (1-f)^{2n-1}(\tau_1 - \tau_f) \end{aligned} \tag{35}$$

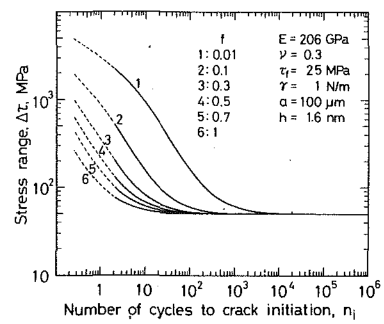

Fig. 10 Effect of the irreversibility factor *f* on the S-N curve for crack initiation given by equation (39)

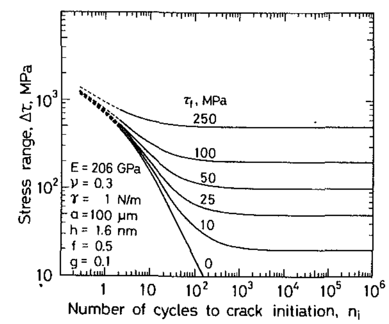

Fig. 12 Effect of the frictional stress τ_f on the S-N crack for crack initiation given by equation (42)

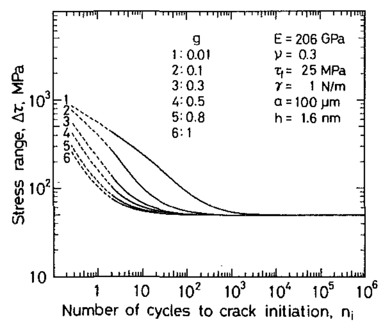

Fig. 11 Effect of the energy-dissipation factor *g* on the S-N curve for crack initiation given by equation (41)

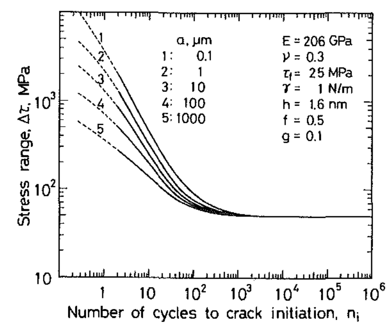

Fig. 13 Effect of the half-length of the PSB *a* on the S-N curve for crack initiation given by equation (42)

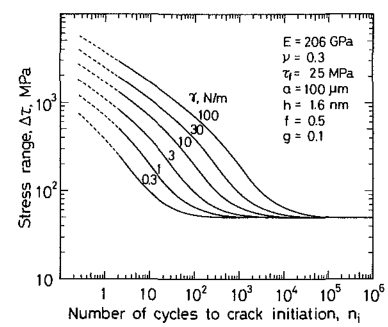

Fig. 14 Effect of the surface energy γ on the S-N curve for crack initiation given by equation (42)

where $f\Delta\tau_1^{(n-1)D}$ and $f\Delta\tau_2^{(n-1)D}$ correspond to $(\tau_{2n+1}^D - \tau_{2n-1}^D)$ in (8) and $(\tau_{2n}^D - \tau_{2n-2}^D)$ in (9). When $f=1$, equations (8) and (9) are recovered. From (35), we have

$$\tau_{2n+1}^D = f\sum_{j=1}^{n+1} \Delta\tau_1^{(j-1)D} = -f\left[(n+1) - \frac{1-(1-f)^{2(n+1)}}{f(2-f)}\right]$$

$$\frac{\Delta\tau - 2\tau_f}{2-f} - \frac{1-(1-f)^{2(n+1)}}{f(2-f)}(\tau_1 - \tau_f)$$

$$\tau_{2n}^D = f\sum_{j=1}^{n} \Delta\tau_2^{(j-1)D} = f\left\{n + \frac{(1-f)[1-(1-f)^{2n}]}{f(2-f)}\right\}\frac{\Delta\tau - 2\tau_f}{2-f}$$

$$-\frac{1(1-f)[1-(1-f)^{2n}]}{f(2-f)}(\tau_1 - \tau_f). \tag{36}$$

For large n, (36) is approximately

$$\tau_{2n+1}^D \approx -\tau_{2n}^D \approx -n(\Delta\tau - 2\tau_f)f/(2-f) \tag{37}$$

and, therefore,

$$D_{2n+1} \approx -D_{2n} \approx n(\Delta\tau - 2\tau_f)xf/\pi A(2-f)(a^2 - x^2)^{1/2}. \tag{38}$$

It is concluded that when fraction (1-f) of newly created dislocations of each cycle of loading or unloading are reversible, the necessary correction for the final formula is to change n to $nf/(2-f)$. When n_i in (28) is replaced by $n_i\, f(2-f)$,

$$(\Delta\tau)^3 - 2\tau_f(\Delta\tau)^2 + \frac{4\mu^2\epsilon\{\log(8/\epsilon) - (3/2)\}}{\pi(1-\nu)^2}\Delta\tau$$

$$-\frac{4\mu^2}{\pi(1-\nu)^2}\left[2\tau_f\epsilon\{\log(8/\epsilon) - (3/2)\} + \frac{(2-f)\gamma}{fan_i}\right] = 0. \tag{39}$$

Equation (39) provides the S-N curves for crack initiation as shown in Fig. 10 where the irreversibility factor f is varied from f = 0.01 to f = 1. The values of the other parameters are chosen so as to be proper ones as shown in the figure. The smaller the factor f, the higher the fatigue strength and the longer the crack initiation life. The dependence of the S-N curve on the other parameters, i.e., τ_f, a, γ, E, and h is similar to that given by (28). It is noted that, in (39), the effect of the surface energy γ is amplified by a factor of $(2-f)/f$ so that a value of the factor f lower than unity gives higher fatigue strength and shifts the knee of an S-N curve to longer n_i range in comparison with the corresponding S-N curve given by (28) $(f=1)$.

Another modification of the theory can be considered for the dislocation energy source W_1. So far 100 percent of W_1 is assumed to be used for the crack initiation. If it is assumed that some fraction g of W_1 is used for the crack initiation, equation (28) is modified to

$$\Delta G = -gW_1 - W_2 + 2c\gamma. \tag{40}$$

Then we have, instead of (39),

$$(\Delta\tau)^3 - 2\tau_f(\Delta\tau)^2 + \frac{4g\mu^2\epsilon\{\log(8/\epsilon) - (3/2)\}\Delta\tau}{\pi(1-\nu)^2}$$

$$-\frac{4\mu^2}{\pi(1-\nu)^2}\left[2g\tau_f\epsilon\log(8/\epsilon) - (3/2)\} + \gamma/an_i\right] = 0. \tag{41}$$

For $g<1$, (41) gives higher fatigue strength and shifts the knee of an S-N curve to longer n_i range in comparison with the

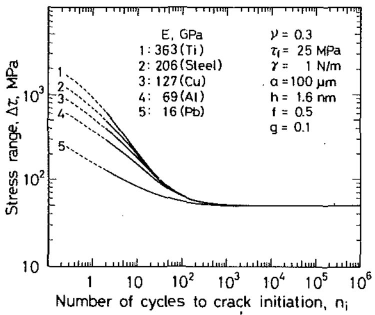

Fig. 15 Effect of Young's modulus *E* on the S-N curve for crack initiation given by equation (42)

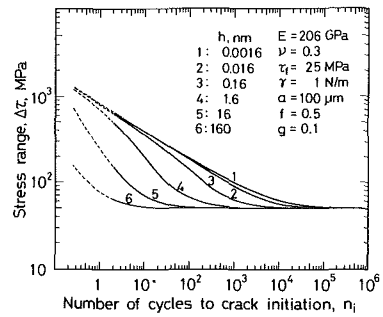

Fig. 16 Effect of the dislocation-dipole height *h* on the S-N curve for crack initiation given by equation (42)

corresponding S-N curve given by (28) ($g = 1$) as shown in Fig. 11. The smaller the factor g, the higher the fatigue strength and the longer the crack initiation life. The residual energy $(1-g)\ W_1$ may be dissipated in the form of heat as often observed during fatigue tests.

Combining (39) and (41), we have

$$(\Delta\tau)^3 - 2\tau_f(\Delta\tau)^2 + \frac{4g\mu^2\epsilon\log(8/\epsilon)}{\pi(1-\nu)^2}\Delta\tau - \frac{4\mu^2}{\pi(1-\nu)^2}$$

$$\left[2g\tau_f\epsilon\log(8/\epsilon) + \frac{2-f)\gamma}{fan_i}\right] = 0. \qquad (42)$$

The dependence of the S-N curve given by (42) on τ_f, a, γ, E, and h is shown in Figs. 12-16, respectively. These figures show that (42), i.e., the introduction of factors f and g can give longer crack initiation life and thus it can bring about more realistic S-N curves than (28). For typical values of the parameters, i.e., E = 206GPa, $\nu = 0.3$, $\tau_f = 25$MPa, $a = 100\mu$m, $\gamma = 1$N/m, $h = 1.6$nm, $f = 0.5$, and $g = 0.1$, the initial crack length c is varied from 0.17 to 0.82 μm as the applied stress range $\Delta\tau$ decreases.

Acknowledgment

This research was supported by the National Science Foundation Grant No. DMR86-17956. We thank Prof. Y. W. Chung and M. E. Fine for stimulating discussions and literature information.

References

Antonopoulos, J. G., Brown, L. M., and Winter, A. T., 1976, "Vacancy Dipoles in Fatigued Copper," *Phil. Mag.*, Vol. 34, pp. 549-563.

Broek, D., 1982, *Elementary Engineering Fracture Mechanics*, Martinus Nijhoff Publishers, p. 289.

Essmann, U., and Mughrabi, H., 1979, "Annihilation of Dislocations during Tensile and Cyclic Deformation and Limits of Dislocation Densities," *Phil. Mag.*, Vol. 40, pp. 731-756.

Forsyth, P. J. E., 1953, "Exudation of Material from Slip Bands at the Surface of Fatigued Crystals of an Aluminum-Copper Alloy," *Nature*, Vol. 171, pp. 172-173.

Griffith, A. A., 1921, "The Phenomena of Rupture and Flow in Solids," *Trans. Roy. Soc.*, Vol. A22a, pp. 163-179.

Hempel, M., 1965, "Einige Probleme der Dauerfestigkeitsprüfung Metallischer Werkstoffe," *Materialprüfung*, Vol. 7, pp. 401-412.

Hirose, Y., and Mura, T., 1985, "Crack Nucleation and Propagation of Corrosion Fatigue in High-strength Steel," *Engn. Frac. Mech.*, Vol. 22, pp. 859-870.

Kato, M., Onaka, S., Mori, T., and Mura, T., 1984, "Statistical Consideration of Plastic Strain Accumulation in Cyclic Deformation and Fatigue Crack Initiation," *Scripta Metallurgica*, Vol. 18, pp. 1323-1326.

Lin, M. R., Fine, M. E., and Mura, T., 1986, "Fatigue Crack Initiation on Slip Bands," *Acta Metall.*, Vol. 34, pp. 619-628.

Mughrabi, H., and Wang, R., 1982, "Cyclic Strain Localization and Fatigue Crack Initiation in Persistent Slip Bands in Face-Centered Cubic Metals and Single-Phase Alloys," *Defects and Fracture*, G. C. Shih and H. Zorski, eds., Martinus Nijhoff Publishers, pp. 15-28.

Mura, T., and Tanaka, K., 1981, "Dislocation Dipole Models for Fatigue Crack Initiation," *Mechanics of Fatigue*, T. Mura, ed., ASME, New York, AMD Vol. 47, pp. 111-131.

Taira, S., Tanaka, K., and Hoshina, M., 1979, "Grain Size Effect" on Crack Nucleation and Growth in Long-Life Fatigue of Low-Carbon Steel," ASTM Special Technical Publications, No. 675, pp. 135-173.

Tanaka, K., and Mura, T., 1981, "A Dislocation Model for Fatigue Crack Initiation," ASME JOURNAL OF APPLIED MECHANICS, Vol. 48, pp. 97-103.

Joseph L. Rose
Professor,
Mechanical Engineering and Mechanics Department,
Drexel University,
Philadelphia, PA 19104

Adnan Nayfeh
Professor,
Aerospace Engineering Department,
University of Cincinnati,
Cincinnati, OH 45221

Aleksander Pilarski[1]
Visiting Associate Professor,
Mechanical Engineering and Mechanics Department,
Drexel University,
Philadelphia, PA 19104

Surface Waves for Material Characterization

Analyses are presented for the propagation of harmonic surface waves on a transversely isotropic layer rigidly bonded to a transversely isotropic substrate of different material. The layer-substrate system is also assumed to be in contact with a liquid and inviscid space. The propagation takes place along an axis of symmetry of both the layer and the substrate. Exact closed-form solutions for the characteristic dispersion relations are presented. Numerical results are presented for material combinations of three classes of centrifugally cast stainless steel material. Results clearly demonstrate the influence of the layer thickness on the propagation speed and, hence, provide a means of material characterization.

Introduction

The need to carry out material characterization analysis, particularly with respect to specific anisotropic character, is well documented. It has recently been recognized that ultrasonic techniques offer potential for material inspection (Jeong, 1987; Kupperman et al., 1987; Ogilvy, 1986; Rose et al., 1988; Silk, 1981; Curtis and Ibrahim, 1981; Sayers, 1982; Delsanto and Clark, 1987; Mase, 1987; Hirao et al., 1987). A detailed description of the problem of grain structure and the various anisotropic character formations of advanced materials is reported by Jeong (1987). Furthermore, many of the existing experimental observations which are associated with unusual inspection can not be fruitful if one does not know where the ultrasonic beam is going or how it is modified by anisotropic influences. As a result, surface wave procedures are introduced either to characterize structural materials directly or as an adjunct to longitudinal or shear waves transversing the bulk material.

Under laboratory conditions, the velocity of longitudinal waves and the ratio of longitudinal to shear wave velocities appear as parameters for the prediction of the microstructure of advanced materials (Kupperman et al., 1987; Ogilvy, 1986; Rose et al., 1988; Silk, 1981; Curtis and Ibrahim, 1981; Sayers, 1981). For example, in centrifugally-cast stainless steel (hereinafter referred to as CCSS) Kupperman et al. found that beam skewing in certain columnar structures is strong enough so that measurements of probe separation at maximum received signal intensities for 45 deg shear waves, pitch-catch transducers, can be correlated with microstructure. Other work associated with anisotropic behavior of welded materials is presented by Ogilvy where a theoretical ray tracing model is presented.

Utilization of quasi-longitudinal waves incident at different angles for material characterization was proposed by Rose et al. The experimental technique described by Rose et al. involves sending the ultrasonic pulse at a specific angle and searching for the maximum amplitude with another probe. The optimal distance between the transmitter when normalized by the plate thickness gives the skip distance factor. Assuming uniform equivalent anisotropic properties, this skip distance factor can be used to characterize the properties of the material with an assumption of a uniform equivalent anistropic model (see Rose et al., 1988). All of the approaches described by Jeong (1987), Kupperman et al. (1987), Ogilvy (1986), and Rose et al. (1988) call for the wave to pass through the solid twice and, hence, depend strongly on the knowledge of the actual local thickness of the inspected component such as a plate or a pipe. Looking for an alternative solution to this problem, utilization of guided waves was proposed by Rose et al. The critical angle or frequency measurements related to the plate wave modes and/or surface wave velocity measurements do not possess these disadvantages of the longitudinal and transverse waves. Such techniques are therefore proposed as complimentary to bulk wave measurements for anisotropy material characterization and the existence of inhomogeneity with depth.

A review of existing literature reveals several aspects of the propagation of surface waves in anisotropic half spaces in the absence of the fluid and layer (see, for example, Delsanto and Clark, 1987; Mase, 1987; Hirao et al., 1987; Kaibichev, 1987; Royer and Dieulesant, 1984). The reflections of ultrasonic

[1]Permanently with the Polish Academy of Sciences, Warsaw, Poland.

Contributed by the Applied Mechanics Division of THE AMERICAN SOCIETY OF MECHANICAL ENGINEERS for presentation at the Winter Annual Meeting, San Francisco, Calif., December 10-15, 1989.

Discussion on this paper should be addressed to the Editorial Department, ASME, United Engineering Center, 345 East 47th Street, New York, N.Y. 10017, and will be accepted until two months after final publication of the paper itself in the JOURNAL OF APPLIED MECHANICS. Manuscript received by the ASME Applied Mechanics Division, March 14, 1988; final revision, February 15, 1989.

Paper No. 89-WA/APM-40.

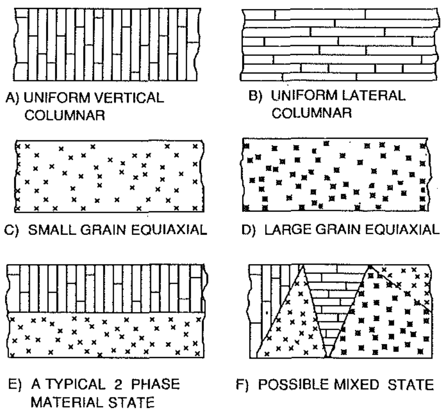

Fig. 1 Possible material state configurations

waves at liquid-cubic solid interfaces are reported by Atalar (1983). The propagation of ultrasonic waves from isotropic solid-fluid interfaces separated by isotropic layers are given by Nayfeh et al. (1981) and Chimenti and Nayfeh (1982).

In the present paper we study the propagation of surface waves on a medium consisting of a transversely-isotropic half space in rigid contact with a transversely-isotropic half space substrate of a different material. The total system is in contact with a fluid space. We then consider the wave that propagates along the fluid-layer interface. The analytical results will be presented in closed form. Results for solids possessing cubic and isotropic material symmetries will be found as special cases of the general solutions by involving the appropriate restrictions on the properties. Furthermore, results for a half space can be deduced by either setting the thickness of the layer equal to zero or by setting the properties of the layer equal to their corresponding properties of the substrate. In all cases, results for the dry medium (i.e., in the absence of the fluid) can be obtained by setting the density of the fluid to zero. Finally, in the numerical illustrations, we shall be concentrating on equiaxial-grain-type structures and columnar dendritic formations that occur in centrifugally-cast stainless steel as representative of transversely isotropic media.

Material State Possibilities

Let us consider some possible configurations of CCSS material grain and anisotropic states as representative examples of the classes of materials under consideration. These are depicted in Fig. 1 and range from a uniform vertical columnar structure representing transverse isotropy to a uniform lateral columnar grain state. We can also have small or large-grain equiaxial configurations. Another situation that has been observed is associated with a two-phase material state as shown in Fig. 1 (*e*) having a columnar material located over an equiaxial configuration, with the transition being approximately halfway through the thickness of the material layer. These unusual grain formations come about as a result of the manufacturing procedure. The last diagram shows a possible, mixed state that could actually occur but will not be pursued any further in this study, however. Our goal in this work is to demonstrate the characterization of the material state in order to optimize inspection procedure.

Theory

In this section we derive an analytical expression for the characteristic equation of surface wave propagation along an isotropic plate in contact with a transversely-isotropic space of similar or different material on one face and fluid on the other. The plane of isotropy for both the plate and the substrate are chosen to coincide with the plane of the interface.

Consider a transversely-isotropic plate having the thickness d rigidly attached to a transversely-isotropic solid half space of similar or different material and separating the latter from a fluid half space. The problem is to study the characteristics of the surface wave propagating along the plate-fluid interface. In order to facilitate the present analysis, we shall use a two-dimensional coordinate system (x_i, $i=1,2$), which has its origin at the substrate-plate interface such that x_1 denotes the propagation direction and x_2 is normal to the interface. The layer will thus occupy the space $0 \le x_2 \le d$.

With this choice of coordinate system it is consistent that all motions will be independent of the x_3-direction and the relevant elastodynamic equations for each solid (including the layer and the substrate) consist of the momentum equations:

$$\sigma_{ij,j}=\rho \ddot{u}_i, \quad i,j=1,2 \tag{1}$$

and the constitutive relations

$$\sigma_{ij}=c_{ijkl}e_{kl}, \quad i,j,k,l=1,2 \tag{2}$$

specialized to transversely-isotropic materials. Here, σ_{ij} are the components of the stress tensor, u_i are the components of the displacements, and ρ and c_{ijkl} are the density and elastic constants of each material. Due to the absence of viscosity in the fluid, its relevant field equations corresponding to equations (1) and (2) can be obtained by appropriate specialization.

Equations (1) and (2) must be supplemented with the appropriate interfacial continuity conditions. For rigid bonding between the plate and substrate these are:

$$\sigma_{i2}=\sigma_{i2}^{(s)}, \ u_i=u_i^{(s)}, \ i=1,2 \tag{3}$$

at $x_2=0$. Here the superscript (s) designates the substrate, whereas the layer is identified by omission of an adscript. Finally, at the fluid-plate interface, the appropriate matching conditions are

$$\sigma_{12}=0, \ \sigma_{22}=\sigma_{22}^{(f)}, \ u_2=u_2^{(f)} \ \text{at } x_2=d. \tag{4}$$

If equations (1) and (2) are combined into two coupled equations in u_1 and u_2, a solution in the form

$$(u_1, u_2)=(U_1, U_2)e^{iq(x_1+\alpha x_2-ct)} \tag{5}$$

is assumed where U_1 and U_2 are constant amplitudes, q is the wave number, c is the phase velocity, and α is the ratio of the x_2 and x_1-directions wave numbers; one obtains a characteristic equation relating α to q. This equation admits four solutions and, by using superposition, one obtains the formal solutions

$$\begin{bmatrix} u_1 \\ u_2 \\ \bar{\sigma}_{22} \\ \bar{\sigma}_{12} \end{bmatrix} = \begin{bmatrix} 1 & 1 & 1 & 1 \\ U_{21} & U_{22} & U_{23} & U_{24} \\ D_{11} & D_{12} & D_{13} & D_{14} \\ D_{21} & D_{22} & D_{23} & D_{24} \end{bmatrix} \begin{bmatrix} U_{11}e^{iq\alpha_1 x_2} \\ U_{12}e^{iq\alpha_2 x_2} \\ U_{13}e^{iq\alpha_3 x_2} \\ U_{14}e^{iq\alpha_4 x_2} \end{bmatrix} \tag{6}$$

which holds for the layer, substrate, and even the fluid under appropriate restrictions. Here

$$\alpha_1 = \frac{-B+\sqrt{(B^2-4AC)}}{2A}, \ \alpha_2=-\alpha_1 \tag{7a}$$

$$\alpha_3 = \frac{-B-\sqrt{(B^2-4AC)}}{2A}, \ \alpha_4=-\alpha_3 \tag{7b}$$

$$B = (C_{11}-\rho c^2)C_{22}-(C_{66}-\rho c^2)C_{66}-(C_{12}+C_{66})^2 \tag{7c}$$

$$C = (C_{11}-\rho c^2)(C_{66}-\rho c^2), \ A=C_{22}C_{66} \tag{7d}$$

and, for each α_p, $p=1, 2, 3, 4$,

$$U_{2p} = \frac{\rho c^2 - C_{11} - C_{66}\alpha_p^2}{(C_{12}+C_{66})\alpha_p}, \ \bar{\sigma}_{mn}=\sigma_{mn}/iq; \ m,n=1,2$$

$$D_{1p} = (C_{12}+C_{22}\alpha_p W_p),\ D_{2p}=C_{66}(\alpha_p+W_p). \tag{8}$$

Equation (6), for the layer, can be used to relate the displacements and stresses at $x_2=0$ to those at $x_2=d$. This can be done by specializing (6) to $x_2=0$ and to $x_2=d$, and eliminating the common amplitude column made up of U_{11}, U_{12}, U_{13}, and U_{14} resulting in

$$\begin{bmatrix} u_1 \\ u_2 \\ \bar{\sigma}_{22} \\ \bar{\sigma}_{12} \end{bmatrix}_{x_2=d} = \begin{bmatrix} a_{11} & a_{12} & a_{13} & a_{14} \\ a_{21} & a_{22} & a_{23} & a_{24} \\ a_{31} & a_{32} & a_{33} & a_{34} \\ a_{41} & a_{42} & a_{43} & a_{44} \end{bmatrix} \begin{bmatrix} u_1 \\ u_2 \\ \bar{\sigma}_{22} \\ \bar{\sigma}_{12} \end{bmatrix}_{x_2=0} \tag{9}$$

where

$$[a_{ij}] = \begin{bmatrix} B_1 & B_2 & B_3 & B_4 \\ U_{21}B_1 & U_{22}B_2 & U_{23}B_3 & U_{24}B_4 \\ D_{11}B_1 & D_{12}B_2 & D_{13}B_3 & D_{14}B_4 \\ D_{21}B_1 & D_{22}B_2 & D_{23}B_3 & D_{24}B_4 \end{bmatrix} \begin{bmatrix} 1 & 1 & 1 & 1 \\ U_{21} & U_{22} & U_{23} & U_{24} \\ D_{11} & D_{12} & D_{13} & D_{14} \\ D_{21} & D_{22} & D_{23} & D_{24} \end{bmatrix}^{-1} \tag{10a}$$

$$B_p = e^{iq\alpha_p d},\ (p=1,2,3,4). \tag{10b}$$

Now, in order to satisfy the continuity conditions (3) and (4) at the substrate-plate and the plate-fluid interfaces, respectively, we need to solve the field equation in the substrate and in the fluid. By inspection, such solutions can be deduced and specialized from the formal solution (6). First, due to the absence of shear deformation, specializing (6) to the fluid half space and insuring boundedness for large values of x_2 yields

$$\begin{bmatrix} U_1^{(f)} \\ U_2^{(f)} \\ \bar{\sigma}_{22}^{(f)} \end{bmatrix} = \begin{bmatrix} 1 & 1 \\ \alpha_f & -\alpha_f \\ \rho_f c^2 & \rho_f c^2 \end{bmatrix} \begin{bmatrix} 0 \\ U^{(f)} e^{-iq\alpha_f x_2 - d} \end{bmatrix} \tag{11a}$$

where

$$\alpha_f^2 = (c^2/c_f^2)-1, \tag{11b}$$

next, specializing (6) to the substrate yields

$$\begin{bmatrix} u_1^{(s)} \\ u_2^{(s)} \\ \bar{\sigma}_{22}^{(s)} \\ \bar{\sigma}_{12}^{(s)} \end{bmatrix} = \begin{bmatrix} 1 & 1 & 1 & 1 \\ U_{21} & U_{22} & U_{23} & U_{24} \\ D_{11} & D_{12} & D_{13} & D_{14} \\ D_{21} & D_{22} & D_{23} & D_{24} \end{bmatrix}_s \begin{bmatrix} U_{11}^{(s)} e^{iq\alpha_1^{(s)} x_2} \\ 0 \\ U_{13}^{(s)} e^{iq\alpha_3^{(s)} x_2} \\ 0 \end{bmatrix}. \tag{12}$$

Notice that in equation (12) the reflected wave amplitudes $U_{12}^{(s)}$ and $U_{14}^{(s)}$ vanish, since solutions must be bounded for large values of x_2 in the substrate half space.

By specializing (11a) and (12) to the fluid-plate interface ($x_2=d$) and plate-substrate interface ($x_2=0$), respectively, and followed by invoking the continuity conditions (3) and (4), their results

$$\begin{bmatrix} \alpha_f & -\alpha_f \\ \rho_f c^2 & \rho_f c^2 \\ 0 & 0 \end{bmatrix} \begin{bmatrix} 0 \\ U^{(f)} \end{bmatrix} = \begin{bmatrix} R_{21} & R_{23} \\ R_{31} & R_{33} \\ R_{41} & R_{43} \end{bmatrix} \begin{bmatrix} U_{11}^{(s)} \\ U_{13}^{(s)} \end{bmatrix} \tag{13}$$

where

$$[R_{ij}] = [a_{ij}][b_{ij}]_s \tag{14}$$

with $[b_{ij}]_s$ as the 4×4 matrix in equation (12). For nontrivial solutions, the matrix equation (13) represents three equations in three unknowns. It can be solved to yield the surface wave characteristic equation

$$G_{31}+QG_{21}=0 \tag{15}$$

where

$$G_{21}=R_{21}R_{43}-R_{23}R_{41},\ G_{31}=R_{31}R_{43}-R_{33}R_{41},\ Q=\frac{\rho_f c^2}{\alpha_f}. \tag{16}$$

In the absence of the fluid, i.e., for $\rho_{fv}=0$, equation (15) reduces to

$$G_{31}=0, \tag{17}$$

which defines the characteristic equation for the Rayleigh surface wave on the dry plate bonded to a semi-infinite solid substrate.

For a given real frequency ω, the real wave number solutions $q=q_r$ of equation (17) define propagating Rayleigh surface modes. It is important to indicate that in the absence of the plate, only a single real solution will exist. This will be the classical surface wave mode which propagates on a half space. In the presence of the liquid these real wave numbers will be perturbed rather mildy and become complex. This statement is confirmed by equation (15), which in general admits the complex solutions

$$q=q_r+i\eta. \tag{18}$$

From equation (18) the phase velocity is given as $c_p=\omega/q_r$ and η is the energy leakage coefficient. Notice that η vanishes in the absence of the fluid and, hence, no attenuation (leaking of energy in the fluid) occurs. Therefore, in the presence of the fluid, these surface wave are called leaky waves. It is also known that c_p is hardly affected by the presence of the fluid (see Nayfeh et al., 1981).

Results of Numerical Simulation

For a numerical simulation of the situations that might occur in realistic structures such as centrifugally-cast stainless steel (CCSS), we have chosen three types of material properties. The first case, corresponding to the equiaxial CCSS, was assumed to be an isotropic one. The second and third cases were chosen as transversely isotropic, corresponding to the columnar CCSS with different degree of anisotropy. These latter materials are described by five independent elastic constants. Which are given in Table 1 along with the properties for the isotropic case.

Our calculations were carried out using combinations of the three kinds of CCSS. As was implied by the theoretical model for materials described by Cases II and III, the appropriate interfaces between the water and the layer or the layer and the

Table 1 Elastic Constants (in GPa) (for three different cases of CCSS)

	Case I (equiaxial)	Case II (columnar I)	Case III (columnar II)
C_{11}	269	282	282
C_{22}	269	242	262
C_{33}	269	282	282
C_{12}	103	140	76
C_{13}	103	100	56
C_{23}	103	140	76
C_{44}	83	135	135
C_{55}	83	91	113
C_{66}	83	135	135

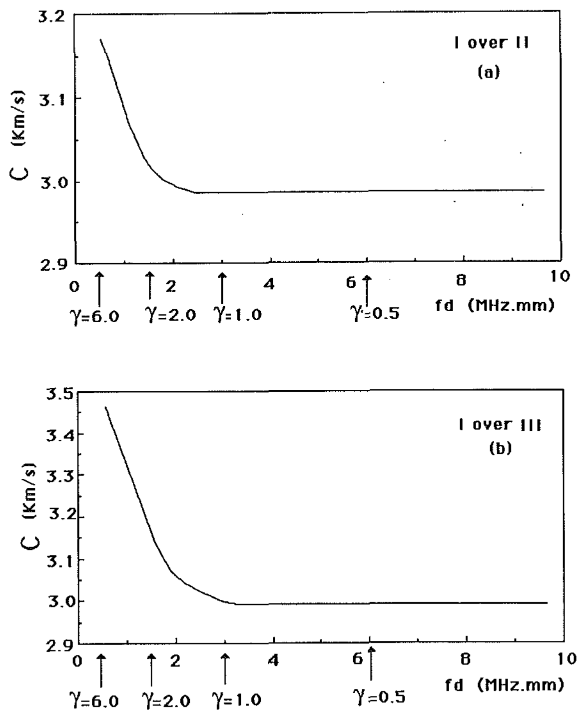

Fig. 2 Dispersion curve for the first mode of surface waves propagating in a layered structure consisting of the upper layer from material I and the substrate: (*a*) from material II; (*b*) from material III. Four ratios or wavelengths to thickness of layer are marked additionally.

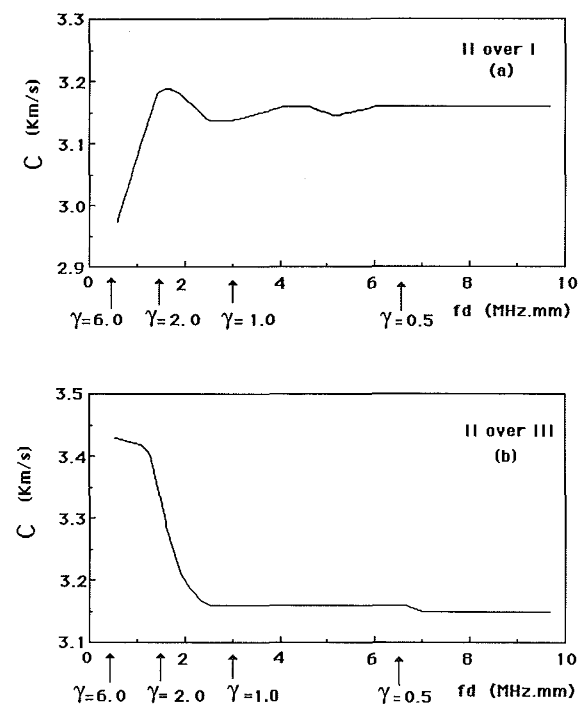

Fig. 3 Dispersion curve for the first mode of surface waves propagating in a layered structure consisting of the upper layer from material II and the substrate: (*a*) from material I; (*b*) from material III. Four ratios of wavelength to thickness of layer are marked additionally.

substrate are assumed to be in the plane of isotropy. Both vectors of anisotropy for each case of columnar CCSS were oriented normally to the wave propagation direction. In Figs. 2, 3, and 4, the dispersion curves of the first modes for the six possible material combinations are given.

These figures illustrate the relationships between the surface wave velocity and the product of frequency and layer

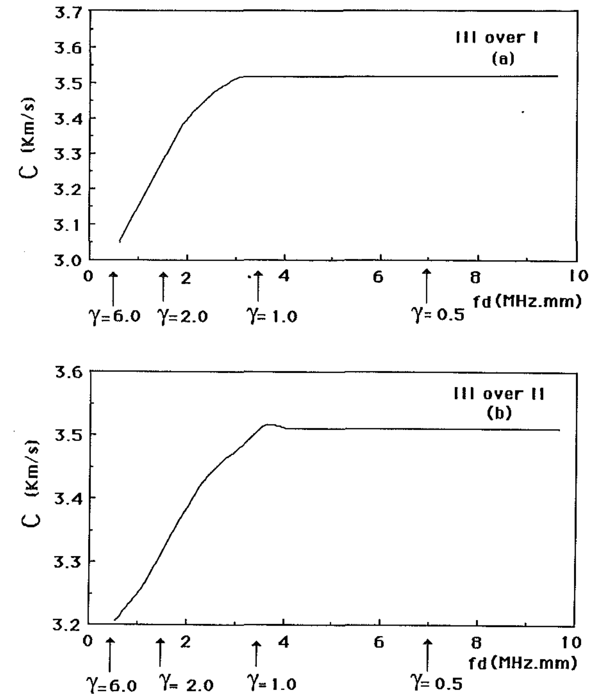

Fig. 4 Dispersion curve for the first mode of surface waves propagating in a layered structure consisting of the upper layer from material III and the substrate: (*a*) from material I; (*b*) from material II. Four ratios of wavelengths to thickness of layer are marked additionally.

Table 2 Surface Wave Velocities (m/s) upper equiaxial layer

Wavelength to thickness of layer ratio $\gamma = (\lambda/d)$

Case I over I	2976	2976	2976	2976
Case I over II	2976	2978	3012	3157
Case I over III	2977	2989	3129	3450

Table 3 Surface Wave Velocities (m/s) upper columnar layer

Wavelength to thickness of layer ratio $\gamma = (\lambda/d)$

	0.5	1.0	2.0	6.0
Case II over II	3145	3145	3145	3145
Case II over I	3145	3133	3176	2971
Case II over III	3145	3153	3288	3415

thickness. There are additionally marked the four values of the ratios of the surface wave wavelengths to layer thickness. It gives us some idea on how large the wavelength of the propagating surface wave should be with respect to the thickness of the layer in order to observe the differences in velocity related to the inhomogeneity generated by the layer thickness. The results of the surface wave velocity calculation for these four ratios are contained in Tables 2 and 3. Note that for small values of these ratios, the surface wave velocity is equal to the velocity appropriate for the material of the upper layer. For ratios larger than six, velocities are almost the same as for the substrate. When the materials of both layer and substrate are identical, the nondispersive case results where the surface wave velocity is frequency independent. This was confirmed both analytically and numerically. These conclusions also serve here as a check on our computations. In Tables 2 and 3 numerical values are listed Case I over II (as the layer), I over III, II over I, and II over III. When the wavelength λ is increased, that is becoming greater than twice the thickness of the plate d, the wave velocity changes significantly (here a 5-10 percent change for such situations are significant). These results indicate how the wave velocity and its dependence on wavelength can be used to distinguish inhomogeneous character with depth.

References

Atalar, A., 1983, "Reflections of Ultrasonic Waves at Liquid-Cubic-Solid Interface," *J. Acoust. Soc. Am.*, Vol. 73, pp. 435–440.

Chimenti, D. E., Nayfeh, A. H., and Butler, D. L., 1982, "Leaky Waves on a Layered-Half-Space," *J. Appl. Phys.*, Vol. 53, pp. 170–176.

Curtis, G. T., and Ibrahim, N., 1981, "Texture Studies of Austenitic Weld Metal Using Elastic Surface Wave," *Metal. Sci.*, Vol. 15, pp. 566–573.

Delsanto, P. P., and Clark, A. V., Jr., 1987, "Rayleigh Wave Propagation in Deformed Orthotropic Materials," *J. Acoustic. Soc. Am.*, Vol. 81, No. 4, pp. 952–960.

Hirao, M., et al., 1987, "Anisotropy Measured with Shear and Rayleigh Waves in Rolled Plates," *Ultrasonics*, Vol. 25, pp. 107–111.

Jeong, P., 1987, "Ultrasonic Characterization of Centrifugally Cast Stainless Steel," EPRI NP-5246.

Kaibichev, I. A., 1987, "Dispersion Relation for Rayleigh Waves in a Medium with Subsurface Inhomogeneities," *Sov. Phys. Acost.*, Vol. 32, No. 5, pp. 430–432.

Kupperman, D. S., Reimann, K. J., and Abrego-Lopez, J., 1987, "Ultrasonic NDE of Cast Stainless Steel," *NDT International*, Vol. 20, No. 3.

Mase, C. T., 1987, "Rayleigh Wave Speeds in Transversely Isotropic Materials," *J. Acoust. Soc. Am.*, Vol. 81, No. 5, pp. 1441–1446.

Nayfeh, A. H., Chimenti, D. E., Adler, L., and Crane, R. L. 1981, "The Influence of Thin Bonding Layers on the Waves at Liquid-Solid Interfaces," *J. Appl. Phys.*, Vol. 52, p. 4985.

Ogilvy, J. A., 1986, "Ultrasonic Beam Profiles and Beam Propagation in an Austenitic Weld Using a Theoretical Ray Tracing Model," *Ultrasonics*, Vol. 24.

Rose, J. L., et al., 1988, "Wave Scattering and Guided Wave Considerations in Anisotropic Media," *Review of Progress in Quantitative NDE*, D. O. Thompson and D. E. Chimenti, eds., Vol. 7.

Rose, J. L., Tverdokhlebov, A., and Balasubramaniam, K., "A Numerical Integration Ultrasonic Wave Scattering Model," JNDE, in press.

Royer, D. and Dieulesant, E., 1984, "Rayleigh Wave Velocity and Displacement in Orthotropic, Tetrogonal, Hexagonal and Cubic Crystals," *J. Acoust. Soc. Am.*, Vol. 76, No. 5, pp. 1438–1444.

Sayers, C. M., 1982, "Ultrasonic Velocities in Anisotropic Polycrystalline Aggregates," *J. Phys. D. Appl. Phys.*, Vol. 15, pp. 2157–2167.

Silk, M. G., 1981, "Relationships Between Metallurgical Texture and Ultrasonic Propagation," *Metal. Sci.*, Vol. 15, pp. 559–565.

Residual Stress Determination Using Acoustoelasticity

J. J. Dike[1]
Assoc. Mem., ASME

G. C. Johnson
Assoc. Mem., ASME

Department of Mechanical Engineering,
University of California,
Berkeley, CA 94720

A technique for the complete nondestructive evaluation of plane states of residual stress is presented. This technique is based on the acoustoelastic effect in which the presence of the residual stress causes a shift in the speed at which a wave propagates through the material. The particular acoustoelastic technique considered here employs longitudinal waves propagating normal to the plane of the stress. Such waves experience a shift in propagation speed which, for an isotropic material, is proportional to the sum of the principal stresses. A Poisson's equation for the in-plane shear stress is obtained from the two-dimensional equilibrium equations in which the forcing function is obtained directly from the measured velocity variations. Once this equation is integrated for the shear stress, the normal stresses may be evaluated directly from the equilibrium equations. In this paper, the basic equations are derived for the case of an anisotropic material. The experimental and numerical procedures are reviewed, and results of residual stresses in an aluminum ring are presented.

Introduction

Experimental methods for the determination of residual stresses in structural components have been the focus of considerable attention through the past several decades. A widely used class of techniques involves either destructive (parting and sectioning techniques) or semi-destructive (blind-hole drilling) methods. In addition to leaving the part examined unfit for service, these techniques require substantial expertise and are fairly costly to perform. A range of nondestructive techniques for stress evaluation have also been developed. One major technique involves diffraction of X-ray or neutron beams as a method of determining the strain on a particular lattice plane of the material. The physics of these processes is well understood and both diffraction techniques are capable of good spatial resolution, although the X-ray technique is limited to measuring the stresses near the surface. Neutrons are more deeply penetrating, but require the presence of a high flux reactor. Thus, there are relatively few facilities that can perform stress evaluation from neutron diffraction measurements.

An alternate nondestructive technique, acoustoelasticity, involves the measurement of the variation of speeds of ultrasonic waves caused by the presence of the stress field. Within the broad heading of acoustoelasticity, there are a range of different methods that have been considered, all of which are limited to the evaluation of plane states of stress. In this paper, attention is focused on this planar case. For the purposes of this introductory section, we also restrict attention to materials which are initially isotropic. The most common acoustoelastic technique is called the birefringence technique (Hsu, 1974; Fukuoka et al., 1983; Pao et al., 1984). This technique is based on the fact that the difference in the speeds at which two shear waves propagating normal to the plane of stress, but polarized in the principal stress directions, is proportional to the difference in the principal stresses. The constant of proportionality is a material constant (called the acoustoelastic constant for birefringence). Another technique, which is currently receiving considerable attention, involves the difference in the speeds of two SH waves propagating in one principal direction and polarized in the other (King and Fortunko, 1983; Thompson et al., 1986; Man and Lu, 1987). In this case, the difference in the square of the SH wave speeds is equal to the difference in principal stresses divided by the material's mass density. There is no acoustoelastic constant which must be determined *a priori* for the SH wave technique. A third technique, called the longitudinal wave technique, involves the change in the speed of a longitudinal wave traveling in the direction normal to the plane of the stress (Kino et al., 1979). This technique, like the birefringence technique, requires that the acoustoelastic constant be known in advance.

Each of the three acoustoelastic techniques discussed in the previous paragraph has certain advantages and disadvantages. A clear advantage of the SH wave technique is the absence of an acoustoelastic constant whose uncertainty affects the precision of the resulting stresses. The birefringence technique has an advantage in that there is a relatively larger velocity variation per unit stress than in either of the other techniques. The advantage of the longitudinal wave technique is the ease with which measurements can be made over a large region of a sample, and the spatial resolution which can be achieved. As will be shown later in this paper, all of the techniques use relative measurements (as opposed to absolute measurements) of velocity variation.

The remainder of this paper addresses the application of the

[1]Presently at Sandia National Laboratories, Division 8242, Livermore, CA 94550.

Contributed by the Applied Mechanics Division of THE AMERICAN SOCIETY OF MECHANICAL ENGINEERS for publication in the JOURNAL OF APPLIED MECHANICS.

Discussion on this paper should be addressed to the Technical Editor, Leon M. Keer, The Technological Institute, Northwestern University, Evanston, IL 60208, and will be accepted until two months after final publication of the paper itself in the JOURNAL OF APPLIED MECHANICS. Manuscript received and accepted by the ASME Applied Mechanics Division, December 1, 1988.

longitudinal wave technique to evaluating the residual stress state throughout a sample. A recent analytical development has made it possible to estimate the complete residual stress state (both normal and shear stress components) everywhere in a planar structure (Johnson and Dike, 1988). Neither of the other acoustoelastic techniques have yet to be demonstrated as having the capability for such whole-field stress determination.

In the next section, the basic theory is presented for the stress evaluation from measurements of variations in longitudinal wave speeds. While the technique should provide exact results for the case of an isotropic material (given perfect data), we consider also the more realistic case of a material which exhibits acoustoelastic anisotropy. Experimental considerations are presented in Section 3, where we provide new equations for the exact determination of spatial velocity variations from measurements of variations in time-of-flight and sample thickness. Section 4 presents certain numerical considerations which must be taken into account in solving the system of equations given the limitations of the measured data. It is shown here that the technique for dealing with the anisotropy provides the correct stress solution, even for rather extreme cases of anisotropy. Finally, experimental results for the residual stresses in an aluminum ring are presented and compared with numerical estimates of the stress state. It is shown that both the spatial variations and the magnitudes of the experimental and numerical estimates are in good agreement.

Theoretical Basis

Consider a body subject to a plane state of residual stress, with cartesian components σ_{xx}, σ_{yy}, and σ_{xy}, and a longitudinal wave propagating in the direction normal to the plane. The material in question is taken to be initially homogeneous and acoustoelastically orthotropic, so that the shift in the speed V of this longitudinal wave from the speed V_o in the unstressed material is (King and Fortunko, 1983; Johnson and Mase, 1984)

$$\frac{V-V_o}{V_o} = A_x\sigma_{xx} + A_y\sigma_{yy}, \tag{1}$$

where A_x and A_y are the acoustoelastic constants, which may be different for an anisotropic material. An alternate form of this equation, which may be more revealing in terms of the eventual stress evaluation, is

$$\frac{V-V_o}{V_o} = A_+(\sigma_{xx}+\sigma_{yy}) + A_-(\sigma_{xx}-\sigma_{yy}), \tag{2}$$

where

$$A_+ = \tfrac{1}{2}(A_x+A_y), \quad A_- = \tfrac{1}{2}(A_x-A_y). \tag{3}$$

Note that for a material which is acoustoelastically isotropic, $A_- = 0$ and the change in wave speed from the unstressed state is proportional to the sum of the in-plane normal stresses. In most engineering materials, the magnitude of A_+ is considerably greater than that of A_-, so that the material can often be considered as being "slightly anisotropic." Although we do not impose a condition of such slight anisotropy, we do assume that $|A_+| > |A_-|$ and that the values of the acoustoelastic constants are known.

The equilibrium equations for the residual stress field in the absence of body forces are

$$\begin{aligned}\sigma_{xx,x}+\sigma_{xy,y}&=0,\\ \sigma_{xy,x}+\sigma_{yy,y}&=0,\end{aligned} \tag{4}$$

where comma denotes partial differentiation with respect to the indicated coordinate. An equation for the shear stress σ_{xy} in terms of the normal stresses may be obtained by differentiating equation $(4)_1$ with respect to y and equation $(4)_2$ with respect to x, and adding. Thus,

$$\nabla^2\sigma_{xy} = -(\sigma_{xx}+\sigma_{yy})_{,xy}, \tag{5}$$

where ∇^2 is the two-dimensional Laplace operator. Equation (5) is a Poisson's equation for the shear stress in terms of derivatives of the sum of the normal stresses.

If an accurate estimate of the sum of the normal stresses can be obtained from acoustoelastic measurements, then equations (4) and (5) can be solved for the entire field in the body. If $A_- = 0$ (acoustoelastic isotropy), the right-hand side of equation (5) is directly related to the acoustoelastic measurements. Let us now focus attention on the problem posed by a material which is acoustoelastically anisotropic.

In order to find a solution for the shear stress by integration of equation (5), the values of σ_{xy} along the boundary must be known. Because the stresses are residual, the boundaries are taken to be traction-free. Consider a point on the boundary with outward unit normal vector n which makes an angle Θ with the x-axis. The stress tensor at this point may be expressed either in terms of the cartesian (x-y) components used, or in terms of normal-tangential (n-t) components, σ_{nn}, σ_{tt}, and σ_{nt}, which are related to the cartesian components as

$$\begin{aligned}\sigma_{nn}&=\sigma_{xx}\cos^2\Theta+\sigma_{yy}\sin^2\Theta+\sigma_{xy}\sin2\Theta\\ \sigma_{tt}&=\sigma_{xx}\sin^2\Theta+\sigma_{yy}\cos^2\Theta-\sigma_{xy}\sin2\Theta\\ \sigma_{nt}&=\tfrac{1}{2}(\sigma_{yy}-\sigma_{xx})\sin2\Theta+\sigma_{xy}\cos2\Theta.\end{aligned} \tag{6}$$

In the case considered here, the only nonvanishing stress component in normal-tangential coordinates is σ_{tt}. Thus, the cartesian components are expressed in terms of σ_{tt} as

$$\sigma_{xx}=\sigma_{tt}\sin^2\Theta, \quad \sigma_{yy}=\sigma_{tt}\cos^2\Theta, \quad \sigma_{xy}=-\tfrac{1}{2}\sigma_{tt}\sin2\Theta. \tag{7}$$

In light of equation (1), the velocity change from the unstressed state is related to the tangential component of stress as

$$\frac{V-V_o}{V_o} = \sigma_{tt}(A_x\sin^2\Theta+A_y\cos^2\Theta). \tag{8}$$

Assuming that measurements of velocity change can be made along the boundary and that the geometry of the boundary (Θ) is known, the shear stress σ_{xy} can be determined through equations $(7)_3$ and (8).

Unfortunately, because the material is not isotropic, we cannot obtain the right-hand side of equation (5) directly from the measurements. Instead, we propose to use an iterative scheme in which the velocity data is used to provide an estimate of $\sigma_{xx} + \sigma_{yy}$ which is updated at the end of each step of the iteration. Specifically, the initial estimate of the sum of the stresses is obtained by letting A_- be zero in equation (2). The boundary values for σ_{xy} and this initial guess are used to solve for the shear stress throughout the sample. The equilibrium equations are then used to estimate the normal stresses. At this point, we have estimates of σ_{xx}, σ_{yy}, and σ_{xy} which are not consistent with equation (2). However, by using these estimates and the actual value of A_-, we obtain at the end of each step of the iteration, a new estimate of the sum of the stresses through the equation

$$(\sigma_{xx}+\sigma_{yy})_{n+1} = \frac{1}{A_+}\left[\frac{V-V_o}{V_o} - A_-(\sigma_{xx}-\sigma_{yy})_n\right], \tag{9}$$

where the subscripts "n" and "$n+1$" refer to the iteration steps involved. It is shown later that this scheme converges for synthetic data to the actual stress field, even for fairly extreme levels of anisotropy.

Experimental Procedures

The algorithm presented in the preceding section assumes that sufficiently precise estimates of the velocity shift with stress can be experimentally determined. Velocity is not, however, a directly measurable quantity. Further, we would like to be able to evaluate the residual stress state without prior knowledge of the unstressed velocity V_o. We show in this section that the use of two scans, which provide spatial variations in the time-of-flight and path length of the longitudinal waves, are sufficient to obtain the necessary velocity shift.

It is important to recognize that there are two types of variations or shifts involved in the experimental work. We refer to these as configurational variations and spatial variations. For the velocities, these variations are associated with the following definitions:

> $\Delta V/V_o$ is the *configurational* velocity change. It is the relative velocity change between the final (stressed) and initial (unstressed) configurations, at the same point.
>
> $\delta V/V$ is the *spatial* velocity variation. It is the relative velocity difference between two points in the final configuration.

The configurational velocity change is the quantity which is needed for the stress evaluation, while spatial variations of the thickness and time-of-flight are actually measured.

In keeping with our previous usage, we let a subscript o denote quantities associated with the initial (unstressed) configuration. Symbols written without a subscript are taken to represent quantities in the final (stressed) configuration. In order to discuss the spatial variation of a quantity, we let X denote any generic material point, and X_r denote a specific reference point. Thus, the velocities in the initial configuration would be written $V_o(X) = V_o(X_r) = V_o$, while the velocities in the final configuration would be written $V(X)$ and $V(X_r)$, where these two velocities would, in general, be different. For simplicity, we often omit the argument X for the generic material point (so that $V(X)$ would be written simply as V).

The configurational velocity change is then just

$$\frac{\Delta V}{V_o} = \frac{V - V_o}{V_o}, \tag{10}$$

while the spatial variation is expressed as

$$\frac{\delta V}{V} = \frac{V - V(X_r)}{V(X_r)}. \tag{11}$$

The measurements made are of two types: spatial variations of the time-of-flight of the longitudinal wave and spatial variations of the thickness of the sample (which is the path length of the wave). The system used for the time-of-flight variations is a slight modification of the double-pulse overlap system described by Ilić et al. (1979). In this system, a single transducer operates in a water-bath and is excited by two rf tone bursts which are timed so that the first echo caused by the second pulse and the second echo caused by the first pulse return to the transducer at the same time. Both tone bursts are operated at the same carrier frequency (typically around 10 MHz) which can be adjusted to provide a particular phase delay between the two overlapping echoes. By using the analog phase-lock loop described by Ilić et al. (1979), this phase delay can be held constant as the time-of-flight changes due to changes in the wave speed and sample thickness. The condition at which such a phase condition is achieved is called a "null" and the associated frequency is denoted f_T, with the subscript indicating that this frequency is related to the time-of-flight.

The system used for the measurement of thickness variation is the two-transducer system proposed by Fisher and Johnson (1984). The two transducers are collinear and are mounted pointing directly at one another on a "rigid" fixture. The sample is placed between the transducers with its major surfaces normal to the axis of the transducers. The fixed distance between the transducers is L, while the distance from each transducer to the nearest face of the sample is l_1 or l_2. Each transducer is excited by a single rf tone burst. If we consider only the first echo returning to each transducer, the total phase delay for each wave is

$$\varphi_i = \frac{2f_d l_i}{V_w}, \quad i = 1,2 \tag{12}$$

where f_d is the carrier frequency of the tone bursts and V_w is the speed at which the waves travel in the water. Adding the two phases, and noting that $L = l_1 + l_2 + d$, gives

$$\Phi = \varphi_1 + \varphi_2 = \frac{2f_d}{V_w}(l_1 + l_2) = \frac{2f_d}{V_w}(L - d). \tag{13}$$

This phase sum can be held constant for changing thickness by varying the frequency f_d. Thus, if V_w is taken to be a constant, the variation in thickness can be related to the variation in frequency through the relation

$$\frac{\delta d}{d}\left[1 + \frac{\delta f_d}{f_d}\right] - \frac{L - d_r}{d_r}\frac{\delta f_d}{f_d} = 0, \tag{14}$$

where the symbol δ is used to denote the spatial nature of the variations, and d_r is the thickness of the sample at X_r. We note that this expression is exact, while the associated relation given by Fisher and Johnson (1984) ignores the term which is nonlinear in the variations.

Given this method for determining the spatial thickness variation, let us return to the single transducer system. The phase delay φ between the two echoes may be written as the product of the frequency and the time-of-flight. Alternatively, the time-of-flight may be eliminated in favor of the thickness and velocity, so that the phase delay becomes

$$\varphi = \frac{2f_T d}{V}. \tag{15}$$

Since φ is held constant at a particular null, the spatial velocity variation is related to the spatial variations in null frequency and thickness as

$$\frac{\delta V}{V} = \frac{\delta d}{d} + \frac{\delta f_T}{f_T} + \frac{\delta d}{d}\frac{\delta f_T}{f_T}, \tag{16}$$

where this expression is again exact.

The importance of retaining the exact expressions in equations (14) and (16) is clear when the acoustoelastic constants of the material being investigated are small. In such cases the maximum velocity change may be on the order of 0.1 percent, while the variations in thickness and null frequency may be much larger (on the order of several percent) and of the opposite sign. The terms which are nonlinear in the variations in these equations may then contribute substantially to the resulting velocity variation.

We now have a method with which to determine the spatial variation in the velocity, but in fact need the configurational variation in order to evaluate the stresses. To obtain this latter variation, we make use of the fact that the residual stress field must be self-equilibrating. Specifically, the volume integrals of the normal stress components over the entire region must vanish. Since we are dealing with the case of plane stress, these integrals over the volumes can be replaced by integrals over the surface of the sample. Given equations (1) or (2), the vanishing of these surface integrals then requires that the integral of the configurational velocity change over the sample must be zero.

Let us now consider the relation between the configurational and spatial variations of velocity. Equation (11) may be expanded as

$$\frac{\delta V}{V} = \frac{V(X) - V_o}{V(X_r)} - \frac{V(X_r) - V_o}{V(X_r)} = \frac{V_o}{V(X_r)}\left[\frac{\Delta V}{V_o} - C\right] \tag{17}$$

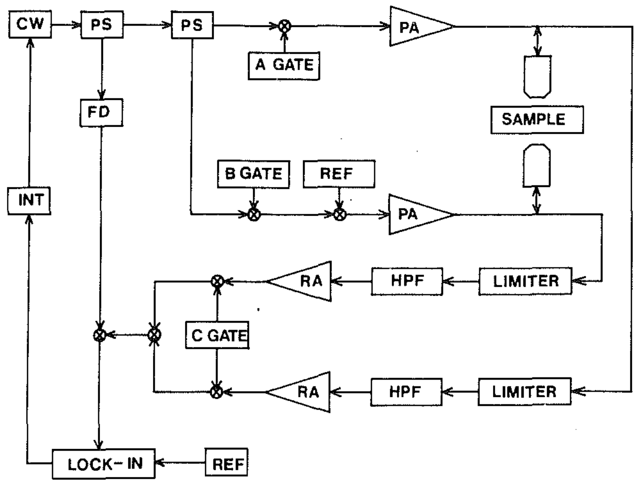

Fig. 1 Electronic block diagram for the two-transducer thickness scanning system. The device abbreviations are: CW = frequency-modulated continuous wave generator, PS = power splitter, PA = power amplifier, HPF = high-pass filter, RA = receiving amplifier, FD = frequency doubler, REF = low frequency reference square wave source, and INT = integrator.

where C is the configurational velocity change at the reference point and will be treated as a constant. The ratio of initial velocity to final velocity at the reference point is taken to be small (almost always less than one percent) so that equation (17) may be rewritten as

$$\frac{\Delta V}{V_o} = \frac{\delta V}{V} + C. \tag{18}$$

Since the integral of the left-hand side of equation (18) must be zero, the constant C may be determined from the integral of the spatial variation over the surface area Σ as

$$C = -\frac{1}{\Sigma}\int \frac{\delta V}{V}\, d\Sigma. \tag{19}$$

Thus, the measurement of the spatial variations is sufficient to provide the necessary configurational data.

The electronic system used for the single transducer measurements is essentially that described by Ilić et al. (1979). The electronic system for the two-transducer system is similar, although the analog signal processing is somewhat different. A schematic diagram of the system used for the thickness scans is shown in Fig. 1. In order to isolate Φ, the sum of the individual phases, the rf tone burst which drives one of the transducers, say the second one, is modulated by a low frequency signal. Thus, the returning pulses r_i, $i = 1, 2$, are of the form

$$r_1 = B_1\cos(\omega_d t + \varphi_1), \quad r_2 = B_2\cos(\omega_d t + \varphi_2)\cos\Omega t, \tag{20}$$

where B_i are the waves' amplitudes, $\omega_d = 2\pi f_d$, and Ω is the frequency of the modulation, which is typically in the low kilohertz range. These two signals are electronically mixed and the result is filtered to isolate the second harmonic of the carrier. This component of the signal has the form

$$r_3 = B_3\cos(2\omega_d t + \Phi)\cos\Omega t. \tag{21}$$

This signal is then mixed with a continuous wave whose frequency is $2\omega_d$. The amplitude of the low frequency component of this final signal is proportional to $\cos\Phi$,

$$r_4 = B_4\cos\Phi\,\cos\Omega t. \tag{22}$$

Thus, when this signal is used as input to a lock-in amplifier whose reference frequency is Ω, the output of the lock-in is a d-c signal proportional to $\cos\Phi$. This d-c signal is then integrated and the result is used to drive an FM modulator until the lock-in output reaches zero (a null condition).

The present system uses commercially available 10 MHz, spherically-focused transducers with 50-mm (2-in.) focal lengths. In actually performing the scans for the thickness variation, we must choose the geometry of the transducer holder (spacing L) in recognition that there are two effects which compete with one another and which must be balanced. On the one hand, the use of distinct rf tone bursts for the phase comparison requires that the lengths l_i be sufficiently large, while on the other hand, large path lengths (large L) result in small frequency variations for a given thickness variation.

Most of the measurements made to date have been on the samples that are approximately 10 mm thick with the sample surfaces between 25 and 40 mm from the transducers' faces. The result is somewhat poorer spatial resolution than would be expected if the transducers were operated at their focal lengths. If the transducers are used at their focal lengths, adjacent null frequencies are only 0.07 percent apart and the sensitivity of the thickness evaluation is poor. Thus, we can make measurements to within approximately 2 mm of the edge of the sample. Our current positioning system consists of two perpendicular lead screw stages driven by stepping motors, and has a nominal spatial resolution of 50 μm. When scans of the same region of a sample are repeated, it is found that the null frequencies for these systems have a repeatability of .005 percent over a 1-percent maximum variation, as determined by the RMS difference in the null frequencies over all points of the scans.

Numerical Procedures

The basic equations have been cast into a finite difference scheme for the solution of the residual stress field. For the present we have restricted attention to disks or annuli which are most conveniently described in plane polar coordinates. In this section we describe results obtained using synthetic velocity data generated from a known stress state. This numerical example does not use a residual stress state, but the requirement that the stresses be residual is not operative as long as the appropriate boundary values of σ_{xy} and the initial velocity V_o are known. We demonstrate that the proposed procedure for stress evaluation in materials which exhibit anisotropic acoustoelastic response converges, and that the solution is basically in agreement with the actual stress state. Experimental results for a residually stressed aluminum ring are presented in the following section.

We consider for this example the stress state generated by the far-field tension of an infinite plate of elastically isotropic material containing a circular hole. We know the exact stress state in terms of components expressed in either polar or cartesian coordinates. Our approach is to use the known normal stresses in equation (1) to generate the synthetic velocity variations given various choices of acoustoelastic constants. The known shear stresses σ_{xy} along the edges of an annular region are used with the velocity variations to estimate the stress state in the interior of the annulus.

Contours of the shear stress and the normal stress in the loading direction are shown in Fig. 2 for an annular region of the plate under a far-field tension of 100 MPa. The stresses displayed in Fig. 2 result from velocity data at discrete grid points within the interior of the region assuming that the material is acoustoelastically isotropic and that $A_+ = 10\ \text{TPa}^{-1}$ (typical of many aluminums). In the results shown, there are nine radial locations between the inner and outer boundaries, and the grid points are spaced at 5-deg intervals in the circumferential direction. This is a rather coarse grid (only 153 data points in the interior of the region), but it serves to show that the algorithm provides stress values which are everywhere within 1 MPa of the exact values.

When the material is taken to be acoustoelastically anisotropic, the same stress state leads to a different velocity var-

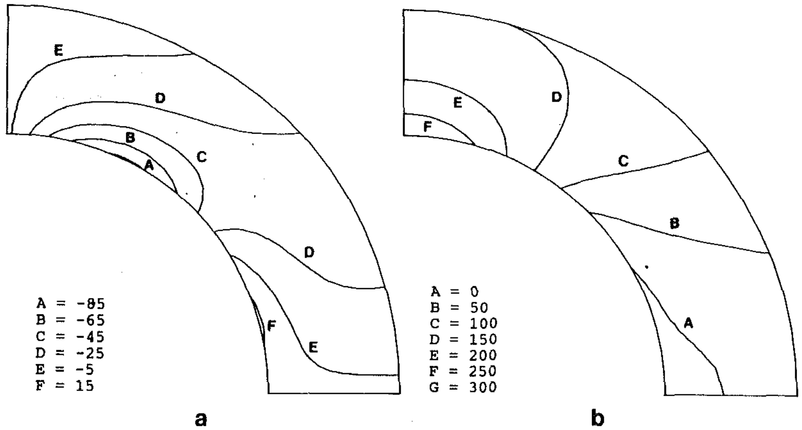

Fig. 2 Contours of (a) shear stress σ_{xy}, and (b) normal stress σ_{xx} in an annular region of an infinite plate subject to far-field tension in the x-direction of 100 MPa, obtained by numerically integrating equations (4) and (5) given synthetic velocity data at the grid points. Contour levels given in MPa.

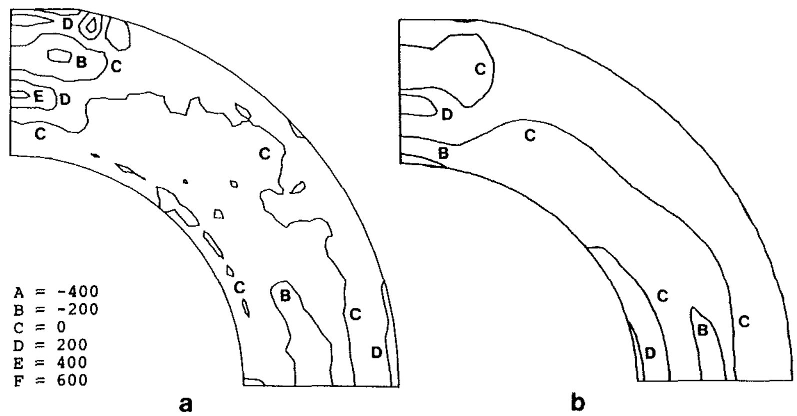

Fig. 3 Contours of the sum of normal residual stresses $\sigma_{xx} + \sigma_{yy}$ obtained (a) experimentally and (b) numerically for a 6061-T6 aluminum ring subject to diametral compression and unloaded. Contour levels given in MPa.

Table 1 Number of iterations required for convergence in anisotropic materials. In all cases, $A_+ = 10$ TPa^{-1}.

A_-	Iterations
1	3
2	4
4	5
6	7
8	9
9	11
10	14

iation. However, the same stress pattern emerges after the iterative process described above. Table 1 gives the number of iterations required to reduce the maximum stress difference between subsequent iterations to within 0.1 MPa for a range of different anisotropies. We find that the technique converges for all cases. In particular, the last case shown is an extreme case corresponding to $A_x = 20$ TPa^{-1}, $A_y = 0$ TPa^{-1}.

Experimental Results

An annulus of 6061-T6 aluminum, with nominal thickness of 12.7 mm, inside diameter of 38.1 mm, and outside diameter of 63.5 mm, was loaded in diametral compression until permanently deformed and then completely unloaded. Loading was performed using ball-in-socket compression platens acting on flat regions which had been machined on the top and bottom of the annulus. One quadrant of the specimen was scanned over a 1 mm radial, 2.5 deg circumferential grid. Experimentally determined stress contours are compared with those estimated by the NIKE2D finite element code (Hallquist, 1986).

Because measurements cannot be made at the very edge of the sample, the interior measurements are extrapolated to obtain the boundary values of the stresses. The extrapolation procedure used for the results shown next involved a linear least-squares fit to the points near the boundary. The interior data is used where it is available, with extrapolated data used only where necessary.

The contours of the sum of the residual normal stresses shown in Fig. 3 indicate generally good agreement between the experimental and numerical estimates. Note, in particular, the results of the two approaches for the zero contour (C). While the experimental contour is somewhat noisier than the numerical contour, the overall agreement indicates that the method for evaluating the constant C, and so the sum of stresses, is valid. The fact that the experimental contours are noisier than the numerical contours is to be expected due to the intrinsic uncertainty in the measurements. This noise is especially noticeable in the low-stress regions of the annulus. We also note that the contours generally have the correct shape and are properly located spatially.

Figure 4 presents the experimental and numerical estimates of the shear stress σ_{xy}. Again, the zero-stress contour (E) has the same basic pattern throughout the region and is noisier in the experimental plot. The regions of positive and negative shear are in uniform agreement, though there are again certain regions within which the magnitudes are somewhat different. Under the corner of the flat at the top, for example, the experimental contours accurately denote the stress concentration

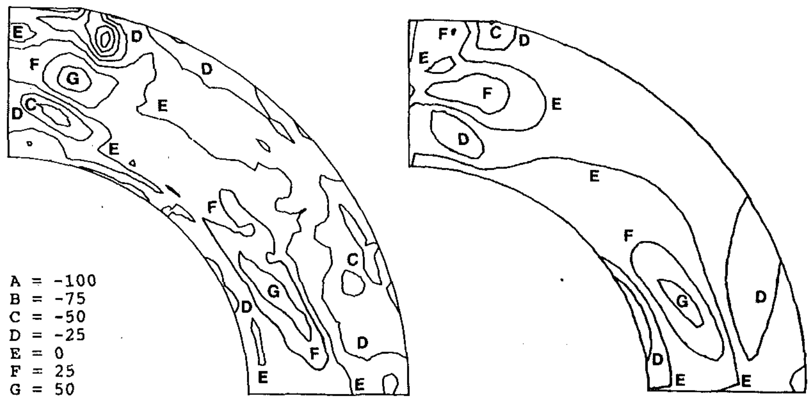

a b

Fig. 4 Contours of the residual shear stress σ_{xy} obtained (*a*) experimentally and (*b*) numerically for a 6061-T6 aluminum ring subject to diametral compression and unloaded. Contour levels given in MPa.

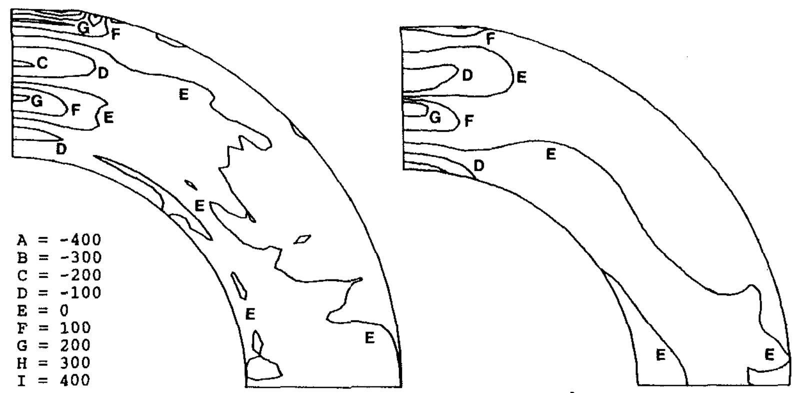

a b

Fig. 5 Contours of the residual normal stress σ_{xx} obtained (*a*) experimentally and (*b*) numerically for a 6061-T6 aluminum ring subject to diametral compression and unloaded. Contour levels given in MPa.

at the edge of the flat, but overpredict the magnitude of the shear stress at this point.

Figure 5 presents contours for the normal stress σ_{xx}, which is the hoop stress at the top of the sample. The region in which this stress component is small is accurately delineated and, as in the previous plots, the zero-stress contours agree reasonably well. The regions of tension and compression are in spatial agreement, though the magnitudes of the experimental estimates are slightly higher at the boundaries than are the numerical estimates.

Extrapolation tends to be an inherently inaccurate process, and as noted previously, can cause difficulties at the boundaries. It was found that while various extrapolation procedures yielded large differences in the values of stresses at the boundary, the interior values were affected very little. The larger the ratio of area where measured data is available to that where extrapolated values must be used, the better the results of this method can be expected to be.

Acknowledgments

This work was supported by the Lawrence Livermore National Laboratory through the Engineering Research and Development Program and by IBM Almaden Research Center.

References

Fisher, M. J., and Johnson, G. C., 1984, "Acoustic Velocity Variations due to Finite Grain Size in Polycrystalline Materials," *Review of Progress in Quantitative NDE*, Vol. 3B, D. O. Thompson and D. E. Chimenti, eds., Plenum Press, New York, pp. 1119–1128.

Fukuoka, H., Toda, H., and Naka, N., 1983, "Nondestructive Residual Stress Measurement in a Wide-Flanged Rolled Beam by Acoustoelasticity," *Experimental Mechanics*, Vol. 23, pp. 120–128.

Hallquist, J. O., 1979, "NIKE2D - A Vectorized Implicit, Finite Deformation, Finite Element Code for Analyzing the Static and Dynamic Response of 2-D Solids with Interactive Rezoning and Graphics, Lawrence Livermore National Laboratory, UCID No. 19677, Livermore, Calif.

Hsu, N. N., 1974, "Acoustical Birefringence and the Use of Ultrasonic Waves for Experimental Stress Analysis," *Experimental Mechanics*, Vol. 14, pp. 169–176.

Ilić, D. B., Kino, G. S., and Selfridge, A. R., 1979, "Computer Controlled System for Measuring Two-Dimensional Velocity Fields," *Review of Scientific Instrumentation*, Vol. 50, pp. 1527–1533.

Johnson, G. C., and Dike, J. J., 1988, "Complete Evaluation of Residual Stress States using Acoustoelasticity," *Review of Progress in Quantitative NDE*, Vol. 7B, D. O. Thompson and D. E. Chimenti, eds., Plenum Press, New York, pp. 1391–1398.

Johnson, G. C., and Mase, G. T., 1984, "Acoustoelasticity in Transversely Isotropic Materials," *Journal of the Acoustical Society of America*, Vol. 75, pp. 1741–1747.

King, R. B., and Fortunko, C. M., 1983, "Determination of in-plane Stress States in Plates Using Horizontally Polarized Shear Waves," *Journal of Applied Physics*, Vol. 54, pp. 3027–3035.

Kino, G. S., Hunter, J. B., Johnson, G. C., Selfridge, A. R., Barnett, D. M., Herrmann, G., and Steele, C. R., 1979, "Acoustoelastic Imaging of Stress Fields," *Journal of Applied Physics*, Vol. 50, pp. 2607–2613.

Man, C.-S., and Lu, W. Y., 1987, "Towards an Acoustoelastic Theory for Measurement of Residual Stress," *Journal of Elasticity*, Vol. 17, pp. 159–182.

Pao, Y.-H., Sachse, W., and Fukuoka, H., 1984, "Acoustoelasticity and Ultrasonic Measurements of Residual Stress," *Physical Acoustics*, Vol. 17, W. P. Mason and R. N. Thurston, eds., Academic Press, New York, Chapter 2, pp. 61–143.

Thompson, R. B., Lee, S. S., and Smith, J. F., 1986, "Angular Dependence of Ultrasonic Wave Propagation in a Stressed Orthorhombic Continuum: Theory and Application to the Measurement of Stress and Texture," *Journal of the Acoustical Society of America*, Vol. 80, pp. 921–931.

Raphael T. Haftka
Virginia Polytechnic Institute and State University,
Blacksburg, VA 24061

Gerald A. Cohen
Structures Research Associates,
Laguna Beach, CA 92651

Zenon Mróz
Institute of Fundamental Technological Research,
Warsaw, Poland

Derivatives of Buckling Loads and Vibration Frequencies With Respect to Stiffness and Initial Strain Parameters

A uniform variational approach to sensitivity analysis of vibration frequencies and bifurcation loads of nonlinear structures is developed. Two methods of calculating the sensitivities of bifurcation buckling loads and vibration frequencies of nonlinear structures, with respect to stiffness and initial strain parameters, are presented. A direct method requires calculation of derivatives of the prebuckling state with respect to these parameters. An adjoint method bypasses the need for these derivatives by using instead the strain field associated with the second-order post-buckling state. An operator notation is used and the derivation is based on the principle of virtual work. The derivative computations are easily implemented in structural analysis programs. This is demonstrated by examples using a general purpose, finite element program and a shell-of-revolution program.

Introduction

Sensitivity analysis provides methods for calculating the variation of structural response with respect to variations of structural parameters. These are useful for structural redesign and gradient-based structural optimization, as well as for parameter identification, imperfection sensitivity, and statistical structural analysis of geometric and material imperfections.

The sensitivity of vibration frequencies and buckling loads to changes in structural stiffness has been treated both in the framework of calculus of variations (e.g., Haichang (1984)) and finite element analysis (e.g., Adelman and Haftka (1986)). Whereas calculation of sensitivity of natural frequencies is simple in that it requires only knowledge of vibration modes, (cf., Haichang (1984), Adelman and Haftka (1986)), this is not the case when buckling loads or vibration frequencies of loaded structures are considered. The calculation then requires also the sensitivity of the prebuckling state. Because of computational cost and complexity, the effect of variation of prebuckling stresses is often neglected (cf., Khot (1981)).

Mróz and Haftka (1988) present an adjoint-structure approach to the calculation of vibration frequency and buckling load variations of a plate due to variations in stiffness and initial-strain parameters. The use of the adjoint structure obviated the need to calculate the sensitivities of the prebuckling stresses. The purpose of the present paper is to generalize the procedure of Mróz and Haftka (1988) to more general structures and nonlinear prebuckling behavior. The paper is based on the general method of sensitivity analysis of nonlinear structural behavior developed in Mróz et al. (1985), Mróz (1987), Szefer et al. (1988), and Barthelemy et al. (1989). A general operator notation previously used by Budiansky and Hutchinson (1964) and Cohen (1968) is employed and guarantees wide applicability of the results. This wide applicability is demonstrated by examples obtained with a general purpose, finite element program EAL (Whetstone, 1983) and a general shell-of-revolution program FASOR (Cohen, 1981).

Vibration and Bifurcation Buckling Analysis

We denote the generalized displacement, strain, and stress fields by u, ϵ, and σ. The strain-displacement relationship has the form

$$\epsilon = L_1(u) + \frac{1}{2} L_2(u) \tag{1}$$

where L_1 and L_2 are first and second-degree homogeneous operators. For example, for a beam under lateral and axial loads, the generalized strain has one component of axial strain ϵ_x and one component of curvature κ, u has components of axial displacement u_x and lateral displacement u_z and equation (1) is written as

$$\begin{Bmatrix} \epsilon_x \\ \kappa \end{Bmatrix} = \begin{Bmatrix} u_{x,\,x} \\ -u_{z,\,xx} \end{Bmatrix} + \frac{1}{2} \begin{Bmatrix} (u_{z,\,x})^2 \\ 0 \end{Bmatrix}. \tag{2}$$

Contributed by the Applied Mechanics Division of The American Society of Mechanical Engineers for presentation at the Winter Annual Meeting, San Francisco, Calif., December 10-15, 1989.

Discussion on this paper should be addressed to the Editorial Department, ASME, United Engineering Center, 345 East 47th Street, New York, N.Y. 10017, and will be accepted until two months after final publication of the paper itself in the Journal of Applied Mechanics. Manuscript received by the ASME Applied Mechanics Division, May 18, 1988; final revision, March 20, 1989.

Paper No. 89-WA/APM-44.

The variation of strain is specified in terms of displacement variation as

$$\delta\epsilon = L_1(\delta u) + L_{11}(u, \delta u) \tag{3}$$

where L_{11} is a symmetric bilinear operator, i.e., $L_{11}(u, v) = L_{11}(v, u)$, defined by

$$L_2(u+v) = L_2(u) + L_2(v) + 2L_{11}(u, v). \tag{4}$$

In particular, equation (4) yields $L_{11}(u, u) = L_2(u)$. We assume a linear stress-strain law

$$\sigma = D(\epsilon - \epsilon^i) = D\epsilon^r \tag{5}$$

where σ is the generalized stress tensor, D is the material stiffness tensor, and ϵ^i is the initial strain (such as the initial strain generated by a temperature field). In our example of a beam under axial and lateral loads, the diagonal elements of D are the stretching and bending stiffnesses.

The equations of equilibrium and static boundary conditions are obtained from the principle of virtual work as

$$\sigma \cdot \delta\epsilon = \lambda q \cdot \delta u \tag{6}$$

where a dot between two vector or tensor fields denotes the integral of their inner product over the structural domain and λ is a load amplitude parameter. Here the unit load vector q includes conservative live loads and is given by

$$q = q_0 + q_1(u) \tag{7}$$

where q_1 is a linear operator satisfying, for any two admissible displacement vectors u and v, the reciprocal relation

$$q_1(u) \cdot v = q_1(v) \cdot u. \tag{8}$$

Consider now small, free harmonic vibrations with frequency ω superimposed on the equilibrium state u_0, ϵ_0, σ_0 associated with load level λ_0. We denote the vibration mode fields by u_1, ϵ_1, and σ_1. They satisfy the following linear equations.

$$\begin{aligned} &\epsilon_1 = L_1(u_1) + L_{11}(u_0, u_1) \\ &\sigma_1 = D\epsilon_1 \\ &\sigma_1 \cdot \delta\epsilon_0 + \sigma_0 \cdot L_{11}(u_1, \delta u) - \lambda_0 q_1(u_1) \cdot \delta u = \omega^2 M u_1 \cdot \delta u \end{aligned} \tag{9}$$

where M denotes the mass matrix and

$$\delta\epsilon_0 = L_1(\delta u) + L_{11}(u_0, \delta u). \tag{10}$$

Setting $\delta u = u_1$ in equation (9c), we obtain the Rayleigh quotient for the vibration frequency

$$\omega^2 = \frac{\sigma_1 \cdot \epsilon_1 + \sigma_0 \cdot L_2(u_1) - \lambda_0 q_1(u_1) \cdot u_1}{M u_1 \cdot u_1}. \tag{11}$$

Under static loading the structure buckles at a load λ_c corresponding to the state $u_0^* = u_0(\lambda_c)$, $\epsilon_0^* = \epsilon_0(\lambda_c)$, $\sigma_0^* = \sigma_0(\lambda_c)$. The buckling load corresponds to a zero vibration frequency. Therefore, the buckling mode u_1, ϵ_1, σ_1 satisfies equations (9) with $\omega = 0$ and $\lambda_0 = \lambda_c$, $u_0 = u_0^*$, $\sigma_0 = \sigma_0^*$.

Direct Calculation of Sensitivities

We consider now a parameter p variations of which can represent variations in the material stiffness matrix, the initial strain field, or both. That is

$$\begin{aligned} \delta D &= D_p \delta p \\ \delta\epsilon^i &= \epsilon_p^i \delta p \end{aligned} \tag{12}$$

where a subscript p indicates differentiation with respect to the parameter. We seek to determine the derivatives of the vibration frequency and buckling load with respect to p. We assume that the equilibrium state u_0, ϵ_0, σ_0 depends analytically on the design parameter p and the load parameter λ. We also assume that the fundamental vibration frequency and buckling load represent nonrepeated eigenvalues, so that the eigenfields u_1, ϵ_1, σ_1 are unique up to a mulitplicative constant. Under these conditions the derivatives of the eigenfields, with respect to p, can be shown to exist. We start by differentiating equations (9) with respect to p and then substitute $\delta u = u_1$; thus

$$\begin{aligned} &\epsilon_{1p} = L_1(u_{1p}) + L_{11}(u_{0p}, u_1) + L_{11}(u_0, u_{1p}) \\ &\sigma_{1p} = D_p \epsilon_1 + D\epsilon_{1p} \\ &\sigma_{1p} \cdot \epsilon_1 + \sigma_1 \cdot L_{11}(u_{0p}, u_1) + \sigma_{0p} \cdot L_2(u_1) \\ &\qquad + \sigma_0 \cdot L_{11}(u_{1p}, u_1) - \lambda_0 q_1(u_{1p}) \cdot u_1 = (\omega^2)_p M u_1 \cdot u_1 \\ &\qquad + \omega^2 M_p u_1 \cdot u_1 + \omega^2 M u_{1p} \cdot u_1. \end{aligned} \tag{13}$$

The derivatives of the vibration mode, σ_{1p}, u_{1p}, can be eliminated from equation (13c) by first setting $\delta u = u_{1p}$ in equation (9c) to give

$$\begin{aligned} &\sigma_1 \cdot [L_1(u_{1p}) + L_{11}(u_0, u_{1p})] \\ &\qquad + \sigma_0 \cdot L_{11}(u_1, u_{1p}) - \lambda_0 q_1(u_1) \cdot u_{1p} = \omega^2 M u_1 \cdot u_{1p} \end{aligned} \tag{14}$$

then subtracting equation (14) from equation (13c) and using equations (8), (13a) can (13b) to get

$$(\omega^2)_p = \frac{D_p \epsilon_1 \cdot \epsilon_1 + 2\sigma_1 \cdot L_{11}(u_{0p}, u_1) + \sigma_{0p} \cdot L_2(u_1) - \omega^2 M_p u_1 \cdot u_1}{M u_1 \cdot u_1}. \tag{15}$$

Equation (15) contains derivatives of the static field u_0, σ_0 with respect to p. Equations for these can be obtained by differentiating equations (1), (5), and (6) at $\lambda = \lambda_0$ to get

$$\begin{aligned} &\epsilon_{0p} = L_1(u_{0p}) + L_{11}(u_0, u_{0p}) \\ &\sigma_{0p} = D_p \epsilon_0^r + D\epsilon_{0p}^r = D_p(\epsilon_0 - \epsilon^i) + D(\epsilon_{0p} - \epsilon_p^i) \\ &\sigma_{0p} \cdot \delta\epsilon_0 + \sigma_0 \cdot L_{11}(u_{0p}, \delta u) - \lambda_0 q_1(u_{0p}) \cdot \delta u = 0. \end{aligned} \tag{16}$$

The derivative of a bifurcation buckling load is obtained from the condition that $\omega^2 = 0$. As p changes λ_c must change with it so that $d(\omega^2) = 0$. Thus

$$d(\omega^2) = (\omega^2)_p dp + (\omega^2)' d\lambda_c = 0 \tag{17}$$

where prime denotes derivative with respect to λ. From equation (17),

$$(\lambda_c)_p = -\frac{(\omega^2)_p}{(\omega^2)'}. \tag{18}$$

To calculate the derivative of the frequency with respect to the load parameter λ, we start by differentiating equation (9) with respect to λ and setting $\delta u = u_1$

$$\begin{aligned} &\epsilon_1' = L_1(u_1') + L_{11}(u_0', u_1) + L_{11}(u_0, u_1') \\ &\sigma_1' = D\epsilon_1' \\ &\sigma_1' \cdot \epsilon_1 + \sigma_1 \cdot L_{11}(u_0', u_1) + \sigma_0' \cdot L_2(u_1) + \sigma_0 \cdot L_{11}(u_1', u_1) \\ &\qquad - [\lambda_0 q_1(u_1') + q_1(u_1)] \cdot u_1 = (\omega^2)' M u_1 \cdot u_1 + \omega^2 M u_1' \cdot u_1. \end{aligned} \tag{19}$$

Next we eliminate the derivatives of the vibration field with respect to λ by setting $\delta u = u_1'$ in equation (9c)

$$\begin{aligned} &\sigma_1 \cdot [L_1(u_1') + L_{11}(u_0, u_1')] + \sigma_0 \cdot L_{11}(u_1, u_1') \\ &\qquad - \lambda_0 q_1(u_1) \cdot u_1' = \omega^2 M u_1 \cdot u_1' \end{aligned} \tag{20}$$

and then subtracting equation (20) from equation (19c) and using equations (8), (9b), (19a), and (19b) to get

$$(\omega^2)' = \frac{2\sigma_1 \cdot L_{11}(u_0', u_1) + \sigma_0' \cdot L_2(u_1) - q_1(u_1) \cdot u_1}{M u_1 \cdot u_1}. \tag{21}$$

Finally, substituting equations (15) and (21) evaluated at the buckling load into equation (18) gives

$$(\lambda_c)_p = -\frac{D_p \epsilon_1 \cdot \epsilon_1 + 2\sigma_1 \cdot L_{11}(u_{0p}^*, u_1) + \sigma_{0p}^* \cdot L_2(u_1)}{2\sigma_1 \cdot L_{11}(u_0'^*, u_1) + \sigma_0'^* \cdot L_2(u_1) - q_1(u_1) \cdot u_1} \tag{22}$$

where the asterisk denotes prebuckling quantities evaluated at the buckling load. Note that the field u_1, σ_1 now denotes the zero-frequency or buckling mode. Here, the derivatives of the prebuckling field with respect to λ are required, as well as its derivatives with respect to p (cf. equations (16)). Equations for these are obtained by differentiating equations (1), (5), and (6), with respect to λ, to get

$$\begin{aligned}&\epsilon_0' = L_1(u_0') + L_{11}(u_0, u_0')\\&\sigma_0' = D\epsilon_0'\\&\sigma_0' \bullet \delta\epsilon_0 + \sigma_0 \bullet L_{11}(u_0', \delta u) - \lambda_0 q_1(u_0') \bullet \delta u = q \bullet \delta u.\end{aligned} \tag{23}$$

These equations represent the tangent incremental problem along the fundamental equilibrium path, and equation (23c) is a weak formulation of incremental equilibrium. This transient solution is typically available in structural analysis programs as a by-product of the nonlinear solution strategy.

Determination of Sensitivity by Adjoint Method

The direct approach to sensitivity calculation requires the calculation of the sensitivities of the static field (prebuckling state), equation (16). This calculation can become expensive when we need sensitivities with respect to a large number of structural parameters. In that case an adjoint method that eliminates the need for static sensitivities is appropriate. Following Mróz and Haftka (1988) and Szefer et al. (1988), we introduce an adjoint field u_2, ϵ_2, σ_2 satisfying

$$\begin{aligned}&\epsilon_2 = L_1(u_2) + L_{11}(u_0, u_2)\\&\sigma_2 = D(\epsilon_2 + \frac{1}{2}L_2(u_1)) = D\epsilon_2^r\\&\sigma_2 \bullet \delta\epsilon_0 + \sigma_0 \bullet L_{11}(u_2, \delta u) - \lambda_0 q_1(u_2) \bullet \delta u\\&\qquad + \sigma_1 \bullet L_{11}(u_1, \delta u) = 0.\end{aligned} \tag{24}$$

Equations (24), the homogeneous form of which is identical to the buckling equations (equation (9) with $\omega = 0$), may be thought of as the field equations of an "adjoint" or "tangent" structure for which the second term in parenthesis in equation (24b) is an initial strain term and the last term in equation (24c) corresponds to a body-force loading. For $\lambda_0 = \lambda_c$, the adjoint field is identical to the second-order field generated in an asymptotic expansion of post-buckling response in the common case of symmetric bifurcation (i.e., when the first post-buckling coefficient $a = 0$) (cf., Cohen, 1968).

In view of equation (24), the second and third terms of the numerator of equation (15) can be transformed as follows

$$\begin{aligned}A &\equiv 2\sigma_1 \bullet L_{11}(u_{0p}, u_1) + \sigma_{0p} \bullet L_2(u_1)\\&= 2\sigma_1 \bullet L_{11}(u_{0p}, u_1) + 2\sigma_{0p} \bullet (\epsilon_2^r - \epsilon_2).\end{aligned} \tag{25}$$

Setting $\delta u = u_2$ in equation (16c) we obtain

$$\sigma_{0p} \bullet \epsilon_2 + \sigma_0 \bullet L_{11}(u_{0p}, u_2) - \lambda_0 q_1(u_{0p}) \bullet u_2 = 0 \tag{26}$$

so that we can rewrite equation (25) as

$$\begin{aligned}A = 2[&\sigma_1 \bullet L_{11}(u_{0p}, u_1) + \sigma_{0p} \bullet \epsilon_2^r\\&+ \sigma_0 \bullet L_{11}(u_{0p}, u_2) - \lambda_0 q_1(u_{0p}) \bullet u_2].\end{aligned} \tag{27}$$

Next, we set $\delta u = u_{0p}$ in equation (24c). In making this substitution as well as the above substitution of $\delta u = u_2$ in equation (16c), it is tacitly assumed that the prebuckling state satisfies the same kinematic constraints as the buckling or vibration mode. We then use (16a) to obtain

$$\begin{aligned}&\sigma_2 \bullet \epsilon_{0p} + \sigma_0 \bullet L_{11}(u_2, u_{0p}) + \sigma_1 \bullet L_{11}(u_1, u_{0p})\\&\qquad - \lambda_0 q_1(u_2) \bullet u_{0p} = 0,\end{aligned} \tag{28}$$

and from equations (16b) and (24b),

$$\sigma_2 \bullet \epsilon_{0p} = D\epsilon_2^r \bullet \epsilon_{0p} = (\sigma_{0p} + D\epsilon_p^i - D_p\epsilon_0^r) \bullet \epsilon_2^r. \tag{29}$$

Using equations (8), (28), and (29), equation (27) becomes

$$A = 2(D_p\epsilon_0^r - D\epsilon_p^i) \bullet \epsilon_2^r. \tag{30}$$

Hence, equations (15) and (22) become

$$(\omega^2)_p = \frac{D_p\epsilon_1 \bullet \epsilon_1 + 2(D_p\epsilon_0^r - D\epsilon_p^i) \bullet \epsilon_2^r - \omega^2 M_p u_1 \bullet u_1}{M u_1 \bullet u_1} \tag{31}$$

and

$$(\lambda_c)_p = -\frac{D_p\epsilon_1 \bullet \epsilon_1 + 2(D_p\epsilon_0^{r*} - D\epsilon_p^i) \bullet \epsilon_2^r}{2\sigma_1 \bullet L_{11}(u_0'^*, u_1) + \sigma_0'^* \bullet L_2(u_1) - q_1(u_1) \bullet u_1}. \tag{32}$$

Equation (32) is based on the prebuckling state calculated at $\lambda_0 = \lambda_c$. The usual practice, however, is to estimate the bifurcation buckling load by solving a linearized eigenvalue problem based on the prebuckling state at a load $\lambda_0 < \lambda_c$. It is shown in the appendix that the error introduced in the derivative $(\lambda_c)_p$ due to such approximation is of the order of $(\lambda_c - \lambda_0)^2$.

Equation (32) can be specialized to the case of plate buckling under in-plane loads and temperature that is uniform through the thickness (Mróz and Haftka, 1988). In this case the L_2 operator contains the terms $(\partial w/\partial x)^2$, $(\partial w/\partial y)^2$ and $(\partial w/\partial x)(\partial w/\partial y)$ for the in-plane strains. The prebuckling response is then linear and ϵ_0 consists of only in-plane components while σ_0 contains the membrane resultants N_{ij}. The buckling mode, on the other hand, consists only of the normal displacement w, so that $L_{11}(u_0, u_1) = 0$, and ϵ_1 contains only the curvature tensor κ_1. Under these conditions equation (32) becomes

$$(\lambda_c)_p = -\frac{D_p^B \kappa_1 \bullet \kappa_1 + 2(D_p^A \epsilon_0^r - D^A \epsilon_p^i) \bullet \epsilon_2^r}{\sigma_0' \bullet L_2(u_1)} \tag{33}$$

where D^A and D^B denote the membrane and bending parts, respectively, of the plate wall stiffness matrix. Equation (33) is equivalent to equations (38) and (50) of Mróz and Haftka (1988) except that the adjoint strain field used in Mróz and Haftka (1988) is $-2\epsilon_2$.

Applications to Plane Frames

The general expressions obtained in this paper can be specialized to the case of a plane frame with m members. The axial force N and bending moment M are the generalized stresses, and the axial strain ϵ_x and curvature κ are the conjugate generalized strains. For the sake of simpler notation, the lateral displacement in a frame member is denoted w instead of u_z. The strain displacement relation, equations (2), is rewritten as

$$\begin{Bmatrix}\epsilon_x\\ \kappa\end{Bmatrix} = \begin{Bmatrix}u_{x,x}\\ -w_{,xx}\end{Bmatrix} + \frac{1}{2}\begin{Bmatrix}w_{,x}^2\\ 0\end{Bmatrix}. \tag{34}$$

Assuming no initial bending strains Hooke's law for a frame member, equation (5), is written as

$$N = EA(\epsilon_x - \epsilon_x^i), \qquad M = EI\kappa \tag{35}$$

where E, A, and I denote the Young's modulus, cross-sectional area, and moment of inertia of a frame member (not necessarily the same for all members). The virtual work equation (6) becomes

$$\sum_i \int_o^{l_i} (M\delta\kappa + N\delta\epsilon_x)dx = \lambda q \bullet \delta u \tag{36}$$

where l_i denotes the axial length of the ith member.

The load q is a combination of point and distributed forces. We assume that the mechanical and initial strain loading induce negligible bending in the frame, so that w_0, κ_0, and M_0 are zero in all members. We consider small harmonic lateral vibrations of the frame with negligible member extension, so that the lateral displacements are given as

$$\overline{w_1}(x, t) = w_1(x)\cos\omega t \tag{37}$$

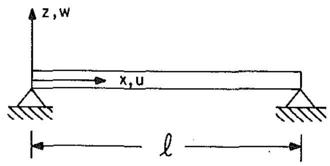

Fig. 1 Beam geometry

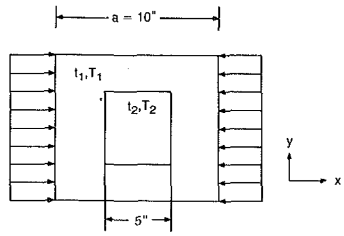

Boundary conditions: Simply supported on all sides

Material properties: Young's modulus $E = 10^7$ psi
Poisson's ratio $\nu = 0$
Coefficient of thermal expansion
$\alpha = 1.3 \times 10^{-5}$/°F

Nominal design: $t_1 = t_2 = 0.05"$, $T_1 = T_2 = 0°$

Fig. 2 Geometry and loading of square plate

for each member. The vibration eigenproblem, equation (9), becomes

$$\kappa_1 = -w_{1,xx}$$
$$M_1 = EI\kappa_1$$

$$\sum_i \int_o^{l_i} (M_1 \delta\kappa + N_0 w_{1,x} \delta w_{,x}) dx = \omega^2 \sum_i \int_o^{l_i} \rho A w_1 \delta w dx \quad (38)$$

where ρ is the mass density of a frame member. The vibration frequency ω is given by the Rayleigh quotient

$$\omega^2 = \frac{\sum_i \int_o^{l_i} (EI\kappa_1^2 + N_0 w_{1,x}^2) dx}{\sum_i \int_o^{l_i} \rho A w_1^2 dx}. \quad (39)$$

We consider a parameter p that affects the cross-sectional areas and moments of inertia of the members. The adjoint problem, equation (24) becomes

$$\epsilon_{x2} = u_{x2,x} \qquad \kappa_2 = -w_{2,xx}$$
$$N_2 = EA\epsilon_{x2}^r \qquad M_2 = EI\kappa_2 \quad (40)$$

$$\sum_i \int_o^{l_i} (M_2 \delta\kappa + N_2 \delta\epsilon_x + N_0 w_{2,x} \delta w_{,w}) dx = 0$$

where

$$\epsilon_{x2}^r = \epsilon_{x2} + \frac{1}{2} w_{1,x}^2. \quad (41)$$

Thus, the only adjoint load is the initial strain $-1/2\ w_{1,x}^2$. Equation (31), for the frequency derivative, can now be written as

$$(\omega^2)_p = \frac{\sum_i \int_o^{l_i} [EI_p \kappa_1^2 + 2(EA_p \epsilon_{x0}^r - EA\epsilon_{xp}^i)\epsilon_{x2}^r - \omega^2 \rho A_p w_1^2]\, dx}{\sum_i \int_o^{l_i} \rho A w_1^2 dx}. \quad (42)$$

Note that the first term in the numerator of equation (42) accounts for the change in bending stiffness, the second term accounts for change in axial forces, and the third term accounts for the change in inertia properties.

Consider, for example, a simply-supported beam shown in Fig. 1. The beam is heated to a temperature T above its stress-free state, resulting in an axial member force and mechanical strain

$$N_0 = -EA\alpha T, \quad \epsilon_{x0}^r = N_0/EA = -\alpha T \quad (43)$$

where α is the coefficient of thermal expansion. The temperature T is selected to produce a member force equal to half of the buckling load

$$T = \frac{\pi^2 I}{2A\alpha l^2}. \quad (44)$$

The vibration mode for the beam is in the form

$$w_1 = B \sin \frac{\pi x}{l} \quad (45)$$

where B is an arbitrary constant. The vibration frequency, equation (39) is given by

$$\omega^2 = \frac{\pi^4 EI + \pi^2 N_0 l^2}{\rho A l^4}. \quad (46)$$

The adjoint initial strain $-1/2\ w_{1,x}^2$ is equivalent to nonuniform cooling of the beam. It results in a tensile member force N_2 producing a constant strain $\epsilon_{x2}^r = N_2/AE$ which counteracts the required shortening due to the initial strain

$$\epsilon_{x2}^r l = \int_o^l \left(-\frac{1}{2}\right) w_{1,x}^2 dx = \pi^2 B^2 / 4l. \quad (47)$$

Equation (42) can now be evaluated with the aid of equations (43), (44), (46), and (47) as

$$(\omega^2)_p = \frac{\pi^4 E}{A \rho l^4} \left(I_p - \frac{A_p I}{2A} - \frac{A_p I}{2A} \right). \quad (48)$$

The reason that the two identical terms in equation (48) are written separately is to preserve the correspondence with equation (42). It is seen that the second term associated with the change in axial load due to change in area is of equal magnitude with the third term, which accounts for the change in inertia. Equation (48) can be easily verified directly by differentiating equations (43) and (46) with respect to p.

Plate Example

The first example that demonstrates the use of the adjoint approach for derivatives of buckling loads is the square plate under uniaxial edge compression shown in Fig. 2. The plate is divided into two regions, and the effects of increasing the thickness or the temperature in the central region are investigated. The calculations are performed using the EAL finite element program (Whetstone, 1983) which supports a programming language (Engineering Analysis Language). A procedure written in that language for applying initial strain loading was used, but it was limited to uniform strains in an element.

To produce the initial strain for the adjoint structure, $L_2(u_1)$ (cf., equation (24)) was calculated at the four nodes of each element and the average value used. The first term in the numerator of equation (32) was calculated using the equivalent $U^T K_p U$ where U is the buckling mode and K the global stiffness matrix. The derivative K_p was calculated by forward difference with a step size of one percent of the thickness. The second term was calculated at the element level because it cannot be expressed in terms of global matrices. The denominator of equation (32), not including live loads, is normalized to unity in EAL.

The plate was modeled using square grids with 4 to 16 EAL elements, type E43, per side. These elements model both the in-plane prebuckling deformations as well as the out-of-plane displacements associated with buckling. The results for the buckling load and its derivative with respect to temperature change in region 1 are given in Table 1. The analytical derivatives are compared to finite difference derivatives. It is seen that the convergence of the semianalytical derivatives with mesh refinement is slower than that of the finite difference derivatives. This is due to the constant-strain modeling in the EAL procedure. The agreement, however, is quite good except for the crudest mesh.

Similar results are given in Table 2 for derivatives of the buckling load with respect to change in thickness in region 2. It is seen that the term accounting for the change in prebuckling stresses is responsible for about ten percent of the derivative.

Composite Cylindrical Panel

The second example is an infinitely long 2-layer composite cylindrical panel under edge shear loading. This is shown in Fig. 3, which also gives geometric data, lamina moduli, and boundary conditions.

The panel wall is a regular antisymmetric angle-ply laminate. The sensitivity parameter is the outer layer fiber angle, α, measured from the longitudinal direction, with positive α corresponding to rotation of the layer towards the direction of maximum tension under the pure shear load (see Fig. 3.). As the outer layer rotates, it is assumed that the inner layer rotates by the same angle, α, but in the opposite direction. Thus, in general, the stacking sequence is [90 deg-α, α].

The calculations were performed using FASOR, a shell-of-revolution program (Cohen, 1981). The FASOR model for an infinitely long, cylindrical panel is a large radius toroidal shell of revolution with a circular arc meridian, as depicted in Fig. 3. Note that the circumferential direction of the toroidal model corresponds to the longitudinal direction of the panel. For large values of the ratio of circumferential radius r of the toroid to panel-width B, the toroid behaves like a long, cylindrical panel.

Studies of panels based on the approximate Karman-Donnell shell theory have shown that their geometry is specified by the curvature parameter $\theta = B/(Rh)^{1/2}$ (e.g., Hui and Du, 1987). Thus, for a given value of θ, the response should be relatively insensitive to R/h. Indeed, a spot check for $\alpha = 0$ deg on the effect of changing R/h from 100 to 1000 showed a change of 0.5 percent in critical stress and 2.6 percent in its sensitivity derivative.

It should be noted that the cross-ply laminate ($\alpha = 0$ deg) is orthotropic in panel coordinates; hence, no shear-extension coupling exists. Since an antisymmetric cross-ply laminate also has no shear-twist coupling (Jones, 1975), its prebuckling state is a membrane state of pure shear. On the other hand, for $\alpha \neq 0$ deg the laminate is anisotropic with coupling between shear and extension/flexure. Therefore, in this case the possible effect of prebuckling rotation and nonlinearity on buckling must be considered.

The effect of α on the buckling of the panel is shown in Fig. 4 in terms of the dimensionless buckling load $\tau^* = N_{xy}^* R/E_2 h^2$ and the second post-buckling coefficient b^1 (Cohen and Haftka, 1989). From the results in Fig. 4 it is seen that, initially, rotation of the fibers towards the direction of maximum tension (and, hence, away from the direction of maximum compression) increases panel stability. As α increases from

[1] b-values are based on a buckling mode normalized such that its maximum normal deflection equals the panel thickness.

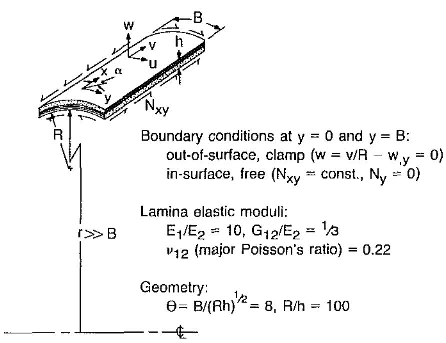

Fig. 3 Two-Ply composite [90 deg-α, α] long cylindrical panel

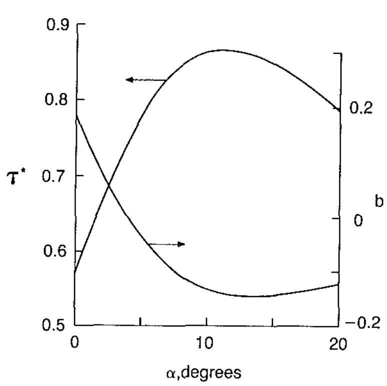

Fig. 4 Critical shear stress τ^* and postbuckling coefficient b as a function of ply angle α for panel of Fig. 3

Table 1 Buckling loads and their derivatives with respect to temperature change in region 1 of plate of Fig. 2

Mesh	Buckling load[a] (lb)	Adjoint method derivative (lb/°F)	Finite difference derivative[b] (lb/°F)
4×4	412.40	−37.61	−29.11
8×8	411.31	−32.16	−30.23
12×12	411.25	−31.30	−30.46
16×16	411.24	−31.01	−30.54

[a]Exact value $= 4\pi^2 D/a = 411.234$ lb

[b]Central differences with 1°F increment

Table 2 Derivatives of buckling loads with respect to thickness change in region 2 of plate of Fig. 2

	Analytical Derivative (lb/in)			
Mesh	due to change in prebuckling stress	due to change in stiffness	Total	Finite difference derivative[a] (lb/in)
4×4	−852	8586	7734	7708
8×8	−799	8622	7823	7886
12×12	−775	8622	7847	7916
16×16	−766	8623	7857	7927

[a]Forward difference with 1 percent increment

Table 3 Dimensionless buckling load ($\tau^* = N_{xy}^* R/E_2 h^2$) and its derivative with respect to ply-angle α of panel of Fig. 3

			$d\tau^*/d\alpha$ (deg^{-1})	
α(deg)	τ^*	$L/2B$[a]	Adjoint method[b]	Finite difference method[c]
0	0.5734	0.600	0.0459	0.0462
10	0.8652	1.672	0.0018	0.0002
20	0.7863	1.754	−0.0114	−0.0120

[a] L = longitudinal buckle wave length
[b] Equation ($A8$) using $\Delta D/\Delta\alpha$ ($\Delta\alpha = 1$ deg) for D_p
[c] $\Delta\tau^*/\Delta\alpha$ ($\Delta\alpha = 1$ deg)

Table 4 Effect of $\Delta\alpha$ on $d\tau^*/d\alpha$ for $\alpha = 10$ deg for panel of Fig. 3

	$d\tau^*/d\alpha$ (deg^{-1})	
$\Delta\alpha$ (deg)	Adjoint method	Finite difference method
1.0	0.00185	0.00025
0.1	0.00256	0.00187
0.05	0.00260	0.00208
0.025	0.00262	0.00226

zero to ten degrees, the panel is stabilized by the appearance of longitudinal tension arising from the shear-extension coupling. However, as also shown in Fig. 4, this increase in critical shear stress is accompanied by a transition from insensitivity to geometric imperfections ($b>0$) to imperfection-sensitivity ($b<0$) at $\alpha \doteq 4$ deg. Beyond ten degrees the longitudinal tension peaks and the effect of rotating the fibers away from the direction of maximum compression asserts itself so that the buckling load decreases.

Results for the critical shear load and its derivative, with respect to α, are given for $\alpha = 0$, 10 deg, 10 deg and 20 deg in Table 3. Buckling deflection profiles at two longitudinal stations spaced one-quarter wavelength apart are shown for $\alpha = 0$ deg in Fig. 5.

For $\alpha = 10$ deg, near the maximum of τ^* there is a large discrepancy between the adjoint and finite difference results. This is due to $\Delta\alpha$ of one deg being inappropriately large near a stationary point. Table 4 shows that the two values converge as $\Delta\alpha$ is decreased. However, the exact value of the derivative at $\alpha = 10$ deg is of little value because it is practically zero.

Concluding Remarks

A uniform variational approach to sensitivity analysis of vibration frequencies and bifurcation loads in nonlinear structures has been developed. Two methods of calculating sensitivities of vibration frequencies of loaded structures and bifurcation buckling loads with respect to stiffness and initial strain parameters have been presented. A direct method requires calculation of the sensitivity of the prebuckling state with respect to the parameters. An adjoint method bypasses the need for these derivatives by using instead an adjoint field. The adjoint field is the same as the second-order post-buckling field for symmetric bifurcation. This fact provides a link between post-buckling and sensitivity analysis. In particular, imperfection sensitivity can be incorporated into the general framework of sensitivity analysis, with respect to stiffness and shape parameters.

The derivation, based on the principle of virtual work, is easily implemented in structural analysis programs. This has been demonstrated by two examples. The EAL general finite element program is used to obtain derivatives of buckling loads of a square plate with respect to initial strain and thickness changes. The FASOR shell-of-revolution program is used to obtain derivatives of buckling loads of an angle-ply cylindrical panel with respect to ply angles. In both cases good agreement of analytical and finite difference derivatives is obtained.

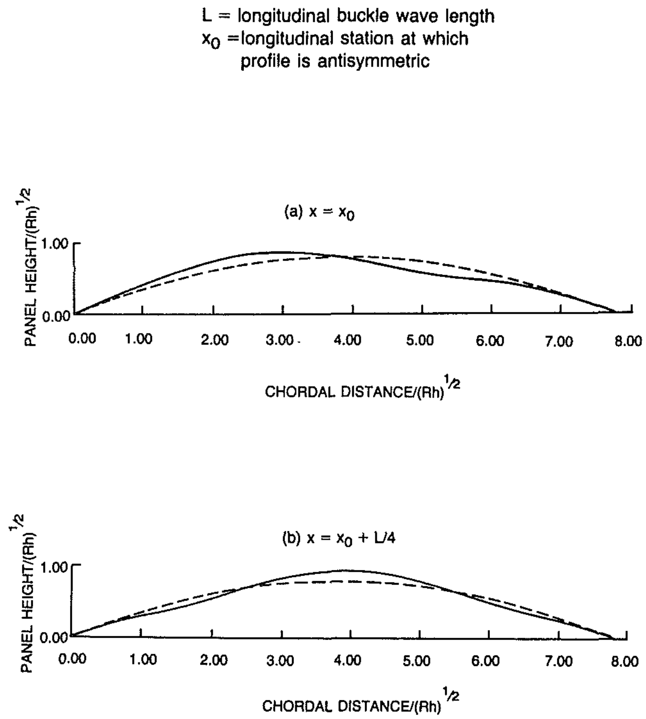

Fig. 5 Undeformed profiles (dashed lines) and buckled profiles (solid lines) of cylindrical panel of Fig. 3, $\alpha = 0$

Acknowledgment

This work was supported in part by NASA grant NAG-1-224.

References

Adelman, H. M., and Haftka, R. T., 1986, "Sensitivity Analysis for Discrete Structural Systems," *AIAA Journal*, Vol. 24, pp. 823–832.

Barthelemy, B. M., Haftka, R. T., and Cohen, G. A., 1989, "Physically Based Sensitivity Derivatives for Structural Analysis Programs," *Computational Mechanics*, Vol. 4, pp. 465–476.

Budiansky, B., and Hutchinson, J. W., 1964, "Dynamic Buckling of Imperfection Sensitive Structures," *Proceeding XI International Congress of Applied Mechanics*, H. Gortner, ed., Springer-Verlag, Berlin, pp. 636–651.

Cohen, G. A., 1968, "Effect of Nonlinear Prebuckling State on the Postbuckling Behavior and Imperfection Sensitivity of Elastic Structures," *AIAA Journal*, Vol. 6, pp. 1616–1619.

Cohen, G. A., 1981, "FASOR—A Program for Stress, Buckling, and Vibration of Shells of Revolution," *Advances in Engineering Software*, Vol. 3, pp. 155–162.

Cohen, G. A., and Haftka, R. T., 1989, "Sensitivity of Buckling Loads of Anisotropic Shells of Revolution to Geometric Imperfections and Design Changes," *Computers and Structures*, Vol. 31, pp. 985–995.

Haichang, Hu, 1984, *Variational Principles of Theory of Elasticity with Applications*, Gordon and Breach Sci. Publ., New York.

Hui, D., and Du, I.H.Y., 1987, "Imperfection-Sensitivity of Long Antisymmetric Cross-Ply Cylindrical Panels under Shear Loads," ASME Journal of Applied Mechanics, Vol. 54, pp. 292–298.

Jones, R. M., 1975, *Mechanics of Composite Materials*, McGraw-Hill, New York, p. 168.

Khot, N. S., 1981, "Optimal Design of a Structure for System Stability for a Specified Eigenvalue Distribution," *International Symposium on Optimum Structural Design*, Tucson, Ariz., Oct., pp. 1–3.

Mróz, Z., 1987, "Sensitivity Analysis and Optimal Design with Account for

Varying Shape and Support Conditions," *Computer Aided Optimal Design, Structural and Mechanical Systems*, C.A. Mota Soares, ed., Springer-Verlag, New York, pp. 407-438.

Mróz, Z., and Haftka, R. T., 1988, "Sensitivity of Buckling Loads and Vibration Frequencies of Plates," *Josef Singer Anniversary Volume*, Springer-Verlag, New York.

Mróz, Z., Kamat, M. P., and Plaut, R. H., 1985, "Sensitivity Analysis and Optimal Design of Non-linear Beams and Plates," *J. Struct. Mech.*, Vol. 13, pp. 245-266.

Szefer, G., Mróz, Z., and Demkowicz, L., 1988, "Variational Approach to Sensitivity Analysis in Nonlinear Elasticity," *Arch. Mech.*, in press.

Whetstone, W. D., 1983, *EISI EAL Engineering Analysis Language Reference Manual*, Engineering Information Systems, Inc., July.

APPENDIX

Error in Bifurcation Buckling Load Derivative due to Linearized Buckling Solution

Typically, equations (9) are solved for the buckling load λ_c by setting $\omega=0$ and using a linear approximation for the critical prebuckling state based on the response at a lower level λ_0, viz.

$$\begin{aligned} u_0^* &\doteq \bar{u}_0 = u_0(\lambda_0) + \mu u_0'(\lambda_0) \\ \epsilon_0^* &\doteq \bar{\epsilon}_0 = \epsilon_0(\lambda_0) + \mu\epsilon_0'(\lambda_0) \\ \sigma_0^* &\doteq \bar{\sigma}_0 = \sigma_0(\lambda_0) + \mu\sigma_0'(\lambda_0) \end{aligned} \tag{A1}$$

where $\mu = \lambda_c - \lambda_0$. Equations (9) are then approximated by

$$\begin{aligned} &\epsilon_1 = L_1(u_1) + L_{11}(\bar{u}_0, u_1) \\ &\sigma_1 = D\epsilon_1 \\ &\sigma_1 \cdot [L_1(\delta u) + L_{11}(\bar{u}_0, \delta u)] + \bar{\sigma}_0 \cdot L_{11}(u_1, \delta u) - \lambda_c q_1(u_1)\cdot\delta u = 0. \end{aligned} \tag{A2}$$

Differentiating equations ($A2$) with respect to p, and then setting $\delta u = u_1$, we get

$$\begin{aligned} &\epsilon_{1p} = L_1(u_{1p}) + L_{11}(\bar{u}_{0p} + \mu_p u_0', u_1) + L_{11}(\bar{u}_0, u_{1p}) \\ &\sigma_{1p} = D_p\epsilon_1 + D\epsilon_{1p} \\ &\sigma_{1p}\cdot\epsilon_1 + \sigma_1\cdot L_{11}(\bar{u}_{0p} + \mu_p u_0', u_1) \\ &+ (\bar{\sigma}_{0p} + \mu_p\sigma_0')\cdot L_2(u_1) + \bar{\sigma}_0\cdot L_{11}(u_1, u_{1p}) \\ &\qquad - \lambda_c q_1(u_{1p})\cdot u_1 - \mu_p q_1(u_1)\cdot u_1 = 0 \end{aligned} \tag{A3}$$

where $\bar{u}_{0p} = u_{0p} + \mu u_{0p}'$ and $\bar{\sigma}_{0p} = \sigma_{0p} + \mu\sigma_{0p}'$ are the derivatives with respect to p of the linear approximation state. We first eliminate the derivaties of the buckling field with respect to p by setting $\delta u = u_{1p}$ in equation ($A2c$) and using equations ($A3a$, b) and ($A2b$) to get

$$\mu_p = -\frac{D_p\epsilon_1\cdot\epsilon_1 + 2\sigma_1\cdot L_{11}(\bar{u}_{0p}, u_1) + \bar{\sigma}_{0p}\cdot L_2(u_1)}{2\sigma_1\cdot L_{11}(u_0', u_1) + \sigma_0'\cdot L_2(u_1) - q_1(u_1)\cdot u_1}. \tag{A4}$$

Equation ($A4$) is identical in form to equation (22), with starred quantities in equation (22) replaced by linear approximations. To calculate $\bar{u}_{0p}$ and $\bar{\sigma}_{0p}$ we differentiate equations (16) with respect to λ to get

$$\begin{aligned} &\epsilon_{0p}' = L_1(u_{0p}') + L_{11}(u_0, u_{0p}') + L_{11}(u_0', u_{0p}) \\ &\sigma_{0p}' = D\epsilon_{0p}' + D_p\epsilon_0' \\ &\sigma_{0p}'\cdot\delta\epsilon_0 + \sigma_0'\cdot L_{11}(u_{0p}, \delta u) + \sigma_{0p}\cdot L_{11}(u_0', \delta u) \\ &\qquad + \sigma_0\cdot L_{11}(u_{0p}', \delta u) - [\lambda_0 q_1(u_{0p}') + q_1(u_{0p})]\cdot\delta u = 0. \end{aligned} \tag{A5}$$

Multiplying equations ($A5$) by μ and adding to equations (16) we have

$$\begin{aligned} &\bar{\epsilon}_{0p} = L_1(\bar{u}_{0p}) + L_{11}(\bar{u}_0, \bar{u}_{0p}) - \mu^2 L_{11}(u_0', u_{0p}') \\ &\bar{\sigma}_{0p} = D(\bar{\epsilon}_{0p} - \epsilon_p^i) + D_p\bar{\epsilon}_0^r \\ &\bar{\sigma}_{0p}\delta\bar{\epsilon}_0 + \bar{\sigma}_0\cdot L_{11}(\bar{u}_{0p}, \delta u) - \lambda_c q_1(\bar{u}_{0p})\cdot\delta u \\ &- \mu^2[\sigma_{0p}'\cdot L_{11}(u_0', \delta u) + \sigma_0'\cdot L_{11}(u_{0p}', \delta u) + q_1(u_{0p}')\cdot\delta u] = 0. \end{aligned} \tag{A6}$$

Except for the terms in μ^2, equations ($A6$) are of the form of equations (16).

The adjoint equations (24) are approximated by

$$\begin{aligned} &\epsilon_2 = L_1(u_2) + L_{11}(\bar{u}_0, u_2) \\ &\sigma_2 = D(\epsilon_2 + \frac{1}{2}L_2(u_1)) = D\epsilon_2^r \\ &\sigma_2\cdot\delta\bar{\epsilon}_0 + \bar{\sigma}_0\cdot L_{11}(u_2, \delta u) - \lambda_c q_1(u_2)\cdot\delta u + \sigma_1\cdot L_{11}(u_1, \delta u) = 0. \end{aligned} \tag{A7}$$

Equations ($A6$) and ($A7$) can be used to eliminate $\bar{u}_{0p}$ and $\bar{\sigma}_{0p}$ in equations ($A4$), in the same manner that equations (16) and (24) were used to elminate u_{0p}^* and σ_{0p}^* in equation (22), to yield the result

$$\mu_p = -\frac{D_p\epsilon_1\cdot\epsilon_1 + 2(D_p\bar{\epsilon_0}^r - D\epsilon_p^i)\cdot\epsilon_2^r + 0(\mu^2)}{2\sigma_1\cdot L_{11}(u_0', u_1) + \sigma_0'\cdot L_2(u_1) - q_1(u_1)\cdot u_1}. \tag{A8}$$

Except for terms of order μ^2, equation ($A8$) has the same form as equation (32). In practice, equation ($A8$) with $0(\mu^2)$ neglected is used to calculate $(\lambda_c)_p = \mu_p$.

M. Y. Sheh
Mem. ASME

D. C. Stouffer
Mem. ASME

Department of Aerospace Engineering and Engineering Mechanics,
University of Cincinnati,
Cincinnati, Oh 45221-0070

A Crystallographic Model for the Tensile and Fatigue Response for René N4 at 982°C[1]

An anisotropic constitutive model based on crystallographic slip theory was formulated for nickel-base single crystal superalloys. The current equations include both drag stress and back stress state variables to model the local inelastic flow. Specially designed experiments have been conducted to evaluate the existence of back stress in single crystals. The results showed that the back stress effect of reverse inelastic flow on the unloading stress is orientation dependent, and a back stress state variable in the inelastic flow equation is necessary for predicting anelastic behavior. Model correlations and predictions of experimental data are presented for the single crystal supperalloy René N4 at 982°C.

I Introduction

Nickel-base single crystal superalloys attract considerable interest for use in rocket and gas turbine engines because their high temperature properties are superior to those of polycrystalline nickel-base superalloys. In high temperature applications, grain boundaries in polycrystalline alloys provide passages for fast diffusion and oxidation. Thus, intercrystalline cracks frequently occur at the grain boundaries and cause rupture failure. The development of superalloy single crystals has led to far superior thermal, fatigue, and creep properties than conventional superalloys. However, the absence of grains in single crystal alloys leads to material anisotropy which produces orientation-dependent material response in addition to other time-dependent inelastic properties found in polycrystalline materials. Hence, constitutive modeling of the single crystal alloys is more difficult and requires a more comprehensive understanding of the structural and mechanical properties and the associated deformation mechanisms.

Single crystal alloys exhibit cubic symmetry and the response is quite different from polycrystalline materials. The elastic stress-strain relationship is orientation dependent. Three material elastic constants, i.e., elastic modulus, shear modulus, and Poisson's ratio, are required to describe the single crystal elastic behavior (Yang, 1984).

The yield strength of single crystal alloys is a function of the material orientation relative to the direction of the applied stress (Shah and Duhl, 1984). Single crystal superalloys also exhibit significant tension/compression asymmetry in yield strength (Lall et al., 1979; Ezz et al., 1982; Umakoshi et al., 1984; Heredia and Pope 1986; Miner et al., 1986a). This behavior is primarily due to slip on the octahedral slip system. The tension/compression asymmetry is negligible near the [111] orientation where cube slip was found to be the primary slip system. Above a critical temperature, approximately 700–760°C, there is a sharp drop in the yield strength, cube slip becomes more predominant, and the tension/compression asymmetry is less significant (Shah and Duhl, 1984; Heredia and Pope, 1986; Gabb et al., 1986). Single crystal superalloys also exhibit strain rate sensitivity and cyclic hardening (Swanson et al., 1984).

The active slip systems in single crystal superalloys depend upon crystal orientation with respect to the applied loads, temperature, and strain rate, and could involve one or more types of slip. Three primary slip systems include:

- slip on the four {111} octahedral planes in the three directions similar to the ⟨110⟩ direction.
- slip on the four {111} octahedral planes in the three directions similar to the ⟨112⟩ direction.
- slip on the three ⟨100⟩ cube planes in the two directions similar to the ⟨110⟩ direction.

There are 30 possible slip components in total as shown in Table 1. Generally, these slip components are not all operative simultaneously. For high strain-rate loading, both octahedral and cube slip in the ⟨110⟩ directions were found for many nickel-base single crystal alloys (Miner et al., 1986a; Milligan and Antolovich, 1987), whereas for low strain-rate loading such as creep, the active slip systems and associated crystal lattice rotation are different from one alloy to another (Leverant and Kear, 1970; MacKay and Maier, 1982; Hopgood and Martin, 1986). The modeling for low strain is discussed elsewhere (Sheh, 1988).

The model proposed in this study is based on a previous work by Dame and Stouffer (1986), where the Bodner-Partom (1975) equation, with only the drag stress, was used to model the local inelastic response in each slip system. The Dame and Stouffer model was based on a unified strain theory. The elastic strains were calculated by using cubic symmetry. The

[1] This research was supported by NASA Grant NAG3-511 to the University of Cincinnati.

Contributed by the Applied Mechanics Division of THE AMERICAN SOCIETY OF MECHANICAL ENGINEERS for publication in the JOURNAL OF APPLIED MECHANICS.

Discussion on this paper should be addressed to the Technical Editor, Prof. Leon M. Keer, The Technological Institute, Northwestern University, Evanston, IL 60208, and will be accepted until two months after final publication of the paper itself in the JOURNAL OF APPLIED MECHANICS. Manuscript received by the ASME Applied Mechanics Division, August 16, 1988; final revision, April 24, 1989.

Table 1 Designated slip number, slip plane normal, and slip direction for each slip system

Slip No.	α*	l*	Slip No.	α	l
		Octahedral Slip $a/2\langle 110\rangle\{111\}$			
1	[1 1 1]	[1 0 −1]	7	[1 −1 −1]	[1 1 0]
2	[1 1 1]	[0 −1 1]	8	[1 −1 −1]	[0 −1 1]
3	[1 1 1]	[1 −1 0]	9	[1 −1 −1]	[1 0 1]
4	[−1 1 −1]	[1 0 −1]	10	[−1 −1 1]	[0 1 1]
5	[−1 1 −1]	[1 1 0]	11	[−1 −1 1]	[1 0 1]
6	[−1 1 1]	[0 1 1]	12	[−1 −1 1]	[1 −1 0]
		Octahedral Slip $a/2\langle 112\rangle\{111\}$			
13	[1 1 1]	[−1 2 −1]	19	[1 −1 −1]	[−1 1 −2]
14	[1 1 1]	[2 1 −1]	20	[1 −1 −1]	[2 1 1]
15	[1 1 1]	[−1 1 2]	21	[1 −1 −1]	[−1 −2 1]
16	[−1 1 −1]	[1 2 1]	22	[1 −1 1]	[−2 1 −1]
17	[−1 1 1]	[1 −1 −2]	23	[−1 −1 1]	[1 −2 −1]
18	[−1 1 −1]	[−2 −1 1]	24	[−1 −1 1]	[1 1 2]
		Cube Slip $a/2\langle 110\rangle\{100\}$			
25	[1 0 0]	[0 1 1]	28	[0 1 0]	[1 0 −1]
26	[1 0 0]	[0 1 −1]	29	[0 0 1]	[1 1 0]
27	[0 1 0]	[1 0 1]	30	[0 0 1]	[−1 1 0]

*The direction expressed by the Miller indices does not represent the unit vector in the direction.
α: slip plane normal; **l**: slip direction

inelastic strain rate was calculated by summing the contributions of slip in each slip system. The inelastic slip rate on each slip system was computed from a local inelastic constitutive equation that depended on the resolved shear stress component in each slip direction and a local state variable. A non-Schmid's law was used for slip on the first octahedral system, $a/2\{111\}\langle 110\rangle$, to model the tension/compression asymmetry and orientation dependence. This was achieved by incorporating the "core width" effect proposed by Lall, Chin, and Pope (1979). A Schmid's law component in the flow equation was used to model the inelastic flow in the cube slip system because tension/compression asymmetry was insignificant.

The objective of the present paper is to present an anisotropic consitituve model for nickel-base single crystal superalloys under isothermal loading conditions. In the proposed model, a back-stress state variable has been incorporated into the local slip equation based on the observed experimental evidence. As a result of this modification, fatigue loop prediction is significantly improved and material behavior such as anelasticity can be modeled. Comparisons of the model predictions and experimental data for single crystal superalloy René N4 at 982°C are presented.

II The Presence of Back Stress

Dame and Stouffer (1986) assumed that back stress should not be present or, if present, it should be negligible in single crystal alloys because of the lack of grain boundaries (the primary source of back stress build-up). Thus, only the drag stress was included in their model. At about the same time, Walker and Jordan (1985) proposed a model with back stress for single crystal superalloys similar to earlier work by Walker (1981). Thus, the presence of back stress is an issue that needs clarification. Recent experimental observation supports the existence of the back stress in single crystals. Milligan and Antolovich (1987) showed for PWA1480, that when dislocations emerge from precipitates, constrictions of the dislocations occur because of high antiphase boundary energy (APBE); thus portions of the dislocations are split because of elastic repulsion. This suggests that back stress should be a component in the local force equilibrium equation. Other mechanisms have also been suggested for establishing back stress in single crystals (Jackson, 1986). These include cross-slip, which establishes a framework of dislocation cells; secondary slip, which completes the formation of relatively stress-free dislocation cells; and local slip within dislocation-rich load-bearing cell walls.

An early goal in this research was to confirm the need for a back stress state variable in the current model. To achieve this goal, an experiment was designed based on the structure of the inelastic flow equation with back stress Ω_{ij}:

$$\dot{\epsilon}^{I}_{ij} = \lambda(\sigma_{ij} - \Omega_{ij}), \tag{1}$$

where λ is a scalar function of macroscopic and state variables that maps the overstress, $\sigma_{ij} - \Omega_{ij}$, onto the inelastic strain rate, $\dot{\epsilon}^{I}_{ij}$. Equation (1) reveals that inelastic flow can be present even when the applied stress, σ_{ij}, is zero, as long as the back stress is large enough to produce meaningful strain rates. Using this hypothesis, two experiments at 982°C were conducted on René N4 samples. Figure 1 shows the results of a double tensile test in the [100] and [111] orientations. In both tests, the sample was loaded to 1.5 percent strain at a strain rate of 1×10^{-4}/sec, unloaded to zero stress within 10 seconds, followed by the 120-second zero-stress hold period, and then reloaded at a higher strain rate of 6×10^{-4}/sec. The reverse inelastic strain histories during the hold period are shown for both samples in Fig. 2. (The model predictions expressed in solid lines in these figures will be discussed later). Significant anelastic recovery was observed during the zero stress hold period for the [100] sample whereas the recovery was minimal for the sample in the [111] orientation.

These results clearly demonstrate the existence of back stress and the orientation dependency of the recovery mechanism. They also suggest that without the back-stress term in the flow equation similar to equation (1), anelastic recovery cannot be predicted. These experiments motivated the development of a new model using back stress and drag stress for single crystal superalloys at elevated temperatures as will be discussed.

III Constitutive Equations

The constitutive model is based on a unified theory that separates the total strain in the principal axes of the material into elastic and inelastic components; that is:

$$\epsilon_{ij}^T = \epsilon_{ij}^E + \epsilon_{ij}^I, \tag{2}$$

where ϵ_{ij}^T is the total strain, ϵ_{ij}^E is the elastic strain component, and ϵ_{ij}^I is the inelastic strain components in the principal material system. The thermal strain is not included in equation (2) because the proposed model is developed for isothermal conditions. The elastic constitutive equation for cubic symmetry in the material principal axes can be written as

$$\begin{bmatrix} \epsilon_{11} \\ \epsilon_{22} \\ \epsilon_{33} \\ \epsilon_{23} \\ \epsilon_{31} \\ \epsilon_{12} \end{bmatrix}^E = \begin{bmatrix} \frac{1}{E} & -\frac{\nu}{E} & -\frac{\nu}{E} & 0 & 0 & 0 \\ -\frac{\nu}{E} & \frac{1}{E} & -\frac{\nu}{E} & 0 & 0 & 0 \\ -\frac{\nu}{E} & -\frac{\nu}{E} & \frac{1}{E} & 0 & 0 & 0 \\ 0 & 0 & 0 & \frac{1}{2G} & 0 & 0 \\ 0 & 0 & 0 & 0 & \frac{1}{2G} & 0 \\ 0 & 0 & 0 & 0 & 0 & \frac{1}{2G} \end{bmatrix} \begin{bmatrix} \sigma_{11} \\ \sigma_{22} \\ \sigma_{33} \\ \sigma_{23} \\ \sigma_{31} \\ \sigma_{12} \end{bmatrix}, \tag{3}$$

where the stress is denoted by σ_{ij}. The compliance matrix in equation (3) contains three independent material constants: Young's modulus E, Poisson's ratio ν, and the shear modulus G. Using this elastic stress-strain relationship, the orientation dependence in the elastic range can be modeled by transforming equation (3) into any other orientation.

Since the inelastic constitutive equations are applied at the crystallographic level, a kinematic relationship is required to relate the stress tensor in the material principal axes to the resolved shear stresses on each slip system. In addition, the inelastic strain rate in the material principal axes must be determined from the components of slip in each slip system. The required stress and infinitesimal strain relations were developed by Bishop (1952) and Paslay et al. (1970) and are used in this study.

The orientation dependence of the hardening characteristics in the inelastic region is modeled by using the inelastic flow equation. The inelastic flow is calculated by summing the contributions of the first octahedral and cube slip systems, that is:

$$\dot{\epsilon}_{ij}^I = (\dot{\epsilon}_{ij}^I)_{\text{OCT}} + (\dot{\epsilon}_{ij}^I)_{\text{CUBE}}, \tag{4}$$

where $(\dot{\epsilon}_{ij}^I)_{\text{OCT}}$ and $(\dot{\epsilon}_{ij}^I)_{\text{CUBE}}$ represent the inelastic strain rates resulting from octahedral and cube slip in the $\langle 110\rangle$ directions, respectively. It has been shown (Leverant and Kear, 1970; MacKay and Maier, 1982) that slip in the second octahedral system, $a/2\langle 112\rangle\{111\}$, occurs only during low strain-rate loading and is not included in the formulation for the tensile and fatigue response at this time. The inelastic strain rate in the principal material direction is calculated by summing the contributions from each of the crystallographic slip systems using results in Bishop (1952) or Pasley et al. (1970). The total inelastic strains are then obtained by integrating the inelastic strain rate with time. Formulation of the local inelastic flow equation for each of the two slip systems is introduced next.

Octahedral Slip of $a/2\langle 100\rangle\{111\}$ Type. Based on the work of Ramaswamy on René 80 (1986), a polycrystalline nickel-base superalloy with similar chemical composition as René N4, the octahedral flow equation for the inelastic shear strain rate, $\dot{\gamma}_{\text{OCT}}^{\alpha\beta}$, in the β direction on the α slip plane is assumed to have similar exponential form with both drag and back stress; that is:

$$\dot{\gamma}_{\text{OCT}}^{\alpha\beta} = D_1 \exp\left[-A_1\left(\frac{Z_1^{\alpha\beta}}{|\tau^{\alpha\beta} - \Omega_1^{\alpha\beta}|}\right)^{n_{11}}\right] \frac{\tau^{\alpha\beta} - \Omega_1^{\alpha\beta}}{|\tau^{\alpha\beta} - \Omega_1^{\alpha\beta}|}, \tag{5}$$

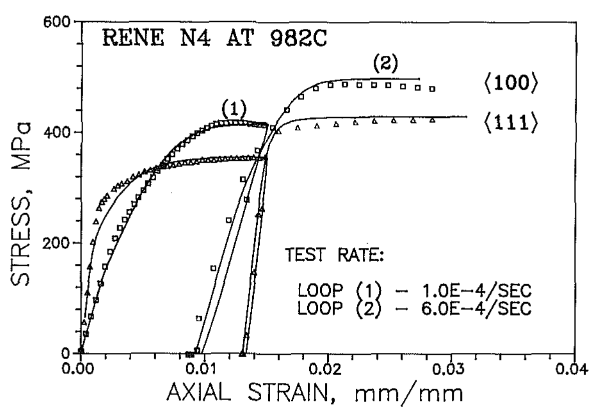

Fig. 1 Double tensile test with 120-second zero-stressd hold in the [100] and [111] orientations for René N4 at 982°C

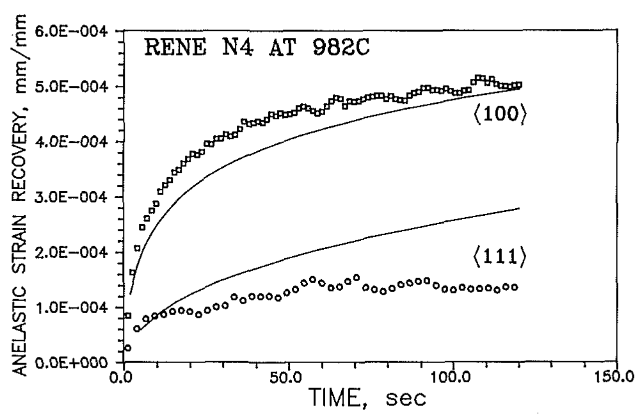

Fig. 2 Anelastic strain recovery during the 120-second zero-stress hold for the double tensile tests in the [100] and [111] orientations

where $Z_1^{\alpha\beta}$ is the drag stress state variable to characterize the mobile dislocation resistance to motion due to precipitates, and $\Omega_1^{\alpha\beta}$ is the back stress state variable used to describe dislocation interaction and/or rearrangements. The difference between the resolved shear stress, $\tau^{\alpha\beta}$, and the back stress, $\Omega_1^{\alpha\beta}$, serves as the driving force for the inelastic flow. The direction of the local slip rate, $\dot{\gamma}_{OCT}^{\alpha\beta}$, is then dependent on the sign of the overstress $\tau^{\alpha\beta}-\Omega_1^{\alpha\beta}$. Constants D_1 and A_1 are scale factors and n_{11} is the strain-rate sensitivity exponent.

Formulation of the back stress component varies among different investigators. Ramaswamy (1986) suggested that the back stress can be written in elastic and inelastic components; that is:

$$\dot{\Omega}^{\alpha\beta}=(\dot{\Omega}^{\alpha\beta})^E+(\dot{\Omega}^{\alpha\beta})^I, \tag{6}$$

where elastic back stress rate is assumed to be linearly proportional to the resolved shear stress rate, and is motivated by the release of dislocation pile-ups when the stress is removed. The inelastic component, similar to Walker's (1981) and Ramaswamy's (1986) models, is given by:

$$(\dot{\Omega}_1^{\alpha\beta})^I=F_1\,|\dot{\gamma}_{OCT}^{\alpha\beta}|^{n_{12}}\left[\operatorname{sign}(\dot{\gamma}_{OCT}^{\alpha\beta})-\frac{\Omega_1^{\alpha\beta}}{\Omega_{SAT}{}^1}\right], \tag{7}$$

except for an exponent n_{12} which is added for more generality. Combining equations (6) and (7) gives the initial formulation for the back-stress evolution equation used in this study:

$$(\dot{\Omega}_1^{\alpha\beta})=F_1\,|\dot{\gamma}_{OCT}^{\alpha\beta}|^{n_{12}}\left[\operatorname{sign}(\dot{\gamma}_{OCT}^{\alpha\beta})-\frac{\Omega_1^{\alpha\beta}}{\Omega_{SAT}{}^1}\right]+G_1\dot{\tau}^{\alpha\beta}, \tag{8}$$

where n_{12}, F_1, G_1, and Ω_{SAT1} are material constants. The saturated back stress at high strain-rate loading conditions is denoted as Ω_{SAT1}; and, at strain rates in the creep range the saturated back stress is not constant (Ramaswamy (1986)). As shown in equation (8), the current formulation uses $|\dot{\gamma}_{OCT}^{\alpha\beta}|$ and $\dot{\gamma}^{\alpha\beta}$ as measures of back stress growth to control the strain-hardening behavior during high strain-rate loading.

According to the structure of the back stress evolution equation, the anelastic recovery effect is primarily controlled by the $G_1\dot{\gamma}^{\alpha\beta}$ term. If the elastic coefficient G_1 has a large value, the changes in back stress during elastic loading and unloading will be significant. Thus, for the double tensile test described earlier, the back stress may decrease significantly during unloading and result in a near zero back stress at the beginning of the 120-sec hold period. This small back stress might not be large enough to produce meaningful anelastic recovery during the hold period. However, if the material is less sensitive to the elastic component (e.g., smaller G_1), the anelastic recovery may be significant during the hold period because of the larger remaining back stress in the beginning of the hold period. This was found to be true for René N4 at 982°C and G_1 was taken as zero.

Dynamic thermal recovery is included through the $-\Omega_1^{\alpha\beta}/\Omega_{SAT1}$ term. Static thermal recovery was not evaluated in the current study. It should be noted that the back stress in the current model has a scalar form rather than the tensorial back stress in other models because local slip is unidirectional.

The variable $Z_1^{\alpha\beta}$ in equation (5) includes work or strain hardening which arises from the development of a dislocation substructure and includes a measure of tension/compression asymmetry. The drag stress, $Z_1^{\alpha\beta}$, used in this study is given by:

$$Z_1^{\alpha\beta}=H_1^{\alpha\beta}+V_1\,\tau_1^{\alpha\beta}+V_2\,|\tau_2^{\alpha\beta}|+V_3\tau_3^{\alpha\beta}, \tag{9}$$

where the parameter $H_1^{\alpha\beta}$ is a measure of work hardening, and $\tau_1^{\alpha\beta}$ and $\tau_2^{\alpha\beta}$ are the shear stress components associated with the "core width" effect and the cross-slip mechanism suggested by Lall et al. (1978). This mechanism was used to explain the tension/compression asymmetry in many $L1_2$ single crystal alloys (Ezz et al., 1982; Umakoshi et al., 1984; Heredia and Pope, 1986; Miner et al., 1986a). The shear stress $\tau_1^{\alpha\beta}$ is on the same octahedral plane and is perpendicular to $\tau^{\alpha\beta}$. The direction of $\tau_1^{\alpha\beta}$ controls the constriction or separation of the two Shockley partial dislocations in the γ' precipitates and, therefore, affects the ability of the dislocation to cross-slip from the octahedral plane to the cube plane. Thus, the tension/compression asymmetry is caused by the magnitude and sign of $\tau_1^{\alpha\beta}$. The shear stress $\tau_2^{\alpha\beta}$ is the resolved shear stress on the cube plane in the same direction as $\tau^{\alpha\beta}$. The magnitude of $\tau_2^{\alpha\beta}$ controls the potential of cross-slip in either direction on the cube plane, and therefore the absolute value of $\tau_2^{\alpha\beta}$ is used in equation (9).

Table 2 Slip system numbers for resolved shear stresses, τ_1, τ_2, and τ_3 in equation (9)

τ	τ_1	τ_2	τ_3	τ	τ_1	τ_2	τ_3
1*	13	28	16	7	19	29	17
2	14	26	20	8	20	26	14
3	15	30	24	9	21	27	23
4	16	28	13	10	22	25	18
5	17	29	19	11	23	27	21
6	18	25	22	12	24	30	15

*slip system number

Lall, Chin, and Pope's model was later modified by Paidar, Pope, and Vitek (1984) to include the resolved shear stress, $\tau_3^{\alpha\beta}$, in the ⟨121⟩ direction on the secondary octahedral slip plane. Paidar et al. (1984) found that $\tau_3^{\alpha\beta}$ has a similar effect to $\tau_1^{\alpha\beta}$, which also affects the anomalous yield behavior in $L1_2$ alloys. Thus, $\tau_3^{\alpha\beta}$, is included in the proposed equation. The constant parameters V_1, V_2, and V_3 are then used to establish the tension/compression asymmetry. A listing of the corresponding slip system number for τ_1, τ_2, and τ_3 is given in Table 2.

The increase in flow resistance caused by cyclic hardening, $H_1^{\alpha\beta}$, is governed by the evolution equation:

$$\dot{H}_1^{\alpha\beta}=m_1(H_{12}-H_1^{\alpha\beta})\tau^{\alpha\beta}\dot{\gamma}^{\alpha\beta}. \tag{10}$$

Replacing the inelastic work rate, $\tau^{\alpha\beta}\dot{\gamma}^{\alpha\beta}$, with the symbol $(\dot{W}^I)^{\alpha\beta}$, rearranging, and integrating with respect to time gives

$$H_1^{\alpha\beta}=H_{12}+(H_{11}-H_{12})\exp(-m_1(W^I)^{\alpha\beta}). \tag{11}$$

The quantities H_{11} and H_{12} are the initial and saturated values of $H_1^{\alpha\beta}$, respectively. The cylic hardening or softening is modeling by the increase or decrease of $H_1^{\alpha\beta}$ depending upon the values of H_{11} and H_{12}. The accumulated inelastic work is used as the measure of cyclic hardening. The parameter m_1 is the exponent associated with $(W^I)^{\alpha\beta}$ to model the rate of cyclic hardening or softening.

Cube Slip of $a/2\langle 100\rangle\{100\}$ Type. Cube slip components are active for loading near the [111] orientation. Mixed cube slip and octahedral slip components were operative during tensile tests in the orientations away from the [111]. Similar to equation (5), the flow equation for the inelastic shear strain-rate on the α-cube plane in the β-direction is given by

$$\dot{\gamma}_{CUBE}^{\alpha\beta}=D_2\exp\left[-A_2\left(\frac{Z_2^{\alpha\beta}}{|\tau^{\alpha\beta}-\Omega_2^{\alpha\beta}|}\right)^{n_{21}}\right]\frac{\tau^{\alpha\beta}-\Omega_2^{\alpha\beta}}{|\tau^{\alpha\beta}-\Omega_2^{\alpha\beta}|}, \tag{12}$$

where $Z_2^{\alpha\beta}$ and $\Omega_2^{\alpha\beta}$ are the drag stress and back stress state variables for the cube slip, respectively. Constants D_2 and A_2 are scaling factors and n_{21} is the strain-rate sensitivity exponent for cube slip.

The back-stress evolution equation for cube slip is also similar to the octahedral slip and has the form:

$$(\dot{\Omega}_2^{\alpha\beta})=F_2\,|\dot{\gamma}^{\alpha\beta}|^{n_{22}}\left[\operatorname{sign}(\dot{\gamma}^{\alpha\beta})-\frac{\Omega_2^{\alpha\beta}}{\Omega_{SAT}{}^2}\right]+G_2\dot{\tau}^{\alpha\beta}, \tag{13}$$

where n_{22}, F_2, and G_2 are material constants. The saturated back stress for the cube slip is denoted as Ω_{SAT2}. Parameter G_2 was also found to be near zero.

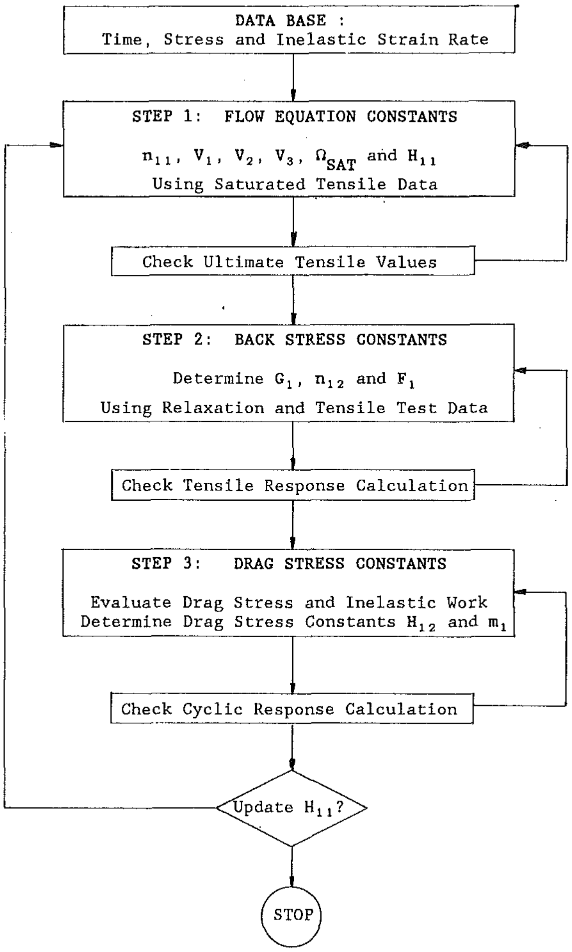

Fig. 3 Flow chart for inelastic material constant evaluation

The drag-stress evolution equation for cube slip is similar to equation (9) but it does not contain the tension/compression dependence terms (i.e., τ_1, τ_2, and τ_3 terms) because tension/compression asymmetry is insignificant for samples deformed primarily by cube slip; therefore, the formulation is similar to Schmid's law. The drag-stress evolution equation for the cube slip system in integrated form is given by:

$$Z_2^{\alpha\beta} = H_{22} + (H_{21} - H_{22}) \exp(-m_2 (W^I)^{\alpha\beta}), \qquad (14)$$

where H_{21}, H_{22}, and m_2 are determined from the fatigue response of the cube slip system. The static thermal recovery term is not included.

In summarizing, the current model uses a similar form of equations for both the octahedral and cube slip systems. The drag stress is used to capture the long-term cyclic hardening whereas the back stress is used for the short-time strain hardening and recovery in the monotonic tensile tests. This is distinctly different from the model proposed by Dame and Stouffer (1986) where a single drag stress was used to account for both the strain and cyclic hardening mechanisms.

IV Experimental Program and Material Constants

All the mechanical tests were performed at 982°C on a MTS closed-loop mechanical test system with a 20,000 kip load frame. These were axial-strain controlled tests in which load and axial strain were monitored using a microcomputer. The test specimens were 14.0 cm long with 3.0 cm long René N4 bars in the gage section. All samples were electron-polished and Laué X-ray photography was taken to determine the actual specimen orientation prior to each mechanical test.

Ten experiments have been performed in five nominal crystal orientations. The test matrix included three monotonic tensile tests, two double tensile tests with a 120-sec hold period at zero stress, three fully-reversed fatigue tests, one fatigue test with a peak tensile strain hold in each cycle, and one fatigue test with a peak compressive strain hold in each cycle. The five nominal orientations were [321], [110], [210], [100], and [111]. Because of the limited number of samples, each test was not repeated for consistency of the response.

Table 3 Material constants for René N4 at 982°C

Material Parameter		OCT ($i=1$)	CUBE ($i=2$)
D_i	1/sec	0.10000E+01	0.10000E+01
A_i	–	0.50000E+00	0.50000E+00
n_{i1}	–	0.53000E+00	0.70000E+00
H_{i1}	MPa	0.20510E+05	0.71841E+04
H_{i2}	MPa	0.20510E+05	0.71841E+04
m_i	1/MPa	0.00000E+00	0.00000E+00
V_1	–	−0.40415E+02	0.00000E+00
V_2	–	−0.28231E+02	0.00000E+00
V_3	–	0.17661E+02	0.00000E+00
F_i	MPa/sec	0.21619E+07	0.16000E+06
n_{i2}	–	0.12108E+01	0.11202E+01
Ω_{SATi}	MPa	0.95293E+02	0.61838E+02

A method for determining elastic constants E, G, and ν for nickel-base single cyrstal superalloys has been developed (Yang, 1984). In the current study, the elastic responses in the [100], [111], and [110] orientations were used to calculate these values. The values of E, G, and ν for René N4 at 982°C are 81.2GPa, 90.9GPa, and 0.398, respectively.

The procedure to determine inelastic material constants consists of three major steps that can be performed separately or in a loop as shown in Fig. 3. Because the model is developed primarily for high strain-rate loading conditions, only tensile and fatigue tests were evaluated. Using octahedral slip constants as an example, in the first step the strain-rate sensitivity exponent, n_{11}, orientation dependence factors, V_1, V_2, and V_3, saturated state variable values, Ω_{SAT1} and H_{11}, are determined by using saturated data from the tensile tests. The second step uses both strain hardening and anelastic recovery data from the double tensile test to evaluate the back stress constants G_1, n_{12}, and F_1. In the third step, the remaining constants in the drag stress evolution equation, H_{12} and m_1, can be evaluated using the cyclic softening or hardening data from the fatigue tests. Since the material was almost cyclically stable, the hardening equation was not activated, and only the initial value H_{11} was used from the tensile data to predict all the fatigue responses. The constitutive model prediction program is used after each step to provide validation of the constants. The material constants determined for single crystal René N4 at 982°C are given in Table 3.

V. Results

The constitutive model has been implemented in a computer code to predict and correlate the material response for each of the loading conditions. Correlations and predictions for the double tensile tests with a 120-sec hold time in the [100] and [111] orientations are shown in Fig. 1. The first loading loop was used to calculate the constants. Note that the hardening characteristics for the reloading, the recovery (anelasticity) at zero stress, and the rate sensitivity effect in these two orientations are all reasonably modeled. The predicted inelastic strain histories during the hold period are given in Fig. 2. This prediction is very good considering that the measured strain values are very small compared to the total strain during the test. Using material constants determined from the two previous tests, predictions of the response were made for the [110] and [321] orientations and are shown in Fig. 4. The elastic moduli, strain-hardening characteristics (knee of the

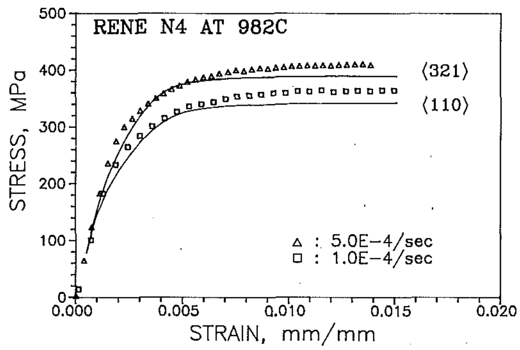

Fig. 4 Comparison between experimental data and predicted tensile responses in the [110] and [321] orientations for René N4 at 982°C

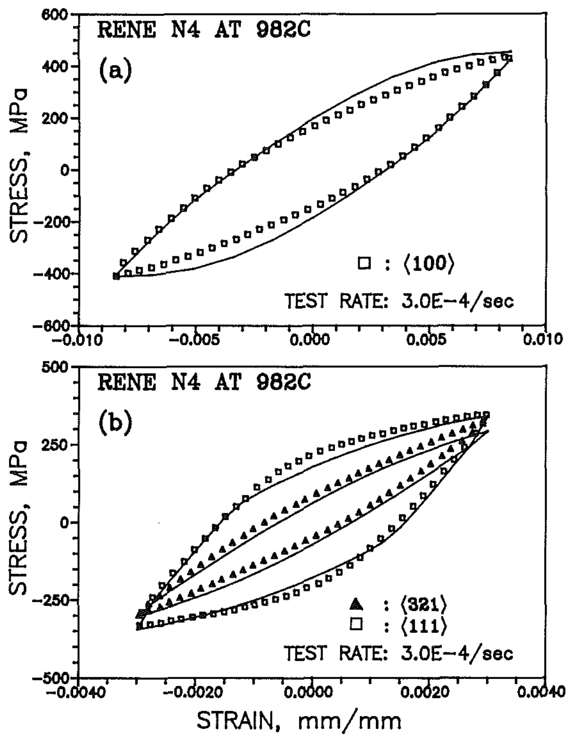

Fig. 5 Comparison between experimental data and predicted saturated fatigue loop in the: (*a*) [100]; and (*b*) [111] and [321] orientations for René N4 at 982°C

curve), ultimate stress values, and the strain-rate sensitivity are all modeled reasonably well for these two orientations.

The experimental results for fatigue in [100], [111], and [123] orientations at 982°C stabilized within five loops and exhibited almost no work hardening or softening throughout the specimen life; therefore, the drag stress remained constant. The only information used from the fatigue data in determining constants was the tension/compression asymmetry for the evaluation of V_1, and V_2, and V_3. This information is used to estimate the compressive yield stress since no individual compressive tests were performed. The predictions of the loops are based purely on constants determined from the tensile tests. These predictions are shown in Fig. 5(*a*) for the [100] orientation and Fig. 5(*b*) for the [111] and [321] orientations. The model has predicted the shape of the saturated loop and the tension/compression asymmetry characteristics for each orientation.

The results of fatigue tests with peak-strain holds are shown in Figs. 6 and 7 for the [321] and [210] orientations, respectively. The tensile-hold fatigue experiment in the [210] orientation showed gradual cyclic softening which was not seen in any of

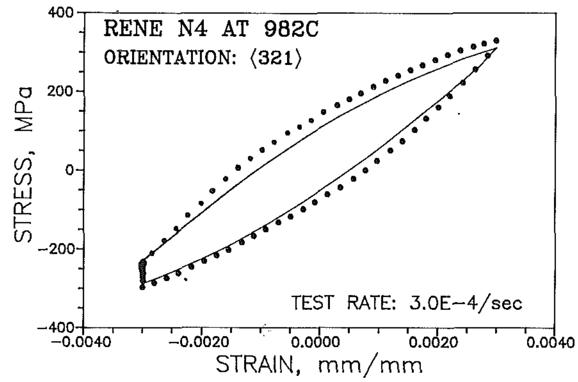

Fig. 6 Comparison between experimental data and predicted fatigue loop with peak compressive strain hold in the [321] orientation for René N4 at 982°C

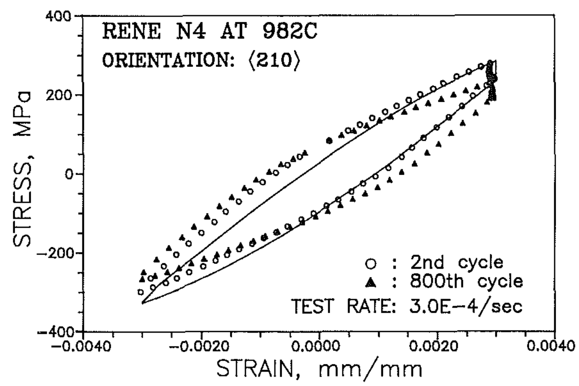

Fig. 7 Comparison between experimental data and predicted fatigue loop with peak tensile strain hold in the [210] orientation for René N4 at 982°C. Note that the material exhibited cyclic softening

the other fatigue tests. The reason for this behavior is not clear. The model predicted the stress relaxation and the shape of the loop quite well for the compressive hold in the [321] orientation.

VI Discussion and Conclusion

As stated earlier, current model can only be used for isothermal loading conditions. Methods for nonisothermal calculations by interpolating parameters at a specific temperature has been suggested by Bodner (1979) for isotropic materials and has been successfully used by Ramaswamy (1986) on René 80. This method may be successful for René N4 because René 80 and René N4 are almost identical in composition. A nonisothermal model might also be formed by allowing the parameter D in the flow equation to be an Arrhenius function of activation energy which is dependent upon temperature (Brown, 1988).

Cyclic hardening or softening behavior for René N4 does not seem to be consistent throughout the experimental program. For example, softening occurred in the tensile-hold fatigue test whereas the other tests were almost cyclically stable. This behavior has to be reexamined carefully and implementation of the drag stress evolution equation may be required.

Finally, latent hardening, e.g., the hardening of inactive slip system due to intersection with active slip system, was not considered in the current model. Latent hardening is generally considered to be an important part of the theoretical basis for hardening in single crystal plasticity (Asaro, 1983; Havner and co-workers, 1977 and 1983; Weng, 1979). However, nonproportional tests on René 80 (Ramaswamy, 1986) did not show any latent-hardening behavior. Thus, in the current model with René N4, latent hardening was assumed insignificant. Extension of the present theory to nonproportional loading still needs to be established.

In conclusion, a back stress/drag stress constitutive model based on crystallographic approach to model single crystal anisotropy was presented. The experimental results demonstrated the need for the back stress variable in the inelastic flow equations. Experimental findings also suggested that the back stress is orientation dependent and controlling both the strain hardening and recovery characteristics. The observed stable fatigue loops at 982°C led to the conclusion that the drag stress is constant for this temperature. The constitutive model, operated with constants determined only from tensile data, was evaluated by using uniaxial tensile, fatigue, and strain-hold tests. The model predicted those conditions very well. This result verifies a major step in relating the macroscopic response to the microstructure of the material.

Acknowledgment

This research work was sponsored by NASA Grant NAG3-511. The authors appreciate the help of Dr. N. Jayaraman and Mr. D. Alden for their work in performing the mechanical tests.

References

Asaro, R. J., 1983 "Crystal Plasticity," ASME JOURNAL OF APPLIED MECHANICS, Vol. 50, pp. 921-934.

Bishop, J., 1952, "A Theoretical Examination of the Plastic Deformation of Crystals by Glide," *Philosophical Magazine*, p. 51.

Bodner, S. R., and Partom, Y. 1975, "Constitutive Equations for Elastic-Viscoplastic Strain-Hardening Materials," ASME JOURNAL OF APPLIED MECHANICS, Vol. 42, p. 385.

Bodner, S. R., 1979, "Representation of Time Dependent Mechanical Behavior of René 95 by Constitutive Equations," AFML Report, AFML-TR-79-4116.

Brown, S. B., 1988, "Experiments for the Evaluation of Internal Variable Constitutive Models," Symposium on Constitutive Equations and Life Prediction Models for High Temperature Applications, ASME/SES Summer Annual Meeting, Berkeley, Calif., June 20-22, 1988.

Dame, L. T., and Stouffer, D. C., 1986, "Anisotropic Constitutive Model for Nickel Base Single Crystal Alloys: Development and Finite Element Implementation. NASA CR-1751015, Lewis Research Center, Cleveland, Ohio.

Ezz, S., Pope, D., and Paidar, V., 1982, "The Tension/Compression Flow Stress Asymmetry in Ni_3 (Al, Nb) Single Crystals," *Acta Metallurgica*, Vol. 30, p. 921.

Gabb, T., Gayda, J., and Miner, R., 1986, "Orientation and Temperature Dependence of Some Mechanical Properties of the Single-Crystal Nickel-Base Superalloy Renê, N4: Part II. Low Cycle Fatigue Behavior," *Metall. Trans.*, Vol. 17A, p. 497.

Havner, K., and Shalaby, A., 1977, "A Simple Mathematical Theory of Finite Distortional Latent Hardening in Single Cyrstals," *Proc. R. Soc. Lond.*, Vol. A358, p. 47.

Havner, K., and Salpekar, S., 1983, "Theoretical Latent Hardening of Crystals in Double-Slip-II. F.C.C. Crystals Slipping on Distinct Planes," *J. Mech. Phys. Solids*, pp. 31-231.

Heredia, F., and Pope, D., 1986, "The Tension/Compression Flow Asymmetry in a High γ' Volume Fraction Nickel Base Alloy," *Acta Metall.*, Vol. 34, pp. 279-285.

Hopgood, A. A., and Martin, J. W., 1986, "The Creep Behavior of a Nickel-Based Single Crystal Superalloy," *Mat. Sci. Eng.*, Vol. 82, pp. 27-36.

Jackson, P. J., 1986, "The Mechanisms of Plastic Relaxation in Single-Crystal Deformation," *Mat. Sci. Engr.*, Vol. 81, pp. 169-174.

Lall, C., Chin, S., and Pope, D., 1979, "The Orientation and Temperature Dependence of the Yield Stress of Ni_3 (Al, Nb) Single Crystals," *Metall. Trans.*, Vol. 10A, p. 1323.

Leverant, G., and Kear, A. H., 1970, "The Mechanism of Creep in Gamma Prime Precipitation-Hardened Nicke-Base Alloys at Intermediate Temperatures," *Metall. Trans.*, Vol. 1, pp. 491-498.

MacKay, R. A., and Maier, R. D., 1982, "The Influence on the Stress Rupture Properties of Nickel-Base Single Crystals," *Metall. Trans.*, Vol. 13A, p. 1747.

Milligan, W. W., and Antolovich, S. D., 1987, "Yielding and Deformation Behavior of the Single Crystal Superalloy PWA 1480," *Metall. Trans.*, Vol. 18A, 85p.

Miner, R., Voigt, R., Gayda, J., and Gabb, T., 1986a, "Orientation and Temperature Dependence of Some Mechanical Properties of the Singly-Crystal Nickel-Base Superalloy René N4: Part I. Tensile Behavior," *Metall. Trans.*, Vol. 17A, p. 491.

Miner, R., Gabb, T., Gayda, J., and Hemker, K. J., 1986b, "Orientation and Temperature Dependence of Some Mechanical Properties of the Single Crystal Nickel-Base Superalloy René N4: Part III. Tensile-Compression Anisotropy," *Metall. Tran.*, Vol. 17A, p. 507.

Paidar, V., Pope, D. P., and Vitek, V., 1984, "A Theory of the Anomalous Yield Behavior in $L1_2$ Ordered Alloys," *Acta Metallurgica*, Vol. 32, pp. 435-448.

Paslay, P., Wells, C., and Leverant, G., 1970, "An Analysis of Primary Creep of Nickel-Base Superalloy Single Crystals," ASME JOURNAL OF APPLIED MECHANICS, Vol. 37, p. 759.

Ramaswamy, V. G., 1986, "A Constitutive Model for the Inelastic Multiaxial Cyclic Response of a Nickel-Base Superalloy René 80," NASA CR-3998.

Shah, D., and Duhl, D., 1984, "The Effect of Orientation, Temperature and Gamma Prime Size on the Yield Strength of a Single Crystal Nickel Base Superalloy," Proceedings of he Fifth International Symposium on Superalloys, ASM, Metals Park, Ohio.

Sheh, M. Y., 1988, "Anisotropic Constitutive Modeling for Nickel-Base Single Crystal Superalloys," Ph.D. Dissertation, Department of Aerospace Engineering Mechanics, University of Cincinnati, Cincinnati, Ohio.

Swanson, G., et al., 1984, Life Prediction and Constitutive Models for Engine Hot Section Anisotropic Materials Program, Contract NAS3-23939, Monthly Report PWA-5968-9, Aug. 1984.

Umakoshi, Y., Pope, D., and Vitek, V., 1984, "The Asymmetry of the Flow Stress in Ni_3 (Al,Ta) Single Crystals," *Acta Metallurgica*, Vol. 32, p. 449.

Walker, K. P., 1981, "Research and Development Program for Nonlinear Structural Modeling with Advanced Time-Temperature Dependent Constitutive Relationships," NASA CR165533.

Walker, K. P., and Jordan, E. H., 1985, "Biaxial Constitutive Modelling and Testing of a Singel Crystal Superalloy at Elevated Temperatures," Biaxial and Mutliaxial Fatigue, EGF3, M. W. Brown and K. J. Miller eds., Mechanical Engineering Publications, London, pp. 145-170.

Weng, G., 1979, "Kinematic Hardening Rule in Single Crystals," *Int. J. Solids Structures*, Vol. 15, p. 861.

Yang S., 1984, "Elastic Constants of a Monocrystalline Nickel-Base Superalloy," *Metallurgical Transactions*, Vol. 16A, p. 661.

Plane-Strain Shear Dislocations Moving Steadily in Linear Elastic Diffusive Solids

J. W. Rudnicki
Department of Civil Engineering,
Northwestern University,
Evanston, IL 60208
Mem. ASME

E. A. Roeloffs
U. S. Geological Survey,
Menlo Park, CA 94025

This paper derives the stress and pore pressure fields induced by a plane-strain shear (gliding edge) dislocation moving steadily at a constant speed V *in a linear elastic, fluid-infiltrated (Biot) solid. Solutions are obtained for the limiting cases in which the plane containing the moving dislocation* (y = 0) *is permeable and impermeable to the diffusing species. Although the solutions for the permeable and impermeable planes are required to agree with each other and with the ordinary elastic solution in the limits of* V = 0 *(corresponding to drained response) and* V = ∞ *(corresponding to undrained response), the stress and pore pressure fields differ considerably for finite nonzero velocities. For the dislocation on the impermeable plane, the pore pressure is discontinuous on* y = 0 *and attains values which are equal in magnitude and opposite in sign as* y = 0 *is approached from above and below. The solution reveals the surprising result that the pore pressure on the impermeable plane is zero everywhere behind the moving dislocation* (x < 0). *For the dislocation on the permeable plane, the pore pressure is zero on* y = 0 *and attains its maximum at about* (2c/V, 2c/V) *where* c *is the diffusivity, and the origin of the coordinate system coincides with the dislocation. For the impermeable plane, the largest pore pressure change occurs at the origin.*

Introduction

This paper derives the stress and pore pressure fields induced by plane-strain shear (gliding edge) dislocations moving steadily, and quasi-statically, in a linear elastic diffusive solid. In an ordinary linear elastic solid, the solution for the stress field, when viewed in a coordinate system moving with the dislocation, is identical to that for the stationary dislocation. In contrast, solutions in a diffusive solid are velocity dependent. Moreover, this dependence is different when the plane in which the dislocation is moving is permeable, or impermeable, to the diffusing species.

Solutions for dislocations provide elementary models of discontinuities in solids and can be used as a basis for numerical methods for treating more elaborate models of cracks (e.g., Erdogan and Gupta, 1972; Cleary, 1976; Detournay and Cheng, 1987). The work here has been motivated by applications to slip on faults in the earth's crust (Nur and Booker, 1972; Booker, 1974; Rice and Cleary, 1976; Roeloffs and Rudnicki, 1984–1985; Rudnicki and Hsu, 1988). In this case the diffusing species is ground water, and is characterized in terms of an apparent fluid volume fraction and a pore fluid pressure. Although the elementary dislocation solutions are only crude representations of slip on faults, they can be used to construct more realistic slip distributions by superposition. In addition, these solutions yield insight into the effects of coupling between deformation and fluid diffusion.

This paper extends and complements previous work by Cleary (1978) and Simons (1979) on moving dislocations in diffusive solids. Cleary (1978) used the solution for instantaneous introduction of opening (climbing edge) and shear (gliding edge) dislocations to obtain numerical results for steadily-moving dislocations. Simons (1979) formulated the problem of the steadily-moving shear dislocation and, using Fourier transforms, obtained an expression for the shear stress on the plane in which the dislocation is moving.

The solutions of both Cleary (1978) and Simons (1979) are appropriate when the plane on which the shear dislocation is moving is permeable to the diffusing species. They do not make this assumption directly but note that for the shear dislocation on $y = 0$ with Burgers vector in the x-direction (Fig. 1), the pore pressure p is antisymmetric about $y = 0$. Because they assume that the pore pressure is continuous, it must be zero on $y = 0$. However, the flow across $y = 0$, which is proportional to the gradient of the pore pressure $\partial p/\partial y$, is not zero. In recent work on instantaneous dislocation solutions for diffusive solids, Rudnicki (1986, 1987) has noted that an alternative possibility is that the plane, $y = 0$, is impermeable. In this case, $\partial p/\partial y = 0$ on $y = 0$. Because the pore pressure must still be antisymmetric about $y = 0$, it is discontinuous and

Contributed by the Applied Mechanics Division of The American Society of Mechanical Engineers for presentation at the Winter Annual Meeting, San Francisco, Calif., December 10–15, 1989.

Discussion on this paper should be addressed to the Editorial Department, ASME, United Engineering Center, 345 East 47th Street, New York, N.Y. 10017, and will be accepted until two months after final publication of the paper itself in the Journal of Applied Mechanics. Manuscript received by the ASME Applied Mechanics Division, September 19, 1988; final revision, June 12, 1989.
Paper No. 89-WA/APM-47.

takes on equal and opposite values as $y = 0$ is approached from above or below. Surprisingly, the solution to be given here demonstrates that for the steadily-moving dislocation, this value is zero for $x < 0$. Rudnicki (1987) also treats the opening (climbing edge) dislocation for which the assumption of a permeable plane requires that $\partial p/\partial y$ be discontinuous.

The solutions for steadily-moving dislocations can, in principle, be constructed from the solutions for instantaneous dislocations by the superposition procedure described by Carslaw and Jaeger (1959) and implemented numerically by Cleary (1978). However, we prefer to follow the approach used by Simons (1979) and to treat the moving dislocation problem directly using Fourier transforms. This approach is similar to that used by Rice and Simons (1976) to solve the related problem of a steadily-moving semi-infinite shear crack. We begin by summarizing the governing equations for a linear elastic diffusive solid and then formulate the boundary conditions for the dislocation problem. The problem is solved by the application of Fourier transforms and the results for selected field variables are presented graphically.

Governing Equations

The constitutive equations for a linear elastic diffusive solid were first formulated by Biot (1941) within the context of fluid-infiltrated soils, but the equations are sufficiently general to describe the linearized response of any elastic solid containing a diffusing species that can be characterized by two scalar variables. For example, they have been used to model the response of cartilage (Kuei, 1977; Mow and Lai, 1980) and are formally identical to the equations of fully-coupled thermoelasticity (Biot, 1956; Rice and Cleary, 1976; Rice, 1979). For fluid-infiltrated soil or rock, the two scalar variables characterizing the response of the fluid are conveniently taken to be the pore pressure p, measured from some ambient value, and the fluid mass content per unit volume m, measured from a reference value m_o.

Rice and Cleary (1976) achieved an advantageous rearrangement of the equations by exploiting the observation that they reduce to the usual equations of linear elastic response, but with different Poisson's ratios, in the two contrasting limits of drained and undrained response. Drained response, with Poisson's ratio ν, occurs when the deformation is so slow that any alterations in pore fluid pressure are eliminated by fluid mass diffusion. Undrained response, with Poisson's ratio ν_u, occurs when the deformation is too rapid (but still quasi-static) to allow fluid mass to diffuse from material elements. Thus, the fluid mass content per unit volume m is equal to its reference value m_o. In this limit, the alteration of pore fluid pressure p is proportional to the negative of the mean normal stress $\sigma_{kk}/3$:

$$p = -B\sigma_{kk}/3 \tag{1}$$

where the coefficient B is called Skempton's coefficient. Values of B range from zero to unity, taking on the lower limit for a very compressible pore fluid and the upper for separately incompressible solid and fluid constituents. More generally, deformation will be neither drained nor undrained and, in this case, the strains of the solid matrix ϵ_{ij} and the alteration of fluid mass content depend on the stress σ_{ij} and pore pressure p as follows:

$$2G\epsilon_{ij} = \sigma_{ij} - \frac{\nu}{(1+\nu)}\sigma_{kk}\delta_{ij} + \frac{3(\nu_u-\nu)}{B(1+\nu)(1+\nu_u)}p\delta_{ij} \tag{2a}$$

$$m - m_o = \frac{9\rho_o(\nu_u-\nu)}{2GB(1+\nu_u)(1+\nu)}[\sigma_{kk}/3 + p/B] \tag{2b}$$

where G is the shear modulus, ρ_o is the mass density of pore fluid, and δ_{ij} is the Kronecker delta. In (1) and (2), $(i, j) = (1, 2, 3)$ and summation on repeated indices has been assumed. For plane-strain deformation in the xy-plane, $\epsilon_{zz} = 0$ and this condition can be used to eliminate σ_{zz} from (2a), (2b). The results are as follows:

$$2G\epsilon_{\alpha\beta} = \sigma_{\alpha\beta} - \nu(\sigma_{xx}+\sigma_{yy})\delta_{\alpha\beta} + \frac{3(\nu_u-\nu)}{B(1+\nu_u)}p\delta_{\alpha\beta} \tag{3a}$$

$$m - m_o = \frac{3\rho_o(\nu_u-\nu)}{GB(1+\nu_u)}[(\sigma_{xx}+\sigma_{yy})/2 + 3p/2B(1+\nu_u)] \tag{3b}$$

where, now, $(\alpha, \beta) = (1, 2)$. The final constitutive equation is Darcy's law which states that the flow rate per unit area, q_α, is proportional to the negative of the gradient of the pore pressure:

$$q_\alpha = -\rho_o\kappa\partial p/\partial x_\alpha \tag{4}$$

where the coefficient κ is a permeability (Rice and Cleary, 1976).

In addition to the constitutive equations, there are field equations expressing equilibrium, compatibility of strains, and fluid mass conservation. For plane-strain deformation, these can all be written in terms of the stress and pore pressure by using the constitutive equations (Rice and Cleary, 1976). The results are as follows:

$$\partial\sigma_{xx}/\partial x + \partial\sigma_{yx}/\partial y = 0 \tag{5a}$$

$$\partial\sigma_{xy}/\partial x + \partial\sigma_{yy}/\partial y = 0 \tag{5b}$$

$$\nabla^2[\sigma_{xx}+\sigma_{yy}+2\eta p] = 0 \tag{6}$$

$$(c\nabla^2 - \partial/\partial t)[\sigma_{xx}+\sigma_{yy}+(2\eta/\mu)p] = 0 \tag{7}$$

where $\eta = 3(\nu_u - \nu)/[2B(1+\nu_u)(1-\nu)]$, $\mu = (\nu_u - \nu)/(1-\nu)$ and $\nabla^2(\ldots) = \partial^2(\ldots)/\partial x^2 + \partial^2(\ldots)/\partial y^2$. The diffusivity c is given by

$$c = 2G\kappa B^2(1-\nu)(1+\nu_u)^2/[9(1-\nu_u)(\nu_u-\nu)]. \tag{8}$$

Equations (5) express equilibrium in the absence of body forces, (6) compatibility, and (7) fluid mass conservation. As noted by Rice and Cleary (1976), the quantity $[\sigma_{xx} + \sigma_{yy} + (2\eta/\mu)p]$ is proportional to the fluid mass content per unit volume.

Formulation of Boundary Conditions

We consider a shear dislocation on the x-axis moving steadily in the positive x-direction at constant speed V (Fig. 1). The speed is assumed to be low enough that inertial effects can be neglected. For steady motion in the x-direction, the displacements and stresses depend on time only in the combination $X-Vt$. Consequently, explicit dependence on time t can be eliminated by adopting a coordinate system that moves steadily with the dislocation. In this coordinate system, a shear dislocation at the origin corresponds to introducing the following discontinuity in the x-direction displacement:

$$u_x(x, y=0^+) - u_x(x, y=0^-) = b\,H(-x) \tag{9}$$

where b is the magnitude of the discontinuity, $H(\ldots)$ is the unit step function, and the notation $y = 0^+$ (0^-) indicates that the x-axis is to be approached from above (below). Because u_x is antisymmetric with respect to $y = 0$, this equation can be written as

$$u_x(x, y=0^+) = (b/2)H(-x). \tag{10}$$

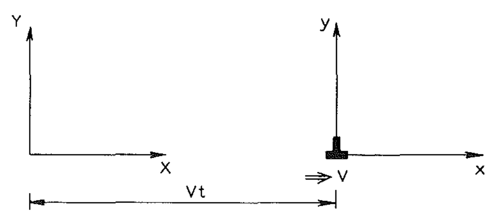

Fig. 1 Coordinate systems for a dislocation steadily moving at a speed V. The xy-system moves with the dislocation.

The normal stress components σ_{xx} and σ_{yy}, and the pore pressure p, are also antisymmetric about $y = 0$. Because the traction on $y = 0$ must be continuous, σ_{yy} equals zero there:

$$\sigma_{yy}(x, y=0)=0. \tag{11}$$

If the pore pressure is required to be continuous, then it also equals zero on the x-axis:

$$p(x, y=0)=0. \tag{12}$$

In this case, $\partial p/\partial y$ will not generally be zero on the x-axis. Consequently, according to Darcy's law (4), flow will occur across this plane and, hence, it is permeable. Another possibility, however, is that the plane is impermeable. In the context of application to a fault in the earth's crust, this can occur because the fault contains clay or fine-grained gouge material that is much less permeable than the surrounding rock. From Darcy's law, the condition enforcing the requirement of no flow across the x-axis is

$$\frac{\partial p}{\partial y}(x, y=0)=0. \tag{13}$$

Now, the pore pressure need not be zero on the x-axis (although we will show that it turns out to be zero on $x < 0$). It is still required, however, to be antisymmetric about $y = 0$ and, hence, will taken on equal and opposite values as the x-axis is approached from above or below.

Because the governing equations (5)–(7) are expressed in terms of the pore pressure and stress, it is convenient to rewrite (10) in terms of these quantities. Differentiating (10) with respect to x yields

$$\epsilon_{xx}(x,0^+)=\frac{\partial u_x}{\partial x}(x,0^+)=(-b/2)\delta_{\mathrm{DIRAC}}(x) \tag{14}$$

where $\delta_{\mathrm{DIRAC}}(x)$ is the Dirac delta function and the first equality in (14) is the result of the strain displacement relation. Using the constitutive equation (3a) to evaluate $\epsilon_{xx}(x, 0^+)$ and (11) yields the desired boundary condition in terms of the stress

$$\sigma_{xx}(x,0^+)+2\eta p(x,0^+)=-[Gb/(1-\nu)]\delta_{\mathrm{DIRAC}}(x) \tag{15}$$

where η has been introduced following (7).

Thus, the problem has been reduced to the solution of the field equations (5)–(7) subject to the boundary conditions (11) and (15) with (12) for the permeable plane and (13) for the impermeable plane.

Solution for the Permeable Plane

The solution procedure is to use the Fourier transform on x. The Fourier transform of a function $f(x, y)$ is defined by

$$\tilde{f}(\kappa,y)=\int_{-\infty}^{\infty} f(x,y)\exp(-\iota\kappa x)dx \tag{16}$$

with inversion

$$f(x,y)=F^{-1}[\tilde{f}(\kappa,y)]=\frac{1}{2\pi}\int_{-\infty}^{\infty}\tilde{f}(\kappa,y)\exp(\iota\kappa x)d\kappa \tag{17}$$

where $\iota = (-1)^{1/2}$. Except for (7), the governing equations are identical in the stationary and moving coordinate systems. Because the dislocation has been assumed to be propagating steadily in the x-direction, the time derivative $\partial(\ldots)/\partial t$ in (7) can be replaced by $-V\partial(\ldots)/\partial x$. Applying (16) to (5)–(7), with the substitution just mentioned in (7), yields equations identical to those solved by Rice and Simons (1976). Their solution for the Fourier transformed stress and pore pressure is as follows:

$$\frac{1}{2}(\tilde{\sigma}_{xx}+\tilde{\sigma}_{yy})=A(\kappa)e^{-m(\kappa)y}+B(\kappa)e^{-n(\kappa)y} \tag{18}$$

$$\eta\tilde{p}=-\mu A(\kappa)e^{-m(\kappa)y}-B(\kappa)e^{-n(\kappa)y} \tag{19}$$

$$\tilde{\sigma}_{xy}=-\left\{\frac{\iota\kappa}{m(\kappa)}C(\kappa)+\iota\kappa yA(\kappa)\right\}e^{-m(\kappa)y}-2(c/V)n(\kappa)B(\kappa)e^{-n(\kappa)y} \tag{20}$$

$$\frac{1}{2}(\tilde{\sigma}_{yy}-\tilde{\sigma}_{xx})=[C(\kappa)+A(\kappa)m(\kappa)y]e^{-m(\kappa)y}+\frac{\kappa^2+n^2(\kappa)}{\kappa^2-n^2(\kappa)}B(\kappa)e^{-n(\kappa)y} \tag{21}$$

where $m^2(\kappa) = \kappa^2$ and $n^2(\kappa) = \kappa^2 - \iota\kappa V/c$. To ensure convergence of the inversion integrals in $y > 0$, $m(\kappa)$ and $n(\kappa)$ are subject to the following restrictions:

$$\mathrm{Re}[m(\kappa)]\geq 0 \tag{22}$$

$$\mathrm{Re}[n(\kappa)]\geq 0 \tag{23}$$

where Re[. . .] stands for "the real part of." The functions A, B, and C are to be determined by the boundary conditions.

Taking the transforms of the boundary conditions for the permeable plane, (11), (12), and (15), substituting (18)–(21), and solving for A, B, and C yield the following results:

$$B(\kappa)=-\mu A(\kappa)=Gb\mu[2(1-\nu_u)] \tag{24}$$

$$C(\kappa)=Gb[1+\mu(2c/V)\iota\kappa]/[2(1-\nu_u)]. \tag{25}$$

When these are substituted back into (18)–(21), terms not involving $n(\kappa)$ can easily be inverted. For example, the first term in the expression for the pore pressure involves the following inversion integral:

$$I(x,y)=\frac{1}{2\pi}\int_{-\infty}^{\infty}\exp[-m(\kappa)y]\exp(\iota\kappa x)d\kappa. \tag{26}$$

This integral can be converted to a Fourier cosine transform by noting that the restriction (22) requires that $m(\kappa)$ be an even function of κ and its value can be obtained from standard tables (e.g., Erdelyi et al., 1954):

$$I(x,y)=y/(\pi r^2) \tag{27}$$

where $r^2 = x^2 + y^2$. Other terms not involving $n(\kappa)$ can be inverted by differentiating or integrating (27). Consequently, the stresses and pore pressure due to steady motion of a shear dislocation on a permeable plane can be written as follows:

$$\frac{1}{2}(\sigma_{xx}+\sigma_{yy})=-\Delta[(2y/r^2)-\mu K(x,y)] \tag{28}$$

$$\eta p=\mu\Delta[(2y/r^2)-K(x,y)] \tag{29}$$

$$\sigma_{xy}=\Delta[2x(x^2-y^2)/r^4]+\Delta(2\mu c/V)\left[\frac{\partial K}{\partial y}+2(y^2-x^2)/r^4\right] \tag{30}$$

$$\frac{1}{2}(\sigma_{yy}-\sigma_{xx})=\Delta(4x^2y/r^4)-\Delta(2\mu c/V)\left[(4xy/r^4)+\frac{\partial K}{\partial x}+(V/2c)K\right] \tag{31}$$

where $\Delta = Gb/[4\pi(1 - \nu_u)]$ and

$$K(x,y)=\int_{-\infty}^{\infty}\exp[\iota\kappa x-n(\kappa)y]d\kappa. \tag{32}$$

Equations (30) and (31) can be written more compactly by combining them as follows in complex form:

$$\tau=\frac{1}{2}(\sigma_{yy}-\sigma_{xx})+\iota\,\sigma_{xy}. \tag{33}$$

The result is then

$$\tau=2\Delta\iota x/\zeta^2-2\Delta\mu(c/V)\{(2\iota/\zeta^2)+(V/2c)K+2\partial K/\partial\zeta\} \tag{34}$$

where $\zeta = x + \iota y$ and $2\,\partial(\ldots)/\partial\zeta = \partial(\ldots)/\partial x - \iota\,\partial(\ldots)/\partial y$. In the limit $V\rightarrow\infty$, the integral $K(x, y)$ vanishes and, consequently, equations (28), (29), and (34) yield the solution for the stresses due to introduction of a shear dislocation in an ordinary elastic solid with Poisson's ratio ν_u. The pore pressure is equal to $-B(1 + \nu_u)(\sigma_{xx} + \sigma_{yy})/3$, as appropriate for undrained plane-strain deformation.

Calculation of the inversion integral (32) can be accomplished by noting that for appropriately chosen branch cuts, the integrand is an analytic function of κ. The restriction (23) can be met by choosing branch cuts for $n(\kappa)$ on the imaginary axis from $\kappa = \iota V/c$ to $\kappa = \infty$ and from $\kappa = 0$ to $\kappa = -\infty$. Now the path of integration can be changed from the real axis to a path on which the exponent is real and negative, subject to the restriction (23). The resulting integration paths (for $x > 0$ and $x < 0$) do not intersect the branch cuts and the integral can be written as follows (some details for calculation of similar integrals are given in the Appendix):

$$K(x,y) = 2y(V/2c)^2 e^{(-Vx/2c)} \int_1^\infty (\xi^2-1)^{1/2} e^{-(Vr/2c)\xi} d\xi. \quad (35)$$

This integral can be expressed in terms of K_1, the modified Bessel function of order one (Abramowitz and Stegun, 9.6.23, 1964), and the result for $K(x, y)$ is

$$K(x,y) = (2y/r^2)(Vr/2c)K_1(Vr/2c)\exp(-Vx/2c). \quad (36)$$

The derivatives of K can be calculated by using the following relation (Lebedev, 1972, p. 110)

$$\frac{d}{dz}[zK_1(z)] = -zK_0(z)$$

where K_0 is the modified Bessel function of order zero. Substituting into (28), (29), and (34) yields the final expressions for the stress and pore pressure due to a shear dislocation moving on a permeable plane:

$$\frac{1}{2}(\sigma_{xx}+\sigma_{yy}) = -\Delta(2y/r^2)\{1-\mu[1-w(x,y)]\} \quad (37)$$

$$\eta p = \mu\Delta(2y/r^2)w(x,y) \quad (38)$$

$$\tau = 2\Delta\iota x/\zeta^2 - (4\Delta\iota\mu/\zeta^2)(c/V)w(x,y) + \Delta\mu(V/c)(y/\zeta)e^{-Vx/2c}K_0(Vr/2c) \quad (39)$$

where

$$w(x,y) = 1-(Vr/2c)\exp(-Vx/2c)K_1(Vr/2c). \quad (40)$$

The expression for the pore pressure (38) has been given previously by Roeloffs and Rudnicki (1984/85) and the expression for σ_{xy} on $y = 0$, obtained from (39), reduces to that given by Simons (1979):

$$\sigma_{xy}(x,0) = (2\Delta/x)\{1-\mu\, g_p(Vx/2c)\} \quad (41)$$

where

$$g_p(z) = z^{-1}\{1-|z|e^{-z}K_1(z)\}. \quad (42)$$

As noted previously, the first term in each expression (i.e., the term not multiplied by μ) is the undrained response appropriate in the limit $V \to \infty$. In the contrasting limit $V \to 0$, $p = 0$ and the expressions for the stress components reduce to the usual ones of linear elasticity with the drained value of Poisson's ratio (ν).

Solution for the Impermeable Plane

Solution for the shear dislocation moving steadily on an impermeable plane proceeds along similar lines. The Fourier transformed solution of the field equations (5)–(7) is again (18)–(21). Now, however, the boundary condition (12) is replaced by (13). The resulting solutions for A, B, and C are as follows:

$$B(\kappa) = -\mu m(\kappa)A(\kappa)/n(\kappa) = 2\pi\Delta\mu m(\kappa)/n(\kappa) \quad (43)$$

$$C(\kappa) = 2\pi\Delta[1+(2c/V)\mu\iota\kappa m(\kappa)/n(\kappa)] \quad (44)$$

where, again, $\Delta = Gb/[4\pi(1 - \nu_u)]$, and $m(\kappa)$ and $n(\kappa)$ are defined following (21). Substituting into (18)–(21) and, as in the case of the permeable plane, inverting terms not involving $n(\kappa)$ yields

$$\frac{1}{2}(\sigma_{xx}+\sigma_{yy}) = \Delta\{(2y/r^2)-\mu H(x,y)\} \quad (45)$$

$$\eta p = \Delta\mu\{(2y/r^2)-H(x,y)\} \quad (46)$$

$$\tau = (2\Delta\iota x/\zeta^2) - \Delta\mu\left\{H(x,y) + (4c/V)\frac{\partial}{\partial\zeta}(H-L)\right\}, \quad (47)$$

where

$$H(x,y) = \int_{-\infty}^{\infty} [m(\kappa)/n(\kappa)]\exp[\iota\kappa x - n(\kappa)y]d\kappa \quad (48)$$

$$L(x,y) = \int_{-\infty}^{\infty} [m(\kappa)/n(\kappa)]\exp[\iota\kappa x - m(\kappa)y]d\kappa \quad (49)$$

and expressions for σ_{xy} and $(\sigma_{yy} - \sigma_{xx})$ have been combined in complex form.

In contrast to the solution for the permeable plane, the integrals (48) and (49) cannot be expressed in terms of tabulated functions. However, they can be simplified and written in a form more suitable for numerical evaluation by means of the same procedure outlined in connection with $K(x, y)$ (see equation (35)): choosing branch cuts appropriately to meet the restrictions (22) and (23) and converting the integral to a contour on which the exponent is real. Some details are given in the Appendix. The results are as follows:

$$H(x,y) = \frac{2y}{r^2} - (V/c)e^{-Vx/2c}\int_{-\cos\theta}^{1}\frac{(1+u\cos\theta)}{(1-u^2)^{1/2}}e^{-(Vr/2c)u}du \quad (50)$$

$$L(x,y) = \frac{2}{r}\int_0^\infty \frac{u^{1/2}e^{-u}\cos\left[\frac{3}{2}\left(\frac{\pi}{2}-\theta\right)-\frac{\psi}{2}\right]du}{|(u-Vx/c)^2+(Vy/c)^2|^{1/4}} \quad (51)$$

where $\tan\theta = y/x$ and

$$\sin\psi = \frac{u\cos\theta - Vr/c}{|(u-Vx/c)^2+(Vy/c)^2|^{1/2}}. \quad (52)$$

Derivatives of H, which appear in (47), can be calculated from (50). However, the derivatives of L can be expressed more compactly by first differentiating (49), then manipulating as to obtain (51). The result is

$$\frac{\partial L}{\partial\zeta} = \frac{\iota}{r^2}\int_0^\infty \frac{u^{3/2}e^{-u}\exp\left\{\iota\left[5\left(\theta-\frac{\pi}{2}\right)-\psi\right]/2\right\}du}{|(u-Vx/c)^2+\quad Vy/c)^2|^{1/4}}. \quad (53)$$

These suffice to determine the full solutions for the stress and pore pressure, but for brevity only the pore pressure and the shear stress σ_{xy} on $y = 0$ are displayed here. The structure of the solution is identical to that for the permeable plane. That is, the first terms in (45)–(47) give the undrained response appropriate to the limit $V \to \infty$; in the limit $V \to 0$, the expressions can be shown to reduce to the usual ones of linear elasticity with Poisson's ratio ν as appropriate to drained response.

The pore pressure, obtained from substitution of (50) into (46), yields

$$\eta p = \Delta\mu(V/c)e^{-Vx/2c}\int_{-\cos\theta}^{1}\frac{(1+u\cos\theta)}{(1-u^2)^{1/2}}e^{-(Vr/2c)u}du. \quad (54)$$

The shear stress on $y = 0$ is obtained by extracting the imaginary part of (47) after substituting (50) and (53) and setting $y = 0$. The result can be expressed in the same form as (41) with g_p replaced by g_i defined as follows:

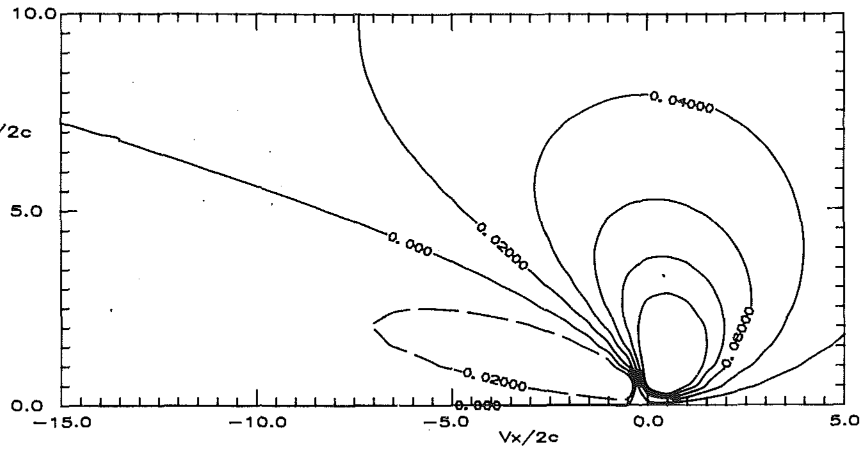

Fig. 2 Contours of constant nondimensional pore pressure (56) for the dislocation on the permeable plane. The dashed contour indicates a negative value. Values for $y < 0$ are equal in magnitude and opposite in sign to those shown.

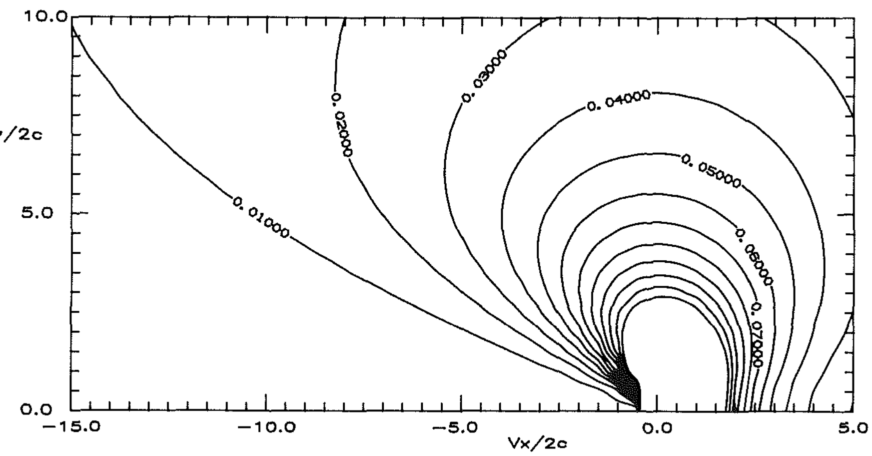

Fig. 3 Same as Fig. 2 for the dislocation on an impermeable plane

$$g_i(z) = 4z\left[\int_1^\infty \frac{u^{3/2}}{(u-1)^{1/2}}\, e^{-2zu}du - \frac{1}{4z^2}\right],\ z>0$$

$$g_i(z) = 4z\left[\int_1^\infty \frac{u^{3/2}}{(1+u)^{1/2}}\, e^{-2|z|u}du - \frac{1}{4z^2}\right],\ z<0. \tag{55}$$

In the next section, some features of these solutions are discussed, compared with the solutions for the permeable plane and displayed graphically.

Discussion

As has already been emphasized, the solutions for the permeable and impermeable planes agree, as they must, in the limits of drained and undrained response corresponding to $V \to 0$ and $V \to \infty$, respectively. Differences in the solutions for finite, nonzero velocities are due to the different boundary conditions for the pore pressure ((12) and (13)) on $y = 0$. In this section, we focus on the differences between the solutions as manifested by the shear stress on $y = 0$ and the pore pressure.

Figures 2 and 3 show contours of the nondimensional pore pressure, defined as

$$P = \frac{4(1-\nu_u)\eta}{G(Vb/c)\mu}\, p, \tag{56}$$

for the permeable (Fig. 2) and impermeable (Fig. 3) planes. These plots are for $y \geq 0$; values for $y < 0$ are equal in magnitude and opposite in sign. As required by the boundary condition (12), the pore pressure change is zero on the permeable plane. The maximum pore pressure change occurs off the dislocation plane at about $(Vx/2c,\ Vy/2c) \approx (1, 1)$. Figure 2 also shows that there is a wake of pore pressure decrease, ($p < 0$), extending behind the edge of the slip discontinuity at the origin. This feature of the solution has been discussed in detail by Roeloffs and Rudnicki (1984/85) and, as noted by them, results from the differing response of the fluid mass content ($m - m_o$) and mean normal stress at a fixed point off the dislocation plane as slip approaches.

Figure 3 shows the corresponding contours of the nondimensional pore pressure for the impermeable plane. As required by the boundary condition (13), the contours intersect the x-axis at right angles. In contrast to the solution for the permeable plane, the maximum pore pressure change occurs on $y = 0$, and, although not evident from the contour plot, at $x = 0$. As a result, the solution predicts flow of pore fluid along $x = 0$ away from the origin. In further contrast to the solution for the permeable plane, the pore pressure change is everywhere positive in $y > 0$. This evidently results because $y = 0$ is a barrier to fluid flow and hence the increase in pore pressure in the first quadrant due to the approaching dislocation cannot be dissipated by flow across $y = 0$ to the region of pore pressure decrease, as occurs for the permeable plane. As indicated in Fig. 3, the pore pressure change is, however, small in magnitude behind the dislocation ($x < 0$). Indeed, as to be discussed shortly, the pore pressure is identically zero for $x < 0$ and $y = 0$.

Figure 4 plots the nondimensional pore pressure change for the permeable (dashed) and impermeable (solid) planes against

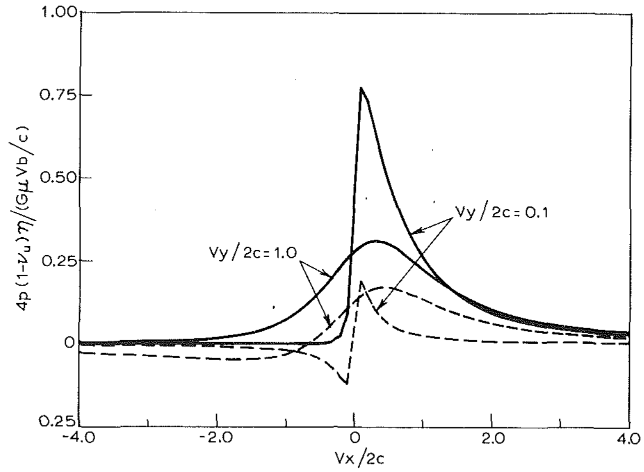

Fig. 4 Comparison of the nondimensional pore pressure induced by dislocations on a permeable (dashed) and impermeable (solid) plane. Results are shown as a function of $Vx/2c$ for $Vy/2c$ = 0.1 and 1.0.

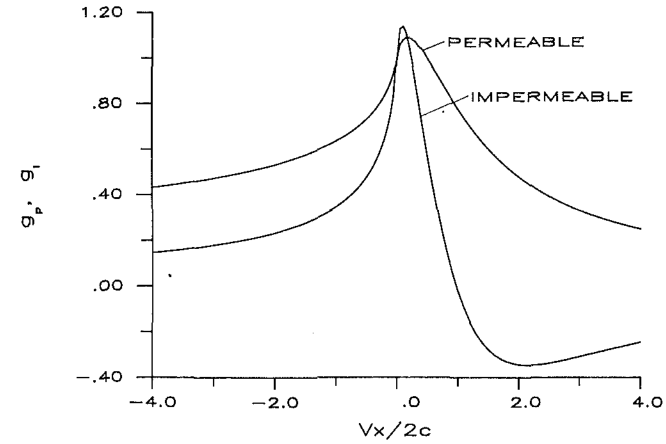

Fig. 5 Comparison of the functions g_p (42) and g_i (55) appearing in the expressions for the shear stress on y = induced by a dislocation moving on a permeable (g_p) and impermeable (g_i) plane

$Vx/2c$ for two fixed distances from the slip plane: $Vy/2c$ = 0.1, 1.0. Because the propagation is steady, these curves, when read from right to left, give the time history of the response at a fixed point as the dislocation moves past. As shown, the magnitude of the pore pressure change is much greater near the impermeable plane than the permeable, but decreases more rapidly with distance from the slip plane. Figure 4 also shows the sign reversal of the pore pressure change for the permeable plane. Also noteworthy is the rapid decrease of the pore pressure change for the impermeable plane for $x < 0$ and $Vy/2c = 0.1$.

Roeloffs and Rudnicki (1986) have given results similar to those shown in Fig. 4, and have discussed their implications for the interpretation of water well level changes in response to propagating slip events in the earth's crust. Their results for the impermeable plane are, however, obtained by direct numerical inversion of the Fourier transformed expression for p rather than by (54). They note that as a result of the sign reversal for the permeable plane, there will be a cancellation of positive and negative contributions to the pore pressure when the elemental dislocations are superimposed to model more elaborate slip distributions. This will further diminish the magnitude of the pressure change for the slip on the permeable plane as compared with that for the impermeable.

A surprising result of the solution is that for the impermeable plane, the pore pressure is identically zero for $y = 0$ and $x < 0$. This is evident from (54), since $\cos(\pi) = -1$, but can also be deduced directly from (48): For $y = 0$, and the branch cuts as specified by (22) and (23), the integrand is analytic for $\mathrm{Im}(\kappa) < 0$; hence, for $x < 0$, the integral can be computed with zero result by closing the contour at infinity in the lower half-plane (see the Appendix for more details). Thus, both p and $\partial p/\partial y$ are zero on $y = 0$ for $x < 0$. For $x > 0$ and $y = 0^+$, (54) can be expressed in terms of tabulated functions as follows:

$$P(x,0^+) = e^{-Vx/2c}\{I_0(Vx/2c) - I_1(Vx/2c)\} \quad (57)$$

where P is given by (56) and I_0 and I_1 are modified Bessel function (Abramowitz and Stegun, 9.6.18, 1964). As $x \to 0$ through positive values, the right-hand side of (57) approaches unity and, hence, the pore pressure induced on the impermeable plane $y = 0^+$ is discontinuous at $x = 0$. This is reflected by the bunching of contours near the origin in Fig. 3. More generally, the behavior of the pore pressure as $r \to 0$ can easily be shown from (54), to be given by

$$\eta p = \mu\Delta(V/c)\left\{\pi - \theta + \frac{1}{2}\sin(2\theta)\right\}. \quad (58)$$

As an example of the effect on the stress field of the fluid flow boundary condition on $y = 0$, Fig. 5 plots the functions $g_p(Vx/2c)$ and $g_i(Vx/2c)$. These appear in the expressions for the shear stress on $y = 0$ (41) for the permeable (42) and impermeable (55) planes. Because these expressions must reduce to the drained value at $V = 0$ and the undrained value as $V \to \infty$, both g_p and g_i equal unity when their arguments are zero and approach zero when their arguments become unbounded. However, as depicted in Fig. 5, the values for finite, nonzero V are considerably different for the permeable and impermeable planes. Interpreted in another way, the distribution of shear stress on $y = 0$ differs in the two cases. In particular, g_i decays more rapidly with distance from the origin than g_p. Moreover, g_i becomes negative at approximately $Vx/2c = 1.0$ and approaches zero through negative values when its argument is positive. (Note, however, that the shear stress itself does not reverse signs.) Because $g_i < g_p$ for $x > 0$, except very close to $x = 0$, the shear stress induced on $y = 0$ ahead of a dislocation moving on an impermeable plane exceeds that for a dislocation on a permeable plane. In addition, because $g_i < 0$ for $Vx/2c < 1$, the shear stress on this portion of the impermeable plane exceeds the undrained value (the first term in (41)). A similar feature was noted in the solution for a dislocation instantaneously introduced on an impermeable plane (Rudnicki, 1986, 1987).

As noted earlier, the expression for g_p has been derived previously by Simons (1979) and has been given graphically by Cleary (1978) who obtained the result by numerically integrating the appropriate expression from the solution for instantaneous introduction of a stationary dislocation (on a permeable plane). Our results appear to agree with those given by Cleary (1978).

Slip on faults in the earth's crust depends not only on the shear stress but also on the effective normal stress: that is, $\sigma_{yy} + p$, the total normal stress plus the pore pressure (e.g., Jaeger and Cook, 1976; Rice, 1980). More specifically, an increase in compressive effective normal stress inhibits slip. For a dislocation propagating on an impermeable plane, the effective normal stress increases in compression on the side where p decreases, ($y = 0^-$), and decreases on the side where p increases ($y = 0^+$). Because the impermeable plane idealizes a narrow, but finite-width fault zone, it is likely that slip propagation will follow the path of least resistance and the reduction of effective compressive stress on one side of the fault promotes slip. The magnitude of this effect is shown in Fig. 6 which plots the following quantity:

$$\psi(Vx/2c) = \frac{4\pi(1-\nu_u)}{GVb/c}\{\sigma_{xy}(x,0^+) + fp(x,0^+)\}. \quad (59)$$

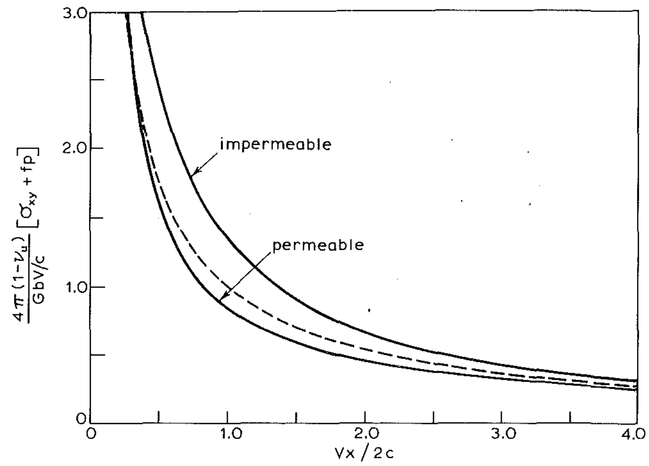

Fig. 6 Plot of $4\pi(1 - \nu_u)[\sigma_{xy} + fp]/(GVb/c)$ on $y = 0^+$ for the dislocation moving on an impermeable plane and a permeable plane ($p = 0$ for the permeable plane). The dashed line shows only the first term for the impermeable plane. Actual plot is for $f = 0.6$, $\mu = 0.2$, $\eta = 1.38\mu$.

The coefficient of friction f (taken to be 0.6) multiplies the effective normal stress $\sigma_{yy} + p$, but σ_{yy} vanishes on $y = 0$. Also shown, for comparison, is the first term alone and the corresponding quantity for the permeable plane. The latter is identical to σ_{xy} because $p = 0$ on $y = 0$ for the permeable plane. As noted in the discussion of Fig. 5, the shear stress ahead of the dislocation on an impermeable plane exceeds that on a permeable plane. Furthermore, the contribution to ψ from the decrease in effective normal compressive stress due to the increase of pore pressure on $y = 0^+$ further elevates the driving force for slip. Because the pore pressure is bounded at $x = 0$, this contribution is overwhelmed there by the shear stress which is singular at $x = 0$. Nevertheless, for more elaborate models of slip that require the shear stress at the edge of the slipping zone to be bounded, the effect of the pore pressure will be significant.

Although we do not consider here problems of steadily-moving opening dislocations, results for the instantaneous introduction of stationary dislocations (Rudnicki, 1987) suggest that the same functions g_i and g_p appear in corresponding expressions for the normal traction (σ_{yy}) on $y = 0$ for an opening dislocation (Burgers vector in the y-direction). That is, if $p = 0$ on $y = 0$, the normal traction induced by an opening dislocation is given by (41) and, if $\partial p/\partial y = 0$ on $y = 0$, by (41) with g_i replacing g_p. More specifically, Rudnicki (1987) found that the time-dependence of the shear traction ahead of a shear dislocation on an impermeable plane is identical to that for the normal traction ahead of an opening dislocation on an impermeable plane. The corresponding result holds for the permeable plane. (For an opening dislocation on $y = 0$, the boundary condition $\partial p/\partial y = 0$ on $y = 0$ arises from symmetry and continuity of the pore pressure, whereas $p = 0$ requires a discontinuity in $\partial p/\partial y$. The latter can be interpreted as the limiting case of a very narrow zone with an extremely high permeability in the x-direction.) Cleary (1978) gives results for the steadily-moving opening dislocation but, unfortunately, the function corresponding to g_i here is expressed as the difference between two functions which are only presented graphically. Our results for g_i appear to be consistent with those given by Cleary (1978), but a detailed comparison is not possible.

A similar correspondence to that for the velocity dependence of tractions for opening and shear dislocations has also been found for cracks, which, of course, can be regarded as continuous distribution of dislocations. Rice and Simons (1978) solved the problem of a shear (Mode II) crack propagating steadily on a permeable plane and Koutsibelas (1988) has recently solved the analogous problem for the impermeable plane. In both cases, the stress field near the edge of the propagating crack has the well-known universal spatial dependence for cracks in linear elastic solids but, in contrast to the results for ordinary elasticity, the stress intensity factor is a function of velocity. The form of this function for the shear crack depends on whether the crack plane is permeable or impermeable. However, Koutsibelas (1988) found that the velocity dependence for the shear crack was identical to that found by Ruina (1978) for the opening crack with the boundary condition $\partial p/\partial y = 0$ imposed on the crack plane.

Acknowledgment

One of us (J. W. R.) thanks Don Simons for several helpful discussions concerning the inversion integrals.

This work was initiated under support from the U. S. Geological Survey Earthquake Hazards Reduction Program and completed under support from the National Science Foundation Earth Sciences Program.

References

Abramowitz, M., and Stegun, I. A., eds., 1964, *Handbook of Mathematical Functions*, (Appl. Math. Ser. 55), National Bureau of Standards, Washington, D.C.

Biot, M. A., 1941, "General Theory of Three-Dimensional Consolidation," *J. Appl. Phys.*, Vol. 12, pp. 155–164.

Biot, M. A., 1956, "Thermoelasticity and Irreversible Thermodynamics," *J. Appl. Phys.*, Vol. 27, pp. 240–253.

Booker, J. R., 1974, "Time-Dependent Strain Following Faulting of a Porous Medium," *J. Geophy. Res.*, Vol. 79, pp. 2037–2044.

Carslaw, H. S., and Jaeger, J. C., 1959, *Conduction of Heat in Solids*, 2nd Ed., Oxford University Press, Oxford, U.K.

Cleary, M. P., 1976, "Continuously-Distributed Dislocation Model for Shear-Bands in Geological Materials," *Int. J. Num. Methods in Eng.*, Vol. 10, pp. 679–702.

Cleary, M. P., 1978, "Moving Singularities in Elasto-Diffusive Solids with Applications to Fracture Propagation," *Int. J. Solids Structures*, Vol. 14, pp. 81–97.

Detournay, E., and Cheng, A. H-D., 1987, "Poroelastic Solution of a Plane Strain Point Displacement Discontinuity," ASME JOURNAL OF APPLIED MECHANICS, Vol. 54, pp. 783–787.

Erdelyi, A., Magnus, W., Oberhettinger, F., and Tricomi, F., 1954, *Tables of Integral Transforms*, Vol. 1, McGraw-Hill, New York.

Erdogan, F., and Gupta, G. D., 1972, "On the Numerical Solution of Singular Integral Equations," *Quart. Appl. Math.*, Vol. 30, pp. 525–534.

Jaeger, J. C., and Cook, N. G. W., 1976, *Fundamentals of Rock Mechanics*, 2nd ed., Halsted Press, New York.

Koutsibelas, D. A., 1988, "Stabilization of Slip in a Fluid-Infiltrated Rock Mass," Ph.D. Thesis, Northwestern University, Chicago, IL.

Kuei, S., 1977, "Rheological Modeling of Synovial Fluid and Application of the Mixture Theory to Articular Cartilage," Ph.D. Thesis, Rensselaer Polytechnic Institute.

Lebedev, N. N., 1972, *Special Functions and Their Applications*, Dover Publications, New York.

Mow, V. C., and Lai, W. M., 1980, "Recent Developments in Synovial Joint Biomechanics," *SIAM Review*, Vol. 22, pp. 275–317.

Nur, A., and Booker, J. R., 1972, "Aftershocks Caused by Fluid Flow?" *Science*, Vol. 175, pp. 885–887.

Rice, J. R., 1979, "The Mechanics of Quasistatic Crack Growth," *Proceeding of the 8th U. S. National Congress of Applied Mechanics*, R. E. Kelley, ed., Western Periodicals, North Hollywood, Calif., pp. 191–216.

Rice, J. R., 1980, "The Mechanics of Earthquake Rupture," *Physics of the Earth's Interior*, (Proc. Int. School Physics "Enrico Fermi", 78), (A. M. Dziewonski and E. Boschi, eds.), North-Holland, Amsterdam, pp. 555–649.

Rice, J. R., and Cleary, M. P., 1976, "Some Basic Stress Diffusion Solutions for Fluid-Saturated Elastic Porous Media With Compressible Constituents," *Rev. Geophys. Space Phys.*, Vol. 14, pp. 227–241.

Rice, J. R., and Simons, D. A., 1976, "The Stabilization of Spreading Shear Faults by Coupled Deformation-Diffusion Effects in Fluid-Infiltrated Porous Materials," *J. Geophys. Res.*, Vol. 81, pp. 5322–5344.

Roeloffs, E., and Rudnicki, J. W., 1984–1985, "Coupled Deformation-Diffusion Effects on Water-Level Changes due to Propagating Creep Events," *Pure and Applied Geophysics*, Vol. 122, pp. 560–582.

Roeloffs, E., and Rudnicki, J. W., 1986, "The Effect of Fault Plane Impermeability on Pore Pressure Changes Induced by Propagating Creep Events," (Abstract), *EOS, Trans. Am. Geophy. Union*, Vol. 67, p. 272.

Rudnicki, J. W., 1986, "Slip on an Impermeable Fault in A Fluid-Saturated Rock Mass," *Earthquake Source Mechanics*, S. Das, J. Boatwright and C. H. Scholz, eds., American Geophysical Union, Geophysical Monograph 37, pp. 81–89.

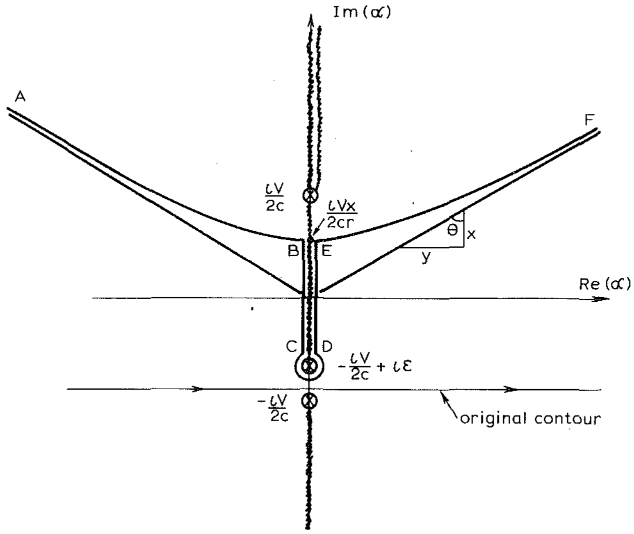

Fig. 7 Branch cuts and integration contours in the complex α-plane (see ($A2$)) used in the evaluation of the integral H ($A1$) for $x > 0$. The branches AB and EF of the hyperbola given by ($A7$) intersect the Im(α) axis at $\iota Vx/2cr$.

Rudnicki, J. W., 1987, "Plane Strain Dislocations in Linear Elastic Diffusive Solids," ASME Journal of Applied Mechanics, Vol. 109, pp. 545–552.

Rudnicki, J. W., and Hsu, T.-C., 1988, "Pore Pressure Changes Induced by Slip on Permeable and Impermeable Faults," *J. Geophys. Res.*, Vol. 93, pp. 3275–3285.

Ruina, A., 1978, "Influence of Coupled Deformation-Diffusion Effects on Retardation of Hydraulic Fracture," *Proc. U. S. Symposium on Rock Mechanics, 19th*, Y. S. Kim, ed., Stateline, Nev., pp. 274–272.

Simons, D. A., 1979, "The Analysis of Propagating Slip Zones in Porous Elastic Media," *Fracture Mechanics, Proceedings of the Symposium in Applied Mathematics of AMS and SIAM*, R. Burridge, ed., SIAM-AMS, New York, pp. 153–169.

APPENDIX

This appendix gives some details of the manipulation of the inversion integral $H(x, y)$ given by (48) and repeated here for convenience:

$$H(x,y) = \int_{-\infty}^{\infty} \frac{m(\kappa)}{n(\kappa)} \exp[\iota\kappa x - n(\kappa)y]d\kappa \qquad (A1)$$

where $m(\kappa)$ and $n(\kappa)$ are defined following (21) and are subject to the restrictions (22) and (23). Manipulation of K (32) and L (49) can be accomplished similarly and will not be discussed in detail. In each case the procedure is to choose the branch cuts consistently with the restrictions (22) and (23), and then transform the integration path to one in the complex plane along which the exponent is real and negative.

It will be convenient to make the change of variable

$$\alpha = \kappa - \iota V/2c \qquad (A2)$$

so that

$$n^2(\alpha) = \alpha^2 + (V/2c)^2. \qquad (A3)$$

To facilitate the choice of the branch cuts, write $n(\alpha)$ as the following product

$$n(\alpha) = n_+(\alpha)n_-(\alpha) \qquad (A4)$$

where $n_\pm(\alpha) = (\alpha \pm \iota V/2c)^{1/2}$. To enforce the restriction (23), the branch cut for $n_+(\alpha)$ is taken along the imaginary α-axis from $-\iota V/2c$ to $-\iota\infty$ and that for $n_-(\alpha)$ from $\iota V/2c$ to $\iota\infty$. Hence, $n_+(\alpha)$ and $n_-(\alpha)$ are analytic in the half-planes $\mathrm{Im}(\alpha) > -\iota V/2c$ and $\mathrm{Im}(\alpha) < \iota V/2c$, respectively. Similarly, we let

$$m(\alpha) = n_+(\alpha)m_-(\alpha) \qquad (A5)$$

where $m_-(\alpha) = \lim_{\epsilon\to 0} \{\alpha + (\iota V/2c) - \epsilon\}^{1/2}$ is analytic for $\mathrm{Im}(\alpha) < -\iota V/2c + \iota\epsilon$. With these definitions, the integral can be written as follows:

$$H(x,y) = \exp(-Vx/2c) \int_{-\infty-\iota V/2c}^{\infty\iota V/2c} \frac{m_-(\alpha)}{n_-(\alpha)} \exp\{\iota\alpha x - n(\alpha)y\}d\alpha \qquad (A6)$$

where the branch cuts and integration contour are shown in Fig. 7. Before proceeding, we note that when $y = 0$, the integration can be accomplished by closing the contour in the upper (lower) half-plane for $x > (<)0$. Because the integrand is analytic in the lower half-plane for $y = 0$, H vanishes for $x < 0$, $y = 0$. Hence, so does the pore pressure, as discussed in the body of the paper.

The integration can be accomplished by wrapping the contour around the branch cuts. However, an expression that is more compact and amenable to numerical evaluation is obtained by transforming the contour of integration to one on which the exponent is real and negative, subject to (23). This contour is given by

$$\alpha_\pm(s) = (\iota xs/r^2) \pm (y/r^2)[s^2 - (Vr/2c)^2]^{1/2} \qquad (A7)$$

where $Vr/2c \le s \le \infty$. For $x > 0$, $\alpha_+(s)$ and α_- describe the right and left branches of a hyperbola in the upper half-plane. As shown in Fig. 7, the hyperbola intersects the branch cut for $m_-(\alpha)$ at $\alpha = \iota Vx/2cr$, corresponding to $s = Vr/2c$. Thus, for $x > 0$, the integral can be evaluated along the contour ABCDEF.

The result is given by (50) where the first term is the due to integration along the arcs of the hyperbola (AB and EF) and the second from integration along the branch cuts (BC and DE). There is no contribution from integration around the branch point (CD). The corresponding calculation for $x < 0$ yields a result of identical form.

Calculation of the integral $K(x, y)$ given by (32) is accomplished by the same method. However, in this case, the integrand does not involve $m(\alpha)$ and, as a consequence, the path of integration involves only the hyperbola specified by ($A7$) and there is no need to detour around the branch cut.

Manipulation of the integral $L(x, y)$ (49) to yield (51) follows similar steps. Begin by letting

$$m(\kappa) = m_+(\kappa)m_-(\kappa)$$

where $m_\pm(\kappa) = \lim_{\epsilon\to 0} (\kappa \pm \iota\epsilon)^{1/2}$ with the branch cut for $m_\pm(\kappa)$ chosen from $\kappa = \mp\iota\epsilon$ to $\mp\iota\infty$. Similarly, decompose $n(\kappa)$ as follows

$$n(\kappa) = m_+(\kappa)n_-(\kappa)$$

with $n_-(\kappa) = (\kappa - \iota V/c)^{1/2}$ having a branch cut from $\kappa = \iota V/c$ to $\kappa = \iota\infty$. With these definitions, the integral becomes

$$L(x,y) = \int_{-\infty}^{\infty} \frac{m_-(\kappa)}{n_-(\kappa)} \exp\{\iota\kappa x - m(\kappa)y\}d\kappa.$$

A contour on which the exponent is real and negative is given by the same form as ($A7$) with $V/2c$ replaced by ϵ. This contour does not intersect any branch cuts. Conversion of the path of integration to this contour yields

$$L(x,y) = \lim_{\epsilon\to 0} 2\int_{r\epsilon}^{\infty} \frac{e^{-s}}{(s^2 - r^2\epsilon^2)^{1/2}} \mathrm{Re}\left\{\frac{m(\kappa_+)m_-(\kappa_+)}{n_-(\kappa_+)}\right\}ds$$

where $\kappa_+ = (ixs/r^2) + (y/r^2)[s^2 - \epsilon^2 r^2]^{1/2}$. The result (51) follows from taking the limit and evaluating $\{\ \ldots\ \}$.

Plane-Strain Crack-Tip Fields for Pressure-Sensitive Dilatant Materials

F. Z. Li
Assoc. Mem. ASME

J. Pan
Assoc. Mem. ASME

Department of Mechanical Engineering and Applied Mechanics,
The University of Michigan,
Ann Arbor, MI 48109

Plane-strain crack-tip stress and strain fields are presented for materials exhibiting pressure-sensitive yielding and plastic volumetric deformation. The yield criterion is described by a linear combination of the effective stress and the hydrostatic stress, and the plastic dilatancy is introduced by the normality flow rule. The material hardening is assumed to follow a power-law relation. For small pressure sensitivity, the plane-strain mode I singular fields are found in a separable form similar to the HRR fields (Hutchinson, 1968a, b; Rice and Rosengren, 1968). The angular distributions of the fields depend on the material-hardening exponent and the pressure-sensitivity parameter. The low-hardening solutions for different degrees of pressure sensitivity are found to agree remarkably with the corresponding perfectly-plastic solutions. An important aspect of the effects of pressure-sensitive yielding and plastic dilatancy on the crack-tip fields is the lowering of the hydrostatic stress and the effective stress directly ahead of the crack tip, which may contribute to the experimentally-observed enhancement of fracture toughness in some ceramic and polymeric composite materials.

1 Introduction

In classical plasticity theories, it is generally assumed that hydrostatic pressure has no effect on material plastic deformation, and plastic dilatancy is neglected. These theories are applicable mainly to dense metals. In contrast, rocks, concretes, soils, and other porous materials exhibit pressure-sensitive yielding and plastic volumetric deformation. Recently toughened structural polymers and ceramics due to their outstanding mechanical properties have attracted tremendous research attention. Experimental results on the mechanical behavior of these two classes of materials support a constitutive description that accounts for pressure-sensitive yielding and plastic dilatancy for these materials.

Spitzig and Richmond (1979) observed that for polymeric materials (polyethylene and polycarbonate) the flow stress has a significant dependence on the hydrostatic stress. Carapellucci and Yee (1986) performed biaxial tension tests on glassy bisphenol A—polycarbonate and found that a modified Mises yield criterion with a dependence on the hydrostatic stress fits their experimental data well. Sue and Yee (1988) investigated the toughening mechanisms in a multiphase alloy of Nylon 6,6/Polyphenylene oxide, and found that there is a considerable amount of plastic volumetric change in the composite material due to the formation of crazes at large strain. They concluded that toughening of this material can be achieved by inducing a large amount of volumetric deformation due to crazing and subsequent shear yielding around a crack tip. The phenomenon of pressure-sensitive yielding is also observed in transformation toughened ZrO_2-containing ceramics (for example, see Chen and Reyes Morel (1986) and Reyes-Morel and Chen (1988)).

From the viewpoint of phenomenological fracture mechanics, the initiation and growth of a crack depend on the surrounding stress and deformation fields near the tip. Therefore, analyses of the crack-tip stress and deformation fields are important to relate continuum stress analyses to micromechanical failure mechanism. The asymptotic crack-tip fields for power-law hardening materials (the well-known HRR fields) have been presented by Hutchinson (1968a, b) and Rice and Rosengren (1968). Recently, Pan and Shih (1986, 1988) obtained the crack-tip fields for power-law hardening orthotropic materials. These fields are of the HRR type, and the deformations of these fields are volume preserving. An example of the HRR type crack-tip fields with volumetric deformation was presented by Hutchinson (1983) for power-law creep materials undergoing creep-constrained grain boundary cavitation.

In this study we investigate the crack-tip stress and strain fields for pressure-sensitive dilatant materials under plane-strain conditions. A simple hydrostatic stress-dependent yield

Contributed by the Applied Mechanics Division of The American Society of Mechanical Engineers for presentation at the Winter Annual Meeting, San Francisco, Calif., December 10-15, 1989.

Discussion on this paper should be addressed to the Editorial Department, ASME, United Engineering Center, 345 East 47th Street, New York, N.Y. 10017, and will be accepted until two months after final publication of the paper itself in the Journal of Applied Mechanics. Manuscript received by the ASME Applied Mechanics Division, December 21, 1988; final revision, April 20, 1989.
Paper No. 89-WA/APM-48.

criterion and the normality flow rule are used to account for the pressure-sensitive yielding and plastic dilatancy. Within a limited degree of pressure sensitivity, mode I crack-tip fields for power-law hardening materials are obtained. The crack-tip fields depend on the pressure sensitivity parameter, μ, and have a separable form. When $\mu = 0$, they exactly match the HRR results. Our low-hardening solutions for power-law hardening pressure-sensitive materials agree well with the corresponding perfectly-plastic slip line solutions.

2 Constitutive Relations

Motivated by the work of Spitzig and Richmond (1979) for polymers and the work of Reyes-Morel and Chen (1988) for ceramics, we adopt a simple pressure-sensitive yielding criterion that contains two stress invariants, the effective shear stress τ_e and the hydrostatic stress σ_m. The yield criterion is written as

$$\psi(\sigma_{ij}) = \tau_e + \mu\,\sigma_m = Q, \qquad (1)$$

where

$$\tau_e = (s_{ij}s_{ij}/2)^{1/2}, \quad s_{ij} = \sigma_{ij} - \sigma_m\delta_{ij}, \quad \sigma_m = \sigma_{kk}/3,$$

and $\psi(\sigma_{ij})$ represents the current yield surface in the stress space. The material constant μ measures the pressure sensitivity of yielding. The characteristic yield strength Q can be taken to depend upon the plastic work W^p. More information on the pressure-sensitive yield criterion can be found, for example, in Drucker (1973).

We introduce the generalized effective shear stress τ_{ge} and the generalized effective stress σ_{ge} as follows:

$$\tau_{ge} = \tau_e + \mu\,\sigma_m \qquad (2)$$

and

$$\sigma_{ge} = \sqrt{3}\,\tau_{ge} = \sigma_e + \sqrt{3}\,\mu\,\sigma_m, \qquad (3)$$

where

$$\sigma_e = \sqrt{3}\,\tau_e = (3s_{ij}\,s_{ij}/2)^{1/2} \qquad (4)$$

is the conventional effective stress. The yield criterion (equation (1)) can be restated as

$$\tau_{ge} = \tau_e + \mu\,\sigma_m = Q(W^p), \qquad (5)$$

or

$$\sigma_{ge} = \sigma_e + \sqrt{3}\,\mu\,\sigma_m = \sqrt{3}\,Q(W^p). \qquad (6)$$

The outward normal of the yield surface in the stress space is

$$\frac{\partial\psi(\sigma_{ij})}{\partial\sigma_{ij}} = \frac{\partial\tau_{ge}}{\partial\sigma_{ij}} = \frac{s_{ij}}{2\tau_e} + \frac{\mu}{3}\,\delta_{ij}. \qquad (7)$$

A direct measurement of the pressure sensitivity factor μ relies on shear experiments under pressure. It can be obtained from the difference between the compressive yield strength σ_c and the tensile yield strength σ_t through the relation (Needleman and Rice, 1978)

$$\mu = \sqrt{3}\,\frac{\sigma_c - \sigma_t}{\sigma_c + \sigma_t}. \qquad (8)$$

An alternative method to determine μ is to perform compressive or tensile tests under pressure p. For compressive tests, let σ_c^0 denote the compressive yield strength in the absence of pressure, and σ_c^p denote the compressive yield strength when superimposed by hydrostatic pressure p. If the experimental data can be fitted by the linear relation (Chen and Reyes Morel, 1986)

$$\sigma_c^p = \sigma_c^0 + \alpha p, \qquad (9)$$

the parameter μ can then be calculated through

$$\mu = \sqrt{3}\,\frac{\alpha}{3+\alpha}. \qquad (10)$$

Note that the relations (8) and (10) give the same upper bound of μ, equal to $\sqrt{3}$. The experimental curves in Carapellucci and Yee (1986) show that the factor μ for glassy bisphenol A—polycarbonate is about 0.14. For ZrO_2-containing ceramics, Chen and Reyes Morel (1986) reported that the constant α in (10) may approach 2.0, which corresponds to $\mu = 0.69$. According to these studies, pressure-sensitive yielding seems to play an important role in the plastic deformation and fracture of polymers and in the transformation plasticity and fracture of toughened ceramics.

In general, pressure-sensitive yielding arises in part from basic flow mechanism in some steels and polymers, phase transformation in some ceramics, and in part from void nucleation and growth in steels as well as craze formation in polymers. The initial and current yielding for these materials may deviate somewhat from the yield criterion (1) (see Drucker (1973) for more discussion). However, in this study we assume that the yield criterion (1) with a constant μ is approximately valid for the range of the stress state of interest near a crack tip for simplicity in order to explore the major effects of pressure sensitivity on the crack-tip field.

In this analysis, we assume that material hardening is specified by the Ramberg-Osgood stress-strain relation in shear:

$$\frac{\gamma}{\gamma_0} = \frac{\tau}{\tau_0} + \alpha\left(\frac{\tau}{\tau_0}\right)^n, \qquad (11)$$

where τ is the shear stress, γ is the shear strain, n is the strain hardening exponent, α is a material constant, and τ_0 and γ_0 are the reference shear stress and the reference shear strain. Within the context of deformation theory of plasticity, we generalize the relation between the shear stress and the plastic shear strain (the second term on the right-hand side of (11)) to multiaxial states by using (5) and (7). In this generalization the yield surface is assumed to expand isotropically and the plastic strain is assumed to obey the plastic normality rule. The resulting relation between the stresses and plastic strains is

$$\frac{\epsilon_{ij}^p}{\gamma_0} = \alpha\left(\frac{\tau_{ge}}{\tau_0}\right)^n\left(\frac{s_{ij}}{2\tau_e} + \frac{\mu}{3}\,\delta_{ij}\right). \qquad (12)$$

The total plastic strain ϵ_{ij}^p in (12) can be decomposed into a deviatoric part and a volumetric part:

$$\epsilon_{ij}^p = \epsilon_{ij}'^p + \frac{1}{3}\,\epsilon_{kk}^p\,\delta_{ij}, \qquad (13)$$

where

$$\frac{\epsilon_{ij}'^p}{\gamma_0} = \alpha\left(\frac{\tau_{ge}}{\tau_0}\right)^n\frac{s_{ij}}{2\tau_e}, \qquad (14)$$

and

$$\frac{\epsilon_{kk}^p}{\gamma_0} = \mu\,\alpha\left(\frac{\tau_{ge}}{\tau_0}\right)^n. \qquad (15)$$

The summation of (14) over i and j gives an expression relating the effective plastic shear strain γ_e^p ($= (2\epsilon_{ij}'^p\,\epsilon_{ij}'^p)^{1/2}$) and the generalized effective shear stress τ_{ge}:

$$\frac{\gamma_e^p}{\gamma_0} = \alpha\left(\frac{\tau_{ge}}{\tau_0}\right)^n. \qquad (16)$$

By comparing (16) with (15), we find that

$$\epsilon_{kk}^p = \mu\,\gamma_e^p. \qquad (17)$$

Equation (17) indicates that the pressure sensitivity factor μ also serves as the plastic dilatancy factor which gives the ratio of plastic volumetric strain ϵ_{kk}^p to the effective plastic shear strain γ_e^p. This results from the plastic normality flow rule that we use to arrive at equation (12).

The stress-strain relation (12) is based on the deformation theory of plasticity. Incremental constitutive equations accounting for pressure sensitivity and plastic dilatancy can be found, for example, in Rudnicki and Rice (1975) and Needleman and Rice (1978). These authors introduced two parameters to allow non-normality flow; one parameter is the pressure-sensitivity factor μ, and the other is the plastic dilatancy factor β. Plastic normality applies only when $\mu = \beta$. In this paper we investigate the asymptotic crack-tip stress and strain fields for the pressure-sensitive dilatant materials to which plastic normality applies.

When the elastic strains are assumed to be negligible compared to the plastic strains, the plane-strain condition requires that, from (12),

$$\frac{s_{33}}{2\tau_e} + \frac{\mu}{3} = 0. \qquad (18)$$

By solving (18) for σ_{33}, the hydrostatic stress, σ_m, and the deviatoric stress components, s_{11} and s_{22}, can be expressed in terms of the three in-plane components, σ_{11}, σ_{22}, and σ_{12}. Substituting the results into (12) yields the following stress-strain relation under plane-strain conditions,

$$\begin{aligned} \frac{\epsilon_{11}}{\gamma_0} &= \frac{1}{2}\alpha\left(\frac{\tau_{ge}}{\tau_0}\right)^n\left[\frac{\sigma_{11}-\sigma_{22}}{2\tau_e} + \mu\right] \\ \frac{\epsilon_{22}}{\gamma_0} &= \frac{1}{2}\alpha\left(\frac{\tau_{ge}}{\tau_0}\right)^n\left[\frac{\sigma_{22}-\sigma_{11}}{2\tau_e} + \mu\right] \\ \frac{\epsilon_{12}}{\gamma_0} &= \frac{1}{2}\alpha\left(\frac{\tau_{ge}}{\tau_0}\right)^n\frac{\sigma_{12}}{\tau_e} \end{aligned} \qquad (19)$$

where

$$\tau_e = \frac{\sigma_e}{\sqrt{3}} = \left[1 - \frac{1}{3}\mu^2\right]^{-1/2}\left[\left(\frac{\sigma_{11}-\sigma_{22}}{2}\right)^2 + \sigma_{12}^2\right]^{1/2}, \qquad (20)$$

and

$$\tau_{ge} = \frac{\sigma_{ge}}{\sqrt{3}} = \left[1 - \frac{1}{3}\mu^2\right]^{1/2} \times\left[\left(\frac{\sigma_{11}-\sigma_{22}}{2}\right)^2 + \sigma_{12}^2\right]^{1/2} + \frac{\mu}{2}(\sigma_{11} + \sigma_{22}). \qquad (21)$$

It is more convenient to use the effective stress σ_e and the generalized effective stress σ_{ge}, (rather than τ_e and τ_{ge}) for the analysis of a crack under mode I loading. With the connections $\sigma_0 = \sqrt{3}\,\tau_0$ and $\epsilon_0 = \gamma_0/\sqrt{3}$, an alternative expression of (19) in terms of σ_0, ϵ_0, σ_e, and σ_{ge} can be easily obtained.

3 Dominant Singularity Analysis

We consider a planar crack problem, where the Cartesian coordinates (x_1, x_2) and the associated polar coordinates (r, θ) are centered at the crack tip and the x_3-axis lies perpendicular to the $x_1 - x_2$ plane. The argument leading to the HRR singular fields has been detailed in Hutchinson (1968a, b) and Rice and Rosengren (1968). In the same fashion, by applying the path-independent J-integral introduced by Rice (1968), the dominant asymptotic crack-tip stress, strain, and displacement fields for pressure-sensitive dilatant materials can be written as

$$\begin{aligned} \sigma_{ij} &= \sigma_0\left[\frac{J}{\alpha\sigma_0\epsilon_0 I(n,\mu) r}\right]^{\frac{1}{n+1}}\tilde{\sigma}_{ij}(\theta;n,\mu) \\ \epsilon_{ij} &= \alpha\epsilon_0\left[\frac{J}{\alpha\sigma_0\epsilon_0 I(n,\mu) r}\right]^{\frac{n}{n+1}}\tilde{\epsilon}_{ij}(\theta;n,\mu) \\ u_i &= \alpha\epsilon_0 r\left[\frac{J}{\alpha\sigma_0\epsilon_0 I(n,\mu) r}\right]^{\frac{n}{n+1}}\tilde{u}_i(\theta;n,\mu) \end{aligned} \qquad (22)$$

where

$$J = \int_\Gamma\left[\frac{n}{n+1}\sigma_{ge}\epsilon_e\nu_1 - \sigma_{ij}\nu_j\frac{\partial u_i}{\partial x_1}\right]ds. \qquad (23)$$

In (23), $\epsilon_e = \gamma_e/\sqrt{3}$ is the effective strain, and ν_j is the jth component of the outward unit normal to an arbitrary path Γ from the lower crack surface to the upper crack surface in the counterclockwise sense. The dimensionless function I and the dimensionless angular functions $\tilde{\sigma}_{ij}$, $\tilde{\epsilon}_{ij}$, and $\tilde{u}_i$ depend on the strain-hardening exponent n, the pressure-sensitivity factor μ, and the conditions of plane strain or plane stress. These angular functions are normalized by setting the maximum value of the generalized effective stress $\tilde{\sigma}_{ge}$ equal to unity. $\tilde{\sigma}_{ge}$ is related to $\tilde{\sigma}_{ij}$ through the following relations:

$$\tilde{\sigma}_{ge} = \tilde{\sigma}_e + \sqrt{3}\,\mu\tilde{\sigma}_m, \qquad (24)$$

$$\tilde{\sigma}_e = \left[1 - \frac{1}{3}\mu^2\right]^{-1/2}\left[\frac{3}{4}(\tilde{\sigma}_{rr} - \tilde{\sigma}_{\theta\theta})^2 + 3\tilde{\sigma}_{r\theta}^2\right]^{1/2}, \qquad (25)$$

$$\tilde{\sigma}_m = \frac{1}{2}(\tilde{\sigma}_{rr} + \tilde{\sigma}_{\theta\theta}) - \frac{\sqrt{3}}{9}\mu\tilde{\sigma}_e. \qquad (26)$$

With the normalization in (22), J represents the amplitude of the singular fields; it cannot be determined by the asymptotic crack-tip analyses since it depends on the geometry of the cracked body and on the external loading. The dimensionless constant I is expressed as:

$$I = \int_{-\pi}^{\pi}\left[\frac{n}{n+1}\tilde{\sigma}_{ge}^{n+1}\cos\theta - [\sin\theta(\tilde{\sigma}_{rr}(\tilde{u}_\theta - \tilde{u}_r') - \tilde{\sigma}_{r\theta}(\tilde{u}_r + \tilde{u}_\theta')) + \frac{\cos\theta}{n+1}(\tilde{\sigma}_{rr}\tilde{u}_r + \tilde{\sigma}_{r\theta}\tilde{u}_\theta)]\right]d\theta \qquad (27)$$

where ( )′ denotes differentiation with respect to θ. Note that the separable form crack-tip fields (22) are of the HRR type, and when $\mu = 0$ they reduce exactly to the HRR fields.

We follow the solution procedures used by Hutchinson (1968a, b), Rice and Rosengren (1968), and Shih (1973, 1974) to obtain the crack-tip fields for pressure-sensitive dilatant materials. We outline these procedures in the following. An Airy stress function of separable form in r and θ is introduced to satisfy the equilibrium equations. The strain components are expressed in terms of the stress function through the plastic stress-strain relation, and then are inserted into the compatibility equation to arrive at a fourth-order nonlinear ordinary differential equation with θ as the independent variable. The traction-free conditions on the crack faces and/or the symmetry (mode I) or antisymmetry (mode II) conditions about the crack line provide the necessary boundary conditions for the differential equation. A shooting method based on a combined fourth-fifth order Runge-Kutta scheme with error and step-size control is employed to generate solutions.

4 Mode I Crack-Tip Fields

We restrict our attention to the mode I crack-tip fields. The angular functions of the fields, $\tilde{\sigma}_{ij}(\theta;n,\mu)$, $\tilde{\epsilon}_{ij}(\theta;n,\mu)$, and $\tilde{u}_i(\theta;n,\mu)$, can be obtained for small μ's. As μ increases for each n, the stress state ahead of the crack approaches the pure hydrostatic stress state and σ_e approaches 0 at $\theta = 0$. This trend for each n will be detailed later in this section. When the elastic strains are neglected, the plane-strain condition at $\theta = 0$ for dilatant materials can not be satisfied under pure hydrostatic stress state unless the materials are incompressible. Furthermore, our constitutive law (12) has a singular behavior and can not describe accurately the constitutive behavior at $\sigma_e = 0$ where a pure hydrostatic stress should induce only a pure dilatational plastic strain. We therefore define a $\mu_{\lim}$ at which the numerical result of σ_e at $\theta = 0$ approaches 0. For each n, when $\mu \geq \mu_{\lim}$, we can not find any solutions based on the present HRR-type formulation. In Table 1 we list the values

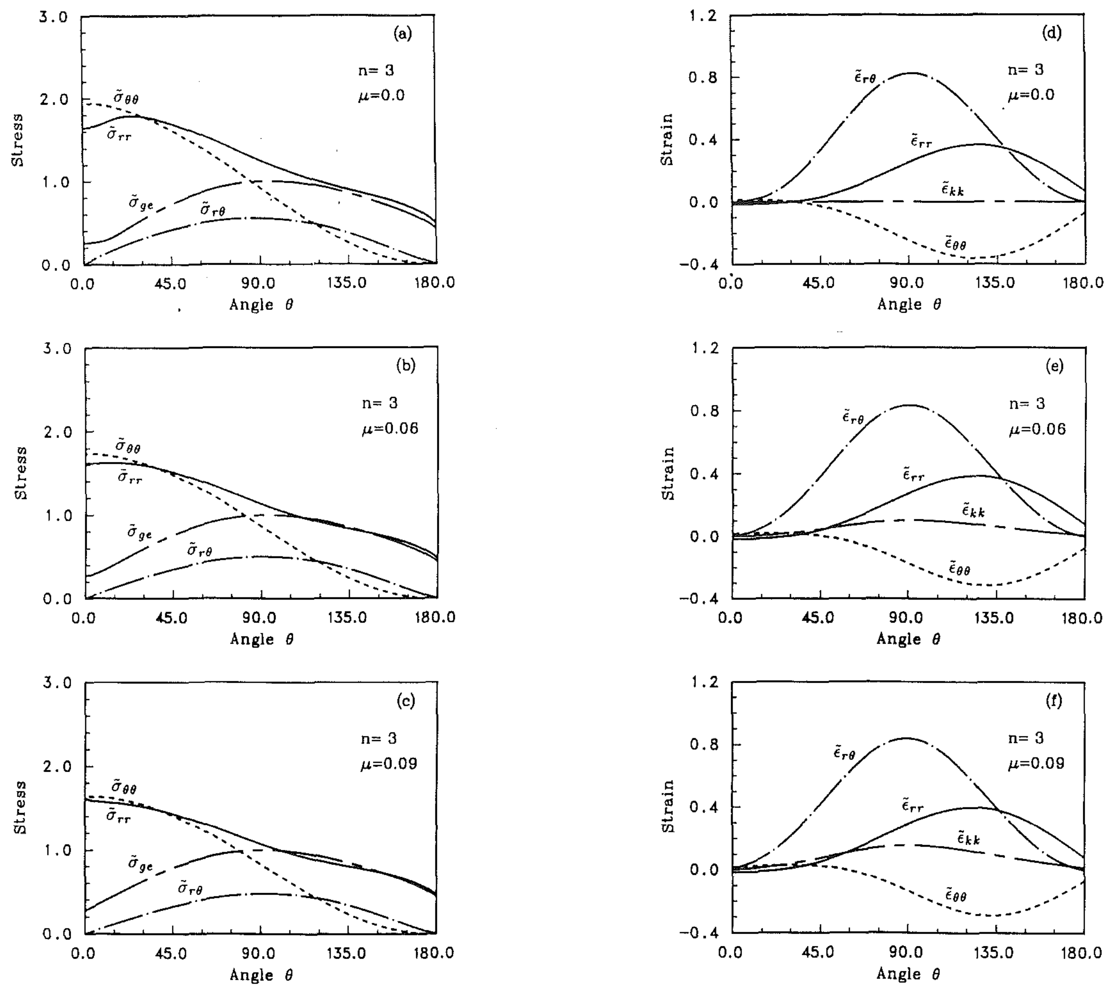

Fig. 1 The θ-variations of the normalized stresses and strains for $n = 3$

Table 1 The numerical values of $I(n,\mu)$ and $\mu_{\lim}(n)$

	$n = 2$	$n = 3$	$n = 5$	$n = 10$	$n = 20$	$n = 100$
$\mu = 0.00$	5.939	5.507	5.024	4.540	4.214	3.835
$\mu = 0.03$	5.880	5.429				
$\mu = 0.06$		5.360				
$\mu = 0.09$		5.307				
$\mu = 0.10$			4.740	4.233	3.894	3.481
$\mu = 0.20$			4.544	3.966	3.609	3.163
$\mu = 0.30$				3.750	3.360	2.876
$\mu = 0.45$					3.078	2.494
$\mu = 0.60$						2.164
$\mu_{\lim}$	0.031	0.098	0.204	0.344	0.461	0.639

of $\mu_{\lim}$ and $I(n,\mu)$ for several n's. It can be seen from this table that the numerical constant I decreases as n or μ increases, and that a large n (representing low-hardening materials) corresponds to a large $\mu_{\lim}$.

The θ-variations of the stresses, $\tilde{\sigma}_{ij}$ and $\tilde{\sigma}_{ge}$, and the strains, $\tilde{\epsilon}_{ij}$ and $\tilde{\epsilon}_{kk}$ are presented in Fig. 1 for $n = 3$ and $\mu = 0$, 0.06, and 0.09 and in Fig. 2 for $n = 10$ and $\mu = 0$, 0.2, and 0.3. The solutions for $n = 3$ and $n = 10$ represent the crack-tip fields for typical high-hardening and low-hardening materials, respectively. For the convenience of comparison with perfectly-plastic solutions which will be detailed in Section 5, the extremely low-hardening solutions for $n = 100$ and $\mu = 0$, 0.4, and 0.6 are also presented in Fig. 3. In each of Figs. 1, 2, and 3, a comparison of the crack-tip stress and strain solutions for $\mu = 0$, the second μ, and the third μ (close to $\mu_{\lim}$), shows the evident effects of μ on the crack-tip fields. It should be mentioned that when $\mu = 0$, our solutions for all the n's match exactly the tabulated values of the HRR solutions given by Shih (1983).

A comparison of the stress plots in Fig. 1 for $n = 3$, in Fig. 2 for $n = 10$, and in Fig. 3 for $n = 100$ shows that for a fixed n, a large μ results in a small $\tilde{\sigma}_{\theta\theta}$, a small $\tilde{\sigma}_{rr}$, and a small $\tilde{\sigma}_{\theta\theta} - \tilde{\sigma}_{rr}$ at $\theta = 0$. The generalized effective stress $\tilde{\sigma}_{ge}$ (reducing to $\tilde{\sigma}_e$ when $\mu = 0$) is found to peak somewhere between 90 deg and 100 deg for all the cases. The shear stress, $\tilde{\sigma}_{r\theta}$, peaks at about 90 deg for $\mu = 0$. It peaks at an angle larger than 90 deg for a large μ, (see Fig. 2 for $n = 10$ and Fig. 3 for $n = 100$). This tendency for the shear stress to peak at an angle larger than 90 deg when $\mu > 0$ is not evident for $n = 3$ because of the small values of μ considered.

Figures 2(d), 2(e), and 2(f) for $n = 10$ and Figs. 3(d), 3(e), and 3(f) for $n = 100$ indicate that the peak value of the strain $\tilde{\epsilon}_{\theta\theta}$ increases as μ increases. In contrast, $\tilde{\epsilon}_{rr}$ weakly depends on μ. As shown in Figs. 1(d), 1(e), and 1(f) for $n = 3$, the angular functions of the strains $\tilde{\epsilon}_{rr}$, $\tilde{\epsilon}_{\theta\theta}$, and $\tilde{\epsilon}_{r\theta}$ are not affected much by the small values of μ considered. However, for $n = 3$ and

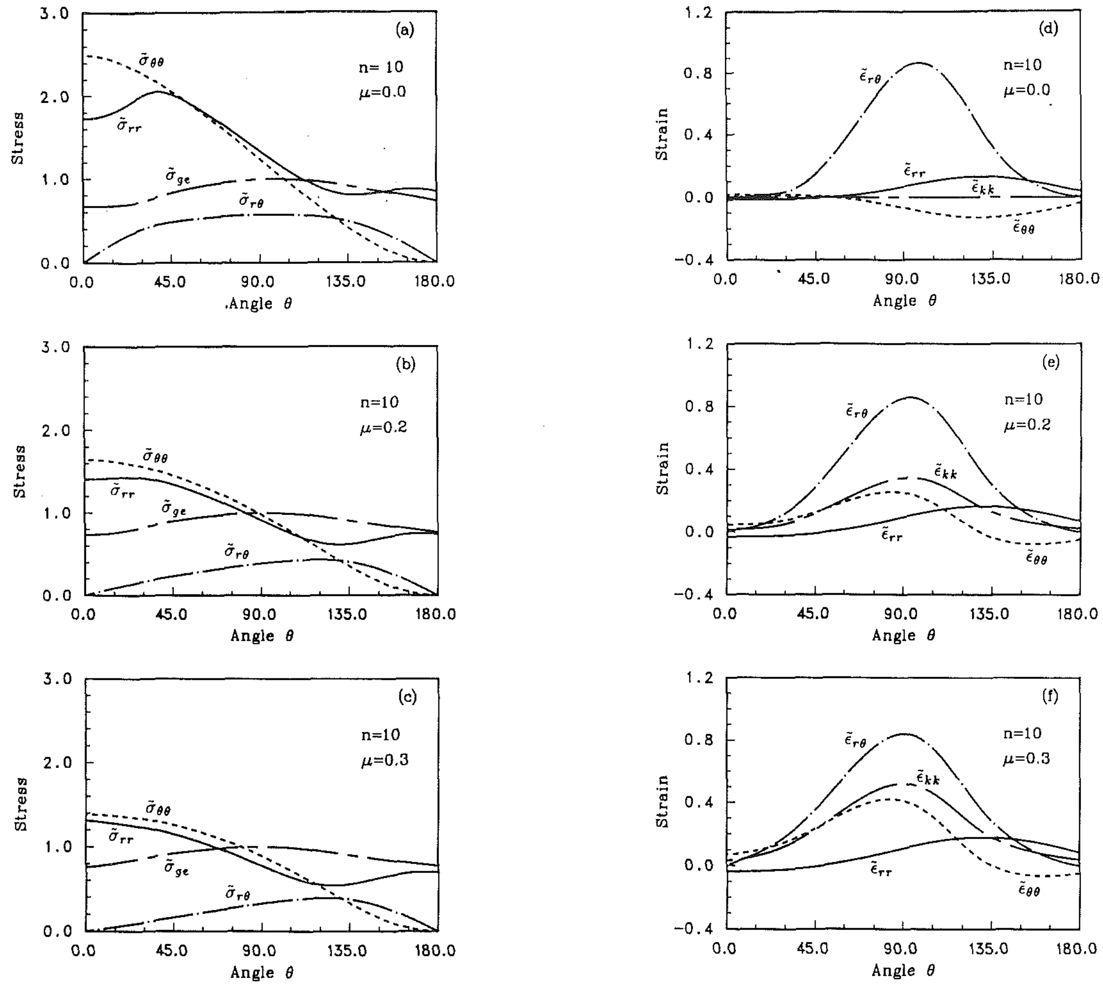

Fig. 2 The θ-variations of the normalized stresses and strains for n = 10

$\mu = 0.09$, the maximum value of the volumetric strain $\tilde{\epsilon}_{kk}$ reaches about 20 percent of the maximum value of the shear strain $\tilde{\epsilon}_{r\theta}$. In all the cases we have studied, the volumetric strain $\tilde{\epsilon}_{kk}$ increases as μ increases and the maximum value of $\tilde{\epsilon}_{kk}$ is attained at about $\theta = 90$ deg.

At this moment, it is worth mentioning Hutchinson's work (1983) on the crack-tip fields for material undergoing creep-constrained grain boundary cavitation. The common feature of his material model and our constitutive equation is that the deformation has a dilatational component. In his constitutive model, the dilatational component of the macroscopic creep strain rate arises from a given density of cavitating grain boundary facets, whereas in our constitutive equation, the dilatational deformation comes from pressure-sensitive yielding and the normality flow rule. We observed from his results that as the density of cavitating grain boundary facets increases, the difference between the hoop stress and the radial stress at $\theta = 0$ deg decreases, and the volumetric strain rate increases with a maximum at about $\theta = 90$ deg. These observations are similar to the effects of pressure sensitivity on the crack-tip fields presented above for the pressure-sensitive dilatant materials.

The contours of the generalized effective stress are plotted in Fig. 4(*a*) for $n = 3$ and $\mu = 0$, 0.06, and 0.09, in Fig. 4(*b*) for $n = 10$ and $\mu = 0$, 0.2, and 0.3, and in Fig. 4(*c*) for $n = 100$ and $\mu = 0$, 0.4, and 0.6. These contours are plotted in the normalized coordinates $x_1/[J/(\alpha\sigma_0\epsilon_0(\sigma_{ge}/\sigma_0)^{n+1})]$ and $x_2/[J/(\alpha\sigma_0\epsilon_0(\sigma_{ge}/\sigma_0)^{n+1})]$. These figures demonstrate that for a fixed n, the contour expands and moves in the positive x_1-direction as μ increases. Note that the contours in these figures should not be confused with the shape of the plastic zone.

The hydrostatic stress contours for $n = 3$ and $\mu = 0$, 0.06, and 0.09 are shown in Fig. 5, whereas the contours for $n = 10$ and $\mu = 0$, 0.2, and 0.3, due to their large size difference, are shown in Figs. 6(*a*), 6(*b*), and 6(*c*). These contours are plotted in the normalized coordinates $x_1/[J/(\alpha\sigma_0\epsilon_0(\sigma_m/\sigma_0)^{n+1})]$ and $x_2/[J/(\alpha\sigma_0\epsilon_0(\sigma_m/\sigma_0)^{n+1})]$. A comparison of the contours in Figs. 5 and 6 shows that for a given n, the contour for a larger μ is smaller in size, flatter in shape, and more extrusive to the positive x_1-direction when compared to those for a small μ. The contour for a large μ is fully enclosed by the one with a small μ. This indicates that the pressure sensitivity reduces the hydrostatic stress in all directions. The observed change in contour shape with μ signifies that the location of the maximum hydrostatic stress moves to $\theta = 0$ deg (directly ahead of the crack) as μ increases. It is worth mentioning that although the maximum hydrostatic stress of the HRR fields ($\mu = 0$) is not located at $\theta = 0$ deg, the values of σ_m at $\theta = 0$ deg for different n's are only about 1–2 percent smaller than their maximums.

5 Perfect-Plasticity Crack-Tip Fields

Here, we construct perfectly-plastic crack-tip fields using slip line theory with the assumption that the material surrounding the crack tip is fully yielded at all angles. The crack-tip fields correspond to the low-hardening limit of the asymptotic crack-tip fields for power-law materials. It is well known that the low-hardening limit of the power-law solutions cor-

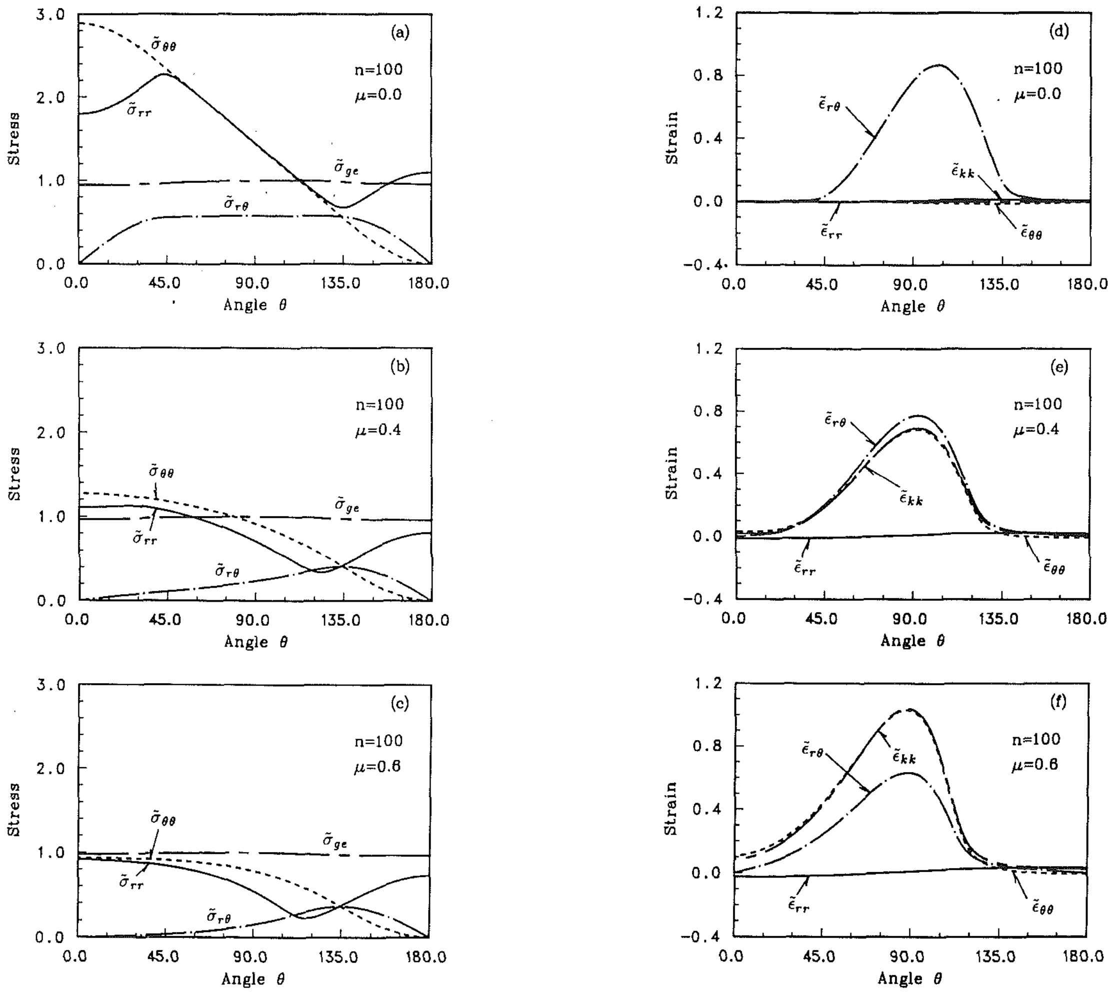

Fig. 3 The θ-variations of the normalized stresses and strains for $n = 100$

responds to solutions for rigid perfectly-plastic materials. However, the material surrounding the crack tip may not always be fully yielded at all angles for elastic perfectly-plastic materials (for example, see Gao (1980), Nemat-Nasser and Obata (1984), and Dong and Pan (1989a, b) for Mises materials).

The crack-tip fields for perfectly-plastic pressure-sensitive materials can be obtained by solving the two equilibrium equations together with the yield condition for the three unknown stress components, σ_{rr}, $\sigma_{\theta\theta}$, and $\sigma_{r\theta}$. The yield condition in the polar coordinates is

$$\tau_{ge} = \left[1 - \frac{1}{3}\mu^2\right]^{1/2}\left[\left(\frac{\sigma_{rr}-\sigma_{\theta\theta}}{2}\right)^2 + \sigma_{r\theta}^2\right]^{1/2} + \mu\,\frac{\sigma_{rr}+\sigma_{\theta\theta}}{2} = \frac{\sigma_0}{\sqrt{3}}. \tag{28}$$

We introduce two parameters, ϕ and c, defined as

$$\sin\phi = \frac{\mu}{\left[1 - \frac{1}{3}\mu^2\right]^{1/2}} \tag{29}$$

and

$$c = \frac{\sigma_0}{\sqrt{3}\left[1 - \frac{4}{3}\mu^2\right]^{1/2}}, \tag{30}$$

and rewrite the yield condition (28) as

$$\left[\left(\frac{\sigma_{rr}-\sigma_{\theta\theta}}{2}\right)^2 + \sigma_{r\theta}^2\right]^{1/2} + \sin\phi\,\frac{\sigma_{rr}+\sigma_{\theta\theta}}{2} = c\cos\phi. \tag{31}$$

The yield condition in the above form allows us to use the slip line theory in soil mechanics and concrete mechanics, where (31) is termed the Coulomb yield criterion and the parameters c and ϕ are frequently called the cohesion and the angle of internal friction, respectively. The details of the slip line theory, based on the Coulomb criterion, can be found in many soil mechanics and concrete mechanics textbooks (see, for example, Wu (1966) and Nielsen (1984)).

With the help of the Mohr diagram, it can be easily shown that when a material element yields, there are two planes (parallel to the x_3-axis) on which the normal stress σ and the shear stress τ satisfy the equation

$$\tau = c - \sigma\tan\phi\,. \tag{32}$$

Equation (32), as an alternative expression of (31), is the original form of the Coulomb criterion. The traces of the planes for which (32) holds form two families of slip lines in the x_1-x_2 plane, α lines and β lines, with one family intersected with the other by an acute angle of $\pi/2 - \phi$ (see Fig. 7). As shown in the figure, the α and β lines incline at an angle of $\pi/4 + \phi/2$ from the major principal axis. Integration of the equilibrium equations along the slip lines shows that (see, for example, Wu (1966))

$$\chi - \psi = \text{constant} \qquad (\text{along } \alpha \text{ lines}) \tag{33}$$

and

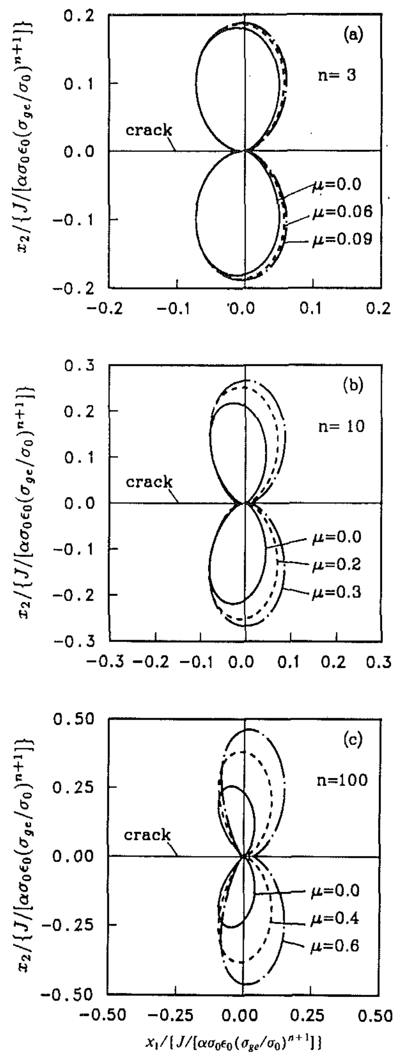

Fig. 4 Contours of the generalized effective stress plotted in the normalized coordinates for (*a*) $n = 3$, (*b*) $n = 10$, and (*c*) $n = 100$

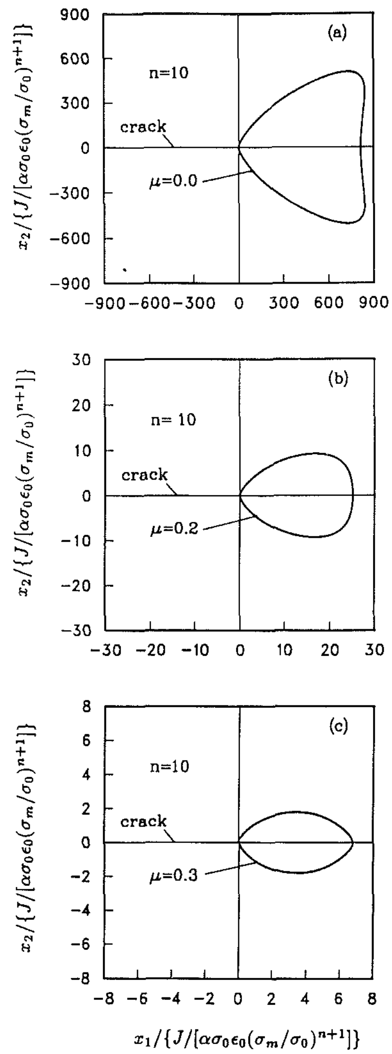

Fig. 6 Contours of the hydrostatic stress plotted in the normalized coordinates fo $n = 10$

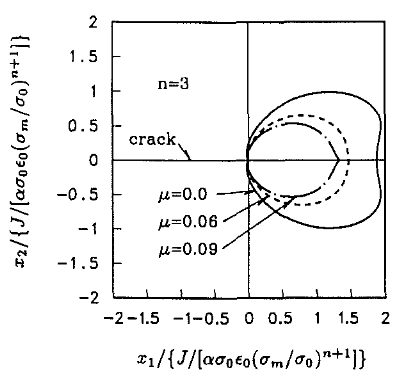

Fig. 5 Contours of the hydrostatic stress plotted in the normalized coordinates for $n = 3$

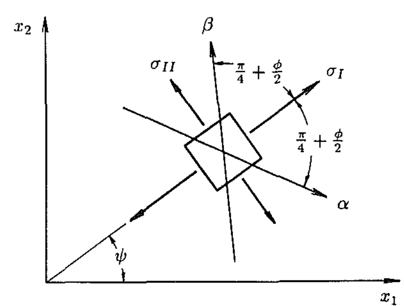

Fig. 7 Slip lines α and β and the major and minor principal stresses σ_I and σ_{II} in the x_1-x_2 plane

$$\chi + \psi = \text{constant} \qquad (\text{along } \beta \text{ lines}), \tag{34}$$

where

$$\chi = -\frac{1}{2\tan\phi}\ln\left(1 - \frac{p}{c}\tan\phi\right), \qquad p = \frac{\sigma_{11}+\sigma_{22}}{2},$$

and ψ is the angle between the major principal axis and the x_1-axis.

Figure 8 shows the slip line fields for $\mu = 0$, 0.4, and 0.8, which correspond to $\phi = 0$ deg, 24.3 deg, and 64.4 deg, respectively. These slip line fields are similar to those in the limit analysis of the Prandtl punch problem in soil mechanics and rock mechanics. As shown in the figure, these crack-tip characteristics fields consist of two constant stress zones (regions I and III) and a centered fan zone (region II). The traction-free boundary conditions require that the material element in region III yield in uniaxial tension or compression. We choose the uniaxial tension which gives tensile stresses ahead of the crack tip. This results in the characteristic lines with an inclination angle of $\pi/4 + \phi/2$ from the x_1-axis. The constant stress state in region III is

$$\sigma_{11} = \frac{2c\cos\phi}{1+\sin\phi}, \qquad \sigma_{22} = \sigma_{12} = 0. \tag{35}$$

As shown in Fig. 8, one family of the characteristic lines (the β lines) leaves the traction-free crack face of region III; then it swings an angle of $\pi/2$ through region II; finally it arrives at the crack line of region I. The slip lines in region I incline at an angle of $\pi/4 - \phi/2$ from the x_1-axis. The constant stress state in region I can be determined by (34) as:

$$\sigma_{11} = \frac{c}{\tan\phi}[1-e^{-\pi\tan\phi}],$$

$$\sigma_{22} = \frac{c}{\tan\phi}\left[1-\frac{1-\sin\phi}{1+\sin\phi}e^{-\pi\tan\phi}\right], \quad \sigma_{12} = 0. \tag{36}$$

The stresses in region II varies with the polar angle θ. They can be also determined by (34) and the stress state in the neighboring constant stress zone. Listed next are the complete crack-tip stress fields expressed in the polar coordinates.

In region I $\left(0\le\theta\le\frac{\pi}{4}-\frac{\phi}{2}\right)$,

$$\frac{\sigma_{rr}}{\sigma_0} = \frac{c\cos\phi}{\sigma_0}\left[\frac{1}{\sin\phi}-\frac{e^{-\pi\tan\phi}}{\sin\phi(1+\sin\phi)}-\frac{e^{-\pi\tan\phi}}{1+\sin\phi}\cos 2\theta\right]$$

$$\frac{\sigma_{\theta\theta}}{\sigma_0} = \frac{c\cos\phi}{\sigma_0}\left[\frac{1}{\sin\phi}-\frac{e^{-\pi\tan\phi}}{\sin\phi(1+\sin\phi)}+\frac{e^{-\pi\tan\phi}}{1+\sin\phi}\cos 2\theta\right] \tag{37}$$

$$\frac{\sigma_{r\theta}}{\sigma_0} = \frac{c\cos\phi}{\sigma_0}\left[\frac{e^{-\pi\tan\phi}}{1+\sin\phi}\sin 2\theta\right].$$

In region II $\left(\frac{\pi}{4}-\frac{\phi}{2}\le\theta\le\frac{3\pi}{4}-\frac{\phi}{2}\right)$,

$$\frac{\sigma_{rr}}{\sigma_0} = \frac{c\cos\phi}{\sigma_0}\left[\frac{1}{\sin\phi}-\frac{1+\sin^2\phi}{\sin\phi(1+\sin\phi)}e^{-2\tan\phi\left(\frac{3\pi}{4}-\frac{\phi}{2}-\theta\right)}\right]$$

$$\frac{\sigma_{\theta\theta}}{\sigma_0} = \frac{c\cos\phi}{\sigma_0}\left[\frac{1}{\sin\phi}-\frac{1-\sin\phi}{\sin\phi}e^{-2\tan\phi\left(\frac{3\pi}{4}-\frac{\phi}{2}-\theta\right)}\right] \tag{38}$$

$$\frac{\sigma_{r\theta}}{\sigma_0} = \frac{c\cos\phi}{\sigma_0}\left[\frac{\cos\phi}{1+\sin\phi}e^{-2\tan\phi\left(\frac{3\pi}{4}-\frac{\phi}{2}-\theta\right)}\right].$$

In region III $\left(\frac{3\pi}{4}-\frac{\phi}{2}\le\theta\le\pi\right)$,

$$\frac{\sigma_{rr}}{\sigma_0} = \frac{c\cos\phi}{\sigma_0}\left[\frac{1}{1+\sin\phi}(1+\cos 2\theta)\right]$$

$$\frac{\sigma_{\theta\theta}}{\sigma_0} = \frac{c\cos\phi}{\sigma_0}\left[\frac{1}{1+\sin\phi}(1-\cos 2\theta)\right] \tag{39}$$

$$\frac{\sigma_{r\theta}}{\sigma_0} = \frac{c\cos\phi}{\sigma_0}\left[-\frac{1}{1+\sin\phi}\sin 2\theta\right].$$

The closed-form slip line solution (37)–(39) is valid for $\phi < \pi/2$, which is equivalent to $\mu < \sqrt{3}/2$ (see (29)). From Table 1, the values of $\mu_{\lim}$ for n = 2, 3, 5, 10, 20, and 100 are 0.031, 0.098, 0.204, 0.344, 0.461, and 0.639, respectively. It seems that $\mu_{\lim}$ for finite n tends to the number $\sqrt{3}/2 = 0.866$, which is the limit for $n = \infty$. Note that the fields for $\mu = 0$ (hence $\phi = 0$ and $c = \sigma_0/\sqrt{3}$) reduce exactly to the plane-strain slip line fields based on the Mises yield criterion (see Rice (1968)).

It can be seen from Fig. 8 that the constant stress region I located in front of the crack forms an angle of $\pi/4-\phi/2$ from the horizontal, while the region III adjacent to the crack face forms an angle of $\pi/4+\phi/2$. Since ϕ increases as μ increases, the slip line patterns become very sharp for a large μ. We emphasize that the boundaries of the slip line fields in Fig. 8 are not intended to represent the boundaries of the plastic zone.

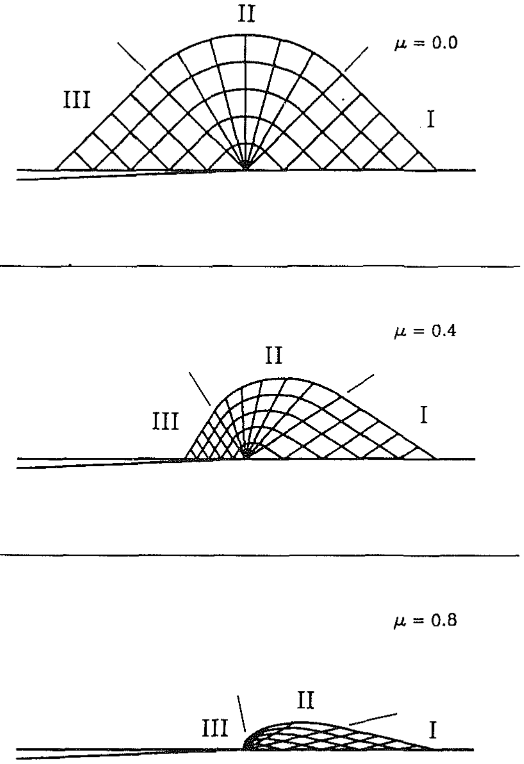

Fig. 8 Plane-strain slip line fields near the tip of a crack under mode I conditions

The angular distributions of the normalized stresses $\bar\sigma_{ij}(=\sigma_{ij}/\sigma_0)$ and $\sigma_{ge}(=\sigma_{ge}/\sigma_0)$ for μ = 0, 0.4, and 0.8, calculated from (37)–(39), are plotted in Figs. 9(a), 9(b), and 9(c), respectively. The generalized effective stress $\bar\sigma_{ge}$ which equals 1 for all θ's is also plotted in these figures. The crack-tip stress distributions for $\mu = 0$ (Fig. 9(a)) are the same as those in Rice (1968). It can be seen from Figs. 9(a), 9(b), and 9(c) that the effects of the pressure sensitivity on the crack-tip stress fields observed from our hardening solutions are also true for perfectly-plastic materials: As μ increases, $\sigma_{\theta\theta}$, σ_{rr}, and $\sigma_{\theta\theta}-\sigma_{rr}$ at $\theta = 0$ deg decreases and these result in a small effective stress, σ_e, and a small hydrostatic stress, σ_m, at $\theta = 0$ deg. As shown in Fig. 9(c), for $\mu = 0.8$ (which closes to $\mu_{\lim} = \sqrt{3}/2$), $\sigma_{\theta\theta}$ almost equals σ_{rr} at $\theta = 0$ deg. A comparison of Fig. 3(b) for n = 100 and $\mu = 0.4$ with Fig. 9(b) for $n = \infty$ and $\mu = 0.4$ indicates that the stress distributions of the low-hardening solution agree remarkably well with those of the perfectly-plastic solution. In addition to the results shown here, for other μ's, we have observed a remarkably good agreement of the n = 100 stress solutions with the perfectly-plastic solutions. This suggests that the perfectly-plastic solutions presented here are indeed the low-hardening limit of the power-law solutions.

6 Concluding Remarks

In this study we have investigated plane-strain mode I crack-tip fields for both power-law hardening and perfectly-plastic, pressure-sensitive dilatant materials. Within a limited degree of pressure sensitivity ($\mu < \mu_{\lim}$), we found that the asymptotic crack-tip fields of separable form in r and θ indeed exist. These solutions of the crack-tip fields for $\mu = 0$ match exactly those of the HRR fields. Furthermore, the angular stress functions of the crack-tip fields for low-hardening materials agree well with those of the corresponding perfect-plasticity solutions.

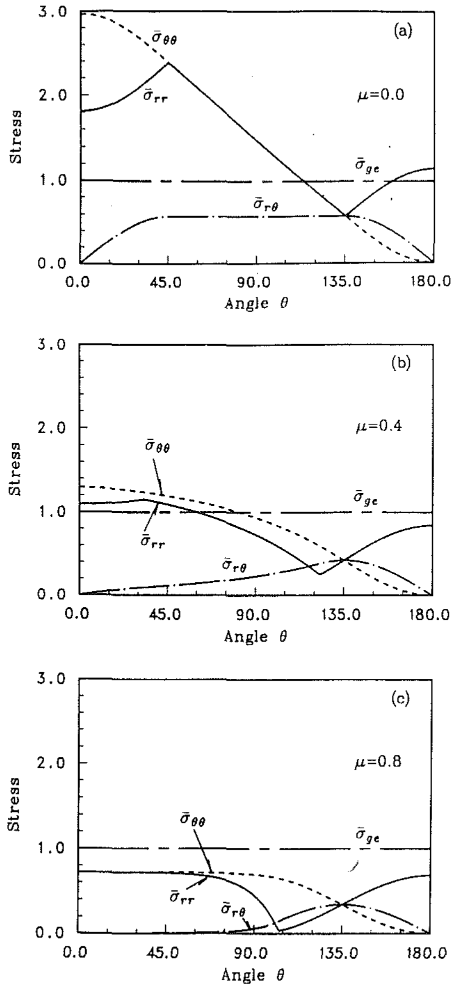

Fig. 9 The θ-variations of the normalized stresses $\tilde{\sigma}_{ij}$ ($= \sigma_{ij}/\sigma_0$) and $\tilde{\sigma}_{ge}$ ($= \sigma_{ge}/\sigma_0$) for perfectly-plastic pressure-sensitive materials

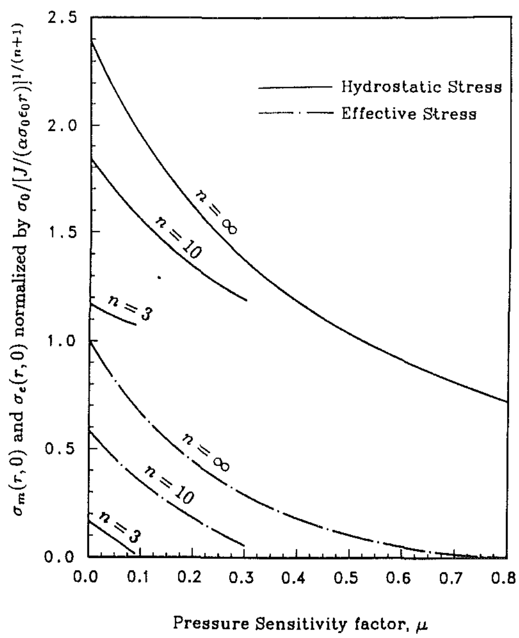

Fig. 10 The hydrostatic stress σ_m (solid line) and the effective stress σ_e (chain-dotted line) ahead of the crack tip versus the pressure sensitivity factor μ for n = 3, 10, and $n = \infty$

It is clear from our hardening solution (22) that J can be regarded as a measure of the amplitudes of the singular crack-tip fields for pressure-sensitive dilatant materials. If the finite deformation zone and the fracture process zone are well contained within the zone of dominance of the singular field, J can be used as a characterizing parameter to correlate the crack initiation and a limited amount of crack growth in these materials. Under small-scale yielding conditions, J can be related to the elastic intensity factor K of the cracked solid. In general, J can be inferred from the geometry and remote loading of the cracked solid by either experiments or computational methods.

The hydrostatic stress ahead of the crack tip seems to play an important role in the initiation of ductile tearing processes. We consider the hydrostatic stress at a small fixed radial distance r ahead of the crack tip (at $\theta = 0$ deg) within the zone dominated by the HRR type fields described by (22) at the same value of J. For a given set of α, σ_0, and ϵ_0, we show in Fig. 10 the μ-dependence of the hydrostatic stress σ_m and the effective stress σ_e ahead of the crack tip (at $\theta = 0$ deg) for $n = 3$ and 10. In this figure, we also show the corresponding results for $n = \infty$. Here, σ_m and σ_e are normalized by $\sigma_0[J/(\alpha\sigma_0\epsilon_0 r)]^{1/(n+1)}$ for hardening materials and by σ_0 for perfectly-plastic materials. The curves for $n = 3$ and 10 represent $[1/I(n,\mu)]^{1/(n+1)}$ $\tilde{\sigma}_m(0;n,\mu)$ and $[1/I(n,\mu)]^{1/(n+1)}$ $\tilde{\sigma}_e(0;n,\mu)$, whereas the curves for $n = \infty$ are obtained from (37) for perfectly-plastic materials. As clearly shown in Fig. 10, both the hydrostatic stress and the effective stress at θ = 0 deg decrease as μ increases, and the effective stress at θ = 0 deg approaches 0 as $\mu \rightarrow \mu_{\lim}$. Under the conditions previously discussed, we also found that for hardening materials the volumetric strain at a given small distance, r, ahead of the crack tip increases from 0 as μ increases from 0. Note that in this study, the pressure sensitivity factor μ also serves as the plastic dilatancy factor which represents the ratio of the volumetric plastic strain to the effective shear strain. Therefore, a large pressure sensitivity accompanied by a large plastic dilatancy relaxes the near-tip hydrostatic and effective stresses. This lowering of the hydrostatic and effective stresses may be used to explain the material toughening observed in some ceramic and polymeric composite materials.

Our plane-strain crack-tip field solutions for both hardening and nonhardening materials show that when $\mu \rightarrow \mu_{\lim}$, σ_e at $\theta = 0$ approaches 0. Our constitutive law (12) can not handle the stress-strain relation at $\sigma_e = 0$. More importantly, in our formulation of the HRR-type crack-tip fields, the plane-strain condition (18) requires $\sigma_e \neq 0$ for dilatant materials. This explains the existence of $\mu_{\lim}$. To explore the near-tip field structure for $\mu \geq \mu_{\lim}$, we have started a full-field elastic-plastic analysis using finite element methods. The results will be reported in the subsequent papers.

Acknowlegment

The authors acknowledge the suppport of this research by the Material Research Group funded by the National Science Foundation under Grant No. DMR-8708405. J. P. also acknowledges the partial support of his research by the National Science Foundation under Grant No. MSM-8613544. Helpful discussions with Prof. A. F. Yee and I.-W. Chen of The University of Michigan and Prof. C. F. Shih of Brown University are greatly appreciated.

References

Carapellucci, L. M., and Yee, A. F., 1986, "The Biaxial Deformation and Yield Behavior of Bisphenol-A Polycarbonate: Effect of Anisotropy," *Polymer Engineering and Science*, Vol. 26, No. 13, pp. 920–930.

Chen, I.-W., and Reyes Morel, P. E., 1986, "Implications of Transformation Plasticity in ZrO_2-Containing Ceramics: I, Shear and Dilatation Effects," *J. Am. Ceram. Soc.*, Vol. 69, No. 3, pp. 181–189.

Dong, P., and Pan, J., 1989a, "Plane-Strain Mixed-Mode Near-Tip Fields in Elastic Perfectly Plastic Solids under Small-Scale Yielding Conditions," *Int. J. Fract.*, submitted for publication.

Dong, P., and Pan, J., 1989b, "Plane-Stress Mixed-Mode Near-Tip Fields in Elastic Perfectly Plastic Solids," *Int. J. Fract.*, to be submitted for publication.

Drucker, D. C., 1973, "Plasticity Theory, Strength-Differential (SD) Phenomenon, and Volume Expension in Metals and Plastics," *Met. Trans.*, Vol. 4, pp. 667–673.

Gao, Y. C., 1980, "Elastic-Plastic Field of a Crack Before Growing in Perfectly Plastic Medium," *Acta Solid Mech. Sinica*, Vol. 1, pp. 69–75.

Hutchinson, J. W., 1968a, "Singular Behavior at the End of a Tensile Crack in a Hardening Material," *J. Mech. Phys. Solids*, Vol. 16, pp. 13–31.

Hutchinson, J. W., 1968b, "Plastic Stress and Strain Fields at a Crack Tip," *J. Mech. Phys. Solids*, Vol. 16, pp. 337–347.

Hutchinson, J. W., 1983, "Constitutive Behavior and Crack Tip Fields for Materials Undergoing Creep-Constrained Grain Boundary Cavitation," *Acta Metallurgica*, Vol. 31, pp. 1079–1088.

Needleman, A., and Rice, J. R., 1978, "Limits to Ductility Set by Plastic Flow Localization," *Mechanics of Sheet Metal Forming*, Donald P. Koistinen and Neng-Ming Wang, eds., Plenum Publishing Corporation, New York.

Nemat-Nasser, S., and Obata, M., 1984, "On Stress Field Near a Stationary Crack Tip," *Mechanics of Materials*, Vol. 3, pp. 235–243.

Nielsen, M. P., 1984, *Limit Analysis and Concrete Plasticity*, Prentice-Hall, Englewood Cliffs, New Jersey.

Pan, J., and Shih, C. F., 1986, "Plane-Strain Crack-Tip Fields for Power-Law Hardening Orthotropic Materials," *Mechanics of Maerials*, Vol. 5, pp. 299–316.

Pan, J., and Shih, C. F., 1988, "Plane-Stress Crack-Tip Fields for Power-Law Hardening Orthotropic Materials," *Int. J. Fract.*, Vol. 37, pp. 171–195.

Reyes-Morel, P. E., and Chen, I.-W., 1988, "Transformation Plasticity of CeO_2-Stabilized Tetragonal Zirconia Polycrystals: I, Stress Assistance and Autocatalysis," *J. Am. Ceram. Soc.*, Vol. 71, No. 5, pp. 343–353.

Rice, J. R., 1968, "A Path Independent Integral and the Approximate Analysis of Strain Concentration by Notches and Cracks," ASME Journal of Applied Mechanics, Vol. 35, pp. 379–386.

Rice, J. R., and Rosengren, G. F., 1968, "Plane Strain Deformation near a Crack Tip in a Power Law Hardening Material," *J. Mech. Phys. Solids*, Vol. 16, pp. 1–12.

Rudnicki, J. W., and Rice, J. R., 1975, "Conditions for the Localization of Deformation in Pressure-Sensitive Dilatant Materials," *J. Mech. Phys. Solids*, Vol. 23, pp. 371–394.

Shih, C. F., 1973, "Elastic-Plastic Analysis of Combined Mode Crack Problems," Ph.D. Thesis, Harvard University, Cambridge, Mass.

Shih, C. F., 1974, "Small-Scale Yielding Analysis of Mixed Mode Plane-Strain Crack Problems," *Fracture Analysis*, ASTM STP-560, pp. 187–210.

Shih, C. F., 1983, "Tables of Hutchinson-Rice-Rosengren Singular Field Quantities," Report MRL E-147, Materials Research Laboratory, Brown University, Providence.

Spitzig, W. A., and Richmond, O., 1979, "Effect of Hydrostatic Pressure on the Deformation Behavior of Polyethylene and Polycarbonate in Tension and Compression," *Polymer Eng. Sci.*, Vol. 19, pp. 1129–1139.

Sue, H.-J., and Yee, A. F., 1988, "Toughening Mechanisms in a Multi-Phase Alloy of Nylon 6,6/Polyphenylene Oxide," *J. Mater. Sci.*, to appear.

Wu, T. H., 1966, *Soil Mechanics*, Allyn and Bacon, Boston, Mass.

ADDENDUM

Interference of a Uniform Open Ring With A Rigid Cylinder, by W. W. King, published in the Sept. 1989 issue of the JOURNAL OF APPLIED MECHANICS, pp. 717–719.

H. S. Fluss has graciously called the author's attention to existing solutions of very closely related problems. The first of these is Prescott's analysis of the constant-thickness, circular piston ring (Prescott, 1924). Although Prescott considered the case of a complete, but open, ring, most of the results of the present work can be deduced readily from his analysis; namely the constant pressure, the contact zone, and the concentrated forces. Fluss himself has extended Prescott's work to the case of an incomplete ring (Fluss 1986). The present Note differs from those earlier works in style, retention of extensibility in the governing equations, and inclusion of the case for which there is only three-point contact.

References

Fluss, H. S., 1986, "Mechanics of Compliant Rings and Cylinders," AT&T Bell Laboratories, 52414-860116-02 TM.

Prescott, J., 1924, *Applied Elasticity*, Longmans, Green and Co., London, (also Dover Publications, New York, 1961), pp. 294–298.

Z. Dursunkaya
Graduate Student.

S. Nair
Associate Professor,
Mem. ASME.

Department of Mechanical and
Aerospace Engineering,
Illinois Institute of Technology,
Chicago, IL 60616

A Moving Boundary Problem in a Finite Domain

The heat conduction and the moving solid-liquid interface in a finite region is studied numerically. A Fourier series expansion is used in both phases for spatial temperature distribution, and the differential equations are converted to an infinite number of ordinary differential equations in time. These equations are solved iteratively for the interface location as well as for the temperature distribution. The results are compared with existing solutions for low Stefan numbers. New results are presented for higher Stefan numbers for which solutions are unavailable.

1 Introduction

Moving boundary problems in melting and solidification have been studied for over a century and various methods have been used in solving these problems. Due to the presence of a moving interface, the boundary conditions are rendered nonlinear. Because of this, exact solutions to these type of problems are very limited and are restricted to semi-infinite mediums (Carslaw and Jaeger, 1954). Exact solutions in forms of infinite series for arbitrary initial and boundary conditions have been found by Tao (1978, 1980, 1981). Various approximate analytical and numerical methods have been used to solve this group of problems. A discussion of these methods has been published in survey articles and books (Fukusako and Seki, 1987; Ockendon and Hogkins, 1975; Rubinstein, 1971; Wilson et al., 1978). The heat balance integral method was introduced by Goodman (1958), and was used by many investigators in semi-infinite domains, initially at the melting temperature, with steady boundary conditions. The method becomes complicated if the initial temperature in the original phase is different from the melting temperature. Yuen (1981) extended the heat balance integral method to account for initial subcooling in a freezing problem in a semi-infinite medium. Numerical methods using finite difference and finite element formulations were also used for solving moving boundary problems. As the location of the interface is not known *a priori*, and is a part of the solution, the numerical formulations are rendered complex near the interface. Another method is the enthalpy formulation, where a single energy equation is written, which covers both domains, and eliminates the moving interface. The resulting equation can be solved using finite difference techniques. Dursunkaya and Nair (1988) used an infinite orthogonal series formulation to solve for the semi-infinite domain problem, which can be extended to include the finite domain with arbitrary initial and boundary conditions.

In a finite medium, if the medium is initially at the melting temperature, the solution to the problem reduces to that of the infinite domain, which can be solved using the available exact solutions or using the heat balance integral method. When the initial temperature is different than the melting temperature, no exact solution to the problem is presently available. Weinbaum and Jiji (1977) applied the singular perturbation theory for the problem in a finite slab, where the medium initially is not at the melting temperature. The location of the interface was found, the results, however, are valid for small Stefan numbers. Charach and Zoglin (1985) used the heat balance integral method and time-dependent perturbation theory to solve the same problem. They found the interface location and temperature distributions for small liquid and solid Stefan numbers.

In this study, infinite orthogonal series are used to represent the temperature distributions in both phases, which satisfy all the boundary conditions. When the series are substituted in the energy equations, the resulting nonlinear ordinary differential equations can be solved iteratively for the time-dependent behavior. When the solution is substituted in the interface heat flux equation, a nonlinear ordinary differential equation is obtained for the location of the interface. This equation can be solved to give the interface location without solving for the temperature distribution. Once the interface location is known, the temperature distribution can be computed using the series summations.

The method of solution presented here has the capability to include variable initial temperature distribution as well as time-dependent boundary conditions. Although an extension of the method to higher dimensions is not obvious at this time, two-dimensional problems with cylindrical symmetry and three-dimensional problems with spherical symmetry are amenable to the type of series expansion introduced here.

2 Formulation

The governing differential equations for the temperature in the two phases are given by,

$$\alpha_1 \frac{\partial^2 T_1}{\partial x^2} = \frac{\partial T_1}{\partial t}, \; 0<x<s, \tag{1}$$

Contributed by the Applied Mechanics Division of THE AMERICAN SOCIETY OF MECHANICAL ENGINEERS for publication in the JOURNAL OF APPLIED MECHANICS.

Discussion on this paper should be addressed to the Technical Editor, Leon M. Keer, The Technological Institute, Northwestern University, Evanston, IL 60208, and will be accepted until two months after final publication of the paper itself in the JOURNAL OF APPLIED MECHANICS. Manuscript received by the ASME Applied Mechanics Division, May 10, 1988; final revision, January 26, 1989.

$$\alpha_2 \frac{\partial^2 T_2}{\partial x^2} = \frac{\partial T_2}{\partial t}, \; s<x<l, \tag{2}$$

where the subscripts 1 and 2 represent the solid and liquid phases, respectively, and α is the thermal diffusivity. The spatial and temporal domains are $0<x<l$ and $0<t<\infty$. The initial and boundary conditions are,

$$T_1(0,t)=U, \; T_2(x,0)=V, \; \frac{\partial T_2}{\partial x}(l,t)=0, \; s(0)=0, \tag{3}$$

and the interface conditions are,

$$T_1(s,t)=T_2(s,t)=T_m, \tag{4}$$

$$k_1 \frac{\partial T_1}{\partial x} - k_2 \frac{\partial T_2}{\partial x} = \rho L \frac{ds}{dt}. \tag{5}$$

Here, $s(t)$ is the interface location, $V>T_m$ and $U<T_m$ are given initial and boundary temperatures, respectively, with T_m representing the melting temperature. The constants k, ρ, L represent thermal conductivity, density, and the latent heat of fusion, respectively. Introducing the dimensionless temperature θ and the other dimensionless quantities,

$$\sigma=s/l, \; \xi=x/l, \; \tau=\alpha_1 t/l^2, \; A=\alpha_2/\alpha_1$$

$$\theta_1 = \frac{T_1-U}{T_m-U} - \frac{x}{s}, \; \theta_2 = \frac{T_2-T_m}{T_m-U}, \; V^* \equiv \frac{V-T_m}{T_m-U}, \tag{6}$$

the governing differential equations, initial, boundary, and interface conditions become,

$$\frac{\partial^2 \theta_1}{\partial \xi^2} = \frac{\partial \theta_1}{\partial \tau} - \frac{\xi}{\sigma^2}\frac{d\sigma}{d\tau}, \tag{7}$$

$$A \frac{\partial^2 \theta_2}{\partial \xi^2} = \frac{\partial \theta_2}{\partial \tau}, \tag{8}$$

$$\theta_1(0,t)=0, \; \frac{\partial \theta_2}{\partial \xi}(1,\tau)=0, \; \theta_2(\xi,0)=V^*, \; \sigma(0)=0, \tag{9}$$

$$\theta_1(\sigma,\tau)=\theta_2(\sigma,\tau)=0, \tag{10}$$

$$k_1 \frac{\partial \theta_1}{\partial \xi} + \frac{k_1}{\sigma} - k_2 \frac{\partial \theta_2}{\partial \xi} = \frac{\rho L \alpha_1}{(T_m-U)} \frac{d\sigma}{d\tau}. \tag{11}$$

A solution of the above system of equations is sought in the form,

$$\theta_1 = \sum_{m=1}^{\infty} \beta_{1m}(\tau)\phi_{1m}(\xi,\sigma(\tau)),$$

$$\theta_2 = V^* \sum_{m=1}^{\infty} \beta_{2m}(\tau)\phi_{2m}(\xi,\sigma(\tau)), \tag{12}$$

where β_{1m} and β_{2m} are unknown functions and ϕ_{1m} and ϕ_{2m} form sequences of linearly independent functions satisfying the boundary conditions. For simplicity we choose,

$$\phi_{1m} = \sin\left(m\pi \frac{\xi}{\sigma}\right), \; \phi_{2m} = \sin\left(\bar{m}\pi \frac{\xi-\sigma}{1-\sigma}\right), \; \bar{m}=m-1/2. \tag{13}$$

Substituting these in differential equations (7) and (8) we get,

$$\sum_{m=1}^{\infty} \beta_{1m}\phi''_{1m} = \sum_{m=1}^{\infty} \phi_{1m}\dot{\beta}_{1m} - \frac{\xi}{\sigma^2}\dot{\sigma} + \sum_{m=1}^{\infty} \beta_{1m}\dot{\phi}_{1m}, \tag{14}$$

$$A\sum_{m=1}^{\infty} \beta_{2m}\phi''_{2m} = \sum_{m=1}^{\infty} \phi_{2m}\dot{\beta}_{2m} + \sum_{m=1}^{\infty} \beta_{2m}\dot{\phi}_{2m}, \tag{15}$$

where dots and primes indicate differentiation with respect to τ and ξ, respectively. Multiplying equation (14) by ϕ_{1n} and (15) by ϕ_{2n}, and integrating (i.e., Galerkin approach), we get,

$$\dot{\beta}_{1n} + \frac{m^2\pi^2}{\sigma^2}\beta_{1n} \frac{2\dot{\sigma}}{\pi\sigma}\frac{(-1)^n}{n} + 2\pi\frac{\dot{\sigma}}{\sigma^3}\sum_{m=1}^{\infty} m\beta_{1m}G_{mn}=0, \; n=1, 2, \ldots, \tag{16}$$

$$\dot{\beta}_{2n} + \frac{A\bar{n}^2\pi^2}{(1-\sigma)^2}\beta_{2n} + \frac{2\pi\dot{\sigma}}{(1-\sigma)^3}\sum_{m=1}^{\infty} \bar{m}\beta_{2m}F_{mn}=0, \; n=1, 2, \ldots, \tag{17}$$

where

$$G_{mn} = \int_0^{\sigma} \xi \cos\left(\frac{m\pi\xi}{\sigma}\right)\sin\left(\frac{n\pi\xi}{\sigma}\right)d\xi, \tag{18}$$

$$F_{mn} = \int_{\sigma}^{1} (\xi-1)\sin\left(\bar{n}\pi\frac{\xi-\sigma}{1-\sigma}\right)\cos\left(\bar{m}\pi\frac{\xi-\sigma}{1-\sigma}\right)d\xi. \tag{19}$$

The equations (16) and (17) can be represented in the following integral forms,

$$\beta_{1m} = -\frac{2(-1)^m}{m\pi}\int_o^{\tau}\frac{\dot{\sigma}}{\sigma}(1+g_m(\zeta)) \times \exp\left(-\int_{\zeta}^{\tau}\left(\frac{\dot{\sigma}}{2\sigma}+\frac{m^2\pi^2}{\sigma^2}\right)d\zeta'\right)d\zeta, \tag{20}$$

$$\beta_{2m} = \frac{2}{\bar{m}\pi}\exp\left[-\int_0^{\tau}\left(\frac{\dot{\sigma}}{2(\sigma-1)}+\frac{A\bar{m}^2\pi^2}{(1-\sigma)^2}\right)d\zeta\right] \times\left\{1+\int_0^{\tau}\frac{\dot{\sigma}}{(1-\sigma)}f_m(\zeta)\left[\exp\int_0^{\zeta}\left(\frac{\dot{\sigma}}{2(\sigma-1)}+\frac{A\bar{m}^2\pi^2}{(1-\sigma)^2}\right)d\zeta'\right]d\zeta\right\}, \tag{21}$$

where,

$$g_m(\tau) = m^2\pi\sum_{\substack{n=1\\ n\neq m}}^{\infty}\frac{(-1)^n n}{m^2-n^2}\beta_{1n}, \tag{22}$$

$$f_m(\tau) = \bar{m}^2\pi\sum_{\substack{n=1\\ n\neq m}}^{\infty}\frac{\bar{n}}{\bar{m}^2-\bar{n}^2}\beta_{2n}. \tag{23}$$

Each of the systems of equations (20) and (21) represents a sequence of coupled integral equations. As the spatial distributions of temperature is smooth, it can be expected that the coupling is of a weak nature and the solutions of these equations can be obtained in an iterative way. In equations (20) and (21), if we neglect $g_m(\tau)$ and $f_m(\tau)$, we obtain the first approximations,

$$\beta_{1m}^{(1)} = -\frac{2(-1)^m}{m\pi}\int_o^{\tau}\frac{\dot{\sigma}}{\sigma}\exp\left[-\int_{\zeta}^{\tau}\left(\frac{\dot{\sigma}}{2\sigma}+\frac{m^2\pi^2}{\sigma^2}\right)d\zeta'\right]d\zeta, \tag{24}$$

$$\beta_{2m}^{(1)} = -\frac{2}{\bar{m}\pi}\exp\left[-\int_0^{\tau}\left(\frac{\dot{\sigma}}{2(\sigma-1)}+\frac{A\bar{m}^2\pi^2}{(1-\sigma)^2}\right)d\zeta\right]. \tag{25}$$

Using these in (22) and (23) we obtain improved values for $g_m(\tau)$ and $f_m(\tau)$, which in conjunction with (20) and (21) give the second approximations,

$$\beta_{1m}^{(2)} = -\frac{2(-1)^m}{m\pi}\int_o^\tau \frac{\dot\sigma}{\sigma}\exp\Big(-\int_\zeta^\tau\Big(\frac{\dot\sigma}{2\sigma}+\frac{m^2\pi^2}{\sigma^2}\Big)d\zeta'\Big)$$

$$\times\Big\{1-2m^2\sum_{\substack{n=1\\n\neq m}}^{\infty}\Big(\int_o^\tau\frac{\dot\sigma}{2\sigma}\exp\Big(\int_\zeta^\tau\frac{(m^2-n^2)\pi^2}{\sigma^2}d\zeta'\Big)\Big/(m^2-n^2)\Big)\Big\}d\zeta, \tag{26}$$

$$\beta_{2m}^{(2)} = \frac{2}{\bar m\pi}\exp\Big(-\int_0^\tau\Big(\frac{\dot\sigma}{2(\sigma-1)}+\frac{A\bar m^2\pi^2}{(1-\sigma)^2}\Big)d\zeta\Big)\Big\{1+2\bar m^2\int_0^\tau\frac{\dot\sigma}{(1-\sigma)}$$

$$\times\sum_{\substack{n=1\\n\neq m}}^{\infty}\Big(\exp\Big(\int_0^\zeta\frac{A(\bar m^2-\bar n^2)\pi^2}{(1-\sigma)^2}d\zeta'\Big)\Big/(\bar m^2-\bar n^2)\Big)d\zeta\Big\}. \tag{27}$$

Further iterations can be carried out if adequate accuracy is not obtained with the second approximation. The examples considered at the end of this paper indicate that the second-order approximations are sufficiently accurate for all cases considered. The interface condition (11) can be expressed in terms of the integrals,

$$I_0(\tau)=\int_\tau^{\tau+\Delta\tau}\frac{d\zeta}{\sigma^2}, \tag{28}$$

$$I_1(m,\tau)=\int_0^\tau\exp\Big(-\int_\zeta^\tau\Big(\frac{\dot\sigma}{2\sigma}+\frac{m^2\pi^2}{\sigma^2}\Big)d\zeta'\Big)\frac{\dot\sigma}{\sigma}d\zeta, \tag{29}$$

$$I_2(m,\tau)=\int_0^\tau\exp\Big(-\int_\zeta^\tau\Big(\frac{\dot\sigma}{2\sigma}+\frac{m^2\pi^2}{\sigma^2}\Big)d\zeta'\Big)\frac{\dot\sigma}{\sigma}g_m^{(2)}(\zeta)d\zeta, \tag{30}$$

$$I_3(\tau)=A\pi^2\int_0^\tau\frac{d\zeta}{(1-\sigma)^2}, \tag{31}$$

$$I_4(\tau)=\sum_{m=1}^{\infty}\bar m^2\exp(-\bar m^2 I_3(\tau))\int_0^\tau\exp(\bar m^2 I_3(\zeta))\frac{\dot\sigma}{(1-\sigma)}\times\sum_{\substack{n=1\\n\neq m}}^{\infty}\frac{\exp(-\bar n^2 I_3(\zeta))}{\bar m^2-\bar n^2}d\zeta, \tag{32}$$

as,

$$\dot\sigma=\frac{S_1}{\sigma}\Big\{1+2\sum_{m=1}^{\infty}I_1(m,\tau)+I_2(m,\tau)\Big\}-\frac{S_2A}{(1-\sigma)^{3/2}}\Big\{2\sum_{m=1}^{\infty}\exp((-\bar m^2 I_3(\tau))+4I_4(\tau)\Big\}, \tag{33}$$

where $S_1=(T_m-U)C_1/L$ and $S_2=(V-T_m)C_2/L$ are the solid and liquid Stefan numbers, respectively, and C_i is the specific heat. The nonlinear ordinary differential equation (33) for the interface location, $\sigma(\tau)$, has to be integrated numerically. The integrals I_0, I_1, I_2, and I_3 can be written in the next time-step, $\tau+\Delta\tau$, as a function of the previous time-step, τ, giving,

$$I_1(m,\tau)=\int_0^\tau\sqrt{\frac{\sigma(\zeta)}{\sigma(\tau)}}\exp\Big(-\int_\zeta^\tau\frac{m^2\pi^2}{\sigma^2}d\zeta'\Big)\frac{\dot\sigma}{\sigma}d\zeta, \tag{34}$$

$$I_1(m,\tau+\Delta\tau)=\sqrt{\frac{\sigma(\tau)}{\sigma(\tau+\Delta\tau)}}\exp\Big(-\int_\tau^{\tau+\Delta\tau}\frac{m^2\pi^2}{\sigma^2}d\zeta\Big)I_1(m,\tau)+I_{11}, \tag{35}$$

where I_{11} is given by,

$$I_{11}=\frac{1}{\sqrt{\sigma(\tau+\Delta\tau)}}\int_\tau^{\tau+\Delta\tau}\frac{\dot\sigma}{\sqrt\sigma}\exp\Big(-\int_\zeta^{\tau+\Delta\tau}\frac{m^2\pi^2}{\sigma^2}d\zeta'\Big)d\zeta, \tag{36}$$

$$I_{11}\simeq\frac{\dot\sigma(\tau+\Delta\tau)}{\sigma(\tau+\Delta\tau)}\int_\tau^{\tau+\Delta\tau}\exp\Big(-\int_\zeta^{\tau+\Delta\tau}\frac{m^2\pi^2}{\sigma^2}d\zeta'\Big)d\zeta. \tag{37}$$

An asymptotic expansion of (37) gives

$$I_{11}\sim\frac{\dot\sigma(\tau+\Delta\tau)}{m^2\pi^2\sigma(\tau+\Delta\tau)}\Big\{[\sigma^2(\tau+\Delta\tau)-\sigma^2(\tau)\exp(-m^2\pi^2 I_0(\tau))]-\frac{2}{m^2\pi^2}[\dot\sigma(/\tau+d\tau)\sigma^3(\tau+\Delta\tau)-\dot\sigma(\tau)\sigma^3(\tau)\exp(-m^2\pi^2 I_0(\tau))]\Big\}. \tag{38}$$

Similarly,

$$I_2(m,\tau)=\int_0^\tau\sqrt{\frac{\sigma(\zeta)}{\sigma(\tau)}}\exp\Big(-\int_\zeta^\tau\frac{m^2\pi^2}{\sigma^2}d\zeta'\Big)\frac{\dot\sigma}{\sigma}(1+g(\zeta))d\zeta \tag{39}$$

$$I_2(m,\tau+\Delta\tau)=\sqrt{\frac{\sigma(\tau)}{\sigma(\tau+\Delta\tau)}}\times\exp\Big(-\int_\tau^{\tau+\Delta\tau}\frac{m^2\pi^2}{\sigma^2}d\zeta\Big)I_2(m,\tau)+I_{22} \tag{40}$$

where I_{22} is

$$I_{22}=\frac{1}{\sqrt{\sigma(\tau+\Delta\tau)}}\int_\tau^{\tau+\Delta\tau}\frac{\dot\sigma}{\sqrt\sigma}\exp\Big(-\int_\zeta^{\tau+\Delta\tau}\frac{m^2\pi^2}{\sigma^2}d\zeta'\Big)(1+g(\zeta))d\zeta \tag{41}$$

$$I_{22}\simeq\frac{\dot\sigma(\tau+\Delta\tau)}{\sigma(\tau+\Delta\tau)}(1+g(\zeta))\int_\tau^{\tau+\Delta\tau}\exp\Big(-\int_\zeta^{\tau+\Delta\tau}\frac{m^2\pi^2}{\sigma^2}d\zeta'\Big)d\zeta. \tag{42}$$

An asymptotic expansion gives

$$I_{22}\sim\frac{\dot\sigma(\tau+\Delta\tau)}{m^2\pi^2\sigma(\tau+\Delta\tau)}(1+g(\zeta))\Big\{[\sigma^2(\tau+\Delta\tau)-\sigma^2(\tau)\exp(-m^2\pi^2 I_0(\tau))]-\frac{2}{m^2\pi^2}[\dot\sigma(\tau+d\tau)\sigma^3(\tau+\Delta\tau)-\dot\sigma(\tau)\sigma^3(\tau)\exp(-m^2\pi^2 I_0(\tau))]\Big\}. \tag{43}$$

The integral I_3 at the next time-step is

$$I_3(\tau+\Delta\tau)=A\pi^2\int_0^{\tau+\Delta\tau}\frac{d\zeta}{(1-\sigma)^2}d\zeta, \tag{44}$$

hence,

$$I_3(\tau+\Delta\tau)=I_3(\tau)+I_{33}, \tag{45}$$

where I_{33} is

$$I_{33}=A\pi^2\int_\tau^{\tau+\Delta\tau}\frac{d\zeta}{(1-\sigma)^2}d\zeta. \tag{46}$$

The integral I_4 at the next time-step is a function of I_3, as given by equation (32), and the interface equation is solved as follows:

(1) The solution is started using the similarity solution for the semi-infinite case, $\sigma(\tau)=\lambda\sqrt{\tau}$, where λ is known (Carslaw and Jaeger, 1954).

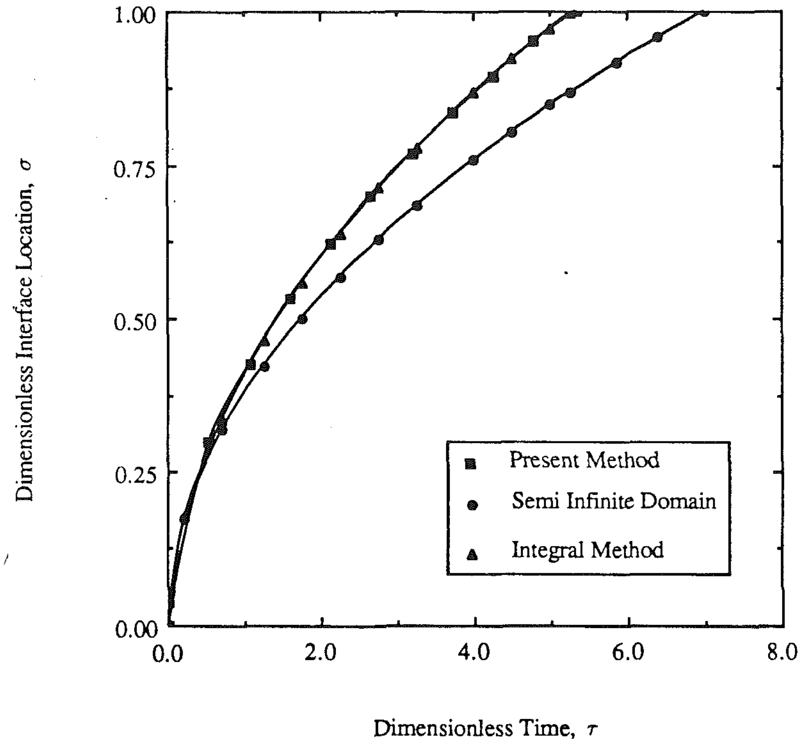

Fig. 1 Dependence of interface location of time

(2) I_0, I_1, I_2, I_3, and I_4 are calculated using a predictor algorithm (Adams-Moulton predictor).

(3) The interface location, σ, and its derivative, $\dot{\sigma}$, are calculated using I_0, I_1, I_2, I_3, and I_4.

(4) New values of I_0, I_1, I_2, I_3, and I_4 are calculated using the σ and $\dot{\sigma}$ values calculated at Step 3.

(5) Corrected values of σ and $\dot{\sigma}$ are calculated (with Adams-Moulton corrector formula) using the I_0, I_1, I_2, I_3, and I_4 calculated at Step 4.

(6) The corrector algorithm is repeated until σ and $\dot{\sigma}$ satisfy a convergence criterion.

Once the location of the interface is calculated, the temperature distribution in both regions can be calculated using,

$$\theta_1(\tau) = \sum_{m=1}^{\infty} \beta_{1m}\phi_{1m},\ \theta_2(\tau) = V^* \sum_{m=1}^{\infty} \beta_{2m}\phi_{2m}, \tag{47}$$

which can be written as,

$$\theta_1(\tau) = \sum_{m=1}^{\infty} \frac{-2(-1)^m}{m\pi} (I_1(m,\tau) + I_2(\tau)) \sin\left(\frac{m\pi\xi}{\sigma}\right), \tag{48}$$

and

$$\begin{aligned}
\theta_2(\tau) = \frac{2V^*}{\sqrt{1-\sigma}} \Bigg\{ & \sum_{m=1}^{\infty} \sin\left(\bar{m}\pi \frac{\xi-\sigma}{1-\sigma}\right) \frac{\exp(-\bar{m}^2 I_3(\tau))}{\bar{m}} \\
& + 2\Bigg[\frac{\dot{\sigma}(1-\sigma)}{A\pi^2} \sum_{m=1}^{\infty} \sin\left(\bar{m}\pi \frac{\xi-\sigma}{1-\sigma}\right) \\
& \times \frac{1-\exp(-\bar{m}^2(I_3(\tau) - I_3(\tau-\Delta\tau)))}{\bar{m}} \\
& \times \sum_{\substack{n=1 \\ n\neq m}}^{\infty} (\exp(-\bar{n}^2 \bar{I}_3)/(\bar{m}^2 - \bar{n}^2)) \\
& - \ln(1-\sigma(\tau-\Delta\tau)) \sum_{m=1}^{\infty} \bar{m} \sin\left(\bar{m}\pi \frac{\xi-\sigma}{1-\sigma}\right) \\
& \times (1-\exp(-\bar{m}^2(I_3(\tau) - I_3(\tau-\Delta\tau)))) \\
& \times \sum_{\substack{n=1 \\ n\neq m}}^{\infty} (\exp(-\bar{n}^2 I_3(\tau-\Delta\tau))/(\bar{\omega}^2 - \bar{n}^2)) \\
& + A\pi^2 \sum_{m=1}^{\infty} \bar{m} \sin\left(\bar{m}\pi \frac{\xi-\sigma}{1-\sigma}\right) \\
& \int_0^{\tau-\Delta\tau} \frac{-\ln(1-\sigma)}{(1-\sigma)^2} \exp(-\bar{m}^2(I_3(\tau) - I_3(\zeta))) \\
& \times \sum_{\substack{n=1 \\ n\neq m}}^{\infty} \exp(-\bar{n}^2 I_3(\zeta))d\zeta\Bigg]\Bigg\}.
\end{aligned} \tag{49}$$

Defining a new dimensionless temperature, φ,

$$\begin{aligned}
\varphi &= \frac{\xi}{\sigma} + \theta_1,\ \xi < \sigma, \\
&= \frac{\theta_2}{V^*} + 1,\ \xi > \sigma.
\end{aligned} \tag{50}$$

The new dimensionless temperature, φ, will be used for the temperature distributions.

3 Results and Discussion

Results are presented for three different cases. The first case is for a solid Stefan number, $S_1 = 0.1$ and a liquid Stefan number, $S_2 = 0.1$ (the diffusivity ratio A, is unity and the liquid is at freezing temperature initially). This case was selected as there are existing perturbation solutions for low Stefan numbers. Figure 1 shows the location of the interface as a

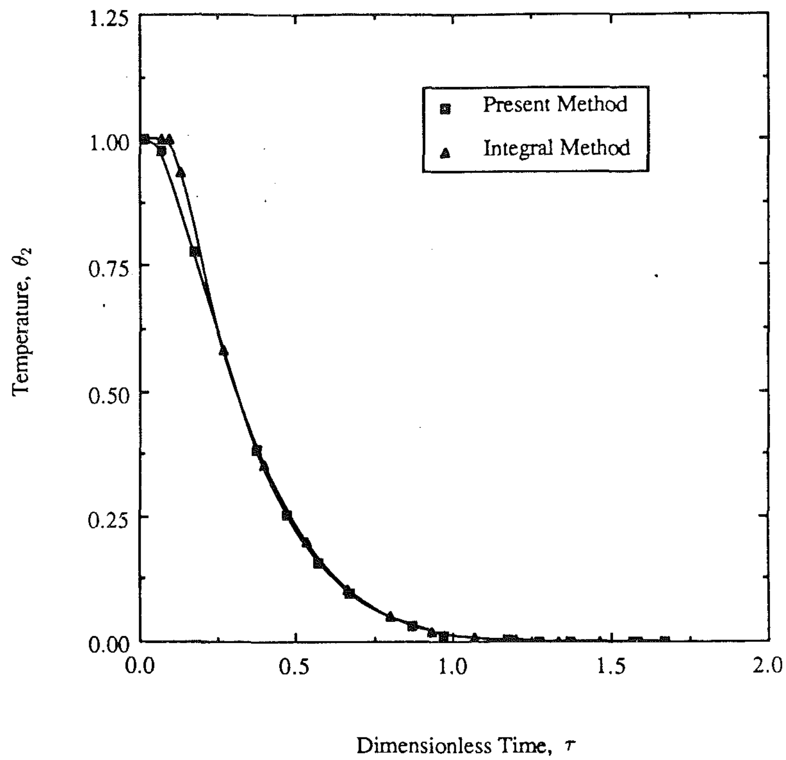

Fig. 2 Insulated wall temperatures

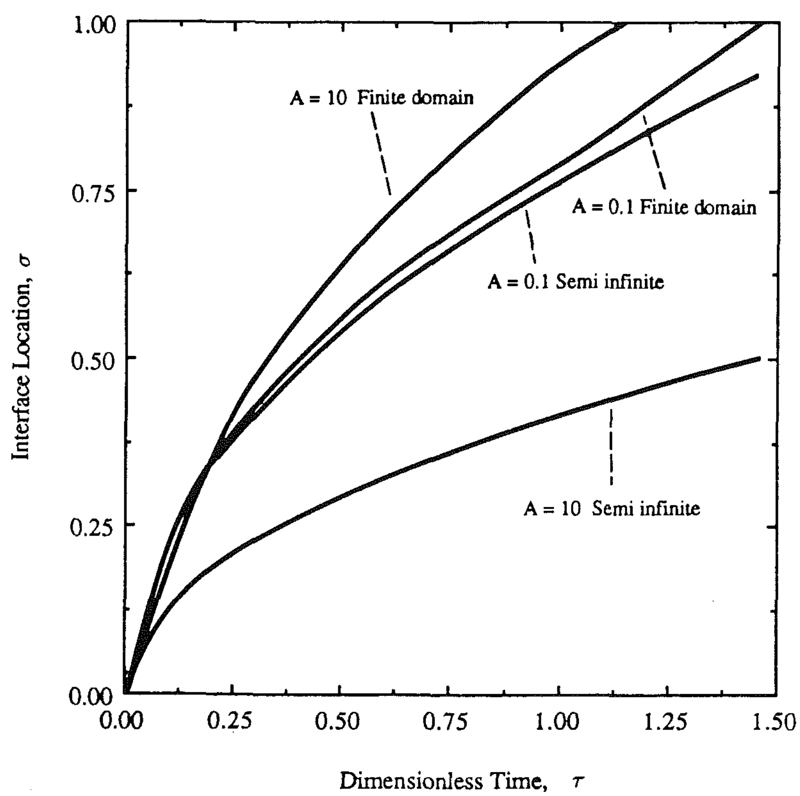

Fig. 3 Interface location for Stefan numbers $S_1 = 0.5$ and $S_2 = 0.5$

function of time. The other two curves are plotted for comparison. The lower curve is the solution for the semi-infinite medium. The upper two curves represent the present solution and the integral solution of Charach and Zoglin (1985). The two curves are in perfect agreement. The solidification time for the finite domain problem is always seen to be shorter than the time given by the semi-infinite solution, i.e., the lower curve. Figure 2 shows the transient insulated wall temperatures. For comparison, the intergral solution (Charach and Zoglin, 1985) is also plotted. Since the integral formulation assumes a finite penetration depth in the liquid phase, the insulated wall temperature remains unchanged until the diffusion front arrives. Therefore, the results of the integral solution for small time are not valid. The results of the

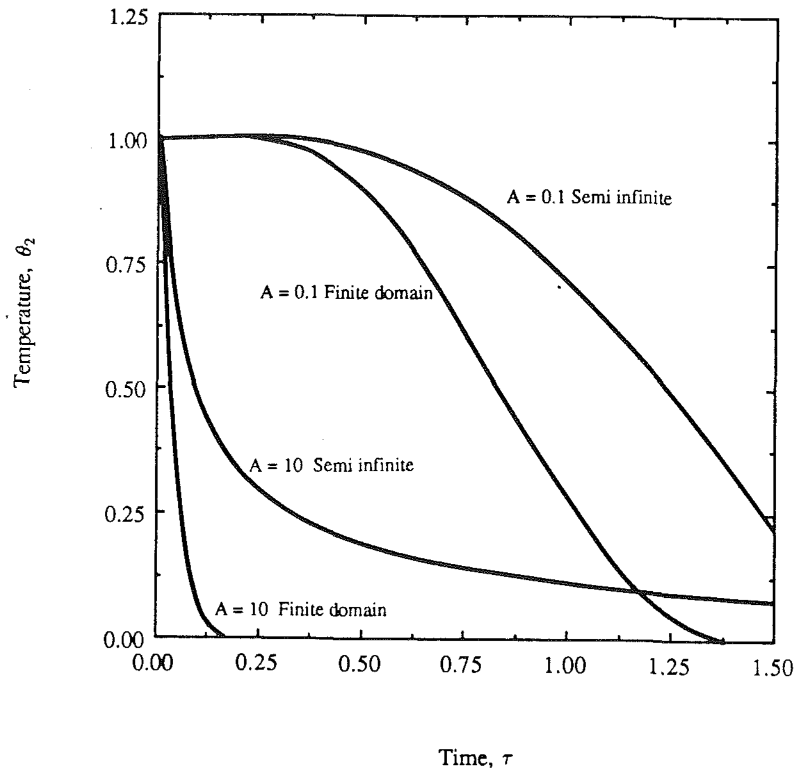

Fig. 4 Insulated wall temperature for Stefan numbers $S_1 = 0.5$ and $S_2 = 0.5$

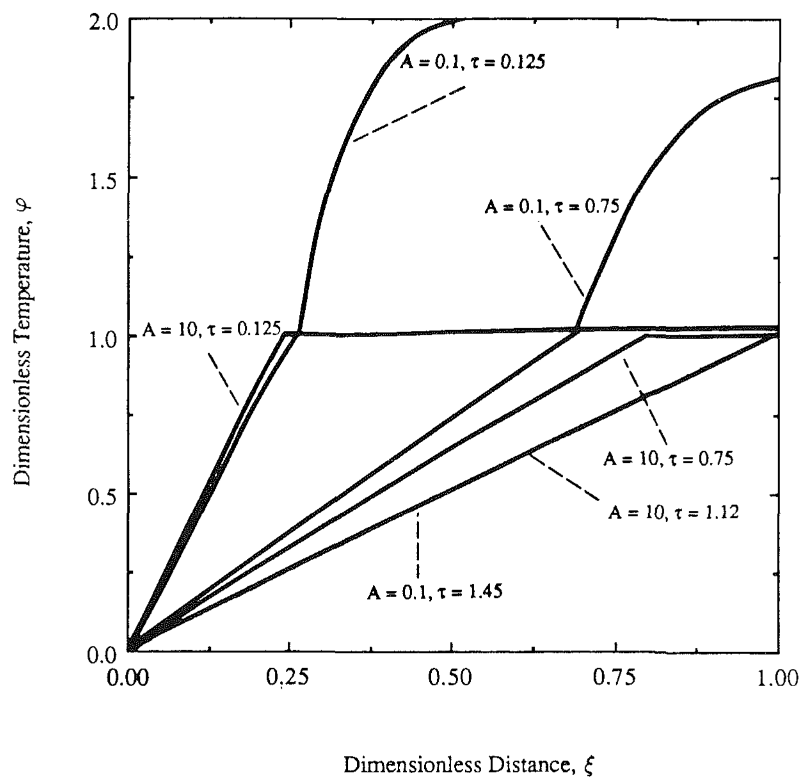

Fig. 5 Temperature distribution for Stefan numbers $S_1 = 0.5$ and $S_2 = 0.5$

present method again match perfectly with the integral solution for larger time. Note that for this set of parameters, the insulated wall temperature drops to the interface temperature at $\tau \approx 1.2$, whereas complete solidification occurs at $\tau \approx 5.3$. The reason is that the diffusivity ratio is unity, i.e., $\alpha_1 = \alpha_2$, and, hence, the heat diffusion in the liquid is not very slow.

The other two cases are presented for solid and liquid Stefan numbers of 0.5 and two different diffusivity ratios, namely $A = 0.1$ and $A = 10$. The liquid is assumed to be at a temperature twice the freezing temperature. The integral solution (Charach and Zoglin, 1985) and the perturbation solution (Weinbaum and Jiji, 1977) are not applicable for these cases. Figure 3 snows the location of the interface for the two diffusivity ratios, given by the present method for the finite medium and the solution for the semi-infinite domain for comparison. For both diffusivity ratios, solidification time is faster in the finite medium. The two cases, however, are very different. For $A = 0.1$, the thermal diffusivity of the liquid is much less than that of the solid and the heat diffusion in the liquid is slow. Therefore, the finite domain solution follows the semi-infinite solution closely, and diverges from it only when the interface gets very close to the insulated boundary. In the other case, the diffusivity of the liquid is ten times higher than that of the solid, and hence the diffusion in the liquid is faster. Therefore, the solution for the finite domain diverges from that of the semi-infinite domain very early. Since both cases have the same Stefan numbers, the total amount of heat lost by the liquid phase during the process is approximately the same. However, when $A = 10$ (higher rate of heat diffusion in the liquid), the rate of heat loss from the liquid and the speed of the interface are higher. Figure 4 shows this effect. Although the soldification time is about the same for both cases, the insulated wall temperature drops very fast and sharply when $A = 10$, reaching the interface temperature at $\tau \approx 0.2$. For $A = 0.1$, on the other hand, the insulated boundary temperature drops gradually to that of the interface at $\tau \approx 1.3$, which is close to the total soldification time. Figure 5 shows the transient temperatures at $\tau = 0.12$, $\tau = 0.75$, and at full solidification. As can be seen, the temperature distribution in the liquid for $A = 10$ drops to the interface temperature very fast, and the temperature distribution in the liquid is almost linear. In the other case, the temperature distribution in the liquid stays above the interface value till very late. The solid temperature distributions in both problems are very close to linear.

Although the method was applied to a problem with constant initial and boundary conditions, it can also be applied to problems with arbitrary boundary and initial conditions. Apart from the verification of the convergence of the iterative solution for the finite domain presented here, this new method has been extensively tested and found to be convergent for the semi-infinite case (Dursunkaya, 1988), for all moderate values of the parameters. The method presented here is particularly suitable for assessing the accuracy of more versatile methods such as finite difference and finite element which could not be tested against existing exact solutions for semi-infinite domains.

Acknowledgments

The authors are indebted to Prof. L. N. Tao for many insightful suggestions.

References

Carslaw, H. S., and Jaeger, J. C., 1954, *Conduction of Heat in Solids*, Oxford University Press, Oxford, U.K.

Charach, Ch., and Zoglin, P., 1985, "Solidification in a finite, initially over heated slab," *International Journal of Heat and Mass Transfer*, Vol. 28, pp. 2261–2268.

Dursunkaya, Z., 1988, "Fourier Series Solution of Moving Boundary Problems in Finite Domain," Ph.D. Dissertation, Illinois Institute of Technology, Chicago, Ill.

Dursunkaya, Z., and Nair, S., 1988, "An Iterated Fourier Series Solution for Moving Boundary Problems," submitted for publication.

Fukusako, S., and Seki, N., 1987, "Fundamental Aspects of Analytical and Numerical Methods on Freezing and Melting Heat-Transfer Problems," *Annual Review of Numerical Fluid Mechanics and Heat Transfer*, Vol. 1, T. C. Chawla, ed., Hemisphere Publishing Corporation, New York, pp. 351–402.

Goodman, T. R., 1958, "The Heat-Balance Integral and Its Application to Problems Involving a Change of Phase," ASME *Journal of Heat Transfer*, Vol. 80, pp. 335–341.

Ockendon, J. R., and Hogkins, W. R., eds., 1975, *Moving Boundary Problems in Heat Flow and Diffusion*, Clarendon Press, Oxford, U.K.

Rubinstein, L. I., 1971, *The Stefan Problem*, (English Translation), American Mathematical Society, Providence, R.I.

Tao, L. N., 1978, "The Stefan Problem with Arbitrary Initial and Boundary Conditions," *Quarterly of Applied Mathematics*, Vol. 36, pp. 223–233.

Tao, L. N., 1980, "The Analyticity of Solutions of the Stefan Problem," *Arch. Rational Mech. Anal.*, Vol. 72, pp. 1–10.

Tao, L. N., 1981, "The Exact Solutions of Some Stefan Problems with Prescribed Heat Flux," ASME Journal of Applied Mechanics, Vol. 48, pp. 732–736.

Weinbaum, S., and Jiji, L. M., 1977, "Singular Perturbation Theory for Melting or Freezing in Finite Domains Initially Not at the Fusion Temperature," ASME Journal of Applied Mechanics, Vol. 44, pp. 25–30.

Wilson, D. G., Solomon, A. D., and Boggs, P. T., eds., 1978, *Moving Boundary Problems*, Academic Press, New York.

Yuen, W. W., 1981, "Application of the Heat Balance Integral to Melting Problems with Initial Subcooling," *International Journal of Heat and Mass Transfer*, Vol. 23, pp. 1157–1160.

S. M. Kulkarni
Graduate Student,
Mem. ASME

G. T. Hahn
Professor.

C. A. Rubin
Professor,
Mem. ASME

V. Bhargava
Research Assistant Professor.

Center for Materials Tribology,
Vanderbilt University,
Nashville, TN 37235

Elastoplastic Finite Element Analysis of Three-Dimensional, Pure Rolling Contact at the Shakedown Limit

This paper describes a three-dimensional elastoplastic finite element model of repeated, frictionless rolling contact. The model treats a sphere rolling on an elastic-perfectly plastic and an elastic-linear-kinematic-hardening plastic, semi-infinite half space. The calculations are for a relative peak pressure (p_o/k) = *4.68 (the theoretical shakedown limit for perfect plasticity). Three-dimensional rolling contact is simulated by repeatedly translating a hemispherical (Hertzian) pressure distribution across an elastoplastic semi-infinite half space. The semi-infinite half space is represented by a finite mesh with elastic boundaries. The calculations describe the distortion of the rim, the residual stress-strain distributions, stress-strain histories, and the cyclic plastic strain ranges in the vicinity of the contact.*

Introduction

Repeated three-dimensional rolling point contact is even more complex than the two-dimensional plane-strain problem. A review by Johnson (1986) examines the possible mechanisms of failure and predicts the nature of the residual stress state. Ponter et al. (1985) apply the kinematical shakedown theorem to investigate the mode of deformation for rolling and sliding point contacts. The authors calculate optimal upper bounds for both the elastic and plastic shakedown limits for varying coefficients of friction and shapes of the loaded ellipse. Bower et al. (1986) used the above-mentioned theorem to closely look at the conditions under which cumulative deformation occurs in the corner of the railhead. The corner of the railhead was idealized as an elastic-perfectly plastic quarter space. The study was further extended to a work-hardening quarter space. Hills and Sackfield (1984) study the yield and shakedown states in the contact of generally curved bodies, with and without friction. Hills and Sackfield (1983a, 1983b, 1986) have done additional work treating the point contact problem mathematically.

Kalker (1979) has developed a computer code for treating elastic three-dimensional rolling contact with dry friction. Kannel and Tevaarwerk (1984) presented a computer model for evaluating the subsurface stresses incurred during rolling/sliding contacts. Hardy et al. (1971) developed a finite element model of a rigid sphere indenting (not rolling on) an elastic-perfectly plastic half space. Equations were obtained by Hamilton and Goodman (1966) for the complete stress field due to a circular contact region carrying a "hemispherical" Hertzian normal pressure and a proportional distributed shearing traction. Chiu and Hartnett (1983) have presented a numerical method of solution for three-dimensional Hertzian contact problems involving layered solids. Hills and Ashelby (1982) have analyzed the residual stresses and their influence on the contact load bearing capacity for three-dimensional rolling. Rydholm and Fredriksson (1981) devised a finite element model for analyzing shakedown problems in three-dimensional rolling contacts for elastic-perfectly plastic and kinematic hardening material responses. As regards plastic deformations in the rim, Martin and Hay (1972) developed a three-dimensional finite element model to analyze yielding of rail material, the subsequent development of residual stresses, and plastic flow due to a moving load. Line contact of two cylinders or of a cylinder and a half space, with plane-strain deformation, has also been studied in detail (Bhargava et al. (1985a, 1985b, 1986), Merwin and Johnson (1963), Johnson and Jefferis (1963)).

Though there exist a number of treatments of the three-dimensional problem of rolling contact, the information obtained is limited. Most of the analyses employ elastic or elastic-perfectly plastic material behavior. Some of them evaluate the shakedown limits and provide peak values of certain normal residual stresses. However, there is very little information on residual stresses, strains, and plastic strain range distributions in the half space, especially in the vicinity of the contact. Only two of the studies deal with the stress-strain history (Ponter et al. (1986), Bower et al. (1986)). Previous analyses have

Contributed by the Applied Mechanics Division of The American Society of Mechanical Engineers for presentation at the Winter Annual Meeting, Dallas, Tex., November 25-30, 1990.

Discussion on this paper should be addressed to the Technical Editor, Prof. Leon M. Keer, The Technological Institute, Northwestern University, Evanston, IL 60201, and will be accepted until two months after final publication of the paper itself in the Journal of Applied Mechanics. Manuscript received by the ASME Applied Mechanics Division, October 10, 1988; final revision, April 10, 1989.

Paper No. 90-WA/APM-2.

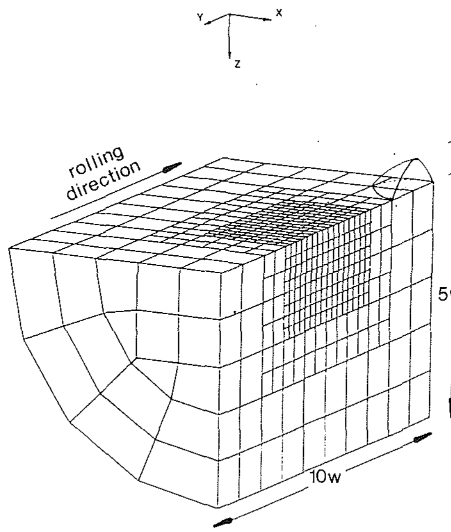

Fig. 1 Three-dimensional finite element mesh

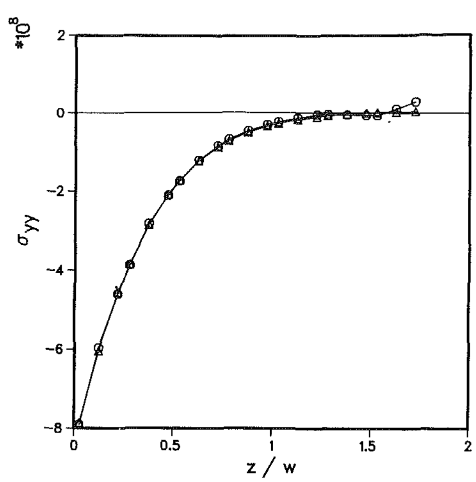

Fig. 2 Comparison of the circumferential stress, σ_{yy}, as a function of normalized depth, z/w, for an elastic indentation of the F.E. mesh (FE) with the closed-form solution (CFS), at a distance $0.125w$ from the YZ plane; Legend: ○ FE, △ CFS

required arbitrary simplifying assumptions; for example, in theoretical studies certain stresses were neglected, and in finite element studies the boundaries were assumed fixed.

The present paper describes a three-dimensional elasto-plastic finite element model of frictionless rolling contact that embodies the elastic-perfectly-plastic, as well as the elastic-linear-kinematic-hardening-plastic, material response. The pressure distribution is assumed to be Hertzian throughout the analysis. The calculations are for a relative peak pressure (p_o/k) of 4.68 (the shakedown limit for a circular contact patch for pure rolling). Unlike other studies, these calculations employ more realistic (elastically displaced) boundaries and provide much more information: residual stress-strain distributions, residual displacements, stress-strain histories and cyclic plastic strain ranges in the half space.

Description of the Finite Element Model

Frictionless rolling of a sphere on a semi-infinite body is simulated by translating a semi-ellipsoidal pressure distribution over one face of a three-dimensional finite element mesh. A finite-sized mesh (Fig. 1) is used to represent a semi-infinite body by appropriately displacing the other faces of the three-dimensional mesh. For this purpose, the semi-ellipsoidal pressure distribution is discretized into numerous concentrated forces. The displacements at the boundary nodes are then calculated for each of these concentrated forces using the solution to Boussinesq's problem of a single normal force acting on the boundary of a semi-infinite solid and then superposing this solution for many loads. All displacements are with reference to a point at the bottom of the mesh directly under the center of the semi-ellipsoidal pressure distribution. To verify the validity of the model, stress versus depth values obtained from a purely elastic indentation of the three-dimensional mesh were compared with those from a program incorporating the closed-form elastic solution. The results show excellent agreement (Fig. 2).

Making use of the symmetry of the pressure distribution about the rolling direction, the three-dimensional mesh has the shape of a quadrant of a circle extended in the third dimension. The present study, in the most general case, pertains to two mechanical components in a three-dimensional rolling situation, and hence, the x-axis will be referred to as the axial direction, the y-axis or the direction of translation as the circumferential direction, and the z-axis as the radial direction. The mesh is dimensionally finer away from the displaced boundaries and coarser towards them. The mesh is $10w$ long (in the circumferential direction) and extends to a distance of $5w$ in the axial and radial directions (the contact patch is assumed to be a circle of radius w). There were some doubts regarding the X and Z dimensions of the mesh. As described earlier, the boundaries are elastically displaced as the pressure translates. These boundaries are restored to their original undeformed state when the mesh is unloaded at the end of a contact cycle. If the mesh were too small, inaccurate answers would result since the residual state produced by the contact will have an effect on the elastic deformation of the half space. For this purpose a larger mesh (the X and Z dimensions four times the size of the original mesh) was devised. The results

Nomenclature

x = axial or out-of-plane coordinate, m
y = circumferential or in-plane coordinate, m
z = radial or depth coordinate, m
p_o = peak pressure, MPa
$k=\sigma_o/1.73$ = von Mises shear yield strength, MPa
$k_k=\sigma_k/1.73$ = kinematic shear yield strength, MPa
$p_o/k, p_o/k_k$ = relative peak pressure
$p(x,y)$ = pressure at any point, MPa
w = radius of the contact circle, m
E = Young's modulus, MPa
ν = Poisson's ratio
M = plastic modulus, MPa
G = shear modulus, MPa
EPP = elastic-perfectly plastic
ELKP = elastic-linear-kinematic-hardening plastic
f^r = parameter f for the residual state
σ_{xx} = axial stress, MPa
σ_{yy} = circumferential stress, MPa
σ_{zz} = radial stress, MPa
τ_{xz}, τ_{yz} = shear stress, MPa
ϵ_{xx} = axial total strain
ϵ_{yy} = circumferential total strain
ϵ_{zz} = radial total strain
$\gamma_{xy}, \gamma_{xz}, \gamma_{yz}$ = shear total strain
$\Delta\epsilon_{zz}{}^p$ = radial plastic strain range
$\Delta\gamma_{yz}{}^p$ = shear plastic strain range
$\Delta eq^p/2$ = half equivalent plastic strain range

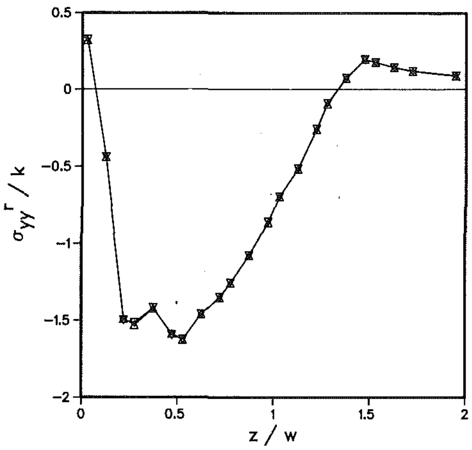

Fig. 3 Comparison of the normalized residual circumferential stress, σ_{yy}^r/k, as a function of the normalized depth, z/w, for the large mesh and the small mesh, for EPP properties, at a distance $0.125w$ from the YZ plane; Legend: △ small mesh, ▽ large mesh

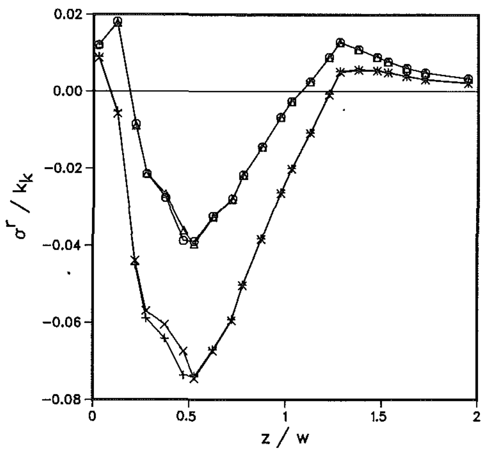

Fig. 5 Comparison of the normalized residual axial, σ_{xx}^r/k_k, and circumferential, σ_{yy}^r/k_k, stress as a function of the normalized depth, z/w, for one and two successive contacts, PS1 and PS2, for ELKP properties; Legend: ○ σ_{xx}^r/k_k – PS1, △ σ_{xx}^r/k_k – PS2, + σ_{xx}^r/k_k – PS1, × σ_{xx}^r/k_k – PS2

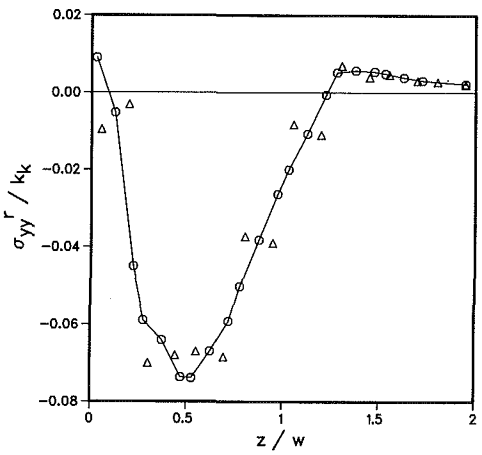

Fig. 4 Comparison of the normalized residual circumferential stress, σ_{yy}^r/k, as a function of the normalized depth, z/w, for the fine mesh and the coarse mesh, at a distance $0.125w$ from the YZ plane; Legend: ○ fine mesh, △ coarse mesh

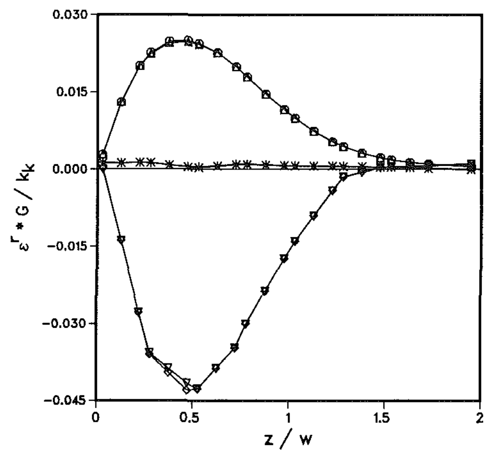

Fig. 6 Comparison of the normalized residual axial, $\epsilon_{xx}^{r}*G/k_k$, circumferential, $\epsilon_{yy}^{r}*G/k_k$, and radial, $\epsilon_{zz}^{r}*G/k_k$, strain as a function of the normalized depth, z/w, for one and two successive contacts, PS1 and PS2, for ELKP properties; Legend: ○ $\epsilon_{xx}^{r}*G/k_k$ – PS1, △ $\epsilon_{xx}^{r}*G/k_k$ – PS2, + $\epsilon_{yy}^{r}*G/k_k$ – PS2, × $\epsilon_{yy}^{r}*G/k_k$ – PS2, ◇ $\epsilon_{zz}^{r}*G/k_k$ – PS1, ▽ $\epsilon_{zz}^{r}*G/k_k$ – PS2

from this large mesh were compared with those from the mesh shown in Fig. 1. As seen in Fig. 3, the stress distributions match very well.

Initial calculations were done using lower-order (8-noded, linear displacement) brick elements. The mesh contained 1392 elements and 1877 nodes. The initial results exhibited poor convergence characteristics. Finally, with CPU time for a contact cycle as the limiting factor, a finer mesh of the same size was developed. This mesh employed higher-order (20 or 27-noded quadratic brick) elements closer to the contact and lower-order (8-noded linear brick) elements away from the contact. It has 1392 elements and 4649 nodes. Figure 4 compares residual stress distributions for the fine and the coarse mesh.

The calculations employed two different material behaviors: (*a*) the more realistic elastic-linear-kinematic-hardening-plastic (ELKP) (Bhargava et al. (1986), Hahn et al. (1987)) behavior with $\sigma_k = 1050$ MPa and $M = 188$ GPa (see Fig. 24), and (*b*) the elastic-perfectly plastic (EPP) behavior with $\sigma_o = 393.98$ MPa, and were performed for $p_o/k = 4.68$. Both models used the following elastic properties: Young's modulus, $E = 207$ GPa, and Poisson's ratio, $\nu = 0.3$. The following assumptions were made for the analyses: (*a*) the contact area is a circle of radius w calculated from the material constants; this does not change after the semi-infinite body begins to deform plastically ($w = 0.8$ mm, and 0.3 mm for ELKP and EPP properties, respectively), and (*b*) the semi-ellipsoidal (here hemispherical) pressure distribution remains Hertzian throughout the analysis. The Hertzian pressure is given by

Table 1 Typical computational times for analyses

Model	Machine	CPU Time For One Contact (Hrs.)
Coarse Mesh	VAX 11/785	150
Coarse Mesh	VAX 8800	15
Fine Mesh	VAX 8800	36
Fine Mesh	CRAY X-MP	1.5

$$p(x,y) = p_o(1 - (x^2 + y^2)/w^2)^{1/2}.$$

The semi-ellipsoidal pressure distribution was applied at one end of the mesh and translated incrementally through a distance of $8w$ to the other end. The translational increments varied according to the location of the pressure distribution. The first increment w was followed by two increments of $0.5w$, sixteen increments of $0.25w$, two increments of $0.5w$, and, finally, one increment of w before the mesh was unloaded. The boundaries of the mesh were appropriately displaced at each increment. The application of the pressure distribution, followed by the 22 translational increments and the unloading, define a single contact cycle. The mesh was subjected to two cycles for each material behavior. The multipurpose finite element package ABAQUS was used for the analyses. The Cray X-MP was used for the calculation with the large mesh. All

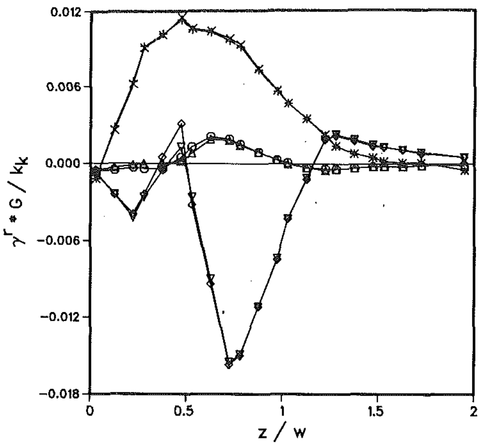

Fig. 7 Comparison of the normalized residual shear strain, γ^r/k_k, as a function of the normalized depth, z/w, for one and two successive contacts, PS1 and PS2, for ELKP properties; Legend: ○ $\gamma_{xy}^{r*}G/k_k$ – PS1, △ $\gamma_{xy}^{r*}G/k_k$ – PS2, + $\gamma_{xz}^{r*}G/k_k$ – PS1, × $\gamma_{xz}^{r*}G/k_k$ – PS2, ◇ $\gamma_{yz}^{r*}G/k_k$ – PS1, ▽ $\gamma_{yz}^{r*}G/k_k$ – PS2

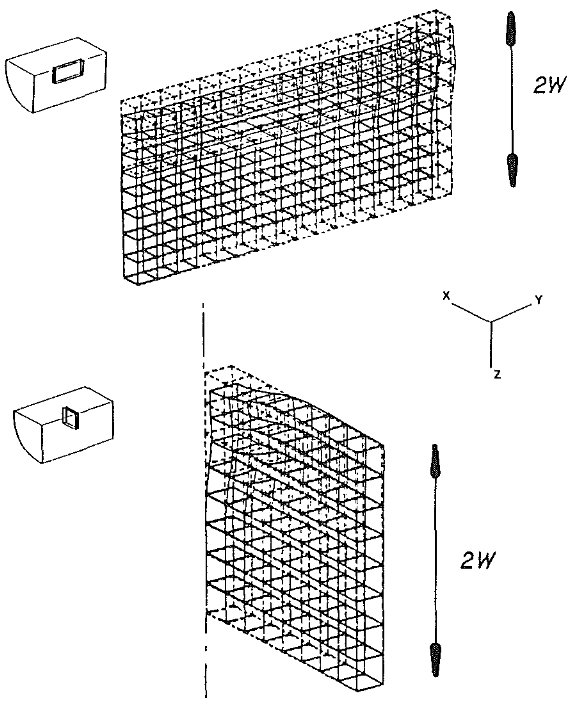

Fig. 8 Residual displaced meshes for a section of the mesh, (*a*) along (mag. fac. = 580) and (*b*) perpendicular (mag. fac. = 440) to the rolling direction for ELKP properties

other calculations were carried out on the VAX 11/785 and the VAX 8800 (Table 1).

Results

The results describe the variation with depth of the residual stresses, residual strains and cyclic plastic strain ranges, sections of the residual displaced mesh, residual stress-strain contours, and stress-strain histories for the two contacts. The residual stresses are normalized with respect to k or k_k, the residual strains with respect to k/G or k_k/G, and the depth with respect to w. All the residual stress, residual strain, and cyclic plastic strain range distributions as functions of depth are presented for integration points located at a distance of $0.125w$ from the plane of symmetry (the YZ plane). Figure 5 shows the residual axial and circumferential stress distributions for the ELKP material. These stresses attain peak compressive

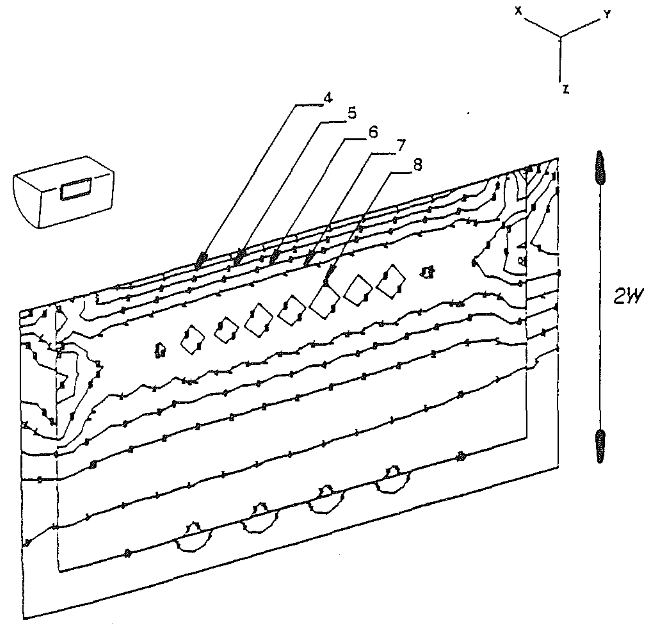

Fig. 9 Residual Mises equivalent stress contours for a section of the mesh along the rolling direction for with ELKP properties (values are in N/m² or Pa); Mises Eq. St.: 4 = 4.0E+06, 5 = 1.2E+07, 6 = 2.0E+07, 7 = 2.8E+07, 8 = 3.6E+07

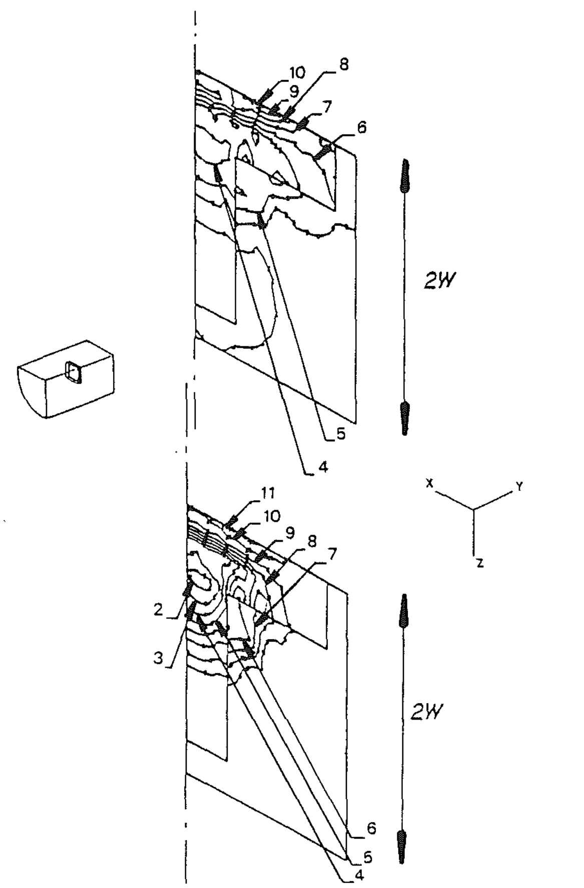

Fig. 10 Residual (*a*) axial and (*b*) circumferential stress contours for a section of the mesh perpendicular to the rolling direction for ELKP properties (values are in N/m² or Pa); (*a*) σ_{xx}^r: 4 = −1.9E+07, 5 = −1.2E+07, 6 = −5.0E+06, 7 = −2.0E+06, 8 = +9.0E+06, 9 = +1.6E+07, 10 = +2.3E+07, and (*b*) σ_{yy}^r: 2 = −4.4E+07, 3 = −3.8E+07, 4 = −3.2E+07, 5 = −2.6E+07, 6 = −2.0E+07, 7 = −1.4E+07, 8 = −8.0E+06, 9 = −2.0E+06, 10 = +4.0E+06, 11 = +1.0E+07

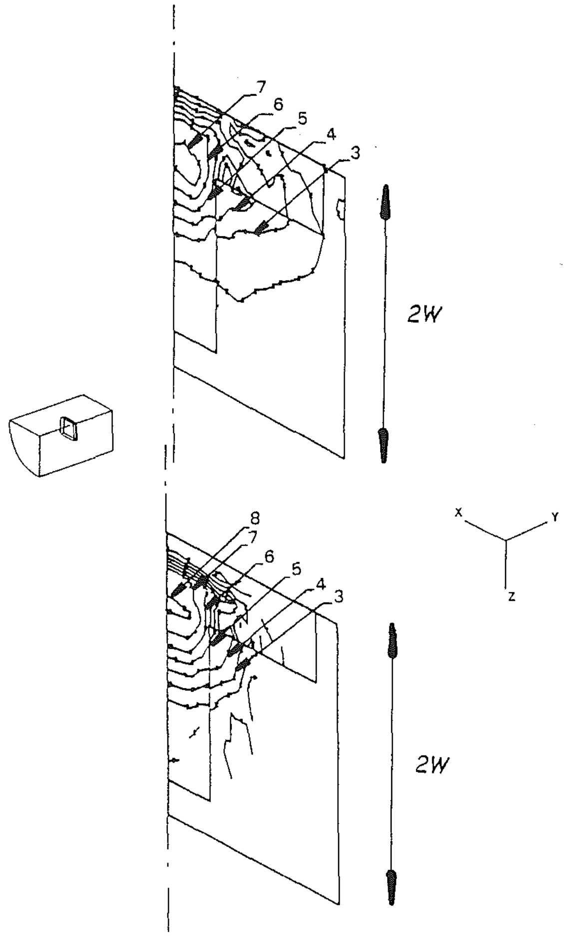

Fig. 11 Residual (*a*) Mises equivalent stress (N/m² or Pa) and (*b*) equivalent plastic strain contours for a section of the mesh perpendicular to the rolling direction for ELKP properties; (*a*) Mises Eq. St.: 3 = 1.2E+07, 4 = 1.8E+07, 5 = 2.4E+07, 6 = 3.0E+07, 7 = 3.6E+07, and (*b*) Eq. Plastic Strain: 3 = 1.2E−04, 4 = 1.8E−04, 5 = 2.4E−04, 6 = 3.0E−04, 7 = 3.6E−04, 8 = 4.2E−04

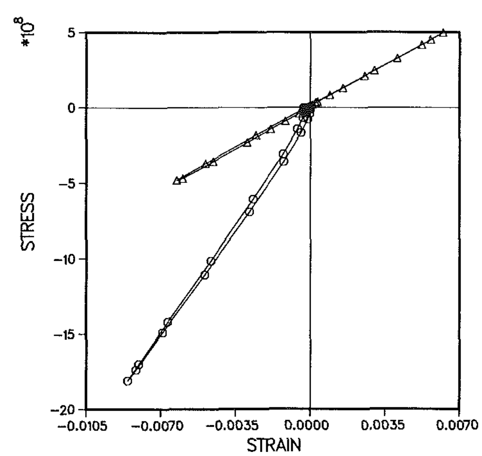

Fig. 12 The radial, *zz*, and shear, *yz*, stress-strain curve for the first contact, at a depth of 0.528*w*, for ELKP properties; Legend: ○ σ_{zz} versus ϵ_{zz}, △ τ_{yz} versus γ_{yz}

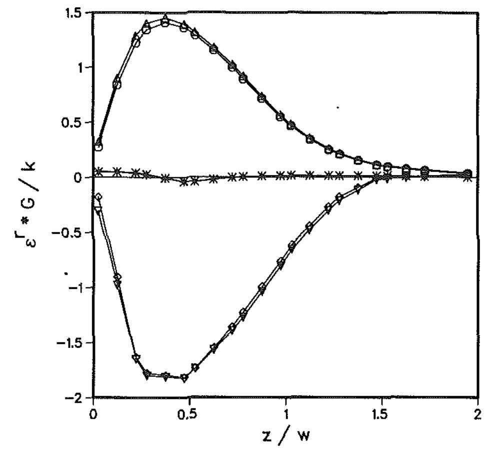

Fig. 13 Comparison of the normalized residual axial, $\epsilon_{xx}{}^{r*}G/k$, circumferential, $\epsilon_{yy}{}^{r*}G/k$, and radial, $\epsilon_{zz}{}^{r*}G/k$, strain as a function of the normalized depth, *z/w*, for one and two successive contacts, PS1 and PS2, for EPP properties; Legend: ○ $\epsilon_{xx}{}^{r*}G/k$ − PS1, △ $\epsilon_{xx}{}^{r*}G/k$ − PS2, + $\epsilon_{yy}{}^{r*}G/k$ − PS1, × $\epsilon_{yy}{}^{r*}G/k$ − PS2, ◇ $\epsilon_{zz}{}^{r*}G/k$ − PS1, ▽ $\epsilon_{zz}{}^{r*}G/k$ − PS2

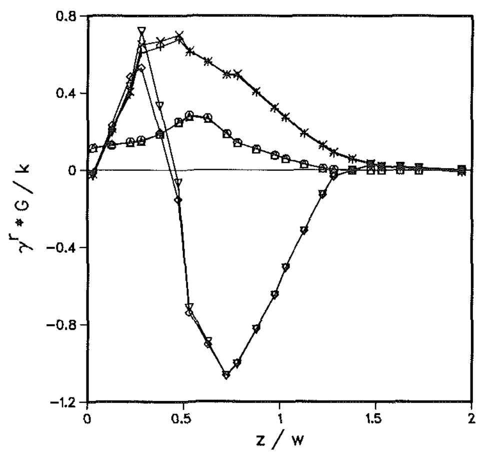

Fig. 14 Comparison of the normalized residual shear strain, γ^r/k, as a function of the normalized depth, *z/w*, for one and two successive contacts, PS1 and PS2, for EPP properties; Legend: ○ $\gamma_{xy}{}^{r*}G/k$ − PS1, △ $\gamma_{xy}{}^{r*}G/k$ − PS2, + $\gamma_{xz}{}^{r*}G/k$ − PS1, × $\gamma_{xz}{}^{r*}G/k$ − PS2, ◇ $\gamma_{yz}{}^{r*}G/k$ − PS1, ▽ $\gamma_{yz}{}^{r*}G/k$ − PS2

values at a depth of about $0.6w$ and become almost zero beyond $1.6w$. It is interesting to note that these stresses are tensile near the surface. Figure 6 shows the residual axial, circumferential, and the radial strain distributions for the ELKP material. These strains also reach a peak value at a depth of about $0.6w$ and become almost zero beyond $1.6w$. Figure 7, on the other hand, presents the residual shear strain distributions for the ELKP material. Here, $\gamma_{xy}{}^r$ is insignificant compared with the other two components; $\gamma_{xz}{}^r$ achieves a peak at $0.6w$ while $\gamma_{yz}{}^r$ does at $0.8w$. Once again they taper off beyond $1.6w$. The presence of large residual axial strains, $\epsilon_{xx}{}^r$ (Fig. 6) and the relatively large residual out-of-plane shear strain (even at a distance of $0.125w$ from the YZ plane), $\gamma_{xz}{}^r$ (Fig. 7), is evidence of ploughing. From Figs. 5, 6, and 7 we observe that for all stresses and strains, the distributions for the second contact virtually overlap those for the first contact. Residual distortions for sections (for Figs. 8, 9, 10, 11, and 16 the sections are indicated by miniature line sketches of the three-dimensional mesh) of the mesh, along and perpendicular to the rolling direction, are shown in Fig. 8. For an ELKP material there is little forward flow during the first contact (of the order of 10^{-5} μm) and none during the second. Figure 9 displays the residual Mises equivalent stress contours for a section of the mesh, along the rolling direction, after one pass. The equivalent stress reaches peak values of about 40 MPa at a depth of $0.6w$. Figures 10 and 11 present additional residual stress and strain contours for a section of the mesh perpendicular to the rolling direction. Figure 10 shows contours for the residual axial and circumferential stresses after one contact. The residual tensile component observed beneath the peak pressure (Fig. 5) extends all the way to the edge of the contact. In Fig. 11, which displays

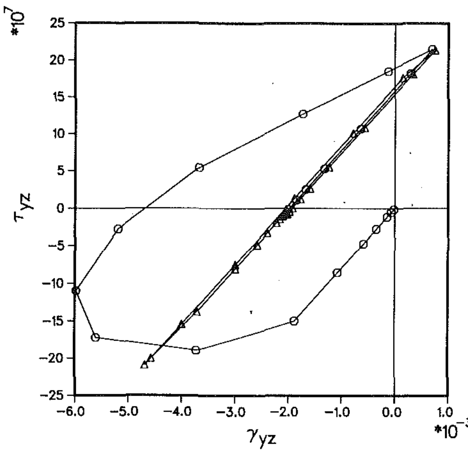

Fig. 15 The shear, yz, stress-strain curve for one and two contacts, at a depth of $0.47w$ for EPP properties; Legend: ○ PASS1, △ PASS2

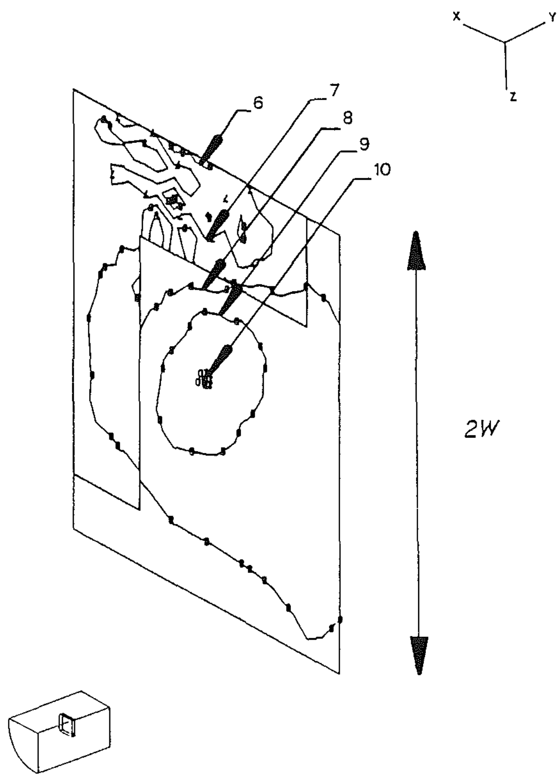

Fig. 16 Residual shear stress $\tau_{xz}{}^{r}$, contours for a section of the mesh perpendicular to the rolling direction for EPP properties. (Values are in N/m² or Pa); $\tau_{xz}{}^{r}$: 6 = −5.0E+07, 7 = −2.0E+07, 8 = +1.0E+07, 9 = +4.0E+07, 10 = +7.0E+07

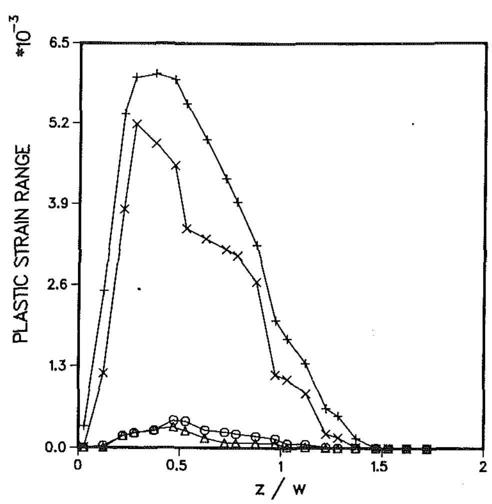

Fig. 17 Comparison of the radial, $\Delta\epsilon_{zz}{}^{p}$, and shear, $\Delta\gamma_{yz}{}^{p}$, cyclic plastic strain range as a function of the normalized depth, z/w, for ELKP and EPP properties; Legend: ○ $\Delta\epsilon_{zz}{}^{p}$ – ELKP, △ $\Delta\gamma_{yz}{}^{p}$ – ELKP, + $\Delta\epsilon_{zz}{}^{p}$ – EPP, × $\Delta\gamma_{yz}{}^{p}$ – EPP

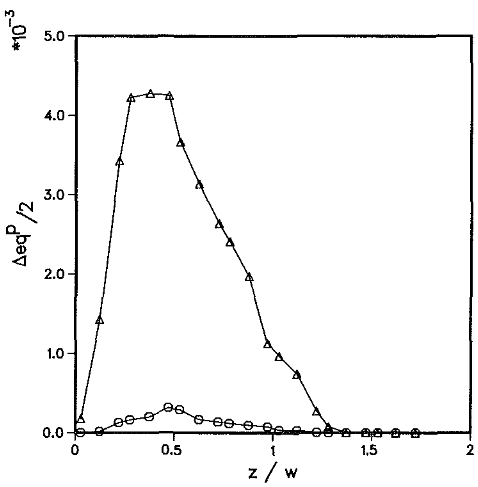

Fig. 18 Comparison of the half equivalent plastic strain range, $\Delta eq^{p}/2$, as a function of the normalized depth, z/w for ELKP and EPP properties; Legend: ○ ELKP, △ EPP

Mises equivalent stress and equivalent plastic strain contours after the first contact for the ELKP material, the plastic region appears to extend in the X and Z directions up to about $1.4w$. Figure 12 presents stress-strain curves for the ELKP study after one cycle at a depth of $0.528w$. The approach to shakedown is hard to observe (the stress-strain loop for the first contact resembles that for a linear elastic material).

Elastic-perfectly plastic calculations were also performed for $p_o/k = 4.68$; Figs. 13 and 14 present the residual strain distributions as a function of depth. Although these results are similar in character to the ELKP case, there is a second-order of magnitude difference in the strains. Also, the forward flow for the EPP case (as is apparent from $\gamma_{yz}{}^{r}$ versus depth in Fig. 14) is larger than for the ELKP material (of the order of 0.01 μm). Figure 15 shows the τ_{yz} versus γ_{yz} plot at a depth of $0.47w$ for two contact cycles. Steady-state appears to have been attained after one cycle for the EPP material. Figure 16 presents contours for the residual shear stress $\tau_{xz}{}^{r}$ after one pass. The peak value, 70 MPa, is at a depth of w and at a distance of w away from the plane of symmetry (the YZ plane).

The results for the EPP and the ELKP behavior are compared in Fig. 17, which describes the radial plastic strain range $\Delta\epsilon_{zz}{}^{p}$, and the shear strain range $\Delta\epsilon_{yz}{}^{p}$ distribution, and in Fig. 18, which exhibits the half equivalent plastic strain increments. The cyclic plastic strain ranges confirm the extension of the active plastic zone to a depth of about $1.4w$. Figures 19 and 20 compare the residual axial and circumferential stress distributions for the ELKP and the EPP material behavior. Figures 6, 7, 13, 14, and 17–20 illustrate that the residual stresses, strains, and cyclic plastic strain ranges for the ELKP case are between one and two orders of magnitude less than those for the EPP calculation, although the depth of the plastic zone remains virtually unchanged. Figures 21 and 22 compare findings for the three-dimensional contact with the earlier results for two-dimensional line contact. Also, the peak residual stresses from the present study are compared with the mathematical predictions of Hills and Sackfield (1984). As observed in Fig. 23, for the EPP material, the peak residual axial stress from this analysis agrees with, but the circumferential stress is 50 percent greater than, that of Hills and Sackfield.

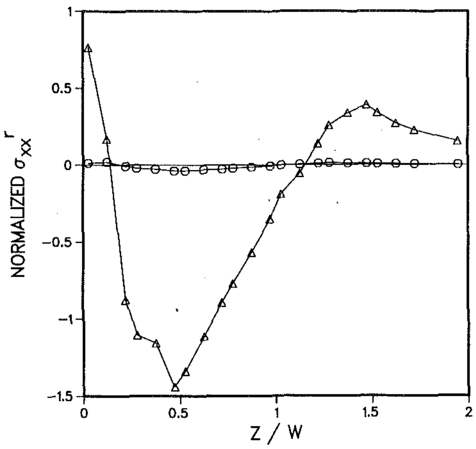

Fig. 19 Comparison of the normalized residual axial, *xx*, stress as a function of normalized depth, *z/w*, after one contact cycle, for ELKP and EPP properties; Legend: ○ ELKP, △ EPP

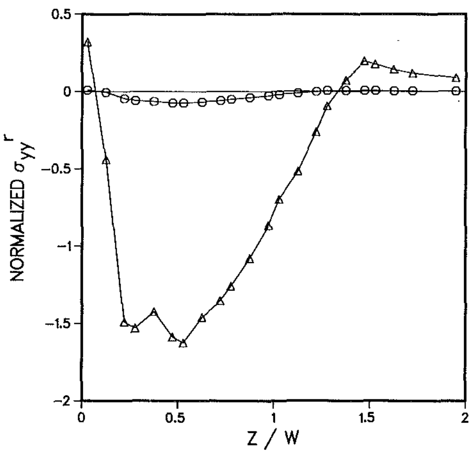

Fig. 20 Comparison of the normalized residual circumferential, *yy*, stress as a function of normalized depth, *z/w*, after one contact cycle, for ELKP and EPP properties; Legend: ○ ELKP, △ EPP

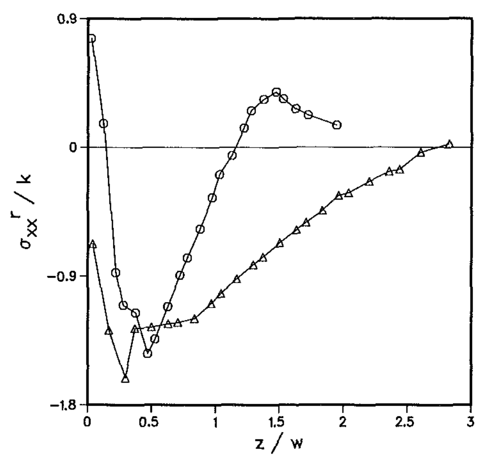

Fig. 21 Comparison of the normalized residual axial stress, $\sigma_{xx}{}^r/k$, as a function of the normalized depth, *z/w*, after one contact cycle for EPP properties for pure rolling 3-D (p_o/k = 4.68) and 2-D plane strain (p_o/k = 5.0) calculations; Legend: ○ 3-D, △ 2-D

Discussion

As reviewed by K. L. Johnson (1986), four regimes of steady-state behavior can be identified for elastic-plastic bodies subjected to repeated rolling contact: (1) purely elastic, (2) elastic shakedown, (3) cyclic plasticity or plastic shakedown, and (4) incremental collapse or ratchetting. Significant contributions

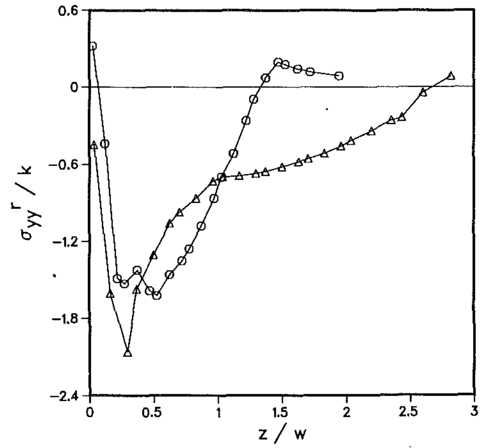

Fig. 22 Comparison of the normalized residual circumferential stress, $\sigma_{yy}{}^r/k$, as a function of the normalized depth, *z/w*, after one contact cycle for EPP properties for pure rolling three-dimensional (p_o/k = 4.68) and two-dimensional plane-strain (p_o/k = 5.0) calculations: Legend: ○ 3-D, △ 2-D

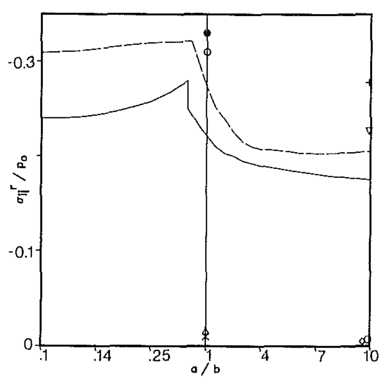

Fig. 23 Peak residual axial and circumferential stress as compared with analytical predictions [18, 19]. (*a/b* = ratio of the axes of the contact ellipse, *a/b* = 1 for the present study) values for *a/b* = 10 are estimated from analyses of line contact for the same material; Legend: $\sigma_{yy}{}^r$ HILLS, $\sigma_{xy}{}^r$ HILLS, ● $\sigma_{yy}{}^r$ EPP—three-dimensional, ○ $\sigma_{xx}{}^r$ EPP—three-dimensional, △ $\sigma_{yy}{}^r$ ELKP—three-dimensional, × $\sigma_{xx}{}^r$ ELKP—three-dimensional, ▽ $\sigma_{yy}{}^r$ EPP—two-dimensional, + $\sigma_{xx}{}^r$ EPP—two-dimensional, ◇ $\sigma_{yy}{}^r$ ELKP—two-dimensional, ○ $\sigma_{xx}{}^r$ ELKP—two-dimensional

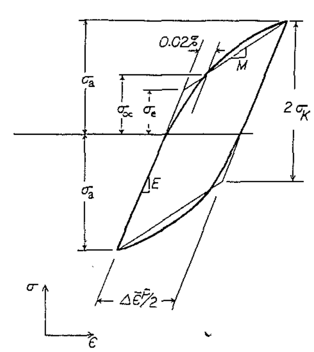

Fig. 24 Schematic representation of the cyclic stress-strain hysteresis loop, showing the bilinear, three parameter: *E*, σ_k and *M*, representation referred to as elastic-linear-kinematic-hardening plastic (ELKP) behavior

to the field of rolling contact have been restricted to two-dimensional plane-strain rolling contact or line contact (a rigid cylinder rolling on the plane surface of an elastoplastic half space). Here, the surface remains flat after rolling and the possible state of residual stress is restricted to four components, namely $\sigma_{xx}{}^r$, $\sigma_{yy}{}^r$, $\sigma_{zz}{}^r$, and $\tau_{yz}{}^r$ (all functions of depth z only). In such a case, the only possible mechanism of ratchetting is shear, parallel to the free surface. Unfortunately, the three-dimensional rolling situation or point contact of a ball rolling on a plane surface is much more complicated. In point contact, all six components of residual stress are possible. (Figs. 5, 10, 16, 19, and 20) and they are functions of the axial distance x and the depth z. When a ball rolls on a plane surface, it creates a groove or a rolling track by ploughing the surface. This ploughing is expected to be promoted by elongation of the contact ellipse in the rolling direction. Contrary to the predictions (Ponter et al., 1985), the large residual axial strains, $\epsilon_{xx}{}^r$ and residual shear strains, $\gamma_{xz}{}^r$ (Figs. 6, 7, 13, and 14), even for a circular contact patch, are evidence of significant ploughing.

Only part of the rolling surface is in direct contact with the translating Hertzian pressure distribution, and, hence, the material at the sides of the rolling track remains permanently undeformed. The only possible mechanism for ratchetting is plastic shear on a single curved surface, whereby a thin segment immediately beneath the rolling track can displace relative to the surrounding material parallel to the rolling direction. For ratchetting to occur in a pure rolling situation, very high contact pressures will have to be applied, a p_o/k of 11.0 for an EPP material (this value was obtained approximately by extrapolating Johnson's (1986) results)). On the other hand, for elastic shakedown, the elastic limit is exceeded during the first cycle, after which steady-state is achieved and for subsequent contacts the deformation is purely elastic. The present study deals with elastic shakedown (p_o/k of 4.68 for a circular contact patch for pure rolling), and for the EPP case this is exactly what is observed (Figs. 13, 14, and 15). On the other hand for the ELKP material response, which is a more realistic model for high strength bearing steels, the plastic strains produced during the first contact cycle are so small that it is difficult to follow the approach to shakedown (Figs. 6, 7, and 12). Also, the residual stresses and strains and the plastic strain ranges for the ELKP case are very small (1-10 percent) compared with those for the EPP material (Figs. 19, 20, 6, 7, 13, 14, 17, and 18). This is because of the high hardening rate—large M value—displayed by hardened steel. Contact pressures above the elastic shakedown limit but below the ratchetting limit, where cyclic plasticity or plastic shakedown would be expected in the steady-state, are dealt with in other papers (Kulkarni et al., 1989a, 1989b).

The ploughing of the surface by three-dimensional rolling contact results in strain gradients in the axial direction. Also, the elastically deformed material, just below the pressure distribution, tries to recover to its original shape when the mesh is unloaded. These two factors result in residual tensile stresses close to the surface extending to the edge of the contact patch (Figs. 5 and 10) and residual shear stresses across the half space (Fig. 16). This could be unfavorable for a mechanical component subjected to repeated rolling contact, at high contact pressures. Such a residual stress state superimposed with the stresses due to a repeated translating contact could promote cyclic crack growth (all modes) eventually resulting in failure. The present three-dimensional model is quite general and has been used to treat the elliptical railwheel contact at pressures above shakedown. Results of these calculations will soon be published (Kulkarni et al. 1989a, 1989b). In addition to treating point contact phenomena, such as a smooth ball in a race, the extension of the present three-dimensional model to rolling plus sliding may provide insights into the contacts of rough surfaces. These would be obtained by applying the model to the microasperity contact.

Earlier results for EPP behavior by Johnson (1986) and Ponter et al. (1985) lead to common solutions for all materials when normalized with respect to p_o/k. The present findings show that the results obtained with the more realistic ELKP cyclic constitutive relations depart radically from those for perfect plasticity. Further, the results are different for materials with different strength levels which display different k_k and M values. Consequently, the present calculations for material parameters appropriate for hardened bearing steels, are not expected to be valid for other materials. In addition, ELKP behavior must also be viewed as an idealization that does not reproduce all the second-order effects, such as the very gradual changes in conformity discussed by Johnson and Kapoor (1987).

Conclusions

(1) Elastic-plastic three-dimensional repeated, pure rolling point contact has been modeled with the finite element method for elastic-perfectly-plastic and elastic-linear-kinematic-hardening-plastic material behavior. The analysis defines the residual stress-strain distributions, stress-strain histories, and the cyclic plastic strain ranges in the vicinity of the contact.

(2) Steady-state was achieved fairly quickly; it was difficult, to follow the approach to steady state for the ELKP case, and steady state was achieved after one cycle for the EPP case, as seen from the stress-strain plots.

(3) As expected for the three-dimensional case and established for the two-dimensional case, the residual stresses, the residual strains and the cyclic plastic strain ranges for the ELKP response are up to two orders of magnitude smaller than those observed in the EPP behavior. The peak residual axial stress after one contact is 25 MPa for the ELKP case, and 340 MPa for the EPP case.

(4) For a p_o/k of 4.68 (shakedown limit), neither the EPP nor the ELKP material exhibited cyclic plasticity after the first contact.

(5) During the first contact, the residual strains perpendicular to the rolling direction (ploughing) far exceed the residual strains in the rolling direction.

(6) At higher loads, the cumulative effect of ploughing, residual tensile stresses on the surface and the complex system of residual stresses across the half space could be detrimental to the fatigue life of a rim.

Acknowledgments

This research was supported by the National Science Foundation under Grant No. DMR-8418097. The authors are grateful to Hibbitt, Karlsson and Sorensen, Inc. for use of their finite element program, ABAQUS, and to the San Diego Supercomputer Center for use of their CRAY X-MP/48.

References

Bhargava, V., Hahn, G. T., and Rubin, C. A., 1985a, "An Elastic-Plastic Finite Element Model of Rolling Contact. Part 1: Analysis of Single Contacts," ASME JOURNAL OF APPLIED MECHANICS, Vol. 52, No. 1, pp. 67-74.

Bhargava, V., Hahn, G. T., and Rubin, C. A., 1985b, "An Elastic-Plastic Finite Element Model of Rolling Contact. Part 2: Analysis of Repeated Contacts," ASME JOURNAL OF APPLIED MECHANICS, Vol. 52, No. 2, pp. 75-82.

Bhargava, V., Hahn, G. T., Ham, G., Kulkarni, S., and Rubin, C. A., 1986, "Influence of Kinematic Hardening on Rolling Contact Deformation," *Proc. 2nd Int. Symp. on Contact Mechanics and Rail/Wheel Systems*, Kingston, R.I.

Bower, A. P., Johnson, K. L., and Kalousek, J., 1986, "A Ratchetting Limit for Plastic Deformation of a Quarter Space under Rolling Contact Loads," *2nd Int. Symposium on Contact Mechanics and Rail/Wheel Systems*, Kingston, R.I.

Chiu, Y. P., and Hartnett, M. J., 1983, "A Numerical Solution for Layered Solid Contact Problems with Application to Bearings," *Journal of Lubrication Technology*, Vol. 195, pp. 585-590.

Hahn, G. T., Bhargava, V., Rubin, C. A., Chen, Q., and Kim, K., 1987, "Analysis of the Rolling Contact Residual Stresses and Cyclic Plastic Deformation of an SAE 52100 Steel Ball Bearing," *Journal of Tribology*, to be published.

Hamilton, G. M., and Goodman, L. E., 1966, "The Stress Field Created by a Circular Sliding Contact," ASME JOURNAL OF APPLIED MECHANICS, Vol. 33, pp. 371-376.

Hardy, C., Baronet, C. N., and Tordion, G. V., 1971, "The Elasto-Plastic Indentation of a Half-Space by a Rigid Sphere," *Int. Journal for Numerical Methods in Engineering*, Vol. 3, pp. 451-462.

Hills, D. A., and Ashelby, D. W., 1982, "The Influence of Residual Stresses on Contact Load Bearing Capacity," *Wear*, Vol. 75, pp. 221–240.

Hills, D. A., and Sackfield, A., 1983a, "Some Useful Results in the Classical Hertz Contact Problem," *Journal of Strain Analysis*, Vol. 18, No. 2, pp. 101–105.

Hills, D. A., and Sackfield, 1983b, "Some Useful Results in the Tangentially Loaded Hertz Contact Problem," *Journal of Strain Analysis*, Vol. 18, No. 2, pp. 101–105.

Hills, D. A., and Sackfield, A., 1984, "Yield and Shakedown States in the Contact of Generally Curved Bodies," *Journal of Strain Analysis*, Vol. 19, No. 1, pp. 9–14.

Hills, D. A., and Sackfield, A., 1986, "The Stress Field Induced by a Twisting Sphere," ASME JOURNAL OF APPLIED MECHANICS, Vol. 53, pp. 372–378.

Johnson, K. L., and Jefferis, J. A., 1963, "Plastic Flow and Residual Stresses in Rolling and Sliding Contact," *Proc. Inst. Mech. Engr.*, London, Vol. 177, pp. 54–65.

Johnson, K. L., 1986, "Plastic Flow, Residual Stresses and Shakedown in Rolling Contact," *2nd Int. Symposium on Contact Mechanics and Rail/Wheel Systems*, Kingston, R.I.

Kalker, J. J., 1979, "The Computation of Three-Dimensional Rolling Contact with Dry Friction," *Int. Journal of Num. Methods in Engineering*, Vol. 14, pp. 1293–1307.

Kapoor, A., and Johnson, K. L., 1987, "Shakedown of Rolling Point Contacts due to Plastic Changes in Conformity," in preparation.

Kulkarni, S., Hahn, G. T., Rubin, C. A., and Bhargava, V., 1989a, "Elastoplastic Finite Element Analysis of Three-Dimensional Pure Rolling Contact above the Shakedown Limit," under preparation; to be submitted to the ASME JOURNAL OF APPLIED MECHANICS.

Kulkarni, S., Hahn, G. T., Rubin, C. A., and Bhargava, V., 1989b, "Elastoplastic Finite Element Analysis of Three-Dimensional Pure Rolling Contact for an Elongated Contact Patch with Rail Steel Properties at a High Relative Peak Pressure," under preparation; to be submitted to the ASME JOURNAL OF APPLIED MECHANICS.

Martin, G. C., and Hay, W. W., 1972, "The Influence of Wheel-Rail Contact Forces on the Formation of Rail Shells," Paper 72-WA/RT-8, ASME, New York.

Merwin, J. E., and Johnson, K. L., 1963, "An Analysis of Plastic Deformation in Rolling Contact," *Proc. Inst. Mech. Engr.*, London, Vol. 177, pp. 676–690.

Ponter, A. R. S., Hearle, A. D., and Johnson, K. L., 1985, "Application of the Kinematical Shakedown Theorem to Rolling and Sliding Point Contacts," *J. Mech. and Phys. of Solids*.

Rydholm, G., and Fredriksson, B., 1981, "Shakedown Analysis of Three-Dimensional Rolling Contact Problems," Linkoping Studies in Science and Technology, Dissertations, No. 61.

Dean G. Duffy
Laboratory for Atmospheres,
NASA/Goddard Space Flight Center,
Greenbelt, MD 20771

The Response of an Infinite Railroad Track to a Moving, Vibrating Mass

We examine vibrations that arise when a moving, vibrating load passes over an infinite railroad track lying on a Winkler foundation. Solutions are presented for both moving and stationary vibrating loads as a function of both the mass and driving frequency of the load as well as the physical properties of the track. For a stationary vibrating load, resonance occurs at lower driving frequencies as the mass of the load increases. For a moving vibrating load, resonance occurs at lower driving frequencies when the velocity and/or mass of the load increases.

Introduction

Railroad tracks vibrate when they are subjected to a moving, vibrating load. Because these vibrations could damage supporting structures, structural engineers have sought to understand them since the mid-nineteenth century.

In one of the earliest and most successful models by Timoshenko (1926), the track is considered to be an elastic beam on a massless Winkler foundation. Using this model, he found the deflection of the track due to a load and examined the system for resonance. For a stationary, vibrating load, resonance occurs at the frequency $(k_W/m)^{1/2}$ where k_W is the Winkler constant and m is the mass of the track per unit length; for a moving, steady load, resonance occurs when the load's speed equals $(4k_W B/m^2)^{1/4}$ where B is the bending stiffness (rigidity) of the beam.

Recently, Patil (1988) extended Timoshenko's analysis by examining the effects of the mass of a stationary, vibrating load on the resonant frequency. He solved the problem by finding the displacement of an initially quiescent beam when it is subjected to an impulsive, vibrating load. Resonant solutions were again found. Resonance will occur at lower and lower driving frequencies as the mass of the vibrating load is increased.

Although Patil's solution is interesting, it is limited because the load is stationary. Furthermore, his solutions only apply to the limit of $t \to \infty$. In this paper we find the response of an infinite railroad at any arbitrary time when a heavy load both moves and vibrates. We may also view our study as a generalization of the work of Mathews (1958) and Chonan (1978) who found the forced solutions generated by a massless, vibrating, impulsive load as it moves along a rail.

Contributed by the Applied Mechanics Division of THE AMERICAN SOCIETY OF MECHANICAL ENGINEERS for publication in the JOURNAL OF APPLIED MECHANICS.

Discussion on this paper should be addressed to the Technical Editor, Prof. Leon M. Keer, The Technological Institute, Northwestern University, Evanston, IL 60201, and will be accepted until two months after final publication of the paper itself in the JOURNAL OF APPLIED MECHANICS. Manuscript received by the ASME Applied Mechanics Division, September 30, 1988; final revision, March 28, 1989.

In Section 2, we introduce the governing equations, boundary conditions and initial conditions. In Section 3, we give the solution for a vibrating, stationary load. Patil's solution is extended and the solutions are illustrated for various parameters. In Section 4, we present the solution for the moving, vibrating load. Finally, we state the conclusions in Section 5.

Governing Equations

For a uniform track, the dimensional vertical displacement w' of the track at the point x' and time t', subjected to the load $p'(x',t')$ is given (Volterra and Zachmanoglou, 1965, p. 374) by

$$B\frac{\partial^4 w'}{\partial x'^4} + m\frac{\partial^2 w'}{\partial t'^2} + k_w w' = p'(x',t'). \qquad (1)$$

The units of B, m, and k_W are Nm^2, kg/m, and N/m^2, respectively. In this paper we assume that the load consists of a wheel of mass M that is in continuous contact with the track and vibrates with the angular frequency ω_0. Consequently, if the wheel moves at the dimensional speed V, the dimensional load is

$$p'(x',t') = \left[P\cos(\omega_0 t') - M\frac{d^2 w'}{dt'^2}\right]\delta(x'-Vt') \qquad (2)$$

where $\delta(\ )$ denotes the delta function and P is the amplitude of the vibration. In (2), the load is initially located at $x'=0$. If we now substitute (2) into (1), and replace the substantial derivative associated with the moving frame with its counterpart in the stationary reference frame, we obtain

$$B\frac{\partial^4 w'}{\partial x'^4} + m\frac{\partial^2 w'}{\partial t'^2} + k_W w' = \Big[P\cos(\omega_0 t')$$
$$-M\left(\frac{\partial^2 w'}{\partial t'^2} + 2V\frac{\partial^2 w'}{\partial x'\partial t'} + V^2\frac{\partial^2 w'}{\partial x'^2}\right)\Big]\delta(x'-Vt'). \qquad (3)$$

Equation (3) may be made dimensionless via the definitions:

$$w' = \frac{P}{m\omega_0^2} w, \; t' = t/\omega_0, \; x' = \left(\frac{4B}{m\omega_0^2}\right)^{1/4} x,$$

$$\alpha^2 = \frac{k_W}{m\omega_0^2}, \; \Delta = \frac{M}{m}, \; U = \frac{V}{\omega_0}\left(\frac{m\omega_0^2}{4B}\right)^{1/4},$$

so that

$$\frac{1}{4}\frac{\partial^4 w}{\partial x^4} + \frac{\partial^2 w}{\partial t^2} + \alpha^2 w = \left[\cos(t) - \Delta\left(\frac{\partial^2 w}{\partial t^2} + 2U\frac{\partial^2 w}{\partial x \partial t} + U^2 \frac{\partial^2 w}{\partial x^2}\right)\right]\delta(x - Ut). \tag{4}$$

The value of α gives the ratio of the natural frequency of the track to the forcing frequency.

Although (4) could be used in our analysis, it is more convenient to define a coordinate system moving with speed U. If we define $z = x - Ut$, then (4) may be written as

$$\frac{1}{4}\frac{\partial^4 w}{\partial z^4} + \frac{\partial^2 w}{\partial t^2} - 2U\frac{\partial^2 w}{\partial z \partial t} + U^2\frac{\partial^2 w}{\partial z^2} + \alpha^2 w = \left[\cos(t) - \Delta\frac{\partial^2 w}{\partial t^2}\right]\delta(z). \tag{5}$$

Turning to the boundary conditions, we require that the solution must vanish as $z \to \pm\infty$. Because the beam is initially at rest, the initial conditions are $w(z,0) = w_t(z,0) = 0$.

We solve (5) using Fourier and Laplace transforms. If we assume that $w(z,t)$ possesses a Fourier transform $W(k,s)$ defined by

$$w(z,t) = \frac{1}{2\pi}\int_{-\infty}^{\infty} W(k,t) e^{ikz} dk, \tag{6}$$

and that $W(k,t)$ possesses a Laplace transform $\bar{W}(k,s)$ defined by

$$\bar{W}(k,s) = \int_0^{\infty} W(k,t) e^{-st} dt, \tag{7}$$

then (5) may be transformed into

$$\left(\frac{1}{4}k^4 - U^2k^2 - 2iUks + s^2 + \alpha^2\right)\bar{W} = \left[\frac{s}{s^2+1} - \Delta s^2 \bar{w}(0,s)\right] \tag{8}$$

in which $\bar{w}(0,s)$ is the Laplace transform of $w(0,t)$. Next, we consider different cases depending upon the value of U.

Stationary Load

The case of a stationary load ($U=0$) was studied by Patil (1988). To find the inverse $w(x,t)$ of (8), we first invert the Fourier transform so that

$$\bar{w}(x,s) = \frac{1}{2\pi}\int_{-\infty}^{\infty} \frac{\dfrac{s}{s^2+1} - \Delta s^2 \bar{w}(0,s)}{\dfrac{1}{4}k^4 + s^2 + \alpha^2} e^{ikx} dk. \tag{9}$$

To evaluate (9), we close the line integral with an infinite semicircle either in the upper half or lower half of the k-plane. According to Jordan's lemma (Hildebrand, 1962, p. 556), the contour must be in the upper half-plane for $x>0$ and in the lower half-plane for $x<0$. Once we close the contour, (9) may be evaluated by Cauchy's residue theorem. Equation (9) has four simple poles located at

$$\begin{aligned} k_1 &= (1+i)(s^2+\alpha^2)^{1/4}, \; k_2 = (-1+i)(s^2+\alpha^2)^{1/4} \\ k_3 &= (1-i)(s^2+\alpha^2)^{1/4}, \; k_4 = (-1-i)(s^2+\alpha^2)^{1/4}. \end{aligned} \tag{10}$$

For positive, real s and the proper choice of the branch $(s^2+\alpha^2)^{1/4}$, k_1 and k_2 lie in the upper half-plane and k_3 and k_4 lie in the lower half-plane. Consequently, after application of the residue theorem, we find that

$$\bar{w}(x,s) = \frac{\dfrac{s}{s^2+1} - \Delta s^2 \bar{w}(0,s)}{2(s^2+\alpha^2)^{3/4}} \exp[-(s^2+\alpha^2)^{1/4}|x|] \times \{\sin[(s^2+\alpha^2)^{1/4}|x|] + \cos[(s^2+\alpha^2)^{1/4}|x|]\}. \tag{11}$$

If we evaluate (11) at $x=0$, we can solve for $\bar{w}(0,s)$ and then eliminate it from (11), so that

$$\bar{w}(x,s) = \frac{s\exp\{-(s^2+\alpha^2)^{1/4}|x|\}}{(s^2+1)[2(s^2+\alpha^2)^{3/4} + \Delta s^2]} \times \{\sin[(s^2+\alpha^2)^{1/4}|x|] + \cos[(s^2+\alpha^2)^{1/4}|x|]\}. \tag{12}$$

If we invert the Laplace transform (12) with the Bromwich's integral (Hildebrand, 1962, p. 602), then we must consider the branch of the multivalued function $(s^2+\alpha^2)^{1/4}$. We derived (12) by assuming that the poles k_1 and k_2 lie in the upper half of the k-plane. This implies that $0<$ arguments of k_1 and $k_2 < \pi$ or, equivalently, $-\pi/4<$ the argument of $(s^2+\alpha^2)^{1/4} < 3\pi/4$ in k_1 and $-3\pi/4<$ the argument of $(s^2+\alpha^2)^{1/4} < \pi/4$ in k_2. Because (12) was obtained by combining terms that depend on both k_1 and k_2, $-\pi/4<$ the argument of $(s^2+\alpha^2)^{1/4} < \pi/4$.

Turning our attention to the inversion of (12), we write the inverse as the contour integral

$$w(x,t) = \frac{1}{2\pi i}\int_{c-i\infty}^{c+i\infty} \frac{s\exp\{st - (s^2+\alpha^2)^{1/4}|x|\}}{(s^2+1)[2(s^2+\alpha^2)^{3/4} + \Delta s^2]} \times \{\sin[(s^2+\alpha)^{1/4}|x|] + \cos[(s^2+\alpha^2)^{1/4}|x|]\} ds \tag{13}$$

in which c is chosen so that the contour passes to the right of any singularities. There are a number of singularities in (13). There are poles at $s = \pm i$, branch points at $s = \pm i\alpha$ and poles at $2(s^2+\alpha^2)^{3/4} + \Delta s^2 = 0$; these poles are found by solving numerically

$$\Delta^4 s^8 - 16s^6 - 48\alpha^2 s^4 - 48\alpha^4 s^2 - 16\alpha^6 = 0. \tag{14}$$

Solutions to (14) consist of four conjugate pairs; only one pair $s = \pm i s_0$ lies on the proper Riemann sheet. The value of s_0 was computed numerically from (14) for various α's and Δ's. It was always found that $0 < s_0 < \alpha$. For a fixed Δ, s_0 increased monotonically with increasing α; for a fixed α, s_0 decreased montonically with increasing Δ. As Δ became very large, s_0 decreased very slowly for moderate values of α.

In addition to determining the location of the singularities, we must lay out our branch cuts. They are taken to run to the left of the branch point, parallel to the real axis, and out to infinity (see Figs. 1, 3, 5) with $-\pi<$ phases of $s \pm i\alpha < \pi$.

At this point, we consider the three cases of $\alpha > 1$, $\alpha = 1$, and $\alpha < 1$.

(a) $\alpha > 1$. When $\alpha > 1$, the contour from $c - \infty i$ to $c + \infty i$ may be closed as shown in Fig. 1. Our choice of contours was dictated by the requirement that $-\pi/4<$ the argument of $(s^2+\alpha^2)^{1/4} < \pi/4$.

From the integration, we obtain contributions both along C_1 and C_4 and along one side of each of the branch cuts C_2 and C_3. Integrations along the arcs AB, CD, and EF vanish because of Jordan's lemma. To evaluate the integral along the line contour C_1, we let $s = -i\rho$, $s - i\alpha = (\rho+\alpha)e^{-i\pi/2}$, $s + i\alpha = (\rho - \alpha)e^{-i\pi/2}$ for $\alpha < \rho < \infty$ and to evaluate along the line contour C_4, we let $s = i\rho$, $s - i\alpha = (\rho - \alpha)e^{i\pi/2}$, $s + i\alpha = (\rho+\alpha)e^{i\pi/2}$ for $\alpha < \rho < \infty$. Direct substitution into (13) and simplification yields

$$I_1(a,b) = \frac{1}{2\pi}\int_a^b$$

$$\times \frac{\rho[\Delta\rho^2 + \sqrt{2}(\rho^2-\alpha^2)^{3/4}]}{(1-\rho^2)\{[\Delta\rho^2+\sqrt{2}(\rho^2-\alpha^2)^{3/4}]^2 + 2(\rho^2-\alpha^2)^{3/2}\}}\,d\rho$$

$$\times\{\exp[-\sqrt{2}(\rho^2-\alpha^2)^{1/4}\,|x|][\sin(\rho t)-\cos(\rho t)]$$

$$+\cos[\rho t-\sqrt{2}(\rho^2-\alpha^2)^{1/4}\,|x|]+\sin[\rho t-\sqrt{2}(\rho^2-\alpha^2)^{1/4}\,|x|]\}$$

$$+\frac{1}{2\pi}\int_a^b \frac{\sqrt{2}\rho(\rho^2-\alpha^2)^{3/4}}{(1-\rho^2)\{[\Delta\rho^2+\sqrt{2}(\rho^2-\alpha^2)^{3/4}]^2+2(\rho^2-\alpha^2)^{3/2}\}}\,d\rho$$

$$\times\{\exp[-\sqrt{2}(\rho^2-\alpha^2)^{1/4}\,|x|][\sin(\rho t)+\cos(\rho t)]$$

$$+\cos[\rho t-\sqrt{2}(\rho^2-\alpha^2)^{1/4}\,|x|]-\sin[\rho t-\sqrt{2}(\rho^2-\alpha^2)^{1/4}\,|x|]\} \quad (15)$$

in which $a=\alpha$ and $b=\infty$.

The integrals along the branch cuts are somewhat more difficult to evaluate. For example, along C_2, we find that $s=-\rho-i\alpha$, $s+i\alpha=\rho e^{i\pi}$ and $s-i\alpha=(\rho^2+4\ \alpha^2)^{1/2}e^{-i\theta}$, $0<\rho<\infty$. The angle θ measures the direction from the branch point $s=i\alpha$ to any arbitrary point s along the contour C_3 (in the negative sense). When these definitions are substituted into (13), we obtain terms containing $e^{i\theta/4}$ and $e^{-3i\theta/4}$. To eliminate these terms we note that $\cos(\theta)=-\rho/(\rho^2+4\alpha^2)^{1/2}$ so that multiple-angle trigonometric identities may be used. After some algebra we obtain

$$I_2=-\frac{1}{2\pi}\int_0^\infty \frac{A}{D}e^{-\rho t}\{e^{-Q|x|}[\cos(\alpha t+P|x|)-\sin(\alpha t+P|x|)]$$

$$-e^{-P|x|}[\cos(\alpha t-Q|x|)+\sin(\alpha t-Q|x|)]\}$$

$$+\frac{B}{D}e^{-\rho t}\{e^{-Q|x|}[\cos(\alpha t+P|x|)+\sin(\alpha t+P|x|)]$$

$$+e^{-P|x|}[\cos(\alpha t-Q|x|)-\sin(\alpha t-Q|x|)]\}d\rho \quad (16)$$

in which

$$A=\rho(1+\alpha^2+\rho^2)[2S-\Delta(\rho^2-\alpha^2)] -\alpha(1-\alpha^2-\rho^2)(2\Delta\alpha\rho+2R)$$

$$B=\rho(1+\alpha^2+\rho^2)[2\Delta\alpha\rho+2R] +\alpha(1-\alpha^2-\rho^2)[2S-\Delta(\rho^2-\alpha^2)]$$

$$D=[(1+\rho^2-\alpha^2)^2+4\alpha^2\rho^2]\{[\Delta(\rho^2-\alpha^2)-2S]^2 +[2\Delta\alpha\rho+2R]^2\}$$

$$P=[\rho(\rho^2+4\alpha^2)^{1/2}]^{1/4}\left\{1+\left[\frac{1}{2}-\frac{\rho}{2(\rho^2+4\alpha^2)^{1/2}}\right]^{1/2}\right\}^{1/2}$$

$$Q=[\rho(\rho^2+4\alpha^2)^{1/2}]^{1/4}\left\{1-\left[\frac{1}{2}-\frac{\rho}{2(\rho^2+4\alpha^2)^{1/2}}\right]^{1/2}\right\}^{1/2}$$

$$R=\frac{1}{2}(P-Q)\left[\frac{1}{2}\rho(\rho^2+4\alpha^2)^{1/2}+\frac{1}{2}\rho^2\right]^{1/2} +\frac{1}{2}(P+Q)\left[\frac{1}{2}\rho(\rho^2+4\alpha^2)^{1/2}-\frac{1}{2}\rho^2\right]^{1/2}$$

$$S=\frac{1}{2}(P-Q)\left[\frac{1}{2}\rho(\rho^2+4\alpha^2)^{1/2}-\frac{1}{2}\rho^2\right]^{1/2} -\frac{1}{2}(P+Q)\left[\frac{1}{2}\rho(\rho^2+4\alpha^2)^{1/2}+\frac{1}{2}\rho^2\right]^{1/2}.$$

There is no contribution from the integration around the branch points at $s=\pm i\alpha$.

In addition to the integrals, there are four simple poles given by $s=\pm i$ and $s=\pm is_0$. However, when $\Delta=2(\alpha^2-1)^{3/4}$, the pole at $s=\pm i$ becomes second order. Thus, we have, in general, that

$$w(x,t)=\frac{\cos(t)\exp[-(\alpha^2-1)^{1/4}\,|x|]\{\sin[(\alpha^2-1)^{1/4}\,|x|]+\cos[(\alpha^2-1)^{1/4}\,|x|]\}}{2(\alpha^2-1)^{3/4}-\Delta}$$

$$+\frac{2\cos(s_0t)\exp[-(\alpha^2-s_0^2)^{1/4}\,|x|]\{\sin[(\alpha^2-s_0^2)^{1/4}\,|x|]+\cos[(\alpha^2-s_0^2)^{1/4}\,|x|]\}}{(1-s_0^2)[3(\alpha^2-s_0^2)^{-1/4}+2\Delta]}$$

$$+I_1(\alpha,\infty)+I_2, \quad (17)$$

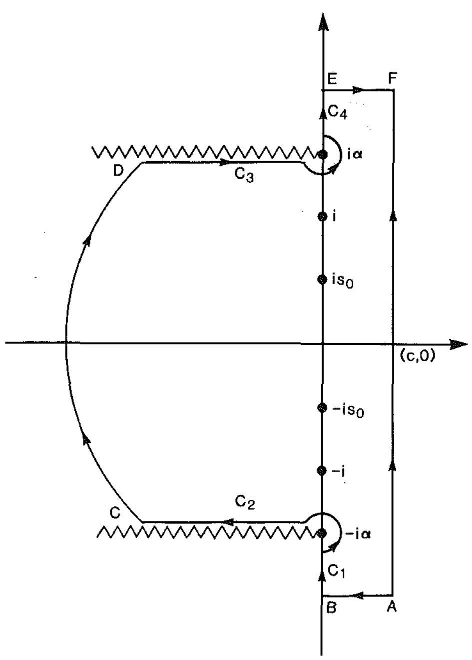

Fig. 1 Contours employed in the inversion of the Laplace transform (11) for $\alpha>1$. A wavy line denotes branch cuts.

and for $\Delta=2(\alpha^2-1)^{3/4}$ we have the resonant solution

$$w(x,t)=\frac{(\alpha^2-1)^{1/4}}{4\left(\alpha^2-\frac{1}{4}\right)}\,t\sin(t)\exp[-(\alpha^2-1)^{1/4}\,|x|]$$

$$\times\{\sin[(\alpha^2-1)^{1/4}\,|x|]+\cos[(\alpha^2-1)^{1/4}\,|x|]\}$$

$$-\frac{|x|\cos(t)\exp[-(\alpha^2-1)^{1/4}\,|x|]}{4\left(\alpha^2-\frac{1}{4}\right)(\alpha^2-1)^{1/2}}\sin[(\alpha^2-1)^{1/4}\,|x|]$$

$$+\frac{3\cos(t)\exp[-(\alpha^2-1)^{1/4}\,|x|]}{64\left(\alpha^2-\frac{1}{4}\right)^2(\alpha^2-1)^{3/4}}$$

$$\times\{\sin[(\alpha^2-1)^{1/4}\,|x|]+\cos[(\alpha^2-1)^{1/4}\,|x|]\}+I_1(\alpha,\infty)+I_2. \quad (18)$$

The most important difference between (17) and (18) is the linear growth with time of the second solution. Physically, this solution corresponds to a case in which the driving force resonates with the beam. From the behavior of s_0 with α and

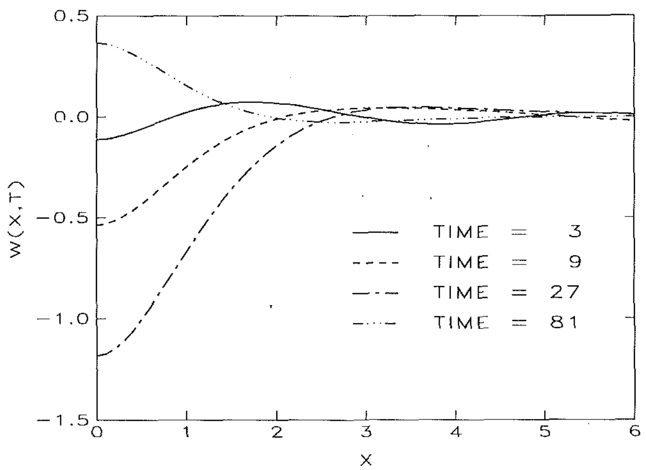

Fig. 2 Deflection of a beam with time as a function of distance from the stationary, vibrating load. Parameters are $\alpha^2 = 2$ and $\Delta = 1$.

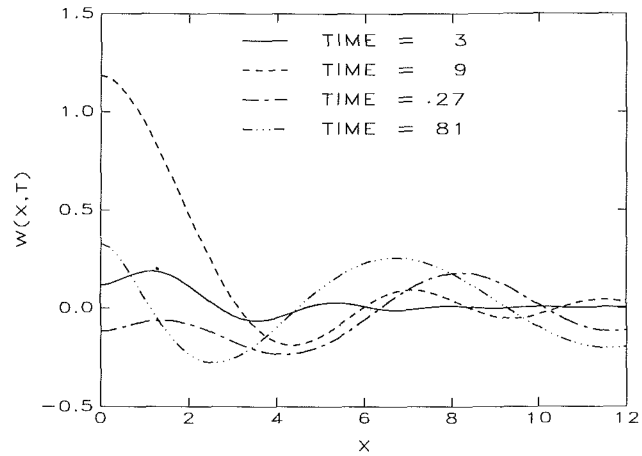

Fig. 4 Same as Fig. 2, except for $\alpha = 1$

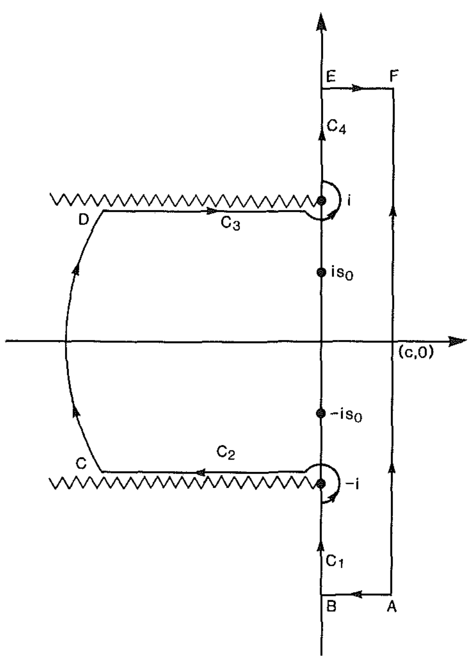

Fig. 3 Same as Fig. 1, except for the $\alpha = 1$ case

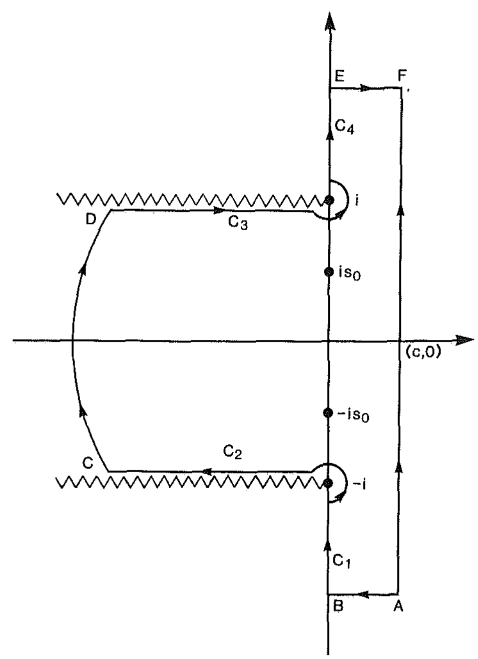

Fig. 5 Same as Fig. 1, except for $\alpha < 1$ case

Δ, we find that as we increase the mass of the load, the resonant driving frequency lowers.

In Fig. 2 we illustrate the solution to (17) when $\alpha^2 = 2$ and $\Delta = 1$ for various times t. The integrals were computed using Simpson's rule. The mesh size was chosen so that $|w(x,0)| \leq 10^{-3}$. We increased the accuracy of the numerical integration of I_2 by introducing a new independent variable $\eta = \ln(\rho)$. Note the skin effect in the wave solution due to the presence of the bending term.

Similar calculations were performed for the resonant case. The spatial dependence is similar to that for the nonresonant case. Eventually the solution grows linearly with time.

(b) $\alpha = 1$. When $\alpha = 1$, the contour from $c - \infty i$ to $c + \infty i$ is closed as shown in Fig. 3. Once again we have contributions from integrals along the contours C_1 to C_4. However, the only singularities within the contour are located at $s = \pm is_0$. Because the singularities at $s = \pm i$ and the branch points coincide, there is a contribution from the integration around the branch points. It is computed by introducing the infinitessimal circle around the branch points $s \pm i = \epsilon e^{i\theta}$ and by preforming the line integrals in the limit as $\epsilon \to 0$. Consequently, the solution for $\alpha = 1$ is

$$w(x,t) = \frac{2\cos(s_0 t)\exp[-(1-s_0^2)^{1/4}|x|]}{(1-s_0^2)[3(1-s_0^2)^{-1/4} + 2\Delta]}$$

$$\times \{\sin[(1-s_0^2)^{1/4}|x|] + \cos[(1-s_0^2)^{1/4}|x|]\}$$

$$-\frac{3\cos(t)}{4\Delta} + I_1(1^+,\infty) + I_2 \tag{19}$$

in which 1^+ denotes a number that is slightly greater than one because I_1 is singular at $a = 1$.

In Fig. 4 we illustrate (19) for the case in which $\Delta = 1$ for various times. We note that the solution propagates away from the origin and eventually covers the entire domain with only a slight decrease in amplitude away from the origin. This is in stark contrast to the case of $\alpha > 1$.

(c) $\alpha < 1$. When $\alpha < 1$, the contour from $c - \infty i$ to $c + \infty i$ is closed as shown in Fig. 5. For this case, the singularities at $s = \pm i$ lie along the contours C_1 and C_4 and are circumvented as shown. Thus, we obtain a contribution equal to one half of the conventional residue at $s = \pm i$. Our integration around the branch points at $s = \pm i\alpha$ vanishes. Consequently, when the arguments of both $s \pm i\alpha$ are carefully considered, we find that

$$w(x,t)=\frac{2\cos(s_0t)\exp[-(\alpha^2-s_0^2)^{1/4}|x|]\{\sin[(\alpha^2-s_0^2)^{1/4}|x|]+\cos[(\alpha^2-s_0^2)^{1/4}|x|]}{(1-s_0^2)[3(\alpha^2-s_0^2)^{-1/4}+2\Delta]}$$

$$+\frac{\Delta+2\sqrt{2}(1-\alpha^2)^{3/4}}{4[\Delta^2+4(1-\alpha^2)^{3/2}+2\sqrt{2}\Delta(1-\alpha^2)^{3/4}]}$$

$$\times\{\sin[t-\sqrt{2}(1-\alpha^2)^{1/4}|x|]-\cos(t)\exp[-\sqrt{2}(1-\alpha^2)^{1/4}|x|]\}$$

$$-\frac{\Delta}{4[\Delta^2+4(1-\alpha^2)^{3/2}+2\sqrt{2}\Delta(1-\alpha^2)^{3/4}]}$$

$$+\{\cos[t-\sqrt{2}(1-\alpha^2)^{1/4}|x|]+\sin(t)\exp[-\sqrt{2}(1-\alpha^2)^{1/4}|x|]\}$$

$$+I_1(\alpha,1^-)+I_1(1^+,\infty)+I_2 \tag{20}$$

in which 1^+ and 1^- are numbers that are slightly greater than or less than one. It is necessary to break I_2 into two parts because of the singularity at one.

In Fig. 6 we illustrate (20) for $\alpha^2=0.5$ and $\Delta=1$ for various times. As in the $\alpha=1$ case, we observe a wave propagating away from the origin; eventually, wave motion envelopes the entire domain.

The Moving, Vibrating Load

For a load that both moves and vibrates, we invert the Fourier-Laplace transform given by (8); this results in

$$\bar{w}(z,s)=\frac{1}{2\pi}\int_{-\infty}^{\infty}\frac{\dfrac{s}{s^2+1}-\Delta s^2\bar{w}(0,s)}{\dfrac{1}{4}k^4-U^2k^2-2iUks+s^2+\alpha^2}e^{ikz}dk. \tag{21}$$

To evaluate (21), we apply Jordan's lemma and close the line integral along the real axis with an infinite semicircle in the upper half of the k-plane if $z>0$ or in the lower half of the k-plane if $z<0$. The integrand of (21) has four simple poles; two of them lie in the upper half-plane (let us call them k_1 and k_2) and two of them in the lower half-plane (k_3 and k_4).

Although the exact values of the k's must be found numerically for given set parameter values α, Δ, U, and s, we can employ the residue theorem to find that

$$\bar{w}(z,s)=i\,\mathrm{sgn}(z)\frac{\dfrac{s}{s^2+1}-\Delta s^2\bar{w}(0,s)}{k_n^3-2U^2k_n-2iUs}e^{ik_nz}$$

$$+i\,\mathrm{sgn}(z)\frac{\dfrac{s}{s^2+1}-\Delta s^2\bar{w}(0,s)}{k_j^3-2U^2k_j-2iUs}e^{ik_jz} \tag{22}$$

where $(n,j)=(1,2)$ for $z\geq 0$ and $(n,j)=(3,4)$ for $z<0$. The sign function $\mathrm{sgn}(z)=1$ for $z\geq 0$ and $\mathrm{sgn}(z)=-1$ for $z<0$.

Upon setting $z=0$ in (22) and solving for $\bar{w}(0,s)$, we can eliminate this quantity from (22). We find that

$$\bar{w}(z,s)=i\,\mathrm{sgn}(z)\frac{Z_je^{ik_nz}+Z_ne^{ik_jz}}{Z_nZ_j+i\,\mathrm{sgn}(z)\,\Delta(Z_n+Z_j)}\frac{s}{s^2+1} \tag{23}$$

in which $Z_n=k_n^3-2U^2k_n-2iUs$

and an identical expression holds for Z_j. Because we no longer have analytical expressions for k, we write the inverse of (23) in terms of the line integral

$$w(z,t)=\frac{\mathrm{sgn}(z)}{2\pi}\int_{c-\infty i}^{c+\infty i}\frac{s\,e^{st}}{s^2+1}$$

$$\times\frac{Z_je^{ik_nz}+Z_ne^{ik_jz}}{Z_nZ_j+i\,\mathrm{sgn}(z)\,\Delta(Z_n+Z_j)}ds. \tag{24}$$

For most values of α, U, Δ, and z, the integrand possess singularities at $s=\pm i$ and simple poles which satisfy

$$Z_nZ_j+i\,\mathrm{sgn}(z)\,\Delta(Z_n+Z_j)=0. \tag{25}$$

However, for certain values of α, (25) has roots at $s=\pm i$ so that $s=\pm i$ becomes a second-order pole and the inverse will grow linearly with time. To determine these α's for given values of Δ and U, $s=i$ was substituted into (25) and the IMSL Library subroutine based upon Muller's method of deflation (Muller, 1956) was used. The speed at which resonance occurs is called the critical speed.

We began our search for resonant solutions by considering the case of $\Delta=0$. As U increased from zero, α^2 decreased from one until at $U=1$ it became negative. When U was increased further, α^2 remained negative although it did approach zero. These results are in agreement with Mathews (1958) and Chonan (1978) who found that resonance only occurs for $0<U<1$ when the mass of the traveling, vibrating load is ignored. Another interpretation of these results is that as the velocity increases from zero to one, the resonant driving frequency is reduced from $(4k_WB/m^2)^{1/4}$ to zero.

When Δ is very small, α^2 again decreases with increasing U and becomes negative at $U=1$. However, for very large U, α^2 eventually becomes slightly positive. Finally, when Δ equals approximately 0.5, α^2 increases montonically with U and the driving frequency becomes even smaller.

For large U, this drop in the resonant driving frequency is quite substantial. For example, resonance for a stationary, vibrating load occurs at $\alpha^2\cong 1.4$ if $\Delta=1$. This α^2 increases to approximately 5 for $U=1$ and slightly less than 29 for $U=2$. This corresponds to a drop in the resonant driving frequency by a factor of 1.9 and 4.5, respectively.

Although we can determine the resonance condition by examining the denominator of the integrand of (24), the actual inversion is computed numerically. For given values of α, U, Δ, and z, the inverse must be computed using a numerical scheme given by Albrecht and Honig (1977). The program was checked by finding the inverse numerically for $U=0$ and comparing it against the results from the previous section. The corresponding k's were computed from

$$k^4-4U^2k^2-8iUks+4(s^2+\alpha^2)=0 \tag{26}$$

for given values of U, s, and α by an IMSL routine which solved (26) by a three-step complex algorithm given by Jenkins and Traub (1972).

Calculations were first performed with $\Delta=0$ for large times.

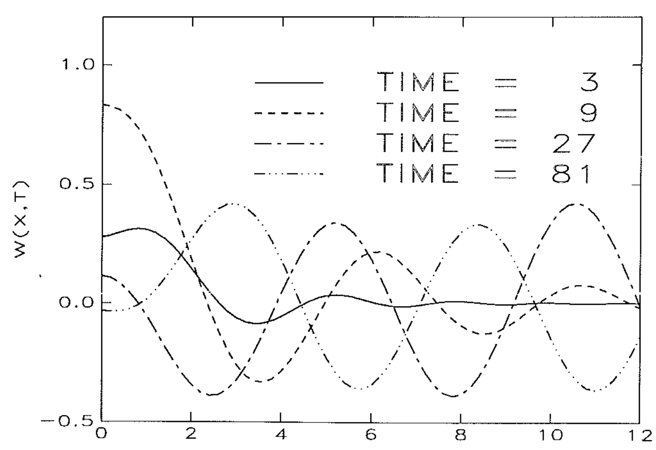

Fig. 6 Same as Fig. 2, except for $\alpha^2=0.5$

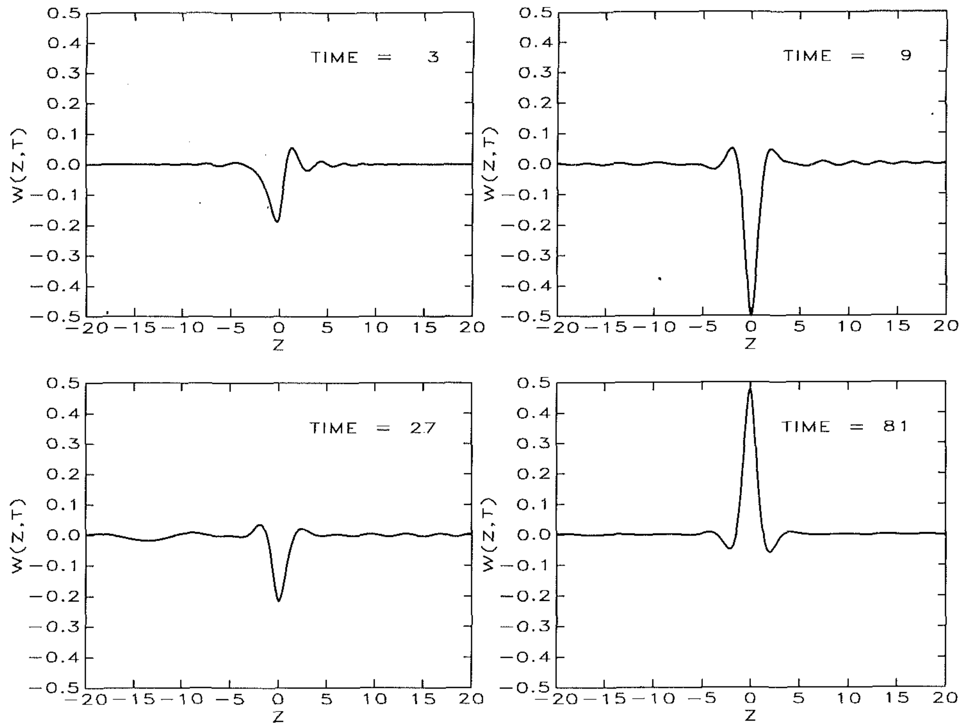

Fig. 7 Deflection of the railroad track with time as a function of distance from the location of the moving, vibrating load. Parameters are $\alpha^2 = 5.54947$, $\Delta = 2$, and $U = 0.5$.

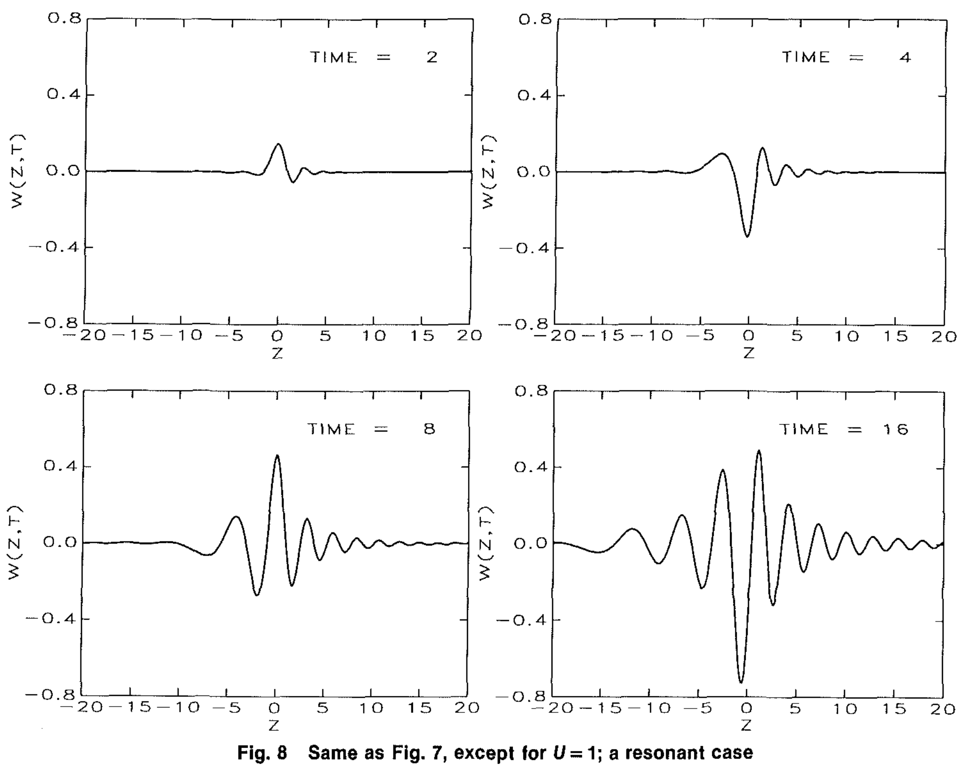

Fig. 8 Same as Fig. 7, except for $U = 1$; a resonant case

For a fixed α, waves were always found before and behind the moving, vibrating load. For speed below the critical speed, the largest amplitude waves occur near the point of forcing. Within a wavelength away from the load, the amplitude decreases dramatically and the wavelength of these waves are uniform before and behind the load. These solutions are very similar to those found for a stationary, vibrating, massless load and are in complete agreement with Mathews (1958) and Chonin (1978).

When the speed of the load becomes larger than the critical

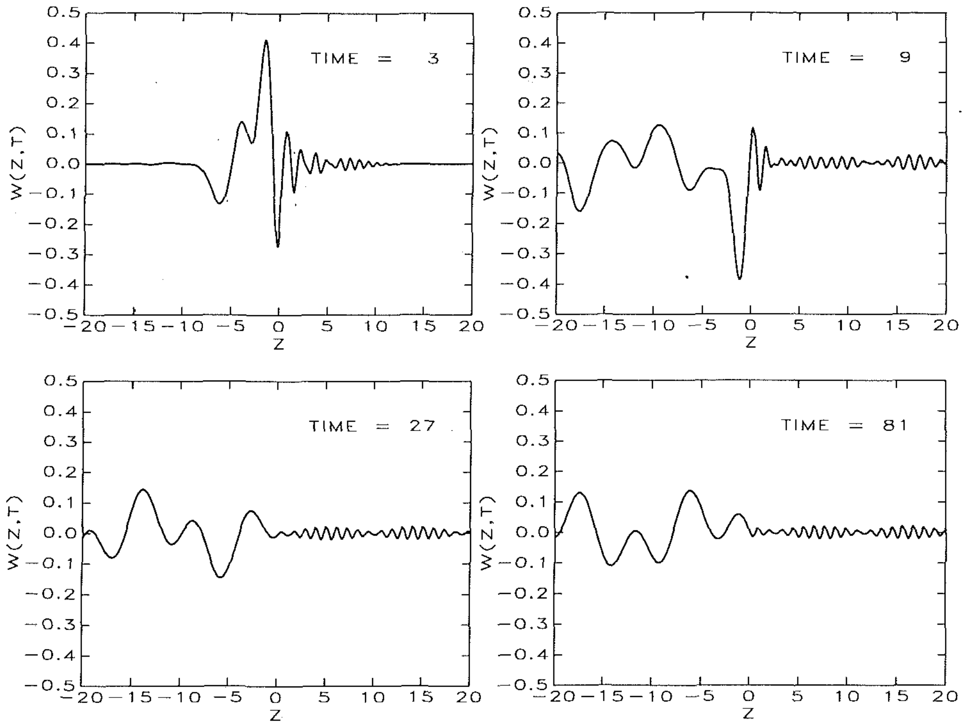

Fig. 9 Same as Fig. 7, except for $U = 3$

speed, several important changes occur. There are two distinct regions. Waves ahead of the load are of smaller wavelength and amplitude compared to those behind the load. As the velocity increases further, both regions exhibit a modulation in the wave amplitudes along with a decrease in the amplitude and wavelength witin the envelope. Eventually, at even higher velocities, the amplitude of the waves ahead of the load approaches zero while a smooth, uniform wave field is set up behind the load. These results are consistent with the findings of Chonan (1978) who found the forced oscillations of a moving, harmonic load on an elastically-supported Timoshenko beam. Our results are not identical to his results because we assumed an Euler beam.

Similar considerations hold for nonzero Δ. For a fixed α and Δ, waves are trapped near the load when the speed is below the critical velocity (see Fig. 7). These solutions are very similar to those found earlier for a stationary, vibrating load shown in Fig. 2.

We illustrate, in Fig. 8, the resonant case $\Delta = 2$, $\alpha^2 = 5.54947$ and $U = 1$. The secular growth of the wave field is clearly seen. At a given time the maximum amplitude is considerably less than its stationary counterpart.

In Fig. 9 we show the solution when we move faster than the critical speed. Waves dominate the entire domain with different wavelengths ahead and behind the load. This is caused by the shorter waves with larger phase speeds running ahead of the source, while the longer, slower waves are left behind. The maximum amplitude has been greatly reduced because some of the wave energy is left behind as the load moves. Additional calculations revealed that the amplitude is also reduced by increasing the mass of the load.

Finally, a particularly interesting solution occurs when $\alpha = 1$ and $U = 1$. Over a large portion of the rail over which the load has passed, the rail vibrates as a rigid body even though resonance does not occur. When $\alpha = 1$ but $U \neq 0$, the rigid body motion is complicated by a superimposed wave motion. This rigid body motion results from the driving frequency equaling the natural frequency.

Conclusions

We have modeled a railroad track as an elastic beam lying on a Winkler foundation to find the vibrations that arise if a vibrating, moving load passed over it. Because we treated the problem as an initial-value problem, we could follow the evolution of the displacement of the beam with time and position as a function of the mass and driving frequency of the load as well as the physical characteristics of the beam.

For a stationary, vibrating load, the Fourier and Laplace transforms were inverted exactly. The nature of the solution depends upon the ratio α of the natural frequency of the beam $(k_W/m)^{1/2}$ and the driving frequency ω_0. For $\alpha > 1$, the beam vibrates but the solutions are trapped near the source of excitation. For $\alpha \leq 1$ the vibrations propagate to infinity.

A reason why this problem is of practical concern is the prediction of resonance at $\alpha = 1$ for a stationary, massless load given by Timoshenko (1926). Resonance also occurs in our problem but now at a larger α. Physically this implies resonance at a lower driving frequency.

When the load moves and vibrates, we inverted the Fourier transform exactly but were forced to invert the Laplace transform numerically. For a given α and Δ, resonance occurs at a particular critical speed given by (25) with $s = i$. For speeds below this critical speed, waves are trapped near the vibrating load. When the load moves faster than the critical speed, shorter, faster waves propagate ahead of the excitation while the longer, slower waves are left behind. Resonance occurs but now both the mass and velocity act to lower the driving frequency at which it occurs. A particularly interesting solution occurs at $\alpha = 1$ and $U = 1$ where a portion of the beam vibrates as a rigid body. This is the best approximation to Timoshenko's original analysis where he stated that the rail would vibrate as a rigid body.

Acknowledgments

The author would like to thank Dr. Wayne Higgins and Prof. John P. Uldrick for their careful reading of the manuscript and many useful suggestions on the manuscript.

References

Albrecht, P., and Honig, G., 1977, "Numerische Inversion der Laplace-Transformierten," *Ang. Info.*, Vol. 19, pp. 336–345.

Chonan, S., 1978, "Moving Harmonic Load on an Elastically Supported Timoshenko Beam," *Z. angew. Math. Mech.*, Vol. 58, pp. 9–15.

Hildebrand, F. B., 1962, *Advanced Calculus for Engineers*, Prentice-Hall, Englewood Cliffs, N.J.

Jenkins, M. A., and Traub, J. F., 1972, "Zeros of a Complex Polynomial," *CACM*, Vol. 15, pp. 97–99.

Mathews, P. M., 1958, "Vibrations of a Beam on Elastic Foundation," *Z. angew. Math. Mech.*, Vol. 38, pp. 105–115.

Muller, D. E., 1956, "A Method for Solving Algebraic Equations Using an Automatic Computer," *Math. Tables and Aids to Computations*, Vol. 10, pp. 208–215.

Patil, S. P., 1988, "Response of Infinite Railroad Track to Vibrating Mass," *J. Eng. Mech.*, Vol. 114, pp. 688–703.

Timoshenko, S. P., 1926, "Method of Analysis of Statical and Dynamical Stresses in Rail," *Proceedings of the Second International Congress for Applied Mechanics*, Zurick, Switzerland, 407–418, see also his *Collected Papers*, pp. 422–435.

Volterra, E., and Zachmanoglou, E. C., 1965, *Dynamics of Vibrations*, Charles E. Merrill, Columbus, OH.

Axisymmetric Inclusion in a Half Space

H. Y. Yu[1]

S. C. Sanday
Mem. ASME
Naval Research Laboratory,
Washington, DC 20375-5000

An alternate method of approach for solving the axisymmetric elastic fields in the half space with an isotropic spheriodal inclusion is proposed. This new approach involves the application of the Hankel transformation method for the solution of prismatic dislocation loops and Eshelby's solution for ellipsoidal inclusions. Existing solutions by other methods for the inclusion with pure dilatational misfit in a half space are shown to be special cases of the present, more general solution.

1 Introduction

The elastic fields caused by an ellipsoidal inclusion with thermal expansion stress-free transformation strains (eigenstrains) in an isotropic infinite body were investigated by Goodier (1937). For more general eigenstrains, solutions were obtained by Eshelby (1957, 1959, 1961). By using the Galerkin vector, Mindlin and Cheng (1950) obtained the solution of the thermoelastic stress field in the semi-infinite solid when a uniform dilatational thermal expansion is given inside a spherical domain. Mindlin's solution (1953) for Green's function in a half space was used by Seo and Mura (1979) to solve the same problem for the domain in the shape of an ellipsoid.

The method of Hankel transformations, elaborated for cylindrically symmetrical problems of the theory of elasticity in Sneddon's book (1951), has been used to solve the stress field of a circular edge dislocation loop with Burger's vector normal to the plane of the loop (prismatic loop) in an unbounded solid (Kroupa, 1960) and in the half space (Bastecka, 1964). A more general elastic solution of a dislocation loop in a two-phase material has been given by Salamon and Dundurs (1971).

In the present study, Eshelby's method for the ellipsoidal inclusion and the Hankel transformation method for the prismatic loop are used for the analysis of the elastic solution of an axisymmetric ellipsoidal inclusion in the half space when a uniform axisymmetric eigenstrain is given inside the inclusion. This approach provides an alternate way for obtaining a more general solution of the stresses in the half space with an spheroidal inclusion. Existing solutions are shown to be special cases of the present one.

2 Fundamental Equations

A semi-infinite domain is defined by $x_3 \geq 0$ as shown in Fig. 1. The surface $x_3 = 0$ is free from external tractions. The present problem is to express the elastic field when the eigenstrain, e_{ij}^T, in an axisymmetric spheroidal subdomain, Ω_1 (with symmetry-axis x_3, semi-axes $a_1 = a_2$, a_3, and center at $x_1 = x_2 = 0$ and $x_3 = c$), of the half space is made up of a uniform dilatation 3ϵ and an extension β parallel to the x_3-axis. Then

$$e_{ij}^T = \delta_{ij}(\epsilon + \beta\delta_{i3}) \quad i, j = 1, 2, 3, \tag{1}$$

where δ_{ij} is the Kronecker delta (the usual summation convention does not apply to any of the expressions in this paper).

For an inclusion Ω centered at $x_1 = x_2 = x_3 = 0$ and with uniform eigenstrain described by equation (1), the stress field in an isotropic infinite body outside Ω can be obtained by using Eshelby's method (1961). The result is given by

$$\sigma_{ij} = \frac{\mu\beta}{4\pi(1-\nu)}[\psi_{,ij33} - 2\nu(1-\delta_{i3})(1-\delta_{j3})(\phi_{,ij} + \delta_{ij}\phi_{,33}) - 2(\delta_{i3}+\delta_{j3})\phi_{,ij}] - \frac{(1+\nu)\mu\epsilon}{2\pi(1-\nu)}\phi_{,ij}, \tag{2}$$

where the numerical suffixes, $i, j = 1, 2, 3$, following a comma denote differentiation with respect to the Cartesian coordinates x_1, x_2, x_3, respectively; μ and ν are the shear modulus and Poisson's ratio, respectively; and ψ and ϕ are the biharmonic and harmonic potential of attracting matter of unit density filling the volume Ω, respectively. Equation (2) can be transformed into cylindrical coordinates (r,θ,z) as follows:

$$\sigma_{rr} = -\frac{\mu\beta}{4\pi(1-\nu)}\left[\phi_{,zz} + z\phi_{,zzz} + \frac{1-2\nu}{r}\phi_{,r} + \frac{z}{r}\phi_{,rz} + f\left(\frac{1}{r}\phi_{,r} + 2\phi_{,zz} + r\phi_{,rzz} + z\phi_{,zzz} + \frac{z}{r}\phi_{,rz}\right] + \frac{(1+\nu)\mu\epsilon}{2\pi(1-\nu)}\left[\frac{\phi_{,r}}{r} + \phi_{,zz}\right],$$

$$\sigma_{\theta\theta} = -\frac{\mu\beta}{4\pi(1-\nu)}\left[2\nu\phi_{,zz} - \frac{1-2\nu}{r}\phi_{,r} - \frac{z}{r}\phi_{,rz} + f\left(\phi_{,zz} - \frac{1}{r}\phi_{,r} - \frac{z}{r}\phi_{,rz}\right)\right] - \frac{(1+\nu)\mu\epsilon}{2\pi(1-\nu)}\frac{\phi_{,r}}{r}, \tag{3}$$

[1]On-site contract employee from Geo-Centers Inc., Fort Washington, MD.

Contributed by the Applied Mechanics Division of THE AMERICAN SOCIETY OF MECHANICAL ENGINEERS for publication in the JOURNAL OF APPLIED MECHANICS.

Discussion on this paper should be addressed to the Technical Editor, Leon M. Keer, The technological Institute, Northwestern University, Evanston, IL 60208, and will be accepted until two months after final publication of the paper itself in the JOURNAL OF APPLIED MECHANICS. Manuscript received by the ASME Applied Mechanics Division, October 14, 1988; final revision, April 15, 1989.

$$\sigma_{zz} = -\frac{\mu\beta}{4\pi(1-\nu)}\Big[\phi_{,zz} - z\phi_{,zzz} - f(3\phi_{,zz} + z\phi_{,zzz}$$

$$+ r\phi_{,rzz}\Big] - \frac{(1+\nu)\mu\epsilon}{2\pi(1-\nu)}\phi_{,zz},$$

$$\sigma_{rz} = \frac{\mu\beta}{4\pi(1-\nu)}\Big[z\phi_{,rzz} + f(2\phi_{,rz} + z\phi_{,rzz}$$

$$- r\phi_{,zzz}\Big] - \frac{(1+\nu)\mu\epsilon}{2\pi(1-\nu)}\phi_{,rz},\ \sigma_{r\theta} = \sigma_{z\theta} = 0,$$

where

$$f = \frac{a_3^2}{a_1^2 - a_3^2}.$$

Equations (3) are obtained with the aid of the relationships between the derivatives of the functions ψ and ϕ given by Eshelby (1962) and the following relationships

$$\nabla^2\phi = 0,$$

$$x_1\phi_{,2} = x_2\phi_{,1}, \tag{4}$$

and

$$\phi_{,r} = \frac{x_1\phi_{,1} + x_2\phi_{,2}}{r},$$

where the letter suffixes following a comma denote differentiation with respect to the cylindrical coordinates r, θ, and z.

For a circular edge dislocation loop with the z-axis (or x_3-axis) as the axis of symmetry in an unbounded medium, the stress field is found by Kroupa (1960) by using Hankel transformations. For $z>0$, Kroupa's solution can be written as

$$\sigma_{rr} = -\frac{\mu ba}{2(1-\nu)}\Big[(I_0^{-1})_{,zz} + z(I_0^{-1})_{,zzz}$$

$$+ \frac{1-2\nu}{r}(I_0^{-1})_{,r} + \frac{z}{r}(I_0^{-1})_{,rz}\Big],$$

$$\sigma_{\theta\theta} = -\frac{\mu ba}{2(1-\nu)}\Big[2\nu(I_0^{-1})_{,zz} - \frac{1-2\nu}{r}(I_0^{-1})_{,r} - \frac{z}{r}(I_0^{-1})_{,rz}\Big],$$

$$\sigma_{zz} = -\frac{\mu ba}{2(1-\nu)}[(I_0^{-1})_{,zz} - z(I_0^{-1})_{,zzz}], \tag{5}$$

$$\sigma_{rz} = \frac{\mu ba}{2(1-\nu)}[z(I_0^{-1})_{,rzz}],\ \sigma_{r\theta} = \sigma_{z\theta} = 0,$$

where

$$I_m^n = I(m, 1; n),$$

$$I(m,p;n) = \int_0^\infty t^n J_m(rt/a) J_p(t) e^{-zt/a} dt,$$

$$I_m^n = -a(I_m^{n-1})_{,z}, \tag{6}$$

$$= -ar^{m-1}(r^{-m+1}I_{m-1}^{n-1})_{,r} \quad (m = 0,1,2,..;\ n = -1,0,1,2,..),$$

and J_m is the Bessel function of the mth order, a is the radius of the circular dislocation loop, and b is the Burger's vector which is normal to the plane of the loop $z=0$.

For the penny-shape inclusion ($a_1 = a_2 = a$ and $a_3 \to 0$) without shear and dilatation eigenstrains (penny-shape prismatic inclusion), the eigenstrains are $e_{11}^T = e_{22}^T = 0$ and $e_{33}^T = \beta$. If we reduce equation (3) for the penny-shape prismatic inclusion, it is interesting to note the similarity between equations (3) and (5). By putting

$$\phi = kI_0^{-1} \qquad (a_3 \to 0), \tag{7}$$

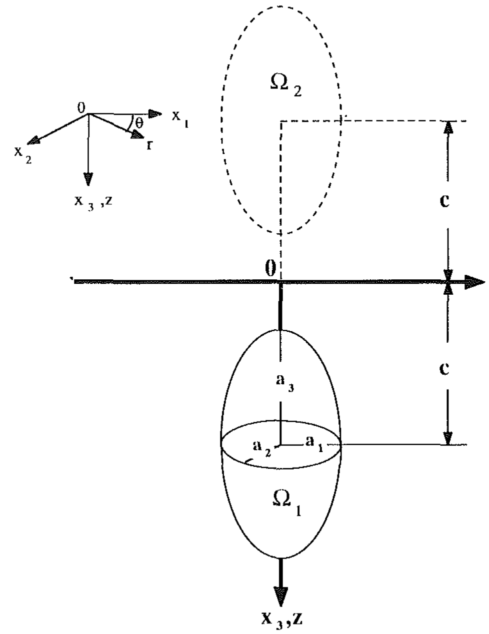

Fig. 1 Spheroidal inclusion Ω_1 with principal half-axes $a_1 = a_2$, a_3 in a half space and its image Ω_2

where $k = 2\pi ba/\beta$, the elastic solutions of the penny-shape prismatic inclusion (equations (3)) and the prismatic loop (equations (5)) are identical. This suggests that the method used to obtain the stress field of a prismatic loop in the half space due to the presence of the free surface can be adapted to solve the elastic field caused by an axisymmetrical inclusion in the half space with its axis of symmetry normal to the plane of the free surface. This approach is believed to be quite reasonable since the solution for the axisymmetrical inclusion can be applied to the penny-shape inclusion after a tedious passage to the limit and the fact that if the inclusion has the same elastic moduli as the matrix, the stress field is the same as that of a small dislocation loop when both the dislocation loop and the inclusion are infinitesimally small (Eshelby, 1961). For example, a small inclusion of volume V and an eigenstrain e_{33}^T in the x_3 direction has the same stress field as that of a prismatic interstitial dislocation loop of area A and Burger's vector b provided that $Ve_{33}^T = Ab$. By using the recurrence relations, equation (6), it can be shown that the function I_0^{-1} satisfies the Laplace equation $\nabla^2 I_0^{-1} = 0$.

3 Elastic Solutions

Consider the half space $x_3 = z > 0$ (Fig. 1) with an axisymmetric inclusion with its center at the point $(0,0,c)$ and its axis of symmetry (z-axis) normal to the plane of the free surface $z=0$. In order that the plane $z=0$ be a surface free of external tractions, the stress components on this plane must satisfy the following boundary conditions

$$(\sigma_{rz})_{z=0} = 0,\ (\sigma_{zz})_{z=0} = 0, \tag{8}$$

and the equilibrium condition

$$\sum_{j=1}^{3} \sigma_{ij,j} = 0. \tag{9}$$

Similar to the work of Bastecka (1964), the stress, σ_{ij}, in the half space, $z \geq 0$, outside the axisymmetric ellipsoidal inclusion centered at the point $(0,0,c)$ can be expressed as

$$\sigma_{ij} = \sigma_{ij}^I + \sigma_{ij}^{II} + \sigma_{ij}', \tag{10}$$

which satisfies the required boundary conditions, equation

(8), the equilibrium condition, equation (9), and also converges to zero for x_1 and x_2 approaching $\pm\infty$ and x_3 approaching ∞. In equation (10), the term σ^I_{ij} is the stress caused by the axisymmetric inclusion Ω_1 centered at $(0,0,c)$, σ^{II}_{ij} is the stress due to the image inclusion Ω_2 centered at the point $(0,0,-c)$, with eigenstrain

$$(e^T_{ij})^{II} = -(e^T_{ij})^I = -\delta_{ij}(\epsilon+\beta\delta_{i3}). \tag{11}$$

The solution for the stresses σ^I_{ij} and σ^{II}_{ij} are obtained by translating the origin of coordinates in equation (2) and equation (3) to points $(0,0,c)$ and $(0,0,-c)$, respectively. The expressions of the Newtonian potential functions ϕ^I and ϕ^{II} for the solutions of σ^I_{ij} and σ^{II}_{ij} can be found in Seo and Mura's paper (1979). The additional stress σ'_{ij} in equation (10) is the fictitious stress necessary to make the surface of the half space free of stresses and it satisfies the boundary conditions

$$(\sigma'_{zz})_{z=0}=0, \tag{12}$$

$$\begin{aligned}(\sigma'_{rz})_{z=0} &= -(\sigma^I_{rz}+\sigma^{II}_{rz})_{z=0}\\ &= \frac{\mu}{2\pi(1-\nu)}\left[c\beta\phi^{II}_{,rzz}+f\beta(c\phi^{II}_{,rzz}+2\phi^{II}_{,rz}\right.\\ &\quad \left. -r\phi^{II}_{,zzz})-2(1+\nu)\epsilon\phi^{II}_{,rz}\right]_{z=0},\end{aligned} \tag{13}$$

where, for $z=0$, $\phi^I_{,rzz}=\phi^{II}_{,rzz}$, $\phi^I_{,rz}=-\phi^{II}_{,rz}$, $\phi^I_{,zzz}=-\phi^{II}_{,zzz}$ and equation (3) is used to obtain equation (13). Now, in the limit when a_3 approaches zero, that is, for the penny-shape inclusion, we can substitute equation (7) into equation (13) to obtain

$$\begin{aligned}(\sigma'_{rz})_{z=0} &= \frac{\mu\beta k}{2\pi(1-\nu)}\left[-(1+f)\frac{c}{a^3}\int_0^\infty t^2J_1(\rho t)J_1(t)e^{-ct/a}dt\right.\\ &\quad \left.+\frac{2f}{a^2}\int_0^\infty tJ_1(\rho t)J_1(t)e^{-ct/a}dt+\frac{f\rho}{a^2}\int_0^\infty t^2J_0(\rho t)J_1(t)e^{-ct/a}dt\right]\\ &\quad -\frac{(1+\nu)\mu\epsilon}{\pi(1-\nu)}\frac{k}{a^2}\int_0^\infty tJ_1(\rho t)J_1(t)e^{-ct/a}dt\end{aligned} \tag{14}$$

where $\rho=r/a$.

For the axisymmetric problem, by the appropriate expression of the elastic displacement as the derivatives of certain function $\varphi(r,z)$ in cylindrical coordinates, the equilibrium and Beltrami equations are replaced by a single equation (Sneddon, 1951),

$$\nabla^4\varphi(r,z)=0, \tag{15}$$

whose general solution is carried out by the method of integral transformations. The function ψ is replaced by its Hankel transform of zeroth order,

$$G(\zeta,z)=\int_0^\infty r\varphi(r,z)J_0(\zeta r)dr, \tag{16}$$

and it can be shown that $G(\zeta, z)$ is, in general, given by the expression

$$G(\zeta,z)=(A+Bz)e^{-\zeta z}+(C+Dz)e^{\zeta z}, \tag{17}$$

where A, B, C, and D are unknown functions of ζ which are determined from the boundary conditions. The stress components are expressed by means of the function $G(\zeta, z)$.

In the present case, we consider the solution to converge to zero for z approaching ∞, thus we set $C=D=0$. In order to determine A and B, from the first boundary condition (equation (12)), we obtain the following relationship

$$A(\zeta)=-\frac{\mu}{\lambda+\mu}\frac{B(\zeta)}{\zeta}, \tag{18}$$

where $\lambda=2\mu\nu/(1-2\nu)$ is Lame's constant. From the relationship between the stress components and the function $G(\zeta,z)$, we have

$$(\sigma'_{rz})_{z=0}=\int_0^\infty \zeta F(\zeta)J_1(\zeta r)d\zeta, \tag{19}$$

where $F(\zeta)$ is the Hankel transformation of the first order of the function $(\sigma'_{rz})_{z=0}$ and

$$F(\zeta)=-2(\lambda+\mu)\zeta^2B(\zeta). \tag{20}$$

By letting $t=a\zeta$, and using equations (14) and (18), $F(\zeta)$ becomes

$$\begin{aligned}F(\zeta) &= -\frac{k\mu\beta}{2\pi(1-\nu)}\left[(c\zeta-2f)J_1(a\zeta)+af\zeta J_0(a\zeta)\right]e^{-c\zeta}\\ &\quad -\frac{(1+\nu)k\mu\epsilon}{\pi(1-\nu)}J_1(a\zeta)e^{-c\zeta}.\end{aligned} \tag{21}$$

This equation is used to calculate the function G which is substituted into the expressions for stress σ'_{ij} (Sneddon, 1951). In the calculation, in addition to the recurrence relations equation (6), the following recurrence (Eason, Noble, and Sneddon, 1955) relation is also used

$$\begin{aligned}I^{II}(m,p-1;n) &= (m+p-n)I^{II}(m,p;n-1)-\frac{r}{a}I^{II}(m-1,p;n)\\ &\quad +\frac{z+c}{a}I^{II}(m,p;n) \qquad (m+n+p>0),\end{aligned} \tag{22}$$

where

$$I^{II}(m,p;n)=\int_0^\infty t^nJ_m(\rho t)J_p(t)e^{-t(z+c)/a}dt, \tag{23}$$

and the transformation relation between two-dimensional harmonic potential, $(I_0^{-1})^{II}$, and three-dimensional harmonic potential, $(\phi)^{II}$, is

$$(\phi)^{II}=k(I_0^{-1})^{II}. \tag{24}$$

The resulting expressions for the fictitious stresses σ'_{ij} are

$$\begin{aligned}\sigma'_{rr} &= -\frac{\mu\beta c}{2\pi(1-\nu)}\left[2\phi^{II}_{,zzz}+z\phi^{II}_{,zzzz}+\frac{2(1-\nu)}{r}\phi^{II}_{,rz}\right.\\ &\quad \left.+\frac{z}{r}\phi^{II}_{,rzz}\right]-\frac{\mu\beta f}{2\pi(1-\nu)}\left[2(2+\nu)\phi^{II}_{,zz}+(5z+2c)\phi^{II}_{,zzz}\right.\\ &\quad +z(z+c)\phi^{II}_{,zzzz}+\frac{2(1-\nu)}{r}\phi^{II}_{,r}+2\frac{(1-\nu)(z+c)+z}{r}\phi^{II}_{,rz}\\ &\quad \left.+\frac{2r^2+z(z+c)}{r}\phi^{II}_{,rzz}+rz\phi^{II}_{,rzzz}\right]+\frac{(1+\nu)\mu\epsilon}{\pi(1-\nu)}\left[2\phi^{II}_{,zz}+z\phi^{II}_{,zzz}\right.\\ &\quad \left.+\frac{2(1-\nu)}{r}\phi^{II}_{,r}+\frac{z}{r}\phi^{II}_{,rz}\right],\end{aligned}$$

$$\begin{aligned}\sigma'_{\theta\theta} &= -\frac{\mu\beta c}{2\pi(1-\nu)}\left[2\nu\phi^{II}_{,zzz}-\frac{2(1-\nu)}{r}\phi^{II}_{,rz}-\frac{z}{r}\phi^{II}_{,rzz}\right]\\ &\quad -\frac{\mu\beta f}{2\pi(1-\nu)}\left[2(1+2\nu)\phi^{II}_{,zz}+[(1+2\nu)z+2\nu c]\phi^{II}_{,zzz}\right.\\ &\quad -\frac{2(1-\nu)}{r}\phi^{II}_{,r}-2\frac{(1-\nu)(z+c)+z}{r}\phi^{II}_{,rz}\\ &\quad \left.+\frac{2\nu r^2-z(z+c)}{r}\phi^{II}_{,rzz}\right]+\frac{(1+\nu)\mu\epsilon}{\pi(1-\nu)}\left[2\nu\phi^{II}_{,zz}\right.\\ &\quad \left.-\frac{2(1-\nu)}{r}\phi^{II}_{,r}-\frac{z}{r}\phi^{II}_{,rz}\right],\end{aligned} \tag{25}$$

$$\sigma'_{zz} = \frac{\mu\beta c}{2\pi(1-\nu)}[z\phi^{II}_{,zzzz}]$$

$$+\frac{\mu\beta f}{2\pi(1-\nu)}z[4\phi^{II}_{,zzz} + (z+c)\phi^{II}_{,zzzz} + r\phi^{II}_{,rzzz}]$$

$$-\frac{(1+\nu)\mu\epsilon}{\pi(1-\nu)}[z\phi^{II}_{,zzz}],\ \sigma'_{rz} = \frac{\mu\beta c}{2\pi(1-\nu)}[\phi^{II}_{,rzz} + z\phi^{II}_{,rzzz}]$$

$$-\frac{\mu\beta f}{2\pi(1-\nu)}[r\phi^{II}_{,zzz} + rz\phi^{II}_{,zzzz} - 2\phi^{II}_{,rz} - (4z+c)\phi^{II}_{,rzz}$$

$$-z(z+c)\phi^{II}_{,rzzz}] - \frac{(1+\nu)\mu\epsilon}{\pi(1-\nu)}[\phi^{II}_{,rz} + z\phi^{II}_{,rzz}],$$

$$\sigma'_{r\theta} = \sigma'_{rz} = 0.$$

It can be easily shown that these stress components satisfy the equilibrium condition, equation (9), and the compatibility equations. Therefore, for points outside Ω_1, the stress field can be obtained by equations (2), (10), and (25). For points inside inclusion Ω_1, the elastic stress σ^*_{ij} is given by

$$\sigma^*_{ij} = (\sigma^I_{ij} - \sigma^{**}_{ij}) + \sigma^{II}_{ij} + \sigma'_{ij}, \tag{26}$$

where the stress $(\sigma^I_{ij} - \sigma^{**}_{ij})$ is the uniform stress inside the inclusion Ω_1 when the medium is infinite and whose solution has been given by Mura (1982, equation 11.20).

For the elastic field in a half space caused by an ellipsoidal inclusion ($a_1 = a_2$) with uniform dilatational eigenstrain only, i.e., $\beta = 0$ equation (25) becomes (in Cartesian coordinates)

$$\sigma'_{ij} = \frac{(1+\nu)\mu\epsilon}{\pi(1-\nu)}[(1-2\nu)(\delta_{i3} + \delta_{j3} - 1)\phi^{II}_{,ij} - \phi^{II}_{,ij}$$
$$+ 2\nu\delta_{ij}\phi^{II}_{,33} - x_3\phi^{II}_{,ij3}] \tag{27}$$

and the stress field outside Ω_1 is

$$\sigma_{ij} = -\frac{(1+\nu)\mu\epsilon}{2\pi(1-\nu)}[\phi^I_{,ij} + \phi^{II}_{,ij} - 2(1-2\nu)(\delta_{i3}$$
$$+ \delta_{j3} - 1)\phi^{II}_{,ij} - 4\nu\delta_{ij}\phi^{II}_{,33} + 2x_3\phi^{II}_{,ij3}]. \tag{28}$$

Equation (28) is the same as Seo and Mura's result (1979) for the elastic field in a half space caused by an ellipsoidal inclusion ($a_1 = a_2$) with uniform dilatational eigenstrain. Mindlin and Cheng's result (1950) for a sphere with a uniform dilatational thermal expansion can also be obtained by taking $a_3 = a$ and $\beta = 0$ in equation (25).

For the elastic field in a half space caused by a penny-shape inclusion ($a_1 = a_2 = a$ and $a_3 \to 0$) without shear and dilatation eigenstrains (penny-shape prismatic inclusion), the eigenstrains are $e^T_{11} = e^T_{22} = 0$ and $e^T_{33} = \beta$. Equation (25) becomes (in Cartesian coordinates)

$$\sigma'_{ij} = -\frac{\mu\beta c}{2\pi(1-\nu)}[(1-2\nu)(\delta_{i3} + \delta_{j3} - 1)\phi^{II}_{,ij3} - \phi^{II}_{,ij3}$$
$$+ 2\nu\delta_{ij}\phi^{II}_{,333} - x_3\phi^{II}_{,ij33}], \tag{29}$$

and the stress field for exterior point of Ω_1 is

$$\sigma_{ij} = \frac{\mu\beta}{4\pi(1-\nu)}[(x_3 - c)(\phi^I_{,ij3} - \phi^{II}_{,ij3})$$
$$-(1-2\nu)(\delta_{i3} + \delta_{j3} - 1)(\phi^I_{,ij} - \phi^{II}_{,ij} + 2c\phi^{II}_{,ij3})$$
$$-2\nu\delta_{ij}(\phi^I_{,33} - \phi^{II}_{,33} + 2c\phi^{II}_{,333}) + 2cx_3\phi^{II}_{,ij33}]. \tag{30}$$

By substituting equation (7) in equation (30) and expressing it in cylindrical coordinates, the same results as given by Bastecka (1964) for a circular edge dislocation loop in a half space are obtained.

4 Summary

The stress field in the half space ($z \geq 0$) caused by an axisymmetric ellipsoidal inclusion Ω_1 centered at $(0,0,c)$ with eigenstrain $e^T_{ij} = \delta_{ij}(\epsilon + \beta\delta_{i3})$ is found by the superposition of the following three stress fields: (*a*) the stress field of the inclusion Ω_1 centered at $(0,0,c)$ with eigenstrain e^T_{ij} in an infinite medium, (*b*) the stress field of the image inclusion Ω_2 centered at $(0,0,-c)$ with eigenstrain $-e^T_{ij}$, and (*c*) the additional fictitious stress field that makes all stress fields satisfy the equilibrium and boundary conditions.

The stress field of the inclusion in an infinite medium obtained by Eshelby is compared with the stress field of a prismatic loop in an infinite medium as obtained by Kroupa. A relationship is found between the potential function ϕ of the inclusion and the integral function I_0^{-1}, which involves the product of Bessel functions J_m, for the solution of the prismatic loop.

The fictitious stress field is solved first for the two-dimensional problem by using the Hankel transformation method and then it is transformed into the three-dimensional case by use of the relationship between ϕ and I_0^{-1}.

The solution of the elastic field in the half space with ellipsoidal inclusions with uniform dilatational eigenstrains obtained by Seo and Mura (1979) has been rearranged into three terms corresponding to the stress field of the inclusion Ω_1 in an infinite medium centered at $(0,0,c)$ with eigenstrain $\delta_{ij}\epsilon$, the stress field of the image inclusion Ω_2 centered at $(0,0,-c)$ with eigenstrain $-\delta_{ij}\epsilon$, and the additional fictitious stress field. It has also been shown that when $a_1 = a_2$, Seo and Mura's results are a special case of the present solution.

References

Bastecka, J., 1964, "Interaction of Dislocation Loop with Free Surface," *Czechoslovak Journal of Physics*, Vol. B14, pp. 430–442.

Eason, G., Noble, B., and Sneddon, J. N., 1955, "On Certain Integrals of Lipschitz-Hankel Type Involving Products of Bessel Functions," *Philosophical Transactions of the Royal Society of London*, Vol. A247, pp. 529–551.

Eshelby, J. D., 1957, "The Determination of the Elastic Field of an Ellipsoidal Inclusion and Related Problems," *Proceedings of the Royal Society of London*, Vol. A241, pp. 376–396.

Eshelby, J. D., 1959, "The Elastic Field Outside an Ellipsoidal Inclusion," *Proceedings of the Royal Society of London*, Vol. A252, pp. 561–569.

Eshelby, J. D., 1961, "Elastic Inclusions and Inhomogeneities," *Progress in Solid Mechanics*, Vol. 2, I.N. Sneddon and R. Hill, eds., North-Holland, Amsterdam, pp. 89–140.

Goodier, J. N., 1937, "On the Integration of the Thermo-Elastic Equations," *Philosophical Magazine and Journal of Science*, Vol. 23, pp. 1017–1032.

Kroupa, F., 1960, "Circular Edge Dislocation Loop," *Czechoslovak Journal of Physics*, Vol. B10, pp. 284–293.

Mindlin, R. D., and Cheng, D. H., 1950, "Thermoelastic Stress in the Semi-Infinite Solid," *Journal of Applied Physics*, Vol. 21, pp. 931–933.

Mindlin, R. D., 1953, "Force at a Point in the Interior of a Semi-Infinite Solid," *Proceedings First Midwestern Conference on Solid Mechanics*, pp. 55–59.

Mura, T., 1982, *Micromechanics of Defects in Solid*, Martinus-Nijhoff, The Hague.

Salamon, N. J., and Dundurs, J., 1971, "Elastic Fields of a Dislocation Loop in a Two-Phase Material," *J. Elasticity*, Vol. 1, pp. 153–164.

Seo, T., and Mura, T., 1979, "The Elastic Field in Half Space Due to Ellipsoidal Inclusions with Uniform Dilatational Eigenstrains," ASME Journal of Applied Mechanics, Vol. 46, pp. 568–572.

Sneddon, I. N., 1951, *Fourier Transforms*, McGraw-Hill, New York.

Du Chen
Visiting Scholar.

Shun Cheng
Professor,
Department of Engineering Mechanics.

University of Wisconsin,
Madison, WI 53706

Stress Distribution in Plane Scarf and Butt Joints

The stress distribution in a plane scarf joint, which may have an arbitrary angle of scarf as well as arbitrary elastic parameters for its adherends and adhesive, is analyzed. The analysis is based on the two-dimensional elasticity theory in conjunction with the variational principle of complementary energy. Minimizing the energy functional leads to a specific optimization problem with two variables for the determination of the stresses. Some typical features of the stress distribution are shown by numerical examples. Criteria for uniformly distributed adhesive stresses which are of importance in practice are deduced. The butt joint is treated as a special case of scarf joints.

Introduction

An adhesive-bonded plane scarf joint is one of the most common types of specimens employed for various adhesive testings, and with the development of new adhesive materials, it has also become one of those extensively used structural elements in the manufacturing of light structures (Patrick, 1976). A comprehensive analysis of the stress distribution around the joint region and in the adhesive layer of the joint is therefore of importance in the application of adhesive joints (Goland and Reissner, 1944; Chen and Cheng, 1983a).

Because of the difficulties in the analysis of scarf joints, only a few theoretical studies have appeared in the literature since the early work by Lubkin (1957a). Lubkin intended to establish the conditions under which a wide or narrow adhesive scarf joint can have uniformly distributed adhesive stresses. In Lubkin's analysis (1957b) the free-edge stress boundary conditions of the joint are neglected, and to some extent the stress distribution in the adhesive layer is oversimplified. This unavoidably limits the overall application of the analysis. By using some known stress functions in two-dimensional elasticity theory to represent the stresses in the two adherends and to satisfy approximately the conditions of equilibrium and compatibility of the adhesive layer, Thein Wah (1976a) tried a series of numerical solutions to the problem. Wah's numerical data (1976b) exposed the complexities in the pattern of the stress distribution for the joint region, and hence a few, if any, general conclusions may be drawn from his analysis. Besides, the expected stress concentration near the free edges of the joint is not fully demonstrated.

In the present analysis, all boundary stress conditions of the joint are strictly satisfied and the stress distribution in the joint region is analyzed and demonstrated by numerical examples. Through the use of two-dimensional elasticity theory in conjuntion with the variational theorem of complementary energy, a specific optimization problem with two variables is derived for the determination of the stresses. The solution may then be obtained by some numerical procedures. Numerical examples are given to show the influence that the scarf angle and the material properties may have on the stress distribution. As a by-product of the present study, Lubkin's criterion (1957c) for the uniform stress distribution is reexamined and a new criterion presented.

Formulation of the Problem

Figure 1 is a schematic diagram of a plane scarf joint where the two adherends (seen as two sheet strips) may have unequal Young's moduli E_1 and E_2 and unequal Poisson's ratios ν_1 and ν_2. The thickness of the adhesive layer is t, which is small when compared with the width b' of the adherends, or compared with the length b of the bonding region ($b=b'/\cos\alpha$). Let the Young's modulus and Poisson's ratio for the adhesive be E_3 and ν_3, respectively. The joint may have arbitrary scarf angle α, and the special case $\alpha=0$ (refers to butt joint) is also under consideration. The tensile forces are assumed to be applied at some distance from the scarf. The corresponding tensile stress is denoted by σ_o.

The main problem is the determination of the stress distribution in the joint region and this is treated as a problem in plane stress.

Description of Stresses in the Joint

To fit the geometry of the joint, an oblique rectilinear coordinate system oxy_1 is chosen, with axis x placed at one of the bonding surfaces and axis y_1 parallel to the tensile forces as shown in Fig. 1. For convenience, coordinate $y_2=y_1+t$ is also used occasionally. Figure 1 depicts the definition and sign convention for the stress components σ_x, σ_y, τ_{xy} ($\tau_{xy}=\tau_{yx}$, Boresi and Chong, 1987) in this oblique coordinate system, and, as a reference, the stress components $\sigma_{x'}$, $\sigma_{y'}$, $\tau_{x'y'}$ associated

Contributed by the Applied Mechanics Division of THE AMERICAN SOCIETY OF MECHANICAL ENGINEERS for publication in the JOURNAL OF APPLIED MECHANICS.

Discussion on this paper should be addressed to the Technical Editor, Leon M. Keer, The Technological Institute, Northwestern University, Evanston, IL 60208, and will be accepted until two months after final publication of the paper itself in the JOURNAL OF APPLIED MECHANICS. Manuscript received and accepted by the ASME Applied Mechanics Division, January 1, 1989.

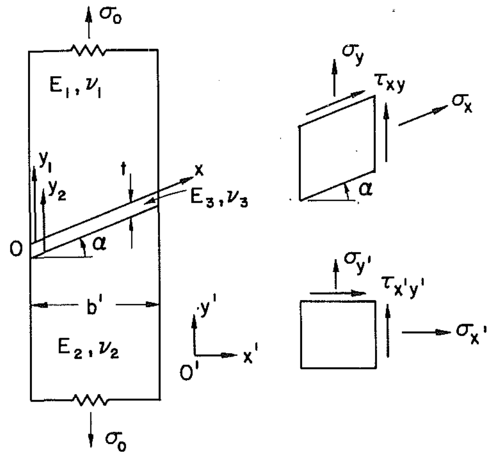

Fig. 1 Scarf joint, coordinate system, and convention for stress components

with the rectangular coordinate system $o'x'y'$ are expressed in the same figure. x' is also measured from the left edge of the joint as $x(x' = x\cos\alpha)$. The relation between the two sets of stress components may be written in matrix form as

$$[\sigma_{x'}, \sigma_{y'}, \tau_{x'y'}]^T = [A][\sigma_x, \sigma_y, \tau_{xy}]^T \tag{1}$$

in which

$$[A] = \begin{bmatrix} \cos\alpha & 0 & 0 \\ \sin\alpha\ \tan\alpha & (\cos\alpha)^{-1} & 2\ \tan\alpha \\ \sin\alpha & 0 & 1 \end{bmatrix}$$

and T denotes the transpose of matrix. From equation (1) it follows

$$[\sigma_{x'}, \sigma_{y'}, \tau_{x'y'}] = [\sigma_x, \sigma_y, \tau_{xy}][A]^T$$

and

$$[\sigma_x, \sigma_y, \tau_{xy}]^T = [A]^{-1}[\sigma_{x'}, \sigma_{y'}, \tau_{x'y'}]^T \tag{2}$$

where

$$[A]^{-1} = \begin{bmatrix} \cos^{-1}\alpha, & 0 & 0 \\ \sin\alpha\ \tan\alpha, & \cos\alpha, & -2\sin\alpha \\ -\tan\alpha & 0 & 1 \end{bmatrix}$$

where $[A]^{-1}$ is the inverse matrix of A. In what follows, the oblique components σ_x, σ_y, τ_{xy} are mainly concerned. It may be shown that these oblique components satisfy the same equations of equilibrium as those for rectangular components of stress:

$$\frac{\partial\sigma_x}{\partial x} + \frac{\partial\tau_{xy}}{\partial y} = 0, \qquad \frac{\partial\tau_{xy}}{\partial x} + \frac{\partial\sigma_y}{\partial y} = 0. \tag{3}$$

Let $(\sigma_{x1}, \sigma_{y1}, \tau_{xy1})$, $(\sigma_{x2}, \sigma_{y2}, \tau_{xy2})$, $(\sigma_{x3}, \sigma_{y3}, \tau_{xy3})$ be the oblique stress components in the upper adherend, the lower adherend, and the adhesive, respectively. These stress components should satisfy equation of equilibrium (3), conditions of continuity of stress across the dividing surfaces ($y_1 = 0$ and $y_2 = 0$), and all those boundary stress conditions. In this section, the possible stress distributions that satisfy all these stress conditions are investigated. The satisfaction of compatibility conditions is treated in the next section. We start with two simplifications that form the basis of the analysis to be developed:

(1) According to the well-known principle of Saint-Venant, the stress components σ_{x1} and σ_{x2} in the upper and lower adherends of the joint may be considered decaying exponentially with the increasing distance from the bonding surfaces, i.e.,

$$\sigma_{x1} = \sigma_1(x)e^{-\lambda_1(y_1/b)}$$
$$\sigma_{x2} = \sigma_2(x)e^{\lambda_2(y_2/b)} \tag{4}$$

where $\sigma_1(x)$ and $\sigma_2(x)$ are two unknown functions of x and λ_1 and $\lambda_2(\lambda_1, \lambda_2 > 0)$ are two unknown decaying exponents yet to be determined.

(2) Since the adhesive layer is rather thin, the stress component τ_{xy3} in this thin layer may be assumed as varying linearly with the coordinate y_1 (or y_2), and this is sufficient to cover the possible influence of the scarf angle on the stress patterns in the layer (cf., the case of butt joint). Similar assumptions were employed in dealing with adhesive-bonded single-lap joints (Chen and Cheng, 1983b).

Based on the first assumption, i.e. (4), making use of the equations of equilibrium (3) and also the known boundary stress conditions of the joint, it is readily deduced that in the upper and lower adherend the other two stress components must be

$$\tau_{xy1} = \frac{b}{\lambda_1}\sigma_1'(x)e^{-\lambda_1(y_1/b)}$$
$$\sigma_{y1} = \left(\frac{b}{\lambda_1}\right)^2 \sigma_1''(x)e^{-\lambda_1(y_1/b)} + \sigma_o\cos\alpha \tag{5}$$

$$\tau_{xy2} = -\frac{b}{\lambda_2}\sigma_2'(x)e^{\lambda_2(y_2/b)}$$
$$\sigma_{y2} = \left(\frac{b}{\lambda_2}\right)^2 \sigma_2''(x)e^{\lambda_2(y_2/b)} + \sigma_o\cos\alpha, \tag{6}$$

respectively, in which primes stand for derivatives, i.e. $\sigma' = d\sigma/dx$, $\sigma'' = d^2\sigma/dx^2$. We note that the boundary conditions at large distances $y_1 = \infty$ and $y_2 = -\infty$,

$$\sigma_{y'1} = \sigma_{y'2} = \sigma_o,\ \sigma_{x'1} = \sigma_{x'2} = 0,\ \tau_{x',y'1} = \tau_{x'y'2} = 0$$

are satisfied. Furthermore, there should be four edge conditions on the two sides $x = 0$ and $x = b$ for each of the two unknown functions σ_1 and σ_2 of x:

$$\sigma_1|_{x=0} = 0,\ \sigma_1'|_{x=0} = 0,\ \sigma_1|_{x=b} = 0,\ \sigma_1'|_{x=b} = 0,$$
$$\sigma_2|_{x=0} = 0,\ \sigma_2'|_{x=0} = 0,\ \sigma_2|_{x=b} = 0,\ \sigma_2'|_{x=b} = 0. \tag{7}$$

From (5) and (6), the stress components acting on the two bonding surfaces are, therefore,

$$y_1 = 0:\ \tau_{xy1} = \frac{b}{\lambda_1}\sigma_1'(x), \quad \sigma_{y1} = \left(\frac{b}{\lambda_1}\right)^2 \sigma_1''(x) + \sigma_o\cos\alpha$$

$$y_2 = 0:\ \tau_{xy2} = -\frac{b}{\lambda_2}\sigma_2'(x), \quad \sigma_{y2} = \left(\frac{b}{\lambda_2}\right)^2 \sigma_2''(x) + \sigma_o\cos\alpha \tag{8}$$

Based on the second assumption and by applying the equations of equilibrium (3) and boundary stress conditions (7) and (8), the stress distributions in the adhesive layer can also be similarly deduced:

$$\tau_{xy3} = -\left(\frac{b}{\lambda_2}\right)\sigma_2'(x) + \frac{y_2}{t}\left[\left(\frac{b}{\lambda_1}\right)\sigma_1'(x) + \left(\frac{b}{\lambda_2}\right)\sigma_2'(x)\right]$$

$$\sigma_{x3} = -\frac{1}{t}\left[\left(\frac{b}{\lambda_1}\right)\sigma_1(x) + \left(\frac{b}{\lambda_2}\right)\sigma_2(x)\right]$$

$$\sigma_{y3} = y_2\left(\frac{b}{\lambda_2}\right)\sigma_2''(x) - \frac{y_2^2}{2t}\left[\left(\frac{b}{\lambda_1}\right)\sigma_1''(x) + \frac{b}{\lambda_2}\sigma_2''(x)\right] + \left(\frac{b}{\lambda_2}\right)^2 \sigma_2''(x) + \sigma_o\cos\alpha \tag{9}$$

where the continuity conditions for stresses across the bonding surface $y_2 = 0$ have been considered and satisfied. From equations (8) and (9), the stress continuity condition across the bonding surface $y_1 = 0$, i.e.,

$$\sigma_{y3}|_{y_1=0,\,(y_2=t)} = \sigma_{y1}|_{y_1=0} \tag{10}$$

may be written as

$$t\left(\frac{b}{\lambda_2}\right)\sigma_2''(x) - \frac{t}{2}\left[\left(\frac{b}{\lambda_1}\right)\sigma_1''(x) + \left(\frac{b}{\lambda_2}\right)\sigma_2''(x)\right]$$
$$+\left(\frac{b}{\lambda_2}\right)^2 \sigma_2''(x) + \sigma_o\cos\alpha = \left(\frac{b}{\lambda_1}\right)^2 \sigma_1''(x) + \sigma_o\cos\alpha$$

or, after integration and applying the edge condition (7), yield

$$\sigma_2(x) = \beta \bullet \sigma_1(x) \tag{11}$$

where

$$\beta = \left[\frac{t}{2}\left(\frac{b}{\lambda_1}\right) + \left(\frac{b}{\lambda_1}\right)^2\right] \Big/ \left[\frac{t}{2}\left(\frac{b}{\lambda_2}\right) + \left(\frac{b}{\lambda_2}\right)^2\right].$$

Relation (11) may be seen as a condition of "constraint" imposed on $\sigma_1(x)$ and $\sigma_2(x)$ for satisfying the condition (10). Thus, all the stress components in the joint can now be expressed in terms of only one unknown function, $\sigma_1(x)$, and two unknown decaying exponents, λ_1 and λ_2.

Variational Method Based on the Principle of Complementary Energy

In the preceding analysis, only equations of equilibrium and boundary stress conditions are satisfied. To obtain further equations for the determination of σ_1, λ_1, and λ_2, use has to be made of the compatibility of stresses. In what follows, this is done approximately by means of the variational theorem of complementary energy (Washizu, 1968), which states that for all stresses satisfying the equilibrium conditions in the interior of an elastic body and on that part of its boundary surface where the surface forces are prescribed, the actual state of the stress, i.e., the stresses that satisfy the conditions of compatibility, is such that the variation of the complementary energy of the body vanishes.

For the present problem, one of plane stress, the expression for the complementary energy to be minimized may be written as

$$V = \sum_{i=1}^{3} \frac{1}{2E_i} \iint [\sigma_{x'i}^2 + \sigma_{y'i}^2 - 2\nu_i \sigma_{x'i}\sigma_{y'i} + 2(1+\nu_i)\tau_{x'y'i}]\,dx'idy'i$$
$$= \sum_{i=1}^{3} \frac{1}{2E_i} \iint [\sigma_{x'i},\ \sigma_{y'i},\ \tau_{x'y'i}][B_i] \begin{bmatrix} \sigma_{x'i} \\ \sigma_{y'i} \\ \tau_{x'y'i} \end{bmatrix} dx'idy'i \tag{12}$$

where

$$[B_i] = \begin{bmatrix} 1 & -\nu_i & 0 \\ -\nu_i & 1 & 0 \\ 0 & 0 & 2(1+\nu_i) \end{bmatrix}.$$

Applying equation (1) yields

$$V = \frac{1}{2E_1}\int_0^b \int_0^l [\sigma_{x1},\ \sigma_{y1},\ \tau_{xy1}][A]^T[B_1]$$
$$\times [A][\sigma_{x1},\ \sigma_{y1},\ \tau_{xy1}]^T \cos\alpha\, dxdy_1$$
$$+ \frac{1}{2E_2}\int_0^b \int_{-l}^0 [\sigma_{x2},\ \sigma_{y2},\ \tau_{xy2}][A]^T[B_2]$$
$$\times [A][\sigma_{x2},\ \sigma_{y2},\ \tau_{xy2}]^T \cos\alpha\, dxdy_2$$
$$+ \frac{1}{2E_3}\int_0^b \int_0^t [\sigma_{x3},\ \sigma_{y3},\ \tau_{xy3}][A]^T[B_3]$$
$$\times [A][\sigma_{x3},\ \sigma_{y3},\ \tau_{xy3}]^T \cos\alpha\, dxdy_2 \tag{13}$$

in which l represents the length of the adherends (l has actually no effect on the calculation because of the rapid decaying terms in the expressions for the stresses in the adherends).

After substituting expressions (4), (5), (6), and (9) into (13), integrating with respect to y_1 (or y_2), eliminating $\sigma_2(x)$ in the integrand by relation (11), and simplifying the results through the use of edge conditions (7), we obtain

$$V = \frac{1}{2}E_3 b^2 \cos\alpha \int_0^1 W(\bar{\sigma}_1,\ \lambda_1,\ \lambda_2)\,d\xi + \text{constant} \tag{14}$$

in which

$$\bar{\sigma}_1 = \sigma_1/E_3, \quad \xi = x/b$$

$$W(\bar{\sigma}_1,\ \lambda_1,\ \lambda_2) = A_1\left(\frac{d^2\bar{\sigma}_1}{d\xi^2}\right)^2$$
$$+ A_2\left(\frac{d\bar{\sigma}_1}{d\xi}\right)^2 + A_3(\bar{\sigma}_1)^2 + 2A_4\bar{\sigma}_1 \tag{15}$$

where

$$A_1 = \frac{1}{\cos^2\alpha}\left[\left(\frac{E_3}{E_1}\right)\frac{1}{2\lambda_1^5} + \left(\frac{E_3}{E_2}\right)\frac{\beta^2}{2\lambda_2^5} + \frac{1}{3}\left(\frac{\beta}{\lambda_2}\right)^2\left(\frac{t}{b}\right)^3\right.$$
$$+\frac{1}{20}\left(\frac{t}{b}\right)^3\left(\frac{1}{\lambda_1}+\frac{\beta}{\lambda_2}\right)^2 + \left(\frac{t}{b}\right)\frac{\beta^2}{\lambda_2^4} - \frac{1}{4}\left(\frac{t}{b}\right)^3\frac{\beta}{\lambda_2}\left(\frac{1}{\lambda_1}\right.$$
$$\left.\left.+\frac{\beta}{\lambda_2}\right) + \left(\frac{t}{b}\right)^2\frac{\beta^2}{\lambda_2^3} - \frac{1}{3}\left(\frac{t}{b}\right)^2\frac{\beta}{\lambda_2^2}\left(\frac{1}{\lambda_1}+\frac{\beta}{\lambda_2}\right)\right]$$

$$A_2 = \left(\frac{E_3}{E_1}\right)\frac{1+\nu_1}{\lambda_1^3} + \left(\frac{E_3}{E_2}\right)\frac{(1+\nu_2)\beta^2}{\lambda_2^3} + \left(\frac{t}{b}\right)\frac{2(1+\nu_3)\beta^2}{\lambda_2^2}$$
$$-\left(\frac{t}{b}\right)\frac{2(1+\nu_3)\beta}{\lambda_2}\left(\frac{1}{\lambda_1}+\frac{\beta}{\lambda_2}\right) + \frac{2}{3}\left(\frac{t}{b}\right)(1+\nu_3)\left(\frac{1}{\lambda_1}+\frac{\beta}{\lambda_2}\right)^2$$
$$+(\tan^2\alpha-\nu_3)\left(\frac{t}{b}\right)\left(\frac{1}{\lambda_1}+\frac{\beta}{\lambda_2}\right)\frac{\beta}{\lambda_2} - \frac{1}{3}(\tan^2\alpha-\nu_3)\left(\frac{t}{b}\right)\left(\frac{1}{\lambda_1}\right.$$
$$\left.+\frac{\beta}{\lambda_2}\right)^2 - \left(\frac{E_3}{E_1}\right)\frac{\tan^2\alpha-\nu_1}{\lambda_1^3} - \left(\frac{E_3}{E_2}\right)\frac{\tan^2\alpha-\nu_2}{\lambda_2^3}\beta^2$$
$$+2(\tan^2\alpha-\nu_3)\left(\frac{1}{\lambda_1}+\frac{\beta}{\lambda_2}\right)\frac{\beta}{\lambda_2^2}$$

$$A_3 = \frac{1}{\cos^2\alpha}\left[\frac{E_3}{E_1}\,\frac{1}{2\lambda_1} + \frac{E_3}{E_2}\,\frac{\beta^2}{2\lambda_2} + \left(\frac{b}{t}\right)\left(\frac{1}{\lambda_1}+\frac{\beta}{\lambda_2}\right)^2\right]$$

$$A_4 = \frac{\sigma_o}{E_3}\cos\alpha\left[\left(\frac{E_3}{E_1}\right)\frac{\tan^2\alpha-\nu_1}{\lambda_1}\right.$$

$$\left.+\beta\left(\frac{E_3}{E_2}\right)\frac{\tan^2\alpha-\nu_2}{\lambda_2}-(\tan^2\alpha-\nu_3)\left(\frac{1}{\lambda_1}+\frac{\beta}{\lambda_2}\right)\right]. \quad (16)$$

The two unknown parameters λ_1 and λ_2 in (14) cannot be determined by minimizing the functional W through the direct variational procedure, and specific optimization techniques should be designed for the case. The steps taken by the authors are as follows:

(1) Carrying out the variation $\delta V=0$ under the edge conditions (7), or their nondimensional form

$$\bar\sigma_{1|\xi=0}=0,\quad \frac{d\bar\sigma_1}{d\xi}\bigg|_{\xi=0}=0,$$

$$\bar\sigma_{1|\xi=1}=0,\quad \frac{d\bar\sigma_1}{d\xi}\bigg|_{\xi=1}=0 \quad (17)$$

the variational equation for the $\bar\sigma_1$ which renders the complementary energy a minimum (for the given λ_1 and λ_2) is obtained:

$$A_1\frac{d^4\bar\sigma_1}{d\xi^4}-A_2\frac{d^2\bar\sigma_1}{d\xi^2}+A_3\bar\sigma_1+A_4=0. \quad (18)$$

This is a fourth-order differential equation with constant coefficients.

(2) The solution of equation (18) may be written as

$$\bar\sigma_1=\bar\sigma_1^*(\xi,\lambda_1,\lambda_2)=k_1e^{\gamma_1\xi}+k_2e^{\gamma_2\xi}+k_3e^{-\gamma_1\xi}+k_4e^{-\gamma_2\xi}-\frac{A_4}{A_3} \quad (19)$$

in which $\pm\gamma_i(i=1,2)$ are the characteristic roots of the homogeneous solution of equation (18), i.e.,

$$A_1\gamma_i^4-A_2\gamma_i^2+A_3=0.$$

We note that k_i and γ_i depend on the two parameters λ_1 and λ_2 yet to be determined, and k_i may be found from the boundary conditions (17).

(3) Substituting (15) into (14), and integrating the first two terms by parts with the aid of (17) yield

$$\int_0^1 A_1[(\bar\sigma_1^*)'']^2d\xi=A_1\int_0^1(\bar\sigma^*)''d(\bar\sigma^*)'=A_1\int_0^1(\bar\sigma_1^*)''''\bar\sigma_1^*d\xi$$

$$\int_0^1 A_2[(\bar\sigma_1^*)']^2d\xi=A_2\int_0^1(\bar\sigma_1^*)'d(\bar\sigma_1^*)=-A_2\int_0^1(\bar\sigma_1^*)''\bar\sigma_1^*d\xi.$$

With the preceding expressions and equation (18), equation (14) becomes:

$$V=\frac{1}{2}E_3b^2\cos\alpha\int_0^1 A_4\bar\sigma_1^*(\xi,\lambda_1,\lambda_2)d\xi+\text{constant}=V(\lambda_1,\lambda_2) \quad (20)$$

which means that the complementary energy can now be considered as a known function of λ_1 and λ_2.

(4) Searching for the minimum point $(\lambda_1^*, \lambda_2^*)$ for the complementary energy function $V(\lambda_1,\lambda_2)$ (cf. (20)) is a typical problem of unconstrained optimization (Wolfe, 1978a). To solve the problem, a modified Newton method may be used. In the present numerical calculations, the first and second derivatives of the function appearing in the iteration procedures of the Newton method are replaced by their difference approximations.

(5) Having found the minimum point $(\lambda_1^*, \lambda_2^*)$, $\bar\sigma_1^*(\xi,\lambda_1^*,\lambda_2^*)$ together with λ_1^* and λ_2^* will determine the stress distribution in the joint through the use of (5), (6), (9), and (11) and the stresses acting on the bonding surfaces can be obtained through the use of (8).

Numerical Examples

Example (1). Butt joints ($\alpha=0$) with parameters $b'/t=20$, $\nu_1=\nu_2=\nu_3=0.25$ are considered. To show the influence of the different stiffnesses of the two adherends, three combinations of adherend stiffness are used in calculation:

(1) $E_1/E_3=20$, $E_2/E_3=5$
(1) $E_1/E_3=20$, $E_2/E_3=20$
(1) $E_1/E_3=20$, $E_2/E_3=100$.

The two decaying exponents λ_1^* and λ_2^* obtained for the present example are given in Table 1.

The shear and normal stresses σ_{t1}, σ_{t2}, σ_{n1}, σ_{n2} acting on the two bonding surfaces are shown in Fig. 2 and Fig. 3, respectively. From Fig. 2 it is seen that the shear stresses all have drastic variations in the edge zones of the joint and these variations are effected evidently by the different combinations of the two adherend stiffnesses. We note that the magnitudes of these stresses are manifestly much smaller than those of normal stresses. Figure 3 reveals that the normal stresses are also changing rapidly (from below the average tensile stress σ_o

Table 1 Decaying exponents for example (1)

E_1/E_3	E_2/E_3	λ_1^*	λ_2^*
20	5	45.7	4.8
20	20	41.6	41.6
20	100	30.1	103.0

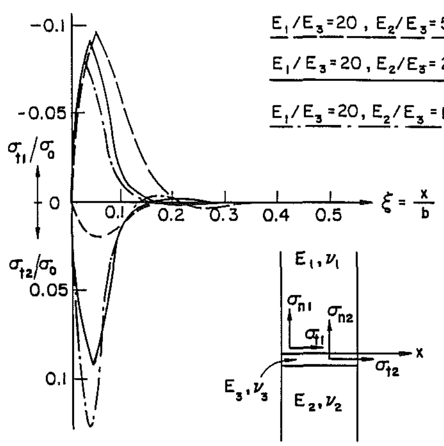

Fig. 2 Shear stresses acting on the bonding surfaces for example (1) (butt joints with $b'/t=20$, $\nu_i=0.25$, $E_1/E_3=20$)

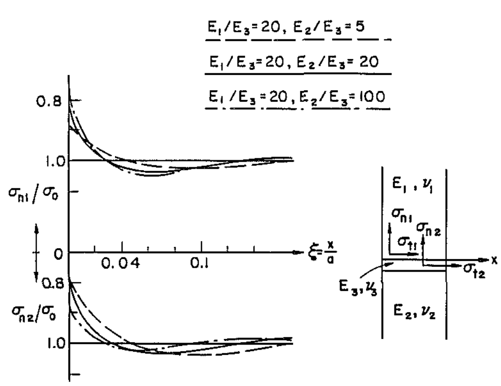

Fig. 3 Normal stresses acting on the bonding surfaces for example (1) (butt joints with $b'/t=20$, $\nu_i=0.25$, $E_1/E_3=20$)

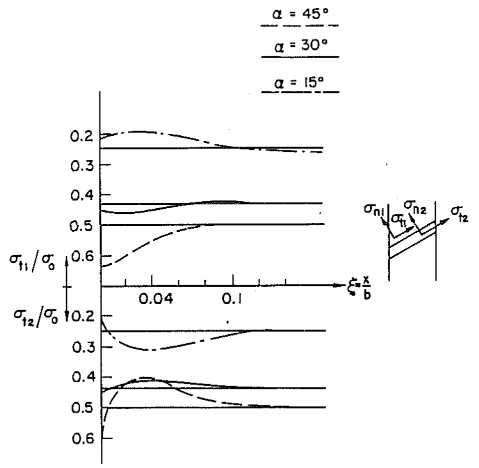

Fig. 4 Shear stresses acting on the bonding surfaces for example (2) (scarf joints with $b'/t = 20$, $\nu_i = 0.25$, $E_1 = E_2$)

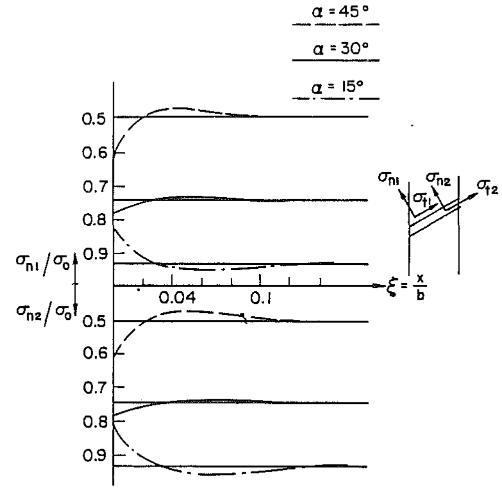

Fig. 5 Normal stresses acting on the bonding surfaces for example (2) (scarf joints with $b'/t = 20$, $\nu_i = 0.25$, $E_1 = E_2$)

to slightly greater than σ_o) in the narrow regions near the edge of the joint but the variations are not so strongly effected by the stiffness combinations of the two adherends as in the case of shear stresses. Figures 2 and 3 also show that for most parts of the bonding surfaces (except the narrow regions near the edge of the joint), the distribution of both shear stresses and normal stresses can be considered uniform (i.e., $\sigma_{t1} = \sigma_{t2} = 0$, $\sigma_{n1} = \sigma_{n2} = \sigma_0$) and this is true for all three stiffness combinations.

Example (2). Scarf joints with parameters $E_1/E_3 = E_2/E_3 = 20$, $b'/t = 20$, $\nu_1 = \nu_2 = \nu_3 = 0.25$ but with different scarf angles ($\alpha = 15$ deg, 30 deg, 45 deg) are considered. This is an example for scarf joints with two identical adherends. The shear and normal stresses acting on the bonding surfaces are partly shown in Figs. 4 and 5. Here, some rapid changes for these stresses in the edge zones of the joint still exist, and as can be expected with the increasing of the scarf angle, on the whole, the shear stresses increase and the normal stresses decrease. An important fact is still that for the central part of the bonding surfaces, the stress distribution can be seen as being uniform (i.e., $\sigma_{t1} = \sigma_{t2} = \sigma_o \sin\alpha \cos\alpha$, $\sigma_{n1} = \sigma_{n2} = \sigma_o \cos^2\alpha$) for all three scarf angles. Because of the equal stiffness of the two adherends, the two decaying exponents in this example are equal, and given in Table 2.

The data in Table 2 as well as what is given in Table 1 for the case $E_1/E_3 = E_2/E_3 = 20$, $\alpha = 0$ deg seem to suggest that for a scarf joint with two identical adherends, the decaying exponent for stresses increases with the increasing scarf angle (varying from 0 deg to 45 deg). But things are not necessarily so. We should note that in this calculation, the geometrical parameter t/b' is kept constant, meaning that the actual thickness of the adhesive layer (which is $t' = t \cdot \cos\alpha$; cf., Fig. 1) is decreasing with the increasing scarf angle. And it must also have some influence on the decaying exponents.

Conditions for Uniformly Distributed Adhesive Stresses

Lubkin (1957c) has shown, by means of an elementary analysis, that the stress distribution in the adhesive layer of a scarf joint was uniform for all scarf angles provided its adherends had identical elastic properties. He also deduced the scarf angle which would result in a uniform stress distribution for a joint with two different adherends. Lubkin's conclusions (1957d) give some insight into the situation but all the complexities in the local stresses near the edge of the joint are ignored. Now we are in a position to establish conditions for uniform distribution of adhesive stresses in scarf joints.

Returning to the variational equation (18), it is easy to see that the coefficient A_4 of the equation plays a key role in the

Table 2 Decaying exponents for example (2)

α	λ_1^*	λ_2^*
15 deg	43.7	43.7
30 deg	50.1	50.1
40 deg	59.6	59.6

uniformity of stresses. In fact, if $A_4 \equiv 0$, which means equation (18) is always homogeneous, the direct results in steps (2) and (3) will be

$$\bar{\sigma}_1^*(\xi, \lambda_1, \lambda_2) \equiv 0, \ V = \text{constant}$$

and the only possible solution for the problem is precisely the uniformly distributed stresses as may be seen from equation (9) ($\tau_{xy3} = \sigma_{x3} = 0$, $\sigma_{y3} = \sigma_o \cos\alpha$). From the expression for A_4 in (16), it is seen that $A_4 \equiv 0$ (for all possible λ_1 and λ_2) is equivalent to the conditions

$$\frac{E_3}{E_1}(\tan^2\alpha - \nu_1) = \tan^2\alpha - \nu_3,$$

$$\frac{E_3}{E_2}(\tan^2\alpha - \nu_2) = \tan^2\alpha - \nu_3. \quad (22)$$

For a scarf joint with two adherends having different elastic properties, (22) has generally no solutions for the scarf angle unless it happens that

$$\left(\nu_3 - \frac{E_3}{E_1}\nu_1\right) \Big/ \left(1 - \frac{E_3}{E_1}\right) = \left(\nu_3 - \frac{E_3}{E_2}\nu_2\right) \Big/ \left(1 - \frac{E_3}{E_2}\right) > 0$$

and, in this case,

$$\alpha = \tan^{-1}\sqrt{\frac{\nu_3 - (E_3/E_1)\nu_1}{1 - E_3/E_1}} \quad (23)$$

is the expected value which results in the uniformly distributed adhesive stresses.

As for a scarf joint with identical adherends, the two conditions in (22) become identical, so (23) is generally a solution (and is the only solution) for the expected value of the scarf angle, provided the quantity under the radical sign is positive. For instance, based on the parameters given in example (2), the expected scarf angle for uniform adhesive stresses will be $\alpha = 26.6$ deg. This is also justified by the relatively even curves for $\alpha = 30$ deg in Figs. 4 and 5.

So in a more rigorous sense, Lubkin's conclusion should be replaced by the criterion (22) or (23). On the other hand, if the term "uniformity" for the adhesive stresses is restricted only in the sense that all these stress components in the thin layer are almost independent of the coordinate x along the bonding surface (not excluding possible variations in the y direction), then the examples given in the last section and some further numerical data obtained by the present method seem to suggest that in the middle portion of a wide joint the adhesive stresses are generally uniform and seldom effected by the stiffness combinations of the joint.

Acknowledgment

The authors are grateful to the competitive research Grants Office of the U.S. Department of Agriculture for the partial support of this research through Grant 88-33521-4087.

References

Boresi, A. P., and Chong, K. P., 1987, *Elasticity in Engineering Mechanics*, Elsevier Science Publishing Co., Inc., p. 414.

Chen, D., and Cheng, S., 1983, "An Analysis of Adhesive-Bonded Single-Lap Joints," ASME JOURNAL OF APPLIED MECHANICS, Vol. 50, pp. 109-115.

Goland, M., and Reissner, E., 1944, "The Stresses in Cemented Joints," ASME JOURNAL OF APPLIED MECHANICS, Vol. 11, pp. A17-A22.

Lubkin, J. L., 1957, "A Theory of Adhesive Scarf Joints," ASME JOURNAL OF APPLIED MECHANICS, Vol. 24, p. 255.

Patrick, R. L., ed., 1976, *Treatise on Adhesion and Adhesives*, Vol. 4, Marcel Dekker, Inc., New York.

Thein Wah, 1976, "Plane Stress Analysis of a Scarf Joint," *J. Solids Structures*, Vol. 12, p. 491.

Washizu, K., 1968, *Variational Methods in Elasticity and Plasticity*, Pergamon Press, New York.

Wolfe, M. A., 1978, *Numerical Methods for Unconstrained Optimization*, Van Nostrand Reinhold Company, New York.

J. W. Klintworth
Engineering Department,
Cambridge University,
Cambridge, CB2 1PZ, U.K.

W. J. Stronge
Lecturer,
Engineering Department,
Cambridge University,
Cambridge, CB2 1PZ, U.K.

Plane Punch Indentation of Anisotropic Elastic Half Space

The stress distribution within a planar anisotropic half space is determined for normal or tangential displacements imposed over a small part of the surface. The general punch problem is then considered as a combination of these basic solutions. Results are presented for the normal, tangential, and rotary indentation of an arbitrarily-oriented half space by a flat frictional punch.

Introduction

Indentation of a punch into the surface of an elastic half space is a fundamental problem for explaining forming and contact damage processes. This is a mixed boundary value problem where stresses and displacements induced in the half space depend on friction at the contact surface. Johnson (1985) summarized the solutions of similar planar punch problems for isotropic materials. When the half space is anisotropic, the stress field is distorted by the effects of material orientation and the relative magnitudes of the elastic moduli. Lekhnitskii (1981) described solutions for stresses induced by line forces on the surface of an anisotropic half space two-dimensional Boussinesq and Cerruti problems). These solutions were obtained by a method of complex variable functions. That technique has also been employed for fomulating boundary integral methods that are used when tractions act on the boundaries of two-dimensional bodies of arbitrary shape (Benjumea and Sikarskie, 1972). In the present paper we use a potential function approach to construct solutions for planar punch problems in a anisotropic half space where there is no slip on the surface of a flat punch. This problem was previously investigated by Galin (1961) who showed that a coefficient of friction $\mu = 0.5$ is sufficient to prevent slip over most of the contact surface.

Elastic Constants of Anisotropic Materials

The elastic properties of a homogeneous, linear-elastic, anisotropic body in Cartesian x-y-z space can be described by 21 independent elastic coefficients which relate strains at any point to the stresses applied at that point. If the body is symmetrical about the x-y plane, the number of independent coefficients reduces to 13 (Lekhnitskii, 1981, p. 35)

$$\begin{bmatrix} \epsilon_x \\ \epsilon_y \\ \epsilon_z \\ \gamma_{yz} \\ \gamma_{xz} \\ \gamma_{xy} \end{bmatrix} = \begin{bmatrix} s_{11} & s_{12} & s_{13} & 0 & 0 & s_{16} \\ & s_{22} & s_{23} & 0 & 0 & s_{26} \\ & & s_{33} & 0 & 0 & s_{36} \\ & & & s_{44} & s_{45} & 0 \\ & & & & s_{55} & 0 \\ & & & & & s_{66} \end{bmatrix} \begin{bmatrix} \sigma_x \\ \sigma_y \\ \sigma_z \\ \tau_{yz} \\ \tau_{xz} \\ \tau_{xy} \end{bmatrix} \tag{1}$$

where $s_{ij} = s_{ji}$. If the body is in a state of plane stress in the x-y plane (i.e., $\sigma_z = \tau_{yz} = \tau_{xz} = 0$), the stress distribution in this plane is determined by the constitutive relations

$$\begin{bmatrix} \epsilon_x \\ \epsilon_y \\ \gamma_{xy} \end{bmatrix} = \begin{bmatrix} s_{11} & s_{12} & s_{16} \\ & s_{22} & s_{26} \\ & & s_{66} \end{bmatrix} \begin{bmatrix} \sigma_x \\ \sigma_y \\ \tau_{xy} \end{bmatrix}. \tag{2}$$

However, if the body is in a state of plane strain (i.e., $\epsilon_z = \gamma_{yz} = \gamma_{xz} = 0$) then $\tau_{yz} = \tau_{xz} = 0$ and $\sigma_z = - s_{13}\sigma_x/s_{33} - s_{23}\sigma_y/s_{33} - s_{36}\tau_{xy}/s_{33}$. Consequently, the effective in-plane constitutive relations become

$$\begin{bmatrix} \epsilon_x \\ \epsilon_y \\ \gamma_{xy} \end{bmatrix} = \begin{bmatrix} (s_{11} - s_{13}{}^2/s_{33}) & (s_{12} - s_{13}s_{23}/s_{33}) & (s_{16} - s_{13}s_{36}/s_{33}) \\ & (s_{22} - s_{23}{}^2/s_{33}) & (s_{26} - s_{23}s_{36}/s_{33}) \\ & & (s_{66} - s_{36}{}^2/s_{33}) \end{bmatrix} \begin{bmatrix} \sigma_x \\ \sigma_y \\ \tau_{xy} \end{bmatrix}. \tag{3}$$

The case of plane stress will be considered further for reasons of clarity.

Many anisotropic materials can be considered as orthotropic; i.e., they have three mutually perpendicular planes of symmetry. The elastic behavior of an orthotropic material in the $\xi - \eta$ plane of symmetry can be expressed in terms of the

Contributed by the Applied Mechanics Division of The American Society of Mechanical Engineers for publication in the Journal of Applied Mechanics.

Discussion on this paper should be addressed to the Editorial Department, ASME, United Engineering Center, 345 East 47th Street, New York, N.Y. 10017, and will be accepted until two months after final publication of the paper itself in the Journal of Applied Mechanics. Manuscript received by ASME Applied Mechanics Division, June 2, 1988; final revision, February 16, 1989.

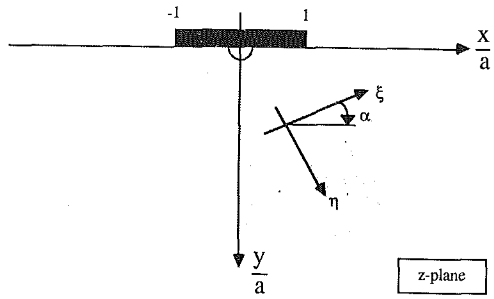

Fig. 1 Flat punch attached to an anisotropic half space

engineering elastic moduli E_ξ, E_η, $G_{\xi\eta}$, and Poisson's ratios $\nu_{\xi\eta}$, $\nu_{\eta\xi}$ (where $\nu_{\eta\xi}=\nu_{\xi\eta}E_\eta/E_\xi$). If the material axes $\xi-\eta$ are rotated through an angle α from the reference axes $x-y$ as shown in Fig. 1, the compliances are related to the engineering elastic constants by (Lekhnitskii, 1981, p. 48)

$$s_{11} = \frac{\cos^4\alpha}{E_\xi}+\left(\frac{1}{G_{\xi\eta}}-\frac{2\nu_{\xi\eta}}{E_\xi}\right)\sin^2\alpha\,\cos^2\alpha+\frac{\sin^4\alpha}{E_\eta} \tag{4}$$

$$s_{22} = \frac{\sin^4\alpha}{E_\xi}+\left(\frac{1}{G_{\xi\eta}}-\frac{2\nu_{\xi\eta}}{E_\xi}\right)\sin^2\alpha\,\cos^2\alpha+\frac{\cos^4\alpha}{E_\eta} \tag{5}$$

$$s_{12} = \left(\frac{1}{E_\xi}+\frac{1}{E_\eta}+\frac{2\nu_{\xi\eta}}{E_\xi}-\frac{1}{G_{\xi\eta}}\right)\sin^2\alpha\,\cos^2\alpha-\frac{\nu_{\xi\eta}}{E_\xi} \tag{6}$$

$$s_{66} = 4\left(\frac{1}{E_\xi}+\frac{1}{E_\eta}+\frac{2\nu_{\xi\eta}}{E_\xi}-\frac{1}{G_{\xi\eta}}\right)\sin^2\alpha\,\cos^2\alpha+\frac{1}{G_{\xi\eta}} \tag{7}$$

$$s_{16} = \left[2\left(\frac{\sin^2\alpha}{E_\eta}-\frac{\cos^2\alpha}{E_\xi}\right)+\left(\frac{1}{G_{\xi\eta}}-\frac{2\nu_{\xi\eta}}{E_\xi}\right)(\cos^2\alpha-\sin^2\alpha)\right]\sin\alpha\,\cos\alpha \tag{8}$$

$$s_{26} = \left[2\left(\frac{\cos^2\alpha}{E_\eta}-\frac{\sin^2\alpha}{E_\xi}\right)+\left(\frac{1}{G_{\xi\eta}}-\frac{2\nu_{\xi\eta}}{E_\xi}\right)(\cos^2\alpha-\sin^2\alpha)\right]\sin\alpha\,\cos\alpha. \tag{9}$$

The anisotropy of an orthotropic material in the $\xi-\eta$ plane can be represented by the nondimensional modulus parameters

$$\hat{E}=E_\xi/E_\eta \tag{10}$$

$$\hat{G}=2G_{\xi\eta}\,(2+\nu_{\xi\eta}+\nu_{\eta\xi})/(E_\xi+E_\eta) \tag{11}$$

and the compressibility is indicated by

$$\hat{\nu}=\nu_{\xi\eta}/\sqrt{E_\xi/E_\eta}=\nu_{\eta\xi}/\sqrt{E_\eta/E_\xi}. \tag{12}$$

If $\hat{\nu}=1$ the material appears incompressible when loaded along its principal axes. An isotropic material can only appear incompressible in a plane when loaded in plane strain.

Stress Functions for a Planar Anisotropic Half Space

The stress state of the body in the $x-y$ plane can be expressed in terms of the Airy stress function ϕ as a function of the complex spatial variable $z=x+iy$. In the absence of body forces, the equation for ϕ which satisfies the constitutive relations (2.2) and the condition of compatibility is given by (Green and Zerna, 1968, p. 204)

$$S^{11}_{22}\frac{\partial^4\phi}{\partial z^4}-4S^{11}_{12}\frac{\partial^4\phi}{\partial z^3\partial\bar{z}}+2(S^{11}_{11}+2S^{12}_{12})\frac{\partial^4\phi}{\partial z^2\partial\bar{z}^2}-4S^{12}_{11}\frac{\partial^4\phi}{\partial z\partial\bar{z}^3}+S^{22}_{11}\frac{\partial^4\phi}{\partial\bar{z}^4}=0 \tag{13}$$

where $\bar{z}$ denotes the complex conjugate of z, and

$$S^{11}_{22} = [s_{11}+s_{22}-s_{66}-2s_{12}+i(2s_{16}-2s_{26})]/4$$

$$S^{11}_{12} = [s_{11}-s_{22}+i(s_{16}+s_{26})]/4$$

$$S^{11}_{11} = [s_{11}+s_{22}+s_{66}-2s_{12}]/4$$

$$S^{12}_{12} = [s_{11}+s_{22}+2s_{12}]/4$$

$$S^{12}_{11} = \bar{S}^{11}_{12}$$

$$S^{22}_{11} = \bar{S}^{11}_{22}.$$

For half-space problems, it is convenient to define new spatial variables ζ_1 and ζ_2 by the transformation (Green and Zerna, 1968, p. 330)

$$\zeta_1 = x+i\left(\frac{1-\gamma_1}{1+\gamma_1}\right)y \tag{14}$$

$$\zeta_2 = x+i\left(\frac{1-\gamma_2}{1+\gamma_2}\right)y \tag{15}$$

where γ_1, γ_2 are defined by

$$|\gamma_1|<1;\ |\gamma_2|<1 \tag{16}$$

$$\bar{S}^{11}_{22}\gamma^4-4\bar{S}^{11}_{12}\gamma^3+2(S^{11}_{11}+2S^{12}_{12})\gamma^2-4\bar{S}^{12}_{11}\gamma+\bar{S}^{22}_{11}=0. \tag{17}$$

Then the stress σ_x, σ_y, τ_{xy} and displacement u, v at any point (x, y) in the anisotropic half space $y>0$ can be expressed in terms of the complex potentials f, g as follows (Green and Zerna, 1968, p. 331)

$$\theta = \sigma_x+\sigma_y=\frac{4\gamma_1}{(1+\gamma_1)^2}f''(\zeta_1)+\frac{4\bar{\gamma}_1}{(1+\bar{\gamma}_1)^2}\bar{f}''(\bar{\zeta}_1)+\frac{4\gamma_2}{(1+\gamma_2)^2}g''(\zeta_2)+\frac{4\bar{\gamma}_2}{(1+\bar{\gamma}_2)^2}\bar{g}''(\bar{\zeta}_2) \tag{18}$$

$$\Phi = \sigma_x-\sigma_y+2i\tau_{xy}=-\frac{4{\gamma_1}^2}{(1+\gamma_1)^2}f''(\zeta_1)-\frac{4}{(1+\bar{\gamma}_1)^2}\bar{f}''(\bar{\zeta}_1)-\frac{4{\gamma_2}^2}{(1+\gamma_2)^2}g''(\zeta_2)-\frac{4}{(1+\bar{\gamma}_2)^2}\bar{g}''(\bar{\zeta}_2) \tag{19}$$

$$D = u+iv=\frac{\delta_1}{1+\gamma_1}f'(\zeta_1)+\frac{\rho_1}{1+\bar{\gamma}_1}\bar{f}'(\bar{\zeta}_1)+\frac{\delta_2}{1+\gamma_2}g'(\zeta_2)+\frac{\rho_2}{1+\bar{\gamma}_2}\bar{g}'(\bar{\zeta}_2) \tag{20}$$

where

$$\delta_1 = -2(S^{11}_{11}{\gamma_1}^2-2S^{11}_{12}\gamma_1+S^{11}_{22})/\gamma_1$$

$$\delta_2 = -2(S^{11}_{11}{\gamma_2}^2-2S^{11}_{12}\gamma_2+S^{11}_{22})/\gamma_2$$

$$\rho_1 = -2(S^{11}_{11}-2S^{11}_{12}\bar{\gamma}_1+S^{11}_{22}{\bar{\gamma}_1}^2)$$

$$\rho_2 = -2(S^{11}_{11}-2S^{11}_{12}\bar{\gamma}_2+S^{11}_{22}{\bar{\gamma}_2}^2).$$

The complex potentials, f and g, can be determined by considering the appropriate loading conditions.

For the surface loading, the forms of the complex potentials on the boundary $y=0$ can be simplified by defining new complex potentials h and k by (Green and Zerna, 1968, p. 332)

$$h(\zeta)=\frac{2\gamma_1}{1+\gamma_1}f(\zeta)+\frac{2\gamma_2}{1+\gamma_2}g(\zeta) \tag{21}$$

$$k(\zeta)=\frac{2}{1+\gamma_1}f(\zeta)+\frac{2}{1+\gamma_2}g(\zeta) \tag{22}$$

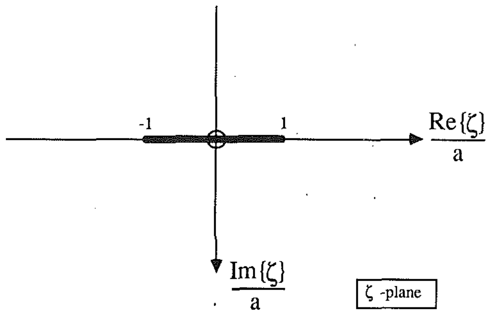

Fig. 2 ζ-plane with a cut on the loaded section

Writing equations (18) and (19) in terms of h'' and k'', then solving for the stresses σ_y and τ_{xy} gives

$$\sigma_y + i\tau_{xy} = \{h''(\zeta_1) - h''(\zeta_2) + \gamma_1 k''(\zeta_2) - \gamma_2 k''(\zeta_1)\}/(\gamma_1 - \gamma_2) + \{\bar{\gamma}_1 \bar{h}''(\bar{\zeta}_1) - \bar{\gamma}_2 \bar{h}''(\bar{\zeta}_2) - \bar{\gamma}_1 \bar{\gamma}_2 [\bar{k}''(\bar{\zeta}_1) - \bar{k}''(\bar{\zeta}_2)]\}/(\bar{\gamma}_1 - \bar{\gamma}_2) \tag{23}$$

$$\sigma_y - i\tau_{xy} = \{\bar{h}''(\bar{\zeta}_1) - \bar{h}''(\bar{\zeta}_2) + \bar{\gamma}_1 \bar{k}''(\bar{\zeta}_2) - \bar{\gamma}_2 \bar{k}''(\bar{\zeta}_1)\}/(\bar{\gamma}_1 - \bar{\gamma}_2) + \{\gamma_1 h''(\zeta_1) - \gamma_2 h''(\zeta_2) - \gamma_1 \gamma_2 [k''(\zeta_1) - k''(\zeta_2)]\}/(\gamma_1 - \gamma_2). \tag{24}$$

At the surface of the half space, $y=0$ and $\zeta_1 = \zeta_2 = \zeta = x$. Consequently, the stresses at the surface can be written directly in terms of $h''(\zeta)$ and $k''(\zeta)$.

$$\sigma_y = [h''(\zeta) + \bar{h}''(\bar{\zeta}) + k''(\zeta) + \bar{k}''(\bar{\zeta})]/2 \tag{25}$$

$$\tau_{xy} = [-h''(\zeta) + \bar{h}''(\bar{\zeta}) + k''(\zeta) - \bar{k}''(\bar{\zeta})]/2i \tag{26}$$

Similarly, the displacements in the anisotropic half space can be written in terms of $h'(\zeta)$ and $k'(\zeta)$. Since $\zeta = x$ at the surface of the half space, the rate of change of the displacement along the surface $\overset{\square}{D} = \partial D/\partial x|_{y=0}$ (the "surface displacement variation rate") can be related to $h''(\zeta)$ and $k''(\zeta)$ as follows

$$\overset{\square}{D} = \overset{\square}{u} + i\overset{\square}{v} = [C_1 h''(\zeta) + C_3 \bar{h}''(\bar{\zeta}) - C_3 k''(\zeta) - C_2 \bar{k}''(\bar{\zeta})]/2 \tag{27}$$

$$\overset{\square}{u} = [(C_1 + \bar{C}_3) h''(\zeta) + (C_3 + C_1)\bar{h}''(\bar{\zeta}) - (C_3 + C_2) k''(\zeta) - (C_2 + \bar{C}_3]\bar{k}''(\bar{\zeta})]/4 \tag{28}$$

$$\overset{\square}{v} = [(C_1 - \bar{C}_3) h''(\zeta) + (C_3 - C_1)\bar{h}''(\bar{\zeta}) - (C_3 - C_2) k''(\zeta) - (C_2 - \bar{C}_3)\bar{k}''(\bar{\zeta})]/4i \tag{29}$$

where

$$C_1 = \bar{C}_1 = -2\left(S_{11}^{11} - \frac{S_{22}^{11}}{\gamma_1\gamma_2}\right)$$

$$C_2 = \bar{C}_2 = 2\left(S_{11}^{11} - S_{22}^{11}\bar{\gamma}_1\bar{\gamma}_2\right)$$

$$C_3 = \frac{S_{22}^{11}}{\gamma_1\gamma_2}[\gamma_1 + \gamma_2 - \gamma_1\gamma_2(\bar{\gamma}_1 + \bar{\gamma}_2)].$$

These constants depend on the elastic properties of the half space as illustrated in Table 1. C_1 and C_2 take on real values and the difference $(C_1 - C_2)$ reflects the compressibility of the material when loaded along its principal axes. C_3 takes on a complex value which depends on the orientation of the principal directions ξ, η relative to the surface.

The solution of the complex potentials h and k is simplified by extending the definition of the potentials to the entire ζ-plane. The potentials can be specified arbitrarily in the region $\mathrm{Im}(\zeta) < 0$ without affecting the problem. Therefore, we can replace the definition of one potential in the half space $\mathrm{Im}(\zeta) > 0$ in terms of the other potential in the notational region $\mathrm{Im}(\zeta) < 0$. As a result, the elastic state of the body can be expressed in terms of the two complex functions h and k defined over the whole plane. The relationship between these complex potentials is chosen so that their derivatives are continuous over the unloaded portion of the surface $y = \mathrm{Im}(\zeta) = 0$. Consequently, they are analytic over the whole ζ-plane with a cut on the load section as shown in Fig. 2. The potentials can then be evaluated by complex integration along a contour surrounding the cut.

Defining h and k in the half plane $\mathrm{Im}(\zeta) < 0$ by (Green and Zerna, 1968, p. 332),

$$h(\zeta) = -\bar{k}(\zeta) \tag{30}$$

$$k(\zeta) = -\bar{h}(\zeta) \tag{31}$$

it follows that in the half plane $\mathrm{Im}(\zeta) > 0$,

$$h(\bar{\zeta}) = -\bar{k}(\bar{\zeta}) \tag{32}$$

$$k(\bar{\zeta}) = -\bar{h}(\bar{\zeta}). \tag{33}$$

Therefore, the stresses at the surface $y=0$ can be expressed in terms of h'' and k'' by substituting for $\bar{h}''(\bar{\zeta})$ and $\bar{k}''(\bar{\zeta})$ in (4.14) and (4.15)

$$\sigma_y = \{[h''(x)]^+ - [h''(x)]^- + [k''(x)]^+ - [k''(x)]^-\}/2 \tag{34}$$

$$\tau_{xy} = \{-[h''(x)]^+ + [h''(x)]^- + [k''(x)]^+ - [k''(x)]^-\}/2i \tag{35}$$

where $[h(x)]^+$ denotes $\lim_{y \to 0+} h(\zeta)$. Similarly, the surface displacement variation can be expressed by

$$\overset{\square}{u} = \{(C_1 + \bar{C}_3)[h''(x)]^+ + (C_2 + \bar{C}_3)[h''(x)]^- - (C_3 + C_2)[k''(x)]^+ - (C_3 + C_1)k''(x)]^-\}/4 \tag{36}$$

$$\overset{\square}{v} = \{(C_1 - \bar{C}_3)[h''(x)]^+ + (C_2 - \bar{C}_3)[h''(x)]^- - (C_3 - C_2)[k''(x)]^+ - (C_3 - C_1)[k''(x)]^-\}/4i. \tag{37}$$

The relationship between the complex potentials h and k is determined by the resultant force on the half space. If the stresses and rotations vanish at infinity, it can be shown that

$$h''(\zeta) = -\frac{P}{2\pi}\frac{1}{\zeta} + O\left(\frac{1}{\zeta^2}\right) \tag{38}$$

$$k''(\zeta) = \frac{\bar{P}}{2\pi}\frac{1}{\zeta} + O\left(\frac{1}{\zeta^2}\right). \tag{39}$$

Therefore a relationship between the complex functions k'' and h'' can be defined in terms of the resultant force due to the tractions acting on the half space.

Normal Tractions ($k_1 = h_1$). For a force $P = iY$ which acts perpendicular to the surface, equations (38) and (39) are satisfied if $h_1 = k_1$. This particular solution has been obtained by Green and Zerna (1968, pp. 341–344). The equations for stresses at the surface $y=0$ reduce to

$$\sigma_y = [h''_1(x)]^+ - [h''_1(x)]^- \tag{40}$$

$$\tau_{xy} = 0 \tag{41}$$

and the rate of change of the normal component of surface displacement is given by

$$\overset{\square}{v}_1 = \{[h''_1(x)]^+ + [h''_1(x)]^-\}(C_1 + C_2 - C_3 - \bar{C}_3)/4i. \tag{42}$$

If the surface is free of tractions except for the interval $-a<x<a$ where the normal component of surface displacement is prescribed,

$$[h''_1(x)]^+ + [h''_1(x)]^- = 4i\dot{v}_1/(C_1+C_2-C_3-\bar{C}_3),\ |x|<a \tag{43}$$

$$[h''_1(x)]^+ - [h''_1(x)]^- = 0, \qquad |x|>a. \tag{44}$$

The solution to the Hilbert problem is

$$h''_1(\zeta) = \frac{2}{\pi(C_1+C_2-C_3-\bar{C}_3)\sqrt{a^2-\zeta^2}} \times \int_{-a}^{a} \frac{\dot{v}_1(x)\sqrt{a^2-x^2}}{(x-\zeta)}dx - \frac{Y}{2\pi\sqrt{a^2-\zeta^2}} \tag{45}$$

where Y is the magnitude of the resultant indentation force. As a result of the prescribed normal displacement, there is a secondary rate of change in the tangential component of surface displacement

$$\dot{u}_1 = \{[(C_1+\bar{C}_3)-(C_3+C_2)]h''_1(\zeta) + [(C_3+C_1)-(C_2+\bar{C}_3]\bar{h}''_1(\bar{\zeta})\}/4. \tag{46}$$

Tangential Tractions ($k_2=-h_2$). For a force $P=X$ which acts tangential to the surface, equations (38) and (39) are satisfied if $k_2=-h_2$. Then, the equations for the stresses at the surface $y=0$ reduce to

$$\sigma_y = 0 \tag{47}$$

$$\tau_{xy} = \{-[h''_2(x)]^+ + [h''_2(x)]^-\}/i \tag{48}$$

and the rate of change of the tangential component of surface displacement is given by:

$$\dot{u}_2 = \{[h''_2(x)]^+ + [h''_2(x)]^-\}(C_1+C_2+C_3+\bar{C}_3)/4. \tag{49}$$

If the surface is free of tractions, expect for the interval $-a<x<a$ where the tangential component of surface displacement is prescribed,

$$[h''_2(x)]^+ + [h''_2(x)]^- = 4u_2/(C_1+C_2+C_3+\bar{C}_3), \quad |x|<a \tag{50}$$

$$[h''_2(x)]^+ - [h''_2(x)]^- = 0, \quad |x|>a. \tag{51}$$

The solution to the Hilbert problem is

$$h''_2(\zeta) = -\frac{2i}{\pi(C_1+C_2+C_3+\bar{C}_3)\sqrt{a^2-\zeta^2}} \times \int_{-a}^{a} \frac{\dot{u}_2(x)\sqrt{a^2-x^2}}{(x-\zeta)}dx + \frac{iX}{2\pi\sqrt{a^2-\zeta^2}} \tag{52}$$

where X is the magnitude of the resultant indentation force. As a result of the prescribed tangential displacement, there is a secondary rate of change of the normal component of surface displacement

$$\dot{v}_2 = \{[(C_1-\bar{C}_3)+(C_3-C_2)]h''_2(\zeta) + [(C_3-C_1)+(C_2-\bar{C}_3)]\bar{h}''_2(\bar{\zeta})\}/4i. \tag{53}$$

General Punch Problems

The general problem of indentation by a rigid block is called the punch problem. For a given punch without slip on the contact surface, the boundary conditions at the surface of the halfspace are

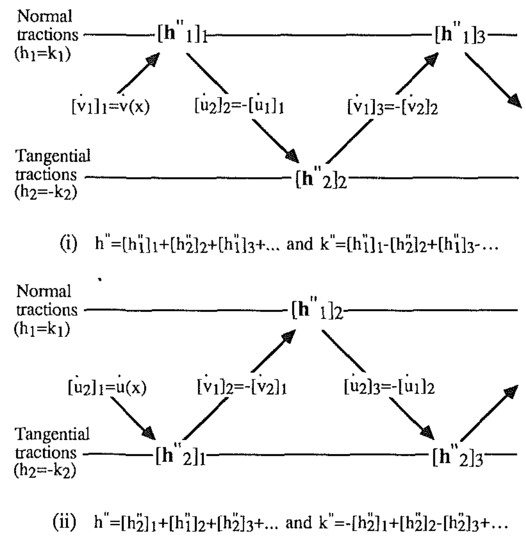

Fig. 3 Solution procedure for coupled punch problem; (*i*) normal and (*ii*) tangential loading

$$u=u(x);\ v=v(x), \quad |x|<a \tag{54}$$

$$\sigma_y=0;\ \tau_{xy}=0, \qquad |x|>a.$$

The solution to this problem can be obtained by superimposing independent solutions for normal and tangential tractions only. Substituting $\dot{u}=\dot{u}_1+\dot{u}_2$ and $\dot{v}=\dot{v}_1+\dot{v}_2$ into (45) and (52) we obtain two coupled integral equations which must be solved for $h''_1(\zeta)$ and $h''_2(\zeta)$.

$$h''_1(\zeta) = \frac{2}{\pi(C_1+C_2-C_3-\bar{C}_3)\sqrt{a^2-\zeta^2}} \times \int_{-a}^{a} \frac{[\dot{v}-\dot{v}_2(h''_2)]\sqrt{a^2-x^2}}{(x-\zeta)}dx - \frac{Y}{2\pi\sqrt{a^2-\zeta^2}} \tag{55}$$

$$h''_2(\zeta) = -\frac{2i}{\pi(C_1+C_2+C_3+\bar{C}_3)\sqrt{a^2-\zeta^2}} \times \int_{-a}^{a} \frac{[\dot{u}-\dot{u}_2(h''_1)]\sqrt{a^2-x^2}}{(x-\zeta)}dx - \frac{iX}{2\pi\sqrt{a^2-\zeta^2}} \tag{56}$$

Then the stress and displacement fields can be calculated using the potentials

$$h''(\zeta)=h''_1(\zeta)+h''_2(\zeta) \text{ and } k''(\zeta)=h''_1(\zeta)-h''_2(\zeta).$$

An iterative solution can be obtained by initially neglecting the tangential tractions under normal loading, and vice versa. The resulting secondary surface displacements beneath the punch can then be counteracted by superimposing further complex functions until the corrections are negligibly small, as shown in Fig. 3(*i*) and 3(*ii*) for normal and tangential loading, respectively.

The magnitudes of the secondary displacements reflect the coupling between normal and tangential displacements and this depends on the elastic properties of the half space. For example, when a frictionless flat punch indents as isotropic half space under plane-strain conditions, the material at the edge of the punch deforms towards its center if the material is compressible (effective Poisson's ratio $\nu/(1-\nu)<1$). But if the material is incompressible, the tangential displacement at the surface is zero. Many anisotropic composite materials appear relatively incompressible because their bulk modulus is large compared with their shear moduli. In particular, low-density cellular materials are highly compliant in shear because the flexural rigidity of the cell walls is small. In this case, the first

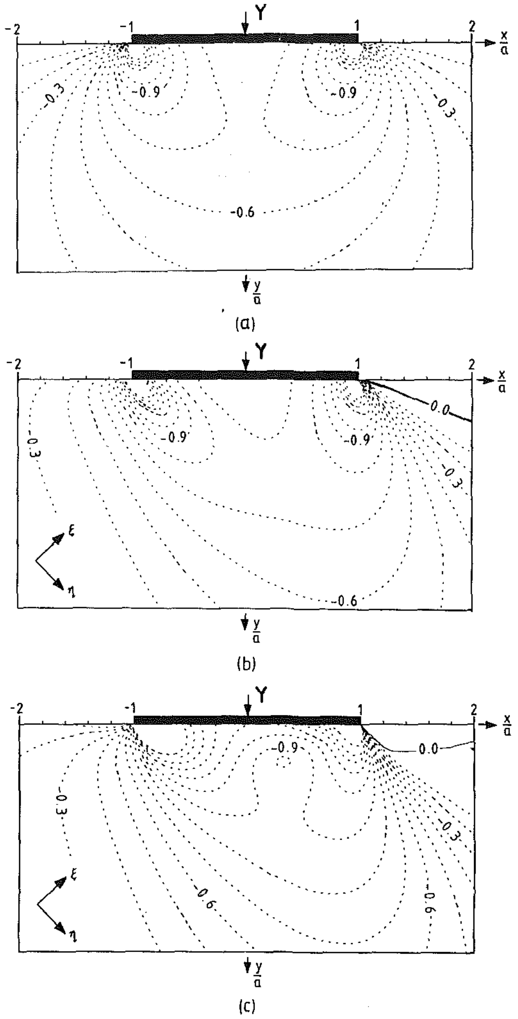

Fig. 4 Ratio of principal compressive stress to average normal tractions for normal indentation; (*a*) isotropic incompressible, (*b*) anisotropic incompressible, and (*c*) anisotropic compressible materials

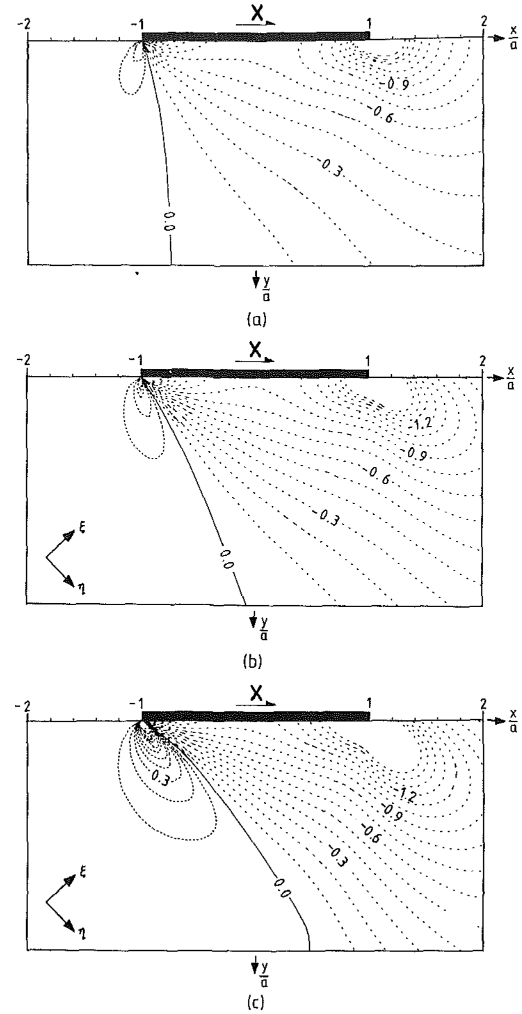

Fig. 5 Ratio of principal compressive stress to average tangential tractions for tangential identation; (*a*) isotropic incompressible, (*b*) anisotropic incompressible, and (*c*) anisotropic compressible materials

Table 1 Material properties

Description	(*a*) Isotropic Incompressible	(*b*) Anisotropic Incompressible	(*c*) Anisotropic Compressible
$\hat{E}$	$\cong 1$	¼	¼
$\hat{G}$	1	1	1
ν	1	1	0
α	–	45 deg	45 deg
C_1	$\cong 4.00$	5.03	7.53
C_2	$\cong 4.00$	5.03	2.53
C_3	$\cong 0.00$	$0.00 - i\,1.68$	$0.00 - i\,1.68$

approximations given in the previous section are sufficiently accurate for most purposes.

Here we consider the general problem of a flat punch attached to the half space, so that $\overset{\square}{u}(x)=0$ and $\overset{\square}{v}(x)=\text{constant}$. This problem can be considered as a combination of the limiting cases of normal, tangential, or rotational resultant forces on the punch. These cases will be solved to a second approximation in order to estimate the likely error of the basic solution.

Normal Indentation. Consider a punch applying a normal force on the half space. If $\overset{\square}{v}(x)=0$, the complex potential $[h_1'']_1$ is given by

$$[h_1''(\zeta)]_1 = -\frac{Y}{2\pi\sqrt{a^2-\zeta^2}}. \tag{57}$$

This causes a secondary surface displacement variation rate beneath the punch

$$[\overset{\square}{u}_1]_1 = \{(C_1 - C_2 - C_3 + \bar{C}_3)[h''_1(\zeta)]_1 + (C_1 - C_2 + C_3 - \bar{C}_3)[\bar{h}''_1(\bar{\zeta})]_1\}/4 = -\frac{(C_1 - C_2)Y}{4\pi\sqrt{a^2-x^2}}. \tag{58}$$

The tangential displacement is canceled by applying tangential tractions on the half space such that $[\overset{\square}{u}_2]_2 = -[\overset{\square}{u}_1]_1$. The equation for the required complex potential $[h_2'']_2$ is given by

$$[h_2''(\zeta)]_2 = -\frac{i(C_1-C_2)Y}{2\pi^2(C_1+C_2+C_3+\bar{C}_3)\sqrt{a^2-\zeta^2}}\int_{-a}^{a}\frac{1}{(x-\zeta)}dx$$
$$= -\frac{i(C_1-C_2)Y}{2\pi^2(C_1+C_2+C_3+\bar{C}_3)\sqrt{a^2-\zeta^2}}\ln\left(\frac{\zeta-a}{\zeta+a}\right). \tag{59}$$

When the magnitude of this secondary complex potential is large, it causes a significant normal surface displacement variation rate $[\overset{\square}{v}_2]_2$. This can be canceled by superimposing additional complex potentials $[h_1'']_3$, etc., until the secondary displacements are negligibly small.

Contours of principal compressive stress divided by the average normal traction are presented in Fig. 4 for the material specifications listed in Table 1. Material (*a*) is almost isotropic and incompressible while material (*b*) is anisotropic and incompressible. Here the stress distribution is determined solely by the primary complex function $[h_1''(\zeta)]_1$. In contrast, material (c) is compressible and the stress distribution is altered by the secondary complex function $[h_2''(\zeta)]_2$. The effect of the secondary displacements is noticeable near the corners of the punch but diffuses rapidly away from the loaded surface.

Tangential Indentation. In the same manner, we consider a punch applying a tangential force on the half space. If $\mathring{u}(x)=0$, the complex potential $[h_2'']_1$ is given by

$$[h_2''(\zeta)]_1=\frac{iX}{2\pi\sqrt{a^2-\zeta^2}}. \tag{60}$$

This causes a secondary surface displacement variation rate beneath the punch

$$[\mathring{v}_2]_1=\{C_1-C_2+C_3-\bar{C}_3)[h_2''(\zeta)]_1$$
$$+(-C_1+C_2+C_3-\bar{C}_3)[\bar{h}_2''(\bar{\zeta})]_1/4i=\frac{(C_1-C_2)X}{4\pi\sqrt{a^2-x^2}}. \tag{61}$$

The coupling is reflected by the factor $(C_1-C_2)/2$ as before. The normal displacement is cancelled by applying fictitious tractions on the half space such that $[\mathring{v}_1]_2=-[\mathring{v}_2]_1$. The equation for the required complex potential $[h_1'']_2$ is given by

$$[h_1''(\zeta)]_2=-\frac{(C_1-C_2)X}{2\pi^2(C_1+C_2-C_3-\bar{C}_3)\sqrt{a^2-\zeta^2}}\int_{-a}^{a}\frac{1}{(x-\zeta)}dx$$
$$=-\frac{(C_1-C_2)X}{2\pi^2(C_1+C_2-C_3-\bar{C}_3)\sqrt{a^2-\zeta^2}}\ln\left(\frac{\zeta-a}{\zeta+a}\right). \tag{62}$$

Contours of principal compressive stress divided by the average tangential traction are presented in Fig. 5 for three material specifications.

Rotary Indentation. We assume that the problem is dominated by normal tractions. Then if the punch rotates through $\mathring{v}(x)=\epsilon$ when loaded by a moment M, the complex potential $[h_1'']_1$ is given by

$$[h_1''(\zeta)]_1=\frac{2\epsilon}{\pi(C_1+C_2-C_3-\bar{C}_3)\sqrt{a^2-\zeta^2}}\int_{-a}^{a}\frac{\sqrt{a^2-x^2}}{(x-\zeta)}dx$$
$$=\frac{2i\epsilon}{(C_1+C_2-C_3-\bar{C}_3)}\left(1+\frac{i\zeta}{\sqrt{a^2-\zeta^2}}\right) \tag{63}$$

where the integral is evaluated by replacing it with a contour integral around the cut $[-a{:}a]$. The moment M is related to the punch rotation by

$$M=-\int_{-a}^{a}\sigma_y x dx=\frac{2\pi a^2\epsilon}{(C_1+C_2-C_3-\bar{C}_3)} \tag{64}$$

and the complex potential can be written

$$[h_1''(\zeta)]_1=\frac{iM}{\pi a^2}\left(1+\frac{i\zeta}{\sqrt{a^2-\zeta^2}}\right). \tag{65}$$

This causes a secondary surface displacement variation rate beneath the punch of

$$[\mathring{u}_1]_1=\{(C_1-C_2-C_3+\bar{C}_3)[h_1''(\zeta)]_1$$
$$+(C_1-C_2+C_3-\bar{C}_3)[\bar{h}_1''(\bar{\zeta})]_1\}/4$$
$$=-\frac{iM}{2\pi a^2}\left[(C_3-\bar{C}_3)-\frac{i(C_1-C_2)x}{\sqrt{a^2-x^2}}\right]. \tag{66}$$

The tangential displacement is canceled by applying tangential tractions on the half space such that $[\mathring{u}_2]_2=-[\mathring{u}_1]_1$. The equation for the required complex potential $[h_2'']_2$ is given by

$$[h_2''(\zeta)]_2=\frac{M}{\pi^2a^2(C_1+C_2+C_3+\bar{C}_3)\sqrt{a^2-\zeta^2}}$$

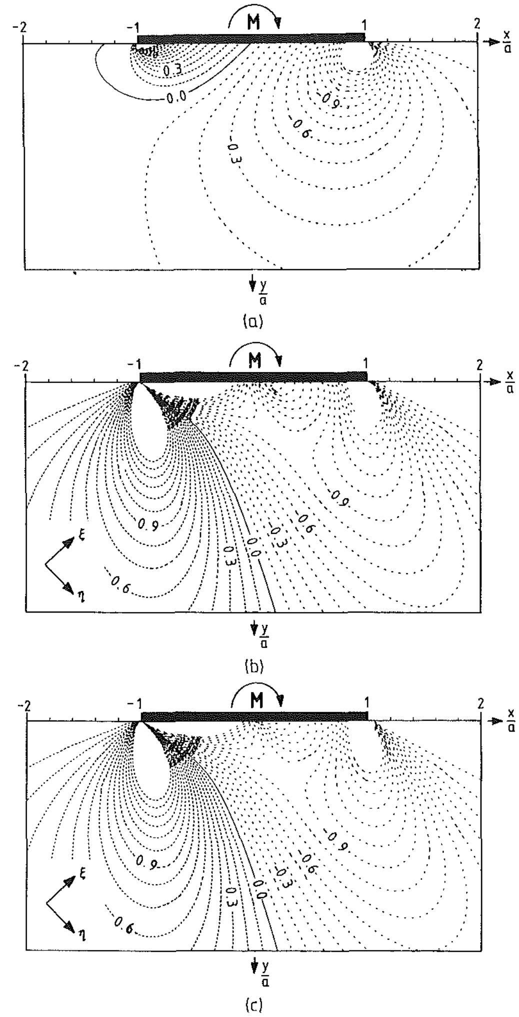

Fig. 6 Ratio of principal compressive stress to average normal tractions for rotary indentation; (*a*) isotropic incompressible, (*b*) anisotropic incompressible, and (*c*) anisotropic compressible materials

$$\times\left\{(C_3-\bar{C}_3)\int_{-a}^{a}\frac{\sqrt{a^2-x^2}}{(x-\zeta)}dx-i(C_1-C_2)\int_{-a}^{a}\frac{x}{(x-\zeta)}dx\right\}$$
$$=\frac{iM}{\pi^2a^2(C_1+C_2+C_3+\bar{C}_3)}$$
$$\times\left\{\pi(C_3-\bar{C}_3)\left(1+\frac{i\zeta}{\sqrt{a^2-\zeta^2}}\right)\right.$$
$$\left.-\frac{(C_1-C_2)}{\sqrt{a^2-\zeta^2}}\left[2a+\zeta\ln\left(\frac{\zeta-a}{\zeta+a}\right)\right]\right\}. \tag{67}$$

Contours of principal compressive stress, divided by the average normal traction, are presented in Fig. 6 for three material specifications.

Discussion

The punch problem in the absence of slip can be considered as a superposition of particular solutions for purely normal or shear tractions. An iterative method for solving the general punch problem is proposed whereby a basic solution is modified by higher-order potentials. The basic solution reflects the net force on the punch, while the higher-order potentials apply corrections near the contact region. In general, the magnitude of each succeeding potential compared with its predecessor is of the order

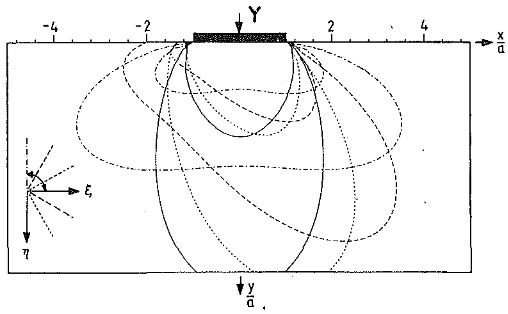

Fig. 7 Variation of principal compressive stress contours with material orientation for $\hat{E} = 1/4$ and $\alpha = 0$ deg, 30 deg, 60 deg, 90 deg

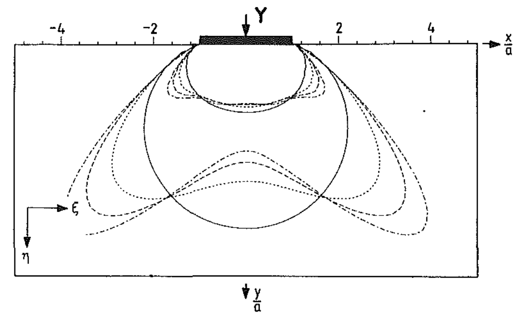

Fig. 8 Variation of principal compressive stress contours for $\hat{G} = 1$, 2, 3, 4

$$[h'']_{i+1}/|[h'']_i| = O\{(C_1 - C_2)/(C_1 + C_2 + C_3 + \bar{C}_3)\}$$

$$\text{or } O\{(C_3 - \bar{C}_3)/C_1 + C_2 + C_3 + \bar{C}_3)\} \tag{68}$$

so that erroneous displacements decrease exponentially with each iteration. In particular, the basic solution tends towards the true solution as the compressibility of the material decreases, the principal axes of the material become aligned with the surface and the distance from the punch increases.

Contours of stress are elongated in the direction of high modulus. Figure 7 illustrates the transformation of contours of principal compressive stress in an anisotropic material with $\hat{E} = 1/4$ as it is rotated relative to the surface of the half space. The stress distribution is highly asymmetrical when the material axes do not coincide with the surface. The shear modulus indicates the stiffness of the material at 45 deg to its principal axes. Figure 8 shows the expansion of contours of principal compressive stress in these directions as the non-dimensional shear modulus parameter $\hat{G}$ increases.

An anisotropic elastic material is likely to have an anisotropic failure criterion. Hill (1950) proposed a simple yield criterion for orthotropic materials which reduces to von Mises' law for vanishing anisotropy. For plane stress this criterion reduces to

$$(G+H)\sigma_\xi{}^2 - 2H\sigma_\xi\sigma_\eta + (F+H)\sigma_\eta{}^2 + 2N\tau_{\xi\eta}^2 = 1 \tag{69}$$

where F, G, H and N can be calculated from experimental results. If, for example, the yield stresses are proportional to the moduli in the principal directions, the yield criterion can be written as

$$\frac{(1+\hat{E})^2}{4\hat{E}^2}\sigma_\xi{}^2 - \frac{(1+2\hat{E}-2\hat{E}^2+2\hat{E}^3+\hat{E}^4)}{4\hat{E}^2}\sigma_\xi\sigma_\eta + \frac{(1+\hat{E})^2}{4}\sigma_\eta{}^2 + \frac{3}{\hat{G}}\tau_{\xi\eta}^2 = Y^2 \tag{70}$$

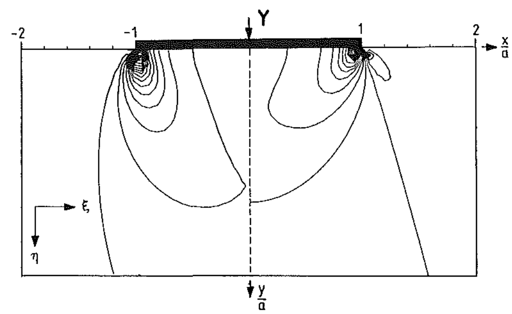

Fig. 9 Contours of effective von Mises (left half) and Hill (right half) yield stress for $\hat{E} = 1/4$

where Y is the average yield stress for the principal directions. Contours of effective yield stress in an anisotropic half space according to the von Mises and Hill criteria are compared in Fig. 9. This suggests that the distribution of yielding beneath a punch is highly sensitive to the anisotropy of the yield criterion.

References

Benjumea, L. A., and Sikarskie, D. L. 1972, "On the Solution of Plane, Orthotropic Elasticity Problems by an Integral Method," ASME Journal of Applied Mechanics, Vol. 39, pp. 801–808.

Galin, L. A. 1961, *Contact Problems in the Theory of Elasticity*, translation from Russian, I.N. Sneddon, ed., North Carolina State College, Raleigh, N.C.

Green, A. E. and Zerna, W., 1968, *Theoretical Elasticity*, Oxford University Press, Oxford, U.K.

Hill, R., 1950, *The Mathematical Theory of Plasticity*, Oxford University Press, Oxford, U.K.

Johnson, K. L., 1985, *Contact Mechanics*, Cambridge University Press, Cambridge, U.K.

Lekhnitski, S. G., 1981, *Theory of Elasticity of an Anisotropic Body*, Mir Publishers, Moscow.

Chien H. Wu
Professor,
Fellow ASME

Chao-Hsun Chen
Graduate Student.

Department of Civil Engineering,
Mechanics, and Metallurgy,
University of Illinois at Chicago,
Chicago, IL 60680

A Crack in a Confocal Elliptic Inhomogeneity Embedded in an Infinite Medium

A family of confocal ellipses may be characterized by a single parameter, $\rho > 1$. In the limit as $\rho \to 1$, the ellipse degenerates into a straight line of length 2. It tends to a circle of infinite radius as $\rho \to \infty$. The geometry of the title problem is fixed by the crack ($\rho = 1$) and the size of an elliptic inhomogeneity ($\rho = \rho_o$). Both the inhomogeneity and the infinite medium are assumed to be homogeneous and isotropic. Plane and anti-plane solutions associated with remote loading conditions are obtained. The solutions depend, among other parameters, on the size of the inhomogeneity ρ_o. Special attention is placed on determining the various limits as $\rho_o \to 1$.

1 Introduction

When a crack is wholly embedded in an inhomogeneity or when the crack tips are separately lodged in disjointed inhomogeneities, differences between the moduli of the inhomogeneity and the matrix material can cause the stress intensity factor (SIF) to be greater or less than that prevailing in a homogeneous body. With the problem of crack damage interaction in mind, the inhomogeneities are taken to be vanishingly small and softer than the matrix. This is the range in which we place our emphasis, even though the title problem is solved for the full ranges of the parameters.

For a finite crack with tips lodged in vanishingly small tip inhomogeneities, the asymptotic limit is the solution for a semi-infinite crack lodged in an inhomogeneity of finite size. The case of a semi-infinite crack penetrating a circular inhomogeneity was studied by Steif (1987). Noncircular inhomogeneities were considered by Hutchinson (1986). The class of problems may be approximated by a simple calculation (Wu, 1988) and accurately solved by a straightforward numerical scheme (Wu and Chen, 1989).

The present problem differs from the previous one in that the complete crack is wholly surrounded by the inhomogeneity even if the size of the inhomogeneity is let to tend to zero. Moreover, the chosen confocal geometry permits a simple mathematical formulation so that parametric dependence may be fully examined. In particular, the limit for a vanishingly small inhomogeneity may be accurately extrapolated from the series solution. Ideally, such a limit should be directly deduced from a thin-airfoil asymptotic expansion (Van Dyke, 1975). This possibility is being pursued by us. Without the availability of such a direct asymptotic result, the confocal geometry is perhaps the only benchmark problem that can be used for extrapolation. This desired limit is successfully deduced in this paper.

Section 2 summarizes the formulation in terms of a complex variable. The exact solution for the antiplane shear case is presented in Section 3. Explicit asymptotic limits for large and small inhomogeneities are extracted from the exact formula. Plane problems are dealt with in Section 4. The case of equal shear modulus and unequal Poisson's ratio is solved exactly, and the general case is presented as a series solution.

A large number of references on inclusion problems may be found in Mura (1982, 1988), but we have not found any reference dealing with the consideration of a crack in a vanishingly small inclusion. The closest situation is the one given by Warren (1983), who considered the edge dislocation inside an elliptical inclusion, including vanishingly small inclusions. For our purpose, the series approach appears to be most expedient.

Numerical results for the plane problems are presented only for plane strain and Mode-I conditions. Parametric dependence of SIF on the size of the inhomogeneity is discussed in detail in Section 5 for the range where the inhomogeneity is softer than the matrix. It is conjectured that the SIF associated with an inhomogeneity of arbitrary size and shape is bounded within a specifically defined region. A number of known solutions are shown to satisfy the conjecture.

2 Formulation

Let (z_1, z_2) be rectangular Cartesian coordinates and $z = z_1 + iz_2$ the associated complex variable in the z-plane. A crack of length 2 in the z-plane is mapped onto a unit circle in a new complex ζ-plane via the mapping function, Fig. 1,

$$z = m(\zeta) = \frac{1}{2}\left(\zeta + \frac{1}{\zeta}\right) \tag{1}$$

Contributed by the Applied Mechanics Division of THE AMERICAN SOCIETY OF MECHANICAL ENGINEERS for presentation at the Winter Annual Meeting, San Francisco, Calif., December 10-15, 1989.

Discussion on this paper should be addressed to the Editorial Department, ASME, United Engineering Center, 345 East 47th Street, New York, N.Y. 10017, and will be accepted until two months after final publication itself in the JOURNAL OF APPLIED MECHANICS. Manuscript received by the Applied Mechanics Division, November 4, 1988; final revision, March 31, 1989.

Paper No. 89-WA/APM-38.

where $\zeta=\zeta_1+i\zeta_2=\rho e^{i\theta}$ and $\rho>1$. The image of the circle $\zeta=\zeta_o=\rho_o e^{i\theta}$ is the ellipse

$$(z_1/a)^2+(z_2/b)^2=1 \tag{2}$$

where

$$a=\frac{1}{2}\left(\rho_o+\frac{1}{\rho_o}\right), \quad b=\frac{1}{2}\left(\rho_o-\frac{1}{\rho_o}\right). \tag{3}$$

The infinite z-plane is now conveniently divided into two regions: D_1 and D_2 by the single parameter ρ_o, viz.,

$$D_1:\ \ 1<\rho<\rho_o, \quad D_2:\ \ \rho>\rho_o. \tag{4}$$

We shall call D_1 the inhomogeneity and D_2 the matrix. The two regions are of different elastic materials characterized by shear moduli μ_α and plane-elasticity constants

$$\kappa_\alpha=\begin{cases}3-4\nu_\alpha & \text{plane strain}\\ (3-\nu_\alpha)/(1+\nu_\alpha) & \text{plane stress}\end{cases} \tag{5}$$

where ν_α are Poisson's ratios. The infinite plane is loaded at infinity by

$$\text{Antiplane:} \quad \tau_{3\alpha}=\sigma_{3\alpha} \quad \text{as } |z|\to\infty, \tag{6}$$

$$\text{Plane:} \quad \tau_{\alpha\beta}=\sigma_{\alpha\beta} \quad \text{as } |z|\to\infty, \tag{7}$$

where τ_{ij} are the stress components.

For the antiplane problem the displacement $u_3(z_1,z_2)$, stresses $\tau_{3\alpha}(z_1,z_2)$, and resultant force R_3 along an arc may be expressed in terms of a single complex function $F(z)$. We have

$$u_3=\frac{1}{2}\left(\Phi(\zeta)+\overline{\Phi(\zeta)}\right), \tag{8}$$

$$\tau_{31}-i\tau_{32}=\mu\Phi'(\zeta)/m'(\zeta), \tag{9}$$

$$R_3=-i\frac{\mu}{2}\left(\Phi(\zeta)-\overline{\Phi(\zeta)}\right), \tag{10}$$

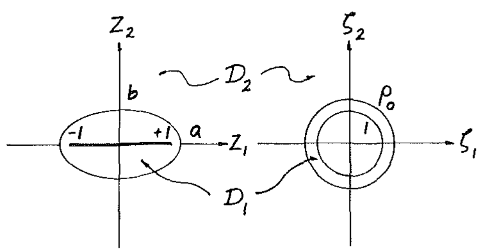

Fig. 1 A crack in a confocal elliptic inhomogeneity

where $\Phi(\zeta)=F(m(\zeta))$ and $m(\zeta)$ is the mapping function (equation (1)).

For the plane problem the displacements $u_\alpha(z_1,z_2)$, stresses $\tau_{\alpha\beta}(z_1,z_2)$, and resultant force $R_1+iR_2=R$ along an arc may be expressed in terms of two complex functions $W(z)$ and $w(z)$. We have

$$2\mu(u_1+iu_2)=\kappa\Omega(\zeta)-\frac{m(\zeta)}{\overline{m'(\zeta)}}\overline{\Omega'(\zeta)}-\overline{\omega(\zeta)} \tag{11}$$

$$iR=\Omega(\zeta)+\frac{m(\zeta)}{\overline{m'(\zeta)}}\overline{\Omega'(\zeta)}+\overline{\omega(\zeta)}, \tag{12}$$

where $\Omega(\zeta)=W(m(\zeta))$ and $\omega(\zeta)=w(m(\zeta))$.

The complex functions must be determined for the two regions D_1 and D_2 subjected to the loading conditions, (6) and (7), and the continuity conditions along the interface boundary characterized by ρ_o. The crack surface is assumed to be traction free. The traction-free condition may be integrated along the crack to become a resultant-free condition. Similarly, traction continuity along the interface may be integrated to become a resultant continuity condition. The integrated forms of these conditions will be used in the calculations to follow.

We shall place a subscript α on a complex function to indicate its region of definition. For example, $F_\alpha(z)$ and $\Phi_\alpha(\zeta)$ are defined for region D_α.

3 Antiplane Shear

The problem may be most conveniently solved in the ζ-plane. The integrated traction-free, integrated traction continuity, displacement continuity, and loading conditions are

$$\Phi_1(e^{i\theta})-\overline{\Phi_1(e^{i\theta})}=0, \tag{13}$$

$$\mu_1[\Phi_1(\zeta_o)-\overline{\Phi_1(\zeta_o)}]=\mu_2[\Phi_2(\zeta_o)-\overline{\Phi_2(\zeta_o)}], \tag{14}$$

$$\Phi_1(\zeta_o)+\overline{\Phi_1(\zeta_o)}=\Phi_2(\zeta_o)+\overline{\Phi_2(\zeta_o)}, \tag{15}$$

$$\Phi_2=\Phi\zeta \quad \text{as } \zeta\to\infty, \tag{16}$$

where $\zeta_o=\rho_o e^{i\theta}$ and

$$\Phi=\frac{1}{2}\frac{1}{\mu_2}(\sigma_{31}-i\sigma_{32}). \tag{17}$$

The solution is

$$\Phi_1(\zeta)=A\zeta+\frac{A}{\zeta} \quad (1<|\zeta|<\rho_o) \tag{18}$$

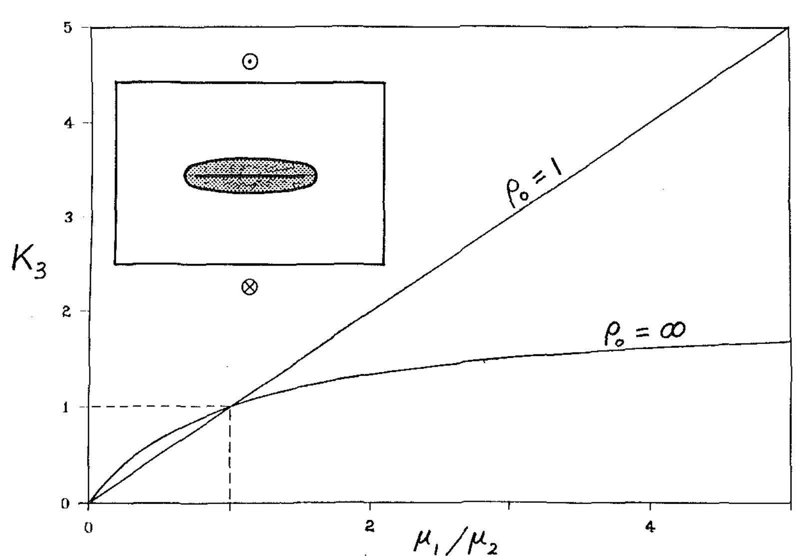

Fig. 2 K_3 as a function of μ_1/μ_2

$$\Phi_2(\zeta)=\Phi\zeta+[(1+\rho_o^2)\bar{A}-\rho_o^2\bar{\Phi}]\frac{1}{\zeta}\quad(|\zeta|>\rho_o)\tag{19}$$

where

$$A=2\rho_o^2\Phi\Big/\left[(\rho_o^2+1)+\frac{\mu_1}{\mu_2}(\rho_o^2-1)\right].\tag{20}$$

The stress intensity factor may be readily determined. It is convenient to normalize the SIF K_{III} by the factor $\sigma_{32}\sqrt{\pi}$, and the result is

$$K_3\left(\rho_o,\frac{\mu_1}{\mu_2}\right)=\frac{K_{III}}{\sigma_{32}\sqrt{\pi}}.$$

$$=\frac{\mu_1}{\mu_2}\left[\frac{2\rho^2{}_o}{\rho_o^2+1}\frac{1}{1+\dfrac{\mu_1}{\mu_2}\dfrac{\rho_o^2-1}{\rho_o^2+1}}\right].\tag{21}$$

The following limits may be easily obtained

$$K_3\left(\infty,\frac{\mu_1}{\mu_2}\right)=2\frac{\mu_1}{\mu_2}\Big/\left(1+\frac{\mu_1}{\mu_2}\right)\tag{22}$$

$$K_3\left(1,\frac{\mu_1}{\mu_2}\right)=\frac{\mu_1}{\mu_2}.\tag{23}$$

These two limits are plotted in Fig. 2. The sign of $\partial K_3/\partial\rho_o$ is governed by $(1-\mu_1/\mu_2)$. Thus

$$K_3\left(1,\frac{\mu_1}{\mu_2}\right)\lesseqgtr K_3\left(\rho_o,\frac{\mu_1}{\mu_2}\right)\lesseqgtr K_3\left(\infty,\frac{\mu_1}{\mu_2}\right)$$

$$\text{if }\frac{\mu_1}{\mu_2}\lesseqgtr 1.\tag{24}$$

It is noted that the bounds are of practical significance for the cases where the inhomogeneity is softer than the matrix.

A very slender inhomogeneity may be defined by $\rho_o=1+\epsilon$ where $\epsilon\ll 1$. The exact result (21) may be used to obtain

$$K_3\left(1+\epsilon,\frac{\mu_1}{\mu_2}\right)\sim\frac{\mu_1}{\mu_2}\left[1+\epsilon\left(1-\frac{\mu_1}{\mu_2}\right)+\dots\right]\tag{25}$$

provided that $\epsilon(\mu_1/\mu_2)\to 0$ as $\epsilon\to 0$. It is, therefore, clear that such a two-term asymptotic expansion is valid only for the cases where the inhomogeneity is either softer or slightly harder than the matrix.

4 Plane Problems

Since the plane problems cannot be solved exactly, we begin by constructing a series solution in the ζ-plane. The traction-free condition on the unit circle unables us to introduce the stress continuation (England, 1971)

$$\omega_1(\zeta)=-\overline{\Omega_1(1/\bar{\zeta})}-\frac{\overline{m(1/\bar{\zeta})}}{m'(\zeta)}\Omega_1'(\zeta).\tag{26}$$

The function $\Omega_1(\zeta)$ is now extended to the region $1/\rho_o<\rho<\rho_o$, and the traction-free condition on $\rho=1$ is identically satisfied. The conditions (7) are met if

$$\Omega_2(\zeta)=\Omega\zeta+0\left(\frac{1}{\zeta}\right)\quad|\zeta|\to\infty,\tag{27}$$

$$\omega_2(\zeta)=\omega\zeta+0\left(\frac{1}{\zeta}\right)\quad|\zeta|\to\infty,\tag{28}$$

where

$$\Omega=\frac{1}{8}(\sigma_{11}+\sigma_{22}),\quad\omega=\frac{1}{4}[(\sigma_{22}-\sigma_{11})+i2\sigma_{12}].\tag{29}$$

The integrated form of the traction continuity condition along ζ_o may be obtained from (12), i.e.,

$$\Omega_2(\zeta_o)+\frac{m(\zeta_o)}{\overline{m'(\zeta_o)}}\overline{\Omega_2'(\zeta_o)}+\overline{\omega_2(\zeta_o)}$$
$$=\Omega_1(\zeta_o)-\Omega_1\left(\frac{1}{\bar{\zeta}_o}\right)+\left[m(\zeta_o)-m\left(\frac{1}{\bar{\zeta}_o}\right)\right]\frac{\overline{\Omega_1'(\zeta_o)}}{\overline{m'(\zeta_o)}}\tag{30}$$

where (26) has been applied. Continuity in displacements along ζ_o yields

$$\frac{1}{\mu_2}\left\{\kappa_2\Omega_2(\zeta_o)-\frac{m(\zeta_o)}{\overline{m'(\zeta_o)}}\overline{\Omega_2'(\zeta_o)}-\overline{\omega_2(\zeta_o)}\right\}=\frac{1}{\mu_1}\left\{\kappa_1\Omega_1(\zeta_o)\right.$$
$$\left.+\Omega_1\left(\frac{1}{\bar{\zeta}_o}\right)-\left[m(\zeta_o)-m\left(\frac{1}{\bar{\zeta}_o}\right)\right]\frac{\overline{\Omega_1'(\zeta_o)}}{\overline{m'(\zeta_o)}}\right\}\tag{31}$$

which, after applying (30), may be reduced to

$$\Omega_1(\zeta_o)=\gamma\Omega_2(\zeta_o)+\gamma^*\left\{\Omega_2(\zeta_o)+\frac{m(\zeta_o)}{\overline{m'(\zeta_o)}}\overline{\Omega_2'(\zeta_o)}+\overline{\omega_2(\zeta_o)}\right\}\tag{32}$$

where

$$\gamma=\frac{(1+\kappa_2)\mu_1}{(1+\kappa_1)\mu_2},\quad\gamma^*=\frac{1}{1+\kappa_1}\left(1-\frac{\mu_1}{\mu_2}\right)\tag{33}$$

are two composite parameters (Dundurs, 1969). We note that (30) may be deduced from (31) via the relation

$$(30)\equiv[\text{Letting }\mu_1=\mu_2=1\text{ and }\kappa_1=\kappa_2=-1\text{ in (31)}].\tag{34}$$

Before proceeding, we shall first consider the special case $\mu_1=\mu_2$.

4.1 Exact Solution for Equal Shear Modulus. For this case, the composite parameters defined by (33) become

$$\gamma=\gamma_o=\frac{1+\kappa_2}{1+\kappa_1},\quad\gamma^*=0\tag{35}$$

and (32) becomes

$$\Omega_1(\zeta_o)=\gamma_o\Omega_2(\zeta_o),\tag{36}$$

which serves as an analytic continuation of the two functions $\Omega_1(\zeta)$ and $\Omega(\zeta)$. Making the substitution $\Omega_1(\zeta)=\zeta_o\Omega_2(\zeta)$, we obtain from (30)

$$\overline{\omega_2(\rho_o^2/\bar{\zeta}_o)}+\frac{m(\zeta_o)}{\overline{m'(\rho_o^2/\bar{\zeta}_o)}}\overline{\Omega_2'(\rho_o^2/\bar{\zeta}_o)}-\gamma_oM(\zeta_o)\overline{\Omega_2'(\rho_o^2/\bar{\zeta}_o)}$$
$$=(\gamma_o-1)\Omega_2(\zeta_o)-\gamma_o\Omega_2(\zeta_o/\rho_o^2)\tag{37}$$

where

$$M(\zeta_o)=\frac{m(\zeta_o)-m(1/\bar{\zeta}_o)}{\overline{m'(\zeta_o)}}=-\frac{\rho_o^2(\rho_o^2-1)(\zeta_o^2-\rho_o^2)}{\zeta_o(\zeta_o^2-\rho_o^4)}.\tag{38}$$

It follows from (37) that the function $H(\zeta)$ defined by

$$H(\zeta)=\begin{cases}(\gamma_o-1)\Omega_2(\zeta)-\gamma_o\Omega_2(\zeta/\rho_o^2), & (|\zeta|>\rho_o)\\ \overline{\omega_2(\rho_o^2/\bar{\zeta})}+\dfrac{m(\zeta)}{\overline{m'(\rho_o^2/\bar{\zeta})}}\overline{\Omega_2'(\rho_o^2/\bar{\zeta})}-\gamma_oM(\zeta)\overline{\Omega_2'(\rho_o^2/\bar{\zeta}_o)}, & \end{cases}$$

$$(|\zeta|<\rho_o)\tag{39}$$

is holomorphic in the whole ζ-plane. Moreover, its properties at $\zeta=0$ and ∞ are governed by the right-hand side of (39). The complete solution is

$$H(\zeta)=\left[-1+\gamma_o\left(1-\frac{1}{\rho_o^2}\right)\right]\Omega\zeta$$
$$+\left\{\bar{\omega}\rho_o^2+[1+\gamma_o(\rho_o^2-1)]\Omega\right\}\frac{1}{\zeta},\tag{40}$$

$$\Omega_2(\zeta)=\Omega\zeta-\left[\Omega+\frac{\bar{\omega}\rho_o^2}{1+\gamma_o(\rho_o^2-1)}\right]\frac{1}{\zeta},\tag{41}$$

$$\omega_2(\zeta)=\overline{H(\rho_o^2/\bar\zeta)}+\gamma_o\overline{M(\rho_o^2/\bar\zeta)}\Omega_2'(\zeta)$$
$$-[\overline{m(\rho_o^2/\bar\zeta)}/m'(\zeta)]\Omega_2'(\zeta), \tag{42}$$
$$\Omega_1(\zeta)=\gamma_o\Omega_2(\zeta). \tag{43}$$

Let us use the factors $\sigma_{22}\sqrt{\pi}$ and $\sigma_{12}\sqrt{\pi}$ to normalize the SIF's K_I and K_{II}, and write

$$K_1=K_I/\sigma_{22}\sqrt{\pi},\quad K_2=K_{II}/\sigma_{12}\sqrt{\pi}. \tag{44}$$

The following explicit results are readily obtained

$$K_1=\frac{\gamma_o[(\rho_o^2+1)+\gamma_o(\rho_o^2-1)]}{2[1+\gamma_o(\rho_o^2-1)]}-\frac{\gamma_o(1-\gamma_o)(\rho_o^2-1)}{2[1+\gamma_o(\rho_o^2-1)]}\frac{\sigma_{11}}{\sigma_{22}}, \tag{45}$$

$$K_2=\frac{\gamma_o\rho_o^2}{1+\gamma_o(\rho_o^2-1)}. \tag{46}$$

There are the following exact limits

$$\lim_{\rho_o\to 1}K_1 \quad\text{and}\quad K_2=\gamma_o=\frac{1+\kappa_2}{1+\kappa_1}, \tag{47}$$

$$\lim_{\rho_o\to\infty}K_1=\frac{1}{2}(1+\gamma_o)-\frac{1}{2}(1+\gamma_o)\frac{\sigma_{11}}{\sigma_{22}}, \tag{48}$$

$$\lim_{\rho_o\to\infty}K_2=1. \tag{49}$$

4.2 Series Solution. The complex functions Ω_1, Ω_2, and ω_2, together with their regions of definition, admit the following series representations

$$\Omega_1(\zeta)=\sum_{n=1}^{\infty}\rho_o^{1-n}(A_n\zeta^n+a_n\zeta^{-n}), \tag{50}$$

$$\Omega_2(\zeta)=\Omega\zeta+\sum_{n=1}^{\infty}\rho_o^{1+n}B_n\zeta^{-n}, \tag{51}$$

$$\omega_2(\zeta)=\omega\zeta+\sum_{n=1}^{\infty}\rho_o^{1+n}b_n\zeta^{-n}, \tag{52}$$

where $n=1,3,5,\ldots$. The factors ρ_o^{1-n} and ρ_o^{1+n} are included for convenience and pose no restrictions on the validity of the series representations. They are nevertheless conceived from the fact that u_α along $|\zeta|=\rho_o$ must be of the order of ρ_o as $\rho_o\to\infty$.

Substituting (50)–(52) into (31), setting $\zeta=\rho_o e^{i\theta}$, and equating coefficients of $e^{in\theta}$ to zero, we obtain

$$-n\left(1-\frac{1}{\rho_o^2}\right)\bar A_n+(n+2)\left(1-\frac{1}{\rho_o^2}\right)\bar A_{n+2}-\left(1+\frac{\kappa_1}{\rho_o^{2n}}\right)a_n$$
$$+\frac{1}{\rho_o^2}\left(1+\frac{\kappa_1}{\rho_o^2(n+2)}\right)a_{n+2}+\frac{\mu_1}{\mu_2}\kappa_2\left(B_n-\frac{1}{\rho_o^2}B_{n+2}\right)$$
$$=\begin{cases}\dfrac{\mu_1}{\mu_2}\bar\omega+\dfrac{1}{\rho_o^2}\Omega\ \text{for } n=1\\[2ex] 0 \qquad\qquad \text{for } n=3,5,7,\ldots\end{cases}, \tag{53}$$

$$-\left(\kappa_1+\frac{1}{\rho_o^2}\right)A_1+\left(1-\frac{1}{\rho_o^2}\right)\bar A_1$$
$$+\frac{1}{\rho_o^2}\left(1-\frac{1}{\rho_o^2}\right)\bar a_1+\frac{1}{\rho_o^2}\left(1+\frac{\kappa_1}{\rho_o^2}\right)a_1$$
$$+\frac{\mu_1}{\mu_2}\left[\frac{1}{\rho_o^2}\bar B_1-\bar b_1-\frac{\kappa_2}{\rho_o^2}B_1\right]=$$
$$-\frac{\mu_1}{\mu_2}\left[(\kappa_2-1)\Omega+\frac{1}{\rho_o^2}\bar\omega\right], \tag{54}$$

and

$$-\left(\kappa_1+\frac{1}{\rho_o^{2n}}\right)\bar A_n+\frac{1}{\rho_o^2}\left(\kappa_1+\frac{1}{\rho_o^{2(n-2)}}\right)A_{n-2}$$
$$+\frac{n}{\rho_o^{2n}}\left(1-\frac{1}{\rho_o^2}\right)\bar a_n-\frac{n-2}{\rho_o^{2(n-2)}}\left(1-\frac{1}{\rho_o^2}\right)\bar a_{n-2}$$
$$+\frac{\mu_1}{\mu_2}\left[(n-2)\bar B_{n-2}+\frac{n}{\rho_o^2}\bar B_n-\bar b_n+\frac{1}{\rho_o^2}\bar b_{n-2}\right]$$
$$=\begin{cases}\dfrac{\mu_1}{\mu_2}\kappa_2\dfrac{\Omega}{\rho_o^2} & \text{for } n=3\\[2ex] 0 & \text{for } n=5,7,9,\ldots\end{cases} \tag{55}$$

The relations derived from (30) are obtained by the substitution (34), i.e.,

[Letting $\mu_1=\mu_2=1$ and $\kappa_1=\kappa_2=-1$ in (53), (54), (55)]. (56)

The infinite system (53)–(56) are truncated and the resulting finite system is inverted numerically. The SIF's

$$K_I-iK_{II}=2(\pi)^{1/2}\Omega_1'(1) \tag{57}$$

are then normalized in accordance with (44). Values of plane-strain K_1 are plotted in Fig. 3 for the case $\nu_1=\nu_2=0.2$ and $\sigma_{11}=0$. The numerical results approach to a limit very rapidly as $\rho_o\to\infty$. The analytic expression for this limit is determined in the next subsection.

The convergence of the numerical scheme becomes extremely slow as $\rho_o\to 1$. For this reason, values of K_1 for fixed values of μ_1/μ_2 are plotted as functions of $1/\rho_o^2$ in Fig. 4. It is seen that all curves tend to finite limits as $\rho_o\to 1$. The $\rho_o=1$ curve indicated in Fig. 3 is extrapolated from Fig. 4.

4.3 Very Large Inhomogeneity. We have indicated before that the factors ρ_o^{1+n} built in (50)–(52) are conceived from the fact that the displacements u_α along $|\zeta|=\rho_o$ must be of the order of ρ_o as $\rho_o\to\infty$. Thus the series representation may also be interpreted as an asymptotic expansion for large ρ_o. In this interpretation, however, the four sets of constants must be reexpanded in powers of ρ_o^{-2}, i.e.,

$$(A,a,B,b)_n=(\ )_{no}+\frac{1}{\rho_o^2}(\ )_{n1}+\ldots \tag{58}$$

Substituting (58) into (53)–(56), and equating to zero the coefficients of powers of ρ_o^{-2}, we obtain an infinite system of infinitely many equations for the determination of the coefficients $(\ )_{nm}$. The asymptotic limit for the case of a very large inhomogeneity is thus governed by the coefficients $(\ )_{no}$.

The system governing $(\ )_{no}$ actually decouples into finite systems and the first cluster of equations are

$$-\bar A_{10}+3\bar A_{30}-a_{10}+\frac{\mu_1}{\mu_2}\kappa_2B_{10}=\frac{\mu_1}{\mu_2}\bar\omega, \tag{59}$$

$$-\bar A_{10}+3\bar A_{30}-a_{10}-B_{10}=\bar\omega, \tag{60}$$

$$-\kappa_1A_{10}+\bar A_{10}-\frac{\mu_1}{\mu_2}\bar b_{10}=-\frac{\mu_1}{\mu_2}(\kappa_2-1)\Omega, \tag{61}$$

$$A_{10}+\bar A_{10}-\bar b_{10}=2\Omega, \tag{62}$$

$$-\kappa_1A_{30}+\frac{\mu_1}{\mu_2}(\bar B_{10}-\bar b_{30})=0, \tag{63}$$

$$A_{30}+\bar B_{10}-\bar b_{30}=0, \tag{64}$$

which may be explicitly solved to yield

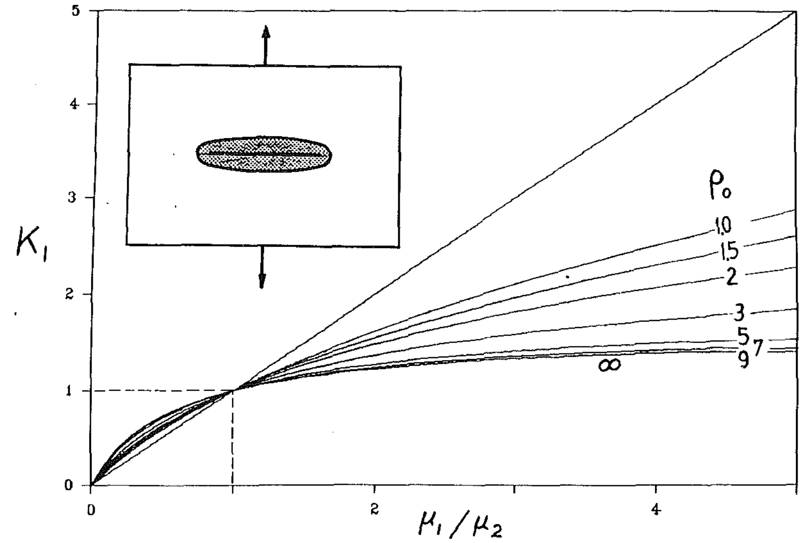

Fig. 3 K_1 as a function of μ_1/μ_2 with ρ_o as a parameter ($\nu_1 = \nu_2 = 0.2$, $\sigma_{11} = \sigma_{12} = 0$ and plane strain)

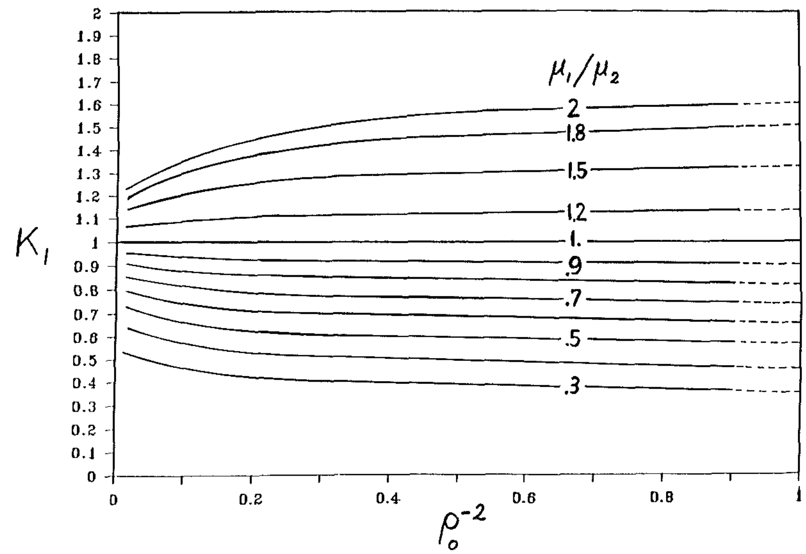

Fig. 4 K_1 as a function of ρ_o^{-2} with μ_1/μ_2 as a parameter

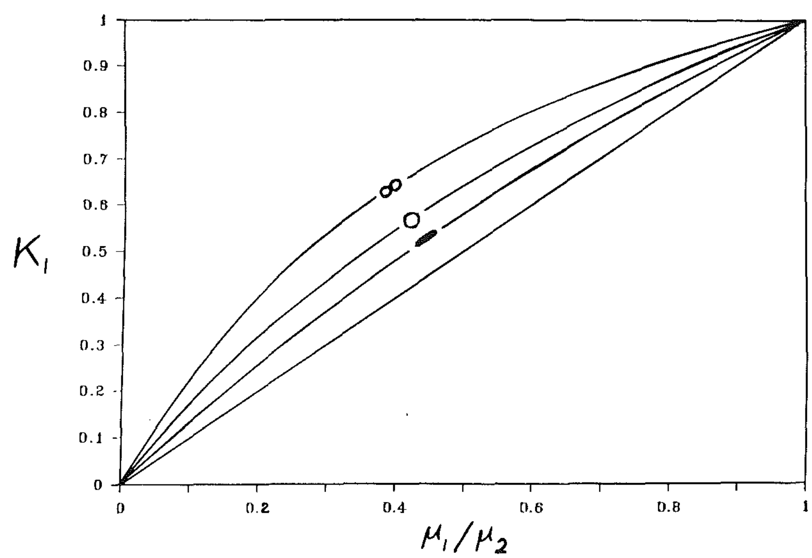

Fig. 5 K_1 is shown to be bounded by (71); (∞: infinitely large inhomogeneity, $-$: vanishingly thin inhomogeneity, 0: vanishingly; small circular crack-tip inhomogeneity)

$$A_{10}=\frac{\mu_1}{\mu_2}\;(\kappa_2+1)\Omega\Big/\left(\kappa_1-1+2\,\frac{\mu_1}{\mu_2}\right),$$

$$B_{10}=b_{30}=\left(\frac{\mu_1}{\mu_2}-1\right)\bar{\omega}\Big/\left(\frac{\mu_1}{\mu_2}\,\kappa_2+1\right), \tag{65}$$

$$A_{10}=-B_{10}-A_{10}-\bar{\omega}$$

$$A_{30}=0,\quad b_{10}=2(A_{10}-\Omega).$$

In fact, the second cluster of equations yields

$$A_{50}=a_{30}=B_{30}=b_{50}=0. \tag{66}$$

The asymptotic limit for Ω_1 is merely

$$\Omega_1(\zeta)\sim\left(A_{10}\zeta+a_{10}\,\frac{1}{\zeta}\right)+0\left(\frac{1}{\rho_o^2}\right) \tag{67}$$

and

$$\Omega_1'(1)\sim(A_{10}-a_{10})+0\left(\frac{1}{\rho_o^2}\right). \tag{68}$$

Equations (44), (57) and (67)–(68) lead to the explicit asymptotic limits

$$K_1\sim\frac{1}{2}\,\frac{\mu_1}{\mu_2}\,(1+\kappa_2)\left[\frac{1-\dfrac{\sigma_{11}}{\sigma_{22}}}{1+\dfrac{\mu_1}{\mu_2}\,\kappa_2}+\frac{1+\dfrac{\sigma_{11}}{\sigma_{22}}}{\kappa_1-1+2\,\dfrac{\mu_1}{\mu_2}}\right], \tag{69}$$

$$K_2\sim\frac{\mu_1}{\mu_2}\,(1+\kappa_2)\Big/\left(1+\frac{\mu_1}{\mu_2}\,\kappa_2\right). \tag{70}$$

Equation (69) is in perfect agreement with the numerical asymptotic limit given in Fig. 3.

While we have not been able to find any references dealing with cracks in vanishingly thin inhomogeneities, solutions for cracks in multiphase regions are many. In particular, the case of a crack in a circular inhomogeneity was solved by Erdogan and Gupta (1975). The aforementioned $\rho_o\to\infty$ limit corresponds to their result deduced for a very large circular inhomogeneity.

The $\rho_o\to\infty$ limit may be obtained by first calculating the uniform stress in an elliptic inhomogeneity. This stress is then used as the remote stress to compute the SIF. The authors are indebted to one of the reviewers for this comment.

5 Discussion and a Conjecture

The plane and antiplane problems associated with a crack in a confocal elliptic inhomogeneity embedded in an infinite medium is solved in detail. In particular, the dependence of the SIF's on the size of the inhomogeneity $\rho_o(1<\rho_o<\infty)$ is examined. The solution for the antiplane problem is exact and the result serves as a qualitative indication of the behaviors of the solutions to the plane problems which cannot be solved exactly.

For plane problems, the case of equal shear modulus and unequal Poison's ratio is also solved exactly. The general case, however, is handled by a series solution. For the latter case, the asymptotic limit for a very large inhomogeneity ($\rho_o\to\infty$) is also explicitly determined. Numerical results are only produced for Mode-I conditions and for $\nu_1=\nu_2=0.2$.

In all cases, the attending SIF's are shown to be bounded by the limits for the large ($\rho_o\to\infty$) and small ($\rho_o\to 1$) inhomogeneities. The case of $\rho_o\to 1$ and $\mu_1/\mu_2<1$ is of special interest in studying crack-damage interaction. For this reason the relevant portion of Fig. 3 is enlarged and reproduced in Fig. 5. It is clear that the effect of the inhomogeneity on the crack tip is strictly of a shielding nature. Moreover, the exact value of the SIF falls in the rather narrow lens-shaped region bounded by the $\rho_o\to\infty$ limit, which is explicitly given by (69), and the 45 deg line. With this observation we conclude our presentation with the following conjecture.

A Conjecture: Let a crack be surrounded by a doubly-symmetric inhomogeneity of moduli μ_1 and $\nu_1=\nu$ which in turn is embedded in an infinite medium of moduli μ_2 and $\nu_2=\nu$. The inhomogeneity may consist of two disjointed inhomogeneities surrounding the tips. The normalized Mode-I SIF is a function of the two composite parameters

$$\gamma=\frac{(1+\kappa_2)\mu_1}{(1+\kappa_1)\mu_2}=\frac{\mu_1}{\mu_2},\quad \gamma^*=\frac{1}{1+\kappa_1}\left(1-\frac{\mu_1}{\mu_2}\right)$$

$$=\frac{1}{1+\kappa}\left(1-\frac{\mu_1}{\mu_2}\right)$$

and is denoted by $K_1(\gamma,\gamma^*)$. It satisfies

$$\gamma\le K_1(\gamma,\gamma^*)\le\frac{\gamma(\gamma+1-\gamma^*)}{2(\gamma+\gamma^*)(1-2\gamma^*)} \tag{71}$$

for $0\le\gamma=\mu_1/\mu_2\le 1$. The right-hand side of (71) is deduced from (69) and equalities hold for $\gamma=\mu_1/\mu_2=0$ and 1.

The solution summarized in Fig. 3 apparently satisfies (71) and the $\rho_o\to 1$ limit is plotted in Fig. 5 to illustrate the situation. The problem of a crack with tips embedded in vanishingly small circular inhomogeneities was solved by Steif (1987). The K_1 curve is reproduced in Fig. 5 and satisfies (71).

Finally, for the case of a vanishingly thin inhomogeneity, the (circumferential) stress concentration factor at the nose of the ellipse would be of practical interest. Let $\rho_o=1+\epsilon$ ($\epsilon\to 0$), then the major and minor axes of the ellipse are $a=1+\frac{1}{2}\epsilon^2$ and $b=\epsilon$. The following explicit results are readily obtained:

$$\tau_{yy}^{(1)}=\frac{2K_1\sigma_{22}}{\epsilon}\quad\text{at}\quad z_1=\rho_o-0,\quad z_2=0, \tag{72}$$

$$\tau_{yy}^{(2)}=\frac{2K_1\sigma_{22}}{\gamma\epsilon}\quad\text{at}\quad z_1=\rho_o+0,\quad z_2=0, \tag{73}$$

where K_1 is the normalized SIF. The SIF K_1 is in general a function of ρ_o and γ, i.e., $K_1(\gamma,\rho_o)$. It is possible to carry out a special asymptotic analysis by using γ as a small parameter and show that

$$\left.\frac{\partial K_1(\gamma,\rho_o)}{\partial\gamma}\right|_{\gamma=0,\rho_o=1}=1. \tag{74}$$

Thus, as $\gamma\to 0$ and $\rho_o\to 1$, (73) becomes $\tau_{yy}^{(2)}=2\sigma_{22}/\epsilon=2\sigma_{22}(a/b)$, which is the stress concentration factor at the nose of a vanishingly thin elliptic hole.

References

Dundurs, J., 1969, discussion on "Edge-Bonded Dissimilar Orthogonal Elastic Wedges Under Normal and Shear Loading," ASME Journal of Applied Mechanics, Vol. 36, pp. 650–652.

England, A. H., 1971, *Complex Variable Method in Elasticity*, John Wiley and Sons, New York.

Erdogan, F., and Gupta, G. D., 1975, "The Inclusion Problems with a Crack Crossing the Boundary," *Int. J. of Fraction*, Vol. 11, pp. 13–27.

Hutchinson, J. W., 1968, "Crack Tip Shielding by Micro-Cracking in Brittle Solids," Harvard University, Mech-87.

Mura, T., 1982, *Micromechanics of Defects in Solids*, Martinus Nijhoff.

Mura, T., 1988, "Inclusion Problems," *Appl. Mech. Review*, ASME, New York, Vol. 41, pp. 15–20.

Steif, P. S., 1987, "A Semi-Infinite Crack Partially Penetrating a Circular Inclusion," ASME Journal of Applied Mechanics, Vol. 54, pp. 87–92.

Van Dyke, M., 1975, *Perturbation Methods in Fluid Mechanics*, Parabolic Press.

Warren, W. E., 1983, "The Edge Dislocation Inside an Elliptical Inclusion," *Mechanics of Materials*, Vol. 2, pp. 319–330.

Wu, C. H., 1988, "A Semi-Infinite Crack Penetrating an Inclusion," ASME Journal of Applied Mechanics, Vol. 55, pp. 736–738.

Wu, C. H., and Chen, C. H., 1989, "Cracks in Thin Inhomogeneities," to be submitted for publication.

Crack-Path Effect on Material Toughness

Asher A. Rubinstein
Department of Mechanical Engineering,
Tulane University,
New Orleans, LA 70118
Mem. ASME

The material-toughening mechanism based on the crack-path deflection is studied. This investigation is based on a model which consists of a macrocrack (semi-infinite crack), with a curvilinear segment at the crack tip, situated in a brittle solid. The effect of material toughening is evaluated by comparison of the remote stress field parameters, such as the stress intensity factors (controlled by a loading on a macroscale), to effective values of these parameters acting in the vicinity of a crack tip (microscale). The effects of the curvilinear crack path are separated into three groups: crack-tip direction, crack-tip geometry pattern-shielding, *and* crack-path length change. *These effects are analyzed by investigation of selected curvilinear crack patterns such as a macrocrack with simple crack-tip kink in the form of a circular arc and a macrocrack with a segment at the crack tip in the form of a sinusoidal wave. In conjunction with this investigation, a numerical procedure has been developed for the analysis of curvilinear cracks (or a system of cracks) in a two-dimensional linear elastic solid. The formulation is based on the solution of a system of singular integral equations. This numerical scheme was applied to the cases of finite and semi-infinite cracks.*

1 Introduction

The modeling of material-toughening mechanisms usually is based on analysis of crack growth from two points of view: crack growth on macroscale, and the crack-tip stress field on microscale. On the macroscale, we consider the material to be homogeneous and the crack to be rectilinear. The characteristics of the applied load are remote stress intensity factors $K_{\rm I}^{\infty}$, $K_{\rm II}^{\infty}$ and the energy release rate per crack advance G^{∞}. These parameters are related to the geometry and loading scheme of the specimens or performing parts. The actual stress field in the vicinity of the crack tip is distorted due to interaction of the crack with the local microstructure; it is characterized by local values $K_{\rm I}^{0}$, $K_{\rm II}^{\infty}$, and G^{0}. The ratio of the local values to the applied values describes the degree of local shielding (*shielding ratio*), or if it is higher than one, anti-shielding. When the crack-tip stress field becomes less intense due to distortion of the applied field by microdefects, the material exhibits higher resistance to crack growth; this is the basic toughening mechanism. There are several toughening mechanisms described in the literature which are based on implantation of inclusions, local microcracking, or phase transformation of material particles. The shielding ratio characterizes the toughening only if one assumes that crack propagation will remain rectilinear. However, the local stress field usually is complex, and consists of two modes of fracture. The expectation that the crack advancing path will be rectilinear is not justifiable. The real crack path usually is curvilinear, and this characteristic in itself represents a toughening mechanism. The aim of this investigation is to establish the main features of the toughening mechanism associated with a curvilinear crack path.

The asymptotic behavior of the stress field in the vicinity of a curved crack tip can be characterized by stress intensity factors as in the case of a straight crack. To prove this it is sufficient to consider an exact solution for the arc crack in a uniform stress field given by Muskhelishvili, 1963. However, the energy release rate per crack advance, G, which can be determined as

$$G = \Lambda[K_{\rm I}{}^2 + K_{\rm II}{}^2], \tag{1}$$

where Λ is a constant, has been defined for the rectilinear crack growth. G is an important fracture mechanics parameter and, therefore, it will be used in our analysis. Physical interpretation of G in the case of a curvilinear path is limited to an infinitesimal crack advance only. The infinitesimal segment of a curvilinear arc can be interpreted as a segment of a straight line, but the curvature of the infinitesimal arc does not vanish with the arc length. Therefore, usefulness of the energy release rate in the form (1) is limited if one tries to draw conclusions regarding the crack growth path curvature. The interpretation of the value of G is limited to potential crack growth in a rectilinear direction only.

The usefulness of the energy release rate is associated with the J-integral introduced by Rice, 1968. The J-integral is a particular case of the integral given by Eshelby, 1970,

$$J_i = \int_{\Gamma} \left[W n_i - \underline{T} \cdot \frac{\partial \underline{u}}{\partial x_i} \right] ds. \tag{2}$$

Contributed by the Applied Mechanics Division of THE AMERICAN SOCIETY OF MECHANICAL ENGINEERS for presentation at the Winter Annual Meeting, San Francisco, Calif., December 10–15, 1989.

Discussion on this paper should be addressed to the Editorial Department, ASME, United Engineering Center, 345 East 47th Street, New York, N.Y. 10017, and will be accepted until two months after final publication of the paper itself in the JOURNAL OF APPLIED MECHANICS. Manuscript received and accepted by the ASME Applied Mechanics Division, July 20, 1988.

Paper No. 89-WA/APM-43.

The case $i=1$ will correspond to the Rice J-integral for the rectilinear crack parallel to an axis x_1. In the case of a rectilinear crack, $J=G$, and J is path independent. In the case of a curvilinear crack, this integral has to be taken in the local coordinate system, which is tangential to the crack tip. With this rotation of the coordinate system, the path independence of the integral (2) is lost in general terms when the contours of integration are ending on the crack surfaces. To observe this, one simply has to note that if n_i is not vanishing on the crack surface, the term with W will not cancel. For the same reason, *the integral (2) is not path independent for any curvilinear crack path in any coordinate system.*

Thus, the actual value of the energy release rate per crack advance obtained from the microscale analysis can be totally different from the value expected from the data on macroscale. Therefore, the finite element techniques based on the evaluation of the energy release rate by employing the J-integral on the contour distant from the crack tip cannot be applied to curvilinear crack-path studies. To obtain complete data characterizing the local stress field in the case of a curvilinear crack path, one has to obtain a complete solution of the problem. The method based on the singular integral equations was chosen in this study.

In the following sections the formulation of the problem, in terms of complex variables, is given with the description of the numerical scheme dealing with a curvilinear crack path. The developed numerical procedure was formulated for the finite and semi-infinite cracks. The numerical scheme was evaluated on an example which has an exact solution (finite crack in the form of a circular arc in uniform stress field). This numerical code was used in the analysis of the effects of crack-tip direction change, local crack-path pattern-shielding (studied on the analysis of a sinusoidal crack pattern), and the total toughness change due to the curvilinear crack path (based on the crack-path length).

2 Formulation

The analysis of the curvilinear crack in this investigation is based on a formulation of two-dimensional linear elasticity in terms of singular integral equations (Muskhelishvili (1963)). The integral equation states a condition of a traction-free crack surface when the total stress field in the plane is given as a superposition of dislocation array along the crack plus external (applied) stress field. This approach is widely used in fracture mechanics. The current approach is different from the standard technique due to curvature of the crack path and due to consideration of a semi-infinite crack. Thus, the stress field is characterized by analytic potentials $\phi(z)$ and $\psi(z)$ resulting from the superposition of the applied (known) stress field ϕ_a, ψ_a and, as mentioned previously, the stress field produced by the array of dislocations, representing the crack, which is given by ϕ_c, ψ_c.

$$\begin{aligned}\phi(z)&=\phi_a(z)+\phi_c(z)\\ \psi(z)&=\psi_a(z)+\psi_c(z)\end{aligned} \tag{3}$$

The stress tensor components in terms of the potentials (3) are

$$\sigma_{\theta\theta}+i\sigma_{r\theta}=\phi'+\bar{\phi}'+e^{2i\theta}(\bar{z}\phi''(z)+\psi'(z)), \tag{4}$$

$$\sigma_{rr}-i\sigma_{r\theta}=\phi'+\bar{\phi}'-e^{2i\theta}(\bar{z}\phi''(z)+\psi'(z)). \tag{5}$$

Functions $\phi_c(z)$ and $\psi_c(z)$ are results of the superposition of dislocations along the crack line. The dislocation density distribution $b(s)$ is an unknown complex valued function, s is the position coordinate along the crack surface. It is convenient to choose s to be a line length of the crack path starting at the crack tip. The potentials ϕ_c and ψ_c in an integral form can be written as

$$\phi_c'(z)=\frac{\alpha}{2\pi i}\int_L\left[\frac{b(s)}{z-t}+\phi_s'(b(s),z,t)\right]ds,\ t=t_x(s)+it_y(s) \tag{6}$$

$$\psi_c'(z)=-\frac{\alpha}{2\pi i}\int_L\left[\frac{\overline{b(s)}}{z-t}-\frac{\bar{t}b(s)}{(z-t)^2}-\psi_s'(b(s),z,t)\right]ds. \tag{7}$$

The analytic functions ϕ_s and ψ_s represent regular parts of the potentials corresponding to the interaction of the dislocation with a defect or the boundary. These functions are analytic in the whole elastic region. The point of consideration is z, and t is a point on the crack line L corresponding to an integration variable s. Here α is a standard coefficient, $\alpha=E/4(1-\nu^2)$ in plain-strain case, and $\alpha=E/4$ in plain-stress case.

The integral equation for evaluation of the dislocation density is formed by a statement of zero tractions on the crack surface; in other words,

$$\sigma_{\theta\theta}+i\sigma_{r\theta}=0. \tag{8}$$

θ is the angle between the x-axis and the tangent to the crack line at any point z on the crack. Substituting in (8) expression (4) with (6), (7) one obtains an integral equation which has to be satisfied for any z on the crack line. The resulting equation can be written in the form

$$\int_0^\infty\left[\frac{N(b(s),\overline{b(s)})}{t(s)-z(v)}+P(\overline{b(s)},b(s),K(s,v))\right]ds=R(v). \tag{9}$$

Functions N and P in (9) are linear functions of their arguments. Function R represents contribution from the applied (remote) stress field given by potentials ϕ_a and ψ_a. $K(s,v)$ here is a Fredholm-type kernel of the integral equation (9). In reality, functions $b(s)$ and the conjugate to it have different Fredholm kernels not shown in (9), explicitly in order to emphasize just the essential features of the equation. Important components of it are functions $t(s)$ and $z(v)$. These functions represent the transformation of the integral equation in a complex plane into a line integral equation in terms of real variables s and v along the crack path L. An important restriction on possible crack trajectories is a requirement that

$$|t(s)-z(v)|\rightarrow 0(|s-v|)\quad \text{as}\quad (s-v)\quad 0. \tag{10}$$

Variables s and v are the real variables on the integration curve, measured as the curve length starting from the crack tip. With condition (10) equation (9) becomes a first-kind Cauchy-type singular integral equation and the integral is understood in terms of Cauchy principal value.

The dislocation density function $b(s)$ in the form defined in (6)–(7) and, consequently, in the equation (9), does not correspond to a standard dislocation density used in fracture mechanics. The difference is in the coefficient. In order to use the standard definition, ds has to be replaced by dt in equations (6), (7), and (9). This definition was used for the convenience of the numerical scheme only, and the difference is accounted for in determination of the stress intensity factors. Essentially, the coefficient dt/ds has been absorbed into the unknown dislocation density for computational convenience. However, the restriction on the integration path, following from the requirements of continuity of the derivative dt/ds, remains. Thus, the crack trajectory has to be a smooth curve with a continuous derivative.

The formulation described above has been applied to finite and semi-infinite cracks. In the case of the finite crack, the upper limit in (9) is equal to the crack length. In the case of a

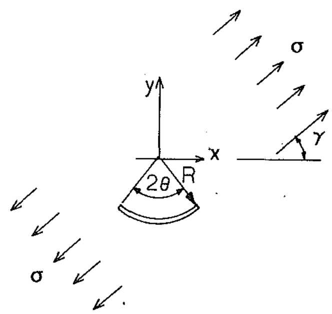

Fig. 1 Configuration of a circular arc crack

semi-infinite crack, the stabilization procedure introduced by Rubinstein (1986) has to be applied. In the case of the infinite crack the right-hand side of the equation (9) becomes equal to zero, and the remote stress field is introduced through the asymptotic behavior of the dislocation density. Thus, we seek the dislocation density in the form

$$b(s) = K^{\infty}\left[\frac{\beta(s)}{\sqrt{s}} + i\,\frac{(1-e^{-s^2})}{\alpha\sqrt{2\pi s}}\right] \tag{11}$$

where K^{∞} is remote (applied) stress intensity factor and function $\beta(s)$ is an unknown function bounded on the integration interval and

$$\beta(s) \to 0 \quad \text{as} \quad s \to \infty. \tag{12}$$

The second term in (11) is a stabilization term. The required property of this term is its behavior at large s. The form chosen here simplifies computations in the vicinity of the crack tip and the evaluation of the stress intensity factors, that is

$$\frac{K_{\mathrm{I}}^{0} + iK_{\mathrm{II}}^{0}}{K^{\infty}} = i\,\overline{\beta(0)}e^{i\theta^0}. \tag{13}$$

Here θ^0 is the angle of the tangential at the crack tip. K with superscript 0 corresponds to local values of the stress intensity factors for Mode I and Mode II accordingly.

After substitution of (11) into (9) the equation is mapped onto a finite interval, and then the collocation procedure is applied in the form given by Rubinstein (1986) for the semi-infinite interval and based on the technique introduced by Erdogan and Gupta (1972). The cases of the finite crack and semi-infinite crack are treated equally after the transformation of the semi-infinite interval of integration onto a finite interval. However, the difference still remains in the formulation of the supplementary condition. The supplementary condition for the semi-infinite crack is condition (12) and it is enforced in the numerical procedure by employing Lagrange formulas for Chebyshev polynomials at the ends of the interval. The supplementary condition in the case of the finite crack is the condition of a single-valued displacement

$$\int_L b(s)ds = 0. \tag{14}$$

L here is the interval along the crack.

The collocation scheme uses Gaus-Chebyshev quadrature formula and requires the node distribution along the roots of Chebyshev polynomials of the first and second kind. In order to secure the accuracy of the integration procedure, a nonlinear equation

$$\int_{x^0}^{x_k} (1 + (y'(x))^2)^{1/2}\,dx = s_k \tag{15}$$

was solved to establish the relation between node s_k and coordinates on the trajectory x,y. In the case of a semi-infinite crack, equation (15) corresponds to a mapped state. Here s_k is a value of corresponding Chebyshev root, x^0 is a coordinate of the crack tip, and function $y(x)$ specifies the crack path.

3 The Circular Arc Crack

The numerical scheme was evaluated in the case of a circular arc crack in the uniform stress field. The analytical solution of this problem is given by Muskhelishvili (1963). The potentials representing the applied load are (see Fig. 1)

$$\phi_a' = \frac{1}{4}\,\sigma_{\infty}, \quad \psi_a' = -\,\frac{1}{2}\,e^{-2i\gamma}. \tag{16}$$

The exact solution for the stress intensity factors derived from the solution given by Muskhelishvili (1963), is

$$\bar{K} = K_{\mathrm{I}} - iK_{\mathrm{II}} = \frac{\sigma}{2}\,e^{\pm i\theta/2}\sqrt{\pi R \sin\theta}\,\left(C_0 + e^{\pm i\theta + 2i\gamma}\right) \tag{17}$$

$$C_0 = i\,\sin 2\gamma\,\sin^2\frac{\theta}{2} + \frac{4 - \cos 2\gamma \sin^2\theta}{2(3-\cos\theta)}\,,$$

here, in the places with $\pm$, the negative sign corresponds to the right crack tip and the positive sign corresponds to the left crack tip. The expression (17), in the case of the right crack tip, is equivalent to one given by Cotterell and Rice (1980).

The computations were performed for the following values of angles γ and θ

$\theta = 0.001$ deg, 10 deg, 20 deg, . . . , 170 deg,

$\gamma = 0$ deg, .15 deg, 30 deg, 45 deg, 60 deg, 75 deg, 90 deg.

The results of the numerical procedure, when compared with an exact expression (17), show excellent agreement. The agreement of these two methods is so good that it would be impossible to illustrate the difference graphically. The data were compared at both crack tips. The summary of the maximal error is given below, where K stands for the right or left crack-tip stress intensity factor, depending where the error is greater.

$$\max\left[\frac{|K_{\mathrm{analytic}}|}{|K_{\mathrm{numeric}}|} - 1\right] < 0.012 \quad \text{at} \quad \theta = 170 \text{ deg}, \gamma = 45 \text{ deg} \tag{18}$$

$$\max|\arg(K_{\mathrm{analytic}}) - \arg(K_{\mathrm{numeric}})| < 0.17 \text{ deg}. \tag{19}$$

A similar numerical approach has been used for a finite length arc crack by Melin (1986a). However, the resulting accuracy did not satisfy the author and, therefore, an additional least-square procedure was invoked by Melin in dealing with this problem. In our case, the results show such good agreement that no additional procedure was necessary to stabilize the scheme. The maximal value of the error given in (18) decreases rapidly with decrease of the angle θ. For example, this number becomes on the order less than 10^{-5} for $\theta = 150$ deg. A maximal value of θ discussed by Melin (1986) is 80 deg.

The above data show that this numerical procedure can be applied successfully to the analysis of curvilinear cracks, excluding, for the reasons mentioned in the previous section, cases with sharp corners and very high curvature.

4 Analysis of the Curvilinear Crack Path Trajectory

During the crack propagation along the curvilinear path, the local stress intensity factors may differ significantly from the remote value. In relation to that, there are several contributing factors to consider. The net result depends on the combined effect of local crack tip orientation and the amplitude of the crack path oscillation. The latter creates a local geometrical effect such that the crack-tip field becomes similar to a field of a small crack in the vicinity of a macrocrack. The complete result of these effects will depend on each individual aspect and their interaction. It can be summarized in evaluating the total effective toughness. To understand the significance of each aspect of the curvilinear path, these effects are investigated separately. The main effects of the crack-path deflection were separated into three groups.

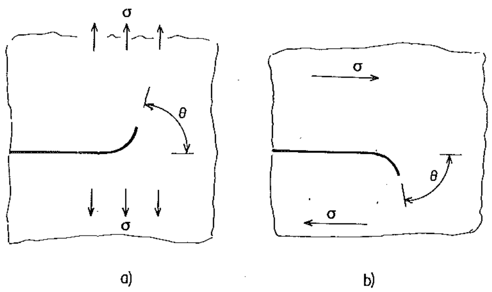

Fig. 2 Geometry of a crack with a circular kink

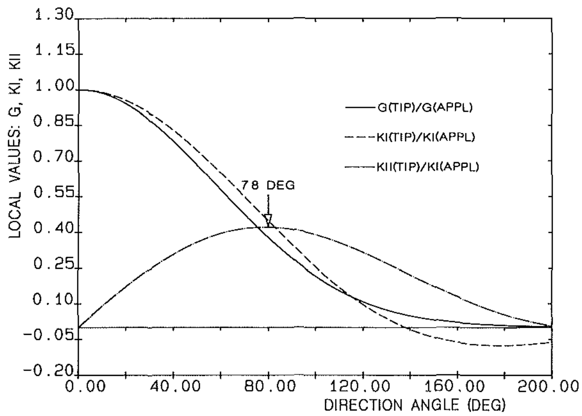

Fig. 3 Variation of the local parameters versus $\theta°$ under Mode I loading

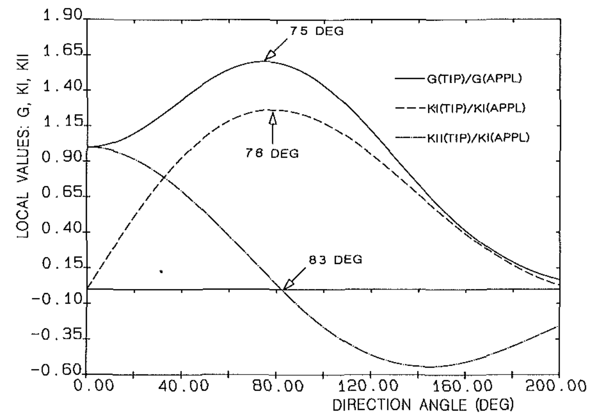

Fig. 4 Variation of the local parameters versus $\theta°$ under Mode II loading

They are: *change in direction, local shape-shielding,* and *effective toughness.* The natural curvilinear crack path takes place due to inhomogenuities which alter the local stress field. The current analysis considers a curvilinear crack in the homogeneous material and does not include these local stress field changes. This puts a certain limitation on the applicability of the effective toughness evaluation. However, the following results will characterize the effects taking place and will give a guideline for the toughness analysis of inhomogeneous materials. The results are given as a ratio of the local values of stress intensity factors to a remote value corresponding to an applied fracture mode. The energy release rate for the infinitesimal crack advance is determined in the form equivalent to rectilinear crack advance. That is

$$G^0/G^\infty = [(K_I^0)^2 + (K_{II}^0)^2]/K^\infty. \tag{20}$$

K^∞ corresponds to an applied stress intensity factor in Mode I or Mode II, respectively.

4.1 Crack Path Direction. The effect of the crack path direction change is analyzed in this section. The semi-infinite crack with a smooth circular kink was subjected to Mode I and Mode II loadings (see Fig. 2). The results in Figs. 3 and 4 show the variations of the local values of the stress intensity factors and energy release rate in ratio to the applied (remote) value of K_I^∞ and K_{II}^∞ for Mode I and Mode II, respectively. The results are given as functions of an angle between the tangential at the crack tip and a parallel to the main part of the crack, angle $\theta°$. The radius of the circular arc should not influence results since the ratio of this radius to the arc length, which is equal to $\theta°$, is the only parameter of the problem. This was used as an additional factor in evaluation of the numerical procedure. The computations were performed on the basis of 40 nodes. The stability and accuracy of the numerical results were evaluated by doubling the number of nodes.

The analysis of the branched cracks was originally given by Lo (1978) where only discrete values of the directional angle are given, that is at $\theta° = 15$ deg, 45 deg, 75 deg. Results given in Figs. 3 and 4 are consistent with the data given by Lo (1978). The energy release rate and local value of the Mode I stress intensity factor decrease with the increase of the directional angle under the Mode I loading condition. The value of the local Mode II stress intensity factor increases in this case and reaches its maximum at $\theta° = 78$ deg. The negative values of Mode I stress intensity factor correspond to the values of the directional angle at which the crack closure will take place. The case of the Mode II loading (Fig. 4) shows increases in the energy release rate and Mode I stress intensity factor as the directional angle increases, up to their maximal positions at 75 deg and 78 deg, respectively. The Mode II stress intensity factor decreases and becomes zero at 83 deg. The maximal value of the energy release rate becomes 60 percent higher than expected from the applied field. This contributes to the instability of the brittle crack growth under Mode II condition and the tendency to change a crack-path direction. The angles of the critical situations usually are associated with potential crack-path direction. These critical directions are: direction of maximal energy release, direction of maximal value of Mode I stress intensity factor, and direction of zero-value Mode II stress intensity factor. Each of these critical directions has a good physical argument to be a preferable direction for the crack-path extension. However, the difference between these directions is significant enough to establish completely different trajectories after any finite crack-growth increment. The experimental observations suggest the preferable crack path to be the direction under which the local stress field will correspond to Mode I loading. These observations are supported by D. G. Smith and C. W. Smith (1972), Smith and Wiersma (1986). Bazzard et al. (1986), using the Mode II loading specimen, observed a tendency of the crack path to turn about 70 deg towards the original Mode II crack direction. Similar results were reported by Banks-Sills and Arcan (1986).

In this report we do not propose any particular criteria for the crack-path formation; it will be the subject of a follow-up paper. The main objective of this investigation is to establish the actual change of local stress field parameters due to the change in crack-tip direction.

4.2 Shielding Due to a Local Crack Pattern. The aim of the investigaton reported in this section is to evaluate the effect of a nonrectilinear crack path on crack-tip stress field parameters. The direction of the crack tip now will remain aligned with the main portion of the macrocrack, but the portion of the crack in the vicinity of the crack tip will have a curvilinear pattern. Specifically, a sinusoidal pattern (21) has been chosen as a representation of a typical wavy crack path, Fig. 5. The equation of this path is

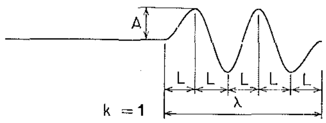

Fig. 5 Geometry of the sinusoidal crack-tip region

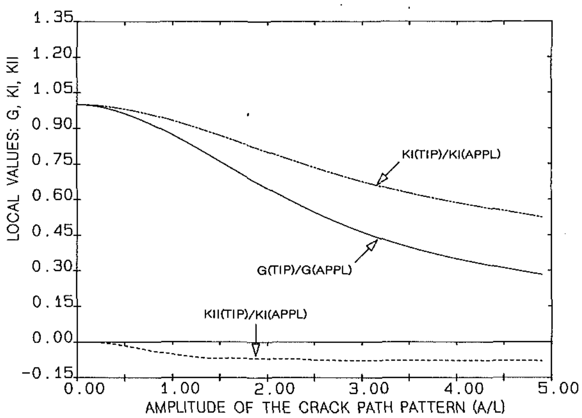

Fig. 6 Local parameters of the crack-tip stress field versus the amplitude of the crack path trajectory (sinusoidal pattern)

$$y=\begin{cases} 0.5A\left(\sin\left(\pi\left(\dfrac{x}{L}-0.5\right)\right)+1\right) & : 0\le x<L \\ A\sin\left(\pi\left(\dfrac{x}{L}-0.5\right)\right) & : L\le x<2L+2kL \\ 0.5A\left(\sin\left(\pi\left(\dfrac{x}{L}-0.5\right)\right)-1\right) & : 2L+2kL\le x\le 3L+2kL \end{cases} \tag{21}$$

$k=0,\ 1,\ 2,\ \ldots$

where k specifies a number of complete periods between the transitional segments, that is, between the segment adjacent to the crack tip and the segment adjacent to the main portion of the crack.

As the amplitude-half-wavelength ratio A/L increases, the region in the vicinity of the crack tip becomes, in a sense, an isolated region, and, therefore, the crack tip acts rather as a small crack in the field of a macrocrack. Thus, the shielding effect takes place. Two aspects are examined here: The first deals with the number of wave periods required for the shielding effect to take place, and the second is the evaluation of the significance of the shielding.

The shielding effect, as it was just described, basically depends on the last curved segment, so the expected result should not depend on the number of intermediate waves. The computations were carried out for the ratio $A/L=1$ and the results are given in Table 1. The values of the local stress intensity factor corresponding to Mode I and the energy release rate are given here versus the number of intermediate waves.

Table 1 Local parameters for a variable number of intermediate waves in the crack pattern

$A/L=1.0$

k	$K_I{}^0$	G^0
0	0.936	0.881
1	0.938	0.886
2	0.937	0.880
3	0.935	0.891
4	0.938	0.888
5	0.942	0.890
6	0.937	0.881
7	0.944	0.891

As k increases, the dependence of the numerical scheme on the number of nodes becomes visible. This is understandable, since the larger number of nodes is required to capture the features of the curved path and surrounding stress field. This minor instability shows in the data given in the Table 1; otherwise, it is clear that the analysis of only one wave ($k=0$) is sufficient to describe the shielding effect.

The results of the shielding analysis are plotted in Fig. 6. The Mode I remote loading only was considered here. The case of Mode II would create a crack closure on the curvilinear segments which will become a different type of shielding mechanism.

The shielding effect in the case of Mode I loading, as shown in Fig. 6, plays a significant role in material toughening. The relatively moderate amplitude may create a significant difference in the actually-acting crack-tip stress intensity factor, or energy release rate. As is well known, fatigue cracks, or any kind of intergranular fracture, are associated with very wavy crack patterns. For the convenience of applications of this phenomenon in fracture mechanics, approximate relations are given for the local values of K_I and the energy release rate.

$$G^0=G^\infty(1.00-0.1682(A/L)^2+0.0485(A/L)^3-0.0042(A/L)^4) \tag{22}$$

$$K_I^0=K_I^\infty(1.00-0.0876(A/L)^2+0.0225(A/L)^3-0.0018(A/L)^4). \tag{23}$$

Relations (22) and (23) were obtained by using the least-square approximation on the data obtained from solution of the integral equation.

4.3 Determination of Material Toughness in the Case of a Curvilinear Crack Path. The important practical aspect of the understanding of the effects of curvilinear crack path is the evaluation of the effective material toughness. There are several ways to interpret the resulting toughness. We are dealing with two aspects. On one hand, the crack growth is controlled by microstructural parameters, that is, local values of the stress intensity factors and energy release rate; on the other hand, the experimental measurements determining the material toughness are, usually, done on a macroscale. On macroscale the crack is assumed to propagate in a rectilinear path. Therefore, the length of the crack path is different in these two cases.

The energy release rate will be used as a parameter in the toughness analysis. It is better suited for that purpose than the stress intensity factor, since the local field always has two stress intensity components while the applied stress field may correspond to only one.

Suppose the crack is growing along the curve (21), and it advances on a full cycle, starting from the horizontal position and ending in the same position. The total crack-path length will be S. On the macroscale, the crack will appear to be advancing horizontally and the crack-path length will be λ. Introduce the *integral toughness* criterion, which will be based on the assumption that the crack is driven by the critical energy release rate G_c^0 along the path. Thus, the total energy released per cycle will be SG_c^0, and on the macroscale, the equivalent measurement of energy release per crack advance λ will be λG_c^∞. The resulting relation between the critical values on macro and microscales is

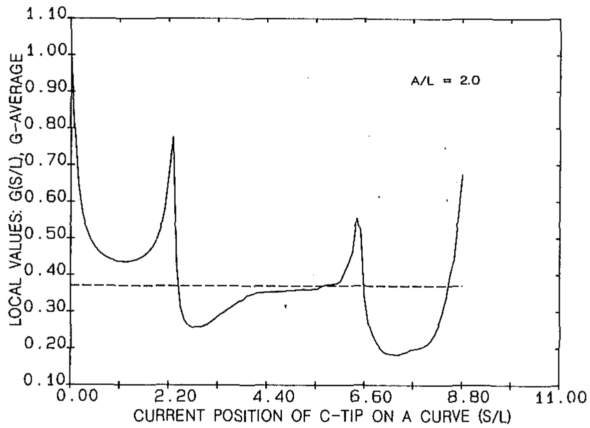

Fig. 7 Variation of the local value of the energy release rate along the crack path, $A/L=2.0$, $k=0$

$$G_c^\infty = \frac{S}{\lambda} G_c^0. \tag{24}$$

The argument against this simple approach is that the assumption $G^0=$ constant along the crack path does not represent the physical situation very well. A typical variation of G^0 along the crack path is shown in Fig. 7. The case corresponding to $A/L=2.0$ and $k=0$, assuming a constant remote load, is given in Fig. 7. The energy release rate varies significantly along the crack path due to direction change and the local shape-shielding. The regions with horizontal tangential have highest values of G^0. Again, as was mentioned previously, this crack path is not a typical case for the homogeneous material. To include the variations of the local fracture mechanics parameters in the toughness evaluation, introduce an *average toughness* criterion. Consider the average value of the energy release rate.

$$G_{\rm av}^0 = \frac{1}{S}\int_0^S G^0(s)ds = \delta\,\frac{\lambda G^\infty}{S} \tag{25}$$

The second equality relates the average value to a remote one by following the same logic as in the case discussed above. The coefficient δ was introduced here to maintain a simple relation. The geometry of the crack path enters this relation through this coefficient only. Assuming that the average value of the energy release rate should reach critical value in order for the crack to propagate through the cycle, the remote value can be written as

$$G_c^\infty = \frac{G^\infty}{G_{\rm av}^0} G_c = \frac{S}{\delta\lambda} G_c. \tag{26}$$

The values of δ were computed for one cycle of a crack path ($k=0$) and for several values of the amplitude-half-wave-length ratio. These data are given in Table 2. It is surprising to observe that δ is practically equal to 1.0 for smaller amplitudes, and, for the cases considered here, did not rise higher than about 1.15. There is no reason to expect that this is a general result for any crack path. The values of δ were computed for intermediate positions along the path as well. These values fluctuate along the crack path, and only for the sinusoidal path at the end do they become so close to unit. Thus, for relatively small amplitudes, two methods practically give equivalent results. The data in Table 2 show that, for the curvilinear crack path, the macrotoughness may appear much higher than the local value. In other words, the crack-path deflection is an important material-toughening mechanism.

5 Conclusions and Discussion

The investigation of the curvilinear crack path demonstrates that the geometry of the crack-path trajectory has to be considered in order to be able accurately to evaluate or to predict the material toughness. The geometry of the crack-path trajectory is as important as other aspects of crack growth on microscale.

Table 2 Toughness parameters for a single cycle of crack path

A/L	$\delta(A/L)$	$S(\lambda=3)$	$G_{\rm av}^0/G^\infty$
0.25	1.000	3.215	0.933
0.50	1.002	3.744	0.803
1.00	1.015	5.232	0.582
1.50	1.045	6.964	0.450
2.00	1.088	8.798	0.370
2.50	1.153	10.685	0.324

This study illustrates several toughening mechanisms associated with the curvilinear crack path. They are: *local crack-tip direction, crack-path oscillation pattern,* and *the length of the curvilinear path.*

The local crack-tip stress field parameters, such as stress intensity factors and energy release rate due to the crack advance, are experiencing significant changes during crack-tip direction change. The typical characteristic of the dominant Mode I crack propagation is higher value of the energy release rate due to the crack advance. The presence of the Mode II component usually reduces the total energy release rate.

The wavy crack path forms a shielding mechanism based on isolation of the crack-tip region, so that it acts as a microcrack in the vicinity of a macrocrack. The examined sinusoidal patterns contributed to the reduction from 1.0 to 0.55 of the ratio of the acting stress intensity factor to the applied one. The corresponding ratio of the energy release rate is 0.30.

The total toughening due to curvilinear path was evaluated on the basis of actual crack-path length and compared with the crack advance length on macroscale. Results show that for relatively small amplitude of the crack-path oscillation, the toughening ratio can be taken equal to the ratio of the corresponding crack-path lengths. This result is applicable to crack trajectories which can be approximated by sinusoidal curves similar to (21).

The material microstructure has an important role in material toughening through several mechanisms. Many of them were widely discussed in the literature. The aim of this work was to give a quantitative description of the crack-path deflection toughening mechanism. The important practical aspect of the curvilinear crack-path formation is the mechanics of the crack-path change. This topic was not addressed here; it will be discussed in detail in a follow-up work, (Rubinstein, 1988).

Acknowledgment

This work was supported by NASA Lewis Research Center under Grant NAG 3-815 and by the Institute for Computational Mechanics in Propulsion at NASA Lewis Research Center.

References

Bazzard, R. J., Gross, B., and Srawley, J. E., 1986, "Mode II Fatigue Crack Growth Specimen Development," ASTM, STP 905, pp. 329-346.

Banks-Sills, L., and Arcan, M., ASTM, STP 905, pp. 347-363.

Erdogan, F., and Gupta, G. D., 1972, "On the Numerical Solutions of Singular Integral Equations," *Quarterly of Applied Mathematics*, Vol. 29, pp. 525-534.

Eshelby, J. D., 1970, "Energy Relations and the Energy-Momentum Tensor in Continuum Mechanics," *Inelastic Behavior of Solids*, M. F. Kanninen, W. F. Adler, A. R. Rosenfield, and R. I. Jaffee, eds., McGraw-Hill, New York, pp. 77-115.

Cotterell, B., and Rice, J. R., 1980, "Slightly Curved or Kinked Cracks," *Int. J. Fracture*, Vol. 16, No. 2, pp. 155-169.

Lo, K. K., 1978, "Analysis of Branched Cracks," ASME JOURNAL OF APPLIED MECHANICS, Vol. 45, No. 4, pp. 797-802.

Melin, S., 1986, "On Singular Integral Equations for Kinked Cracks," *Int. J. Fracture*, Vol. 30, pp. 57-65.

Muskhelishvili, N. I., 1963, *Some Basic Problems in the Mathematical Theory of Elasticity*, P. Noordhoff, Ltd., Holland.

Smith, C. W., and Wiersma, S. J., 1986, "Stress-Fringe Signatures for Propagating Crack," *Engineering Fracture Mechanics*, Vol. 23, No. 1, pp. 229-236.

Smith, D. G., and Smith, C. W., 1972, "Photoelastic Determination of Mixed Mode Stress Intensity Factors," *Engineering Fracture Mechanics*, Vol. 4, pp. 357-366.

Rice, J. R., 1968, "Mathematical Analysis in the Mechanics of Fracture," *Fracture*, Vol. 2, H. Liebowitz, ed., Academic Press, pp. 191-311.

Rubinstein, A. A., 1986, "Macrocrack-Microdefect Interaction," ASME JOURNAL OF APPLIED MECHANICS, Vol. 53, pp. 505-510.

Rubinstein, A. A., 1988, "Mechanics of the Crack Path Formation," submitted for publication.

Fracture Initiation Due to Asymmetric Impact Loading of an Edge Cracked Plate

Y. J. Lee
Research Assistant.

L. B. Freund
Professor of Engineering,
Fellow ASME.

Division of Engineering,
Brown University,
Providence, RI 02912

The two-dimensional elastodynamic problem of a semi-infinite plate containing an edge crack is considered. Initially, the plate is stress-free and at rest. To simulate the asymmetric impact of a projectile on the cracked edge of the plate, a normal velocity is suddenly imposed on the boundary of the plate on one side of the edge crack. The boundary of the plate and the crack faces are otherwise traction-free. Due to the nature of the loading, a combination of transient mode I and mode II deformation fields is induced near the crack tip. The corresponding stress intensity factor histories are determined exactly by linear superposition of several more readily obtainable stress wave propagation solutions, including a fundamental solution arising from a particular problem in the dynamic theory of elastic dislocations. The stress intensity factor histories are determined for the time interval from initial loading until the first wave scattered at the crack tip is reflected at the plate edge and returns to the crack tip. In experiments on fracture initiation in a high-strength steel based on essentially this specimen and loading configuration, Kalthoff and Winkler (1987) reported a fracture grew from the original crack either as a tensile crack inclined to the original crack plane or as a straight-ahead shear fracture, depending on the intensity of the applied velocity. The observations are considered in light of the solution reported here.

1 Introduction

An experimental technique has been proposed by Kalthoff and Winkler (1987) and Kalthoff (1987) for subjecting edge cracks in plate specimens to very high rates of loading that result in a crack tip deformation field that is predominantly mode II, that is, the in-plane shearing mode. A plate specimen with two parallel edge cracks or notches is impacted by a cylindrical projectile of diameter equal to the spacing between the cracks, as shown schematically in Fig. 1. Upon impact, the projectile produces a compressive wave in the part of the specimen between the two cracks, and this wave propagates toward the crack tips while merely grazing the two crack faces that border this part of the specimen. Upon arrival of the wave at the crack tips the constraint of the remainder of the specimen is encountered, and relatively large shear stress is induced on the crack planes ahead of the crack tips resulting in transient mode II stress intensity factors. The same idea has been applied for the case of a plate with a single edge crack.

The wave motion in the part of the specimen between the cracks upon projectile impact is actually much more complicated than the foregoing discussion would suggest. A plane compressive wave is indeed generated upon impact. Because the crack faces are free of traction, cylindrical unloading waves immediately begin to propagate outward from the corners where the crack faces intersect the impacted edge of the plate. The wave front diagram is shown in Fig. 2. These unloading waves have two main effects. They tend to erode the strength of the compressive plane wave as it propagates along the crack faces and they tend to result in outward bulging of the crack faces as the intense compression of the plane wave is relieved due to the presence of the free surface. These features are evident in some early work by Skalak (1957) on longitudinal

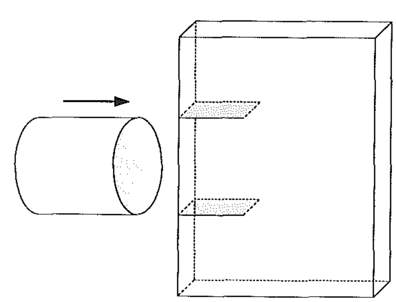

Fig. 1 Experimental configuration introduced by Kalthoff and Winkler (1987) for dynamic fracture initiation studies under mixed-mode conditions

Contributed by the Applied Mechanics Division of The American Society of Mechanical Engineers for presentation at the Winter Annual Meeting, San Francisco, Calif., December 10–15, 1989.

Discussion on this paper should be addressed to the Editorial Department, ASME, United Engineering Center, 345 East 47th Street, New York, N.Y. 10017, and will be accepted until two months after final publication of the paper itself in the Journal of Applied Mechanics. Manuscript received by the ASME Applied Mechanics Division, December 1, 1988; final revision, March 31, 1989. Paper No. 89-WA/APM-41.

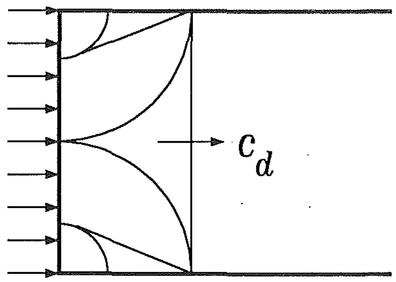

Fig. 2 Pattern of wave fronts generated in the portion of the specimen shown in Fig. 1 between the two cracks due to normal impact of the projectile

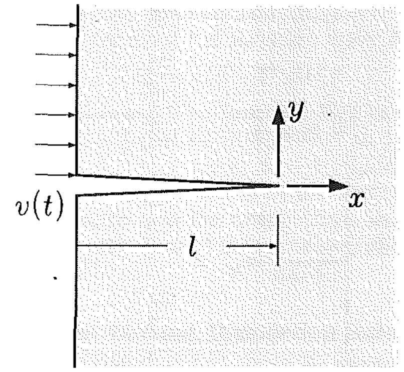

Fig. 3 A schematic representation of the boundary value problem considered here, showing the edge crack of length l and the imposed normal velocity imposed asymmetrically on the edge of the plate

wave propagation in a plate due to impact loading of the edge. The net result of this loading is to induce a transient, mixed-mode stress intensity factor field at the crack tip. The mode II stress intensity factor has a large component due to the main compressive wave, but a time-dependent mode I stress intensity factor is also generated. In view of the tendency for the crack to close that was previously noted, the mode I stress intensity factor will likely be negative.

Data are reported by Kalthoff (1987) for experiments on specimens of a high-strength maraging steel. The plate dimensions were approximately 1 cm × 10 cm × 20 cm, and the crack length, crack separation distance, and projectile diameter were all about 5 cm. Impact velocities were in the range from about 10 m/s to 100 m/s. A particularly interesting feature of the data is that two completely different failure modes were observed to occur, depending on the impacting speed of the projectile. For the lowest impact velocities, fracture occurred in the form of planar crack growth in a direction inclined at about 70 deg to the original crack plane. For impact speed greater than about 20 m/s, on the other hand, failure occurred by the crack-like growth of a shear band in a direction almost coincident with the original crack plane.

The purpose here is to compute the transient mixed-mode stress intensity factors through analysis of a boundary value problem intended to model the experimental conditions. The analysis is based on the assumption of elastic material response; study of the influence of crack tip plasticity is underway.

The particular edge-cracked plate problem to be analyzed is shown schematically in Fig. 3. A rectangular x, y-coordinate system is introduced in the plane of the plate, and the plate occupies the half plane $x \geq -l$. A crack with traction-free faces extends normally inward a distance l from the edge of the plate. Thus, the crack tip is at the origin of coordinates as shown in Fig. 3. The normal stress component σ_{xx} vanishes on the edge of the plate for $y < 0$ and a time-dependent normal velocity is imposed on the edge of the plate for $y > 0$. The shear traction is assumed to vanish everywhere on the plate edge. This boundary condition would be strictly valid if the projectile had the same cross-section as the portion of the plate being impacted. The influence of the different shapes should be small except for points very near to the impacting surfaces.

To solve the problem, the longitudinal displacement potential ϕ and the shear displacement potential ψ are introduced through the Helmholtz decomposition of the displacement vector. The components of displacement in the coordinate directions are derived from the potentials by differentiation according to

$$u_x = \phi_{,x} + \psi_{,y} \quad u_y = \phi_{,y} - \psi_{,x} \tag{1}$$

where the familiar comma-subscript notation is used to denote partial differentiation.

Each of these potential functions satisfies a two-dimensional wave equation,

$$\phi_{,xx} + \phi_{,yy} - a^2\phi_{,tt} = 0 \quad \psi_{,xx} + \psi_{,yy} - b^2\psi_{,tt} = 0 \tag{2}$$

where $a = 1/c_d = \sqrt{\rho/(\lambda+2\mu)}$ and $b = 1/c_s = \sqrt{\rho/\mu}$ are the inverse dilatational and shear waves speeds, respectively, in terms of the Lamé elastic constants λ, μ and the mass density ρ. For future reference, $c = 1/c_R$ is the inverse Rayleigh wave speed.

The stress components can be expressed in terms of the displacement potentials by means of Hooke's law for the material. As already discussed, the portion of the plate edge below the crack in Fig. 3 is completely traction-free. On the other hand, the portion of the edge above the crack is free of shear traction, but the normal speed is imposed beginning at time $t = 0$. Thus, the solution must satisfy the boundary conditions

$$\begin{aligned} &\sigma_{xx}(-l,y,t) = 0, \quad \sigma_{xy}(-l,y,t) = 0, && y<0 \\ &u_x(-l,y,t) = \int_0^t v(\tau)d\tau, \quad \sigma_{xy}(-l,y,t) = 0, && y>0 \qquad (3) \\ &\sigma_{xx}(x,0^{\pm},t) = 0, \quad \sigma_{xy}(x,0^{\pm},t)(=0, && -l<x<0 \end{aligned}$$

where $v(t)$ is prescribed for $t \geq 0$. The formulation is completed by specifying zero initial data. Evidently, the stress intensity factors will be identically zero until time $t = l/c_d$.

The boundary value problem formulated in equation (3) is linear. Nonetheless, it is sufficiently complex so that direct methods of solution are apparently not applicable. By studying the features of a sequence of subproblems, however, it will be shown that mathematically-exact expressions for the mode I and mode II stress intensity factors can be found. The property of linearity is exploited by superposition of these solutions in a certain way. The Laplace transform is useful in approaching some of these problems. The dual transform of the dilatational displacement potential $\phi(x, y, t)$ over time t and spatial coordinate x is defined by

$$\bar{\phi}(\xi,y,s) = \int_{-\infty}^{\infty} e^{-s\xi x} \int_0^{\infty} e^{-st}\phi(x,y,t)dt\, dx \tag{4}$$

where the transform parameters are defined to be s and $s\xi$, respectively. The parameter s may be viewed as a sufficiently large positive real number in considering transform on x.

The superposition scheme is outlined in Figs. 4, 5, and 6. In Fig. 4, is shown that the asymmetric impact problem can be viewed as a superposition of a symmetric impact problem (A) and an antisymmetric impact problem (B). If $v(t)$ is the imposed normal velocity in the problem of interest, then a normal edge velocity of magnitude $½v(t)$ is imposed symmetrically with respect to the crack plane in (A) and antisymmetrically with respect to the crack plane in (B). Thus, solutions of these two problems are required.

Consider the symmetric problem (A). It is shown in Fig. 5 that this problem can be decomposed into a quarter-plane problem (C) and a problem concerned with the motion of

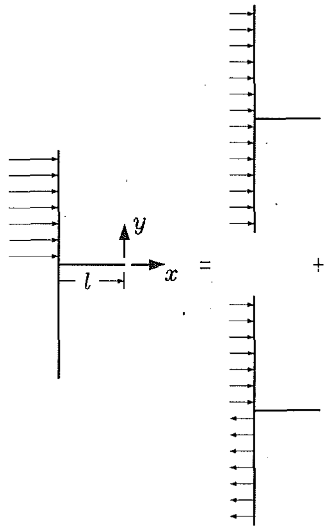

Fig. 4 Decomposition of the asymmetric boundary value problem in Fig. 1 into a symmetric loading system (A) and an antisymmetric loading system (B)

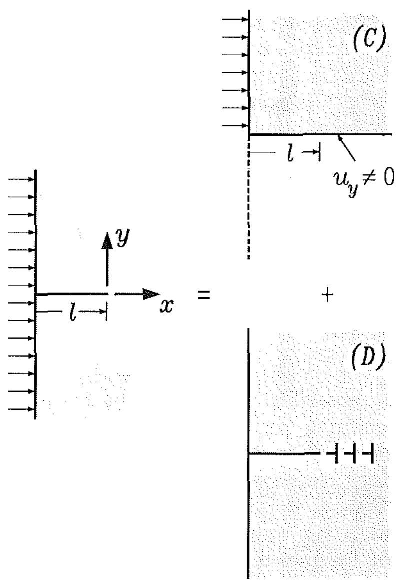

Fig. 5 Decomposition of problem (A) into a quarter-plane problem (C) and a dynamic dislocation propagation problem (D)

dislocations emanating from the tip of a crack (D). The basic idea is as follows. If the imposed velocity begins to act on the edge $x = -l$ of the quarter plane in (C), then a normal displacement is induced on the edge $y = 0$. However, the displacement in the y-direction on $x > 0$, $y = 0$ for the problem of interest (A) is zero. Consequently, the normal displacement induced on $x > 0$, $y = 0$ for the quarter-plane problem (C) is canceled by a distribution of climbing edge dislocations emanating from the crack tip in (D) with a net displacement distribution on $y = 0$, $x > 0$ that exactly negates the normal displacement in (C). The use of dynamic dislocation solutions in this way was introduced by Freund (1974) in order to obtain stress intensity factor solutions for certain problems that are not amenable to direct analysis. These solutions have been used to interpret experimental data by Ravi-Chandar and Knauss (1984) and Kim (1985). A similar superposition scheme can be used to solve the antisymmetric loading problem. The same general approach has been applied to various problems in elastodynamics by Brock (1983) and others.

Finally, the quarter-plane problem can be solved by the superposition shown schematically in Fig. 6. Case (E) is the

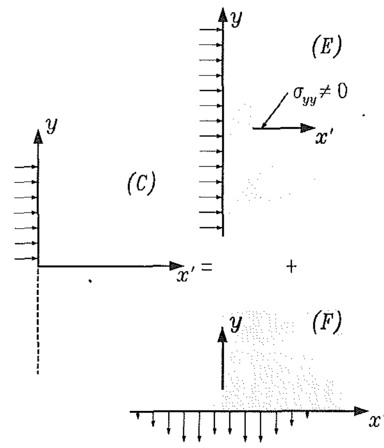

Fig. 6 Decomposition of the quarter-plane problem (C) into two half-plane problems, each of which can be solved by standard methods of analysis

problem of a half plane occupying $x' = x + l \geq 0$ with the surface of the half plane subject to a uniform normal velocity $\frac{1}{2}v(t)$. A result of this loading is that a normal stress is induced on $y = 0$ for $x' < c_d t$. This normal stress is then negated by considering the problem (F) of a half plane occupying $y \geq 0$ subjected to a surface normal traction equal but opposite to that induced on $y = 0$ in (E). This approach was introduced by Wright (1969) and Freund and Phillips (1969) in studies of grazing incidence of a stress pulse on a free surface.

2 Quarter Plane Problem

In this section, the solution of the quarter-plane problem designated as (C) in the preceding discussion is determined. The plane-strain deformation of an elastic material occupying the region $x' \geq 0$, $y \geq 0$ in the x, y-plane is considered, as indicated in Fig. 6. The prime on x is dropped for the development in this section. Initially, the material is stress-free and at rest. At time $t = 0$, a spatially-uniform normal displacement is imposed on the edge $x = 0$, $y > 0$ of the quarter plane. The shear traction is zero on this edge, and the traction is also zero on the other edge $x > 0$, $y = 0$. The resulting wave motion is a plane wave at $x = c_d t$ that carries a unit jump in particle displacement in the x-direction, plus cylindrical dilatational and shear waves centered at the corner of the quarter plane with their associated headwaves. A Rayleigh wave is also expected on the free surface at $x = c_R t$.

For purposes of the superposition step indicated in Fig. 5, and its counterpart for the case of antisymmetric loading, the only feature of the solution of the quarter-plane problem that is required is the displacement on the edge $y = 0$ for all time. It is this displacement that must be negated by a distribution of moving dislocations in (D). The displacement component $u_y(x, 0, t)$ will lead to the mode I stress intensity factor, and likewise the component $u_x(x, 0, t)$ will lead to the mode II stress intensity factor.

The two half-plane problems whose superimposed solutions provide the solution for the quarter-plane problem are labelled (E) and (F); see Fig. 6 for the case of symmetric loading. In (E), a unit step in normal displacement is imposed on the surface at time $t = 0$, and the shear traction on this surface is zero. The elementary solution is simply a plane wave propagating in the x-direction behind which $u_x = 1$. This wave satisfies the quarter-plane boundary conditions on the edge $x = 0$, $y > 0$ but the boundary conditions on the other edge are violated. The plane wave induces no shear stress σ_{xy} on this surface but it does induce a compressive normal stress $-\lambda a \delta(t - x/c_d)$ where $\delta(\ )$ denotes the Dirac delta function. Thus, the solution of the half-plane problem (F) must satisfy the boundary conditions

$$\sigma_{xy}(x,0,t)=0, \quad \sigma_{yy}(x,0,t)=\lambda a\delta(t-x/c_d). \tag{5}$$

In considering the physical dimensions of terms in (5) and of other fields in this section, it should be kept in mind that all expressions are multiplied by a unit displacement.

Application of the Laplace transforms defined in (4) to the wave equations (2) and the boundary conditions (5) leads to the transformed wave potentials for problem (F) given by

$$\bar{\phi}^F(\xi,y,s)=\frac{\lambda}{\mu}\frac{1}{s^2}\frac{a(b^2-2\xi^2)}{R(\xi)}g(\xi)e^{-s\alpha y} \quad \mathrm{Re}(\alpha)\geq 0$$

$$\bar{\psi}^F(\xi,y,s)=\frac{\lambda}{\mu}\frac{1}{s^2}\frac{2a\xi\alpha}{R(\xi)}g(\xi)e^{-s\beta y} \quad \mathrm{Re}(\beta)\geq 0 \tag{6}$$

where $\alpha(\xi)$ and $\beta(\xi)$ are defined by

$$\alpha(\xi)=(a^2-\xi^2)^{1/2}, \quad \beta(\xi)=(b^2-\xi^2)^{1/2} \tag{7}$$

and

$$g(\xi)=\frac{1}{a-\xi}+\frac{1}{a+\xi}$$

$$R(\xi)=(b^2-2\xi^2)^2+4\xi^2\alpha\beta. \tag{8}$$

The superscript F indicates a feature of problem (F). The condition $\mathrm{Re}(\alpha)\geq 0$ is met for all points in the ξ-plane by cutting ξ-plane along $a \leq |\mathrm{Re}(\xi)| < \infty$, $\mathrm{Im}(\xi)=0$, and choosing the branch for which α is a positive real number at $\xi=0$. Similar conditions are imposed on β. The function $R(\xi)$ is recognized as the Rayleigh wave function, and the only roots of $R(\xi)=0$ in the complex plane cut as indicated are at $\xi = \pm c = \pm 1/c_R$. The domain of definition of each of $\bar{\phi}^F$ and $\bar{\psi}^F$ is extended from the common strip of convergence of the integral transforms $-a < \mathrm{Re}(\xi) < a$ to the entire ξ-plane, cut along the line $|\mathrm{Re}(\xi)| > a$, $\mathrm{Im}(\xi)=0$. Both $\bar{\phi}^F$ and $\bar{\psi}^F$ have simple poles at the zeros of $R(\xi)$. Furthermore, $\bar{\phi}^F$ has simple poles at $\xi=\pm a$, which correspond to the point loads on the surface of the half space propagating in opposite directions with the dilatational wave speed. Transformed displacements for (F) can be obtained from potentials in the form

$$\bar{u}_x^F(\xi,0,s)=-\frac{\lambda}{\mu}\frac{1}{s}\frac{ab^2\xi(2\xi^2-b^2+2\alpha\beta)g(\xi)}{R(\xi)}$$

$$\bar{u}_y^F(\xi,0,s)=-\frac{\lambda}{\mu}\frac{1}{s}\frac{a\alpha(\xi)g(\xi)}{R(\xi)}. \tag{9}$$

It is noted that the transformed form of u_x^F is similar to u_y of Lamb's (1904) problem and the transformed form of u_x^F is similar to u_y of Abou-Sayed et al. (1980), with a weighting function $g(\xi)$.

The displacement components in physical coordinates can be obtained by application of the Laplace transform inversion integrals and the Cauchy integral theorem. The displacement components for problem (C) are then obtained by superposition of the results from (E) and (F), that is $u_i^F = u_i^E + u_i^F$. The result is

$$u_x^C(x,0,t)=\begin{cases}\dfrac{\lambda}{\mu}\dfrac{a}{\pi}\displaystyle\int_a^{t/x}\mathrm{Im}\left(\frac{(b^2-2\xi^2)-2\alpha\beta}{R(\xi)}\right)\xi g(\xi)d\xi & ax<t<bx\\[2ex] \dfrac{\lambda}{\mu}\left[\dfrac{a}{\pi}\displaystyle\int_a^{b}\mathrm{Im}\left(\frac{(b^2-2\xi^2)-2\alpha\beta}{R(\xi)}\right)\xi a g(\xi)d\xi \right. \\ \left. +\dfrac{2c^2-b^2+2\sqrt{(c^2-a^2)(c^2-b^2)}}{2\kappa S(c)}g(c)H(t-cx)\right] & bx<t<\infty\end{cases} \tag{10}$$

and

$$u_y^C(x,0,t)=\frac{\lambda}{\mu}\frac{ab^2}{\pi}\int_a^{t/x}\mathrm{Im}\left(\frac{2a}{R(\xi)\sqrt{a^2-\xi^2}}\right)d\xi \quad ax<t<\infty \tag{11}$$

where integration paths are taken on $\mathrm{Im}(\xi)\to 0^-$. The function $S(\xi)$ is defined in terms of the Rayleigh wave function by

$$R(\xi)=\kappa(c^2-\xi^2)S(\xi) \tag{12}$$

where $\kappa = 2(b^2-a^2)$. The function $S(\xi)$ has neither zeros nor poles in the cut ξ-plane and $S(\xi)\to 1$ as $|\xi|\to\infty$. With reference to Fig. 5, the displacement component u_y^C in (10) must be negated by superposition of dislocations in (D). The method to be described in the next section hinges on the observation that u_x^C and u_y^C are homogeneous functions of x and t of degree zero.

3 Fundamental Moving Dislocation Solutions

The next step in the analysis is to determine the crack-tip stress intensity factor for a single edge dislocation climbing at constant speed out of the crack tip; see problem (D) in Fig. 5. The body is stress-free and at rest up until the instant that the dislocation emerges from the crack tip. A solution to this problem that is valid for all time cannot be obtained in the presence of the free boundary at $x=-l$. However, a solution can be found for the case of a semi-infinite crack in an otherwise unbounded body, and the stress intensity factor histories will be identical cases for the two cases for time in the range $0<t<2l/c_d$. When the dislocation begins to move from the crack tip, a Rayleigh wave is initiated on the crack face. This surface wave travels at speed c_R from the crack tip toward the free edge of the plate. The main effect of free surface in this case is to reflect the Rayleigh wave back toward the crack tip at time $t=l/c_R$. The reflected Rayleigh wave can have a significant effect on the stress intensity factor when it arrives back at the crack tip. It is expected that the difference in stress intensity factor histories for dislocation emission between the edge crack problem and the half-plane crack problem will be small for time in the range $2l/c_d < t < 2l/c_R$.

Consider plane-strain deformation of an unbounded elastic solid containing a half-plane crack whose faces are free of traction. The material is initially stress-free and at rest. At time $t=0$, an elastic dislocation with Burgers vector of magnitude 2Δ in the y-direction begins to move at constant speed v in the positive x-direction from the crack tip. In the terminology of elastic dislocation theory, this is an edge dislocation climbing in the x-direction. The speed is assumed to be in the range $0\leq v\leq c_d$, though the solution may be obtained by the same procedure if the speed exceeds the dilatational wave speed of the material.

For the case of mode I, the deformation is symmetric with respect to the plane $y=0$. Thus, a solution is sought for $-\infty < x < \infty$, $0<y<\infty$, and $0\leq t<\infty$ subject to the boundary conditions

$$\begin{aligned}\sigma_{yy}(x,0,t)&=\sigma_+(x,t)\\ \sigma_{xy}(x,0,t)&=0\\ u_y(x,0,t)&=u_-(x,t)+\Delta H(vt-x)\end{aligned} \tag{13}$$

where σ_+ is the unknown normal stress distribution on the plane $y=0$ for $x\geq 0$, and $\sigma_+=0$ for $x<0$. Likewise, u_- is the unknown normal displacement distribution on $y=0$ for $x<0$, and $u_-=0$ for $x>0$.

Following the procedure introduced by Freund (1974), the Wiener-Hopf equation for this case is

$$\frac{-b^2\alpha(\xi)}{\mu R(\xi)}\Sigma_+(\xi)=U_-(\xi)+\frac{\Delta}{\xi+d} \tag{14}$$

where Σ_+ and U_- are the double Laplace transforms of σ_+ and u_-, respectively, and $d = 1/v$. Application of the factorization procedure of the Wiener-Hopf method leads to the solution for the double transform of σ_+ in the form

$$\Sigma_+(\xi)=-\frac{\Delta\mu\kappa}{b^2}\frac{1}{(\xi+d)F_+(\xi)F_+(d)} \tag{15}$$

where

$$F_+(\xi)=\frac{(c+\xi)S_+(\xi)}{\alpha_+(\xi)} \tag{16}$$

and

$$S_\pm(\xi)=\exp\left\{-\frac{1}{\pi}\int_a^b \tan^{-1}\left[\frac{4\eta^2|\alpha|\;|\beta|}{(2\eta^2-b^2)^2}\right]\frac{d\eta}{\eta\pm\xi}\right\}. \tag{17}$$

The transform inversion leads to the expression for σ_+ in the physical domain as

$$\sigma_+(x,t)=-\frac{\Delta}{\pi x}\,\mathrm{Im}\left\{\Sigma_+\left(-\frac{t}{x}+i0\right)\right\}H(t-ax). \tag{18}$$

The stress intensity factor history for mode I due to the dislocation moving at speed v, say $k_I(t;v)$, may be deduced from the asymptiotic behavior of $\Sigma_+(\xi)$ as $\xi \to \infty$, with the result

$$k_I(t;v)=-\sqrt{\frac{2}{\pi}}\frac{\mu\kappa}{b^2}\frac{1}{F_+(d)\sqrt{t}}\quad(\Delta=1). \tag{19}$$

The fact that $\sigma_+(x, t)$ is a homogeneous function of its arguments of order -1 is evident in (18). Furthermore, the dependence of the stress intensity factor on the dislocation velocity v has been indicated explicitly in (19). These observations are important in calculating the transient stress intensity factor $K_I(t)$ for the crack problem (A). Recall that this step requires the superposition of dislocations that reproduces a normal displacement that is exactly equal but opposite to the normal displacement $u_y(x, 0, t)$ of the quarter-plane problem (C); see Fig. 5.

The case of mode II can be handled in an analogous way. The direction of Burgers vector is the negative x-direction, rather than the positive y-direction as in mode I. In addition, the normal stress σ_{yy} vanished on $y = 0$ in the mode II equivalent of problem (D) instead of the component σ_{xy} in mode I. Suppose that $\tau_+(x, t)$ is the unknown shear stress on $y = 0$, $x > 0$ in this case. Without repeating the details, it can be shown that

$$\tau_+(x,t)=\frac{1}{\pi x}\frac{\Delta\mu\kappa}{b^2}\,\mathrm{Im}\left\{\frac{1}{(\xi+d)G_+(\xi)G_+(d)}\right\}_{\xi=-t/x+i0}H(t-ax) \tag{20}$$

where

$$G_+(\xi)=\frac{(c+\xi)S_+(\xi)}{\beta_+(\xi)}. \tag{21}$$

The fundamental stress intensity factor solution is

$$k_{II}(t;v)=-\sqrt{\frac{2}{\pi}}\frac{\mu\kappa}{b^2}\frac{1}{G_+(d)\sqrt{t}}\quad(\Delta=1). \tag{22}$$

The fundamental stress intensity factor solutions (19) and (22) will be used in the next section to construct the full mode I and mode II stress intensity factor histories.

4 Mixed-Mode Stress Intensity Factors

In the preceding section, the stress intensity factor due to the motion of a dislocation away from the tip of the crack at constant speed was considered. Suppose now that a continuous distribution of dislocations is emitted from the crack tip, each moving with a different constant speed. Furthermore, suppose that the time of emission and the amplitude of the Burgers displacement both depend on the speed of the dislocation. For any continuous variation of the amplitude, say $w(v)$, and the time of emission, say $t_o(v)$ with speed v, the continuous distribution represents a displacement distribution that is a homogeneous function of degree zero of position and time. From (19) or (22), the stress intensity factor resulting from this dislocation distribution is

$$K(t)=-\int_{v_1}^{v_2}k(t-t_o;v)\,\frac{dw(v)}{dv}\,dv \tag{23}$$

where v_1 and v_2 are appropriate limits on the actual range of speed.

In the present case, the distribution of climbing edge dislocations giving rise to an opening displacement across the plane $y = 0$ results in the mode I stress intensity factor. If the boundary loading acts at time $t = 0$ and at place $x = -l$, then the time at which the displacement level with speed x/t arrives at $x = 0$ is $t_o(v) = (1 - v/c_d)l/v$. The first displacement level to arrive at $x = 0$ does so with speed c_d, and the range of speeds of all displacement levels involved at time t is $l/t < v < c_d$. Therefore, the mode I stress intensity factor resulting from negation of the displacement distribution u_y, and the corresponding mode II stress intensity factor resulting from negation of u_x, are

$$K_I(t)=-\int_a^{h*}k_I(t-t_o;h)\,\frac{du_y(h)}{dh}\,dh \tag{24}$$

$$K_{II}(t)=-\int_a^{h*}k_{II}(t-t_o;h)\,\frac{du_x(h)}{dh}\,dh \tag{25}$$

where $h^* = t/l$ and the inverse speed $h = 1/v$ has been used as the integration variable for convenience. As indicated in Fig. 4, the solution for the case of a unit boundary condition is obtained by superposition of two fundamental solutions, each with half-unit boundary conditions. Thus, the results of Section 2 must be multiplied by one-half prior to superposition. This is accomplished by u_y in (24) with $u_y^C/2$ from (11). The integral expression for K_I can be evaluated by using the fundamental formula for $k_I(t; v)$ in (19) and the explicit expression for the displacement u_y^C given in (11). The procedure is described by Freund (1974), and only the result is included here, that is,

$$K_I(t)=-\frac{\lambda}{\sqrt{2\pi l}}\begin{cases}\dfrac{\kappa}{\pi}\displaystyle\int_a^{h*}\frac{2a^2(2h^2-b^2)}{(h+a)\sqrt{(h-a)(h^*-h)}}P(h)dh & a<h^*<b\\[2ex] \dfrac{\sqrt{2a}}{S_+(a)\sqrt{h^*+a}}\dfrac{a}{c+a}+\dfrac{2a^2\sqrt{c-a}}{S_-(c)\sqrt{c-h^*}(c^2-a^2)} & b<h^*<c\\[2ex] \dfrac{\sqrt{2a}}{S_+(a)\sqrt{h^*+a}}\dfrac{a}{(c+a)} & c<h^*<3a\end{cases} \tag{26}$$

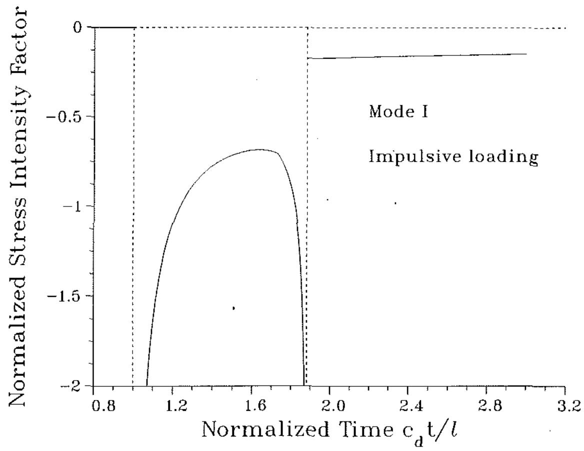

Fig. 7 The mode I stress intensity factor for the case of impulsive imposed velocity $v(t) = \delta(t)$, normalized by $E/[2(1 - \nu^2)\sqrt{\pi l}]$, versus normalized time

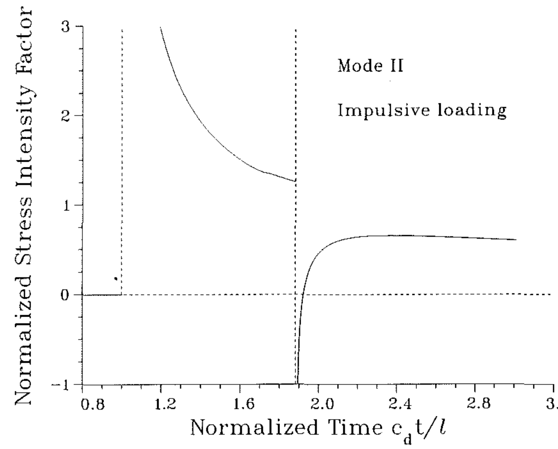

Fig. 8 The mode II stress intensity factor corresponding to the result in Fig. 8

The history of K_I is square root singular at $t/l = c$, but a nonzero, finite value is obtained at $t/l = a$ from the integration. Following a similar process, K_{II} is obtained as

$$K_{II}(t) = -\frac{\lambda}{\sqrt{2\pi l}} \begin{cases} \dfrac{\kappa}{\pi}\displaystyle\int_a^{h^*} \frac{4a^2h\sqrt{b-h}}{\sqrt{(h^2-a^2)(h^*-h)}} P(h)dh & a<h^*<b \\ \dfrac{\kappa}{\pi}\displaystyle\int_a^{b} \frac{4a^2h\sqrt{b-h}}{\sqrt{(h^2-a^2)(h^*-h)}} P(h)dh & b<h^*<c \\ \dfrac{\kappa}{\pi}\displaystyle\int_a^{b} \frac{4a^2h\sqrt{b-h}}{\sqrt{(h^2-a^2)(h^*-h)}} P(h)dh & \\ \quad +\dfrac{2a^2c}{b^2(c^2-a^2)} \dfrac{2c^2-b^2-2\sqrt{(c^2-a^2)(c^2-b^2)}}{S_-(c)\sqrt{c+b}} \dfrac{1}{\sqrt{h^*-c}} & c<h^*<3a. \end{cases} \quad (27)$$

The history of K_{II} has a square root singularity at $t/l = c$, but again a finite value is found at $t/l = a$ from the integration. In the above expressions, $P(h) = (h + c)(2h^2 - b^2)S_+(h)/[(2h^2 - b^2)^4 + 16h^4(h^2 - a^2)(b^2 - h^2)]$.

For numerical evaluation of these expressions Poisson's ratio, ν, is assumed to be equal to 0.25. In this case, the ratios of the slowness are $b^2 = 3a^2$ and $c^2 = 3.549a^2$. The stress intensity factors have been evaluated numerically by application of the appropriate Gaussian quadrature rules with Chebychev polynomial interpolations. The results are shown in Figs. 7 and 8. The results are normalized by the limiting value of the mode II stress intensity factor as $t \to \infty$ for the problem posed in section 1 with $v(t) = \delta(t)$. This stress intensity factor is readily calculated to be $E/[2(1 - \nu^2)\sqrt{\pi l}]$ (times the unit imposed displacement) by means of the M-integral procedure introduced by Freund (1978).

Up to this point, the stress pulse grazing the lower edge of the crack surface has had the form of a displacement with step-function time dependence. The stress intensity factors for general time dependence can be obtained by convolution. If the velocity on the lower edge is prescribed as an arbitrary function of time $v(t)$, then the stress intensity factor for this situation is

$$\mathcal{K}(t) = \int_0^t K(t)-s)v(s)ds. \quad (28)$$

For example, suppose that the velocity is a step function $v(t) = v_oH(t)$, which is essentially the loading condition used by Kalthoff (1987). The resulting values of $\mathcal{K}_I(t)$ and $\mathcal{K}_{II}(t)$ obtained according to (28) are presented in Fig. 9 and Fig. 10. The normalizing factor here is $Ev_o\sqrt{l/\pi}/[2c_d(1 - \nu^2)]$.

5 Discussion

In the foregoing sections, the exact elastodynamic stress intensity factor history has been determined for a particular case of asymmetric impact of an edge-cracked plate. The stress intensity factor results for impulsive imposed velocity $v(t) = \delta(t)$ are presented in Figs. 7 and 8. In themselves, these results are of limited practical significance. However, they provide the fundamental building block for determining the transient stress intensity factors for more realistic imposed velocity boundary conditions. In addition, the existence of an exact solution for a configuration of this sort provides a valuable check on numerical procedures that are being developed to analyze more complex geometries and, eventually, impact with nonlinear material response.

The exact stress intensity factor histories for step velocity loading $v(t) = v_oH(t)$ are given in Figs. 9 and 10. As anticipated, when the imposed velocity on the boundary is in a direction into the material, then the adjacent crack face bulges outward and the resulting mode I stress intensity factor is negative. If the crack is initially closed the faces would press against each other and, in fact, no mode I stress intensity factor would develop. On the other hand, if the crack is initially held open by some background equilibrium load or if the geometry is such that a small opening exists beforehand, then the crack will indeed tend to close upon application of the boundary velocity.

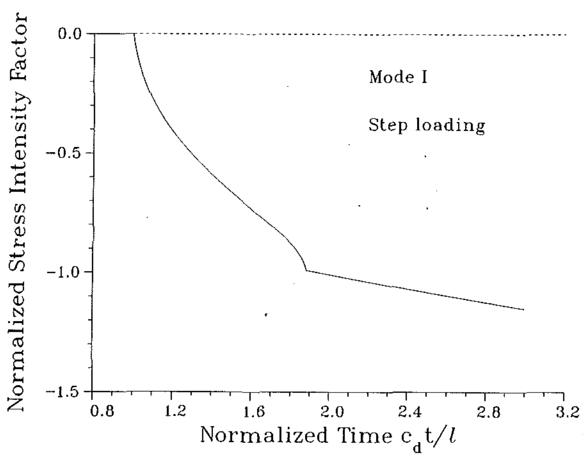

Fig.9 The mode I stress intensity factor for the case of step loading $v(t) = v_o H(t)$, normalized by $Ev_o\sqrt{l/\pi l}\,[2(1-\nu^2)c_d]$, versus normalized time

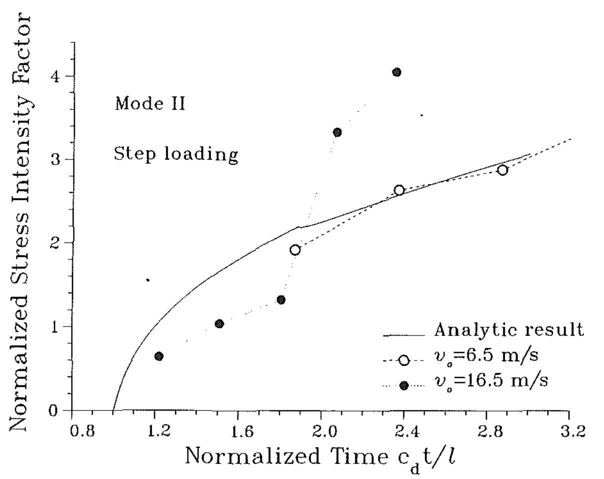

Fig. 10 The mode II stress intensity factor corresponding to the result in Fig. 9. The data points are those reported by Kalthoff (1987).

The magnitude of the mode I stress intensity factor is always less than the magnitude of the corresponding mode II stress intensity factor, but the value is significant. A single parameter that is useful in characterizing the near-tip field under mixed-mode conditions was introduced by Shih (1974). The parameter is defined by

$$\mathfrak{M}^e = \frac{2}{\pi}\tan^{-1}\left(\frac{K_I}{K_{II}}\right) \tag{29}$$

and it is called the mixity parameter. The dependence of the mixity parameter on time for the problem analyzed here is shown in Fig. 11, where it is seen that the value varies only a small amount from -0.25 over the time interval of interest.

If it is assumed that the crack will grow in a direction determined by the condition that the circumferential tensile stress within the asymptotic field is maximum then the angle between the crack line and the direction of growth satisfies

$$3\sin^2\left(\frac{\theta}{2}\right) - \tan\left(\frac{\pi}{2}\,\mathfrak{M}^e\right)\cos\left(\frac{\theta}{2}\right)\sin\left(\frac{\theta}{2}\right) - 1 = 0. \tag{30}$$

The angle θ_e that satisfies this condition for the problem analyzed here is also shown in Fig. 11 where it is seen that this angle varies only slightly from 63 deg in the time interval of interest.

The possible influence of crack face interaction resulting from the tendency for the crack to close under compressive loading is difficult to assess at this point. In the pure mode I problem considered by Freund (1974), the crack could be viewed as closed with normal pressure acting or open with no traction acting. In the mixed-mode case considered here, however, the crack faces would tend to slide with respect to each other if they are in contact so that the two modes are coupled in a way that has not yet been sorted out. Perhaps some progress on this point could be made by considering the case of closed crack faces, that is, continuous normal traction and velocity across the crack, but zero shear traction over the entire crack surface. This problem could be analyzed by the procedure used here.

Data taken from the work of Kalthoff (1987) are also shown in Fig. 10. He measured the speed of the impacting projectile in the configuration of Fig. 1, and the resulting stress intensity factor histories were observed by means of the optical shadow-spot method. In his experiments, interaction between the crack faces was avoided by cutting the cracks into the plate so that there was a finite gap between the crack faces. Thus, both a mode II stress intensity factor and a *compressive* mode I stress intensity factor could be generated, as modeled in the present analysis. To enter the data for steep specimens struck by steel

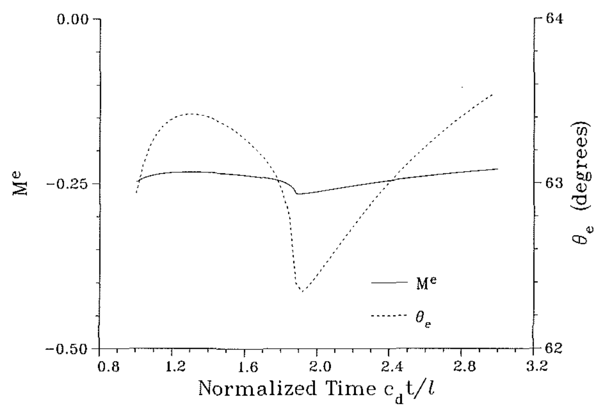

Fig. 11 The mixity parameter defined in (30) for the stress intensity factors given in Figs. 9 and 10, and the corresponding direction of crack growth based on a maximum circumferential tensile stress criterion

projectiles on Fig. 10, the velocity value v_o imposed on the edge of the specimen was determined by assuming that the portion of the specimen struck by the projectile (see Fig. 1) had the same elastic impedance as the projectile itself. Thus, from elementary wave propagation theory, the value of v_o was essentially one-half of the speed of the incident projectile. The agreement between the analytical model results and the experimental results for the low velocity result (v_o = 6.5 m/s) is excellent over the time range for which data are reported. On the other hand, the observed mode II stress intensity factor for the higher velocity impact (v_o = 16.5 m/s) is less than the theoretical result up until the time $c_d t/l \sim 2$, and substantially greater thereafter. Kalthoff (1987) also reported results of one experiment on the brittle plastic Araldite B which, when normalized, were closer to the analytical results than the high impact velocity steel results but which differed in the same general way. Nonetheless the trend between the observed variation of K_{II} with time and the analytical result are consistent in both cases up until $c_d t/l \sim 2$. The differences thereafter could be due to nonlinear material response in the crack tip region or to the influence of other features of the experiment not taken into account in the analytical model, such as the presence of the second crack. Both of these possibilities are being pursued through further work based on detailed numerical simulation of the process.

Acknowledgment

The work described here was supported by the National Science Foundation, through grant DMR87-14665 to Brown

University, and by the Office of Naval Research, through contract N00014-87-K-0481 to Brown University. This research support is gratefully acknowledged.

References

Abou-Sayed, I. S., Burgers, P., and Freund, L. B., 1980, "Stress Intensity Factor Due to Parallel Impact Loading of the Faces of a Crack," *Fracture Mechanics: Twelfth Symposium*, ASTM STP 700, pp. 164-173.

Brock, L. M., 1982, "Shear and Normal Impact Loadings on One Face of a Narrow Slit," *International Journal of Solids and Structures*, Vol. 18, pp. 467-477.

Freund, L. B., 1974, "The Stress Intensity Factor Due to Normal Impact Loading of the Faces of a Crack," *International Journal of Engineering Science*, Vol. 12, pp. 179-189.

Freund, L.B., and Phillips, J. W., 1969, "Stress Pulse Grazing a Free Boundary of an Elastic Solid," Brown University Technical Report, No. A. M. 39.

Freund, L. B., 1978, "Stress Intensity Factor Calculations Based on a Conservation Integral," *International Journal of Solids and Structures*, Vol. 14, pp. 241-250.

Kalthoff, J. K., and Winkler, S., 1987, "Failure Mode Transition at High Rates of Shear Loading," *Impact '87* (International Conference on Impact Loading and Dynamic Behavior of Materials), May, Bremen, West Germany.

Kalthoff, J. K., 1987, "Shadow Optical Analysis of Dynamic Shear Fracture," *International Conference on Photomechanics and Speckel Metrology*, SPIE, Vol. 814, pp. 531-538.

Kim, K. S., 1985, "Dynamic Fracture Under Normal Impact Loading of the Crack Faces," ASME Journal of Applied Mechanics, Vol. 52, pp. 585-592.

Lamb, H., 1904, "On the Propagation of Tremors over the Surface of an Elastic Solid," *Philosophical Transactions of the Royal Society* (*London*), Vol. A203, pp. 1-42.

Ravi-Chandar, K., and Knauss, W. G., 1984, "An Experimental Observation into Dynamic Fracture: I. Crack Initiation and Arrest," *International Journal of Fracture*, Vol. 25, pp. 247-262.

Shih, C. F., 1974, "Small-Scale Yielding Analysis of Mixed Mode Plane-Strain Crack Problems," *Fracture Analysis*, ASTM STP 560, pp. 187-210.

Skalak, R., 1957, "Longitudinal Impact of a Semi-infinite Circular Elastic Bar," ASME Journal of Applied Mechanics, Vol. 24, pp. 59-64.

Wright, T. W., 1969, "Impact on an Elastic Quarter Space," *Journal of the Acoustical Society of America*, Vol. 45, pp. 935-943.

Peter Gudmundson[1]

Sören Östlund

Department of Strength of Materials
and Solid Mechanics,
The Royal Institute of Technology,
S-100 44 Stockholm, Sweden

Stress Singularity at the Free Surface of a Dynamically Growing Crack

The stress singularity at the intersection between the crack front and the free surface of a dynamically growing crack in a linear elastic isotropic material has been numerically evaluated by an especially developed finite element program. The singularity parameter (λ), *defined by* $\sigma \sim R^{\lambda-1}$, *is presented as a function of the crack-tip velocity and the angle* (β) *between the crack front and the free surface. The angle* (β) *at which the singularity* (λ) *equals 0.5 was found to be 101 deg almost independently of the crack-tip velocity.*

1 Introduction

The stress field close to a crack tip in a linear elastic material has a $r^{-0.5}$ singularity, where r denotes the distance from the crack tip. The crack-tip velocity has an influence on the angular dependence but not on the strength of the singularity. It should, however, be emphasized that these facts are only valid inside a body at points where the crack front is smooth. In particular, the aforementioned stress and displacement fields will not be valid close to the point where the crack front meets a free surface. Benthem (1977) was apparently the first one to determine the stress singularity at such a point for a stationary crack. By an application of series expansions of Neuber-Papkovich potentials he found that, for a Poisson ratio of 0.3, the stresses behaved as $r^{-0.4523}$ close to the singular point. Later, Benthem (1980) resolved the same problem by an application of a finite difference technique. He was then able to confirm the previous results. Bažant and Estenssoro (1979) solved the same static problem as Benthem by a finite element technique. They also investigated cases for which the crack plane and the crack front formed arbitrary angles to the free surface. By energy arguments they claimed that the inclination of the crack plane and the crack front must be such that the singularity coincides with the internal $r^{-0.5}$ stress singularity. Their conclusions seem to be confirmed by experimental results, (see Bažant and Estenssoro (1979), (1980)). The energy release rate along a stationary crack front has been numerically studied by Burton et al. (1984) for some crack/surface intersection problems. It is observed that a decay in the energy release rate takes place as the free surface is approached. This decay is expected from the weaker singularity previously mentioned. For the problems treated by Burton et al. (1984), this three-dimensional effect was probably not significant from a fracture toughness testing point of view. However, if the deformation field on the free surface close to the crack tip is used in the analysis of the experiments, this might not be true as will be discussed later. Burton et al. (1984) also points out that three-dimensional effects might be more important if near-surface residual stresses are present.

In the present investigation the previously discussed problem has been analyzed for a dynamically growing crack. The stress singularity has been determined as a function of crack-tip velocity and the angle between the crack front and the free surface. The problem is numerically solved by a finite element formulation which is similar to that used by Bažant and Estenssoro (1979). For a vanishing crack-tip speed the numerical results from Bažant and Estenssoro (1979) could be confirmed, and at nonvanishing crack-tip velocities, the additional dynamic terms had an influence on the results.

The results from this investigation contribute to the understanding of curved crack fronts for dynamically growing cracks. By using the same energy arguments as Bažant and Estenssoro (1979) it can be argued that also for a dynamically growing crack, the crack tip at the free surface is trailing behind the crack tip inside a finite thickness specimen.

Many experimental dynamic fracture mechanics investigations have been based on optical methods combined with high-speed photography for the determination of crack-tip speed and stress intensity factors. Based on the present results, one should be aware of two facts when such experimental data are evaluated. First, the crack length measurement which is based on a surface evaluation can be wrong because of a curved crack front. Secondly, if the displacement fields are measured too close to the crack tip at the free surface, they are governed by the singular fields which have been analyzed in this report. If the determination of the stress intensity factors is then based on the two-dimensional plane-stress solution, errors can occur. For thin sheet specimens, these two error sources are probably negligible. However, if thicker specimens are experimentally investigated, one should be aware of the

[1] Presently at the Swedish Institute of Composites, S-941 26 Piteå, Sweden.

Contributed by the Applied Mechanics Division of THE AMERICAN SOCIETY OF MECHANICAL ENGINEERS for publication in the JOURNAL OF APPLIED MECHANICS.

Discussion on this paper should be addressed to the Technical Editor, Leon M. Keer, The Technological Institute, Northwestern University, Evanston, IL 60208, and will be accepted until two months after final publication of the paper itself in the JOURNAL OF APPLIED MECHANICS. Manuscript received and accepted by the ASME Applied Mechanics Division, April 26, 1988.

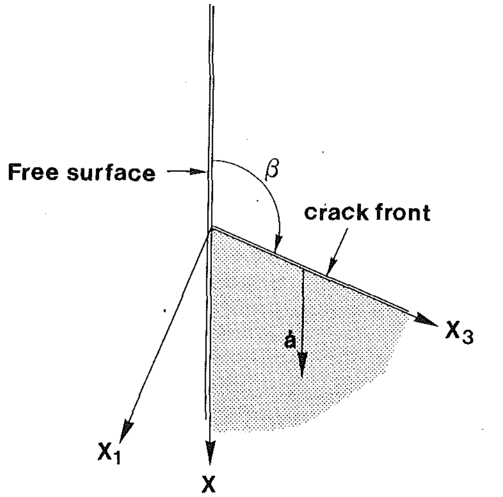

Fig. 1 Definition of coordinate systems and the angle β. The crack propagates in the x-direction, and the shaded area represents the unbroken ligament.

aforementioned problems. The size of the region around the crack tip inside which the two-dimensional plane-stress solution for a stationary crack does not prevail has been experimentally investigated using the method of caustics by Rosakis and Ravi-Chandar (1986). These authors did find that for a straight crack front perpendicular to the free surface there is a region of approximately half the specimen thickness within which the plane-stress solution is no longer applicable and three-dimensional effects cannot be neglected. The same result was observed by Yang and Freund (1985), who explored the three-dimensional crack problem using a boundary layer approach.

In the present report only symmetrical stress fields have been evaluated. This corresponds to mode I loadings in the fracture mechanics terminology. The numerical method could, however, be easily applied to solve antisymmetric problems.

2 Theoretical Basis

A dynamically growing crack in a linear elastic isotropic material is considered. The crack plane is perpendicular to a free surface and the crack front forms an angle, β, to the free surface (see Fig. 1).

For the determination of the stress and displacement fields close to the point where the crack front meets the free surface, it is convenient to introduce a moving Cartesian coordinate system (x_1, x_2, x_3) which is based at this point. The x_3-axis coincides with the crack front, the x_2-axis is perpendicular to the crack plane and lies on the free surface, and the x_1-axis lies in the crack plane and forms an angle β-$\pi/2$ with the free surface (see Fig. 1).

Based on the principle of virtual work, the stress and displacement fields in a volume (V) bounded by the surface (S) can be determined from

$$\int_V \sigma_{ij}\delta\epsilon_{ij}dV + \int_V \rho\ddot{u}_i\delta u_i dV = \int_{S_T} T_i\delta u_i dS, \tag{1}$$

where σ_{ij}, ϵ_{ij}, u_i, and $\ddot{u}_i$ denote the physical components of the stress tensor, the strain tensor, the displacement vector, and the acceleration vector, respectively. T_i is the traction vector and ρ the density. Virtual displacements are denoted by δu_i and virtual strains by $\delta\epsilon_{ij}$.

If it is assumed that a steady-state condition has been reached (the fields are independent of time in the moving coordinate system), the acceleration vector can be written as

$$\ddot{u}_i = \dot{a}^2\frac{\partial^2 u_i}{\partial x^2} \tag{2}$$

where $\dot{a}$ denotes the crack-tip velocity and x is a coordinate in the direction of crack growth (see Fig. 1). The steady-state assumption is not severe since it can be proved that asymptotically close to the origin of (x_1, x_2, x_3), equation (2) is always true.

The introduction of equation (2) in equation (1) and an application of the divergence theorem leads to an alternative expression for the principle of virtual work,

$$\int_V \sigma_{ij}\delta\epsilon_{ij}dV - \int_V \rho\dot{a}^2\frac{\partial u_i}{\partial x}\,\delta\left(\frac{\partial u_i}{\partial x}\right)dV + \int_S \rho\dot{a}^2\frac{\partial u_i}{\partial x}\delta u_i n_x dS = \int_{S_T} T_i\delta u_i dS, \tag{3}$$

where n_x denotes the component of the normal vector in the direction of crack growth.

For the investigation of stresses and displacements close to the origin of the moving coordinate system, it is useful to introduce a spherical coordinate system according to

$$\begin{aligned} x_1 &= R\sin\theta\cos\phi, \\ x_2 &= R\sin\theta\sin\phi, \\ x_3 &= R\cos\theta. \end{aligned} \tag{4}$$

For small R, it can be assumed that the displacements behave like R^{λ}, where λ is an unknown constant (see Benthem (1977), Bažant and Estenssoro (1979)). The reason for this assumption is that no characteristic length exists in the problem. The assumed R dependence implies that

$$u_i(R,\theta,\phi) = R^{\lambda}\bar{u}_i(\theta,\phi), \tag{5}$$

$$\epsilon_{ij}(R,\theta,\phi) = R^{\lambda-1}\bar{\epsilon}_{ij}(\theta,\phi), \tag{6}$$

$$\sigma_{ij}(R,\theta,\phi) = GR^{\lambda-1}\bar{\sigma}_{ij}(\theta,\phi), \tag{7}$$

$$\frac{\partial u_i}{\partial x}(R,\theta,\phi) = R^{\lambda-1}\bar{u}_{i,x}(\theta,\phi). \tag{8}$$

Here, a bar denotes a function which only depends on θ, ϕ. In equation (7), G denotes the shear modulus.

If equations (4)–(8) are introduced in equation (3), the volume integrals can be performed explicity in the R-direction and surface integrals result. This is valid under the assumption that $\mathrm{Re}(\lambda) > -0.5$, which is the condition for a finite strain energy close to the origin (see Benthem, 1977). The surface integral formulation must be valid for arbitrary surfaces defined by $R = R(\theta,\phi)$. If a spherical surface, $R = R_0$, is selected, the resulting equations can, after some rearrangements, be written as

$$\int_\theta \int_\phi [\bar{\sigma}_{ij}\delta\bar{\epsilon}_{ij} - (2\lambda+1)\bar{\sigma}_{ij}n_j\delta\bar{u}_i - M^2(\bar{u}_{i,x}\delta\bar{u}_{i,x} - (2\lambda+1)\bar{u}_{i,x}n_x\delta\bar{u}_i)]\sin\theta d\theta d\phi = 0. \tag{9}$$

Here, the Mach number, M, has been introduced, $M^2 = \dot{a}^2/(G/\rho)$, and the tractions, $\bar{T}_i$, has been written as $\bar{T}_i = \bar{\sigma}_{ij}n_j$.

The stresses, $\bar{\sigma}_{ij}$ can, through Hooke's law, be expressed in terms of the strains $\bar{\epsilon}_{ij}$, which in turn can be determined from the displacements, $\bar{u}_i$. Hence, equation (9) expresses a weak formulation for the determination of $\bar{u}_i$. The problem is homogeneous, and nontrivial solutions can only exist for certain values of λ, the eigenvalues λ_n. Of practical interest are those λ_n for which the real part is larger than -0.5. Smaller λ_n give rise to infinite strain energies which are physically unrealistic. It is also observed that the solution with the minimum λ_n will be the most singular one. Thus, the problem is defined by the determination of the minimum eigenvalue with a real part larger than -0.5.

If a static problem is considered, $M=0$, the same problem as was investigated by Benthem (1977) and Bažant, Estenssoro (1979) results. Bažant and Estenssoro (1979) use a slightly different derivation and an apparently different equation results. It can be shown that their formulation and the present one are equivalent.

Based on equation (9) a finite element formulation can be defined. As is explained in the next section, a generalized nonlinear eigenvalue problem for approximate solutions of λ_n and the corresponding eigenfunctions $\bar{u}_i$ will result.

3 Numerical Procedure

In the derivation of the finite element equations it is convenient to introduce a vector notation. Denote by $\bar{\mathbf{u}}$, $\bar{\boldsymbol{\epsilon}}$, $\bar{\boldsymbol{\sigma}}$, and $\bar{\mathbf{u}}_{,x}$ the vectors formed from the components of the tensors $\bar{u}_i$, $\bar{\epsilon}_{ij}$, $\bar{\sigma}_{ij}$, and $\bar{u}_{i,x}$ in the spherical coordinate system introduced in equation (4). The displacement vector is then written as

$$\bar{\mathbf{u}} = \mathbf{H}\boldsymbol{\alpha} \tag{10}$$

where $\mathbf{H}$ is a matrix containing the shape functions and $\boldsymbol{\alpha}$ is a vector of nodal displacements. The expressions for $\bar{\boldsymbol{\epsilon}}$, $\bar{\boldsymbol{\sigma}}$, and $\bar{\mathbf{u}}_{,x}$ are preferably divided into two parts according to

$$\bar{\epsilon} = \mathbf{B}_1\alpha + \lambda\mathbf{B}_2\alpha \tag{11}$$

$$\bar{\sigma} = \bar{\mathbf{C}}\bar{\epsilon} = \bar{\mathbf{C}}\mathbf{B}_1\alpha + \lambda\bar{\mathbf{C}}\mathbf{B}_2\alpha \tag{12}$$

$$\bar{\mathbf{u}}_{,x} = \mathbf{D}_1\alpha + \lambda\mathbf{D}_2\alpha. \tag{13}$$

Here, $\bar{\mathbf{C}}$ is the constitutive matrix normalized with respect to the shear modulus; $\mathbf{B}_1$ and $\mathbf{B}_2$ are matrices independent of λ formed from the strain-displacement relations in the spherical coordinates, and $\mathbf{D}_1$ and $\mathbf{D}_2$ are matrices independent of λ derived from equation (8). Introducing equations (10)–(13) into equation (9), and taking into consideration that this equation must hold for arbitrary variations $\delta\alpha$ yields

$$\begin{aligned}\Big\{\int_\theta\int_\phi [&\mathbf{B}_1{}^T\bar{\mathbf{C}}\mathbf{B}_1 + \lambda(\mathbf{B}_1{}^T\bar{\mathbf{C}}\mathbf{B}_2 + \mathbf{B}_2{}^T\bar{\mathbf{C}}\mathbf{B}_1) + \lambda^2\mathbf{B}_2{}^T\bar{\mathbf{C}}\mathbf{B}_2\\ &-M^2(\mathbf{D}_1{}^T\mathbf{D}_1 + \lambda(\mathbf{D}_1{}^T\mathbf{D}_2 + \mathbf{D}_2{}^T\mathbf{D}_1) + \lambda^2\mathbf{D}_2{}^T\mathbf{D}_2)\\ &+M^2(\mathbf{H}^T\mathbf{D}_1 + \lambda(2\mathbf{H}^T\mathbf{D}_1 + \mathbf{H}^T\mathbf{D}_2) + 2\lambda^2\mathbf{H}^T\mathbf{D}_2)n_x\\ &-(\mathbf{H}^T\mathbf{N}\bar{\mathbf{C}}\mathbf{B}_1 + \lambda(2\mathbf{H}^T\mathbf{N}\bar{\mathbf{C}}\mathbf{B}_1 + \mathbf{H}^T\mathbf{N}\bar{\mathbf{C}}\mathbf{B}_2)\\ &+2\lambda^2\mathbf{H}^T\mathbf{N}\bar{\mathbf{C}}\mathbf{B}_2)]\sin\theta d\theta d\phi\Big\}\alpha = \mathbf{0}.\end{aligned} \tag{14}$$

In equation (14), $\mathbf{N}$ is a matrix formed from the components of the normal vector n_i so that $\mathbf{N}\bar{\sigma}$ is equivalent to $\bar{\sigma}_{ij}n_j$.

The integration in equation (14) should be performed over the surface of a half sphere surrounding the corner. Since the angle θ is measured from an axis along the crack front, the following limitations on the integration domain can be derived

$$0 \le \phi \le \pi, \tag{15}$$

$$\theta = \theta_b = \arctan\left(\frac{\tan(\pi-\beta)}{\cos\phi}\right), \text{ if } \theta<0 \text{ then } \theta \to \theta + \pi. \tag{16}$$

In equation (15), symmetry, with respect to the crack plane, has been assumed.

Special attention must be given to the matrices $\mathbf{D}_1$ and $\mathbf{D}_2$, and to the component n_x of the normal vector when the crack front is not normal to the free surface. In this case $\mathbf{D}_1$ and $\mathbf{D}_2$ can be derived from

$$\bar{\mathbf{u}}_{,x} = \bar{\mathbf{u}}_{,1}\sin(\pi-\beta) + \bar{\mathbf{u}}_{,3}\cos(\pi-\beta), \tag{17}$$

where $\bar{\mathbf{u}}_{,1}$ and $\bar{\mathbf{u}}_{,3}$ follows from equations similar to equation (8). In the same way the x-component of the normal vector follows as

$$n_x = \sin\theta\cos\phi\sin(\pi-\beta) + \cos\theta\cos(\pi-\beta). \tag{18}$$

The finite elements used in the present analysis were four-noded isoparametric elements in the (θ,ϕ) plane. This means that the basic shape functions included in the matrix $\mathbf{H}$ have been considered as bilinear, i.e., as $a + b\theta + c\phi + d\theta\phi$. The integrals in equation (14) were evaluated by Gaussian numerical integration using nine integration points per element. This leads to the formulation of an eigenvalue problem

$$(\mathbf{K}_0 + \lambda\mathbf{K}_1 + \lambda^2\mathbf{K}_2)\alpha = \mathbf{0}, \tag{19}$$

where the matrices $\mathbf{K}_0$, $\mathbf{K}_1$, and $\mathbf{K}_2$ follow from equation (14) in a straight forward way.

For the solution of the generalized nonlinear eigenvalue problem defined by equation (19), a value of λ is assumed and a specified component, α_k, of the nodal displacement vector is set to 1. A standard equation solving subroutine is then used to solve for the remaining α_i. When all α_i are known, it is possible to calculate the right-hand side, P_k, of equation k. This procedure is iterated and λ is varied according to a modified Powell hybrid method, implemented in a standard library subroutine, until a λ for which $P_k = 0$ is found. To make it possible to search for complex eigenvalues, a subroutine giving the solution to a complex system of equations was used in the finite element code. However, for the problems stated in this report no complex λ was found.

4 Numerical Results

The singularity parameter λ has been determined for symmetrical mode I crack growth as a function of the nondimensionalized crack-tip velocity M and the angle β. The stress boundary conditions on the free surface, $\theta = \theta_b$, and the crack surface, $\phi = \pi$, are automatically satisfied by the finite element method. To impose symmetry with respect to the crack plane, the displacements in the ϕ-direction at $\phi = 0$ were set equal to 0.

To obtain accurate results for λ with the four-noded isoparametric finite elements an extremely fine mesh would have to be used. However, as pointed out by Bažant and Estenssoro (1979), this is not necessary since the convergence pattern can be exploited to greatly improve the accuracy, provided that the grids for various subdivisions are all similar, generated according to the same rule. In this study grids of 32, 50, 72, 128, and 200 finite elements, corresponding to subdivisions 4×8, 5×10, 6×12, 8×16 and 10×20 in the θ and ϕ-directions, respectively were used.

The value λ obtained from an extrapolation to an infinite number of elements was calculated by assuming

$$\log(\lambda_N - \lambda) = \log A + m\log\left(\frac{1}{N}\right) \tag{20}$$

and determining the unknown constants λ, m, and A by a least square fit to the numerical values λ_N obtained from grids of different number of finite elements N. If there were no gradient singularities in the functions $\bar{u}_i(\theta, \phi)$, a value of $m=1$ would be expected. In the present formulation the functions exhibit a gradient singularity for $\theta \to 0$, so that a value of $m<1$ could be expected. For the results presented in this work, m was between 0.94 and 0.96. It was observed that for higher crack-tip velocities it was usually necessary to leave out the value of λ_N obtained from $N=32$, since it did not show an acceptable convergence pattern.

To check the numerical formulation and the implementation into the finite element program, values of λ were compared with the results of Benthem (1977) and Bažant,

Table 1 Values of λ as function of nondimensionalized crack-tip velocity M; $\beta = 90$ deg, $\nu = 0.3$

M	0.0	0.1	0.3	0.5	0.7
λ	0.548	0.548	0.551	0.561	0.600

Estenssoro (1979) for a stationary crack. In general, these results showed very good agreement as will be noted later.

There does not seem to exist any tests which completely check the velocity-dependent terms of equation (14). One test which gives some confidence in the results is to impose symmetry boundary conditions at $\theta = \theta_b$ for $\beta = 90$ deg. In this case the corner singularity reduces to a line singularity, which is known to have a value of λ equal to 0.5 for all M. For this problem the extrapolation to $N \rightarrow \infty$ from values of $N = 18$, 32, 72, and 128 provides a λ which is less than 0.6 percent from the correct value, for cases where $M = 0.0$ and 0.5 and Poisson's ratio $\nu = 0.15$.

All results presented in the remainder of this section are calculated for $\nu = 0.3$. In Table 1 values for λ for $\beta = 90$ deg are presented for different crack-tip velocities. The value for a stationary crack, $\lambda = 0.548$, is in close agreement with the result of Benthem (1977), $\lambda = 0.5477$, Bažant and Estenssoro (1979), $\lambda = 0.548$, and Andersson (1988), $\lambda = 0.5465$. Andersson obtained his result by use of a p-version of the finite element method. In Fig. 2 results for different angles β are presented. Of particular interest is the value, $\beta_{0.5}$, for which a stationary crack has a singularity parameter λ equal to 0.5. The parameter λ depends almost linearly on β and a least square fit of a straight line to the numerical values gives $\beta_{0.5} = 101.1$ deg. This is almost identical to the result of Bažant and Estenssoro (1979), $\beta_{0.5} = 101.16$ deg.

The results for $\beta = 100$ deg need a special comment. Figure 2 indicates that λ is a slightly decreasing function of M except for crack-tip velocities close to the elastic Rayleigh surface wave speed $M \approx 0.9262$, where a pronounced increase takes place. This decrease of λ might be an effect of the extrapolation procedure since the values of λ_N, for all the grids used, is monotonously increasing with crack-tip velocity. A more correct curve for $\beta = 100$ deg might be slightly increasing for low values of M and then show a steeper increase in λ close to the Rayleigh wave speed. One conclusion is that for values of β close to 101 deg, λ is very insensitive to variations in M.

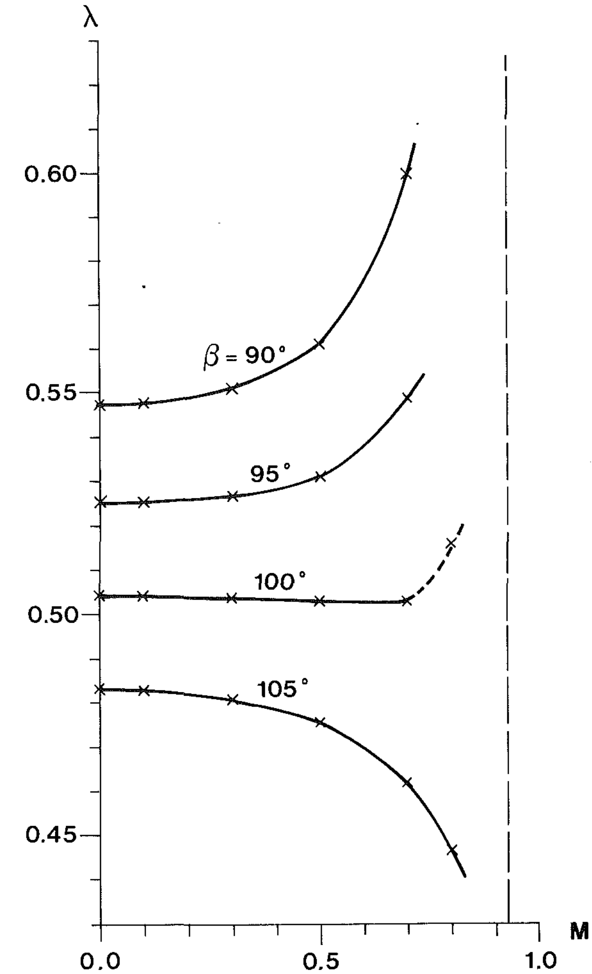

Fig. 2 Values of λ as function of nondimensionalized crack-tip velocity M at $\beta = 90$ deg, 95 deg, 100 deg, and 105 deg, $\nu = 0.3$. Indicated in the figure is the Rayleigh surface wave speed ($M = 0.9262$). The dotted line represents a region where the extrapolation procedure did not converge satisfactory.

5 Discussion

In the present finite element formulation, no special considerations were taken of the square-root singularity in the displacement gradients expected at $\theta = 0$, (i.e., points close to the crack front). If singular finite elements had been applied, a better convergence rate would have been expected. However, in this investigation, the efficiency of the numerical implementation was not the main objective. Judging from comparisons with previously published results for static problems, the present results should have about three significant figures.

The results in Fig. 2 show that the dynamic effects on the singularity are small for moderate crack-tip velocities (M) in comparison with the Rayleigh velocity. This is not surprising, since the crack-tip velocity enters the governing equations, equation (9), as M^2. It can thus immediately be concluded that for small (M), the singularity parameter (λ) will depend on (M) as $\lambda = \lambda_0 + qM^2$, where ($q$) is a constant.

The crack front angle (β) at which the singularity is the same as for an internal crack ($\lambda = 0.5$) seems to be very independent of the crack-tip velocity. Thus, if the arguments put through by Bažant and Estenssoro (1979) hold, the crack front will form an angle ($\beta \approx 101$ deg) almost independently of the crack-tip velocity.

All results in Fig. 2 indicate that the singularity parameter (λ) rapidly varies as the Rayleigh surface wave speed is approached. It was difficult to numerically determine accurate values of λ for these crack-tip velocities. One can only speculate on what the behavior of λ would be for crack-tip velocities close to the Rayleigh speed. Further, more detailed numerical investigations are necessary to resolve this problem.

References

Andersson, B., 1988, *Royal Institute of Technology, Stockholm*, private communication.

Bažant, Z. P., and Estenssoro, L. F., 1979, "Surface singularity and crack Propagation," *Int. J. Solids Structures*, Vol. 15, pp. 405–426.

Bažant, Z. P., and Estenssoro, L. F., 1980, Addendum to the paper, "Surface Singularity and Crack Propagation," *Int. J. Solids Structures*, Vol. 16, pp 479–481.

Benthem, J. P., 1977, "State of Stress at the Vertex of a Quarter-Infinite Crack in a Half-Space," *Int. J. Solids Structures*, Vol. 13, pp. 479–492.

Benthem, J. P., 1980, "The Quarter-Infinite Crack in a Half Space; Alternative and Additional Solutions," *Int. J. Solids Structures*, Vol. 16, pp. 119–130.

Burton, W. S., Sinclair, G. B., Solecki, J. S., and Swedlow, J. L., 1984, "On the Implications for LEFM of the Three-dimensional Aspects in Some Crack/Surface Intersection Problems," *Int. J. Fracture*, Vol. 25, pp. 3–32.

Rosakis, A. J., and Ravi-Chandar, K., 1986, "On Crack-Tip Stress State: An Experimental Evaluation of Three-Dimensional Effects," *Int. J. Solids Structures*, Vol. 22, pp. 121–134.

Yang, W., and Freund, L. B., 1985, "Transverse Shear Effects for Through-Cracks in an Elastic Plate," *Int. J. Solids Structures*, Vol. 21, pp. 977–994.

APPENDIX

The matrices $\mathbf{B}_1$ and $\mathbf{B}_2$ can be derived from the following relations between the strain components, $\bar{\epsilon}$, and the displacements, $\bar{\mathbf{u}}$, in spherical coordinates. It is convenient to write the relation in the form $\bar{\epsilon}=\mathbf{E}\bar{\mathbf{u}}$, where $\mathbf{E}$ is an operator operating on $\bar{\mathbf{u}}$. Defining $\bar{\epsilon}$ and $\bar{\mathbf{u}}$ as

$$\bar{\epsilon}^T=[\bar{\epsilon}_R, \bar{\epsilon}_\theta, \bar{\epsilon}_\phi, \bar{\gamma}_{R\theta}, \bar{\gamma}_{R\phi}, \bar{\gamma}_{\theta\phi}], \tag{A1}$$

$$\bar{\mathbf{u}}^T=(\bar{u}_R, \bar{u}_\theta, \bar{u}_\phi), \tag{A2}$$

the elements of $\mathbf{E}$ can be written as

$$\begin{aligned}
E_{11} &= \lambda,\\
E_{12} &= E_{12}=E_{23}=E_{43}=E_{52}=E_{61}=0,\\
E_{21} &= E_{31}=1,\\
E_{22} &= E_{41}=\frac{\partial}{\partial\theta},\\
E_{32} &= \cot\theta,\\
E_{33} &= E_{51}=E_{62}=1/\sin\theta\frac{\partial}{\partial\phi},\\
E_{42} &= E_{53}=(\lambda-1),\\
E_{63} &= \frac{\partial}{\partial\theta}-\cot\theta.
\end{aligned} \tag{A3}$$

The matrices $\mathbf{D}_1$ and $\mathbf{D}_2$ are derived from the expressions $\bar{\mathbf{u}}_{,1}=\mathbf{F}\bar{\mathbf{u}}$ and $\bar{\mathbf{u}}_{,3}=\mathbf{G}\bar{\mathbf{u}}$. Here, $\mathbf{F}$ and $\mathbf{G}$ are operators given by

$$\begin{aligned}
F_{11}&=F_{22}=F_{33}=\lambda\sin\theta\cos\phi+\cos\theta\cos\phi\frac{\partial}{\partial\theta}-\frac{\sin\phi}{\sin\theta}\frac{\partial}{\partial\phi},\\
F_{12}&=-F_{21}=-\cos\theta\cos\phi,\\
F_{13}&=-F_{31}=\sin\phi,\\
F_{23}&=-F_{32}=\cot\theta\sin\phi,
\end{aligned} \tag{A4}$$

and

$$\begin{aligned}
G_{11}&=G_{22}=G_{33}=\lambda\cos\theta-\sin\theta\frac{\partial}{\partial\theta},\\
G_{12}&=-G_{21}=\sin\theta,\\
G_{13}&=G_{31}=G_{23}=G_{32}=0.
\end{aligned} \tag{A5}$$

Dynamic Mixed Mode I-II Crack Kinking Under Oblique Stress Wave Loading in Brittle Solids

Chien-Ching Ma
Associate Professor,
Department of Mechanical Engineering,
National Taiwan University,
Taipei, Taiwan 10764

The dynamic stress intensity factors of an initially stationary semi-infinite crack in an unbounded linear elastic solid which kinks at some time t_f *after the arrival of a stress wave is obtained as a function of kinking crack tip velocity* v, kinking angle δ, incident stress wave angle α, time t, *and the delay time* t_f. *A perturbation method, using the kinking angle* δ *as the perturbation parameter, is used. The method relies on solving simple problems which can be used with linear superposition to solve the problem of a kinked crack. The solutions can be compared with numerical results and other approximate results for the case of* $t_f = 0$ *and give excellent agreement for a large range of kinking angles. The elastodynamic stress intensity factors of the kinking crack tip are used to compute the corresponding fluxes of energy into the propagating crack-tip, and these results are discussed in terms of an assumed fracture criterion.*

Introduction

When dynamic loading is applied to a body with an internal crack, the stress gradually intensifies at the crack-tip and after some finite delay time, the resulting stress waves may cause the initiation of crack growth and continued crack propagation. A frequently observed fracture event is the kinking or bifurcation of an initially straight crack. The direction of propagation, as well as the velocity of crack propagation, will depend on the local stress field around the crack-tip. To understand the observed bifurcation events in brittle material, the dynamic solution for cracks which suddenly branch or kink is required. The problem of a crack that is branching at an arbitrary angle with the primary crack is difficult to solve, and much of the analytical work is elastostatic in nature. A great deal of progress has been made recently in analyzing the problem of elastodynamic crack branching problems in homogeneous, isotropic elastic solids. One method which seems to have potential for analytic solutions was proposed by Achenbach and Varatharajulu (1974). The method takes advantage of the self-similarity of the particle velocity of the diffracted field, which occurs when appropriate conditions on the incident wave and the crack geometry are satisfied. This method was used by Burgers and Dempsey (1982) to construct exact solutions of symmetric crack bifurcation in antiplane strain for a specific angle. Subsequently, Dempsey, Kuo, and Achenbach (1982) have used a conformal mapping to obtain the analytical solution for the mode III crack kinking problem for stress wave loading. The problem of symmetric and asymmetric crack bifurcation in mode III has been studied by Dempsey, Kuo, and Bentley (1986). The solutions in Burgers and Dempsey (1982) and Dempsey, Kuo and Achenbach (1982) verified the numerical method being applied by Burgers (1982). This method has since been used by Burgers (1983) and Burgers and Dempsey (1984) to provide numerical solutions to the plane-strain crack kinking and bifurcation problems, respectively.

For an important range of kinking angles, the elastodynamic crack kinking stress intensity factors are affected more by the loading of the new crack faces than by the wedge geometry. This suggests that a suitable first-order approximation would be to ignore the wedge geometry and to compute the elastodynamic stress intensity factors by considering a crack propagating in its own plane provided, however, that the new faces are subjected to traction corresponding to those of the branched crack. This approximate method for both mode III and mixed mode I-II crack kinking under stress wave loading was investigated by Achenbach, Kuo, and Dempsey (1984). In all the results mentioned, the problems are restricted to being self-similar; it is assumed that the new crack initiates out of the original crack-tip at an angle at the same time as the stress wave loading arrived at the crack-tip.

It was observed by Achenbach (1970) that if a plane-stress pulse strikes a half-plane crack in an initially undisturbed medium, instantaneous crack propagation can occur only if the stress pulse front carries a square-root singular stress. Hence, it will greatly improve the model by allowing a finite delay time in the initiation of the nonplanar crack. This finite delay time effect also observed in a series of paper by Ravi-Chandar and Knauss (1984a, b, c, d). But if we do so, the problem loses

Contributed by the Applied Mechanics Division of THE AMERICAN SOCIETY OF MECHANICAL ENGINEERS for publication in the JOURNAL OF APPLIED MECHANICS.

Discussion on this paper should be addressed to the Technical Editor, Leon M. Keer, The Technical Institute, Northwestern University, Evanston, IL 60201, and will be accepted until two months after final publication of the paper itself in the JOURNAL OF APPLIED MECHANICS. Manuscript received by the ASME Applied Mechanics Division, May 2, 1988; final revision, April 1, 1989.

its self-similar nature. The only solutions for the newly initiated crack propagating after a delay time have been first obtained by Freund (1973, 1974), and these solutions are restricted to the crack remaining straight. More recently, a finite delay time has been included in the initiation of the nonplanar crack by Ma and Burgers (1986), in which the approximate method in Achenbach, Kuo, and Dempsey (1984) has been used for analyzing the antiplane-strain case. Ma and Burgers (1987) extended the delay time effect to the in-plane case for incident stress wave which is parallel to the crack faces.

The analysis undertaken here is the extension of the previous work in which both the incident longitudinal and transverse stress wave parallel to the crack faces was solved. We consider the dynamic crack growth out of the original semi-infinite crack at an angle to the original crack at some time after the oblique longitudinal (or transverse) stress-wave loading initially interacts with the crack tip. The geometry for the kinked crack under consideration with the wavefront pattern for stress-wave loading is shown in Fig. 1. A perturbation method is used to obtain the first-order solution of the dynamic stress intensity factor near the kinking crack-tip. When the kinking angle is zero, the solutions obtained in this paper reduce to the results of Freund (1973, 1974), and reduce to the solutions of Achenbach, Kuo, and Dempsey (1984) as the delay time tends to zero. The energy flux into the propagating kinked crack-tip can be obtained from the dynamic stress intensity factors, and those results are discussed in terms of an assumed fracture criterion.

Required Fundamental Solutions

Consider a stress-free linear elastic homogeneous isotropic infinite medium that contains a stationary semi-infinite crack, which will be referred to as the original crack, which lies along the negative x-axis with the origin of the coordinate system at the crack-tip. At time $t = 0$, a horizontally-polarized longitudinal wave (or transverse wave) strikes the stationary crack-tip at angle of incidence α. A short time later, at $t = t_f$, a crack referred to as the new crack propagates out of the tip

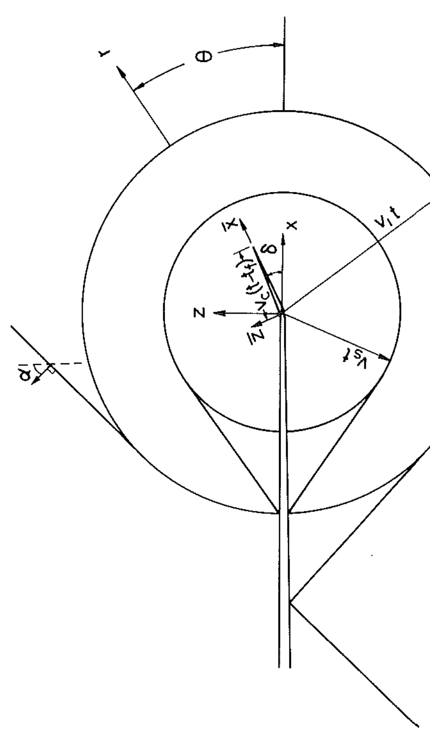

Fig. 1 Stress wave front pattern for a planar stress-wave impacting a kinking crack

of the semi-infinite crack with a constant velocity v (less than the Rayleigh wave speed) making an angle δ with the original crack, thus producing a kinked crack.

The field solution for a kinked-crack geometry can be considered as the superposition of the field generated by diffraction of the incident wave by the stationary crack and the field from the new crack faces subjected to crack-face tractions, which are opposite in sign to the stresses computed from the stationary crack problem. The fields generated by kinking of a semi-infinite crack upon diffraction of a longitudinal or transverse stress wave are extremely difficult to analyze. The analysis involves coupled integral equations, which must be solved numerically. (See Burgers (1983) and Burgers and Dempsey (1984).) We use the first-order approximation of the dynamic stress intensity factor for a kinked crack, which can be expressed by the stress intensity factor for a straight crack, propagating in its own plane, subjected to the negative of the traction computed from the stationary crack problem along the line of the kinked crack. The solutions for the approximation method for the kinking crack under stress-wave loading can be separated into a number of different problems, all of which are relevant problems in their own right. By building up the so-called fundamental solutions of more basic problems, the solution of the final problem can then be solved. Some fundamental solutions needed for solving the dynamic stress intensity factor of the kinking crack will be presented.

In a stationary coordinate x-z system, a homogeneous, isotropic, linearly elastic medium is governed by the two-dimensional wave equations

$$\nabla^2\phi - a^2\ddot{\phi} = 0, \tag{1}$$

$$\nabla^2\psi - b^2\ddot{\psi} = 0, \tag{2}$$

where

$$a = \sqrt{\frac{\rho}{\lambda + 2\mu}} = \frac{1}{v_l},\ b = \sqrt{\frac{\rho}{\mu}} = \frac{1}{v_s}.$$

a and b are the slowness of longitudinal and shear waves, respectively, μ and ρ are the shear modulus and the mass density of the material, and λ is the Lamé elastic constant. The displacements are derived from the potentials according to $u = \phi_{,x} - \psi_{,z}$, $w = \phi_{,z} + \psi_{,x}$, where u and w are the displacements in the x and z directions. The stresses can be written in terms of the potentials by means of Hooke's law.

Diffraction by a Stationary Crack. Consider a special problem for a tensile stress loading applied uniformly on the stationary crack faces $z = 0$. The following mixed boundary conditions on $z = 0$ are considered:

$$\sigma^I_{zz}(x,0,t) = -\sigma_o H(t + xa^*) \text{ for } -\infty < x < 0, \tag{3a}$$

$$\sigma^I_{xz}(x,0,t) = 0 \text{ for } -\infty < x < \infty, \tag{3b}$$

$$w(x,0,t) = 0 \text{ for } 0 < x < \infty. \tag{3c}$$

where $a^* = a \sin\alpha$ and H represents the unit step function. The full field solutions of stresses for $-\pi/2 < \theta < \pi/2$ are

$$\frac{\sigma^I_{zz}}{A} = -\int_{ar}^{t} \mathrm{Im}\left[\frac{(2\lambda^2 - b^2)^2\Phi(s)}{(a+\lambda)^{1/2}}\right]_{\lambda=\lambda_L} ds - \int_{br}^{t} \mathrm{Im}[4\lambda^2(a-\lambda)^{1/2}(b^2-\lambda^2)^{1/2}\Phi(s)]_{\lambda=\lambda_T}\, ds, \tag{4a}$$

$$\frac{\sigma^I_{xz}}{A} = -\int_{ar}^{t} \mathrm{Im}[2\lambda(2\lambda^2 - b^2)(a-\lambda)^{1/2}\Phi(s)]_{\lambda=\lambda_L} ds + \int_{br}^{t} \mathrm{Im}[2\lambda(2\lambda^2 - b^2)(a-\lambda)^{1/2}\Phi(s)]_{\lambda=\lambda_T}\, ds, \tag{4b}$$

$$\frac{\sigma_{xx}^I}{A} = \int_{ar}^{t} \mathrm{Im}\left[\frac{(2\lambda^2-b^2)(2\lambda^2+b^2-2a^2)\Phi}{(a+\lambda)^{1/2}}\right]_{\lambda=\lambda_L} ds$$

$$+ \int_{br}^{t} \mathrm{Im}[4\lambda^2(a-\lambda)^{1/2}(b^2-\lambda^2)^{1/2}\Phi]_{\lambda=\lambda_T}\, ds, \qquad (4c)$$

where

$$A = \frac{\sigma_o \omega_+^o(a^*)}{\pi k},\ k=2(b^2-a^2),$$

$$\omega_+^o(\lambda) = \frac{(a+\lambda)^{1/2}}{(c+\lambda)S_+^o(\lambda)},$$

$$\lambda_L(s) = -\frac{s}{r}\cos\theta + i\left(\frac{s^2}{r^2}-a^2\right)^{1/2}\sin|\theta|,$$

$$\lambda_T(s) = -\frac{s}{r}\cos\theta + i\left(\frac{s^2}{r^2}-b^2\right)^{1/2}\sin|\theta|,$$

$$S_\pm^o(\lambda) = \exp\left(-\frac{1}{\pi}\int_a^b \tan^{-1}\left[\frac{4y^2(y^2-a^2)^{1/2}(b^2-y^2)^{1/2}}{(b^2-2y^2)^2}\right]\frac{dy}{y\pm\lambda}\right),$$

$$\Phi(s) = \frac{\partial\lambda/\partial s}{(\lambda-a^*)(\lambda-c)S_-^o(\lambda)}.$$

$c = 1/v_R$ is the slowness of the Rayleigh wave and satisfies the equation

$$(2c^2-b^2)^2+4c^2(a^2-c^2)^{1/2}(b^2-c^2)^{1/2}=0.$$

The first two terms of the asymptotic expansion as $r \to 0$ of the stresses are

$$\sigma_{zz}^I \approx \frac{2}{\pi}\sigma_o\omega_+^o(a^*)\left(\frac{t}{r}\right)^{1/2}\cos\frac{\theta}{2}\left[1+\sin\frac{\theta}{2}\sin\frac{3\theta}{2}\right]-\sigma_o+o(1),$$

$$\sigma_{xz}^I \approx \frac{2}{\pi}\sigma_o\omega_+^o(a^*)\left(\frac{t}{r}\right)^{1/2}\cos\frac{\theta}{2}\sin\frac{\theta}{2}\cos\frac{3\theta}{2}+o(1), \qquad (5)$$

$$\sigma_{xx}^I \approx \frac{2}{\pi}\sigma_o\omega_+^o(a^*)\left(\frac{t}{r}\right)^{1/2}\cos\frac{\theta}{2}\left[1-\sin\frac{\theta}{2}\sin\frac{3\theta}{2}\right]-\sigma_oC_{xx}+o(1),$$

where

$$C_{xx} = \frac{b^2-2a^2}{b^2} + \frac{\sqrt{a}(2c^2-b^2)}{c^2S_+^o(0)S_-^o(c)(a+c)}.$$

The second term in (5), which is $O(1)$ in the asymptotic expansion, will play a significant role in the crack kinking analysis.

For the shear loading applied uniformly on the crack faces, the deformation will occur in mode II. The mixed boundary conditions are then

$$\sigma_{zz}^{II}(x,0,t)=0 \text{ for } -\infty<x<\infty, \qquad (6a)$$

$$\sigma_{xz}^{II}(x,0,t)=-\sigma_oH(t+xa^*) \text{ for } -\infty<x<0, \qquad (6b)$$

$$u^*(x,0,t)=0 \text{ for } 0<x<\infty, \qquad (6c)$$

where u^* is the component of displacement in the x-direction. The full-field solutions for stresses evaluated for $-\pi/2 < \theta < \pi/2$ are

$$\frac{\sigma_{zz}^{II}}{B} = \int_{ar}^{t}\mathrm{Im}[2\lambda(b^2-2\lambda^2)(b-\lambda)^{1/2}\Phi(s)]_{\lambda=\lambda_L}ds$$

$$-\int_{br}^{t}\mathrm{Im}[2\lambda(b^2-2\lambda^2)(b-\lambda)^{1/2}\Phi(s)]_{\lambda=\lambda_T}\,ds, \qquad (7a)$$

$$\frac{\sigma_{xz}^{II}}{B} = -\int_{ar}^{t}\mathrm{Im}[4\lambda^2(b-\lambda)^{1/2}(a^2-\lambda^2)^{1/2}\Phi(s)]_{\lambda=\lambda_L}ds$$

$$-\int_{br}^{t}\mathrm{Im}\left[\frac{(2\lambda^2-b^2)^2\Phi(s)}{(b+\lambda)^{1/2}}\right]_{\lambda=\lambda_T}ds, \qquad (7b)$$

$$\frac{\sigma_{xx}^{II}}{B} = \int_{ar}^{t}\mathrm{Im}[2\lambda(b-\lambda)^{1/2}(2\lambda^2+b^2-2a^2)\Phi]_{\lambda=\lambda_L}ds$$

$$+\int_{br}^{t}\mathrm{Im}[2\lambda(b-\lambda)^{1/2}(b^2-2\lambda^2)\Phi]_{\lambda=\lambda_T}\,ds, \qquad (7c)$$

where

$$B=\frac{\sigma_ou_+^o(a^*)}{\pi k},\ u_+^o(\lambda)=\frac{(b+\lambda)^{1/2}}{(c+\lambda)S_+^o(\lambda)}.$$

For $r \to 0$, the leading two terms of the asymptotic expansion of (7) are

$$\sigma_{zz}^{II}\approx\frac{2}{\pi}\sigma_ou_+^o(a^*)\left(\frac{t}{r}\right)^{1/2}\cos\frac{\theta}{2}\sin\frac{\theta}{2}\cos\frac{3\theta}{2}+o(1), \qquad (8a)$$

$$\sigma_{xz}^{II}\approx\frac{2}{\pi}\sigma_ou_+^o(a^*)\left(\frac{t}{r}\right)^{1/2}\cos\frac{\theta}{2}\left[1-\sin\frac{\theta}{2}\sin\frac{3\theta}{2}\right]-\sigma_o+o(1), \qquad (8b)$$

$$\sigma_{xx}^{II}\approx-\frac{2}{\pi}\sigma_ou_+^o(a^*)\left(\frac{t}{r}\right)^{1/2}\sin\frac{\theta}{2}\left[2+\cos\frac{\theta}{2}\cos\frac{3\theta}{2}\right]+o(1). \qquad (8c)$$

Point Moving Loads of Growing Crack. Consider a crack-tip which is at rest at $x = 0$, and suppose there are no loads acting on the body for $t < 0$. At time $t = 0$, the crack-tip begins to move in the x direction at speed v and, simultaneously, a symmetric pair of concentrated normal forces appears at the crack-tip. For $t > 0$, the concentrated forces increase linearly in time and begin to move in the x-direction with speed $u < v$. The boundary conditions are

$$(\sigma_{zz}^F)_1(x,0,t)=(mt+n)\Delta(x-ut)H(t) \quad \text{for} \quad -\infty<x<vt,$$
$$(\sigma_{xz}^F)_1(x,0,t)=0 \quad \text{for} \quad -\infty<x<\infty,$$
$$w_1(x,0,t)=0 \quad \text{for} \quad vt<x<\infty, \qquad (9)$$

where Δ is the Dirac delta function and m and n are arbitrary parameters. The stress intensity factor of this problem was obtained by Freund (1973)

$$K_I^F=\frac{2mh^2\omega_+'\sqrt{2t}}{\sqrt{\pi}(1-a/d)^{1/2}}-\frac{\sqrt{2}\,nh\omega_+(h)}{(1-a/d)^{1/2}\sqrt{\pi t}}, \qquad (10)$$

where

$$\omega_+'(h)=\frac{\partial\omega_+(h)}{\partial h},\ \omega_+(\lambda)=\frac{\alpha_+(\lambda)}{(\lambda+c_2)S_+(\lambda)}.$$

$$S_\pm(\lambda)=\exp\left(-\frac{1}{\pi}\int_{a_{2,1}}^{b_{2,1}}\right.$$
$$\left.\times\tan^{-1}\left[\frac{4\eta^2|\alpha|\ |\beta|}{(2\eta^2-b^2-b^2\eta^2/d^2\mp2b^2\eta/d)^2}\right]\frac{d\eta}{\eta\pm\lambda}\right),$$

$$\alpha(\lambda)=(a^2-\lambda^2+a^2\lambda^2/d^2-2a^2\lambda/d)^{1/2},$$
$$\beta(\lambda)=(b^2-\lambda^2+b^2\lambda^2/d^2-2b^2\lambda/d)^{1/2},$$
$$\alpha_\pm=[a\pm\lambda(1\mp a/d)]^{1/2},$$

$$a_2=\frac{a}{1-a/d},\ b_2=\frac{b}{1-b/d},\ c_2=\frac{c}{1-c/d}.$$

$d = 1/v$ is the slowness of the crack velocity. The parameter $h = 1/(v - u)$ is the inverse of the relative speed between the moving load and the crack-tip. The other fundamental solution needed is that produced by concentrated shear forces appearing at the crack-tip and then moving in the x direction with speed u. The boundary conditions are

$$(\sigma_{zz}^F)_2(x,0,t)=0 \quad \text{for} \quad -\infty<x<\infty,$$
$$(\sigma_{xz}^F)_2(x,0,t)=(mt+n)\Delta(x-ut)H(t) \quad \text{for} \quad -\infty<x<vt,$$
$$u^*(x,0,t)=0 \quad \text{for} \quad vt<x<\infty. \tag{11}$$

The stress intensity factor for this case is

$$K_{II}^F=\frac{2mh^2u_+'\sqrt{2t}}{\sqrt{\pi}(1-b/d)^{1/2}}-\frac{\sqrt{2}nhu_+(h)}{(1-b/d)^{1/2}\sqrt{\pi t}}, \tag{12}$$

where

$$u_+(\lambda)=\frac{\beta_+(\lambda)}{(\lambda+c_2)S_+(\lambda)},$$
$$\beta_\pm(\lambda)=[b\pm\lambda(1\mp b/d)]^{1/2}.$$

With these fundamental solutions at hand, we are now able to construct the solution of the stress intensity factor for the kinking crack.

Crack Kinking Due to an Incident Longitudinal Wave

Consider the incident longitudinal step-stress tensile wave of the form

$$\sigma_{\bar z\bar z}^i=\sigma_o H(t+ar\sin(\alpha-\theta)). \tag{13}$$

The stresses of the stationary crack problem can be obtained by superimposing the solutions of the symmetric and antisymmetric problems proposed in the previous section. Relative to polar coordinates,

$$\sigma_{\theta\theta}^s=\sigma_{\theta\theta}^i+\sigma_{\theta\theta}^d,\ \sigma_{\theta r}^s=\sigma_{\theta r}^i+\sigma_{\theta r}^d, \tag{14}$$

where

$$\sigma_{\theta\theta}^i=\sigma_o\left[1-2\left(\frac{a}{b}\right)^2\sin^2(\alpha-\theta)\right], \tag{15}$$

$$\sigma_{\theta r}^i=-\sigma_o\left(\frac{a}{b}\right)^2\sin 2(\alpha-\theta), \tag{16}$$

$$\sigma_{\theta\theta}^d=\frac{1}{2}(1-\cos 2\theta)\sigma_{xx}^L+\frac{1}{2}(1+\cos 2\theta)\sigma_{zz}^L-\sin 2|\theta|\sigma_{xz}^L, \tag{17}$$

$$\sigma_{\theta r}^d=\left[-\frac{1}{2}\sin 2|\theta|\sigma_{xx}^L+\frac{1}{2}\sin 2|\theta|\sigma_{zz}^L+\cos 2\theta\ \sigma_{xz}^L\right]\mathrm{sgn}(\theta) \tag{18}$$

and

$$\sigma_{ij}^L=\left[1-2\left(\frac{a}{b}\right)^2\sin^2\alpha\right]\sigma_{ij}^I-\left(\frac{a}{b}\right)^2\sin 2\alpha\sigma_{ij}^{II}\ \mathrm{sgn}(\theta)$$
$$ij=xx,zz,xz,$$

where $\sigma_{\theta\theta}^i$ represents the incident field and $\sigma_{\theta\theta}^d$ is the diffraction field. σ_{xx}^I, σ_{xz}^I, and σ_{zz}^I are given in (4). The first-order approximation of the dynamic stress intensity factor for a kinked crack with delay time t_f can be expressed by the stress intensity factor for a straight crack propagating in its own plane subjected to the negative of the traction given in (14) on the new crack faces. This approximation method is discussed more fully by Achenbach and Kuo (1985). The appropriate boundary conditions are:

(1) for the mode I stress intensity factor

$$\sigma_{\bar z\bar z}=0 \quad \text{for} \quad \bar x<0, \tag{19a}$$
$$\sigma_{\bar z\bar z}=-\sigma_{\theta\theta}^s(\bar x/t,\theta=\delta) \quad \text{for} \quad 0<\bar x<v(t-t_f) \tag{19b}$$

and

(2) for the mode II stress intensity factor

$$\sigma_{\bar z\bar x}=0 \quad \text{for} \quad \bar x<0, \tag{20a}$$
$$\sigma_{\bar z\bar x}=-\sigma_{\theta r}^s(\bar x/t,\theta=\delta) \quad \text{for} \quad 0<\bar x<v(t-t_f), \tag{20b}$$

where the $\bar x$-axis lies along the kinked crack line and δ is the kinked angle as shown in Fig. 1.

Mode I Stress Intensity Factor. The stress intensity factor of the kinking crack due to the loading from the diffraction part of the stationary crack field can be constructed from the fundamental solution of equation (10) by choosing $m=-1$, $n=-t^*=-ht_f/d$, replacing t by $t-t^*$, and integrating over the appropriate range of $u=\bar x/t$. The mode I stress intensity factor for the propagating kinked crack is

$$(K_I^L)_d(t,v,\delta)=\int_0^{v(t-t_f)/t}K_I^F(m=-1,n=-t^*,t-t^*)\sigma_{\theta\theta}^d\left(\frac{1}{u},\delta\right)du$$
$$=-\int_d^{d^*}2\left[\frac{2t_f}{\pi d(1-a/d)}\right]^{1/2}\left[\omega_+(h)(d^*-h)^{1/2}\right]_h\sigma_{\theta\theta}^d\left(\frac{h}{vh-1},\delta\right)dh, \tag{21}$$

where

$$d^*=\frac{t}{vt_f}.$$

The integral in (21) is suited to integration by parts. It gives a more tractable form than (21) and allows us to get very simple closed-form results in some special cases. By careful analysis, we find that the function $\sigma_{\theta\theta}^d$ has a square-root singularity at $h=d$. Hence, if integration by parts is applied, neither the integrated term nor the remaining integral will exist, even though the sum exists. To get around this difficulty, the method suggested by Freund (1973) is applied. The lower limit of integration in (21) is replaced by $d+\epsilon$, $\epsilon<<d$. It can be shown that those terms which are singular at $\epsilon=0$ exactly cancel each other, and the desired result can be obtained by taking the limit as $\epsilon\to 0$.

Integration by parts of (21) and making use of the explicit expression for $\sigma_{\theta\theta}^d$ yields

$$(K_I^L)_d(t,v,\delta)=\lim_{\epsilon\to 0}2\left[\frac{2t_f}{\pi d(1-a/d)}\right]^{1/2}\left\{\sigma_o\omega_+(d)(d^*-d)^{1/2}\left[\frac{2d\Gamma_L}{\pi\epsilon^{1/2}(c+a^*)S_+^o(a^*)}-\Sigma_L\right]+\int_{d+\epsilon}^{d^*}\omega_+(h)(d^*-h)^{1/2}(\sigma_{\theta\theta}^d)_h dh\right\}+o(1)$$
$$=2\sigma_o\left[\frac{2t_f}{\pi d(1-a/d)}\right]^{1/2}\left\{-\omega_+(d)(d^*-d)^{1/2}\Sigma_L+\frac{d\omega_+(d)\Gamma_L}{(c+a^*)S_+^o(a^*)}+\frac{d}{\pi(c+a^*)S_+^o(a^*)}\int_d^{d^*}\frac{(d^*-h)^{1/2}}{(h-d)^{1/2}}\times\left[\frac{\omega_+(d)\Gamma_L}{(h-d)}-\frac{\omega_+(h)d^{5/2}}{k(h-d)^3}(\sigma_{\theta\theta}^L)_h^*\right]dh\right\}+o(1), \tag{22}$$

where

$$\Gamma_L=\left[1-2\left(\frac{a}{b}\right)^2\sin^2\alpha\right]\cos^3\frac{\delta}{2}(a+a^*)^{1/2}+\frac{3}{4}\left(\frac{a}{b}\right)^2\sin 2\alpha\left(\sin\frac{\delta}{2}+\sin\frac{3\delta}{2}\right)(b+a^*)^{1/2},$$

$$\Sigma_L = \left[1 - 2\left(\frac{a}{b}\right)^2 \sin^2\alpha\right](\cos^2\delta + C_{xx}\sin^2\delta) + \left(\frac{a}{b}\right)^2 \sin 2\alpha \sin 2\delta.$$

The complete form of $(\sigma_{\theta\theta}^L)_h^*$ is shown in Appendix A. The stress intensity factor due to the incident field (15) can be easily obtained as follows

$$(K_I^L)_i(t,v,\delta) = \int_0^{v(t-tf)} K_I^F\left(m=0, n=-1, t-t_f-\frac{x_o}{v}\right)\sigma_{\theta\theta}^i dx_o$$

$$= \frac{2\sqrt{2}\sigma_o t_f^{1/2}\omega_+(d)(d^*-d)^{1/2}}{\sqrt{\pi}(1-a/d)^{1/2}d^{1/2}}\left[1 - 2\left(\frac{a}{b}\right)^2 \sin^2(\alpha-\delta)\right]. \quad (23)$$

The first-order approximation of the mode I stress intensity factor, including the delay time effect for the kinking crack due to the normal loading on the original crack faces, is expressed in (22), and the solution for the step longitudinal stress-wave loading is the sum of the contributions due to diffracted and incident fields given in (22) and (23),

$$K_I^L = (K_I^L)_d + (K_I^L)_i. \quad (24)$$

Mode II Stress Intensity Factor. Following a similar analysis as in the mode I case, the mode II stress intensity factor due to the diffracted field (18) can be expressed as follows

$$(K_{II}^L)_d(t,v,\delta) = \int_0^{v(t-tf)/t} K_{II}^F(m=-1, n=-t^*, t-t^*)\sigma_{\theta r}^d\left(\frac{1}{u},\delta\right)du$$

$$= 2\sigma_o\left[\frac{2t_f}{\pi d(1-b/d)}\right]^{1/2}\left\{u_+(d)(d^*-d)^{1/2}\Lambda_L + \frac{du_+(d)\Pi_L}{(c+a^*)S_+^o(a^*)} + \right.$$

$$+ \frac{d}{\pi(c+a^*)S_+^o(a^*)}\int_d^{d^*}\frac{(d^*-h)^{1/2}}{(h-d)^{1/2}}\left[\frac{u_+(d)\Pi_L}{(h-d)} - \left.\frac{u_+(h)d^{5/2}}{k(h-d)^3}(\sigma_{\theta r}^L)_h^*\right]dh\right\} + o(1), \quad (25)$$

where

$$\Pi_L = \frac{1}{4}\left[1 - 2\left(\frac{a}{b}\right)^2 \sin^2\alpha\right]\left(\sin\frac{\delta}{2} + \sin\frac{3\delta}{2}\right)(a+a^*)^{1/2} - \frac{1}{4}\left(\frac{a}{b}\right)^2 \sin 2\alpha\left(\cos\frac{\delta}{2} + 3\cos\frac{3\delta}{2}\right)(b+a^*)^{1/2}$$

$$\Lambda_L = \frac{1}{2}\left[1 - 2\left(\frac{a}{b}\right)^2 \sin^2\alpha\right](C_{xx}-1)\sin 2\delta + \left(\frac{a}{b}\right)^2 \sin 2\alpha \cos 2\delta.$$

Details of $(\sigma_{\theta r}^L)_h^*$ are given in Appendix A. The mode II stress intensity factor due to the incident field (16) is

$$(K_{II}^L)_i(t,v,\delta) = \int_0^{v(t-tf)} K_{II}^F\left(m=0, n=-1, t-t_f-\frac{x_o}{v}\right)\sigma_{\theta r}^i dx_o$$

$$= -\frac{2\sqrt{2}\sigma_o t_f^{1/2}u_+(d)(d^*-d)^{1/2}}{\sqrt{\pi}(1-b/d)^{1/2}d^{1/2}}\left(\frac{a}{b}\right)^2 \sin 2(\alpha-\delta). \quad (26)$$

Hence,

$$K_{II}^L = (K_{II}^L)_d + (K_{II}^L)_i. \quad (27)$$

Crack Kinking Due to an Incident Transverse Wave

Consider the incident transverse stress-wave of the form

$$\sigma_{\dot{x}\dot{z}}^i = \sigma_o H(t + br\sin(\alpha-\theta)). \quad (28)$$

The stress components in the polar coordinate for incident and diffracted fields of the stationary crack are

$$\sigma_{\theta\theta}^i = \sigma_o \sin 2(\alpha-\theta), \quad (29)$$

$$\sigma_{\theta r}^i = \sigma_o \cos 2(\alpha-\theta), \quad (30)$$

$$\sigma_{\theta\theta}^d = \frac{1}{2}(1-\cos 2\theta)\sigma_{xx}^T + \frac{1}{2}(1+\cos 2\theta)\sigma_{zz}^T - \sin 2|\theta|\sigma_{xz}^T, \quad (31)$$

$$\sigma_{\theta r}^d = \left[-\frac{1}{2}\sin 2|\theta|\sigma_{xx}^T + \frac{1}{2}\sin 2|\theta|\sigma_{zz}^T + \cos 2\theta\sigma_{xz}^T\right]\mathrm{sgn}(\theta), \quad (32)$$

where

$$\sigma_{ij}^T = \sin 2\alpha(\sigma_{ij}^I)^* + \cos 2\alpha(\sigma_{ij}^{II})^*\mathrm{sgn}(\theta),\ ij = xx, zz, xz.$$

Here $(\sigma_{ij}^I)^*$ and $(\sigma_{ij}^{II})^*$ are almost the same as σ_{ij}^I and σ_{ij}^{II}, which are defined in (4) and (7), respectively, except that a^* should be replaced by $b^* = b \sin\alpha$.

The analysis for the stress intensity factor due to the incident transverse wave on a kinked crack proceeds in a similar manner as discussed in the previous section for the incident longitudinal wave. We will not report the solution procedure and only present the results.

Mode I Stress Intensity Factor.

$$K_I^T = (K_I^T)_d + (K_I^T)_i, \quad (33)$$

$$(K_I^T)_d(t,v,\delta) = 2\sigma_o\left[\frac{2t_f}{\pi d(1-a/d)}\right]^{1/2}\left\{-\omega_+(d)(d^*-d)^{1/2}\Sigma_T + \frac{d\omega_+(d)\Gamma_T}{(c+b^*)S_+^o(b^*)} + \frac{d}{\pi(c+b^*)S_+^o(b^*)}\int_d^{d^*}\frac{(d^*-h)^{1/2}}{(h-d)^{1/2}}\left[\frac{\omega_+(d)\Gamma_T}{(h-d)} - \frac{\omega_+(h)d^{5/2}}{k(h-d)^3}(\sigma_{\theta\theta}^T)_h^*\right]dh\right\} + o(1), \quad (34)$$

where

$$\Gamma_T = \sin 2\alpha \cos^3\frac{\delta}{2}(a+b^*)^{1/2} - \frac{3}{4}\cos 2\alpha\left(\sin\frac{\delta}{2} + \sin\frac{3\delta}{2}\right)(b+b^*)^{1/2},$$

$$\Sigma_T = \sin 2\alpha(\cos^2\delta + C_{xx}\sin^2\delta) - \cos 2\alpha \sin 2\delta,$$

and

$$(K_I^T)_i(t,v,\delta) = \frac{2\sqrt{2}\sigma_o t_f^{1/2}\omega_+(d)(d^*-d)^{1/2}}{\sqrt{\pi}(1-a/d)^{1/2}d^{1/2}}\sin 2(\alpha-\delta). \quad (35)$$

Mode II Stress Intensity Factor.

$$K_{II}^T = (K_{II}^T)_d + (K_{II}^T)_i, \quad (36)$$

$$(K_{II}^T)_d(t,v,\delta) = 2\sigma_o\left[\frac{2t_f}{\pi d(1-b/d)}\right]^{1/2}\left\{u_+(d)(d^*-d)^{1/2}\Lambda_T + \frac{du_+(d)\Pi_T}{(c+b^*)S_+^o(b^*)} + \frac{d}{\pi(c+b^*)S_+^o(b^*)}\int_d^{d^*}\frac{(d^*-h)^{1/2}}{(h-d)^{1/2}}\left[\frac{u_+(d)\Pi_T}{(h-d)} - \frac{u_+(h)d^{5/2}}{k(h-d)^3}(\sigma_{\theta r}^T)_h^*\right]dh\right\} + o(1), \quad (37)$$

where

$$\Pi_T = \frac{1}{4}\sin 2\alpha\left(\sin\frac{\delta}{2}+\sin\frac{3\delta}{2}\right)(a+b^*)^{1/2}$$

$$+\frac{1}{4}\cos 2\alpha\left(\cos\frac{\delta}{2}+3\cos\frac{3\delta}{2}\right)(b+b^*)^{1/2},$$

$$\Lambda_T = \frac{1}{2}\sin 2\alpha(C_{xx}-1)\sin 2\delta-\cos 2\alpha\cos 2\delta$$

and

$$(K_{II}^T)_i(t,v,\delta)=\frac{2\sqrt{2}\sigma_o t_f^{1/2}\dot{u}_+(d)(d^*-d)^{1/2}}{\sqrt{\pi}(1-b/d)^{1/2}d^{1/2}}\cos 2(\alpha-\delta). \tag{38}$$

Details of $(\sigma_{\theta\theta}^T)_h^*$ and $(\sigma_{\theta r}^T)_h^*$ are given in Appendix B.

Special Cases and Numerical Results

Some special cases are discussed to give simple closed-form results and can be used as a check for the numerical calculation of the general cases. For the kinking angle $\delta = 0$, the new crack propagates straight out of the original crack. The stress intensity factor can then be simplified as

$$K_I^L = 2\sqrt{\frac{2}{\pi}}\,\sigma_o\left(1-2\frac{a^{*2}}{b^2}\right)\omega_+^o(a^*)\kappa_I(d)[t+v(t-t_f)a^*]^{1/2}, \tag{39}$$

$$K_{II}^L = -2\sqrt{\frac{2}{\pi}}\,\sigma_o\frac{a^2}{b^2}\sin 2\alpha\, u_+^o(a^*)\kappa_{II}(d)[t+v(t-t_f)a^*]^{1/2} \tag{40}$$

$$K_I^T = 2\sqrt{\frac{2}{\pi}}\,\sigma_o\sin 2\alpha\,\omega_+^o(b^*)\kappa_I(d)[t+v(t-t_f)b^*]^{1/2}, \tag{41}$$

$$K_{II}^T = 2\sqrt{\frac{2}{\pi}}\,\sigma_o\cos 2\alpha\, u_+^o(b^*)\kappa_{II}(d)[t+v(t-t_f)b^*]^{1/2}, \tag{42}$$

where

$$\kappa_I(d)=\frac{d}{S_+(d)(d+c_2)(1-a/d)^{1/2}},$$

$$\kappa_{II}(d)=\frac{d}{S_+(d)(d+c_2)(1-b/d)^{1/2}}.$$

The functions $\kappa_I(d)$ and $\kappa_{II}(d)$ depend only on the crack speed $v = 1/d$ and material properties. The values of $\kappa_I(d)$ and $\kappa_{II}(d)$ decrease from unity at $v = 0$ to zero when the crack speed reaches the Rayleigh wave speed. It is worth noting that the solution in (39)–(42) provides exact results, without any approximation made in this case and reduce to the same results obtained by Freund (1974) for a crack propagating straight.

If one wants to study the criterion for a crack kinking event, it is clear that the most significant time scale involved should be in the region when crack kinking has just occurred, in other words, $t - t_f << 1$. The field quantities change very rapidly at this time period and it certainly plays an important role in the crack kinking events. The stress intensity factor just after the kinking occurs has the form

$$K_I^L = 2\sigma_o\left[\frac{2td}{\pi(1-a/d)}\right]^{1/2}\frac{\omega_+(d)\Gamma_L}{(c+a^*)S_+^o(a^*)}, \tag{43}$$

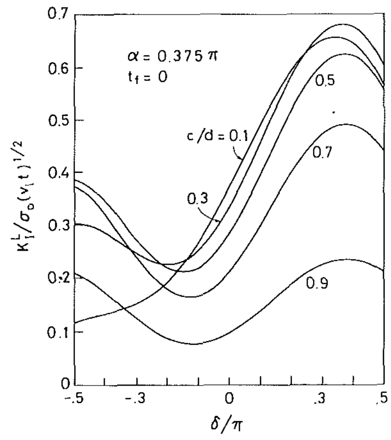

Fig. 2 The normalized mode I stress intensity factor versus kinking angle due to incident longitudinal stress-wave loading for $t_f = 0$ and $\alpha = 0.375\pi$

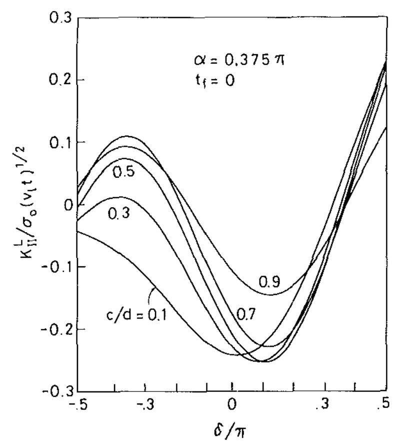

Fig. 3 The normalized mode II stress intensity factor versus kinking angle due to incident longitudinal stress-wave loading for $t_f = 0$ and $\alpha = 0.375\pi$

$$K_{II}^L = 2\sigma_o\left[\frac{2td}{\pi(1-b/d)}\right]^{1/2}\frac{u_+(d)\Pi_L}{(c+a^*)S_+^o(a^*)}, \tag{44}$$

$$K_I^T = 2\sigma_o\left[\frac{2td}{\pi(1-a/d)}\right]^{1/2}\frac{\omega_+(d)\Gamma_T}{(c+b^*)S_+^o(b^*)}, \tag{45}$$

$$K_{II}^T = 2\sigma_o\left[\frac{2td}{\pi(1-b/d)}\right]^{1/2}\frac{u_+(d)\Pi_T}{(c+b^*)S_+^o(b^*)}. \tag{46}$$

Just before kinking, the crack is stationary and the stress intensity factor can be obtained by taking the limit $t \to t_f$ and $d \to \infty$ in equations (39)–(42) or by taking the limit $\delta \to 0$ and $d \to \infty$ in equations (43)–(46).

$$(K_I^L)_s = 2\sigma_o[1-2(a/b)^2\sin^2\alpha](2t/\pi)^{1/2}\omega_+^o(a^*), \tag{47}$$

$$(K_{II}^L)_s = -2\sigma_o(a/b)^2\sin 2\alpha(2t/\pi)^{1/2}u_+^o(a^*), \tag{48}$$

$$(K_I^T)_s = 2\sigma_o\sin 2\alpha(2t/\pi)^{1/2}\omega_+^o(b^*), \tag{49}$$

$$(K_{II}^T)_s = 2\sigma_o\cos 2\alpha(2t/\pi)^{1/2}u_+^o(b^*). \tag{50}$$

Because the crack-tip speed changes discontinuously at $t = t_f$, the stress intensity factor just before and after the kinked crack has a jump, whose magnitude depends on the crack speed v, the incident angle α, and the kinked angle δ.

If we examine the special case of no finite delay time, that is the crack kinks at the instant the incident stress wave strikes the original crack-tip, the solution of (24), (27), (33), and (36) will reduce to the result of Achenbach, Kuo, and Dempsey (1984). Figures 2 and 3 show the dimensionless mode I and

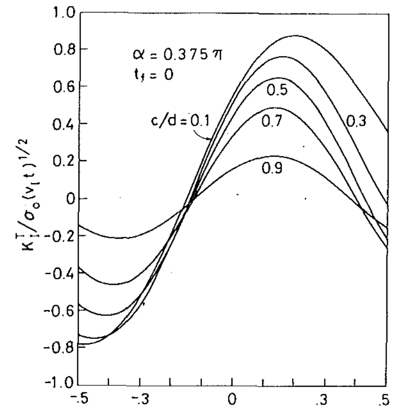

Fig. 4 The normalized mode I stress intensity factor versus kinking angle due to incident transverse stress-wave loading for $t_f = 0$ and $\alpha = 0.375\pi$

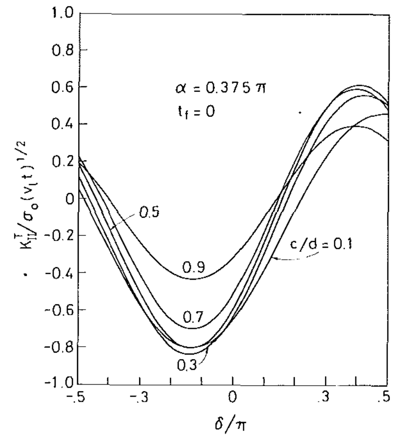

Fig. 5 The normalized mode II stress intensity factor versus kinking angle due to incident transverse stress-wave loading for $t_f = 0$ and $\alpha = 0.375\pi$

Table 1 Comparison of numerical results according to Burgers (1983): (1) Achenbach, Kuo, and Dempsey (1984); (2) and this paper; (3) for an incident longitudinal stress wave $\alpha = 0$ and $t_f = 0$

	v/v_R \ δ		0	.0625	.125	.25	.375	.485
$\frac{K_I^L}{\sigma_o(v_l t)^{1/2}}$	0.1	(1)	1.0070	.9870	.9291	.7241	.4625	.2482
		(2)	.9991	.9797	.9234	.7219	.4610	.2829
		(3)	.9997	.9808	.9247	.7239	.4622	.2448
	0.3	(1)	.8484	.8295	.7747	.5818	.3387	.1435
		(2)	.8625	.8435	.7884	.5937	.3481	.1932
		(3)	.8623	.8434	.7884	.5945	.3495	.1537
	0.5	(1)	.7078	.6911	.6427	.4744	.2674	.1068
		(2)	.7023	.6856	.6373	.4695	.2637	.1356
		(3)	.7019	.6853	.6372	.4701	.2650	.1069
	0.7	(1)	.51[illegible]9	.5011	.4644	.3385	.1895	.0805
		(2)	.5043	.4916	.4549	.3294	.1810	.0899
		(3)	.5040	.4913	.4548	.3299	.1821	.0738
$\frac{K_{II}^L}{\sigma_o(v_l t)^{1/2}}$	0.1	(1)	0	.1287	.2465	.4131	.4564	.3952
		(2)	0	.1257	.2410	.4047	.4458	.3848
		(3)	0	.1251	.2397	.4030	.4439	.3787
	0.3	(1)	0	.1342	.2564	.4260	.4636	.3962
		(2)	0	.1276	.2436	.4023	.4299	.3565
		(3)	0	.1271	.2427	.4009	.4285	.3514
	0.5	(1)	0	.1245	.2373	.3909	.4202	.3551
		(2)	0	.1197	.2277	.3711	.3887	.3155
		(3)	0	.1192	.2268	.3697	.3874	.3115
	0.7	(1)	0	.1069	.2031	.3301	.3479	.2890
		(2)	0	.1029	.1951	.3136	.3220	.2570
		(3)	0	.1025	.1943	.3123	.3209	.2543

mode II stress intensity factor which is valid for $t_f = 0$ and incident longitudinal stress wave angle $\alpha = 3\pi/8$. Note that for all calculations in this paper, a Poisson's ratio of 0.25 is used which gives a ratio of wave speed $v_l = \sqrt{3}v_s$, $v_l = 1.884v_R$. The numerical results of the mode I and mode II stress intensity factor due to incident transverse stress wave for $t_f = 0$ are

Table 2 Comparison of numerical results according to Burgers (1983): (1) Achenbach, Kuo, and Dempsey (1984); (2) and this paper; (3) for an incident transverse stress wave $\alpha = 0$ and $t_f = 0$

	V/V_R \ δ		0	.0625	.125	.25	.375	.485
$\dfrac{K_I^T}{\sigma_0 (v_1 t)^{1/2}}$	0.1	(1)	0	-.3814	-.7365	-1.2803	-1.5241	-1.4983
		(2)	0	-.3840	-.7397	-1.2693	-1.4607	-1.3524
		(3)	0	-.3836	-.7395	-1.2690	-1.4607	-1.3431
	0.3	(1)	0	-.3179	-.6086	-1.0231	-1.1571	-1.0589
		(2)	0	-.3322	-.6347	-1.0558	-1.1560	-1.0130
		(3)	0	-.3319	-.6343	-1.0551	-1.1552	-1.0043
	0.5	(1)	0	-.2648	-.5021	-.8104	-.8479	-.7102
		(2)	0	-.2710	-.5133	-.8229	-.8452	-.6830
		(3)	0	-.2708	-.5129	-.8222	-.8443	-.6781
	0.7	(1)	0	-.1938	-.3622	-.5558	-.5248	-.3790
		(2)	0	-.1950	-.3656	-.5597	-.5239	-.3699
		(3)	0	-.1949	-.3653	-.5592	-.5233	-.3680
$\dfrac{K_{II}^T}{\sigma_0 (v_1 t)^{1/2}}$	0.1	(1)	1.3369	1.2940	1.1695	.7321	.1837	-.2586
		(2)	1.3485	1.3005	1.1610	.6680	.0466	-.5429
		(3)	1.3436	1.2954	1.1575	.6648	.0441	-.4392
	0.3	(1)	1.2351	1.1897	1.0590	.6119	.0871	-.2986
		(2)	1.2247	1.1755	1.0339	.5468	-.0295	-.5266
		(3)	1.2227	1.1736	1.0320	.5453	-.0302	-.4372
	0.5	(1)	1.0823	1.0369	.9070	.4725	-.0095	-.3290
		(2)	1.0784	1.0299	.8910	.4258	-.0906	-.4656
		(3)	1.0770	1.0285	.8897	.4248	-.0910	-.4160
	0.7	(1)	.8920	.8493	.7278	.3297	-.0844	-.3199
		(2)	.8817	.8373	.7110	.2972	-.1315	-.3791
		(3)	.8807	.8363	.7100	.2965	-.1318	-.3626

shown in Figs. 4 and 5. These results agree very well with the numerical results presented by Achenbach, Kuo, and Dempsey (1984). A comparison with the numerical results with Achenbach, Kuo, and Dempsey (1984) and Burgers (1983) is shown in Tables 1 and 2, for both incident longitudinal and transverse waves with $\alpha = 0$. It shows that the first-order approximation method used in this paper agrees quite well with the numerical results of Burgers (1983). For the important range of kinking angles $0 < \delta < \pi/4$, the error introduced by using this approximate method is within 3 percent for mode I stress intensity factor and 5 percent for mode II stress intensity factor due to incident longitudinal wave. For incident transverse wave, the error is within 3 percent for mode I and 10 percent for mode II. This good agreement suggests that the wedge geometry of the kinked crack has only a minor effect on the calculation of the dynamic stress intensity factor.

In order to investigate the stress intensity factor for the whole propagation event of the kinked crack, the normalized time t_f/t is chosen as the parameter. The instant of initiation of the kink is at $t_f/t = 1$, while $t_f/t = 0$ corresponds to the time when the kinked crack has propagated for an infinite time compared to the delay time. The nondimensional stress intensity factor for mode I and mode II versus t_f/t for incident longitudinal wave (or transverse wave) for incident angle $\alpha = 0.375\pi$, and kinking angles $\delta = \pm 0.125\pi$ are calculated and plotted in Figs. 6–9. As we can see from these figures, the dimensionless stress intensity factor is significantly different for $t_f/t = 0$ and $t_f/t = 1$ for some cases. The mode II stress intensity factor has a stronger dependence on delay time effect than mode I case.

Energy Fluxes and Kinking Criterion

For mixed mode I-II fracture, the energy flux into the propagating crack-tip can be written in terms of the corresponding dynamic stress intensity factors in the form

$$E = -\frac{b^2}{2\mu d^3 R(d)} \left[\left(1 - \frac{a^2}{d^2}\right)^{1/2} (K_I)^2 + \left(1 - \frac{b^2}{d^2}\right)^{1/2} (K_{II})^2 \right]$$
$$= \frac{\sigma_o^2 t}{2\mu b^2} E^*, \tag{51}$$

where

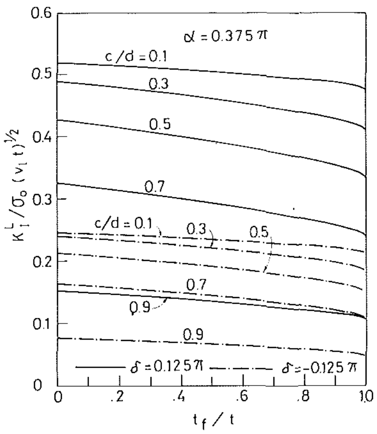

Fig. 6 The time history of mode I stress intensity factor for $\delta = \pi/8$, $-\pi/8$ due to incident longitudinal stress-wave loading for $\alpha = 0.375\pi$

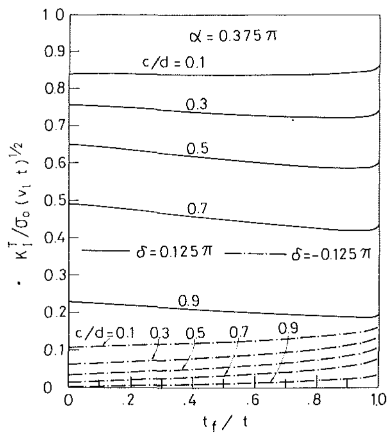

Fig. 8 The time history of mode I stress intensity factor for $\delta = \pi/8$, $-\pi/8$ due to incident transverse stress-wave loading for $\alpha = 0.375\pi$

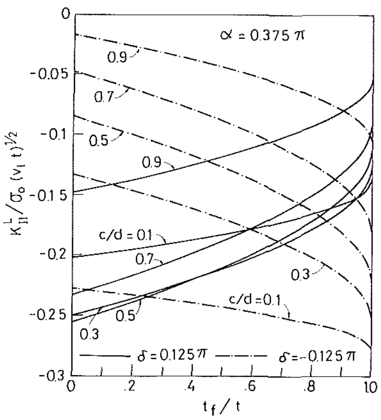

Fig. 7 The time history of mode II stress intensity factor for $\delta = \pi/8$, $-\pi/8$ due to incident longitudinal stress-wave loading for $\alpha = 0.375\pi$

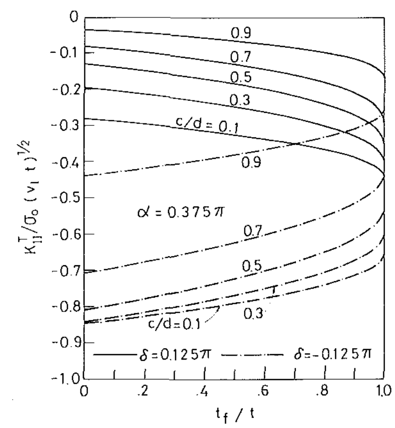

Fig. 9 The time history of mode II stress intensity factor for $\delta = \pi/8$, $-\pi/8$ due to incident transverse stress-wave loading for $\alpha = 0.375\pi$

$$R(d) = \left(\frac{b^2}{d^2} - 2\right)^2 - 4\left(1 - \frac{a^2}{d^2}\right)^{1/2}\left(1 - \frac{b^2}{d^2}\right)^{1/2}.$$

In the following calculations of E^*, the stress intensity factor might show a negative value. A negative mode I stress intensity factor would correspond to the contact of the crack faces near the crack-tip. Hence, we would set K_I identically equal to zero whenever the calculations show it to be negative. The effect on the negative mode II stress intensity factor may be ignored under the smooth, frictionless crack faces assumption. If the maximum energy release rate criterion is accepted as the kinking condition, then the combination of the kinking angle and the crack speed can be determined at which the energy flux into the propagating crack-tip achieves a maximum value. For an incident longitudinal wave, Fig. 10 shows the kinking angle and the crack-tip speed at which E^* attains its maximum value for various values of α for $t_f = 0$. The predicted kinked crack speed increases as the incident angle α increase. For the general case, the delay time is not zero, it is shown in Fig. 11 for incident angle $\alpha = \pi/4$ that the kinking angle and crack tip speed for E^* to achieve its maximum value $E^*_{\max}$ of the whole time history.

Conclusion

With the inclusion of a delay time, the solution of the fracture problem becomes a great deal more realistic physically and more closely models real material response. An approximate method that ignores the corner geometry of the kink angle is used to construct the mixed-mode stress intensity factor for incident longitudinal and transverse stress-wave loading. A very satisfactory result is obtained when compared with the numerical results with no delay time effect. This good agreement suggests that the wedge geometry of the kinked crack has only a minor effect on the calculation of the dynamic stress intensity factor. Hence, for important range of kinking angles, the elastodynamic crack kinking stress intensity factors are affected more by the loading of the new crack faces than by the wedge geometry.

The influence of the delay time effect on the calculation of the dynamic stress intensity factor for kinking crack can be obtained from Figs. 6–9. The figures show that the mode I stress intensity factor is weakly dependent on delay time, while the mode II stress intensity factor has a stronger dependence on delay time. For the kinking angle $\delta = 0$, the crack propagates straight out of the original crack, the stress intensity factors are expressed in (39)–(42). An interesting result is that K_I^L and K_{II}^T are independent of the delay time for $\alpha = 0$.

Frequently, an energy-based fracture criterion is used to look at the initiation of crack-tip motion. The criterion is based on the assumption that the energy release rate at initiation of fracture is a material parameter. For static fracture under small-scale yielding conditions this is well established, but for dynamic fracture, it is not clear that this is a suitable criterion beyond the initiation phase. It is unfortunately not yet clear from experimental results what is a suitable criterion for a bifurcation event. Recent attempts have been made to determine the condition for crack branching from theoretical analysis of the elastodynamic field quantities near the tips of the branches. With these theoretical results for the stress intensity factor of the kinking crack, an attempt can be made to de-

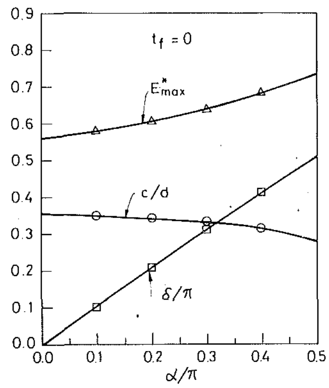

Fig. 10 Kinking angle and crack-tip speed for E^*_{max} of incident various angles of longitudinal wave

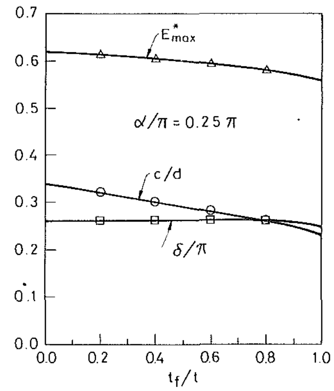

Fig. 11 Kinking angle and crack-tip speed for E^*_{max} in whole time history for $\alpha = \pi/4$

termine the kink angle and the new kinked crack speed using different fracture criteria and to compare them with the experimental results available. For this paper, the maximum energy release rate is adopted for the kinking criterion. This energy criterion suggests that the crack will choose to propagate in the direction and at velocity for which the energy flux into the crack tip has a maximum value. For the special case $t_f = 0$, the general features are that the kinked crack speed v increases as the incident stress wave angle α increases for E^* to achieve its maximum value $E^*_{\max}$, and the kinked angle δ is just slightly larger than α. For the general case, the kinking angle δ is approximately constant until t_f/t reaches 0.8. In general, v and δ are slightly smaller than the corresponding values obtained by assuming no delay time. For incident stress-wave parallel to the crack faces ($\alpha = 0$), the energy criterion predicts that the crack will tend to propagate straight ahead of the original crack which has been observed in experiments, see Ravi-Chandar and Knauss (1984a, b, c, d).

The complete solutions available for the kinked crack geometry that include the corner effect are still restricted to no delay time. There are no other results that can be used to judge the accuracy of the approximation in this paper when the delay time effect is included in the whole kinking angle range. It has been shown, that for $\delta = 0$, the results are exact. It is believed that this approximate method still gives a quite good accuracy for small kinked angles.

Acknowledgments

The research support of the R.O.C. National Science Council through Grant NSC76-0401-E002-17 at National Taiwan University is gratefully acknowledged.

References

Achenbach, J. D., 1970, "Crack Propagation Generated by a Horizontally Polarized Shear Wave," *J. Mech. Phys. Solids*, Vol. 18, pp. 245–259.

Achenbach, J. D., and Kuo, M. K., 1985, "Conditions for Crack Kinking under Stress-Wave Loading," *Engineering Fracture Mechanics*, Vol. 22, pp. 165–180.

Achenbach, J. D., Kuo, M. K., and Dempsey, J. P., 1984, "Mode III and Mixed Mode I-II Crack Kinking under Stress-Wave Loading," *Int. J. Solids Structures*, Vol. 20, pp. 395–410.

Achenbach, J. D., and Varatharajulu, 1974, "Skew Crack Propagation at the Diffraction of a Transient Stress Wave," *Quarterly Appl. Math.*, Vol. 32, pp. 123–135.

Burgers, P., 1982, "Dynamic Propagation of a Kinked or Bifurcated Crack in Anti-plane Strain," ASME Journal of Applied Mechanics, Vol. 49, pp. 371–376.

Burgers, P., 1983, "Dynamic Kinking of a Crack in Plane Strain," *Int. J. Solids Structures*, Vol. 19, pp. 735–752.

Burgers, P., and Dempsey, J. P., 1982, "Two Analytical Solutions for Dynamic Crack Bifurcation in Anti-plane Strain," ASME Journal of Applied Mechanics, Vol. 49, pp. 366–370.

Burgers, P., and Dempsey, J. P., 1984, "Plane Strain Dynamic Crack Bifurcation," *Int. J. Solids Structures*, Vol. 20, pp. 609–618.

Dempsey, J. P., Kuo, M. K., and Achenbach, J. D., 1982, "Mode III Crack Kinking under Stress Wave Loading," *Wave Motion*, Vol. 4, pp. 181–190.

Dempsey, J. P., Kuo, M. K., and Bentley, D. L., 1986, "Dynamic Effects in Mode III Crack Bifurcation," *Int. J. Solids Structures*, Vol. 22, pp. 333–353.

Freund, L. B., 1973, "Crack Propagation in an Elastic Solid Subjected to General Loading—III, Stress Wave Loading," *J. Mech. Phys. Solids*, Vol. 21, pp. 47–61.

Freund, L. B., 1974, "Crack Propagation in an Elastic Solid Subjected to General Loading—IV, Obliquely Incident Stress Pulse," *J. Mech. Phys. Solids*, Vol. 22, pp. 137–146.

Ma, C. C., and Burgers, P., 1986, "Mode III Crack Kinking with Delay Time: An Analytical Approximation," *Int. J. Solids Structures*, Vol. 22, pp. 883–899.

Ma, C. C., and Burgers, P., 1987, "Dynamic Mode I and Mode II Crack Kinking Including Delay Time Effects," *Int. J. Solids Structures*, Vol. 23, pp. 897–918.

Ravi-Chandar, K., and Knauss, W. G., 1984a, "An Experimental Investigation into Dynamic Fracture: I. Crack Initiation and Arrest," *International Journal of Fracture*, Vol. 25, pp. 247–262.

Ravi-Chandar, K., and Knauss, W. G., 1984b, "An Experimental Investigation into Dynamic Fracture: II. Microstructural Aspects," *International Journal of Fracture*, Vol. 26, pp. 65–80.

Ravi-Chandar, K., and Knauss, W. G., 1984c, "An Experimental Investigation into Dynamic Fracture: III. On Steady-State Crack Propagation and Crack Branching," *International Journal of Fracture*, Vol. 26, pp. 141–154.

Ravi-Chandar, K., and Knauss, W. G., 1984d, "An Experimental Investigation into Dynamic Fracture: IV. On the Interaction of Stress Waves with Propagating Cracks," *International Journal of Fracture*, Vol. 26, pp. 189–200.

APPENDIX A

$$(\sigma^I_{\theta\theta})^*_h = (a+a^*)^{1/2}\left[1-2\left(\frac{a}{b}\right)^2\sin^2\alpha\right](\sigma^I_{\theta\theta})^*_h$$

$$-(b+a^*)^{1/2}\left(\frac{a}{b}\right)^2\sin 2\alpha(\sigma^{II}_{\theta\theta})^*_h\operatorname{sgn}(\delta).$$

$$(\sigma^I_{r\theta})^*_h = (a+a^*)^{1/2}\left[1-2\left(\frac{a}{b}\right)^2\sin^2\alpha\right](\sigma^I_{r\theta})^*_h$$

$$-(b+a^*)^{1/2}\left(\frac{a}{b}\right)^2\sin 2\alpha(\sigma^{II}_{r\theta})^*_h\operatorname{sgn}(\delta).$$

$$(\sigma^p_{\theta\theta})^*_h = \frac{1}{2}(1-\cos 2\delta)(\sigma^p_{xx})^*_h + \frac{1}{2}(1$$

$$+\cos 2\delta)(\sigma^p_{zz})^*_h - \sin|2\delta|(\sigma^p_{xz})^*_h,\ p = I \text{ or } II$$

$$(\sigma^q_{\theta r})^*_h = \left[-\frac{1}{2}\sin|2\delta|(\sigma^q_{xx})^*_h + \frac{1}{2}\sin|2\delta|(\sigma^q_{zz})^*_h\right.$$

$$\left.+\cos 2\delta(\sigma^q_{xz})^*_h\right]\operatorname{sgn}(\delta),\ q = I \text{ or } II,$$

and

$$(\sigma_{zz}^I)_h^* = \mathrm{Im}\left\{ -\frac{[2\Theta_a^2 - b^2(vh-1)^2]^2\Omega_a}{\Psi_a[a(vh-1)+\Theta_a]^{1/2}} - \frac{4\Theta_b^2[a(vh-1)-\Theta_b]^{1/2}[b^2(vh-1)^2-\Theta_b^2]^{1/2}\Omega_b}{\Psi_b}\right\},$$

$$(\sigma_{xz}^I)_h^* = \mathrm{Im}\left\{ -\frac{2\Theta_a[a(vh-1)-\Theta_a]^{1/2}[2\Theta_a^2 - b^2(vh-1)^2]\Omega_a}{\Psi_a} + \frac{2\Theta_b[a(vh-1)-\Theta_b]^{1/2}[2\Theta_b^2 - b^2(vh-1)^2]\Omega_b}{\Psi_b}\right\},$$

$$(\sigma_{xx}^I)_h^* = \mathrm{Im}\left\{ \frac{[2\Theta_a^2 - b^2(vh-1)^2][2\Theta_a^2+(b^2-2a^2)(vh-1)^2]\Omega_a}{\Psi_a[a(vh-1)+\Theta_a]^{1/2}} + \frac{4\Theta_b^2[a(vh-1)-\Theta_b]^{1/2}[b^2(vh-1)^2-\Theta_b^2]^{1/2}\Omega_b}{\Psi_b}\right\},$$

and

$$(\sigma_{zz}^{II})_h^* = \mathrm{Im}\left\{ \frac{2\Theta_a[b(vh-1)-\Theta_a]^{1/2}[b^2(vh-1)^2-2\Theta_a^2]\Omega_a}{\Psi_a} - \frac{2\Theta_b[b(vh-1)-\Theta_b]^{1/2}[b^2(vh-1)^2-2\Theta_b^2]\Omega_b}{\Psi_b}\right\},$$

$$(\sigma_{xz}^{II})_h^* = \mathrm{Im}\left\{ -\frac{4\Theta_a^2[b(vh-1)-\Theta_a]^{1/2}[a^2(vh-1)^2-\Theta_a^2]^{1/2}\Omega_a}{\Psi_a} - \frac{[2\Theta_b^2 - b^2(vh-1)^2]^2\Omega_b}{\Psi_b[b(vh-1)+\Theta_b]^{1/2}}\right\},$$

$$(\sigma_{xx}^{II})_h^* = \mathrm{Im}\left\{ \frac{2\Theta_a[b(vh-1)-\Theta_a]^{1/2}[2\Theta_a^2+(b^2-2a^2)(vh-1)^2]\Omega_a}{\Psi_a} + \frac{2\Theta_b[b(vh-1)-\Theta_b]^{1/2}[b^2(vh-1)^2-2\Theta_b^2]\Omega_b}{\Psi_b}\right\}$$

where

$$\Omega_a = -[h^2 - a^2(vh-1)^2]^{1/2}\cos\delta + ih\sin|\delta|,$$

$$\Omega_b = -[h^2 - b^2(vh-1)^2]^{1/2}\cos\delta + ih\sin|\delta|,$$

$$\Theta_a = -h\cos\delta + i[h^2 - a^2(vh-1)^2]^{1/2}\sin|\delta|,$$

$$\Theta_b = -h\cos\delta + i[h^2 - b^2(vh-1)^2]^{1/2}\sin|\delta|,$$

$$\Psi_a = [h^2 - a^2(vh-1)^2]^{1/2}[\Theta_a - a(vh-1)\sin\alpha][\Theta_a - c(vh-1)]S_-^o(\Theta_a/(vh-1)),$$

$$\Psi_b = [h^2 - b^2(vh-1)^2]^{1/2}[\Theta_b - a(vh-1)\sin\alpha][\Theta_b - c(vh-1)]S_-^o(\Theta_b/(vh-1)).$$

APPENDIX B

$$(\sigma_{\theta\theta}^T)_h^* = (a+b^*)^{1/2}\sin 2\alpha(\sigma_{\theta\theta}^I)_h^* + (b+b^*)^{1/2}\cos 2\alpha(\sigma_{\theta\theta}^{II})_h^*\mathrm{sgn}(\delta).$$

$$(\sigma_{r\theta}^T)_h^* = (a+b^*)^{1/2}\sin 2\alpha(\sigma_{r\theta}^I)_h^* + (b+b^*)^{1/2}\cos 2\alpha(\sigma_{r\theta}^{II})_h^*\mathrm{sgn}(\delta).$$

$$(\sigma_{\theta\theta}^p)_h^* = \frac{1}{2}(1-\cos 2\delta)(\sigma_{xx}^p)_h^* + \frac{1}{2}(1+\cos 2\delta)(\sigma_{zz}^p)_h^* - \sin|2\delta|(\sigma_{xz}^p)_h^*,\ p = I \text{ or } II$$

$$(\sigma_{\theta r}^q)_h^* = \left[-\frac{1}{2}\sin|2\delta|(\sigma_{xx}^q)_h^* + \frac{1}{2}\sin|2\delta|(\sigma_{zz}^q)_h^* + \cos 2\delta(\sigma_{xz}^q)_h^* \right]\mathrm{sgn}(\delta),\ q = I \text{ or } II,$$

where $(\sigma_{\theta\theta}^I)_h^*$, $(\sigma_{r\theta}^I)_h^*$, $(\sigma_{\theta\theta}^{II})_h^*$ and $(\sigma_{r\theta}^{II})_h^*$ are exactly the same as Appendix A except changing $a(vh-1)\sin\alpha$ in Ψ_a and Ψ_b to $b(vh-1)\sin\alpha$, that is

$$\Psi_a = [h^2 - a^2(vh-1)^2]^{1/2}[\Theta_a - b(vh-1)\sin\alpha][\Theta_a - c(vh-1)]S_-^o(\Theta_a/(vh-1)),$$

$$\Psi_b = [h^2 - b^2(vh-1)^2]^{1/2}[\Theta_b - b(vh-1)\sin\alpha][\Theta_b - c(vh-1)]S_-^o(\Theta_b/(vh-1)).$$

On Membrane and Plate Problems for Which the Linear Theories are Not Admissible

Arnold D. Kerr
Professor,
Mem. ASME

Douglas W. Coffin
Graduate Student.

Department of Civil Engineering,
University of Delaware,
Newark, DE 19716

A horizontal clamped plate is subjected to the weight of a liquid above it. When the free surface of the liquid coalesces with the plane of the undeformed upper surface of the plate, according to the classical theory of plates (which results in an eigenvalue problem), nonzero deflections will exist only for discrete values of the ratio γ/D*; where* γ *is the specific weight of the liquid and* D *is the flexural stiffness of the plate. The purpose of this paper is to clarify this apparently unreasonble result. It is shown, using a nonlinear analysis, that problems of this type exhibit a bifurcation point from the undeformed state and that the eigenvalues of the linear analysis determine merely the bifurcation points. Thus, for problems of this type, a linear formulation is not suitable. Because of its analytical simplicity, at first, the membrane strip is analyzed in detail. This is followed by the analysis of the plate.*

Introduction

When analyzing plates, the following problem was encountered: An infinite thin elastic strip clamped along both edges is subjected to a fluid, as shown in Fig. 1. The free fluid surface coalesces with the upper surface of the undeformed strip.

For this problem the deflection is $w = w(x)$ and the vertical load is

$$q(x) = \gamma w(x), \tag{1}$$

where γ is the specific weight of the liquid. Using the classical bending theory of plates, the analytical formulation is

$$\left.\begin{array}{ll} Dw^{iv}(x) - \gamma w(x) = 0 & 0 \le x \le L \\ w(0) = 0 \;;\; w(L) = 0 & \\ w'(0) = 0 \;;\; w'(L) = 0 & \end{array}\right\} \tag{2}$$

where

$$D = \frac{Eh^3}{12(1-\nu^2)}, \tag{3}$$

$(\;)' = d(\;)/dx$ and E, ν are the elastic constants.

This formulation constitutes an eigenvalue problem. Except for the meaning of γ, it is identical to the free vibration problem of a clamped plate strip (Volterra and Zachmanoglou, 1965). The condition for the existence of a nonzero solution is

$$\cosh\beta L \cos\beta L = 1 \tag{4}$$

where

$$\beta = \sqrt[4]{\frac{\gamma}{D}}. \tag{5}$$

The corresponding eigenvalues are $(\beta L)_1 = 4.7300$; $(\beta L)_2 = 7.8532$, . . . Because, for the problem under consideration, $w(x) > 0$ in $0 < x < L$, only the first eigenvalue is of interest. Therefore, a nonzero deflection surface will exist only when $\sqrt[4]{\gamma/D} = 4.7300/L$ or, rewritten, when $\gamma = 500.6 \cdot D/L^4$. According to this analysis, for $\gamma \lessgtr 500.6 \cdot D/L^4$, the deflections are identically zero. This does not appear to be a physically reasonable result, especially for $\gamma > 500.6 \cdot D/L^4$. The purpose of this paper is to clarify this situation.

Using a nonlinear formulation, it will be shown that a linear analysis as used above is not suitable for problems of this type. Because of the nature of the nonlinearity included in the following analyses, exact closed-form solutions will be obtained which are very convenient for the planned study. Due to its analytical simplicity, at first, the membrane strip will be analyzed in detail. This will be followed by the analysis of the plate strip.

The Membrane Strip

Linear Analysis. The problem shown in Fig. 2 is analyzed first using the *linear* membrane formulation. Noting that $w = w(x)$ and that the water load is, as before, $q(x) = \gamma w(x)$ the governing equations are

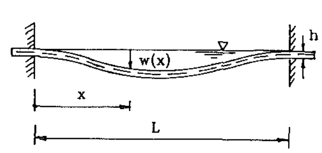

Fig. 1

Contributed by the Applied Mechanics Division of The American Society of Mechanical Engineers for publication in the Journal of Applied Mechanics.

Discussion on this paper should be addressed to the Technical Editor, Leon M. Keer, The Technological Institute, Northwestern University, Evanston, IL 60201, and will be accepted until two months after final publication of the paper itself in the Journal of Applied Mechanics. Manuscript received by the ASME Applied Mechanics Division, October 13, 1988; final revision, January 6, 1989.

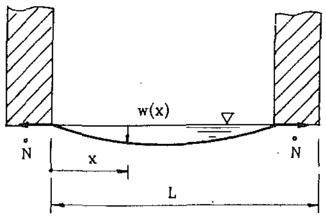

Fig. 2

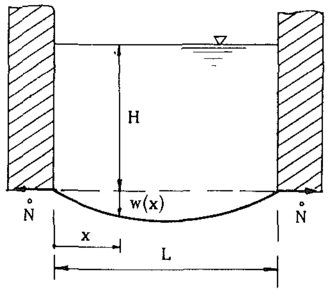

Fig. 3

$$\left.\begin{aligned}&\mathring{N}w''+\gamma w=0 \qquad 0\le x\le L\\ &w(0)=0\ ;\ w(L)=0\end{aligned}\right\} \tag{6}$$

where $\mathring{N}$ is a prescribed constant axial force field and γ is the specific weight of the liquid. In this standard formulation it is assumed (Rayleigh, 1945) that $\mathring{N}$ is very large, and that the additional axial forces due to $q(x)$ are negligible compared to $\mathring{N}$.

The formulation in (6) constitutes an eigenvalue problem. The condition for the existence of a nonzero solution is

$$\sin\mathring{\alpha}L=0 \tag{7}$$

where

$$\mathring{\alpha}=\sqrt{\gamma/\mathring{N}}. \tag{8}$$

The eigenvalues are

$$\mathring{\alpha}_n L=n\pi \qquad n=1,2,3,\ \ldots\ . \tag{9}$$

Since $w(x)>0$ in $0\le x\le L$, it follows that only

$$\mathring{\alpha}_1 L=\pi \tag{10}$$

is of interest. The corresponding eigenfunction is

$$w_1(x)=\sin\frac{\pi x}{L}\ . \tag{10'}$$

Thus, according to the above analysis, a nonzero $w(x)$ may exist only when $\gamma/\mathring{N}=\pi^2/L^2$ and for $\gamma \gtrless \mathring{N}\pi^2/L^2$ the deflection $w(x)\equiv 0$, similar to the plate strip result discussed in the previous section.

In an attempt to clarify this unreasonable result, next the problem shown in Fig. 3 is analyzed and then H is set to zero. This problem corresponds to the actual physical situation when the membrane strip is subjected to a water layer of depth H and then this layer is poured off leaving the water in the space created by the deflected membrane, as shown in Fig. 2.

Since the water pressure is now

$$q(x)=\gamma[H+w(x)], \tag{11}$$

the governing equations are

$$\left.\begin{aligned}&\mathring{N}w''+\gamma w=-\gamma H \qquad 0\le x\le L\\ &w(0)=0\ ;\ w(L)=0\end{aligned}\right\}. \tag{12}$$

The solution of this boundary value problem is

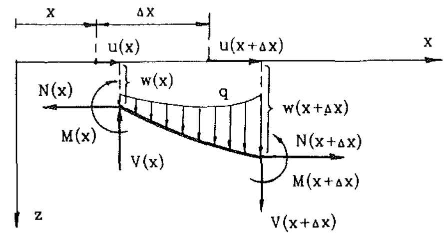

Fig. 4

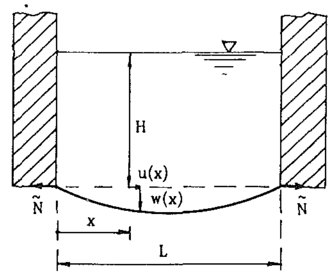

Fig. 5

$$w(x)=H\left[\cos\mathring{\alpha}x+\frac{1-\cos\mathring{\alpha}L}{\sin\mathring{\alpha}L}\sin\mathring{\alpha}x-1\right]. \tag{13}$$

For the case $H\to 0$, the deflection $w(x)\to 0$, unless also $\sin\mathring{\alpha}L/(1-\cos\mathring{\alpha}L)=0$, which leads for $\mathring{\alpha}L=\pi$ to an undetermined $w(x)$. Note that the condition $\sin\mathring{\alpha}L=0$ is the result of the eigenvalue problem discussed previously.

Nonlinear Analysis. To gain a better understanding of the analytical features of this problem a nonlinear analysis is conducted next.

In the following analyses, the differential equations for the membrane strip are based on the equilibrium equations of the free-body diagram shown in Fig. 4 (with $M=0$), the strain displacement relation

$$\epsilon_{xx}(x)=u'(x)+\frac{1}{2}w'^2(x), \tag{14}$$

and Hooke's law. These equations are

$$N'=0\ ;\ -(Nw')'=q \tag{15}$$

where

$$N=Eh\left(u'+\frac{1}{2}w'^2\right). \tag{16}$$

E is Young's modulus of the membrane and h is its thickness in the undeformed state. In Fig. 4, the x-axis coalesces with the undeformed reference plane of the membrane, $(x,\ z)$ are Lagrange coordinates, and $(u,\ w)$ are the components of the displacement vector $\bar{u}(x)$ of the reference plane in the x and z-directions, respectively.

The differential equations in (15) are *nonlinear*. However, since the first equation when integrated once yields $N=$ constant, the second equation reduces to a *linear* ordinary differential equation for $w(x)$. This analytical feature makes it possible to solve these differential equations exactly and in closed form (Marguerre, 1938).

In these derivations, $u(x)$ are assumed to be very small. Therefore, the expression for the vertical load

$$q(x)=\gamma[H+w(x)] \tag{17}$$

is retained, as in equation (11). Also, because the corresponding membrane slopes are very small, the horizontal components of the water pressure are neglected.

With these assumptions, the formulation of the problem shown in Fig. 5 consists of the differential equations

$$\left.\begin{array}{l}\left[Eh\left(u'+\frac{1}{2}w'^2\right)w'\right]'+\gamma w=-\gamma H\\ \left[Eh\left(u'+\frac{1}{2}w'^2\right)\right]'=0\end{array}\right\}\ 0\le x\le L, \tag{18}$$

and the boundary conditions

$$\left.\begin{array}{ll} w(0)=0; & w(L)=0\\ u(0)=0; & u(L)=0\end{array}\right\}. \tag{19}$$

Integration of the second equation in (18) yields

$$Eh\left(u'+\frac{1}{2}w'^2\right)=\text{const}=\tilde{N}\quad 0\le x\le L, \tag{20}$$

$\tilde{N}$ being the axial force field caused by the water pressure. Note that unlike in the linear formulation, there is no initial axial force field $\mathring{N}$. This case will be discussed later.

Utilizing equation (20), the first equation in (18) reduces to a linear ordinary differential equation with constant coefficients

$$\tilde{N}w''+\gamma w=-\gamma H\quad 0\le x\le L. \tag{21}$$

This equation is identical, except for the $\tilde{N}$, with the differential equation in (12). The solution to this equation and the two boundary conditions on w in (19) is

$$w(x)=H\left[\cos\tilde{\alpha}x+\frac{1-\cos\tilde{\alpha}L}{\sin\tilde{\alpha}L}\sin\tilde{\alpha}x-1\right] \tag{22}$$

where $\tilde{\alpha}=\sqrt{\gamma/\tilde{N}}$.

The as yet unknown $\tilde{N}$ is determined next, using the second differential equation in (18) and the remaining boundary conditions in (19).

The first integral, presented in (20), is a nonlinear differential equation of first order. Since, at this point of the analysis, $w(x)$ is a known function given in (22), equation (20) reduces to a linear differential equation for $u(x)$. Namely,

$$u'(x)=\frac{\tilde{N}}{Eh}-\frac{1}{2}w'^2(x)\quad 0\le x\le L. \tag{23}$$

Integrating this relation from 0 to L, noting that according to (19) $u(0)=0$ and $u(L)=0$, it becomes

$$\frac{\tilde{N}L}{Eh}-\frac{1}{2}\int_o^L w'^2(x)dx=0. \tag{24}$$

Substitution of $w(x)$ from (22) into equation (24) and performing the integrations results in

$$\frac{EhH^2}{2\gamma L^4}=\frac{1+\cos\tilde{\alpha}L}{(\tilde{\alpha}L)^3(\tilde{\alpha}L-\sin\tilde{\alpha}L)}. \tag{25}$$

This is the equation for the determination of $\tilde{\alpha}$ (or $\tilde{N}=\gamma/\tilde{\alpha}^2$) for given E, h, γ, L, H.

Equation (22), in conjunction with (25), constitutes a solution of the problem stated in (18) and (19). For completeness, $u(x)$ may be obtained by integrating (23) from 0 to x. The result is

$$u(x)=\frac{\tilde{N}x}{Eh}-\frac{1}{2}\int_o^x w'^2(\xi)d\xi. \tag{26}$$

Next, consider the case when $H\to 0$. For this purpose, equation (25) is solved for H. The result is

$$H=\underset{(-)}{+}\sqrt{\frac{2\gamma L^4}{Eh}\frac{1+\cos\tilde{\alpha}L}{(\tilde{\alpha}L)^3(\tilde{\alpha}L-\sin\tilde{\alpha}L)}}. \tag{27}$$

It is obvious that when $H\to 0$, the condition

$$\cos\tilde{\alpha}L=-1 \tag{28}$$

has to be satisfied. This takes place for

$$\tilde{\alpha}_nL=n\pi\quad n=1,3,5,\ \ldots\ . \tag{29}$$

Because $w(x)>0$, it follows from (22) that only $\tilde{\alpha}_1L=\pi$ is of interest. For this case $\sin\tilde{\alpha}_1L=0$ and $w(x)$ in (22) appears not determined, like in the linear analysis of the previous section.

However, for the present nonlinear analysis, H was shown to depend on $\tilde{\alpha}$ (or vice versa). Therefore, substituting (27) into (22), and noting that

$$\lim_{H\to 0}[H\cos\tilde{\alpha}x]=0,$$

it follows that

$$\lim_{H\to 0}[w(x)]=\lim_{\substack{H\to 0\\ \tilde{\alpha}L\to\pi}}\left[H\frac{1-\cos\tilde{\alpha}L}{\sin\tilde{\alpha}L}\sin\tilde{\alpha}x\right]$$

$$=\lim_{\substack{H\to 0\\ \tilde{\alpha}L\to\pi}}\left[\sqrt{\frac{2\gamma L^4}{Eh}\frac{(1+\cos\tilde{\alpha}L)(1-\cos\tilde{\alpha}L)^2}{(\tilde{\alpha}L)^3(\tilde{\alpha}L-\sin\tilde{\alpha}L)\sin^2\tilde{\alpha}L}}\sin\tilde{\alpha}x\right].$$

Since $\sin^2\tilde{\alpha}L=1-\cos^2\tilde{\alpha}L=(1-\cos\tilde{\alpha}L)(1+\cos\tilde{\alpha}L)$, $\cos\tilde{\alpha}_1L=\cos\pi=-1$, and $\sin\tilde{\alpha}_1L=\sin\pi=0$, the above relation becomes

$$\lim_{H\to 0}[w(x)]=\frac{2L^2}{\pi^2}\sqrt{\frac{\gamma}{Eh}}\sin\frac{\pi x}{L}. \tag{30}$$

The corresopnding tensile force field is $\tilde{N}=\gamma L^2/\pi^2$.

According to the above analysis, for the case $H=0$, a deflected membrane shape does exist for any $\gamma>0$.

It is of interest to establish if equation (30) may be obtained from the nonlinear analysis, by assuming *a priori* that $H=0$. For this case the equations in (18) reduce to

$$\left.\begin{array}{l}Eh\left(u'+\frac{1}{2}w'^2\right)=\text{const}=\tilde{N}\\ \tilde{N}w''+\gamma w=0\end{array}\right\}0\le x\le L. \tag{18'}$$

The boundary conditions are given in (19). The equations for $w(x)$ constitute an eigenvalue problem.

The general solution of the second equation in (18′) is

$$w(x)=A_1\sin\tilde{\alpha}x+A_2\cos\tilde{\alpha}x \tag{31}$$

where $\tilde{\alpha}=\sqrt{\gamma/\tilde{N}}$. From the first boundary condition, $w(0)=0$, it follows that $A_2=0$. The second condition results in $\sin\tilde{\alpha}L=0$. It is satisfied by the eigenvalues

$$\tilde{\alpha}_nL=n\pi\quad n=1,2,3,\ \ldots\ . \tag{32}$$

Since $w(x)>0$, only $n=1$ is of interest. Thus,

$$w(x)=A_1\sin\tilde{\alpha}_1x, \tag{33}$$

with $\tilde{\alpha}_1=\pi/L$. The corresponding axial force is

$$\tilde{N}=\gamma L^2/\pi^2. \tag{34}$$

The unknown A_1 is determined from the remaining equations in (18′) and (19), which reduce to equation (24). Substituting (33) into (24) and performing the indicated integration yields

$$A_1=\frac{2L^2}{\pi^2}\sqrt{\frac{\gamma}{Eh}}. \tag{35}$$

This agrees with the $w(x)$ expression obtained previously, by subjecting the solution for $H>0$ to the limit process $H\to 0$.

To gain a better understanding of the above results, equation (27) was numerically evaluated. The obtained graphs and the corresponding $w(x)$ shapes are shown in Fig. 6.

The results of the numerical evaluation of equation (30) and equation (22), in conjunction with equation (27), are shown in Fig. 7.

In the *linear* analysis presented above, the membrane force

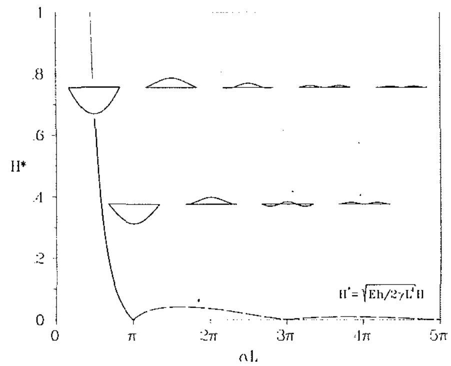

Fig. 6

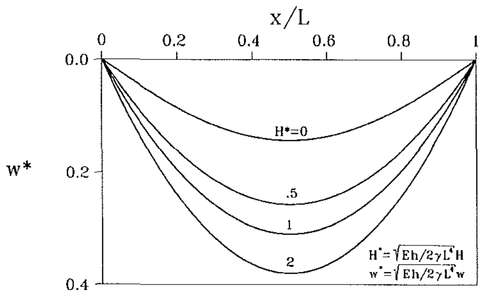

Fig. 7

was $\overset{\circ}{N}$; an *a priori* prescribed large force field. In the *nonlinear* analysis that followed, the axial force was $\tilde{N}$; a force field created by the lateral load. Next, these two cases are combined by first prestretching the membrane strip, by moving the right "wall" laterally by Δ, and then by loading it vertically, as shown in Fig. 8.

The nonlinear formulation is the same as in (18) and (19), except for the last boundary condition, $u(L)=0$, which becomes

$$u(L)=\Delta. \tag{19'}$$

For the following analysis it is convenient to set

$$u(x)=\overset{\circ}{u}(x)+\tilde{u}(x);\quad w(x)=\tilde{w}(x);\quad N=\overset{\circ}{N}+\tilde{N}, \tag{36}$$

where ($^\circ$) are the quantities caused by prestretching only and ($\tilde{\ }$) are the quantities caused when the water is added.

The prestretching case, with $\tilde{u}(x)=0$ and $\tilde{w}(x)=0$, is solved first. For this case the equations in (18) and (19) become

$$\left.\begin{array}{ll} Eh\overset{\circ}{u}''=0 & 0\le x\le L \\ \overset{\circ}{u}(0)=0; & \overset{\circ}{u}(L)=\Delta \end{array}\right\}. \tag{37}$$

The solution is

$$\overset{\circ}{u}(x)=\frac{\Delta}{L}\,x \tag{38}$$

and the corresponding axial force is

$$\overset{\circ}{N}=Eh\overset{\circ}{u}'=Eh\Delta/L. \tag{39}$$

The water is then added. From (18) and (19) it then follows that $\tilde{w}(x)$ is governed by the boundary value problem

$$\left.\begin{array}{ll} N\tilde{w}''+\gamma\tilde{w}=-\gamma H & 0\le x\le L \\ \tilde{w}(0)=0; \quad \tilde{w}(L)=0 & \end{array}\right\}. \tag{40}$$

The solution is

$$\tilde{w}(x)=H\left[\cos\alpha x+\frac{1-\cos\alpha L}{\sin\alpha L}\,\sin\alpha x-1\right], \tag{41}$$

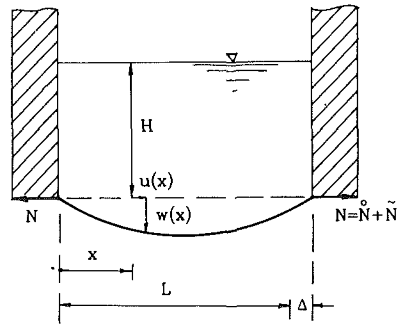

Fig. 8

where $\alpha=\sqrt{\gamma/(\overset{\circ}{N}+\tilde{N})}$.

Whereas $\overset{\circ}{N}$ is given in (39), $\tilde{N}$ is, as yet, unknown. It is determined from the second differential equation in (18) and the remaining boundary conditions $u(0)=0$ and $u(L)=\Delta$. Integrating once, and noting (16), this differential equation becomes

$$Eh\left(u'+\frac{1}{2}\,\tilde{w}'^2\right)=\text{const}=N, \tag{42}$$

or, rewritten

$$u'(x)=\frac{N}{Eh}-\frac{1}{2}\,\tilde{w}'^2(x). \tag{43}$$

Integrating equation (43) from 0 to L, and noting the boundary conditions on u, it becomes

$$\frac{NL}{Eh}-\Delta-\frac{1}{2}\int_o^L \tilde{w}'^2dx=0. \tag{44}$$

Substituting (41) into equation (44) and performing the integrations yields

$$\frac{Eh}{2\gamma L^4}\,H^2=\left[1-\Delta\,\frac{Eh}{\gamma L^3}\,(\alpha L)^2\right]\frac{1+\cos\alpha L}{(\alpha L)^3(\alpha L-\sin\alpha L)}\,. \tag{45}$$

This is the equation for the determination of $\tilde{N}$ for given E, h, γ, L, H, Δ. As expected, for $\Delta=0$ it reduces to equation (25).

In the expression for the axial displacement component, $u(x)=\overset{\circ}{u}(x)+\tilde{u}(x)$, $\overset{\circ}{u}(x)$ is given in (38), but the $\tilde{u}(x)$ is as yet unknown. It is determined by integrating equation (43) from 0 to x. Noting that $u(0)=0$, this results in

$$u(x)=\frac{Nx}{Eh}-\frac{1}{2}\int_o^x \tilde{w}'^2(\xi)d\xi. \tag{46}$$

Then, according to (36) and (38), $\tilde{u}(x)=u(x)-(\Delta/L)x$.

Equations (41), (45), and (46) constitute the solution to the nonlinear problem shown in Fig. 8.

Next, the case $H\to 0$ is considered. For this purpose, equation (45) is solved for H. The result is

$$H=\underset{(-)}{+}\sqrt{\frac{2\gamma L^4}{Eh}\left[1-\Delta\,\frac{Eh}{\gamma L^3}\,(\alpha L)^2\right]\frac{1+\cos\alpha L}{(\alpha L)^3(\alpha L-\sin\alpha L)}}. \tag{47}$$

For the case when $Eh\alpha^2\Delta/(\gamma L)<1$ and $H=0$, the condition $\cos\alpha L=-1$ has to be satisfied. This takes place when

$$\alpha_n L=n\pi \quad n=1,3,5,\ldots \tag{48}$$

where $\alpha=\sqrt{\gamma/(\overset{\circ}{N}+\tilde{N})}$. Because $w(x)>0$, only $\alpha_1 L=\pi$ is of interest. The corresponding axial force is $N=\overset{\circ}{N}+\tilde{N}=\gamma L^2/\pi^2$. Substituting (47) into (41), and forming the limit $H\to 0$, we obtain

$$\lim_{H\to 0}\,[w(x)]=\frac{2L^2}{\pi^2}\sqrt{\frac{\gamma}{Eh}\left[1-\Delta\,\frac{Eh\pi^2}{\gamma L^3}\right]}\,\sin\frac{\pi x}{L}\,. \tag{49}$$

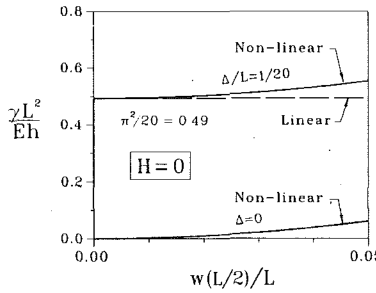

Fig. 9

Thus, when $H=0$, $w(x)$ will be real for an *a priori* prescribed $\gamma L^3/(Eh\pi^2)>\Delta$, but when $\gamma L^3/(Eh\pi^2)\le\Delta$, $w(x)\equiv 0$.

Next, equation (49) is rewritten as

$$\frac{w(x)}{L}=\frac{2}{\pi^2}\sqrt{\gamma^*\left[1-\frac{\Delta}{L}\frac{\pi^2}{\gamma^*}\right]}\sin\frac{\pi x}{L} \tag{49'}$$

where $\gamma^*=\gamma L^2/(Eh)$, and then numerically evaluated for $\Delta/L=1/20$ and $x=L/2$. The result is shown in Fig 9. Also shown is the graph for $\Delta=0$.

From Fig. 9, or equation (49′), it follows that for $\Delta>0$ there exists a bifurcation point at $\gamma^*_{cr}=\pi^2\Delta/L$. Noting that according to (39), $\Delta=\mathring{N}L/(Eh)$, it follows that $\gamma_{cr}=\mathring{N}\pi^2/L^2$. This agrees with the first eigenvalue, equation (10), obtained from the linear analysis. This should have been anticipated, since in the nonlinear solution, for very small deflections, $\tilde{w}(x)\equiv 0$, the axial force $\tilde{N}$ is negligible compared to $\mathring{N}$, which is the *a priori* assumption in the linear formulation presented in (6).

From the above results it follows that, for the case $H=0$, when the membrane strip shown in Fig. 5 is not prestretched, deflections will take place for any $\gamma>0$. However, when the membrane is prestretched by Δ, nonzero deflections will exist only when $\gamma^*>\pi^2\Delta/L$, with a bifurcation point at $\gamma^*=\pi^2\Delta/L$.

The Plate Strip

Nonlinear Analysis. The linear analysis for $H=0$ was presented in the Introduction. In this section this problem is analyzed using a *nonlinear* formulation. In order to simplify the analysis, symmetry is utilized and the origin of the coordinate system is placed in the center, as shown in Fig. 10.

In the following analysis, the differential equations for the plate strip are based on the equilibrium equations for the free-body diagram shown in Fig. 4, the nonlinear strain displacement relation (14), and Hooke's law. An alternative variational formulation is given by Marguerre (1938) and Kerr and El-Aini (1978). Retaining the loading $q(x)=\gamma w(x)$, the resulting formulation consists of the two simultaneous differential equations

$$\left.\begin{aligned}&Dw^{iv}-\left[Eh\left(u'+\frac{1}{2}w'^2\right)w'\right]'-\gamma w=0\\&\left[Eh\left(u'+\frac{1}{2}w'^2\right)\right]'=0\end{aligned}\right\}0\le x\le L/2 \tag{50}$$

where

$$D=\frac{Eh^3}{12(1-\nu^2)} \tag{51}$$

and the boundary conditions

$$\left.\begin{aligned}&w'(0)=0; &&w(L/2)=0\\&w'''(0)=0; &&w'(L/2)=0\\&u(0)=0; &&u(L/2)=0\end{aligned}\right\}. \tag{52}$$

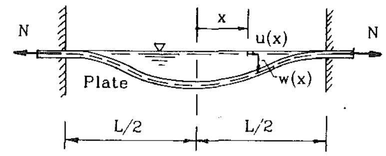

Fig. 10

The method of solution is similar to the one used previously for the membrane strip. Integration of the second equation in (50) results in

$$Eh\left(u'+\frac{1}{2}w'^2\right)=\text{constant}=\tilde{N}. \tag{53}$$

This expression reduces the first equation in (50) to

$$Dw^{iv}-\tilde{N}w''-\gamma w=0 \quad 0\le x\le L/2. \tag{54}$$

The general solution is

$$w(x)=B_1\cosh\rho x+B_2\sinh\rho x+B_3\cos\kappa x+B_4\sin\kappa x \tag{55}$$

where

and

$$\left.\begin{aligned}&\left.\begin{matrix}\rho\\\kappa\end{matrix}\right\}=\sqrt{\sqrt{\left(\frac{\lambda^2}{2}\right)^2+\beta^4}\pm\frac{\lambda^2}{2}}\\&\lambda^2=\frac{\tilde{N}}{D};\quad \beta^4=\frac{\gamma}{D}.\end{aligned}\right\} \tag{56}$$

Differential equation (54) and the four boundary conditions on w in (52) constitute an eigenvalue problem. From the two boundary conditions at $x=0$, it follows that

$$B_2=0;\quad B_4=0. \tag{57}$$

Thus,

$$w(x)=B_1\cosh\rho x+B_3\cos\kappa x. \tag{58}$$

The remaining two boundary conditions yield the two homogeneous algebraic equations

$$\left.\begin{aligned}&B_1\cosh(\rho L/2)+B_3\cos(\kappa L/2)=0\\&B_1\rho\sinh(\rho L/2)-B_3\kappa\sin(\kappa L/2)=0\end{aligned}\right\}. \tag{59}$$

The condition for the existence of a nonzero solution $w(x)$ is

$$\kappa\cosh(\rho L/2)\sin(\kappa L/2)+\rho\sinh(\rho L/2)\cos(\kappa L/2)=0; \tag{60}$$

the equation for the determination of $\tilde{N}$.

Utilizing the first equation in (59), the $w(x)$ in (58) may be written as

$$w(x)=B_1\left[\cosh(\rho x)-\frac{\cosh(\rho L/2)}{\cos(\kappa L/2)}\cos(\kappa x)\right]. \tag{58'}$$

The unknown B_1 is determined next using the second differential equation in (50), or its first integral in (53), and the remaining boundary conditions on u in (52). They reduce to

$$\frac{\tilde{N}L}{Eh}-\int_0^{L/2}w'^2dx=0. \tag{61}$$

Substituting $w(x)$ from (58′) into equation (61), performing the integrations yields B_1. Next, simplifying the resulting expression in (58′), utilizing equation (60), yields

$$w(x)=(\pm)\sqrt{\frac{4D[(\rho L)^2-(\kappa L)^2]}{Eh\Phi}}[\cos(\kappa L/2)\cosh(\rho x)-\cosh(\rho L/2)\cos(\kappa x)] \tag{62}$$

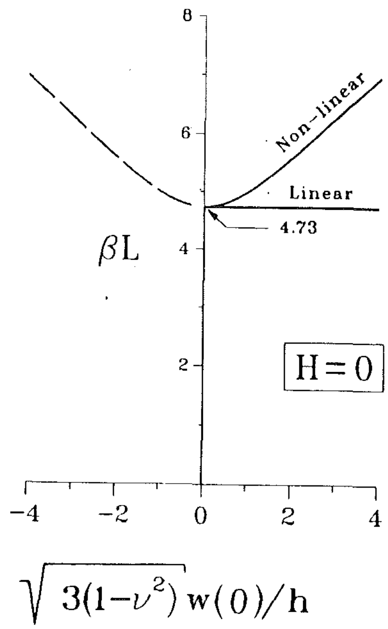

Fig. 11

where

$$\Phi=(\kappa L)^2\cosh^2(\rho L/2)-\rho L[\rho L+2\sinh(\rho L)]\cos^2(\kappa L/2). \quad (62')$$

Next, equation (62) is rewritten for $x=0$, noting that $\rho^2-\kappa^2=\lambda^2$ and $w(x)>0$, as

$$\sqrt{3(1-\nu^2)}\,\frac{w(0)}{h}=\underset{(-)}{+}\frac{\lambda L[\cosh(\rho L/2)-\cos(\kappa L/2)]}{\sqrt{\Phi}}. \quad (63)$$

It is then numerically evaluated, in conjunction with equation (60). At the start it is helpful to note that when $w(x)\equiv 0$, then $\tilde{N}=0$, and thus $\lambda=0$. Therefore, for $w(0)=0$ and $\tilde{N}=0$, $\rho=\kappa=\beta$ and equation (60) reduces to

$$\cosh(\beta L/2)\sin(\beta L/2)+\sinh(\beta L/2)\cos(\beta L/2)=0. \quad (64)$$

This agrees with the result of the corresponding linear eigenvalue problem. The first root of this equation is $\beta_1 L=4.7300$. The numerical evaluation proceeds by choosing βL value>4.73 and determining the corresponding λL-values from equation (60), noting (56). For each λL and βL and the corresponding (ρL, κL) pairs, the deflection $w(0)$ is determined from (63). The results are shown in Fig. 11 and Fig. 12. It is of interest to note that for the range of the considered variables, $\Phi>0$.

Conclusions

The presented nonlinear analyses show that the prestretched membrane and the clamped plate, subjected to a fluid that fills the space created by the deflections, exhibit deflections only for "load parameters" larger than the respective bifurcation points.

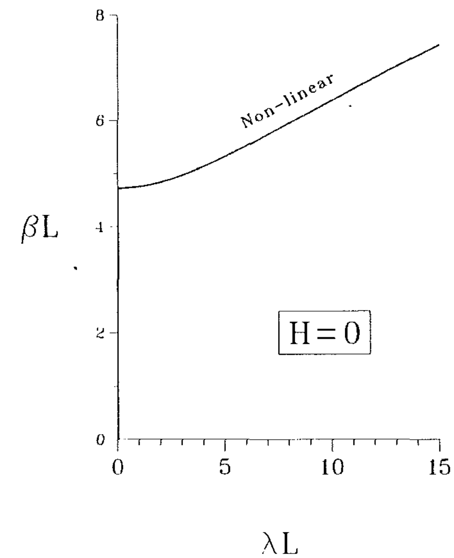

Fig. 12

For example, the plate strip will not deflect when the "load parameter" $\beta L=\sqrt[4]{\gamma L^4/D}\le 4.73$. However, when $\beta L>4.73$, plate deflections will take place. This contradicts the result of the corresponding linear eigenvalue problem, presented in the Introduction, according to which $w(x)\neq 0$ will exist only for discrete values of βL, with $(\beta L)_1=4.73$ as the first eigenvalue. The nonlinear analyses show that the linear eigenvalue problem determines merely the bifurcation points. This suggests that the use of linearized analyses, for the class of problems under consideration (with $H=0$), is not admissible.

The similarity of the obtained "load parameter" versus deflection curves, shown in Fig. 9 and Fig. 11, with those of the elastica theory for compressed beams is noteworthy.

Also noteworthy is the shown relationship of $\mathring{N}$ and $\tilde{N}$ usually ignored in the linear membrane analysis.

References

Kerr, A. D., and El-Aini, Y., 1978, "Determination of Admissible Temperature Increases to Prevent Vertical Track Buckling," ASME JOURNAL OF APPLIED MECHANICS, Vol. 45, pp. 565–573.

Marguerre, K., 1938, "Über die Behandlung von Stabilitätsproblemen mit Hilfe der energetischen Methode," *Zeitschrift für Angewandte Mathematik und Mechanik*, Vol. 18, Nr. 1, pp. 57–73.

Rayleigh, J. W. S., 1945, *The Theory of Sound*, 2nd ed., Vol. I, Chapter 9, McMillan Co., 1984. Republished by Dover Publ., New York.

Volterra, E., and Zachmanoglou, E. C., 1965, *Dynamics of Vibration*, Charles E. Merrill Books, Columbus, OH, p. 316.

J. M. Duva
Assoc. Mem. ASME

J. G. Simmonds
Mem. ASME

Department of Applied Mathematics,
University of Virginia,
Charlottesville, VA 22903

Elementary, Static Beam Theory is as Accurate as You Please[1]

Starting with a solution of elementary beam theory and integrating polynomials in the thickness coordinate, we generate kinematically-admissible strain fields and statically-admissible strain fields whose average approximates the actual two-dimensional strain field in an orthotropic beam to within a relative mean square error of the order of magnitude of an arbitrary power of the ratio of the thickness of the beam to a characteristic wavelength of the elementary beam solution.

Introduction

Building on theories of Rehfield and Murthy (1982) and Levinson (1985), Rychter (1988) has presented a refined theory of orthotropic beams that accounts for the effects of transverse shear strain as well as normal and axial stress. From the solutions of his *one-dimensional* beam equations, Rychter constructs a *two-dimensional* stress field that approximates a certain exact solution of plane-stress elasticity to within a relative mean square error of $O(H^3/l^3)$, where $2H$ is the thickness (depth) of the beam and l is a measure of the wavelength of the beam theory solution. (If the external loads vary smoothly and not too rapidly, l may be replaced by the length, L, of the beam.) Rychter bases his error estimate on the hypercircle method of Prager and Synge (1974) and uses ideas first applied to classical plate theory by Nordgren (1971).

In this paper, we show that *elementary* beam theory suffices to generate approximate, two-dimensional strain (and hence stress) fields of *any* accuracy, provided only that, at the ends of the beam, we demand no more detail than the shear stress resultant for the average vertical displacement and the stress couple or the gross rotation. To foreclose the objection that our conclusions do not apply to beams weak in shear, we analyze an elastically-orthotropic beam.

The secret to obtaining a relatively small mean-square error in the two-dimensional strain field inferred from one-dimensional beam theory is to construct statically-admissible strain fields and kinematically-admissible strain fields[2] whose thickness distributions are nearly equal. In doing so, we find that once we start down this path, we can go as far as we please; specifically, we can construct approximate strain fields with a relative mean-square error of $O(H^{2N}/l^{2N})$ or $O(H^{2N-1}/l^{2N-1})$, where N is any positive integer; for beams weak in shear, the relative error is shown to be $O(HL/l^2)^N$. The rub, of course, is that at the ends of the beam the prescribed stresses or displacements must be compatible with the static or kinematic fields we construct. If the prescribed stresses or displacements are different, then a full-blown, two-dimensional treatment of end effects must be considered and we are asking for information that no beam theory can supply. Thus, higher-order beam theories (and, by extension, higher-order plate theories) are *unnecessary* in the sense that any information that can be gleaned about two-dimensional stresses from a higher-order beam (or plate) theory can be wrung from elementary theory.

Our analysis rests on the well-known but sometimes forgotten assumption that, in a beam, any given stress component varies much more rapidly through the thickness than along the length. If this assumption fails so does *any* beam theory; if this assumption holds, then the two-dimensional equilibrium equations of plane stress theory imply that, if the normal stress, σ_z, is $O(p_0)$, where p_0 is a constant representative of the magnitude of the external face load on the beam, then the transverse shear stress, τ, is $O(p_0 l/H)$, and the axial stress, σ_x, is $O(p_0 l^2/H^2)$. These order-of-magnitude relations suggest an obvious scaling of the stresses; the stress-strain-displacement relations then imply an obvious scaling of the displacements.

The Governing Equations

Let $Oxyz$ denote a fixed, right-handed Cartesian reference frame and consider a rectangular beam which, when undeformed, occupies the region $0 \le x \le L$, $|y| \le B$, $|z| \le H$. For concreteness, we assume that the beam is built-in at $x=0$, stress-free at $x=L$, that there are no body forces, and that the faces of the beam are under the tractions $\sigma_z(x, \pm H) = \pm \frac{1}{2} p_0 p(x/L)$, $\tau(x, \pm H) = 0$, where p is a dimensionless normal load. We further assume that the beam is elastically orthotropic, sufficiently narrow, and loaded sufficiently lightly for linear plane stress theory to apply.

The field equations consist of equilibrium, compatibility, and stress-strain relations. We satisfy equilibrium by introduc-

[1]This work was supported by the National Science Foundation under grant MSM-8618657-02.

[2]A statically-admissible strain field satisfies the equilibrium equations and any stress boundary conditions; a kinematically-admissible strain field satisfies the compatibility conditions and any kinematic boundary conditions. In linear theory, the unique exact solution is both statically and kinematically admissible.

Contributed by the Applied Mechanics Division of The American Society of Mechanical Engineers for presentation at the Winter Annual Meeting, San Francisco, Calif., December 10-15, 1989.

Discussion on this paper should be addressed to the Editorial Department, ASME, United Engineering Center, 345 East 47th Street, New York, N.Y. 10017, and will be accepted until two months after final publication of the paper itself in the Journal of Applied Mechanics. Manuscript received and accepted by the ASME Applied Mechanics Division, March 20, 1989.

Paper No. 89-WA/APM-49.

ing the Airy stress function, F, which we assume satisfies the face traction conditions

$$F_{,xx}(x,\pm H)=\pm\tfrac{1}{2}p_0p(x/L),\ F_{,xz}(x,\pm H)=0, \tag{1}$$

where a subscript preceded by a comma denotes partial differentiation with respect to that subscript. We satisfy compatibility by expressing strains in terms of the axial and normal displacements, U and W.

To incorporate the orthotropic stress-strain relations, we set

$$\Delta e_z\equiv e_z^K-e_z^S=W_{,z}-E_z^{-1}(F_{,xx}-\nu F_{,zz}) \tag{2}$$

$$\Delta\gamma\equiv\gamma^K-\gamma^S=U_{,z}+W_{,x}+G^{-1}F_{,xz} \tag{3}$$

$$\Delta e_x\equiv e_x^K-e_x^S=U_{,x}-E_x^{-1}(F_{,zz}-\nu\tilde{E}F_{,xx}), \tag{4}$$

where the superscripts K and S stand for *kinematically admissible* and *statically admissible*, E_x, E_z, and G are elastic moduli, ν is Poisson's ratio, and

$$\tilde{E}\equiv E_x/E_z. \tag{5}$$

According to the hypercircle error estimate of Prager and Synge (1947),

$$\|e-\tfrac{1}{2}(e^K+e^S)\|=\|\Delta e\|, \tag{6}$$

where e is the actual strain field,

$$\|e\|^2=(1/2)\int_{-H}^{H}\int_0^L[\eta(E_xe_x^2+E_ze_z^2+2\nu E_xe_xe_z)+G\gamma^2]dxdz \tag{7}$$

is the strain energy, and

$$\eta\equiv\frac{1}{1-\nu^2\tilde{E}}. \tag{8}$$

The actual strain field is kinematically and statically admissible and the actual stress function satisfies the compatibility condition

$$F_{,zzzz}+2\bar{E}F_{,xxzz}+\tilde{E}F_{,xxxx}=0, \tag{9}$$

where

$$\bar{E}\equiv\tfrac{1}{2}(E_x/G)-\nu(E_x/E_z). \tag{10}$$

Our aim is to show how, by starting from an approximation to F supplied by elementary beam theory and performing simple integrations through the thickness, we may construct a refined approximation to F with a *formal* error as small as we please. With this approximation in hand, we then use (2) to (4) to construct approximate displacements such that the *computable relative error*, $\|\Delta e\|/\|e^{(0)}\|$, is bounded by as high a power of H/l as we please. Here, $e^{(0)}$ is the lowest-order approximation to the statically-admissible strain field. The *actual* relative error is $\|\Delta e\|/\|e\|$ but cannot be computed because e is unknown.

Solution for the Stress Function

In terms of the dimensionless variables and parameter,

$$\xi=\frac{x}{L},\ \zeta=\frac{z}{H},\ f=\frac{F}{p_0L^2},\ \epsilon=\frac{H}{L}, \tag{11}$$

(9) may be rewritten as

$$f_{,\zeta\zeta\zeta\zeta}=-(2\epsilon^2\bar{E}f_{,\zeta\zeta\xi\xi}+\epsilon^4\tilde{E}f_{,\xi\xi\xi\xi}) \tag{12}$$

and the face traction conditions, (1), as

$$f_{,\xi\xi}(\xi,\pm 1)=\pm\tfrac{1}{2}p(\xi),\ f_{,\xi\zeta}(\xi,\pm 1)=0. \tag{13}$$

Because we have assumed that the stress resultant and couple on the right end of the beam vanish, and because the dimensionless stress function, f, is arbitrary to within linear terms, we may, by integrating with respect to ξ, replace (13) by the alternative conditions

$$f(\xi,\pm 1)=\mp\tfrac{1}{2}m(\xi),\ f_{,\zeta}(\xi,\pm 1)=0, \tag{14}$$

where

$$m=\int_\xi^1(\xi-t)p(t)dt \tag{15}$$

is the dimensionless bending moment of beam theory—elementary or otherwise.

We assume that the prescribed stresses or displacements on the ends of the beam are such that σ_x and U are *odd* in z while τ and W are *even* in z. It follows from these restrictions and (14) that f must be *odd* in ζ. Hence, integrating (12) four times with respect to ζ, we have

$$f=A(\xi)\zeta+B(\xi)\zeta^3-2\epsilon^2\bar{E}\left[\int_0^\zeta(\zeta-t)f(\xi,t)dt\right]_{,\xi\xi} -(1/6)\epsilon^4\tilde{E}\left[\int_0^\zeta(\zeta-t)^3f(\xi,t)dt\right]_{,\xi\xi\xi\xi}, \tag{16}$$

and A and B are unknown functions of integration. Imposition of the boundary conditions (14) reduces (16) to the integro-differential equation

$$f=f^{(0)}+\epsilon^2\bar{E}If_{,\xi\xi}+\epsilon^4\tilde{E}Jf_{,\xi\xi\xi\xi}, \tag{17}$$

where

$$f^{(0)}=(1/4)m(\xi)\zeta(\zeta^2-3), \tag{18}$$

$$If\equiv\zeta\int_0^1(\zeta^2t+2-3t)f(\xi,t)dt-2\int_0^\zeta(\zeta-t)f(\xi,t)dt, \tag{19}$$

and

$$Jf\equiv(1/12)\zeta\int_0^1[\zeta^2(2+t)-3t](1-t)^2f(\xi,t)dt -(1/6)\int_0^\zeta(\zeta-t)^3f(\xi,t)dt. \tag{20}$$

If we seek an asymptotic solution of the form

$$f=f^{(0)}+\epsilon^2f^{(1)}+\ \ldots, \tag{21}$$

then (17) yields the recurrence relation

$$f_n=\bar{E}If_{,\xi\xi}^{(n-1)}+\tilde{E}Jf_{,\xi\xi\xi\xi}^{(n-2)},\ n=1,2,\ \ldots,f_n=0,\ n<0. \tag{22}$$

Applying (22) repeatedly and noting (15) and (18) to (20), we obtain a solution of the form

$$f_n=K_nf^{(0)}=m^{[2n]}(\xi)P^{[2n+3]}(\zeta),\ n=1,2,\ \ldots, \tag{23}$$

where $m^{[k]}$ denotes the kth derivative of m with respect to ξ and $P^{[k]}$ is a polynomial of degree k. In particular,

$$f^{(1)}=-(1/40)\bar{E}m''(\xi)\zeta(1-\zeta^2)^2=(1/40)\bar{E}p(\xi)\zeta(1-\zeta^2)^2, \tag{24}$$

and it may be readily verified that the approximation $f^{(0)}+\epsilon^2f^{(1)}$ leads to the statically-admissible stress distributions given by Rychter's equations (29) to (31) (in the absence of axial stretching). It may also be verified, using (14), (18), and (21), that $f_{,\zeta\zeta}(1,\zeta)$ and $-f_{,\xi\zeta}(1,\zeta)$, the dimensionless normal and shear stresses at the right end of the beam, have a zero stress resultant and couple.

Note from (12) that if $\bar{E}=O(\epsilon^{-1})$, i.e., if $\tfrac{1}{2}(E_x/G)-\nu(E_x/E_z)=O(L/H)$, then (21) must be replaced by an expansion in powers of ϵ instead of ϵ^2, which we shall consider presently. Moreover, if $\bar{E}=O(\epsilon^{-2})$ or if $\tilde{E}=O(\epsilon^{-4})$, then the successive terms in (21) do *not* diminish and *no* beam theory holds: the problem is flat-out two-dimensional.

Approximate Displacements

Let

$$U=(L^3p_0/E_xH^2)u,\ W=(L^4p_0/E_xH^3)w. \tag{25}$$

Then, (2) to (4) take the form

$$\Delta e_z=(p_0/E_x)\epsilon^{-4}(w_{,\zeta}+\epsilon^2\nu\tilde{E}f_{,\zeta\zeta}-\epsilon^4\tilde{E}f_{,\xi\xi}) \tag{26}$$

$$\Delta\gamma=(p_0/E_x)\epsilon^{-3}(u_{,\zeta}+w_{,\xi}+\epsilon^2\hat{E}f_{,\xi\zeta}) \tag{27}$$

$$\Delta e_x = (p_0/E_x)\epsilon^{-2}(u,_{\xi} - f,_{\zeta\zeta} + \epsilon^2 \nu \tilde{E} f,_{\xi\xi}), \tag{28}$$

where

$$\hat{E} \equiv E_x/G. \tag{29}$$

Our aim is to make $\|\Delta e\|/\|e^{(0)}\| = O(\epsilon^{2N})$. As $\|e^{(0)}\| = O(\epsilon^{-2}p_0/E_x)$, we need to construct an approximate stress function and displacement field such that $\|\Delta e\| = O(\epsilon^{2N-2}p_0/E_x)$. To this end, let

$$f = f^{(0)} + \ . \ . \ . + \epsilon^{2N} f^{(N)} \tag{30}$$

$$u = u^{(0)} + \ . \ . \ . + \epsilon^{2N} u^{(N)} \tag{31}$$

$$w = w^{(0)} + \ . \ . \ . + \epsilon^{2N} w^{(N)}. \tag{32}$$

Guided by (26) to (28), and recalling that the f_n's are known (and equal to zero if $n<0$), we choose the coefficients in the expansions for u and w so that

$$w,_{\zeta}^{(n-1)} = -\nu \tilde{E} f,_{\zeta\zeta}^{(n-2)} + \tilde{E} f,_{\xi\xi}^{(n-3)}, \ n=1,2,\ldots,N+1 \tag{33}$$

$$u,_{\zeta}^{(n-1)} = -w,_{\xi}^{(n-1)} - \hat{E} f,_{\xi\zeta}^{(n-2)}, \ n=1,2,\ldots,N+1 \tag{34}$$

$$u,_{\xi}^{(n-1)} = f,_{\zeta\zeta}^{(n-1)} - \nu \tilde{E} f,_{\xi\xi}^{(n-2)}, \ n=1,2,\ldots,N+1, \tag{35}$$

which reduces (26) to (28) to

$$\Delta e_z = (p_0/E_z)\epsilon^{2N-2}[\nu f,_{\zeta\zeta}^{(N)} - f,_{\xi\xi}^{(N-1)} - \epsilon^2 f,_{\xi\xi}^{(N)}] \tag{36}$$

$$\Delta\gamma = (p_0/G)\epsilon^{2N-1} f,_{\xi\zeta}^{(N)} \tag{37}$$

$$\Delta e_x = -(p_0/E_x)\epsilon^{2N-2}[f,_{\zeta\zeta}^{(N)} - \nu f,_{\xi\xi}^{(N-1)} - \epsilon^2 \nu f,_{\xi\xi}^{(N)}]. \tag{38}$$

We may solve (33) to (35) in sequence. Thus, integrating (33) with respect to ζ, we have

$$w^{(n-1)} = v_{n-1}(\xi) - \nu \tilde{E} f,_{\zeta}^{(n-2)} + \tilde{E}\left(\int_0^{\zeta} f^{(n-3)} dt\right),_{\xi\xi}, \tag{39}$$

where v_{n-1} is a function of integration. Inserting (39) into (34), and integrating with respect to ζ, we obtain

$$u^{(n-1)} = -v'_{n-1}(\xi)\zeta + (\nu\tilde{E} - \hat{E}) f,_{\xi}^{(n-2)} - \tilde{E}\left[\int_0^{\zeta} (\zeta - t) f^{(n-3)} dt\right],_{\xi\xi\xi}, \tag{40}$$

there being no function in integration as u must be an odd in ζ. The v_n's are determined by substituting (40) into (35). By (18) we find that, in particular,

$$v''_0 = -(3/2)m(\xi), \tag{41}$$

which is just the basic equation of *elementary* beam theory. By (22), which relates f_n to $f^{(n-1)}$ and $f^{(n-2)}$, we have, in general,

$$v_{n-1} = C_{n-1} + D_{n-1}\xi - \int_0^1 [6\tilde{E} t f^{(n-2)}(\xi,t) + \tfrac{1}{2}\tilde{E}(2+t)(1-t)^2 f,_{\xi\xi}^{(n-3)}(\xi,t)]dt, \quad n=2,\ldots,N+1, \tag{42}$$

where C_{n-1} and D_{n-1} are constants of integration determined by the displacement boundary conditions at the left end of the beam. For example, if the vertical deflection and rotation of elementary beam theory are identified with the *average* vertical deflection and average cross-sectional rotation of two-dimensional plane-stress theory, then, if the beam is built in at the left end,

$$\int_0^1 w(0,\zeta)d\zeta = \int_0^1 \zeta u(0,\zeta)d\zeta = 0. \tag{43}$$

By (31), (32), and (39) to (42), these conditions translate into the well-known boundary conditions of elementary beam theory,

$$v_0(0) = v'_0(0) = 0, \tag{44}$$

plus explicit (but elaborate) formulas for C_{n-1} and D_{n-1} that we shall not state.

Referring back to (36) to (38), we note that the error in $\Delta\gamma$ is smaller than the errors in Δe_z and Δe_x, i.e., our scheme delivers kinematically and statically-admissible shear strains that are closer to one another than necessary to achieve a relative error in the energy norm of $O(\epsilon^{2N})$. On the other hand, if we let n go only up to N and not to $N+1$ in (34), then (37) is replaced by

$$\Delta\gamma = (p_0/G)\epsilon^{2N-3} f,_{\xi\zeta}^{(N-1)}, \tag{45}$$

and the relative error in the energy norm is only $O(\epsilon^{2N-1})$, the major contribution coming from (45) and not (36) and (38).

General expressions for the difference between the kinematically and statically-admissible strains in terms of derivatives of m can be obtained by substituting the right side of (23) into (36) to (38):

$$\Delta e_z = (p_0/E_z)\epsilon^{2N-2}[m^{[2N]}(\xi)Q_z^{\{2N+1\}}(\zeta) - \epsilon^2 m^{[2N+2]} P^{\{2N+3\}}(\zeta)] \tag{46}$$

$$\Delta\gamma = (p_0/G)\epsilon^{2N-1} m^{[2N-1]}(\xi) Q^{\{2N+2\}}(\zeta) \tag{47}$$

$$\Delta e_x = (p_0/E_x)\epsilon^{2N-2}[m^{[2N]}(\xi)Q_x^{\{2N+1\}}(\zeta) - \epsilon^2 \nu m^{[2N+2]} P^{\{2N+3\}}], \tag{48}$$

where $Q_z^{\{k\}}$, $Q^{\{k\}}$, and $Q_x^{\{k\}}$ are polynomials of degree k. These expressions prove convenient in the following determination of the computable relative error.

The last essential piece of our analysis is to define l, the *characteristic wavelength* of the problem. If m is differentiable on [0, 1], then, roughly speaking, the "wavelength" associated with m is the smallest length l such that $dm/d\xi = O(mL/l)$ on [0, 1]. As we are dealing with mean square errors and as the integrands in the error estimate involve high derivatives of m, we instead define the characteristic wavelength of m by

$$\left(\frac{l}{L}\right)^{4N} \equiv \frac{\int_0^1 m^2 d\xi}{\int_0^1 (m^{[2N]})^2 d\xi}. \tag{49}$$

With this definition and Schwarz' inequality, we find for the first term in the expression for $\|\Delta e\|$, upon substitution of (48) into (7),

$$\int_{-H}^{H}\int_0^L \eta E_x (\Delta e_x)^2 dxdz \le 2\eta(HLp_0^2/E_x)(H/l)^{4N}\epsilon^{-4}\int_0^1 m^2 d\xi \int_0^1 [\,|Q_x^{\{2N+1\}}| + \nu^2 (H/l)^2 |P^{\{2N+3\}}|\,]^2 d\zeta. \tag{50}$$

By (7) and (18), the analogous term in the expression for $\|e^{(0)}\|$ is

$$\int_{-H}^{H}\int_0^L \eta E_x (e_x^{(0)})^2 dxdz = (3/2)\eta(HLp_0^2/E_x)\epsilon^{-4}\int_0^1 m^2 d\xi \int_0^1 \zeta^2(\zeta-3)^2 d\zeta. \tag{51}$$

A similar analysis of the other terms composing $\|\Delta e\|$ and $\|e^{(0)}\|$ shows that $\|\Delta e\|/\|e^{(0)}\| = O(H^{2N}/l^{2N})$.

Beams Weak in Shear

Our analysis thus far has assumed that $\tilde{E} = O(1)$. If the beam is weak in shear (as might be the case in a composite beam), we take

$$E_x/G = 2k\epsilon^{-1}, \ k = O(1). \tag{52}$$

In this case, the integro-differential equation, (17), for the dimensionless stress function takes the form

$$f = f^{(0)} + \epsilon(k - \epsilon\nu\tilde{E}) If,_{\xi\xi} + \epsilon^4 \tilde{E} J f,_{\xi\xi\xi\xi}. \tag{53}$$

The assumed asymptotic expansion (21) is now replaced by

$$f=f^{(0)}+\epsilon f^{(1)}+\ .\ .\ . \tag{54}$$

which leads, in place of (22), to the new recurrence relation

$$f_n=kIf,_{\xi\xi}^{(n-1)}-\nu\tilde{E}If,_{\xi\xi}^{(n-2)}$$
$$+Jf,_{\xi\xi\xi\xi}^{(n-4)},\ n=1,\ 2,\ .\ .\ .\ ,f_n=0,\ n<0. \tag{55}$$

Of the three equations for the incremental strains, (27) becomes

$$\Delta\gamma=(p_0/E_x)\epsilon^{-3}(u,_{\zeta}+w,_{\xi}+2\epsilon kf,_{\xi\zeta}) \tag{56}$$

while (26) and (28) remain unchanged.

We now approximate f, u, and w by finite series of the form $f=f^{(0)}+\epsilon f^{(1)}+\ .\ .\ .\ +\epsilon^N f^{(N)}$, etc., so that (33) to (35) are replaced by

$$w,_{\zeta}^{(n-1)}=-\nu\tilde{E}f,_{\zeta\zeta}^{(n-3)}+\tilde{E}f,_{\xi\xi}^{(n-5)},\ n=1,\ 2,\ .\ .\ .\ ,\ N+2 \tag{57}$$

$$u,_{\zeta}^{(n-1)}=-w,_{\xi}^{(n-1)}-2kf,_{\xi\zeta}^{(n-2)},\ n=1,\ 2,\ .\ .\ .\ ,\ N+1 \tag{58}$$

$$u,_{\xi}^{(n-1)}=f,_{\zeta\zeta}^{(n-1)}-\nu\tilde{E}f,_{\xi\xi}^{(n-3)},\ n=1,\ 2,\ .\ .\ .\ ,\ N. \tag{59}$$

This leads, in place of (36) to (38), to incremental strains of the form

$$\Delta e_z=(p_0/E_z))\epsilon^{N-2}[\nu\tilde{E}f,_{\zeta\zeta}^{(N)}+O(\epsilon)] \tag{60}$$

$$\Delta\gamma=2(p_0/E_x)k\epsilon^{N-2}f,_{\xi\zeta}^{(N)} \tag{61}$$

$$\Delta e_x=(p_0/E_x)\epsilon^{N-2}[f,_{\zeta\zeta}^{(N)}+O(\epsilon)]. \tag{62}$$

From (52), (61), and (62) we see that

$$\eta E_x(\Delta e_x)^2+G(\Delta\gamma)^2=(\eta p_0^2/E_x)\epsilon^{2N-4}(f,_{\zeta\zeta}^{(N)})^2[1+O(\epsilon)], \tag{63}$$

with a similar conclusion with E_z and Δe_z in place of E_x and Δe_x. Thus, if we compute terms up to and including $f^{(N)}$, the dominant contribution to $\|\Delta e\|$ will come from Δe_x and e_z. Because $\|e^{(0)}\|^2=O(HLp_0^2/E_x)\epsilon^{-4}\int_0^1 m^2 d\xi$, as before, and $f^{(N)}=O(m^{[2N]})$, it follows that $\|\Delta e\|/\|e^{(0)}\|=O(HL/l^2)^N$.

Conclusions

By a straightforward analysis that may be extended in an obvious way to plates, we have shown that if one wishes to infer approximate two-dimensional strain fields, starting from beam theory as a base, then it is sufficient to start from elementary beam theory. This conclusion, which holds even for beams weak in shear, is based on the Prager-Synge hypercircle method which assumes that the prescribed displacement or stress boundary conditions at the ends of the beam have same thickness distributions, respectively, as do the kinematically or statically-admissible fields we construct. If the boundary conditions do not satisfy this constraint, then there will be end effects and a full two-dimensional treatment, such as given by Gregory and Gladwell (1982), is unavoidable if we want accurate stresses everywhere. On the other hand, as emphasized by Koiter (1971), one rarely knows the exact thickness distribution of the stresses or displacement at the edge of a beam, except if the edge is traction free. In the face of such ignorance, a procedure such as we have outlined is the best one can do.

After the present work was finished, Dr. Rychter kindly brought to our attention a brief note by Donnell (1952) in which he presents expansions for the two-dimensional stresses in an isotropic beam loaded by arbitrary pressures on the upper and lower faces. If these pressures are taken to be equal and opposite, as we have assumed herein, then the stresses which follow from our asymptotic expansion of the dimensionless stress function, equation (21), agree with Donnell's formulae. Our contribution consists of modifying this expansion for orthotropic beams weak in shear and in presenting *explicit, computable* error estimates for these asymptotic aproximations.

References

Donnell, L. H., 1952, "Bending of Rectangular Beams," ASME Journal of Applied Mechanics, Vol. 19, p. 123.

Gregory, R. D., and Gladwell, I., 1982, "The Cantilevered Beam under Tension, Bending, or Flexure at Infinity," *J. Elasticity*, Vol. 12, pp. 317–343.

Koiter, W. T., 1971, "On the Mathematical Foundation of Shell Theory," *Actes du Congrès International de Mathématiciens*, Nice, 1970, (Publ. Paris), Vol. 3, pp. 123–130.

Levinson, M., 1985, "On Bickford's Consistent Higher Order Beam Theory," *Mech. Res. Comm.*, Vol. 12, pp. 1–9.

Nordgren, R. P., 1971, "A Bound on the Error in Plate Theory," *Q. Appl. Math.*, Vol. 28, pp. 587–595.

Prager, W., and Synge, J. L., 1947, "Approximations in Elasticity Based on the Concept of Function Space," *Q. Appl. Math.*, Vol. 5, pp. 241–269.

Rehfield, L. W., and Murthy, P. L. N., 1982, "Toward a New Engineering Theory of Bending; Fundamentals," *AIAA J.*, Vol. 20, pp 693–699.

Rychter, Z., 1988, "A Simple and Accurate Beam Theory," *Acta Mech.*, Vol. 75, pp. 57–62.

A. M. Waas[1]
Graduate Research Assistant,
Mem. ASME

C. D. Babcock, Jr.[2]
Professor of Aeronautics and
Applied Mechanics,
Mem. ASME

W. G. Knauss
Professor of Aeronautics and
Applied Mechanics,
Mem. ASME

Graduate Aeronautical Laboratories,
California Institute of Technology,
Pasadena, CA 91125

A Mechanical Model for Elastic Fiber Microbuckling

A two-dimensional mechanical model is presented to predict the compressive strength of unidirectional fiber composites using technical beam theory and classical elasticity. First, a single fiber resting on a matrix half-plane is considered. Next, a more elaborate analysis of a uniformly laminated, unidirectional fiber composite half-plane is presented. The model configuration incorporates a free edge which introduces a buckling mode that originates at the free edge and decays into the interior of the half-plane. It is demonstrated that for composites of low volume fraction (<0.3), this decay mode furnishes values of buckling strain that are below the values predicted by the Rosen (1965) model. At a higher volume fraction the buckling mode corresponds to a half wavelength that is in violation of the usual assumptions of beam theory. Causes for deviations of the model prediction from existing experimental results are discussed.

1 Introduction

A problem that has received much attention but moderate success is the prediction of compressive strength of fiber composites. Dow and Gruntfest (1960) were apparently the first to identify fiber buckling as a viable mode of compressive failure in composites. Their work was followed by that of Fried and Kaminetsky (1964) and Leventz (1964), who addressed experimentally and theoretically the question of compressive strength. In these investigations, an empirical factor was used to obtain a correlation between the experimentally and theoretically predicted values of compressive strength. In 1965, Rosen (1965) presented an analysis addressing the question of microbuckling which was devoid of any empiricism and laid the foundation for much of the work that was to follow. With a few exceptions, noted later, the analytical research work carried out in the past 20 years is based on the model by Rosen (1965). Due to lack of space and because an excellent literature survey on fiber microbuckling exists (Shuart (1985)), a discussion of the various contributions that have enhanced our understanding of microbuckling will be omitted here. Instead, the discussion will be limited to those aspects that are fundamental in clarifying the state-of-the-art of the subject. The interested reader is referred to the references at the end of this chapter and the review by Shuart (1985), in particular, for a complete and up-to-date account.

The Rosen (1965) model for microbuckling addresses the problem of fiber buckling in glass fiber/epoxy laminates under compressive loading. The model presented, which is two-dimensional, treats the fiber layers as plates supported by an elastic matrix (offering lateral support to the fibers at buckling). When the unidirectional composite of infinite extent undergoes failure, Rosen envisages two possible modes of failure which he calls the extension and shear modes. In the extension mode, the matrix material is predominantly in extension and adjacent fibers deform 180 deg out of phase with each other, as shown in Fig. 1. In the shear mode, adjacent fibers deform in phase, and the matrix material is

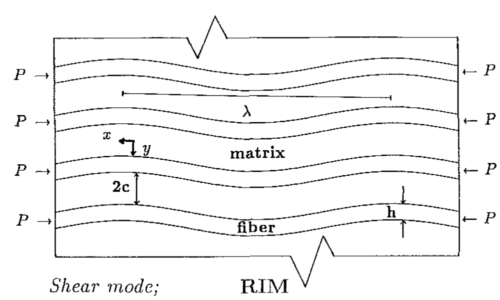

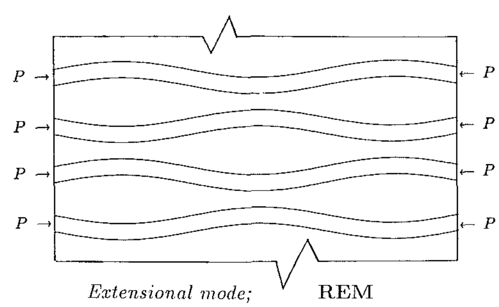

Fig. 1 The configuration studied by Rosen (1965)

[1] Presently at the Department of Aerospace Engineering, University of Michigan, Ann Arbor, MI 48109.

[2] Deceased.

Contributed by the Applied Mechanics Division of THE AMERICAN SOCIETY OF MECHANICAL ENGINEERS for publication in the JOURNAL OF APPLIED MECHANICS.

Discussion on this paper should be addressed to the Technical Editor, Leon M. Keer, The Technological Institute, Northwestern University, Evanston, IL 60208, and will be accepted until two months after final publication of the paper itself in the JOURNAL OF APPLIED MECHANICS. Manuscript received by the ASME Applied Mechanics Division, September 12, 1988; final revision, June 6, 1989.

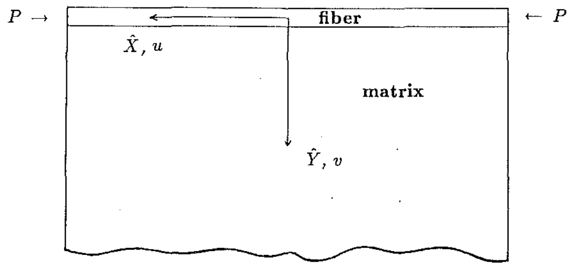

Fig. 2(a) The single fiber composite

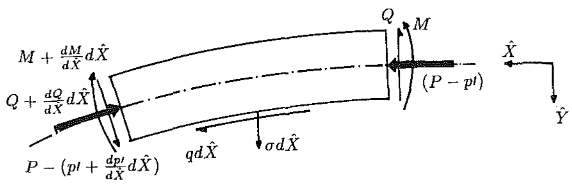

Fig. 2(b) Isolated element of buckled fiber

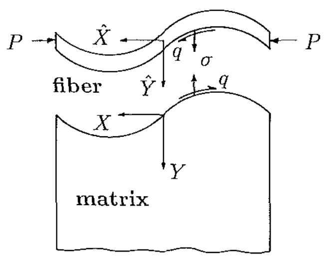

Fig. 2(c) Matrix configuration at buckling

predominantly in shear. Using an energy method to obtain the buckling load, Rosen approximated the buckled mode shape of the fibers to be

$$v = \sum_{n=1}^{\infty} a_n \sin\left(\frac{n\pi x}{L}\right).$$

Here, $L/m = \lambda$, the buckle wavelength, as indicated in Fig. 1. In evaluating the contribution to the potential energy from the matrix at buckling, he assumed the *strains* in the matrix to be independent of y. This amounts to approximating the displacements in the matrix to vary linearly in y. Next, considering the bending energy contribution of the fiber and the work done by the in-plane compressive loads on the fiber, he obtains the following critical values for the extensional and shear modes:

Extensional Mode:

$$\sigma_{cr} = 2V_f\left[\frac{V_f \mathrm{E}_m \mathrm{E}_f}{3(1-V_f)}\right]^{1/2} \tag{1}$$

$$\left(\frac{\lambda}{h}\right)_{cr} = \pi \sqrt[4]{\frac{(1-V_f)}{3V_f}\,\frac{\mathrm{E}_f}{\mathrm{E}_m}}\,. \tag{2}$$

Shear Mode:

$$\sigma_{cr} = \frac{G_m}{1-V_f} + O\left(\left(\frac{h}{\lambda}\right)^2\right) \tag{3}$$

$$\left(\frac{\lambda}{h}\right)_{cr} \gg 1. \tag{4}$$

Here, σ_{cr} = critical compressive stress at buckling, E_m = Young's modulus of the matrix, E_f = Young's modulus of the fiber, V_f = volume fraction of fibers, h = thickness of a fiber plate, and λ = wavelength of the buckled fiber.

Notice that in the shear mode the critical value of σ occurs for $\lambda \gg h$. Thus, unlike the extension mode in which a critical buckle wavelength can be evaluated, no such value λ_{cr} exists in the shear mode. The buckling "load" is continuously dependent on the wavelength λ.

A second viewpoint regarding the mode of failure in compression is referred to as *fiber kinking*. Observations on kinking failure go back as far as 1949 when Orowan (1942) observed that single crystal rods of Cadmium collapse under uniaxial compression into peculiar kinks if the (0001) glide plane is nearly parallel to the axis of compression. It is frequently useful to use four axes (thus four Miller indices), three of them co-planar, to describe the crystal planes for hexagonally close packed (HCP) crystals. The (0001) for HCP Cadmium is the basal plane. The advent of fibrous materials has rekindled interest in the subject, and in recent years, fiber kinking as a viable mode of failure has been observed by, among others, Weaver and Williams (1975), as well as other researchers (Dale and Baer, 1974; Robinson et al., 1986, Evans and Adler, 1983; Chaplin, 1977). Judging from the experimental evidence available, it appears that the formation of compression-induced kink bands is closely associated with the existence of a preferable glide plane in the direction of compression. Budiansky (1983) analyzed kinking by introducing inelastic behavior in the matrix and explained the large scatter in kinking strengths in terms of the composite's sensitivity to initial fiber misalignment. He presents in Budiansky (1983) a result for the compressive strength of the composite which depends on the matrix yield stress in shear and on the initial fiber misalignment. However, the experimental evidence available (Fried and Kaminetsky, 1964; Leventz, 1964; Hahn and Williams, 1986; Sohi, Hahn, and Williams, 1984; Hahn, Sohi, and Moon, 1986; Lager and June, 1969) does not suggest that kinking failures are limited to composites that permit inelastic matrix behavior.

More recently, Hahn and Williams (1986) and Sohi et al. (1984) have reported experimental results related to compression failure in straight fiber-laminated test specimens. In these studies, it was repeatedly observed that failure of the fibers in plies aligned along the loading direction (0 deg plies) originated at a *free edge* and subsequently propagated into the interior of the specimen, precipitating a global failure of the test specimen. This observation is consistent with the findings of Waas and Babcock (1989) as regards the origins of the failure process.

In this paper we consider a simple mechanical model that is capable of demonstrating the origins of compressive failure at a free edge. To do so, the problem of a laminated half-plane subjected to a uniform far-field compression parallel to the surface of the half-plane is considered. Despite the fact that experimental observations strongly suggest that fiber-microbuckling originates at a free edge, a model configuration that allows incorporating a free edge has not been examined with the view of understanding microbuckling.

In developing the analysis, a simple example is considered first in which a single fiber perfectly bonded to a half-plane is subjected to compression. This is done for two reasons: first, to understand the effects of boundary conditions that are applied at the interface of the different materials, particularly from a buckling standpoint, and secondly, to assist in developing the more elaborate analysis that follows, where a more realistic configuration for the composite is chosen in which the entire half-plane is a unidirectionally laminated medium.

2 Problem Formulation

2.1 An Example Problem. Consider the idealized, single fiber composite of unit thickness in the $\hat{z}$-direction, shown in Fig. 2(a). For carity of presentation, upper case letters have been used in the figures for coordinate axes corresponding to their lower case counterparts in the text. The composite is subjected to a uniform compression (P/h) per unit thickness normal to the $\hat{x}$, $\hat{y}$-plane of the figure. The relatively "soft" supporting medium (matrix) acts as an *elastic* foundation offering lateral support to the fiber. For convenience, a composite of infinite extent in the $\hat{x}$-direction occupying the space $0 \leq y \leq \infty$ is considered. Standard notation, such as "E" for Young's modulus and ν for Poisson's ratio is used with the subscripts "f" and "m" to denote properties of the fiber and matrix, respectively. The analysis is carried out for composites typical of those in the aerospace industry where $E_f \gg E_m$. Consequently, the prebuckling deformation of the composite is one of uniform contraction with the compressive load borne essentially by the fiber. Bernoulli-Navier beam theory is used to describe the fiber, while the matrix is modeled as a linearly elastic, homogeneous, and isotropic medium. The prebuckled state for the fiber (a positive sign associated with compression) is described by

$$\epsilon_0 = \frac{P}{E_f h}, \quad v=0. \tag{5}$$

Next, the governing equations for the fiber in the buckled state are developed. With reference to Fig. 2(b), consider an element of the fiber infinitesimally removed from the straight configuration. It is cut by planes that were parallel to the $\hat{y}$, $\hat{z}$ plane at $\hat{x}$ and $\hat{x}+d\hat{x}$ in the undeformed state. These sections remain plane and normal to the deformed middle surface. With the assumption that rotations are small compared to unity, force equilibrium, and moment equilibrium in the $\hat{x}$, $\hat{y}$ plane results in

$$\frac{dQ}{d\hat{x}} + \sigma - P\frac{d^2v}{d\hat{x}^2} = 0 \tag{6a}$$

$$\frac{dp'}{d\hat{x}} + q = 0 \tag{6b}$$

$$-\frac{d^2M}{d\hat{x}^2} - \frac{h}{2}\frac{dq}{d\hat{x}} + \frac{dQ}{d\hat{x}} = 0. \tag{6c}$$

Here, p' (per unit length in the $\hat{z}$-direction) is the change in the axial force P at buckling, M is the bending moment in the fiber, and v the deflection of the fiber in the $\hat{y}$-direction. σ and q are the interface tractions develped at buckling because the fiber and matrix are bonded at their common interface. In writing equation (6a), the product $p'd^2v/d\hat{x}^2$, which is of second order, has been omitted. The buckling under investigation is infinitesimal. Equation (6b) can be further simplified by noting that

$$p' = hE_f\frac{du_0}{d\hat{x}}, \tag{7}$$

where u_0 is the axial displacement of the fiber due to buckling. Also,

$$M = -EI\frac{d^2v}{d\hat{x}^2}. \tag{8}$$

Combining (6) through (8), the following is deduced

$$E_f I\frac{d^4v}{d\hat{x}^4} + P\frac{d^2v}{d\hat{x}^2} - \frac{h}{2}\frac{dq}{d\hat{x}} - \sigma = 0$$

$$q + hE_f\frac{d^2u_0}{d\hat{x}^2} = 0. \tag{9}$$

Continuity of displacements at the common interface requires

$$u_0 - \frac{h}{2}\frac{dv}{d\hat{x}}\bigg|_{\hat{y}=\frac{h}{2}} = u_m|_{y=0}$$

$$v\bigg|_{\hat{y}=\frac{h}{2}} = v_m|_{y=0}. \tag{10}$$

Periodic perturbations in $u(\hat{x})$ and $v(\hat{x})$ of sinusoidal form about the trivial solution (5), with an arbitrary wavelength, λ, are investigated. Then, one seeks the critical value of P required to maintain this disturbance; q and σ are obtained in terms of the fiber displacements v and u_0. This requires the solution of the elastic displacement equations of equilibrium in the matrix.

2.2 The Matrix Problem. With reference to Fig. 2(c), it is necessary to solve

$$2\frac{\partial^2 u_m}{\partial x^2} + (1-\nu_m)\frac{\partial^2 u_m}{\partial y^2} + (1+\nu_m)\frac{\partial^2 v_m}{\partial x \partial y} = 0$$

$$2\frac{\partial^2 v_m}{\partial y^2} + (1-\nu_m)\frac{\partial^2 v_m}{\partial x^2} + (1+\nu_m)\frac{\partial^2 u_m}{\partial x \partial y} = 0, \tag{11}$$

which are the elastic displacement equations of equilibrium with the approximation of *plane stress* in the x, y-plane, subject to the following boundary conditions:

$$\text{at } y=0, \quad u_m = U\cos\alpha x, \quad v_m = V\sin\alpha x \tag{12a}$$

$$\text{as } y\to\infty, \quad u_m \to 0, \quad v_m \to 0. \tag{12b}$$

Here, $\alpha = 2\pi/\lambda$ and U, V are arbitrary constants. In writing (12), the form of the buckled displacements of the fiber is assumed as

$$u_{0f} = B\cos\alpha\hat{x}, \quad v_f = A\sin\alpha\hat{x}. \tag{13}$$

The solution of (11) proceeds in the following manner. Let

$$u_m = \psi(y)\cos\alpha x, \quad v_m = \phi(y)\sin\alpha x. \tag{14}$$

Using (14) in (11), and elimination of ϕ(or ψ), results in the following ordinary differential equation for $\psi(\phi)$

$$\psi^{IV} - 2\alpha^2\psi^{II} + \alpha^4\psi = 0, \tag{15}$$

where $(\ )^I \equiv d/dy$; a similar equation results for ϕ.

The solution of (15), subject to the second condition in (12), is

$$\psi = (C_3 y + C_4)e^{-\alpha y}$$

and similarly, (16)

$$\phi = (D_3 y + D_4)e^{-\alpha y}.$$

Here the Cs and Ds are related by

$$C_4 = \frac{D_3}{\alpha}\left[\frac{(3-\nu_m)}{(1+\nu m)}\right] - D_4, \quad C_3 = -D_3. \tag{17}$$

Equation (17) is obtained by substituting (16) into (11). Incorporating the first of (12), one arrives at

$$u_m(x,0) = \left[\frac{D_3}{\alpha}\frac{(3-\nu_m)}{(1+\nu_m)} - D_4\right]\cos\alpha x, \quad v_m(x,0) = D_4\sin\alpha x \tag{18}$$

with

$$D_4 = V, \quad D_3 = \alpha\frac{(1+\nu_m)}{(3-\nu_m)}U + \alpha\frac{(1+\nu_m)}{(3+\nu_m)}V. \tag{19}$$

Next, the surface tractions q and σ are computed;

$$\tau_{xy} = G_m\left[\frac{\partial u_m}{\partial y} + \frac{\partial v_m}{\partial x}\right] = G_m[\psi' + \alpha\phi]\cos\alpha x.$$

Thus,

$$\tau_{xy}(x,0)\equiv q(x,0)=G_m\left[2\alpha\,\frac{(1-\nu_m)}{(3-\alpha)}\,V\right.$$

$$\left.-\frac{4\alpha}{(3-\nu_m)}\,U\right]\cos\alpha x. \tag{20}$$

The normal stress

$$\sigma_y=\frac{E_m}{(1-\nu_m{}^2)}\left[\frac{\partial v_m}{\partial y}+\nu_m\,\frac{\partial u_m}{\partial x}\right]$$

$$=\frac{E_m}{(1-\nu_m{}^2)}\,[\phi'-\nu_m\alpha\psi]\sin\alpha x.$$

Thus,

$$\sigma_y(x,0)\equiv\sigma(x,0)=$$

$$-\frac{E_m\alpha}{(1+\nu_m)(3-\nu_m)}\,[2V-U(1-\nu_m)]\sin\alpha x. \tag{21}$$

Using (13) and (12a), the following is obtained:

$$V=A$$
$$U=B-\frac{h\alpha}{2}\,A. \tag{22}$$

Substituting (20) through (22) into (9), the following system of equations results

$$(a_1-\epsilon_0)A+b_1B=0$$
$$a_2A+b_2B=0 \tag{23}$$

where

$$a_1=\frac{\rho^2}{12}+\frac{2\mu}{\rho(1+\nu_m)(3-\nu_m)}+\frac{\mu(1-\nu_m)}{2(3-\nu_m)(1+\nu_m)}$$

$$+\frac{\mu(\rho+(1-\nu_m))}{2(1+\nu_m)(3-\nu_m)}$$

$$a_2=\frac{\mu((1-\mu_m)+\rho)}{\rho(1+\nu_m)(3-\nu_m)}$$

$$b_1=\frac{-\mu}{(1+\nu_m)(3-\nu_m)}-\frac{\mu(1-\nu_m)}{\rho(3-\nu_m)(1+\nu_m)}$$

$$b_2=\frac{2\mu}{\rho(1+\nu_m)(3-\nu_m)}+1,$$

and the following nondimensionalizations have been used

$$\rho=h\alpha=\frac{2\pi h}{\lambda}$$
$$\mu=\frac{E_m}{E_f} \tag{24}$$

For nontrivial solutions for A and B, one requires

$$\begin{vmatrix}(a_1-\epsilon_0) & b_1\\ a_2 & b_2\end{vmatrix}=0. \tag{25}$$

The condition (25) implies that

$$\epsilon_0=a_1+a_2\left(\frac{b_1}{b_2}\right). \tag{26}$$

2.3 Results and Discussion. To illustrate the results, the material properties listed in Table 1 have been chosen. These correspond to the two fiber/matrix systems, designated as T300/BP907 and IM7/8551-7. From now on, these shall be referred to as BP907 and IM7, respectively.

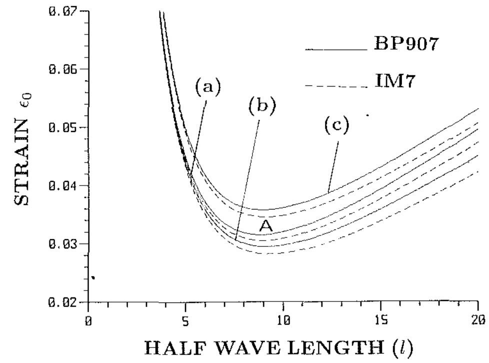

Fig. 3 Variation of ϵ_0 with nondimensional half wavelength l. Comparison of predictive models; curve (a) is Gough (1939), curve (b) is Reissner (1937), and curve (c) is the present; dashed line—IM7, solid line—BP907

Table 1

	BP907	IM7
$\frac{E_f}{E_m}$	74.2	79.3
ν_m	0.38	0.33

Figure 3 shows the variation of ϵ_0, with the nondimensional half wavelength $l\,(l=\lambda/2h)$. In this plot, the present results (solid curve for BP907 and dashed curve for IM7) are compared with those of two other models. The first one, Gough et al. (1939), is obtained by neglecting the presence of the interface shear traction q. In that calculation, instead of the continuity conditions, equations (10) are replaced by the requirement that the surface of the matrix ($y=0$) is constrained to satisfy

$$\epsilon_x=0$$
$$v=v_m. \tag{27a}$$

In the second model (Reissner (1937)) the surface of the matrix is taken to be free from shearing stress. This amounts to satisfying (at $y=0$)

$$v=v_m$$
$$\tau_{xy}=0. \tag{27b}$$

In computing the critical strain, the models of Gough (1939) and Reissner (1937) do not account for the interface shear traction developed at buckling. From Fig. 3 the minimum values of ϵ_0, such as those corresponding to point A, are identified as the buckling strain.

The manner in which the buckling strain in affected as a function of the ratio of Young's moduli of the constituents E_f/E_m is shown in Fig. 4(a). The corresponding critical wavelength variation is depicted in Fig. 4. Notice that a large disparity in Young's moduli between fiber and matrix ($E_f\gg E_m$) leads to a gradually decreasing value of critical strain, with the rate of this decrease diminishing as the limit $E_f/E_m\to\infty$ is approached. Further, as expected, the agreement between the present calculation and those of Gough et al. (1939) and Reissner (1937) improves as this limit is approached. Also, as $E_f/E_m\to\infty$, by holding E_f constant and letting $E_m\to 0$, which corresponds to a gradual disappearence of the matrix, the Euler formula, $\epsilon_{cr}=\rho^2/12$, is obtained from the present result (26). Next, consider the case of $E_f/E_m\to 1$. Here, there is a noticeable difference in the predicted values of ϵ_0 between the three calculations. However, in the range $E_f/E_m\le 20$, the predicted critical nondimensional half wavelength l is less than 5. Thus, in this situation where the critical wavelength becomes comparable to the thickness of the fiber, use of a one-dimensional theory, such as technical beam theory in describing the fiber, is inappropriate. The effect of Poisson's ratio on the buckling strain and critical half

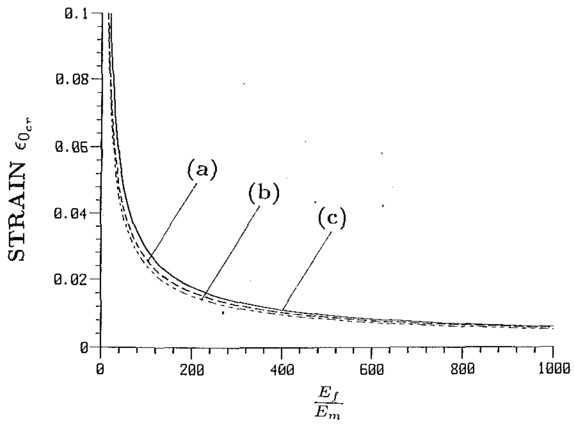

Fig. 4(*a*) Variation of critical ϵ_0 with ratio of Young's moduli E_f/E_m; curves (a), (b), and (c) as in Fig. 3

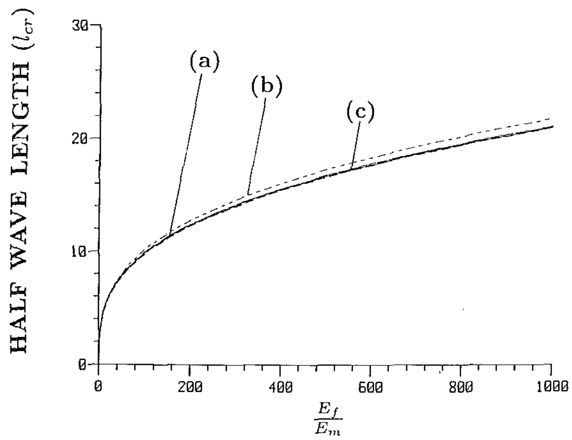

Fig. 4(*b*) Variation of critical half wavelength (l_{cr}) with ratio of Young's moduli E_f/E_m; curves (a), (b), and (c) as in Fig. 3

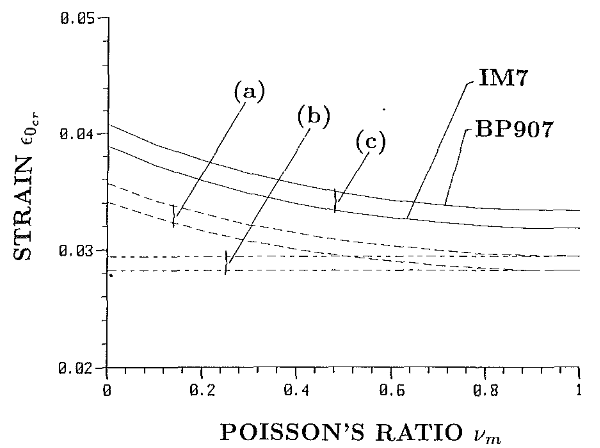

Fig. 5(*a*) Effect of Poisson's ratio on critical strain ϵ_0; curves (a), (b), and (c) as in Fig. 3

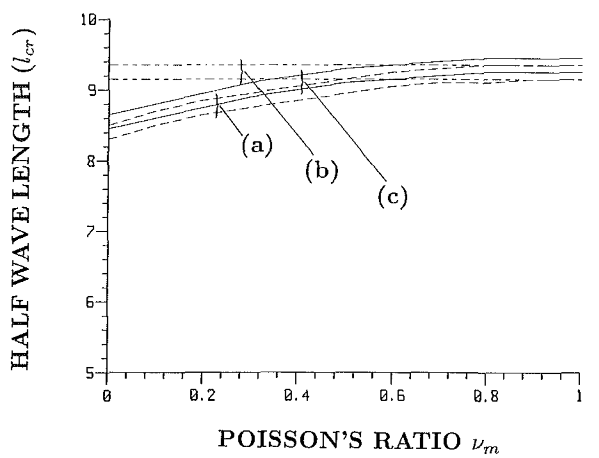

Fig. 5(*b*) Effect of Poisson's ratio on critical half wavelength l_{cr}; curves (a), (b), and (c) as seen in Fig. 3

wavelength can be inferred from Fig. 5. Here, it is seen that when $\nu_m = 0$ (a condition which constrains the matrix to behave such that $\epsilon_y = \epsilon_z = 0$ at buckling), the buckling strain is higher than for cases $\nu_m \geq 0$. This is to be expected because the constraining condition "stiffens" the matrix at buckling.

In summary, it is observed that the effect of the interface shear traction occurring at buckling is to introduce small periodic fluctuations in the axial thrust acting on the fiber (denoted by p' in the formulation). Further, this shear traction also introduces bending moments because of its eccentricity with respect to the centerline of the fiber. These effects have been included in the present formulation.

The stresses in the matrix associated with the sinusoidally-buckled form of the fiber contain the multiplier $e^{-\alpha y}$, and thus diminish as y increases. At a sufficiently large value of y, they may be regarded as negligible. Thus, the coefficient 'α'_{cr} in the exponent characterizes a boundary layer depth into the matrix to which any surface disturbance can be felt. The quantity "αy" can be rewritten as,

$$\alpha y = \frac{2\pi}{\lambda} y = \frac{\pi}{l} \cdot \left(\frac{y}{h}\right). \tag{28}$$

Figure 4(*b*) shows a plot of l_{cr} against the ratio E_f/E_m. It is seen that for a "soft" matrix ($E_f/E_m = 500$, say), the surface disturbance is felt to a larger depth than for a "hard" matrix ($E_f/E_m = 50$, say). This result can be interpreted in the light of more realistic composites. Suppose a unidirectional laminated composite contains several fibers. Then, so long as the fiber spacing is larger than a certain minimum value, the interaction between adjacent fibers will be negligible, and the one-fiber model presented here can be used as a measure of the compressive strength of the composite. However, in order to maximize the specific stiffness of the composite (the E/ρ ratio), one needs to attain a high volume fraction of fibers. This makes the spacing between fibers (expressed more readily in terms of fiber volume fraction $V_f = (h/h + 2c)$ small compared with h. Typical values of V_f range from $0.5 - 0.6$ for fiber-reinforced laminated systems that are currently in use. Thus, it is informative to address the more general problem of a laminated medium containing many fibers under compressive loading (Fig. 6(*a*)). There are several ways to approach this problem. In the spirit of the previous analysis, this can be modeled as a problem of a single fiber resting on an equivalent orthotropic medium (the "smeared" foundation). However, unlike before, the prebuckling stress state in the "foundation" is quite different. No longer can it be assumed that the totality of the load is borne by the surface fiber alone. Indeed, one is compelled to consider a problem in which the "foundation's" initial stressed state on the buckling of the surface fiber has to be accounted for. Such a consideration can pose difficulties in solving for the displacements of the foundation in the presence of the initial stress, since now a two-dimensional stability problem for the foundation itself has to be considered.

Another approach to the problem is to consider individual fibers separately, and account for the interaction effects between adjacent fibers by analyzing the deformation of the sandwiched elastic matrix at buckling. It is this approach that is followed in the next investigation.

3 Buckling of a Layered Medium

3.1 Problem Formulation. The configuration being studied is shown in Fig. 6(*a*). Here, the end compression is indicated as being carried entirely by the fibers. To verify this assumption, let P (per unit length in the $\hat{z}$-direction) be the applied load to a "unit cell" of depth $(h+2c)$ in the prebuckled state. Then, the axial compressive stresses in the fiber and matrix are

$$\sigma_{x_f} = \frac{P}{h\left(1+\dfrac{2c}{h}\dfrac{\mathrm{E}_m}{\mathrm{E}_f}\right)}$$

$$\sigma_{x_m} = \frac{P}{h\left(\dfrac{\mathrm{E}_f}{\mathrm{E}_m}+\dfrac{2c}{h}\right)}$$

with

$$\frac{2c}{h} = \left(\frac{1-V_f}{V_f}\right).$$

These reduce to $\sigma_{xf}=P/h$ and $\sigma_{x_f} \gg \sigma_{x_m}$, so long as $(\mathrm{E}_f/\mathrm{E}_m) \gg ((1-V_f)V_f)$ and $\mathrm{E}_f \gg \mathrm{E}_m$, which is the case in the present investigation. Thus, the prebuckled state of the composite is as described by (5), with the end compression load carried entirely by the fibers. The matrix acts as an elastic foundation. Next, consider the composite in the buckled configuration (Fig. 6(b) and 6(c)). Then, considering the equilibrium of a typical fiber, the following set of equations result for the surface fiber ($N=1$) and the nth fiber ($N=n$), respectively. (Here an extra subscript n designates quantities associated with the nth fiber.)

Surface Fiber.

$$\mathrm{E}_f I \frac{d^4 v_1}{d\hat{x}^4} + P\frac{d^2 v_1}{d\hat{x}^2} - \sigma_{u_1} - \frac{h}{2}\frac{dq_{u_1}}{d\hat{x}} = 0$$
$$q_{u_1} + h\mathrm{E}_f \frac{d^2 u_{0_1}}{d\hat{x}^2} = 0. \qquad (29)$$

nth Fiber.

$$\mathrm{E}_f I \frac{d^4 v_n}{d\hat{x}^4} + P\frac{d^2 v_n}{d\hat{x}^2} - [\sigma_{u_1} - \sigma_{L_{n-1}}]$$
$$- \frac{h}{2}\frac{d}{d\hat{x}}[q_{u_n} + q_{L_{n-1}}] = 0$$
$$[q_{u_n} - q_{L_{n-1}}] + h\mathrm{E}_f \frac{d^2 u_{0_n}}{d\hat{x}^2} = 0. \qquad (30)$$

In order to proceed with the solution of (29) and (30), the shearing and normal tractions (q, σ) developed at the fiber/matrix interface at buckling have to be determined. This can be done by considering the deformation of a typical matrix layer sandwiched between any two fibers. Thus, isolate the nth and $(n+1)$st fibers and the matrix in between (Fig. 6(c)). To proceed, solving for the displacements in the matrix layer, some boundary conditions have to be imposed at the fiber/matrix interface. As before, sinusoidal perturbations in $u(\hat{x})$, $v(\hat{x})$ are investigated about the trivial solution (5). Thus, for the nth fiber it is assumed,

$$u_{0n} = U_{0n}\cos\alpha\hat{x}$$
$$v_n = V_n \sin\alpha\hat{x}. \qquad (31)$$

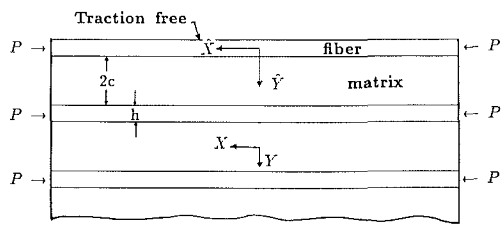

Fig. 6(a) Configuration for unidirectional laminated composite

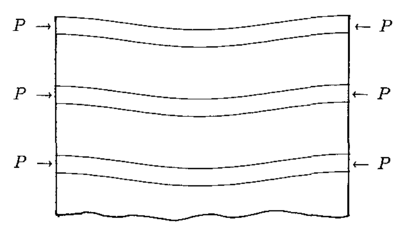

Fig. 6(b) Buckled configuration of laminated composite

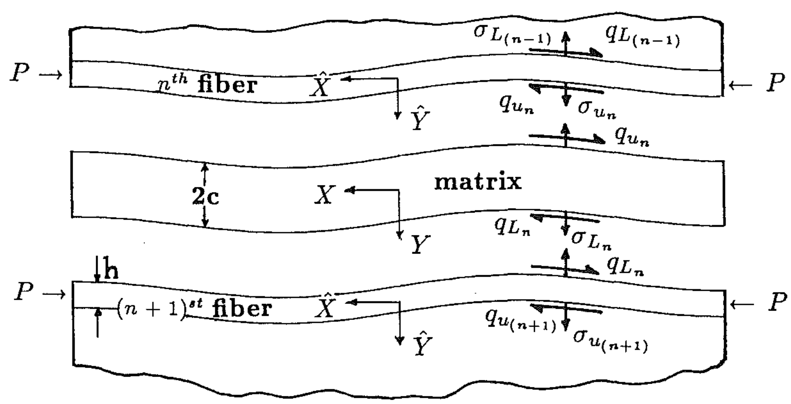

Fig. 6(c) Isolated portion of buckled configuration; nth, $(n+1)$st fibers and sandwiched matrix

U_{0n}, V_n are the unknown amplitudes of the perturbations $u_n(\hat{x})$, $v_n(\hat{x})$, respectively, of the nth fiber.

Next, the deformation of the matrix strip between the nth and $(n+1)$st fibers is considered. With reference to Fig. 6(c), it is required to solve (11) in the matrix subject to the following boundary conditions

nth fiber/matrix interface

$$u_{0n} - \frac{h}{2}\frac{dv_n}{d\hat{x}}\bigg|_{\hat{y}_n = \frac{h}{2}} = u_m\big|_{y=-c} \qquad v_n\bigg|_{\hat{y}_n = \frac{h}{2}} = v_m\big|_{y=-c} \tag{32a}$$

$(n+1)$st fiber/matrix interface,

$$u_{0(n+1)} + \frac{h}{2}\frac{dv_{(n+1)}}{d\hat{x}}\bigg|_{\hat{y}_{n+1} = -\frac{h}{2}} = u_{m|y=c} \qquad v_{(n+1)}\bigg|_{\hat{y}_{n+1} = -\frac{h}{2}} = v_{m|y=c}. \tag{32b}$$

Notice that by confining attention to the nth and $(n+1)$st fibers and the sandwiched matrix in between, it is possible to generate the governing equations for *any fiber*. The interface continuity conditions for displacements are completely specified by (32) in that, at *every* fiber/matrix interface, one of the conditions (32) will apply.

The solution of (11) subject to (32) is,

$$\begin{aligned} u_m(x, y) &= (C_1\cosh\alpha y + C_2\sinh\alpha y + C_3 y\cosh\alpha y + C_4 y\sinh\alpha y)\cos\alpha x \\ v_m(x, y) &= (D_1\cosh\alpha y + D_2\sinh\alpha y + D_3 y\cosh\alpha y + D_4 y\sinh\alpha y)\sin\alpha x, \end{aligned} \tag{33}$$

with

$$\begin{aligned} D_1 &= C_2 - \frac{C_3}{\alpha}\left(\frac{3-\nu_m}{1+\nu_m}\right) \\ D_2 &= C_1 - \frac{C_4}{\alpha}\left(\frac{3-\nu_m}{1+\nu_m}\right) \\ D_3 &= C_4 \\ D_4 &= C_3. \end{aligned} \tag{34}$$

Here, $C_i\,(i=1,4)$ is related to the unknown amplitudes of the adjacent fibers U_{0n}, $U_{0(n+1)}$, V_n, $V_{(n+1)}$ through the conditions (32) by

$$\begin{aligned} C_1 &= m_{11}\left[U_{0(n+1)} + U_{0n} + \frac{\rho}{2}(V_{(n+1)} - V_n)\right] + m_{12}[V_{(n+1)} - V_n] \\ C_2 &= m_{21}\left[U_{0(n+1)} - U_{0n} + \frac{\rho}{2}(V_{(n+1)} + V_n)\right] + m_{22}[V_{(n+1)} + V_n] \\ \frac{C_3}{\alpha} &= m_{31}\left[U_{0(n+1)} - U_{0n} + \frac{\rho}{2}(V_{(n+1)} + V_n)\right] + m_{32}[V_{(n+1)} + V_n] \\ \frac{C_4}{\alpha} &= m_{41}\left[U_{0(n+1)} + U_{0n} + \frac{\rho}{2}(V_{(n+1)} - V_n)\right] + m_{42}[V_{(n+1)} - V_n]. \end{aligned} \tag{35}$$

The constants $m_{11}, \ldots m_{14}$ and $m_{21}, \ldots m_{24}$ are given in Appendix A.

Having obtained the displacement field for the matrix strip (32) in terms of the boundary values $U_{0(n+1)}$, U_n, $V_{(n+1)}$, V_n, the surface tractions σ_{u_n}, $\sigma_{L_{(n-1)}}$, q_{u_n}, $q_{L_{(n-1)}}$ acting on the nth fiber can be computed.

Thus,

$$\begin{aligned} \sigma_{u_n} &= \frac{E_m\alpha}{(1-\nu_m^2)}[U^1{}_nP_{u_1} + U_{(n+1)}P_{u_2} + V_nP_{u_3} + V_{(n+1)}P_{u_4}]\sin\alpha x \\ \sigma_{L_{(n-1)}} &= \frac{E_m\alpha}{(1-\nu_m^2)}[U_{(n-1)}P_{L_1} + U^2{}_nP_{L_2} + V_{(n-1)}P_{L_3} + V_nP_{L_4}]\sin\alpha x \\ q_{u_n} &= G_m\alpha[U^1{}_nR_{u_1} + U_{(n+1)}R_{u_2} + V_nR_{u_3} + V_{(n+1)}R_{u_4}]\cos\alpha x \\ q_{L_{(n-1)}} &= G_m\alpha[U_{(n-1)}R_{L_1} + U^2{}_nR_{L_2} + V_{(n-1)}R_{L_3} + V_nR_{L_4}]\cos\alpha x, \end{aligned} \tag{36}$$

where

$$\begin{aligned} U^1{}_n &= U_{0n} - \frac{\rho}{2}V_n \\ U^2{}_n &= U_{0n} + \frac{\rho}{2}V_n \\ U_{(n+1)} &= U_{0(n+1)} + \frac{\rho}{2}V_{n+1} \\ U_{(n-1)} &= U_{0(n-1)} - \frac{\rho}{2}V_{n-1}. \end{aligned} \tag{37}$$

Expressions for $P_{u_1}, \ldots, R_{u_1}, \ldots$, etc. are given in Appendix A. Substituting (36) into (30), the following system of equations for the nth fiber are obtained:

$$\begin{aligned} &\frac{\rho^2}{12}V_n - \epsilon_0 V_n - \frac{\mu}{\rho(1-\nu_m^2)}F_1(U_{0(n-1)}, U_{0n}, U_{0(n+1)}, V_{n-1}\ldots V_n) + \frac{\mu^*}{2}F_2(U_{0(n-1)}, \ldots) = 0 \\ &\frac{\mu^*}{\rho}F_3(U_{0(n-1)}, \ldots\ldots) - U_{0n} = 0. \end{aligned} \tag{38}$$

Here, $\mu^* = G_m/E_f$. The functions $F_1, \ldots F_3$ are *linear* combinations of the six unknown amplitudes $U_{0(n-1)}$, U_{0n}, $U_{0(n+1)}$, V_{n-1}, V_n, V_{n+1}. These functions are given in Appendix A. Similarly, for the surface fiber from (29), the following equations are obtained

$$\begin{aligned} &\frac{\rho^2}{12}V_1 - \epsilon_0 V_1 - \frac{\mu}{\rho(1-\nu_m^2)}F_4(U_{01}, U_{02}, V_1, V_2) + \frac{\mu^*}{2}F_5(U_{01}, \ldots, V_2) = 0 \\ &\frac{\mu^*}{\rho}F_6(U_{01}, \ldots\ldots V_2) - U_{01} = 0. \end{aligned} \tag{39}$$

The functions $F_4, \ldots F_6$ are also given in Appendix A.

The system of equations (38) and (39) can be conveniently arranged in the following form

$$[\hat{Q}^*][\mathbf{u}_1] + [\bar{Q}][\mathbf{u}_2] = 0 \tag{40a}$$

$$[Q][\mathbf{u}_{n-1}] + [\hat{Q}][\mathbf{u}_n] + [\bar{Q}][\mathbf{u}_{n+1}] = 0, \tag{40b}$$

where elements of the (2×2) matrices Q, $\hat{Q}$, etc., are arranged in Appendix B and

$$\mathbf{u}_n = \begin{bmatrix} u_{0n} \\ v_n \end{bmatrix}.$$

It is of interest to seek solutions to the perturbation amplitudes (U_{0n}, V_n) that exhibit a decay into the interior of the half-plane under consideration. Thus, one seeks values of

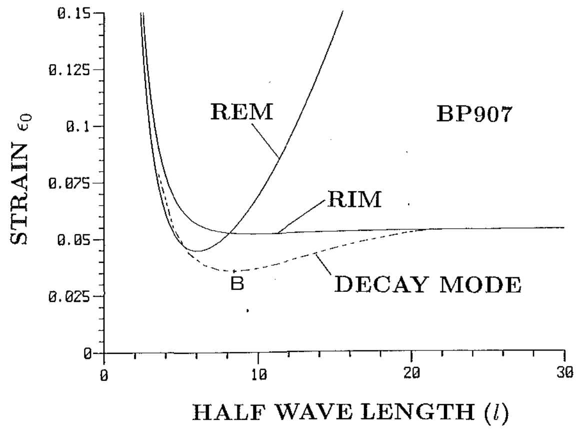

Fig. 7(a) Variation of ϵ_0 with nondimensional half wavelength l for T300/BP907. "decay mode" denotes present results. $V_f = 0.1$

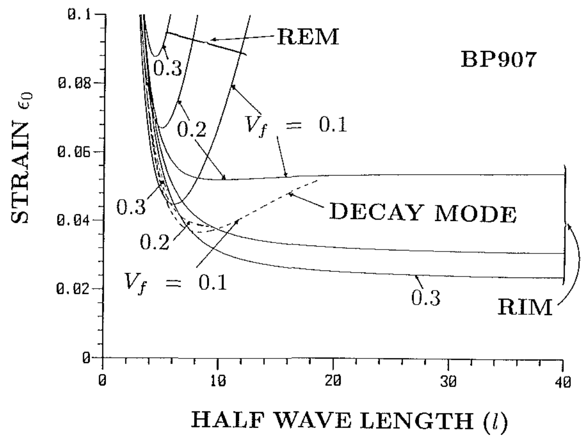

Fig. 7(b) Variation of ϵ_0 with nondimensional half wavelength l for T300/BP907. "decay mode" denotes present results; V_f as a parameter

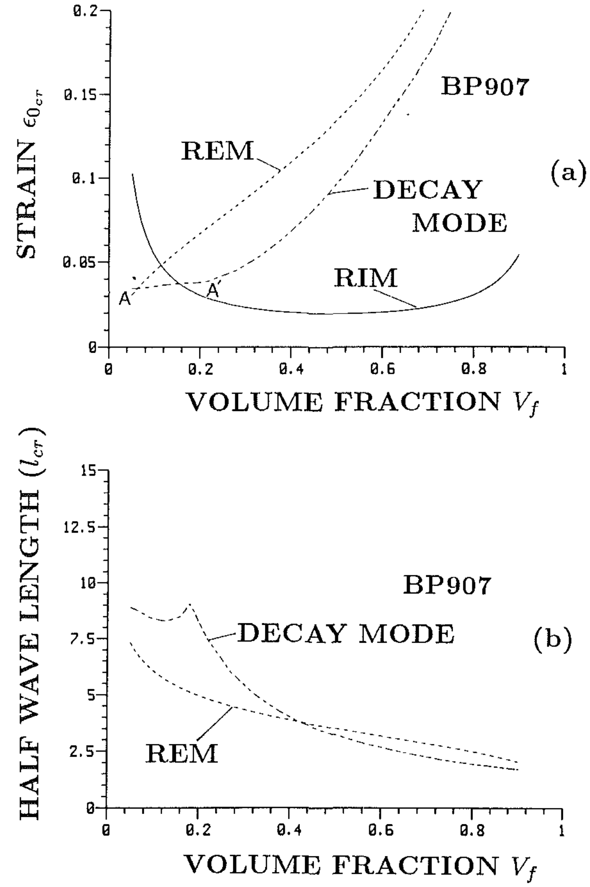

Fig. 8(a) Variation of critical ϵ_0 with fiber volume fraction V_f for T300/BP907 and (b) variation of critical half wavelength l_{cr} with fiber volume fraction V_f for T300/BP907

ϵ_0 that permit this behavior. Of all possible ϵ_0 that fall into this category, the minimum ϵ_0 is identified as the buckling "load" of the system. Thus, the following problem is considered.

We are required to solve (40) subject to the condition

$$\begin{aligned} &U_{01},\ V_1 \quad \text{finite} \\ &U_{0n},\ V_n \to 0 \text{ as } n \to \infty. \end{aligned} \tag{41}$$

Notice that (40) subject to (41) is a *difference equation eigenvalue problem*. Here, ϵ_0 is the eigenvalue sought and the amplitudes U_{0n}, V_n are the associated eigenfunctions. The boundary conditions (41) are physically motivated to conform to the experimental observations discussed in (Hahn and Williams, 1986; Sohi, Hahn, and Williams, 1984; Waas and Babcock, 1989). The solution proceeds in the following manner: First, (40*b*) is solved using the boundary condition for large n. This enables one to find the general solution for U_{0n}, V_n up to two arbitrary constants. Then, using the first of conditions (41) and the obtained general solution, substitute for U_{01}, V_1 into (40*a*). This results in a (2×2) system of homogeneous equations for the two as yet undetermined constants. Vanishing of the determinant associated with this system gives the required condition to obtain ϵ_0. Unlike in the previous case, it is not possible to obtain an explicit expression for ϵ_0 (see (26)). This is because each member of the matrix associated with the final system of equations is a function of ϵ_0. Thus, we obtain an equation implicit in ϵ_0 of the form

$$G(\epsilon_0, l) = 0. \tag{42}$$

Newton's method is used to solve (42) for a specified l. Details of the solution process can be found in Waas 1987. Depending on the geometry and material properties of the composite, several cases will be discussed next.

3.2 Results and Discussion. Results are computed for composites whose material properties are listed in Table 1. For clarity of presentation, the results are displayed in the (ϵ_0, l) plane. In the discussion to follow, the term "decaying solution" is used to refer to solutions of (40) subject to (41). For comparison purposes we first present solutions to (40) subject to

$$U_{0n} = 0, \ \ldots \ V_{(n-1)} = V_{(n)} = V_{(n+1)} \ \ldots \tag{43}$$

which is the displacement field assumed in RIM (abbreviation for Rosen's in-plane mode (1965)). The value of ϵ_0 predicted by such a specialization is obtained by substituting (43) into (40*b*). One then finds

$$\epsilon_0 = \hat{q}_{12}. \tag{44}$$

Values of (ϵ_0, l) conforming to (44) are indeed the RIM prediction. However, in order that (44) be a solution to (40), it must in addition satisfy the required boundary condition for large n. Clearly, this is not the case. The reason is that the Rosen shear mode result holds only for a composite of infinite extent, without recourse to a traction-free edge. Furthermore, the Rosen result

$$\sigma_{cr}\,|_{\min} = \frac{G_m}{(1 - V_f)}$$

is obtained in the limit $l \to \infty$, implying a mode of buckling with a long wavelength. Thus, the Rosen prediction corresponds to buckling of an *infinite* medium where *all* wavelengths $(l \gg 1)$ are admissible solutions. Physically, the RIM prediction furnishes values of ϵ_0 corresponding to the equilibrium of the composite in a nontrivial configuration in which *every fiber buckles in an identical manner*. Where appropriate, the RIM prediction is included in the results presented for comparison purposes.

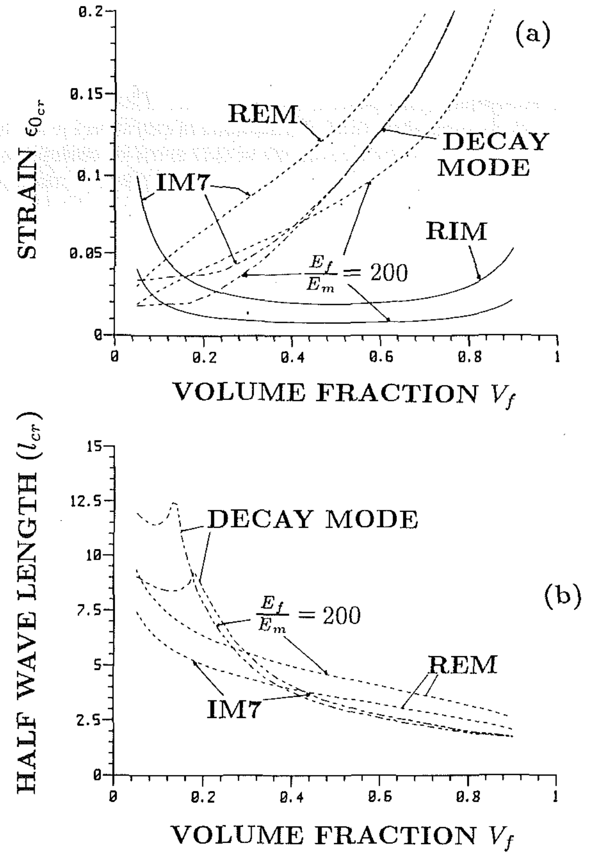

Fig. 9(*a*) Variation of critical ϵ_0 with fiber volume fraction V_f; comparison of IM7/8551-7 with composite of $E_f/E_m = 200$, and (*b*) variation of critical half wavelength l_{cr} with fiber volume fraction V_f; comparison of IM7/8551-7 with composite of $E_f/E_m = 200$.

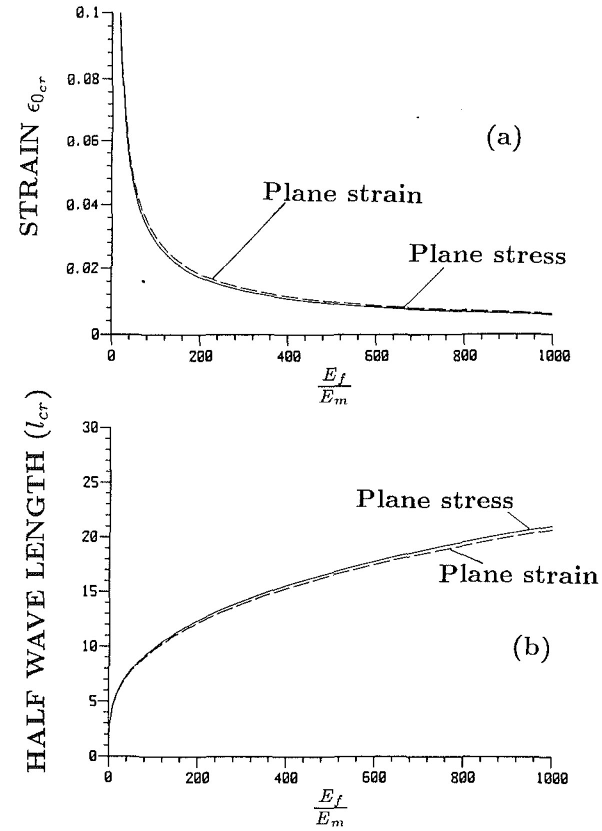

Fig. 10 Comparison of plane-stress and plane-strain approximations for BP907 single fiber composite; (*a*) $\epsilon_{0_{cr}}$ variation and (*b*) l_{cr} variation

In Fig. 7(*a*), a plot of variation of strain with l for a composite with a low fiber volume fraction $V_f = 0.1$ is shown. In this figure, the result obtained from the present analysis has been compared with those of RIM and REM (Rosen extensional mode). Notice that the buckling strain as predicted by the present analysis, and marked as point B, is lower than both the RIM and REM predictions. Similar curves for other values of V_f are shown in Fig. 7(*b*). Here, the minimum point of the curves marked as "decay mode" shifts to the right with increasing values of V_f. Beyond a certain value of V_f, the minimum is found to disappear. The nonexistence of a true minimum implies a continuous dependence of ϵ_0 on the half wavelength l. Thus, for a fixed value of E_f/E_m, a critical decay buckling mode of short wavelength exists below a certain V_f. Above this value of V_f, a short wavelength buckling instability is still present but shows a continous dependence on l. With increasing V_f, the buckling strain increases, while the corresponding critical half wavelength decreases as is shown in Figs. 8(*a*) and 8(*b*). However, in this limit ($V_f \rightarrow 1$), the critical half wavelength becomes comparable to the thickness of a fiber ($l \approx 1$). In such cases, treating the fiber via beam theory is inadequate. To properly address this question requires modeling a fiber as a two-dimensional continuum. This aspect is not considered in this presentation.

A critical strain (ϵ_{cr}) is defined by points corresponding to such as B in Fig. 7(*a*), and when a true minimum does not exist, the minimum of all admissible (ϵ_0,l). Then, Fig. 9(*a*) shows plots of ϵ_{cr} against the volume fraction V_f. In this figure, curves for a composite of large E_f/E_m (=200) and $\nu_m = 0.3$ have also been included for comparison purposes. The corresponding plots for the corresponding critical wavelength are shown in Fig. 9(*b*). In Fig. 8(*a*), the portion of the curve marked A-A′ is a region of almost constant strain. This region spans a range of V_f that is large for small values of the composite's E_f/E_M. This can be inferred from Fig. 9(*a*). The "section" A-A′ corresponds to the value of ϵ_0 obtained from the previous analysis for a single-fiber composite. Physically, this implies that for values of V_f, less than that corresponding to point A′, the fiber spacing is large enough that there are no interactions between fibers. Thus, the buckling is as predicted for a single-fiber composite. Beyond point A′, one can no longer ignore this interaction effect. That this is so was emphasized in our previous discussion on a single-fiber composite. There, the existence of a certain critical depth into the matrix to which any surface effects were felt was discussed. It was noted that for a "soft" composite ($E_f/E_m \approx 200$, say) this depth was larger than for a "hard" composite ($E_f/E_m \approx 50$, say). Thus, here it is not surprising that the region of constant strain A-A′ persists further for the harder composite (Fig. 9(*a*)). However, it is seen that in situations where the interaction effect is present, the present decay mode prediction yields a higher value of buckling strain as compared with the RIM prediction for a composite of infinite extent. Experimental results reported in the literature show some scatter (Shuart, 1985) in the data on compressive strength. The RIM prediction, when compared with this data, can be in error by as little as 40 percent (June et al. 1969) to as large as by an order of magnitude (Shuart, 1985; Hahn and Williams, 1986; Sohi, Hahn, and Williams, 1984; Lager and June, 1969; Waas and Babcock, 1989; Waas, 1987).

Before discussing possible causes for such a discrepancy, the difference in the results between a *plane-stress* and *plane-strain* approximation for the perturbation problem will be addressed. The plane-strain result can be generated by making appropriate substitutions for the elastic constants. Results are computed for the BP907 composite. For the single fiber case, Fig. 10 shows the critical strain and critical half wavelength

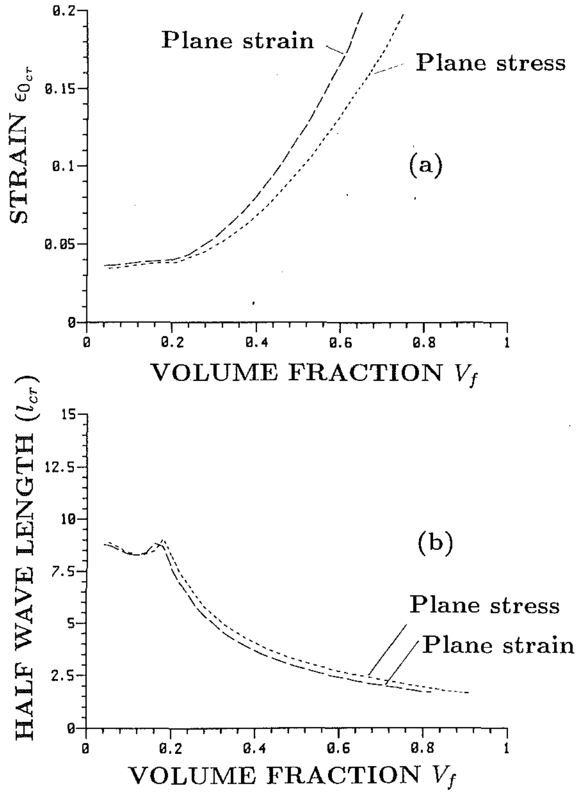

Fig. 11 Comparison of plane-stress and plane-strain approximations for BP907 unidirectional composite; (a) $\epsilon_{0_{cr}}$ variation; (b) l_{cr} variation

variation as a function of (E_f/E_m). With the plane-strain approximation, the computed $\epsilon_{0_{cr}}$ is slightly larger than the corresponding plane-stress result, while l_{cr} is slightly lower. The Poisson's ratio of the fiber is assumed as 0.2. The corresponding results for the unidirectional composite exhibit a similar trend as shown in Fig. 11.

It was seen that values of $\epsilon_{0_{cr}}$ calculated for the RIM result and the present investigation overestimated the experimentally observed buckling strains. In addition, the present decay mode result is higher than the RIM result. The reason for this latter discrepancy is that the decay mode, which accounts for interaction between adjacent fibers, yields a critical wavelength that is a small multiple of the fiber diameter as compared with the longer wavelength RIM result. Further, the decay buckling mode is two-dimensional involving a dependence on both the $\hat{x}$ and $\hat{y}$-directions, while the RIM is essentially one-dimensional, presuming that *all fibers* buckle in an identical manner. Thus, the RIM model is less constrained than the present model. However, it is unrealistic as compared with recent experimental findings reported by Hahn and Williams (1986), Sohi et al. (1984), Hahn et al. (1986), and Waas et al. (1989), which indicate a decay mode type of buckling. For example, in Waas and Babcock (1989), real-time holographic interferometry coupled with optical microscopy are used to capture the origins of compressive failure, which is seen to originate at a traction-free edge. In Hahn and Williams (1986) and Sohi, Hahn, and Williams (1984) evidence of multiple fracture in the damage area was presented. It was also postulated that microbuckling of fibers originated with the buckling of a single fiber, which caused tensile stresses to develop in the matrix in between, thus reducing the buckling load of the adjacent straight fiber. This process progressively involved additional fibers as the damage propagated. Both the RIM and the present model enforce perfect bonding conditions between fibers and matrix. In addition, the fibers are assumed to be perfectly aligned in a regular fashion. Both of these simplifications are unrealistic from a physical viewpoint in that neither are the fibers perfectly aligned nor are they perfectly bonded to the matrix. (Evidence to this effect is presented in Hahn et al. (1986) for example, that show SEM micrographs of the cross-section of typical virgin specimens.) An attempt was made to characterize the imperfect bonding between fibers and matrix in Kulkarni et al. (1973). However, no specific parameter was identified that enables quantifying the imperfect nature of the bonding by a suitable measurement in the laboratory. A recent investigation by Minahen and Knauss (1989), addressing the influence of the bond conditions on the buckling strian, has revealed a fivefold reduction in $\epsilon_{0_{cr}}$ when the displacement constraint at the interface is released. The reasons stated above are the primary causes for the discrepancy between the predictive microbuckling models (RIM and present) and the experimental results reported in the literature (Hahn and Williams, 1986; Sohi, Hahn, and Williams, 1984; Hahn, Sohi, and Moon, 1986; Lager and June, 1969; Waas and Babcock, 1989; Waas, 1987).

5 Conclusions

A simple mechanical model for fiber microbuckling has been considered with a view to understanding the effects of a traction-free edge in initiating the buckling process. For low fiber volume fractions, it is demonstrated that a decay buckling mode furnishes values of critical strain which are below the predictions of the classical Rosen model (1965). At high volume fractions, the predicted critical half wavelength becomes comparable to the fiber thickness, invalidating treating the fibers via technical beam theory. A two-dimensional description of the fibers is employed in another investigation.

These preliminary results have highlighted some drawbacks of existing models for fiber microbuckling and are suggestive of the need for future research in understanding the compressive behavior of fiber composites.

Acknowledgments

This work was supported by NASA Grant No. NSG-1483. The authors are appreciative of this support. The interest and encouragement of Dr. J. H. Starnes, Jr. of NASA-Langley is gratefully acknowledged.

References

Biezeno, C. B., and Hencky, H., 1928, "On the general theory of elastic stability," *Koninklijke akademie van wetenschappen te Amsterdam, Proc.*, Vol. 31.

Biot, M., 1939, "A non-linear theory of elasticity and the linearized case for a body under initial stress," *Phil. Mag.*, Vol. 27, p. 468.

Budiansky, B., 1983, "Micromechanics," *Computers and Structures*, Vol. 16, pp. 3-12.

Chaplin, C. R., 1977, "Compressive fracture in unidirectional glass reinforced plastics," *Journal of Materials Science*, Vol. 12, pp. 347-352.

Dale, W. C., and Baer, E., 1974, "Fiber buckling in composite systems: A model for the ultra-structure of uncalcified collagen tissues," *Journal of Materials Science*, Vol. 9, pp. 369-382.

Dow, N. J., and Gruntfest, I. J., 1960, "Determination of most-needed, potentially possible improvements in materials for ballistic and space vehicles," General Electric Company, Air Force Contract AF 04(647)-269, June.

Evans, A. G., and Adler, W. F., 1983, "Kinking as a mode of structural degradation in carbon fiber composites," *Acta Metallurgica*, Vol. 26, pp. 725-738.

Fried, N., and Kaminetsky, J., 1964, "The influence of material variables on the compressive properties of parallel filament reinforced plastics," *Proceedings of the 19th Annual Technical and Management Conference*, Reinforced Plastics Division, Soc. of the Plastics Industry, Inc., February, pp. (9-A) 1-10.

Goodier, J. N., 1946, "Cylindrical Buckling of Sandwich Plates," ASME Journal of Applied Mechanics, Vol. 13, pp. A253-A260.

Gough, G. S., et al., 1939, "The stabilization of a thin sheet by a continuous supporting medium," *Journal of the Royal Aero. Society*, August, pp. 12-43.

Hahn, H. T., Sohi, M., and Moon, S., 1986, "Compression failure mechanisms of composite structures," NASA-CR-3988.

Hahn, H. T., and Williams, J. G., 1986, "Compression failure mechanisms in unidirectional composites, March, NASA-TM-85834.

Hoff, N. J., and Mautner, S. E., 1945, "Buckling of sandwich type panels," *Journal of Aero. Science*, Vol. 12, pp. 285–297.

Hoff, N. J., and Mautner, S. E., 1948, "Bending and buckling of sandwich beams," *Journal of Aero. Science*, Vol. 15, December, pp. 707–720.

Kulkarni, S. V., Rice, J. S., and Rosen, B. W., 1973, "An investigation of the compressive strength of PRD 49-3/Epoxy composites," NASA-CR-112334.

Lager, J., and June, R., 1969, "Compressive strength of Boron/Epoxy composites," *Journal of Composite Materials*, Vol. 3, pp. 48–56.

Leventz, B., 1964, "Compressive applications of large diameter fiber reinforced plastics," *Proc. of the 19th Annual Technical and Management Conference*, Reinforced Plastics Div., Society of the Plastics Industry, Inc., pp. (14-D) 1–18.

Minahen, T., and Knauss, W. G., 1989, "A note on microbuckling in unidirectional fibrous composites," submitted to ASME JOURNAL OF APPLIED MECHANICS.

Orowan, E., 1949, "A type of plastic deformation new in metals," *Nature*, Vol. 149, pp. 643–644.

Reissner, M. E., 1937, "On the theory of beams resting on a yielding foundation," *Proc. of the National Academy of Sciences*, Vol. 23, pp. 328–333.

Robinson, I. M., et al., 1986, "Stress induced twinning of polydiacetylene single crystal fibers in composites," *Journal of Materials Sciences*, Vol. 21, pp. 3440–3444.

Rosen, B. W., 1965, "Mechanics of composite strengthening," *Fiber Composite Materials*, American Society for Metals," pp. 37–75.

Shuart, M. J., 1985, "Short wave-length buckling and shear failures of compression-loaded composite laminates," November, NASA-TN-87640.

Sohi, M. S., Hahn, H. T., and Williams, J. G., 1984, "The effect of resin toughness and modulus on compressive failure modes of quasi-isotropic GR/epoxy laminates," August, NASA-TM-87604.

Waas, A., 1987, "Compression failure of fibrous laminated composites in the presence of stress gradients: Experiment and theory, Ph.D. thesis, California Institute of Technology, Pasadena, Calif.

Waas, A., and Babcock, C. D., 1989, "An experimental study of the initiation and progression of damage in compressively loaded composite laminates in the presence of a circular cutout," Proceedings of the 30th AIAA/SDM Conference, Mobile, Ala., AIAA, Paper No. 89-1274.

Weaver, C. W., and Williams, J., 1975, "Deformation of a carbon-epoxy composite under hydrostatic pressure," *Journal of Materials Science*, Vol. 10, pp. 1323–1333.

Williams, D., Leggett, D. M., and Hopkins, H. G., 1941, "Flat sandwich panels under compressive end loads," A.R.C., R&M No. 1987, pp. 484–507.

APPENDIX A

$$
\begin{aligned}
m_{11} &= \frac{-Ch + \frac{2\bar{k}}{\rho r} Sh}{\Delta^*} \\
m_{12} &= \frac{Sh}{\Delta^*} \\
m_{21} &= \frac{-Sh + \frac{2\bar{k}}{\rho r} Sh}{\Delta^{**}} \\
m_{22} &= \frac{Ch}{\Delta^{**}} \\
m_{31} &= \frac{2Ch}{\rho r \Delta^{**}} \\
m_{32} &= \frac{2Sh}{\rho r \Delta^{**}} \\
m_{41} &= \frac{2Sh}{\rho r \Delta^*} \\
m_{42} &= \frac{2Ch}{\rho r \Delta^*}
\end{aligned}
\tag{A1}
$$

With

$$
\begin{aligned}
\Delta^* &= \frac{2\bar{k}}{\rho r} \sinh \rho r - 2 \\
\Delta^{**} &= \frac{2\bar{k}}{\rho r} \sinh \rho r + 2 \\
Ch &\equiv \cosh\left(\frac{\rho r}{2}\right) \\
Sh &\equiv \sinh\left(\frac{\rho r}{2}\right) \\
\rho &= \frac{2\pi h}{\lambda} \\
\bar{k} &= \frac{3 - \nu_m}{1 + \nu_m} \\
r &= \frac{2c}{h}
\end{aligned}
\tag{A2}
$$

$$
\begin{aligned}
P_{u_1} &= (1-\nu_m) Chm_{11} + (1-\nu_m) Shm_{21} \\
&\quad + \left[(1-\bar{k}) Sh + \frac{\rho r}{2}(1-\nu_m) Ch\right] m_{31} \\
&\quad + \left[(1-\bar{k}) Ch + \frac{\rho r}{2}(1-\nu_m) Sh\right] m_{41} \\
P_{u_2} &= (1-\nu_m) Chm_{11} - (1-\nu_m) Shm_{21} \\
&\quad - \left[(1-\bar{k}) Sh + \frac{\rho r}{2}(1-\nu_m) Ch\right] m_{31} \\
&\quad + \left[(1-\bar{k}) Ch + \frac{\rho r}{2}(1-\nu_m) Sh\right] m_{41} \\
P_{u_3} &= -(1-\nu_m) Chm_{12} - (1-\nu_m) Shm_{22} \\
&\quad + \left[(1-\bar{k}) Sh + \frac{\rho r}{2}(1-\nu_m) Ch\right] m_{32} \\
&\quad + \left[(1-\bar{k}) Ch + \frac{\rho r}{2}(1-\nu_m) Sh\right] m_{42} \\
P_{u_4} &= (1-\nu_m) Chm_{12} - (1-\nu_m) Shm_{22} \\
&\quad + \left[(1-\bar{k}) Sh + \frac{\rho r}{2}(1-\nu_m) Ch\right] m_{32} \\
&\quad - \left[(1-\bar{k}) Ch + \frac{\rho r}{2}(1-\nu_m) Sh\right] m_{42}
\end{aligned}
\tag{A3}
$$

$$
\begin{aligned}
R_{u_1} &= -2Shm_{11} - 2Chm_{21} - [(1-\bar{k}) Ch + \rho r Sh] m_{31} \\
&\qquad - [(1-\bar{k}) Sh + \rho r Ch] m_{41} \\
R_{u_2} &= -2Shm_{11} + 2Chm_{21} + [(1-\bar{k}) Ch + \rho r Sh] m_{31} \\
&\qquad - [(1-\bar{k}) Sh + \rho r Ch] m_{41} \\
R_{u_3} &= 2Shm_{12} + 2Chm_{22} - [(1-\bar{k}) Ch + \rho r Sh] m_{32} \\
&\qquad - [(1-\bar{k}) Sh + \rho r Ch] m_{42} \\
R_{u_4} &= -2Shm_{12} + 2Chm_{22} - [(1-\bar{k}) Ch + \rho r Sh] m_{32} \\
&\qquad + [(1-\bar{k}) Sh + \rho r Ch] m_{42},
\end{aligned}
\tag{A4}
$$

the following relations hold between the P's and R's.

$$
\begin{aligned}
P_{L_1} &= P_{u_2} \\
P_{L_2} &= P_{u_1} \\
P_{L_3} &= -P_{u_4} \\
P_{L_4} &= -P_{u_3} \\
R_{L_1} &= -R_{u_2}
\end{aligned}
\tag{A5a}
$$

$$R_{L_2} = -R_{u_1}$$
$$R_{L_3} = R_{u_4}$$
$$R_{L_4} = R_{u_3} \quad \text{(A5}b\text{)}$$

$$F_1 = -P_{L_1} U_{n-1} + P_{u_1} U_n{}^1 - P_{L_2} U_n{}^2 + P_{u_2} U_{n+1} - V_{n-1} P_{L_3} + V_n (P_{u_3} - P_{L_4}) + V_{n+1} P_{u_4}$$
$$F_2 = R_{L_1} U_{n-1} + R_{u_1} U_n{}^1 + R_{L_2} U_n{}^2 + R_{u_2} U_{n+1} + V_{n-1} R_{L_3} + V_n (R_{u_3} + R_{L_4}) + V_{n+1} R_{u_4} \quad \text{(A6)}$$
$$F_3 = -R_{L_1} U_{n-1} + R_{u_1} U_n{}^1 - R_{L_2} U_n{}^2 + R_{u_2} U_{n+1} - V_{n-1} R_{L_3} + \dot{V}_n (R_{u_3} - R_{L_4}) + V_{n+1} R_{u_4}.$$

APPENDIX B

$$Q = \begin{pmatrix} q_{11} & q_{12} \\ q_{21} & q_{22} \end{pmatrix}$$

and, similarly for $[\hat{Q}]$, etc.,

$$q_{11} = \frac{\mu}{\rho(1-\nu_m{}^2)} [P_{L_1}] + \frac{\mu^*}{2} [R_{L-1}]$$

$$q_{12} = \frac{-\mu}{\rho(1-\nu_m{}^2)} \left[\frac{\rho}{2} P_{L_1} - P_{L_3} \right] + \frac{\mu^*}{2} \left[-\frac{\rho}{2} R_{L_1} + R_{L_3} \right]$$

$$q_{21} = \frac{\mu^*}{\rho} [-R_{L_1}]$$

$$q_{22} = \frac{\mu^*}{\rho} \left[\frac{\rho}{2} R_{L_1} - R_{L_3} \right]$$

$$\hat{q}_{11} = 0$$

$$\hat{q}_{12} = \frac{\rho^2}{12} - \epsilon_0 - \frac{\mu}{\rho(1-\nu_m{}^2)} \left[-\frac{\rho}{2} (P_{u_1} + P_{L_2}) + 2P_{u_3} \right] + \frac{\mu^*}{2} \left[-\frac{\rho}{2} (R_{u_1} - R_{L_2}) + 2R_{u_3} \right]$$

$$\hat{q}_{21} = \mu^* \rho [2R_{u_1}] - 1$$

$$\hat{q}_{22} = 0$$

$$\bar{q}_{11} = -q_{11}$$
$$\bar{q}_{12} = q_{12}$$
$$\bar{q}_{21} = q_{21}$$
$$\bar{q}_{22} = -q_{22} \quad \text{(B1)}$$

$$\hat{q}_{11}{}^* = \frac{-\mu}{\rho(1-\nu_m{}^2)} [P_{u_1}] + \frac{\mu^*}{2} R_{u_1}$$

$$\hat{q}_{12}{}^* = \frac{\rho^2}{12} - \epsilon_0 - \frac{\mu}{\rho(1-\nu_m{}^2)} \left[\frac{-\rho}{2} P_{u_1} + P_{u_3} \right] + \frac{\mu^*}{2} \left[-\frac{\rho}{2} R_{u_1} + R_{u_3} \right]$$

$$\hat{q}_{21}{}^* = \frac{\mu^*}{\rho} [R_{u_1}] - 1$$

$$\hat{q}_{22}{}^* = \frac{\mu^*}{\rho} \left[-\frac{\rho}{2} R_{u_1} + R_{u_3} \right].$$

The above expressions for the matrix elements have been simplified by using relations (A5) between the R'and P's.

Large Axisymmetric Deformation of a Laminated Composite Membrane

S. P. Joshi[1]
Assistant Professor,
Department of Aerospace and Mechanical Engineering,
University of Arizona,
Tucson, AZ 85721
Assoc. Mem. ASME

L. M. Murphy
Solar Energy Research Institute,
Golden, CO 80401
Mem. ASME

The formulation and solution of the large elastic axisymmetric deformation problem corresponding to a membrane shell from an initially flat laminated composite material is provided. The numerical solution method developed is found to be very stable and accurate and is easily implemented on a personal computer. The results which consider initial pretension in the membrane are compared with the finite element results and with results obtained by assuming an approximate deflected shape in conjunction with the energy methods. The deformed profile, surface slope, and in-plane tensions are presented as a function of radial distance. Their variation with initial tension and normal pressure parameters is also shown. This problem is of importance in the design of large-diameter membrane concentrators for solar applications.

1 Introduction

Laminated composites are slowly being used outside the aerospace industry. New and innovative applications of high-strength and high-modulus properties of composites are being sought because the cost of the light-weight advance composites continues to drop rapidly. For example, the use of pretensioned laminated membranes has been recognized as being a very effective way of using the material where transverse deflection and slope are critical design considerations. These design variables are of concern in aerospace, as well as ground-based applications such as solar panels, dish antennae, solar reflectors, etc. These applications typically deal with large deformations.

The large deformation problem for axisymmetric membranes having composite material properties does not appear to have been studied in the literature. However, membranes with isotropic material properites have been studied extensively in the past and continue to be investigated, as noted in recent works (e.g., see Cook (1982), Fried (1982), and Murphy (1987)). The general problem of the axisymmetric membrane was studied in a classical work by Adkins and Rivlin (1952), where both geometric and material nonlinearities were considered for the membrane. Though the method developed by Adkins and Rivlin (1952), and extended by others, was quite powerful for the study of inflatable membranes made from isotropic rubber-like materials, it still required significant computational effort to employ.

Other less general methods were found to give adequate solutions for many common engineering applications in the context of plate and thin shell theory (Soedel, 1981; Nielan, 1982; Murphy, 1987). Further, these more approximate methods give good indications of overall surface deformations and equilibrium loads in the membrane for structural design purposes (Murphy, 1987) and where deformations are constrained to be only moderately large, but the degree of approximation is unacceptably high if fine details of surface contour, including slope, are required. For instance, in Nielan (1982) and Murphy (1987), a variational principle is used to describe the load/deformation relationship where the Rayleigh-Ritz technique is applied assuming a parabolic transverse displacement. However, at various loading levels, the surface shape deviates significantly from the ideal parabolic shape needed for solar concentrator application; thus, deviations from the parabolic shape, which can seriously degrade the optical performance, are not predicted with this approach.

In recent work, the analysis of general membrane response has been carried out using the finite element method (Cook, 1982; Fried, 1982). Although this method is quite powerful and general, it can also be quite cumbersome and expensive to implement, especially for design problems, primarily because of the nonlinear geometric stiffness effect which must be considered in membrane problems.

The purpose of this work is to provide a highly accurate design assessment analysis method for evaluating the load, large deformation response of membrane structures composed of composite materials that is adequate for optical surface evaluations. Further, the model should be capable of being adaptable to a range of initial shape contours other than flat.

We base our study of large deformation of laminated membranes on the elasticity theory provided by Green and Adkins (1970). The formulation results in a system of algebraic and ordinary differential equations, where the derivatives of the pertinent variables are presented in explicit form. The derivatives are used in performing the integration at a point by using the Taylor series expansion. From the initial guess at a point, the solution is successively extended toward the known boundaries and the initial guess is modified till the boundary

[1] Currently at the Aerospace Engineering Department, University of Texas at Arlington, Arlington, TX 76019.

Contributed by the Applied Mechanics Division of The American Society of Mechanical Engineers for publication in the Journal of Applied Mechanics.

Discussion on this paper should be addressed to the Editorial Department, ASME, United Engineering Center, 345 East 47th Street, New York, N.Y. 10017, and will be accepted until two months after final publication of the paper itself in the Journal of Applied Mechanics. Manuscript received by the ASME Applied Mechanics Division, September 22, 1987; final revision, January 12, 1988.

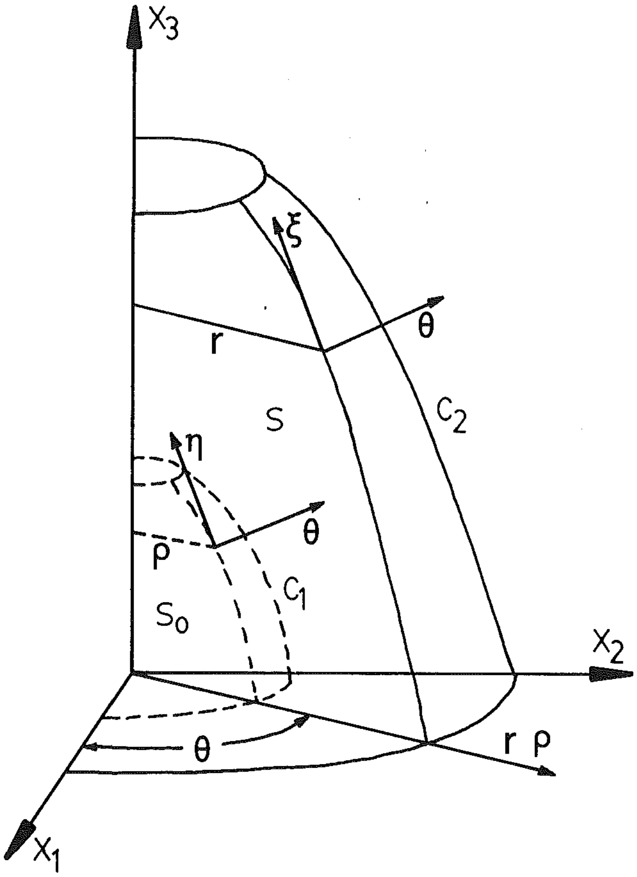

Fig. 1 Description of geometry and coordinates corresponding to the undeformed and deformed membranes

conditions are matched. The method is found to be very stable and accurate and is easily implemented on an IBM PC or compatible computer.

2 Problem Statement

We consider the large elastic deformations of initially flat membranes with axisymmetric geometry and loads. The axis of symmetry is the same in the deformed and the undeformed cases. It should be noted that preservation of the axis of symmetry does not require assumptions of uniformity, isotropy, and incompressibility. The material is assumed to behave linearly, which is a good assumption for a wide range of composite materials. The deviations from isotropy which are permissible under the assumption of an axially symmetric system of deforming forces are cylindrical orthotropy and quasi-isotropy. The axisymmetric membrane is subjected to uniformly distributed in-plane loads along the edges and a continuous distribution of normal traction on the surface. It is assumed that no singularities are present in the system of forces and in the surface of revolution defining the elastic body.

3 Problem Formulation

The plane curve C_1 (Fig. 1) generates an undeformed membrane surface by complete revolution about the axis x_3 in its plane. The curve C_1 has no double points and does not cut the axis x_3 except possibly at one or both of its endpoints. Similarly, the plane curve C_2 generates a deformed surface (Fig. 1). These curves thus become meridian curves on the middle surface; lines of latitude are formed by the family of curves which are orthogonal to the meridians at every point.

We choose a cylindrical polar coordinate system (ρ, θ, x_3) for the undeformed membrane surface, S_0, and a coordinate system (r, θ, x_3) for the deformed membrane surface, S. Another orthogonal curvilinear coordinate system can also be defined by two-dimensional curvilinear surface coordinates (η, θ) and (ξ, θ) in the undeformed (S_0) and deformed (S) surfaces, respectively, where η and ξ are coordinates along the meridian and θ along the latitudes.

From the symmetry of the system, it follows that the prinicipal directions of strain at a point coincide with the meridians, the lines of latitude, and the normal to the deformed middle surfaces y_3 (S and S_0). We denote the principal extension ratios in these directions by λ_1, λ_2, and λ_3, respectively. We then have

$$\left.\begin{aligned} \lambda_1 &= \frac{d\xi}{d\eta} \\ \lambda_2 &= \frac{r}{\rho} \\ \lambda_3 &= \frac{1}{\lambda_1\lambda_2} \text{ (incompressible)} \end{aligned}\right\}. \tag{1}$$

The variables, λ_1, λ_2, λ_3, r, ξ, and η, are independent of θ and may be regarded as functions of the single variable ρ. Alternatively, r, ξ, or η may be chosen as the independent variable.

3.1 Deformation Relationships. A line element of length dS in the surface of the deformed membrane is given by

$$dS = d\xi^2 + r^2 d\theta^2. \tag{2}$$

The expression for the corresponding element dS_0 in the undeformed middle surface is

$$dS_0^2 = d\eta^2 + \rho^2 d\theta^2. \tag{3}$$

Expressing the undeformed length in terms of the deformed coordinate system, we get, from equations (3) and (1),

$$dS_0^2 = \frac{1}{\lambda_1^2} d\xi^2 + \frac{r^2}{\lambda_2^2} d\theta^2. \tag{4}$$

The covariant and contravariant metric tensors associated with the coordinates in the middle plane of the deformed and undeformed membrane are [obtained from equations (2) and (4)]

$$A_{\alpha\beta} = \begin{bmatrix} 1 & 0 \\ 0 & r^2 \end{bmatrix}, \quad A_{\alpha\beta} = \begin{bmatrix} 1 & 0 \\ 0 & \dfrac{1}{r^2} \end{bmatrix}, \quad A = r^2 \tag{5}$$

$$a_{\alpha\beta} = \begin{bmatrix} \dfrac{1}{\lambda_1^2} & 0 \\ 0 & \dfrac{r^2}{\lambda_2^2} \end{bmatrix}, \quad a_{\alpha\beta} = \begin{bmatrix} \lambda_1^2 & 0 \\ 0 & \dfrac{\lambda_2^2}{r^2} \end{bmatrix}, \quad a = \frac{r^2}{\lambda_1^2\lambda_2^2} = \lambda_3^2 r^2. \tag{6}$$

The component of the Green strain tensor for the curvilinear coordinate system are obtained from equations (2) and (4) and are

$$\left.\begin{aligned} \gamma_{11} &= \frac{1}{2}\left(1 - \frac{1}{\lambda_1^2}\right) \\ \gamma_{22} &= \frac{r^2}{2}\left(1 - \frac{1}{\lambda_2^2}\right) \\ \gamma_{12} &= 0 \end{aligned}\right\} \tag{7}$$

The physical components of the strains are defined as

$$\epsilon_{\alpha\beta}=\frac{\gamma_{\alpha\beta}}{\sqrt{A_{\alpha\alpha}A_{\beta\beta}}}\,. \tag{8}$$

3.2 Constitutive Relationships. Let's consider an orthotropic layer with principal material directions 1 and 2. The stress-strain relationship is given by Jones (1975)

$$\begin{Bmatrix}\sigma_{11}\\ \sigma_{22}\\ \sigma_{12}\end{Bmatrix}=\begin{bmatrix}Q_{11} & Q_{12} & 0\\ & Q_{22} & 0\\ \text{sym} & & Q_{66}\end{bmatrix}\begin{Bmatrix}\epsilon_{11}\\ \epsilon_{22}\\ \epsilon_{12}\end{Bmatrix}. \tag{9}$$

The stress-strain relations (9) in the orthogonal coordinate system rotated by an angle (say, α) in a 1-2 plane are given by

$$\begin{Bmatrix}\sigma_{\xi\xi}\\ \sigma_{\theta\theta}\\ \sigma_{\xi\theta}\end{Bmatrix}=\begin{bmatrix}\bar{Q}_{11} & \bar{Q}_{12} & \bar{Q}_{16}\\ & \bar{Q}_{22} & \bar{Q}_{26}\\ \text{sym} & & \bar{Q}_{66}\end{bmatrix}\begin{Bmatrix}\epsilon_{\xi\xi}\\ \epsilon_{\theta\theta}\\ \epsilon_{\xi\theta}\end{Bmatrix} \tag{10}$$

(see the Appendix for definitions of Q_{ij} and $\bar{Q}_{ij}$). Figure 1 illustrates the coordinate system.

In the general case with body coordinates, there is coupling between shear strain and normal stresses and between shear stress and normal strains. Thus, in body coordinates, even an orthotropic layer behaves as an anisotropic layer. If we laminate these layers together, with each layer oriented at an arbitrary angle from the body coordinate system, the integrated constitutive relations become

$$\begin{Bmatrix}N_{\xi\xi}\\ N_{\theta\theta}\\ N_{\xi\theta}\end{Bmatrix}=\begin{bmatrix}A_{11} & A_{12} & A_{16}\\ & A_{22} & A_{26}\\ \text{sym} & & A_{66}\end{bmatrix}\begin{Bmatrix}\epsilon_{\xi\xi}\\ \epsilon_{\theta\theta}\\ \epsilon_{\xi\theta}\end{Bmatrix} \tag{11}$$

where

$$N_{\xi\xi}=\int_{-t/2}^{t/2}\sigma_{\xi\xi}dy_3,\ N_{\theta\theta}=\int_{-t/2}^{t/2}\sigma_{\theta\theta}dy_3,$$

$$N_{\xi\theta}=\int_{-t/2}^{t/2}\sigma_{\xi\theta}dy_3 \tag{12}$$

and

$$A_{ij}=\int_{-t/2}^{t/2}\bar{Q}_{ij}dy_3=\sum_{k=1}^{K}(\bar{Q}_{ij})_k(y_{3k}-y_{3k-1}), \tag{13}$$

where K is the total number of orthotropic layers and t is the total thickness of the laminated membrane. The laminates, with layers arranged in such a way that the stiffness coefficients A_{16} and A_{26} are zero and the others are related in such a way that the material behaves in the membrane plane like an isotropic material, are called quasi-isotropic material. An example of such a laminate is given in the Appendix. Note that a symmetric lay-up is required to get membrane strains and bending curvature decoupling. Equation (11) can be reduced for quasi-isotropic laminated membranes as

$$\begin{Bmatrix}N_{\xi\xi}\\ N_{\theta\theta}\end{Bmatrix}=\begin{bmatrix}A_{11} & A_{21}\\ A_{12} & A_{22}\end{bmatrix}\begin{Bmatrix}\epsilon_{\xi\xi}\\ \epsilon_{\theta\theta}\end{Bmatrix}, \tag{14}$$

$$N_{\xi\theta}=0\ .$$

3.3 Equilibrium Equations. The ξ and θ curves are the lines of principal curvature of the deformed middle surface. Let the normal curvatures in these directions be denoted by κ_ξ and κ_θ, respectively. The equilibrium equations for a general shell are derived by Green and Adkins (1970). These equilibrium equations reduce to

$$\left.\begin{aligned}&\frac{d}{d\xi}N_{\xi\xi}r=N_{\theta\theta}\frac{dr}{d\xi}\\ &\kappa_\xi N_{\xi\xi}+\kappa_\theta N_{\theta\theta}=P\\ &P=p_1-p_2\end{aligned}\right\}. \tag{15}$$

for the membrane case, where P is the resultant pressure in the direction of outward normal to the deformed middle surface.

3.4 Compatibility Conditions. The Mainardi-Codazzi equation ($C_{\alpha 1}\|_2=C_{\alpha 2}\|_1$) with $\alpha=2$ yields

$$\frac{d}{d\xi}(\kappa_\theta r)=\kappa_\xi\frac{dr}{d\xi}\,. \tag{16}$$

Also, from the elementary formula for the curvature of a plane curve, we obtain for a meridian curve in the deformed membrane

$$\kappa_\xi=\frac{d^2r/d\xi^2}{\left[1-\left(\dfrac{dr}{d\xi}\right)^2\right]^{1/2}}\,. \tag{17}$$

Substituting κ_ξ into equation (16) and integrating the resulting equation, we get

$$\kappa_\theta r=\left[1-\left(\frac{dr}{d\xi}\right)^2\right]^{1/2}. \tag{18}$$

If we assume that κ_θ is finite and the surface cuts the axis of symmetry orthogonally at r equal to zero, then from equation (18),

$$\left.\frac{dr}{d\xi}\right|_{r=0}=1.$$

We get the alternative relation from equations (17) and (18):

$$\kappa_\xi\kappa_\theta r=-\frac{d^2r}{d\xi^2}\,. \tag{19}$$

From equations (15) and (16), we obtain

$$N_{\xi\xi}\frac{d}{d\xi}(\kappa_\theta r)+\kappa_\theta\frac{d}{d\xi}(N_{\xi\xi}r)=P\frac{dr}{d\xi}\,. \tag{20}$$

Integrating equation (20), we get

$$\kappa_\theta N_{\xi\xi}=\frac{1}{r^2}\int^r Prdr+\frac{L}{r^2}\,, \tag{21}$$

where L is constant. When P is constant, this becomes

$$\kappa_\theta N_{\xi\xi}=\frac{1}{2}P+\frac{L}{r^2}\,. \tag{22}$$

If the deformed sheet cuts the axis of symmetry orthogonally, we have at the point $r=0$

$$\kappa_\xi=\kappa_\theta=\kappa;\quad \lambda_1=\lambda_2=\lambda\ (\text{say});\quad N_{\xi\xi}=N_{\theta\theta}=N\ (\text{say}).$$

Equation (22) and second part of equation (15) yield

$$2\kappa N=P,\quad L=0. \tag{23}$$

4 Deformation of Circular Quasi-Isotropic Membrane

Let's consider the undeformed body to be a uniform laminated membrane consisting of incompressible orthotropic layers. The membrane is clamped at a radius "a" with initial in-plane tension N_0. The membrane is inflated by a uniform pressure P applied transverse to the surface so that it takes an axisymmetric form. The deformation thus produced may be examined by using the results of an axially symmetric membrane. The procedure follows Green and Adkins' (1970) approach, with the exception that the constitutive relations being used are for a laminated composite membrane. The commonly used engineering constants for the orthotropic material are incorporated in the analysis. The constitutive relations used by Green and Adkins are of physical significance only in the case of rubber-like materials. In equation (10), we have

$$\eta=\rho, \quad \lambda_1=\frac{d\xi}{d\rho} \tag{24}$$

and, in the remainder of the equations, the independent variable may be changed from ξ to ρ by making use of equation (24). These equations can be solved for the determination of the unknowns r, λ_1, λ_2, λ_3, $N_{\xi\xi}$, $N_{\theta\theta}$, κ_ξ, and κ_θ as functions of ρ. Equation (24) defines the geometric relationship among coordinates in an undeformed shape. Appropriate relationships may be used for other undeformed shapes.

If the values of λ_1, λ_2, λ_3, κ_ξ, and κ_θ are known at the point P initially at (ρ, θ) in the middle plane of the undeformed membrane, the remaining quantities and their first derivatives may be found from the scheme given here:

(1) $$\lambda_3=\frac{1}{\lambda_1\lambda_2} \tag{25}$$

(7),(8),(14) $$\begin{Bmatrix} N_{\xi\xi} \\ N_{\theta\theta} \end{Bmatrix} = \begin{bmatrix} A_{11} & A_{21} \\ A_{12} & A_{22} \end{bmatrix} \begin{Bmatrix} \dfrac{1}{2(1-1/\lambda_1^2)} \\ \dfrac{1}{2(1-1/\lambda_2^2)} \end{Bmatrix} \tag{26}$$

(1) $$r=\lambda_2\rho \tag{27}$$

(18) $$\frac{dr}{d\rho}=\lambda_1(1-\kappa_\theta^2 r^2)^{1/2} \tag{28}$$

(27) $$\frac{d\lambda_2}{d\rho}=\frac{1}{\rho}\left(\frac{dr}{d\rho}-\lambda_2\right) \tag{29}$$

(16) $$\frac{d\kappa_\theta}{d\rho}=\frac{1}{r}\frac{dr}{d\rho}(\kappa_\xi-\kappa_\theta) \tag{30}$$

(15) $$\frac{dN_{\xi\xi}}{d\rho}=-\frac{1}{r}\frac{dr}{d\rho}(N_{\xi\xi}-N_{\theta\theta}) \tag{31}$$

(26) $$\frac{d\lambda_1}{d\rho}=\frac{\lambda_1^3}{2A_{11}}\left(\frac{dN_{\xi\xi}}{d\rho}-\frac{2A_{12}}{\lambda_2^3}\frac{d\lambda_2}{d\rho}\right) \tag{32}$$

(26) $$\frac{dN_{\theta\theta}}{d\rho}=2\left[\frac{A_{12}}{\lambda_1^3}\frac{d\lambda_1}{d\rho}+\frac{A_{22}}{\lambda_2^3}\frac{d\lambda_2}{d\rho}\right] \tag{33}$$

(15) $$\frac{d\kappa_\xi}{d\rho}=-\frac{1}{N_{\xi\xi}}\left(\kappa_\xi\frac{\partial N_{\xi\xi}}{\partial p}+\kappa_\theta\frac{\partial N_{\theta\theta}}{\partial\rho}+N_{\theta\theta}\frac{\partial\kappa_\theta}{\partial\rho}\right). \tag{34}$$

Equations (25)–(34) are derived by proper substitution or differentiation from the equation numbers given on the left side. In each of these equations, the quantity on the left side is expresed as a function of the known quantities λ_1, λ_2, κ_ξ, and κ_θ, or quantities that can be determined from them by means of the preceding equations in the scheme. All the quantities are defined as a function of ρ only.

Expressions for the second and higher-order derivatives of r, λ_1, λ_2, κ_ξ, κ_θ, $N_{\xi\xi}$, and $N_{\theta\theta}$ in terms of quantities previously determined may be obtained by successive differentiation of equations (28)–(34). Alternatively, for the second derivative of r, we obtain from equations (19) and (24),

$$\frac{d^2r}{d\rho^2}=\frac{1}{\lambda_1}\left(\frac{dr}{d\rho}\frac{d\lambda_1}{d\rho}-\kappa_\xi\kappa_\theta r\lambda_1^3\right). \tag{35}$$

Now, we will consider the center of the deformed membrane where r is equal to zero where the symmetric conditions exist:

$$\kappa_\xi=\kappa_\theta=\kappa;\ \lambda_1=\lambda_2=\lambda;\ N_{\xi\xi}=N_{\theta\theta}=N;$$
$$\frac{dr}{d\rho}=\lambda;\ \lambda_3=\frac{1}{\lambda^2}. \tag{36}$$

It is assumed that κ, λ, and N are finite and nonzero at the center of the deformed membrane. Equations (26) and the second part of equation (15) yield

$$N=\frac{1}{2}(A_{11}+A_{12})(1-1/\lambda^2) \tag{37}$$

$$2\kappa N=P, \tag{38}$$

respectively, when $r=0$. Substituting the symmetric conditions (36) into equations (29)–(35), it follows that at the center of the deformed membrane

$$\frac{d^2r}{d\rho^2}=\frac{d\lambda_1}{d\rho}=\frac{d\lambda_2}{d\rho}=\frac{d\kappa_\xi}{d\rho}=\frac{d\kappa_\theta}{d\rho}$$
$$=\frac{dN_{\xi\xi}}{d\rho}=\frac{dN_{\theta\theta}}{d\rho}=0. \tag{39}$$

Rewriting equation (15) in the form (using equation (24))

$$\frac{d}{d\rho}(N_{\xi\xi}r)=N_{\theta\theta}\frac{dr}{d\rho}, \tag{40}$$

differentiating twice, and inserting the conditions (36) and (37) at the center, we get

$$3\frac{d^2N_{\xi\xi}}{d\rho^2}=\frac{d^2N_{\theta\theta}}{d\rho^2}. \tag{41}$$

Similarly, from equation (20) we have

$$3\frac{d^2\kappa_\theta}{d\rho^2}=\frac{d^2\kappa_\xi}{d\rho^2}. \tag{42}$$

With the use of equations (37)–(42), the second derivative of the second part of equation (15) yields

$$\kappa\frac{d^2N_{\xi\xi}}{d\rho^2}+N\frac{d^2\kappa_\theta}{d\rho^2}=0. \tag{43}$$

Again, by differentiating equation (35) and using the symmetric conditions at the center, we have

$$\frac{d^3r}{d\rho^3}-\frac{d^2\lambda_1}{d\rho^2}=-\kappa^2\lambda^2, \tag{44}$$

and by differentiating equation (27) three times, we get

$$\frac{d^3r}{d\rho^3}=3\frac{d^2\lambda_2}{d\rho^2}. \tag{45}$$

Equations (44) and (45) yield

$$3\frac{d^2\lambda_2}{d\rho^2}-\frac{d^2\lambda_1}{d\rho^2}=-\kappa\lambda^3. \tag{46}$$

Two more relations are obtained by differentiating equation (26) twice and introducing the symmetric conditions at the center. Thus,

$$\frac{\partial^2N_{\xi\xi}}{d\rho^2}=\frac{2}{\lambda^3}\left(A_{11}\frac{d^2\lambda_1}{d\rho^2}+A_{12}\frac{d^2\lambda_2}{d\rho^2}\right) \tag{47}$$

$$\frac{\partial^2N_{\theta\theta}}{d\rho^2}=\frac{2}{\lambda^3}\left(A_{12}\frac{d^2\lambda_1}{d\rho^2}+A_{22}\frac{d^2\lambda_2}{d\rho^2}\right). \tag{48}$$

Rearranging equations (41) and (46)–(48), we get

$$\frac{d^2\lambda_1}{d\rho^2}=\frac{3A_{12}-A_{22}}{9A_{11}-A_{22}}\kappa^2\lambda^3 \tag{49}$$

$$\frac{d^2\lambda_2}{d\rho^2}=\frac{A_{12}-3A_{11}}{9A_{11}-A_{22}}\kappa^2\lambda^3 \tag{50}$$

$$\frac{d^2N_{\xi\xi}}{d\rho^2}=\frac{A_{12}^2-A_{11}A_{22}}{9A_{11}-A_{22}}2\kappa^2. \tag{51}$$

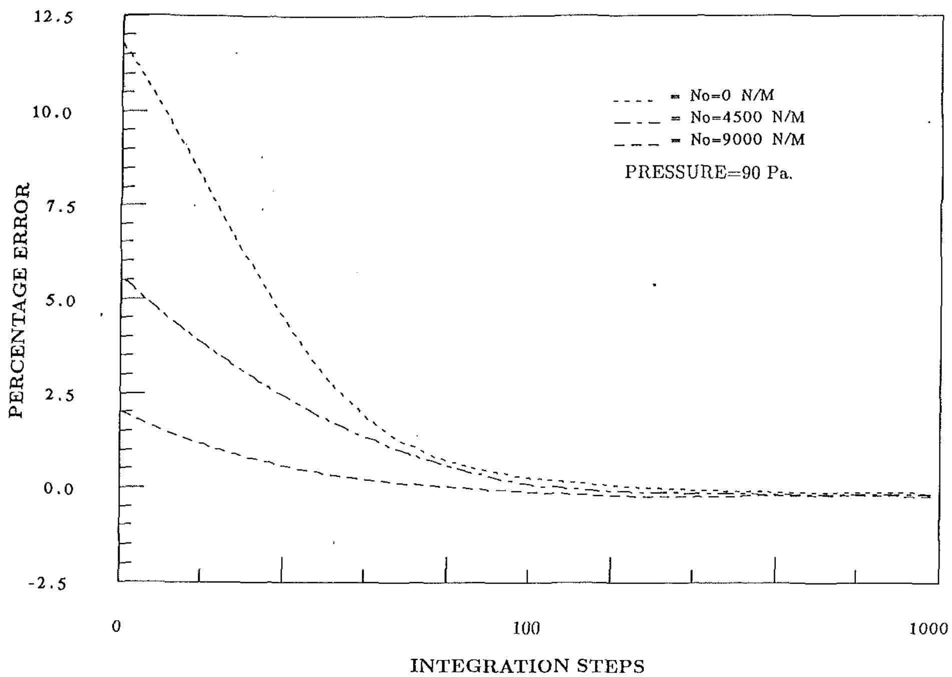

Fig. 2 Convergence of center deflection with number of integration steps

Substituting these equations into equations (41)-(43) yields expressions for second derivatives of $N_{\theta\theta}$, κ_ξ, and κ_θ at the center. By continued differentiation of equations (27)-(35), one can show that all odd-order derivatives of λ_1, λ_2, K_ξ, κ_θ, T_ξ, T_θ, and $dr/d\rho$ vanish at $\rho = 0$. The fourth and higher-order derivatives of these quantities can be evaluated by a procedure similar to the foregoing, but the resulting expressions will be of increasing complexity.

4.1 Numerical Algorithm. The numerical algorithm is based on the use of a Taylor series expansion to do numerical step-by-step integration. The following steps are incorporated into the numerical computation:

1 Assume λ at the center of the membrane.

2 Calculate N and κ from equations (37) and (38).

3 Evaluate values of the second derivatives of λ_1, λ_2, κ_ξ, κ_θ, $N_{\xi\xi}$, and $N_{\theta\theta}$ at the center by means of equations (49)-(51) and (41)-(43).

4 Approximate values of λ_1, λ_2, κ_ξ, κ_θ, $N_{\xi\xi}$, and $N_{\theta\theta}$ at the point $(\Delta\rho, \theta)$ can then be calculated from a Taylor series expansion (truncated) of the type

$$[\lambda_1]_{\Delta\rho} = \lambda_{\rho=0} + \frac{1}{2}\left[\frac{d^2\lambda_1}{d\rho^2}\right]_{\rho=0} (\Delta\rho)^2.$$

5 First derivatives of λ_1, λ_2, κ_ξ, and κ_θ are obtained by means of the system of equations (25)-(34) at the point $\Delta\rho$.

6 The values of λ_1, λ_2, κ_ξ, κ_θ, $N_{\xi\xi}$, and $N_{\theta\theta}$ at $n\Delta\rho$ from the values at $(n-1)\Delta\rho$ are obtained by using the Taylor series expansion of the type

$$[\lambda_1]_{n\Delta\rho} = [\lambda_1]_{(n-1)\Delta\rho} + \left[\frac{d\lambda_1}{d\rho}\right]_{(n-1)\Delta\rho} \Delta\rho + \ldots .$$

7 Steps 5 and 6 are repeated until the boundary is reached.

8 If the boundary conditions are matched, the process is terminated; otherwise the initial assumptions at the center are modified appropriately and the algorithm is repeated.

4.2 Profile of the Inflated Membrane. To determine the shape of the profile of the inflated membrane, we observe that

$$\left(\frac{d\xi}{d\rho}\right)^2 = \left(\frac{dr}{d\rho}\right)^2 + \left(\frac{dx_3}{d\rho}\right)^2. \tag{52}$$

This relation, with equations (24) and (28), yields

$$\frac{dx_3}{d\rho} = -\kappa_\theta\lambda_1 r. \tag{53}$$

The sign is chosen to be negative because x_3 is a decreasing function of ρ. This relation and those obtained from it by differentiation, with respect to ρ, enable the derivatives of x_3 to be calculated from the previously determined values of κ_θ, λ_1, and r and their derivatives. The successive determination of x_3 at all points of the membrane proceeds with the help of a Taylor series. The values of x_3 at ρ equal to zero are adjusted so that x_3 is equal to zero at the fixed boundary.

5 Discussion of Results

Representative results showing the applicability and accuracy of the aforementioned numerical modeling procedure for the study of a typical membrane are described next. All the results presented are for an initially flat, quasi-isotropic, glass-epoxy laminated membrane with glass fibers oriented in the $[0/90/\pm 45]$ directions. The material properties used in the numerical calculation are as given below:

$$E_1 = 29.94 \text{ GPa} \qquad G_{12} = 4.0 \text{ GPa}$$
$$E_2 = 8.45 \text{ GPa} \qquad \nu_{12} = 0.32 \tag{54}$$

The equivalent isotropic properties for the laminated membrane are used in the energy method and the finite element method. These equivalent isotropic properties, as derived from the relationships provided in the Appendix, are

$$E = 32.1 \text{ GPa}, \qquad \nu = 0.276. \tag{55}$$

A 15-m diameter circular membrane clamped at the edge is considered. The thickness of the membrane is 0.254 mm, and a 90 Pa uniform pressure load normal to the membrane surface is assumed. Finally, various levels of initial pretension are used to illustrate the relative dominance of various response mechanisms.

Figure 2, which gives error size (defined as the difference in

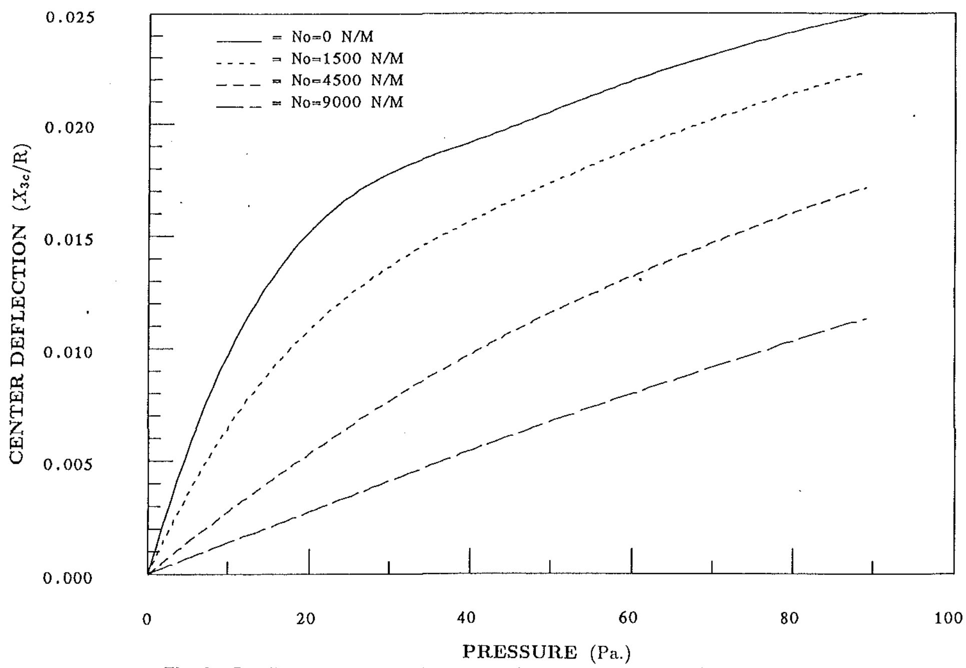

Fig. 3 Predicted variation of center deflection with the applied normal pressure for several values of initial membrane pretension

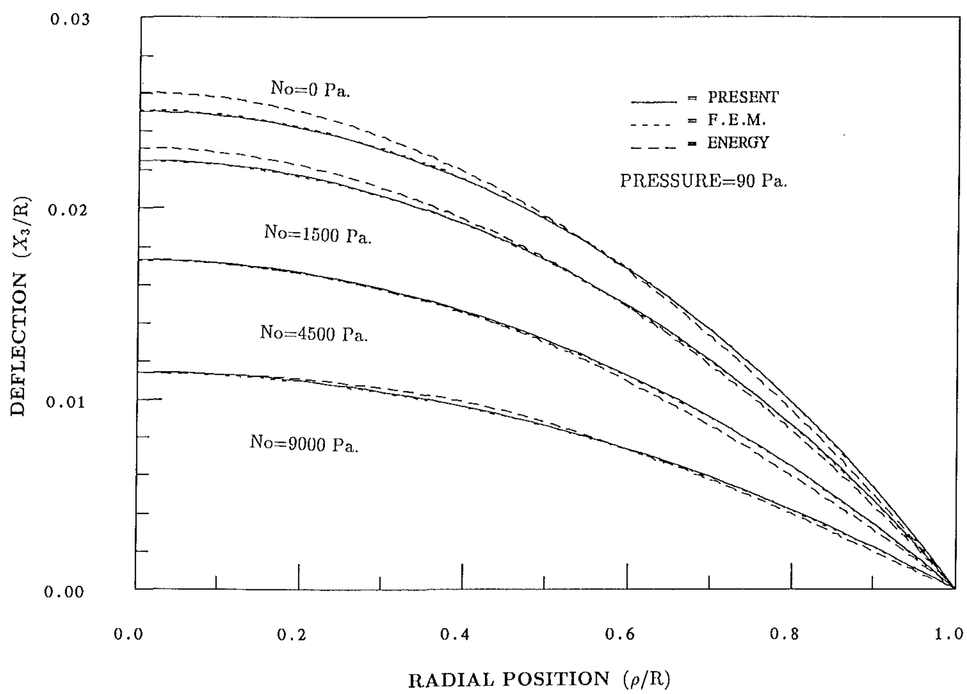

Fig. 4 Deflected shape profile of a circular simply-supported membrane

the predicted membrane center deflection calculated by the finite element method and the current method, respectively) as a function of the number of integration steps, shows the convergence of the center displacement for several different membrane pretension levels. The displacement converges rapidly as the number of integration steps is increased. The pretensioning of the membrane results in relatively lower error, even with a large step size. This is caused primarily by a geometric stiffening effect introduced by higher levels of pretension. The error in center deflection is within one percent of the final value for all pretension cases when the number of integration steps is greater than 100.

The variation in center deflection with pressure is presented in Fig. 3 for four different membrane pretension levels. The center deflection decreases as pretension increases for a given uniform pressure. This occurs because higher pretensions add higher levels of stiffness as the membrane changes shape to carry the load. Further, the center deflection variation with pressure becomes more linear as pretension increases. The variation is, however, quite nonlinear for lower pretensions. The deflection will increase rapidly with an initial change in pressure, but the membrane will become stiffer at higher pressures as the geometric stiffness starts dominating.

Deformed profiles of a membrane for various initial tensions are shown in Fig. 4. They are compared with the nonlinear ANSYS finite element solutions and the energy

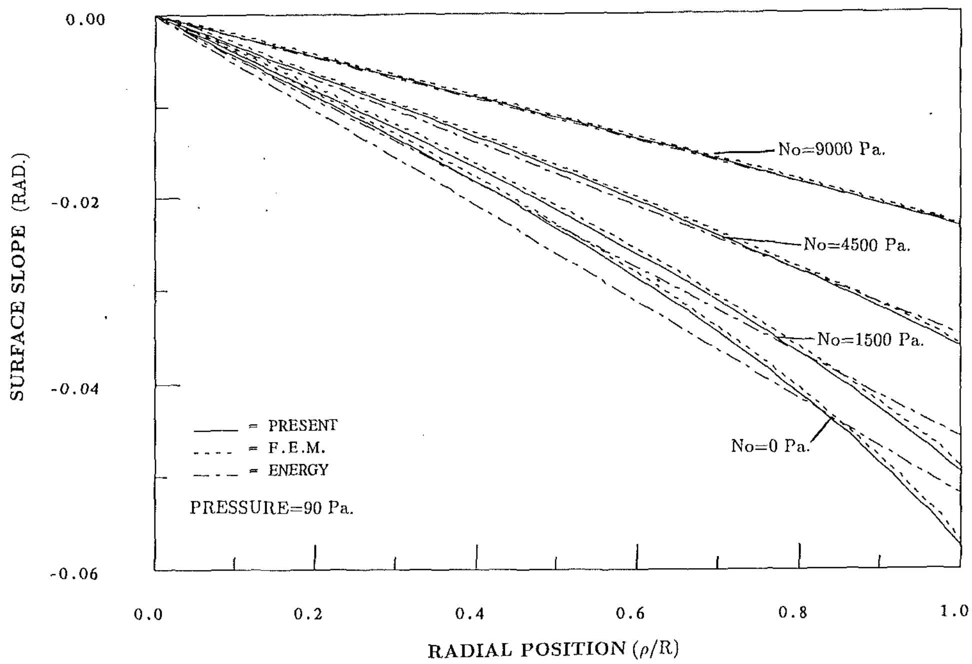

Fig. 5 Comparison of predicted surface slope variations with radial position using three analysis methodologies

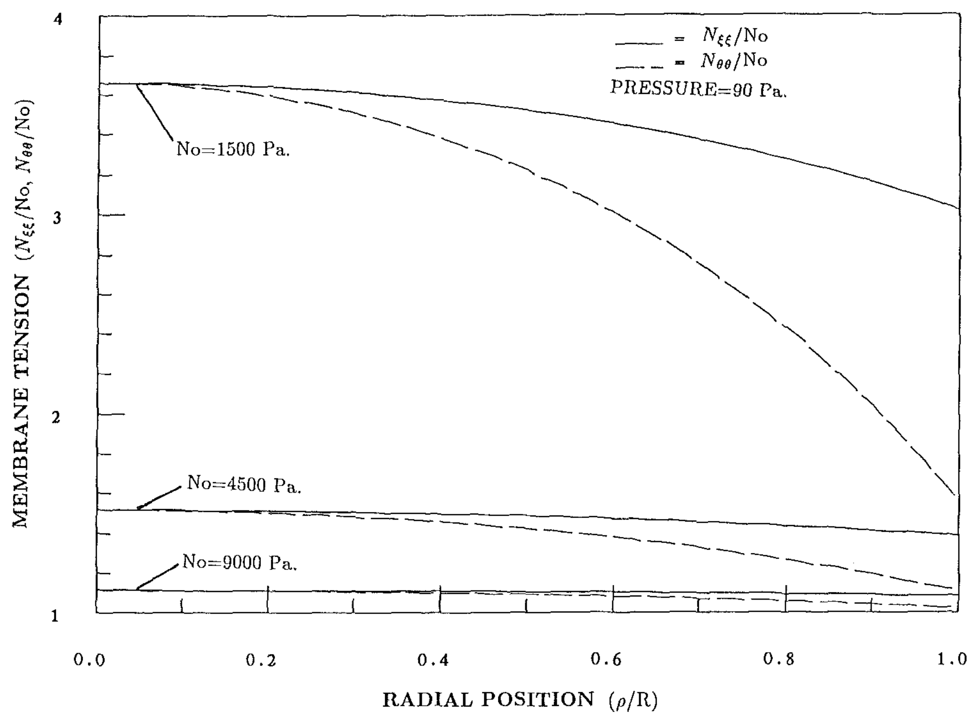

Fig. 6 Predicted variation in meridinal and latitudinal tension with radial position for three initial pretension values

method with assumed parabolic deformed shape (Murphy, 1987). Forty-one axisymmetric, conical shell elements were used in the finite element simulation. As shown in Fig. 4, the present analysis results are in excellent agreement with the nonlinear finite element analysis; similar agreement has been obtained in numerous other membrane design comparisons using the finite element and the current analysis procedures. Also shown in Fig. 4, for comparison purposes, are predicted results using the variational method (Murphy, 1987) which assumes an initially parabolic shape. It is seen that these results agree less well with the other predictions, especially at higher initial pretensions.

A more stringent comparison for the predicted results is given in Fig. 5, where the predicted surface slope as a function of position is illustrated for four initial pretension levels, using each of three predictive methodologies. Local surface slopes are important, especially in applications where the deformed surface is used for reflection of the incident solar radiation. It is evident that the surface slope deviates considerably from the linear slope variation of the parabolic deformed surface,[2]

[2]Actually, a uniform pressure loading with uniform membrane tension would result in a spherical shape. We refer to parabolic contours here because that is the desired shape from an optical concentrator perspective and also because the slope differences between the ideal parabola and the best spherical approximation to the parabola is quite small for the deformation levels considered here.

especially for very large deformations and low initial pretensions (Fig. 5). In the case of the finite element method, the surface slopes are obtained by simple differencing techniques from the nodal displacements. Therefore, their accuracy depends on the number of finite elements. It is seen that the surface slope results obtained from the finite element analysis are in good agreement with the results from the present analysis, although it should be noted that the one obtained from the finite element analysis depends on the number of elements. The obvious inadequacy of the simple variational technique using an assumed parabolic displacement field is also seen.

The predicted meridinal and latitudinal tension variations with radial position are shown in Fig. 6 for three pretension levels. It is seen that the tensions vary increasingly in a nonlinear manner at lower initial tensions. This is because the relative superimposed tension due to deflection decreases as the initial tension increases. Further, both tension components tend to be uniform for a higher initial tension. Finally, the latitudinal tension decreases at a faster rate with radius than does the meridinal tension.

The results presented here demonstrate that the method based on large elastic deformations can easily be implemented and may be used to get the accurate quantitative information related to laminated membrane design. The technique is capable of handling very large deformations of laminated membranes with initial tension. The method is easily implemented on a microcomputer, and the analysis can be preformed inexpensively and in relatively little time compared to finite element analysis. The critical results (e.g., surface slopes) are obtained with a high degree of accuracy as compared with the finite element analysis.

References

Adkins, J. E., and Rivlin, R. S., 1952, "Large Elastic Deformations of Isotropic Materials—The Deformation of Thin Shells," *Philosophical Transactions of the Royal Society of London*, Vol. 244, No. 888, pp. 505-531.

Cook, W. A., 1982, "A Finite Element Model for Nonlinear Shells of Revolution," *Internatioanl Journal for Numerical Methods in Engineering*, Vol. 18, pp. 135-149.

Fried, I., 1982, "Finite Element Computation of large Rubber Membrane Deformations," *International Journal for Numerical Methods in Engineering*, Vol. 18, pp. 653-660.

Green, A. E., and Adkins, J. E., 1970, *Large Elastic Deformations*, Clarendon Press, Oxford, U.K., pp. 161-169.

Jones, R. M., 1975, *Mechanics of Composite Materials*, McGraw-Hill, New York, pp. 45-59.

Murphy, L. M., 1987, "Moderate Axisymmetric Deformations of Optical Membrane Surfaces," ASME *Journal of Solar Energy Engineering*, Vol. 109, pp. 111-120.

Nielan, P. E., 1982, "Large Elastic Deformation of Nonlinear Axisymmetric Membrane: A Variational Approach," Report No. DE83-001851, Sandia Labs., Livermore, Calif.

Soedel, W., 1981, *Vibration of Shells and Plates*, Marcel Dekker, New York, pp. 124-148.

APPENDIX

$$Q_{11}=\frac{E_1}{1-\nu_{12}\nu_{21}}$$

$$Q_{22}=\frac{E_2}{1-\nu_{12}\nu_{21}}$$

$$Q_{12}=\frac{\nu_{12}E_2}{1-\nu_{12}\nu_{21}}=\frac{\nu_{21}E_1}{1-\nu_{12}\nu_{21}}$$

$$Q_{66}=G_{12}$$

$$\bar{Q}_{11}=U_1+U_2\cos(2\alpha)+U_3\cos(4\alpha)$$

$$\bar{Q}_{12}=U_4-U_3\cos(4\alpha)$$

$$\bar{Q}_{22}=U_1-U_2\cos(2\alpha)+U_3\cos(4\alpha)$$

$$\bar{Q}_{16}=\frac{1}{2}U_2\sin(2\alpha)+U_3\sin(4\alpha)$$

$$\bar{Q}_{26}=\frac{1}{2}U_2\sin(2\alpha)-U_3\sin(4\alpha)$$

$$\bar{Q}_{66}=U_5-U_3\cos(4\alpha)$$

where

$$U_1=(3Q_{11}+3Q_{22}+2Q_{12}+4Q_{66})/8$$

$$U_2=(Q_{11}-Q_{22})/2$$

$$U_3=(Q_{11}+Q_{22}-2Q_{12}-4Q_{66})/8$$

$$U_4=(Q_{11}+Q_{22}+6Q_{12}-4Q_{66})/8$$

$$U_5=(Q_{11}+Q_{22}-2Q_{12}+4Q_{66})/8.$$

For a $[0\text{ deg}/90\text{ deg}/\pm 45\text{ deg}]_s$ quasi-isotropic laminate,

$$A_{11}=A_{22}=4tU_1$$

$$A_{12}=4tU_4$$

$$A_{66}=4tU_5$$

$$A_{16}=A_{26}=0$$

where t is total thickness.

Effective Elastic Moduli of Ribbon-Reinforced Composites

Y. H. Zhao[1]

G. J. Weng
Professor,
Mem. ASME

Department of Mechanics and
Materials Science,
Rutgers University,
New Brunswick, NJ 08903

Based on the Eshelby-Mori-Tanaka theory the nine effective elastic constants of an orthotropic composite reinforced with monotonically aligned elliptic cylinders, and the five elastic moduli of a transversely isotropic composite reinforced with two-dimensional randomly-oriented elliptic cylinders, are derived. These moduli are given in terms of the cross-sectional aspect ratio and the volume fraction of the elliptic cylinders. When the aspect ratio approaches zero, the elliptic cylinders exist as thin ribbons, and these moduli are given in very simple, explicit forms as a function of volume fraction. It turns out that, in the transversely isotropic case, the effective elastic moduli of the composite coincide with Hill's and Hashin's upper bounds if ribbons are harder than the matrix, and coincide with their lower bounds if ribbons are softer. These results are in direct contrast to those of circular fibers. Since the width of the Hill-Hashin bounds can be very wide when the constituents have high modular ratios, this analysis suggests that the ribbon reinforcement is far more effective than the traditional fiber reinforcement.

1 Introduction

The effective elastic property of a two-phase composite is known to depend on the microgeometry of the reinforcing phase. While considerable work apparently has been done to estimate the elastic behavior of the particle and fiber-reinforced composites, the cross-section of fibers in the latter case has mostly been treated as circular. When the fibers exist in the form of elliptic cylinders such that the aspect ratio of the cross-section (the ratio of thickness to width) is not necessarily one, this shape parameter may have a significant effect on the overall moduli of the composite. In particular, when the aspect ratio approaches zero, the reinforcing fibers become ribbons, which, being able to be easily processed, will have great potential applications if the resulting composite property is superior to that reinforced with circular fibers. Motivated by such an observation, our objective here is to examine the influence of the aspect ratio on the effective moduli of the composite, with a special reference to the property of ribbon-strengthened solids.

Two types of composites will be considered here. The first one, as shown in Fig. 1(*a*), is reinforced with monotonically-aligned, uniformly-dispersed elliptic cylinders or ribbons, so that the material, as a whole, is orthotropic. Nine independent elastic constants are to be determined as a function of aspect ratio, α, and volume fraction, c_1, of the cylinders. The second type, as depicted in Fig. 1(*b*), contains randomly-oriented elliptic cylinders or ribbons in the transverse plane, resulting in a transversely-isotropic composite. The five independent elastic moduli associated with such a composite will be derived, and the results will be checked against Hill's (1964) and Hashin's (1965) bounds.

The shape of the elliptic cylinders and ribbons will be represented, for simplicity, by an ellipsoid, with the principal axis extending to infinity marked as axis 1. We only need to consider

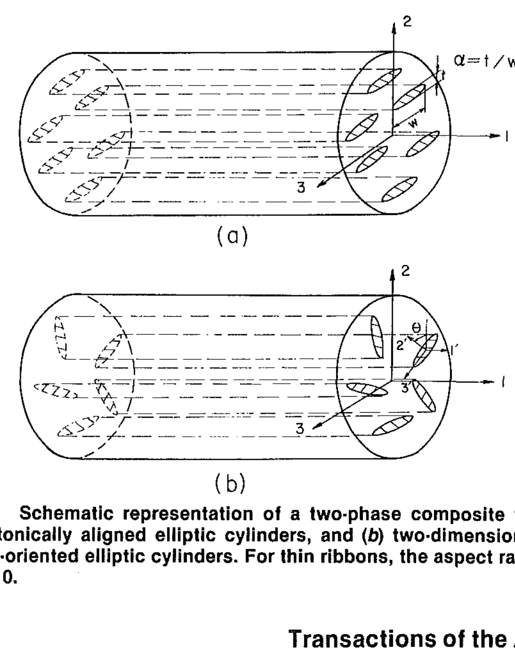

Fig. 1 Schematic representation of a two-phase composite with (*a*) monotonically aligned elliptic cylinders, and (*b*) two-dimensional randomly-oriented elliptic cylinders. For thin ribbons, the aspect ratio $\alpha = t/w \to 0$.

[1]Visiting Scholar from Shenyang Institute of Architectural Engineering, Shenyang, Liaoning, People's Republic of China.

Contributed by the Applied Mechanics Division of THE AMERICAN SOCIETY OF MECHANICAL ENGINEERS for publication in the JOURNAL OF APPLIED MECHANICS.

Discussion on this paper should be addressed to the Technical Editor, Leon M. Keer, The Technological Institute, Northwestern University, Evanston, IL 60201, and will be accepted until two months after final publication of the paper itself in the JOURNAL OF APPLIED MECHANICS. Manuscript received by the ASME Applied Mechanics Division, August 23, 1988; final revision, April 10, 1989.

the range of aspect ratio from 0 to 1, as the corresponding results from 1 to ∞ can be readily recovered from those results by interchanging the 2 and 3-axes. This representation, together with the assumption that fibers and the matrix are perfectly bonded, allows one to make use of Eshelby's (1957) solution of an ellipsoidal inclusion. To deal with the condition of finite concentration of reinforcing phase, Mori-Tanaka's (1973) mean-field theory will be employed. This method has previously been used by Chow (1978), Taya and Chou (1981), Taya and Mura (1981), and Weng (1984), among others, to examine various elastic properties of composites, and has proven to be reliable. In particular, it was shown (Weng, 1984) that when the inclusions are spherical, the derived bulk and shear moduli of the composite coincide with Hashin and Shtrikman's (1963) lower bounds if the inclusion is the harder phase, and coincide with their upper bounds if the inclusion is the softer. When the three-dimensional, randomly-oriented inclusions are spheroidal in shape, the resulting bulk and shear moduli—with the aspect ratio varying from 0 to ∞—were found by Tandon and Weng (1986) to always lie on or within the Hashin-Shtrikman bounds (1963), with the spherical inclusions and thin disks taking the opposite ends. Moreover, when both phases possess an identical shear rigidity, the bulk modulus of the composite containing spherical particles coincides with Hill's (1963) exact solution. Comparisons with experimental data from some two and three-phase composites have also shown good agreement (see Weng, 1984, for other implications).

To pave the way for the subsequent analysis, let us first briefly recapitulate the Mori-Tanaka method (1973) in the following section for the simple monotonically aligned composite. For brevity, the familiar symbolic notation, with a bold-faced Greek letter representing the second-order tensor, and the ordinary capitol letter representing the fourth-order one, will be adopted there. Throughout the text, the matrix phase will be referred to as phase 0, and the elliptic cylinders or ribbons (the inclusions) as phase 1. The bulk and shear moduli of the rth phase will be denoted by κ_r and μ_r, respectively, and its volume fraction will be denoted by c_r.

2 The Mori-Tanaka Method for a Monotonically Aligned Composite

Consider a two-phase composite containing homogeneously dispersed inclusions. To facilitate the determination of mean stress in the two constituent phases, we may introduce an identically-shaped comparison material, with the property of the matrix. We now subject both the composite and the comparison material to the same boundary traction which would give rise to a homogeneous stress $\bar{\boldsymbol{\sigma}}$. The strain in the comparison material is then given by

$$\boldsymbol{\epsilon}^0 = L_0^{-1}\bar{\boldsymbol{\sigma}}, \tag{1}$$

where L_0 is the elastic moduli tensor of the matrix, and its inverse indicates its elastic compliance.

Due to the presence of inclusions, the mean strain of the matrix in the composite material generally differs from $\boldsymbol{\epsilon}^0$, and so does it mean stress from the externally applied $\bar{\boldsymbol{\sigma}}$. If we denote these differences from $\boldsymbol{\epsilon}^0$ and $\bar{\boldsymbol{\sigma}}$ by $\tilde{\boldsymbol{\epsilon}}$ and $\tilde{\boldsymbol{\sigma}}$ respectively, the average stress of the matrix in the composite system is given by

$$\boldsymbol{\sigma}^{(0)} = \bar{\boldsymbol{\sigma}} + \tilde{\boldsymbol{\sigma}} = L_0(\boldsymbol{\epsilon}^0 + \tilde{\boldsymbol{\epsilon}}). \tag{2}$$

The average stress and strain of the inclusions further differ from those of the surrounding matrix, say, by some additional perturbed values $\boldsymbol{\sigma}^{pt}$ and $\boldsymbol{\epsilon}^{pt}$. Then, by means of Eshelby's (1957) equivalence principle the average stress of the inclusions can be written as

$$\begin{aligned}\boldsymbol{\sigma}^{(1)} = \bar{\boldsymbol{\sigma}} + \tilde{\boldsymbol{\sigma}} + \boldsymbol{\sigma}^{pt} &= L_1(\boldsymbol{\epsilon}^0 + \tilde{\boldsymbol{\epsilon}} + \boldsymbol{\epsilon}^{pt}) \\ &= L_0(\boldsymbol{\epsilon}^0 + \tilde{\boldsymbol{\epsilon}} + \boldsymbol{\epsilon}^{pt} - \boldsymbol{\epsilon}^*),\end{aligned} \tag{3}$$

where L_1 is the elastic moduli tensor of the inclusions, and $\boldsymbol{\epsilon}^*$ is Eshelby's equivalence transformation strain (or eigenstrain, Mura, 1987), introduced into the regions occupied by the inclusions so that L_1 could be replaced by L_0 to provide the same $\boldsymbol{\sigma}^{(1)}$. The perturbed strain $\boldsymbol{\epsilon}^{pt}$ is taken to be related to $\boldsymbol{\epsilon}^*$ through Eshelby's relation

$$\boldsymbol{\epsilon}^{pt} = S\boldsymbol{\epsilon}^*, \tag{4}$$

where S is Eshelby's transformation tensor. The fourth-rank S tensor possesses the symmetry $S_{ijkl} = S_{jikl} = S_{ijlk}$; its components for an elliptic cylinder are given in the Appendix (A1).

Since the weighted average of $\boldsymbol{\sigma}^{(r)}$ must be in balance with the externally applied $\bar{\boldsymbol{\sigma}}$ (namely $\bar{\boldsymbol{\sigma}} = c_1\boldsymbol{\sigma}^{(1)} + c_0\boldsymbol{\sigma}^{(0)}$), one has

$$\tilde{\boldsymbol{\sigma}} = -c_1\boldsymbol{\sigma}^{pt}, \text{ or } \tilde{\boldsymbol{\epsilon}} = -c_1(\boldsymbol{\epsilon}^{pt} - \boldsymbol{\epsilon}^*). \tag{5}$$

By substituting (4) and (5) into the last of (3), one can find $\boldsymbol{\epsilon}^*$ in terms of $\boldsymbol{\epsilon}^0$, which is further related to $\bar{\boldsymbol{\sigma}}$ by (1).

Similarly, by considering the weighted mean of the strain components, one finds that the total strain of the composite is given by

$$\bar{\boldsymbol{\epsilon}} = \boldsymbol{\epsilon}^0 + c_1\boldsymbol{\epsilon}^*. \tag{6}$$

This $\bar{\boldsymbol{\epsilon}}$ allows one to determine the effective elastic moduli tensor L through $\bar{\boldsymbol{\sigma}} = L\bar{\boldsymbol{\epsilon}}$.

Thus, central to the determination of the overall moduli is the evaluation of $\boldsymbol{\epsilon}^*$ for the considered problem.

3 Effective Elastic Moduli of a Two-Phase Composite with Monotonically Aligned Elliptic Cylinders

The infinitely-extended principal axis is taken as axis 1, the one along the thickness (t) of the elliptic cross-section as axis 2, and the other along the width (w) as axis 3. Then following the foregoing process—submitting (4) and (5) into the last of (3)—we arrive at the connection between the normal components of ϵ_{ij}^* and ϵ_{ij}^0 (henceforth, all indicial notations) as

$$\begin{pmatrix} B_1 & B_2 & B_3 \\ B_4 & B_5 & B_6 \\ B_7 & B_8 & B_9 \end{pmatrix}\begin{pmatrix} \epsilon_{11}^* \\ \epsilon_{22}^* \\ \epsilon_{33}^* \end{pmatrix} + \begin{pmatrix} D_1 & 1 & 1 \\ 1 & D_1 & 1 \\ 1 & 1 & D_1 \end{pmatrix}\begin{pmatrix} \epsilon_{11}^0 \\ \epsilon_{22}^0 \\ \epsilon_{33}^0 \end{pmatrix} = 0, \tag{7}$$

where

$$\begin{aligned}
B_1 &= c_1D_1 + D_2 + c_0(S_{2211} + S_{3311}) \\
B_2 &= c_1 + D_3 + c_0(S_{2222} + S_{3322}) \\
B_3 &= c_1 + D_3 + c_0(S_{2233} + S_{3333}) \\
B_4 &= c_1 + D_3 + c_0(D_1S_{2211} + S_{3311}) \\
B_5 &= c_1D_1 + D_2 + c_0(D_1S_{2222} + S_{3322}) \\
B_6 &= c_1 + D_3 + c_0(D_1S_{2233} + S_{3333}) \\
B_7 &= c_1 + D_3 + c_0(D_1S_{3311} + S_{2211}) \\
B_8 &= c_1 + D_3 + c_0(D_1S_{3322} + S_{2222}) \\
B_9 &= c_1D_1 + D_2 + c_0(D_1S_{3333} + S_{2233}),
\end{aligned} \tag{8}$$

and in terms of the Lamè constants of the rth phase,

$$\begin{aligned}
D_1 &= 1 + 2(\mu_1 - \mu_0)/(\lambda_1 - \lambda_0), \\
D_2 &= (\lambda_0 + 2\mu_0)/(\lambda_1 - \lambda_0), \\
D_3 &= \lambda_0/(\lambda_1 - \lambda_0).
\end{aligned} \tag{9}$$

Inversion of the B-matrix in (7) leads to the following solutions for ϵ_{ij}^*:

$$\begin{pmatrix} \epsilon_{11}^* \\ \epsilon_{22}^* \\ \epsilon_{33}^* \end{pmatrix} = \frac{1}{A}\begin{pmatrix} A_1 & A_2 & A_3 \\ A_4 & A_5 & A_6 \\ A_7 & A_8 & A_9 \end{pmatrix}\begin{pmatrix} \epsilon_{11}^0 \\ \epsilon_{22}^0 \\ \epsilon_{33}^0 \end{pmatrix}, \tag{10}$$

where

$$A_1 = D_1(B_6B_8 - B_5B_9) + B_3(B_5 - B_8) + B_2(B_9 - B_6)$$
$$A_2 = D_1(B_2B_9 - B_3B_8) + B_6(B_8 - B_2) + B_5(B_3 - B_9)$$
$$A_3 = D_1(B_3B_5 - B_2B_6) + B_8(B_6 - B_3) + B_9(B_2 - B_5)$$
$$A_4 = D_1(B_4B_9 - B_6B_7) + B_1(B_6 - B_9) + B_3(B_7 - B_4)$$
$$A_5 = D_1(B_3B_7 - B_1B_9) + B_4(B_9 - B_3) + B_6(B_1 - B_7) \quad (11)$$
$$A_6 = D_1(B_1B_6 - B_3B_4) + B_9(B_4 - B_1) + B_7(B_3 - B_6)$$
$$A_7 = D_1(B_5B_7 - B_4B_8) + B_2(B_4 - B_7) + B_1(B_8 - B_5)$$
$$A_8 = D_1(B_1B_8 - B_2B_7) + B_5(B_7 - B_1) + B_4(B_2 - B_8)$$
$$A_9 = D_1(B_2B_4 - B_1B_5) + B_7(B_5 - B_2) + B_8(B_1 - B_4),$$

and

$$A = B_1(B_5B_9 - B_6B_8) + B_2(B_6B_7 - B_4B_9) + B_3(B_4B_8 - B_5B_7).$$

The shear components are uncoupled, having the simpler expressions:

$$\epsilon_{12}^* = -\frac{(\mu_1 - \mu_0)}{\mu_0 + (\mu_1 - \mu_0)(c_1 + 2\,c_0 S_{1212})}\,\epsilon_{12}^0,$$

$$\epsilon_{13}^* = -\frac{(\mu_1 - \mu_0)}{\mu_0 + (\mu_1 - \mu_0)(c_1 + 2\,c_0 S_{1313})}\,\epsilon_{13}^0, \quad (12)$$

$$\epsilon_{23}^* = -\frac{(\mu_1 - \mu_0)}{\mu_0 + (\mu_1 - \mu_0)(c_1 + 2\,c_0 S_{2323})}\,\epsilon_{23}^0.$$

With (10) and (12), we now proceed to determine the nine independent elastic constants for the orthotropic composite: E_{11}, E_{22}, E_{33}, μ_{12}, μ_{13}, μ_{23}, ν_{12}, ν_{13}, and ν_{32}. The algebraic processes are sometimes tedious; only the end results will be presented in the following.

3.1 Longitudinal Young's Modulus E_{11}. To derive E_{11}, we apply a pure tension, $\bar{\sigma}_{11}$, on both the composite and the comparison material. This leads to

$\bar{\sigma}_{11} = E_{11}\bar{\epsilon}_{11}$ for the composite, and

$\bar{\sigma}_{11} = E_0\epsilon_{11}^0$, $\epsilon_{22}^0 = \epsilon_{33}^0 = -\nu_0\epsilon_{11}^0$ for the comparison material.

Since from (6) $\bar{\epsilon}_{11} = \epsilon_{11}^0 + c_1\,\epsilon_{11}^*$, and ϵ_{11}^* is further given by (10), one finds

$$\frac{E_{11}}{E_0} = \frac{\epsilon_{11}^0}{\epsilon_{11}^0 + c_1\epsilon_{11}^*} = \frac{1}{1 + c_1[A_1 - \nu_0(A_2 + A_3)]/A}. \quad (13)$$

3.2 Transverse Young's Modulus Along the Thickness of the Elliptic Cylinders E_{22}. For this we apply $\bar{\sigma}_{22}$. A similar analysis leads to

$$\frac{E_{22}}{E_0} = \frac{1}{1 + c_1[A_5 - \nu_0(A_4 + A_6)]/A}. \quad (14)$$

3.3 Transverse Young's Modulus Towards the Width of the Elliptic Cylinder E_{33}. Similarly, by applying $\bar{\sigma}_{33}$, we have

$$\frac{E_{33}}{E_0} = \frac{1}{1 + c_1[A_9 - \nu_0(A_7 + A_8)]/A}. \quad (15)$$

3.4 Longitudinal Shear Modulus Parallel to the Surface of Thickness μ_{12}. To determine this value we apply a pure shear stress $\bar{\sigma}_{12}$ (= $\bar{\sigma}_{21}$). The responses in the composite and the comparison material are now given by

$$\bar{\sigma}_{12} = 2\,\mu_{12}\bar{\epsilon}_{12}, \text{ and } \bar{\sigma}_{12} = 2\,\mu_0\epsilon_{12}^0,$$

respectively. Since $\bar{\epsilon}_{12} = \epsilon_{12}^0 + c_1\epsilon_{12}^*$ and ϵ_{12}^* is related to ϵ_{12}^0 through (12), one finds

$$\frac{\mu_{12}}{\mu_0} = 1 + \frac{c_1}{2\,c_0 S_{1212} + \mu_0/(\mu_1 - \mu_0)}. \quad (16)$$

3.5 Longitudinal Shear Modulus Parallel to the Edge of Width μ_{13}. In this case we apply $\bar{\sigma}_{13}$, and the result is

$$\frac{\mu_{13}}{\mu_0} = 1 + \frac{c_1}{2\,c_0 S_{1313} + \mu_0/(\mu_1 - \mu_0)}. \quad (17)$$

3.6 In-Plane Shear Modulus μ_{23}. Similarly, by applying $\bar{\sigma}_{23}$, we arrive at

$$\frac{\mu_{23}}{\mu_0} = 1 + \frac{c_1}{2\,c_0 S_{2323} + \mu_0/(\mu_1 - \mu_0)}. \quad (18)$$

3.7 Longitudinal Poisson's Ratio Perpendicular to the Surface of Thickness ν_{12}. This property is the measure of shrinkage in the thickness (t) direction when the composite is under a pure tensile stress $\bar{\sigma}_{11}$. By definition, $\bar{\epsilon}_{22} = -\nu_{12}\bar{\epsilon}_{11}$. Then with (6), (10), and $\epsilon_{22}^0 = \epsilon_{33}^0 = -\nu_0\epsilon_{11}^0$, one has

$$\nu_{12} = \frac{\nu_0 - c_1[A_4 - \nu_0(A_5 + A_6)]/A}{1 + c_1[A_1 - \nu_0(A_2 + A_3)]/A}. \quad (19)$$

3.8 Longitudinal Poisson's Ratio Toward the Edge of Width ν_{13}. This Poisson's ratio is defined by $\bar{\epsilon}_{33} = -\nu_{13}\,\bar{\epsilon}_{11}$ under the action of pure tension $\bar{\sigma}_{11}$. Following a similar consideration as in (19), one obtains

$$\nu_{13} = \frac{\nu_0 - c_1[A_7 - \nu_0(A_8 + A_9)]/A}{1 + c_1[A_1 - \nu_0(A_2 + A_3)]/A}. \quad (20)$$

3.9 In-Plane Poisson's Ratio ν_{32}. The property defines the contraction in the thickness direction under a tensile stress $\bar{\sigma}_{33}$; namely, $\bar{\epsilon}_{22} = -\nu_{32}\,\bar{\epsilon}_{33}$. As in (19) and (20), a parallel consideration leads to

$$\nu_{32} = \frac{\nu_0 - c_1[A_6 - \nu_0(A_4 + A_5)]/A}{1 + c_1[A_9 - \nu_0(A_7 + A_8)]/A}. \quad (21)$$

With the compoonent of S-tensor given in the Appendix, equations (13) to (21) provide the variations of the nine independent elastic moduli of the orthotropic composite as a function of volume fraction c_1 and aspect ratio α (= t/w) of the elliptic cylinders.

4 Composites Reinforced With Monotonically Aligned Ribbons

When the aspect ratio of the cross-section of the elliptic cylinders approaches zero ($\alpha = t/w \to 0$), the components of the S-tensor can be greatly simplified. The resulting nonvanishing components, now given in the Appendix ($A2$), are seen to depend only on the Poisson ratio of the matrix ν_0. The A_i-components, which appear in most of the nine independent moduli, can also be simplified accordingly. After substituting the new S-components for ribbons into (8) for B_i, and then into (11) for A_i, one finds

$$A_1 = A_9 = -\left[\frac{c_0\nu_0}{1-\nu_0}(D_1 - 1)(D_2 - D_1D_3) - (1 + D_3)(c_1 + D_3)(D_1 - 1) + D_1(D_1 + D_2)(c_1D_1 + D_2) - (c_1 + D_3)(D_1 + D_2 - D_3 - 1) - (1 + D_3)(c_1D_1 + D_2)\right],$$

$$A_2 = A_8 = (D_2 - D_1D_3)[c_1(1 - D_1) - (D_2 - D_3)],$$

$$A_3 = A_7 = (D_2 - D_1D_3)\left[\frac{c_0\nu_0}{1-\nu_0}(D_1 - 1) - (D_1 + D_2 - D_3 - 1)\right],$$

$$A_4 = A_6 = \left[c_1 (D_1 - 1) - (D_2 - D_3) \right] \cdot \left[\frac{c_0 \nu_0}{1-\nu_0} (D_1 - 1)(D_2 + 2) + D_1 D_3 - D_2 \right],$$

$$A_5 = \left[c_1 (D_1 - 1) + (D_2 - D_3) \right] \left[(c_1 + D_3)(2 - D_1) - D_1 (c_1 D_1 + D_2) \right],$$

$$A = \left[c_1 (D_1 - 1) + (D_2 - D_3) \right] \left[\frac{2 c_0 \nu_0}{1-\nu_0} (D_1 D_3 - D_2) + 2(1 + D_3)(c_1 + D_3) - (D_1 + D_2)(c_1 D_1 + D_2 + D_3 + c_1) \right], \tag{22}$$

where, once again, c_r is the volume fraction of rth phase, and D_1, D_2, and D_3 are given in (9).

With these simplified S_{ijkl} components and A_i values for ribbons, the nine independent elastic moduli given in (13) to (21) for the orthotropic composite can be written explicitly in terms of the elastic moduli and volume fractions of the two constituent phases. Keeping in mind that axis 1 is the longitudinal direction, axis 2 the direction perpendicular to the surface of the ribbons, and axis 3 the one extending to the width of the ribbons one finds, after some lengthy algebra,

$$\mathrm{E}_{11} = \mathrm{E}_{33} = c_1 \mathrm{E}_1 + c_0 \mathrm{E}_0 + \frac{4 c_1 c_0 (\nu_1 - \nu_0)^2}{c_1 \left(\frac{1}{\bar{\kappa}_0} + \frac{1}{\mu_0} \right) + c_0 \left(\frac{1}{\bar{\kappa}_1} + \frac{1}{\mu_1} \right)}, \tag{23}$$

$$\mathrm{E}_{22} = \frac{c_1 \mathrm{E}_1 \bar{\kappa}_1 (\bar{\kappa}_0 + \mu_0) + c_0 \mathrm{E}_0 \bar{\kappa}_0 (\bar{\kappa}_1 + \mu_1)}{c_1 c_0 (\mu_1 - \mu_0)[3(\bar{\kappa}_1 - \bar{\kappa}_0) - (\mu_1 - \mu_0)] + c_1 \bar{\kappa}_1 \mu_0 + c_0 \bar{\kappa}_0 \mu_1 + \bar{\kappa}_1 \bar{\kappa}_0}, \tag{24}$$

$$\frac{1}{\mu_{12}} = \frac{1}{\mu_{23}} = \frac{c_1}{\mu_1} + \frac{c_0}{\mu_0}, \tag{25}$$

$$\mu_{13} = c_1 \mu_1 + c_0 \mu_0, \tag{26}$$

$$\nu_{12} = \nu_{32} = c_1 \nu_1 + c_0 \nu_0 + \frac{c_1 c_0 (\nu_1 - \nu_0)(\nu_1 \mu_0 - \nu_0 \mu_1)}{c_1 \mu_1 (1 - \nu_0) + c_0 \mu_0 (1 - \nu_1)}, \tag{27}$$

$$\nu_{13} = \frac{c_1 \nu_1 \mu_1 (1 - \nu_0) + c_0 \nu_0 \mu_0 (1 - \nu_1)}{c_1 \mu_1 (1 - \nu_0) + c_0 \mu_0 (1 - \nu_1)}, \tag{28}$$

where $\bar{\kappa}_r$ is the plane-strain bulk modulus of the rth phase. Equations (23), (25), and (27) indicate that, since the aspect ratio of the ribbons are taken to approach zero, directions 1 and 3 are now on equal footing. In addition, the three in-plane properties are found to satisfy the isotropic constraint $\mathrm{E}_{11} = 2\mu_{13} (1 + \nu_{13})$. Thus, there are only five independent elastic moduli in this limiting case.

A tedious examination on these five moduli also reveals that they are exactly identical to those of a laminated medium (see Christensen, 1979, p. 140, equation (5.8) after changing C_{ij} to these moduli) and that the properties of the matrix and thin ribbons appear symmetrically.

5 Effective Elastic Moduli of a Two-Phase Composite With Two-Dimensional Randomly-Oriented Elliptic Cylinders

We now consider the case when the elliptic cylinders or ribbons are randomly oriented in the 2–3 plane as depicted in Fig. 1(*b*). The five independent elastic constants can also be derived by the mean-field theory outlined in Section 2, but, since the average stress in the inclusions, $\boldsymbol{\sigma}^{(1)}$ in (3), is now orientation-dependent, slight modifications are necessary. While (1) and (2) remain unchanged, (4) should be referred to the local coordinates aligned along the three pincipal axes of the considered inclusion orientation, as

$$\epsilon_{ij}^{pt\prime} = S_{ijkl} \epsilon_{kl}^{*\prime}, \tag{29}$$

where the primed quantities are referred to the said local coordinates, say along axes $1'$-$2'$-$3'$.

Keeping axis $1'$ to coincide with the material axis 1, the directional cosines between the local i'-axis and the global j-axis are

$$Q_{ij} = \begin{pmatrix} 1 & 0 & 0 \\ 0 & \cos\theta & \sin\theta \\ 0 & -\sin\theta & \cos\theta \end{pmatrix}, \tag{30}$$

where θ is the angle defining the orientation of inclusions. Then, the strain and stress components follow the ordinary transformation

$$\epsilon_{ij}' = Q_{ik} Q_{jl} \epsilon_{kl}. \tag{31}$$

Following a similar analysis as outlined in Section 2, equation (5) now takes the form

$$\tilde{\sigma}_{ij} = -c_1 \langle \sigma_{ij}^{pt} \rangle, \text{ or } \tilde{\epsilon}_{ij} = -c_1 \langle \epsilon_{ij}^{pt} - \epsilon_{ij}^{*} \rangle, \tag{32}$$

where $\langle \cdot \rangle$ is the orientational average, with θ varying from 0 to π, of the indicated quantity. Such a general relation has also been derived by Takao et al. (1982) in their study of the effect of fiber misorientation on the longitudinal Young's modulus.

Likewise, equation (6) now becomes

$$\bar{\epsilon}_{ij} = \epsilon_{ij}^{0} + c_1 \langle \epsilon_{ij}^{*} \rangle. \tag{33}$$

Thus, as in the unidirectional case, central to the determination of the effective moduli is the evaluation of $\langle \epsilon_{ij}^{*} \rangle$. This process, in turn, requires the information of $\epsilon_{ij}'^{*}$ in the local coordinates.

This can be accomplished by recognizing that the equivalence principle—or the last of equation (3)—continues to hold in the primed, local coordinates for the considered inclusion orientation. Then, following the same procedure as in (7) to (10), but keeping the primed $\tilde{\epsilon}_{ij}'$ together with the primed $\epsilon_{ij}^{0\prime}$, one arrives, in parallel to (10),

$$\begin{pmatrix} \epsilon_{11}^{*\prime} \\ \epsilon_{22}^{*\prime} \\ \epsilon_{33}^{*\prime} \end{pmatrix} = \frac{1}{a} \begin{pmatrix} a_1 & a_2 & a_3 \\ a_4 & a_5 & a_6 \\ a_7 & a_8 & a_9 \end{pmatrix} \begin{pmatrix} \epsilon_{11}^{0\prime} + \tilde{\epsilon}_{11}' \\ \epsilon_{22}^{0\prime} + \tilde{\epsilon}_{22}' \\ \epsilon_{33}^{0\prime} + \tilde{\epsilon}_{33}' \end{pmatrix}, \tag{34}$$

where, with the help of (11), constants a_i are given by

$a_i = A_i$ and $a = A$ by setting $c_1 = 0$,

and $C_0 = 1$ in (11) and (8). (35)

Similarly, the shear components can be readily established by way of (12), as

$$\epsilon_{12}^{*\prime} = -\frac{(\mu_1 - \mu_0)}{\mu_0 + 2(\mu_1 - \mu_0) S_{1212}} (\epsilon_{12}^{0\prime} + \tilde{\epsilon}_{12}'),$$

$$\epsilon_{13}^{*\prime} = -\frac{(\mu_1 - \mu_0)}{\mu_0 + 2(\mu_1 - \mu_0) S_{1313}} (\epsilon_{13}^{0\prime} + \tilde{\epsilon}_{13}'),$$

$$\epsilon_{23}^{*\prime} = -\frac{(\mu_1 - \mu_0)}{\mu_0 + 2(\mu_1 - \mu_0) S_{2323}} (\epsilon_{23}^{0\prime} + \tilde{\epsilon}_{23}'), \tag{36}$$

by setting $c_1 = 0$ and $C_0 = 1$ in those equations.

The orientational average $\langle \epsilon_{ij}^{*} \rangle$ then can be evaluated from

$$\langle \epsilon_{ij}^{*} \rangle = \frac{1}{\pi} \int_0^{\pi} \epsilon_{ij}^{*} d\theta = \frac{1}{\pi} \int_0^{\pi} Q_{ki} Q_{lj} \epsilon_{kl}^{*\prime} d\theta, \tag{37}$$

where $\epsilon_{ij}^{*\prime}$ are now given in terms of $\epsilon_{ij}^{0\prime} + \tilde{\epsilon}_{ij}'$, which in turn are related to $\epsilon_{ij}^{0} + \tilde{\epsilon}_{ij}$ through the usual tensor transformation. After carrying out this process one has, for a general multiaxial loading,

$$\langle \epsilon_{11}^* \rangle = \frac{1}{a}\left[a_1(\epsilon_{11}^0 + \tilde{\epsilon}_{11}) + \frac{1}{2}(a_2+a_3)(\epsilon_{22}^0 + \tilde{\epsilon}_{22} + \epsilon_{33}^0 + \tilde{\epsilon}_{33}) \right],$$

$$\langle \epsilon_{22}^* \rangle = \frac{1}{8a}\left[4(a_4+a_7)(\epsilon_{11}^0 + \tilde{\epsilon}_{11}) + \left(3a_5 + a_6 + a_8 + 3a_9 - \frac{2a}{2\,S_{2323} + \mu_0/(\mu_1-\mu_0)} \right) \cdot (\epsilon_{22}^0 + \tilde{\epsilon}_{22}) + \left(a_5 + 3a_6 + 3a_8 + a_9 + \frac{2a}{2\,S_{2323} + \mu_0/(\mu_1-\mu_0)} \right) \cdot (\epsilon_{33}^0 + \tilde{\epsilon}_{33}) \right],$$

$$\langle \epsilon_{33}^* \rangle = \frac{1}{8a}\left[4(a_4+a_7)(\epsilon_{11}^0 + \tilde{\epsilon}_{11}) + \left(a_5 + 3a_6 + 3a_8 + a_9 + \frac{2a}{2\,S_{2323} + \mu_0/(\mu_1-\mu_0)} \right)(\epsilon_{22}^0 + \tilde{\epsilon}_{22}) + \left(3a_5 + a_6 + a_8 + 3a_9 - \frac{2a}{2\,S_{2323} + \mu_0/(\mu_1-\mu_0)} \right)(\epsilon_{33}^0 + \tilde{\epsilon}_{33}) \right],$$

$$\langle \epsilon_{12}^* \rangle = -\frac{1}{2}\left[\frac{1}{2\,S_{1212} + \mu_0/(\mu_1-\mu_0)} + \frac{1}{2\,S_{1313} + \mu_0/(\mu_1-\mu_0)} \right](\epsilon_{12}^0 + \tilde{\epsilon}_{12}),$$

$$\langle \epsilon_{13}^* \rangle = -\frac{1}{2}\left[\frac{1}{2\,S_{1212} + \mu_0/(\mu_1-\mu_0)} + \frac{1}{2\,S_{1313} + \mu_0/(\mu_1-\mu_0)} \right](\epsilon_{13}^0 + \tilde{\epsilon}_{13}),$$

$$\langle \epsilon_{23}^* \rangle = \left[\frac{a_5 - a_6 - a_8 + a_9}{4a} - \frac{1}{2}\frac{1}{2\,S_{2323} + \mu_0/(\mu_1-\mu_0)} \right](\epsilon_{23}^0 + \tilde{\epsilon}_{23}). \tag{38}$$

It is now evident that in order to determine $\langle \epsilon_{ij}^* \rangle$, we must find $\epsilon_{ij}^0 + \tilde{\epsilon}_{ij}$, or $\tilde{\epsilon}_{ij}$ first. The last quantity is given by (32); when cast in the integral form, it reads

$$\tilde{\epsilon}_{ij} = -\frac{c_1}{\pi}\int_0^{\pi} (\epsilon_{ij}^{pt} - \epsilon_{ij}^*)\,d\theta$$

$$= -\frac{c_1}{\pi}\int_0^{\pi} Q_{ki}Q_{lj}(S_{klmn} - I_{klmn})\epsilon_{mn}^{*\prime}\,d\theta, \tag{39}$$

where I_{klmn} is the fourth-rank identity tensor. This integration, after some rearrangements, leads to

$$\begin{pmatrix} 1+c_1b_1 & c_1b_2 & c_1b_2 \\ c_1b_3 & 1+c_1b_4 & c_1b_5 \\ c_1b_3 & c_1b_5 & 1+c_1b_4 \end{pmatrix} \begin{pmatrix} \epsilon_{11}^0 + \tilde{\epsilon}_{11} \\ \epsilon_{22}^0 + \tilde{\epsilon}_{22} \\ \epsilon_{33}^0 + \tilde{\epsilon}_{33} \end{pmatrix} = \begin{pmatrix} \epsilon_{11}^0 \\ \epsilon_{22}^0 \\ \epsilon_{33}^0 \end{pmatrix} \tag{40}$$

and

$$b_6(\epsilon_{12}^0 + \tilde{\epsilon}_{12}) = \epsilon_{12}^0,$$
$$b_6(\epsilon_{13}^0 + \tilde{\epsilon}_{13}) = \epsilon_{13}^0,$$
$$b_7(\epsilon_{23}^0 + \tilde{\epsilon}_{23}) = \epsilon_{23}^0, \tag{41}$$

where

$$b_1 = -a_1/a,$$
$$b_2 = -(a_2+a_3)/(2a),$$

$$b_3 = \left[a_1(S_{2211} + S_{3311}) + a_4(S_{2222} + S_{3322} - 1) + a_7(S_{2233} + S_{3333} - 1) \right]/(2a),$$

$$b_4 = \frac{1}{8a}\Big[(3a_2+a_3)S_{2211} + (a_2+3a_3)S_{3311} + (3a_5+a_6)(S_{2222}-1) + (a_5+3a_6)S_{3322} + (3a_8+a_9)S_{2233} + (a_8+3a_9)(S_{3333}-1) \Big] + \frac{1}{4}\cdot\frac{2\,S_{2323}-1}{2S_{2323} + \mu_0/(\mu_1-\mu_0)},$$

$$b_5 = \frac{1}{8a}\Big[(a_2+3a_3)S_{2211} + (3a_2+a_3)S_{3311} + (a_5+3a_6)(S_{2222}-1) + (3a_5+a_6)S_{3322} + (a_8+3a_9)S_{2233} + (3a_8+a_9)(S_{3333}-1) \Big] + \frac{1}{4}\cdot\frac{2\,S_{2323}-1}{2S_{2323} + \mu_0/(\mu_1-\mu_0)},$$

$$b_6 = 1 - \frac{c_1}{2}\left[\frac{2\,S_{1212}-1}{2\,S_{1212} + \mu_0/(\mu_1-\mu_0)} + \frac{2\,S_{1313}-1}{2\,S_{1313} + \mu_0/(\mu_1-\mu_0)} \right],$$

$$b_7 = 1 + \frac{c_1}{4a}\Big[(a_2-a_3)(S_{2211}-S_{3311}) + (a_5-a_6)(S_{2222}-S_{3322}-1) + (a_8-a_9)(S_{2233}-S_{3333}+1) \Big] - \frac{c_1}{2}\cdot\frac{2\,S_{2323}-1}{2\,S_{2323} + \mu_0/(\mu_1-\mu_0)}, \tag{42}$$

Now that $\langle \epsilon_{ij}^* \rangle$ is given in terms of $\epsilon_{ij}^0 + \tilde{\epsilon}_{ij}$ by (38), and which in turn is given in terms of ϵ_{ij}^0 by (40) and (41), we are in a position to evaluate the five independent elastic moduli: E_{11}, μ_{12}, μ_{23}, ν_{12}, and κ_{23}.

5.1 Longitudinal Young's Modulus E_{11}. For this we apply a uniaxial stress $\bar{\sigma}_{11}$ to both the composite and the comparison material. As in (13), one finds

$$\frac{E_{11}}{E_0} = \frac{\epsilon_{11}^0}{\epsilon_{11}^0 + c_1\langle \epsilon_{11}^* \rangle}, \tag{43}$$

where $\langle \epsilon_{11}^* \rangle$ is given by the first of (38), in which $\epsilon_{ij}^0 + \tilde{\epsilon}_{ij}$ are given in terms of (40), with $\epsilon_{22}^0 = \epsilon_{33}^0 = -\nu_0\epsilon_{11}^0$ for the pure tension. It follows that

$$\langle \epsilon_{11}^* \rangle = p_{11}\epsilon_{11}^0, \tag{44}$$

where

$$p_{11} = \frac{a_1}{a}\left[1 - c_1\cdot\frac{b_1(c_1b_4 + c_1b_5 + 1) - 2\,c_1b_2b_3 - 2\,\nu_0b_2}{(c_1b_1+1)(c_1b_4+c_1b_5+1) - 2\,c_1^2b_2b_3} \right] - \frac{a_2+a_3}{a}\left[\nu_0 + c_1\cdot\frac{b_3 - \nu_0(b_4+b_5)(c_1b_1+1) + 2\,\nu_0c_1b_2b_3}{(c_1b_1+1)(c_1b_4+c_1b_5+1) - 2\,c_1^2b_2b_3} \right]. \tag{45}$$

The longitudinal Young's modulus is then given by

$$\frac{E_{11}}{E_0} = \frac{1}{1 + c_1p_{11}}. \tag{46}$$

5.2 Longitudinal Shear Modulus Parallel to the Axis of Cylinders μ_{12} (= μ_{13}). Now we apply $\bar{\sigma}_{12}$ (= $\bar{\sigma}_{21}$), to yield ϵ_{12}^0 (= ϵ_{21}^0), with other $\epsilon_{ij}^0 = 0$. The shear modulus is given by

$$\frac{\mu_{12}}{\mu_0} = \frac{\epsilon_{12}^0}{\epsilon_{12}^0 + c_1\langle \epsilon_{12}^* \rangle}. \tag{47}$$

After evaluating $\langle \epsilon_{12}^* \rangle$ from (38) and (41), one finds

$$\langle \epsilon_{12}^* \rangle = p_{12}\epsilon_{12}^0, \tag{48}$$

where

$$p_{12} = -\left[\frac{1}{2\,S_{1212}+\mu_0/(\mu_1-\mu_0)} + \frac{1}{2\,S_{1313}+\mu_0/(\mu_1-\mu_0)}\right] \Bigg/ \left\{2 - c_1\left[\frac{2\,S_{1212}-1}{2\,S_{1212}+\mu_0/(\mu_1-\mu_0)} + \frac{2\,S_{1313}-1}{2\,S_{1313}+\mu_0/(\mu_1-\mu_0)}\right]\right\}. \tag{49}$$

The axial shear modulus then follows as

$$\frac{\mu_{12}}{\mu_0} = \frac{1}{1+c_1 p_{12}}. \tag{50}$$

5.3 Transverse Shear Modulus in the Isotropic Plane μ_{23}. For this we apply $\bar{\sigma}_{23}$ to yield ϵ_{23}^0. The effective shear modulus is then given by

$$\frac{\mu_{23}}{\mu_0} = \frac{\epsilon_{23}^0}{\epsilon_{23}^0 + c_1\langle \epsilon_{23}^* \rangle}. \tag{51}$$

From (38) and (41), we can write

$$\langle \epsilon_{23}^* \rangle = p_{23}\epsilon_{23}^*,$$

with

$$p_{23} = \left[\frac{a_5-a_6-a_8+a_9}{4a} - \frac{1}{2}\,\frac{1}{2\,S_{2323}+\mu_0/(\mu_1-\mu_0)}\right]\Big/ b_7. \tag{52}$$

It follows that

$$\frac{\mu_{23}}{\mu_0} = \frac{1}{1+c_1 p_{23}}. \tag{53}$$

5.4 Major Poisson's Ratio ν_{12} ($= \nu_{13}$). This property defines the lateral contraction of the composite under a pure tension $\bar{\sigma}_{11}$, and is defined as

$$\nu_{12} = -\frac{\bar{\epsilon}_{22}}{\bar{\epsilon}_{11}} = -\frac{\epsilon_{22}^0 + c_1\langle \epsilon_{22}^* \rangle}{\epsilon_{11}^0 + c_1\langle \epsilon_{11}^* \rangle}, \tag{54}$$

where $\epsilon_{22}^0 = -\nu_0\epsilon_{11}^0$. The connection between $\langle \epsilon_{11}^* \rangle$ and ϵ_{11}^0 is already given by (44), and for $\langle \epsilon_{22}^* \rangle$ it can be found from (38) and (40) to be

$$\langle \epsilon_{22}^* \rangle = p_{21}\epsilon_{11}^0, \tag{55}$$

where

$$p_{21} = \frac{a_4+a_7}{2a}\left[1 - c_1\cdot\frac{b_1(c_1b_4+c_1b_5+1) - 2\,c_1b_2b_3 - 2\,\nu_0 b_2}{(c_1b_1+1)(c_1b_4+c_1b_5+1) - 2\,c_1^2 b_2 b_3}\right] - \frac{a_5+a_6+a_7+a_8}{2a} \times \left[\nu_0 + c_1\,\frac{b_3 - \nu_0(b_4+b_5)(c_1b_1+1) + 2\,\nu_0 c_1 b_2 b_3}{(c_1b_1+1)(c_1b_4+c_1b_5+1) - 2\,c_1^2 b_2 b_3}\right]. \tag{56}$$

The major Poisson's ratio then follows as

$$\nu_{12} = \frac{\nu_0 - c_1 p_{21}}{1+c_1 p_{11}}. \tag{57}$$

5.5 Plane-Strain Bulk Modulus κ_{23}. To determine the plane-strain bulk modulus κ_{23}, we apply $\bar{\sigma}_{22} = \bar{\sigma}_{33}$ and set $\bar{\epsilon}_{11} = 0$ *on the composite. To fulfill the latter plane-strain condition*, a longitudinal stress $\bar{\sigma}_{11} = \nu_{12}\,(\bar{\sigma}_{22} + \bar{\sigma}_{33})$ must be applied on the composite, and also on the comparison material to provide the same $\bar{\sigma}_{ij}$. The plane-strain bulk modulus of the composite is defined through

$$\bar{\sigma}_{22} + \bar{\sigma}_{33} = 2\,\kappa_{23}(\bar{\epsilon}_{22} + \bar{\epsilon}_{33}),\ \text{or}\ \bar{\sigma}_{22} = 2\,\kappa_{23}\bar{\epsilon}_{22}. \tag{58}$$

The strain components in the comparison material are

$$\epsilon_{22}^0 = \epsilon_{33}^0 = \bar{\sigma}_{22}[1 - \nu_0(1+2\,\nu_{12})]/\mathrm{E}_0, \qquad \epsilon_{11}^0 = 2\,\bar{\sigma}_{22}(\nu_{12}-\nu_0)/\mathrm{E}_0. \tag{59}$$

It then follows from (58) and (59) that

$$\frac{\kappa_{23}}{\bar{\kappa}_0} = \frac{(1+\nu_0)(1-2\nu_0)}{1-\nu_0(1+2\nu_{12})}\cdot\frac{\epsilon_{22}^0+\epsilon_{33}^0}{\bar{\epsilon}_{22}+\bar{\epsilon}_{33}}, \tag{60}$$

where the relation $\mathrm{E}_0 = 2\,(1+\nu_0)\,(1-2\,\nu_0)\,\bar{\kappa}_0$ has been used.

Since $\bar{\epsilon}_{22} + \bar{\epsilon}_{33} = \epsilon_{22}^0 + \epsilon_{33}^0 + c_1 < \epsilon_{22}^* + \epsilon_{33}^* >$, we need to evaluate the orientational average. From (38), (40), and (59), one can write

$$<\epsilon_{22}^* + \epsilon_{33}^*> = \bar{p}_{23} < \epsilon_{22}^0 + \epsilon_{33}^0 >, \tag{61}$$

where

$$\bar{p}_{23} = \frac{a_4+a_7}{a}\left\{\frac{\nu_{12}-\nu_0}{1-\nu_0(1+2\nu_{12})} - c_1 \cdot \frac{b_2 + \dfrac{\nu_{12}-\nu_0}{1-\nu_0(1+2\nu_{12})}\,[b_1(c_1b_4+c_1b_5+1) - 2\,c_1b_2b_3]}{(c_1b_1+1)(c_1b_4+c_1b_5+1) - 2\,c_1^2b_2b_3}\right\} + \frac{a_5+a_6+a_7+a_8}{2a} \times \left\{1 - c_1\,\frac{\dfrac{2b_3(\nu_{12}-\nu_0)}{1-\nu_0(1+2\nu_{12})} + (c_1b_1+1)(b_4+b_5) - 2\,c_1b_2b_3}{(c_1b_1+1)(c_1b_4+c_1b_5+1) - 2\,c_1^2b_2b_3}\right\}. \tag{62}$$

The bulk modulus then follows from (60), as

$$\frac{\kappa_{23}}{\bar{\kappa}_0} = \frac{(1+\nu_0)(1-2\,\nu_0)}{1-\nu_0(1+2\,\nu_{12})}\cdot\frac{1}{1+c_1\bar{p}_{23}}, \tag{63}$$

where the major Poisson's ratio ν_{12} is given in (57).

6 Composites Reinforced With Two-Dimensional Randomly-Oriented Ribbons, and the Realization of the Hill-Hashin Bounds

When the cross-sectional aspect ratio approaches zero, the elliptic cylinders become thin ribbons and the a_i and b_i components, which appear in the five independent elastic moduli, can be greatly simplified. Again, using the nonvanishing components of the S-tensor listed in Appendix ($A2$), we have

$a_i = A_i$ and $a = A$ by setting $c_1 = 0$ and $c_0 = 1$ in (22) (64)

for the ten a_i coefficients. Also, with these simplified S_{ijkl} components, one can deduce from (42) the following expressions for b_i

$$b_1 = -a_1/a,$$

$$b_2 = -(a_2+a_3)/(2a),$$

$$b_3 = \frac{1}{2(1-\nu_0)a}\,[\nu_0 a_1 - (1-2\,\nu_0)a_3],$$

$$b_4 = \frac{1}{8a}\left[-3a_1 - a_2 + \frac{\nu_0}{1-\nu_0}(a_1+6a_2+a_3)\right],$$

$$b_5 = \frac{1}{8a}\left[-a_1 - 3a_2 + \frac{\nu_0}{1-\nu_0}(3a_1+2a_2+3a_3)\right],$$

$$b_6 = 1 + \frac{c_1(\mu_1-\mu_0)}{2\,\mu_0},$$

$$b_7 = 1 + \frac{c_1}{4a(1-\nu_0)}\,[-a_1+a_2+\nu_0(a_2-a_3)]. \tag{65}$$

These simplified expressions allow one to write the five independent elastic constants more explicitly for the ribbon-reinforced composites.

This process involves the simplification of the five parameters p_{11}, p_{12}, p_{23}, p_{21}, and $\bar{p}_{23}$ given in the preceding section. After some lengthy algebra, we found that the five elastic constants of the transversely-isotropic composite can be written as

$$\mathrm{E}_{11} = c_1\mathrm{E}_1 + c_0\mathrm{E}_0 + \frac{4\, c_1 c_0 (\nu_1 - \nu_0)^2}{\dfrac{c_1}{\bar{\kappa}_0} + \dfrac{c_0}{\bar{\kappa}_1} + \dfrac{1}{\mu_1}}, \tag{66}$$

$$\mu_{12} = \mu_1 + \frac{c_0}{-\dfrac{1}{\mu_1 - \mu_0} + \dfrac{c_1}{2\mu_1}}, \tag{67}$$

$$\mu_{23} = \mu_1 + \frac{c_0}{-\dfrac{1}{\mu_1 - \mu_0} + \dfrac{c_1(\bar{\kappa}_1 + 2\mu_1)}{2\mu_1(\bar{\kappa}_1 + \mu_1)}}, \tag{68}$$

$$\kappa_{23} = \bar{\kappa}_1 + \frac{c_0}{-\dfrac{1}{\bar{\kappa}_1 - \bar{\kappa}_0} + \dfrac{c_1}{\bar{\kappa}_1 + \mu_1}}, \tag{69}$$

$$\nu_{12} = c_1\nu_1 + c_0\nu_0 + \frac{c_1 c_0 (\nu_1 - \nu_0)\left(\dfrac{1}{\bar{\kappa}_0} - \dfrac{1}{\bar{\kappa}_1}\right)}{\dfrac{c_1}{\bar{\kappa}_0} + \dfrac{c_0}{\bar{\kappa}_1} + \dfrac{1}{\mu_1}}. \tag{70}$$

Upon inspection, it becomes evident that these expressions coincide with those of the Hill (1964) and Hashin (1965) bounds. Indeed, when the ribbons are harder than the matrix, such that $\bar{\kappa}_1 \geq \bar{\kappa}_0$ and $\mu_1 \geq u_0$, the four moduli E_{11}, μ_{12}, μ_{23}, and κ_{23} coincide with their upper bounds. For the major Poisson ratio, it also coincides with Hill's upper bound if $\nu_1 > \nu_0$, but if $\nu_1 < \nu_0$—as in many fiber/polymer matrix cases—it will coincide with his lower bound. However, if we write the bounds of ν_{12} in Hill's original forms, again assuming $\mu_1 > \mu_0$

$$\frac{c_1 c_0}{\dfrac{c_1}{\bar{\kappa}_0} + \dfrac{c_0}{\bar{\kappa}_1} + \dfrac{1}{\mu_0}} \leq \frac{\nu_{12} - (c_1\nu_1 + c_0\nu_0)}{(\nu_1 - \nu_0)\left(\dfrac{1}{\bar{\kappa}_0} - \dfrac{1}{\bar{\kappa}_1}\right)} \leq \frac{c_1 c_0}{\dfrac{c_1}{\bar{\kappa}_0} + \dfrac{c_0}{\bar{\kappa}_1} + \dfrac{1}{\mu_1}} \tag{71}$$

so that the bounds of $\dfrac{\nu_{12} - (c_1\nu_1 + c_0\nu_0)}{(\nu_1 - \nu_0)\left(\dfrac{1}{\bar{\kappa}_0} - \dfrac{1}{\bar{\kappa}_1}\right)}$ are sought for, the present result—as for the other four moduli—will also coincide with Hill's upper bound.

On the contrary, if the ribbons are softer than the matrix, the five independent elastic moduli—with the bounds ν_{12} expressed in the form of (71)—will coincide with Hill's and Hashin's lower bounds.

The fact that ribbons provide a superior reinforcement than fibers here is similar to the conclusion reported by Christensen (1979) on the superior platelet-type reinforcements in the three-dimensional isotropic composites.

7 Numerical Results

It is now of interest to see how the shape of the reinforcing phase—when it changes from circular fibers ($\alpha = 1$) to thin ribbons ($\alpha \to 0$)—would affect the nine elastic constants of an orthotropic composite and the five of a transversely isotropic one. To this end we used the properties of glass fibers and epoxy matrix in our calculations. The elastic constants are

$$\kappa_0 = 3.07 \text{ GPa}, \quad \mu_0 = 1.02 \text{ GPa}, \quad \text{or} \quad \mathrm{E}_0 = 2.76 \text{ GPa}, \quad \nu_0 = 0.35,$$

$$\kappa_1 = 40.2 \text{ GPa}, \quad \mu_1 = 30.2 \text{ GPa}, \quad \text{or} \quad \mathrm{E}_1 = 72.4 \text{ GPa}, \quad \nu_1 = 0.20.$$

The corresponding plane-strain bulk modulus of course can be evaluated from the usual isotropic relation, $\bar{\kappa} = \mu/(1 - 2\nu)$, for each phase. The values of $\alpha = 0$, 0.01, 0.1, 0.5, and 1 were chosen for demonstrations.

The nine normalized elastic constants of an orthotropic composite as a function of c_1 are depicted in Figs. 2 to 4. In these figures, the three tensile Young's moduli are grouped into one, the three shear moduli are grouped into the other, and the three Poisson's ratios are put together as the third, each having the same scale. In reading these results, we are reminded once again that direction 1 is the infinitely extended direction, direction 2 is perpendicular to the surface of the thickness, and direction 3 is along the width. As the aspect ratio decreases from 1 to 0 it is evident, from Fig. 2, that it has very little effect on E_{11} and E_{22}, which apparently can be well represented by the rule of mixture for the moduli and for the compliances, respectively. The Young's modulus, E_{33}, along the width direction is seen to be very sensitive to α, and continues to

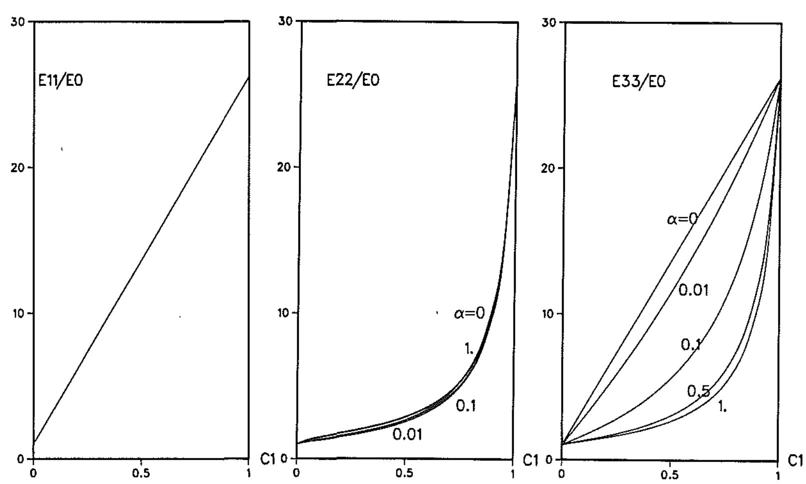

Fig. 2 The variations of the three Young's moduli of the orthotropic composite

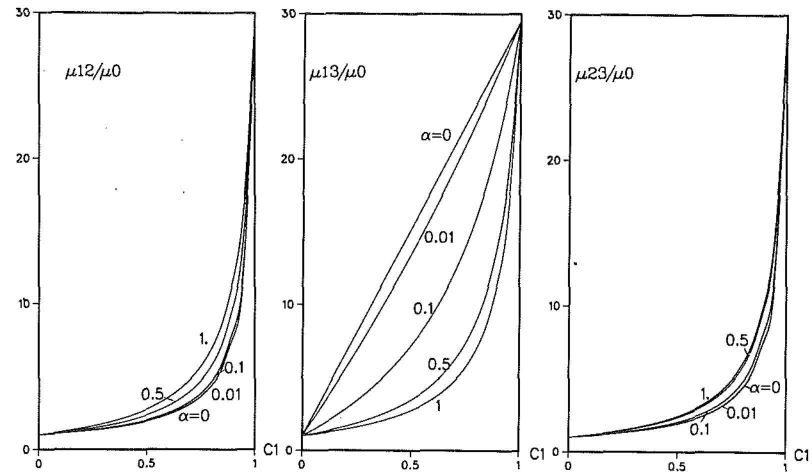

Fig. 3 The variations of the three shear moduli of the orthotropic composite

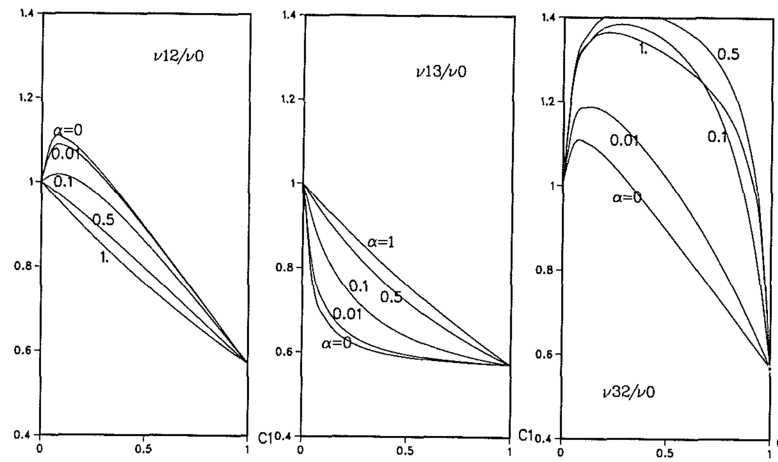

Fig. 4 The variations of the three Poisson's ratios of the orthotropic composite

increase as the thickness of the elliptic cylinder continues to decrease, approaching the linear dependence as $\alpha \rightarrow 0$. Of course, when $\alpha = 0$, $E_{33} = E_{11}$ and when $\alpha = 1$, $E_{33} = E_{22}$ as required.

The variations of the three shear moduli are shown in Fig. 3. The shear modulus μ_{13} is seen to be particularly sensitive to the aspect ratio, but moduli μ_{12} and μ_{23} are less so. On the other hand, if we read the axial moduli μ_{12} and μ_{13} together we see that, as the "shape" of the shearing surface of the elliptic cylinder change from a "flat" surface ($\alpha = 0$ in μ_{12}) to a sharp edge ($\alpha = 0$ in μ_{13}), the shear modulus increases dramatically. These two limiting conditions approach those of constant stress and constant strain distributions, respectively, thereby exhibiting such a consequence. It is also noted that $\mu_{12} = \mu_{13}$ when $\alpha = 1$, and that $\mu_{12} = \mu_{23}$ when $\alpha = 0$, as expected.

The three Poisson's ratios are depicted in Fig. 4, with all three showing strong sensitivity to the aspect ratio α. Poisson ratio ν_{12} tends to increase when the aspect ratio decreases. As α decreases, the shrinkage in the 2-direction is more dominated by the behavior of the matrix (which has a higher Poisson's ratio than the fibers), and therefore such a trend is somewhat anticipated. The same argument may also apply to ν_{13}, which shows an opposite effect. However, in ν_{12} when α is low and in ν_{32} for all α, it appears that these two Poisson ratios can exceed those of both constituents over certain range of c_1. Such a synergistic effect has also been reported by Hashin and Rosen (1964) for ν_{32}, for the special case of circular fibers ($\alpha = 1$).

The five normalized elastic moduli for the two-dimensional randomly-oriented composite are shown in Figs. 5 to 9. The first four moduli, E_{11}, μ_{12}, μ_{23}, and κ_{23}, as already proven in Section 6, coincide with Hill's and Hashin's upper bounds for the thin ribbons ($\alpha = 0$), and now since $\nu_1 < \nu_0$, the major Poisson's ratio ν_{12} also coincides with Hill's lower bound. When the aspect ratio becomes 1 such that the reinforcing phase is in the form of circular cylinders, these four constants have been shown to coincide with Hill's and Hashin's lower bounds if the inclusions are the harder phase (see Tandon, 1986 and Zhao et al., 1989) and the major Poisson's ratio ν_{12}, under the present circumstance ($\nu_1 < \nu_0$), also coincides with Hill's upper bound. To show how the aspect ratio would affect the transverse Young's modulus E_{22} ($= E_{33}$), we have also plotted its variations (by the usual transversely-isotropic relation; see, for instance, Christensen, 1979) in Fig. 10, which also shows a similar effect. Indeed it is evident that, with the exception of E_{11}, the other four measures of stiffness — E_{22}, μ_{12}, μ_{23} and κ_{23} — can all be significantly improved if the circular fibers are replaced by thin ribbons in the composite. Such an improvement can be very significant. For instance, from these figures at $c_1 = 0.2$, these four moduli with ribbon reinforcement are, respectively, 2.0, 2.6, 2.1, and 1.8 times those reinforced with circular fibers. Generally speaking, the thinner the ribbons, the stiffer the composite.

In closing it is sometimes desirable to see how the ribbon width would affect the overall properties of the composite. If the thickness and volume fraction of ribbons are to be kept constant, an increase in the ribbon width will have to be ac-

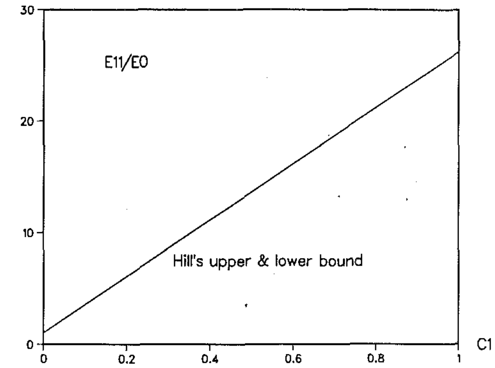

Fig. 5 The variations of the longitudinal Young's modulus of the transversely-isotropic composite

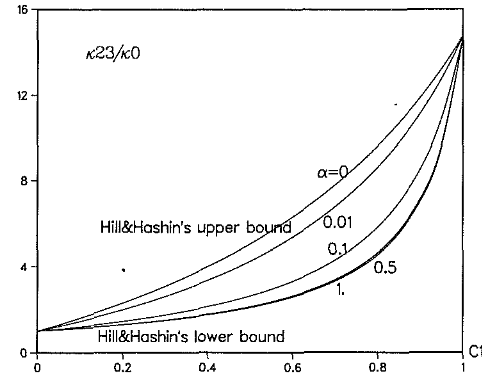

Fig. 8 The variations of the plane-strain bulk modulus of the transversely-isotropic composite

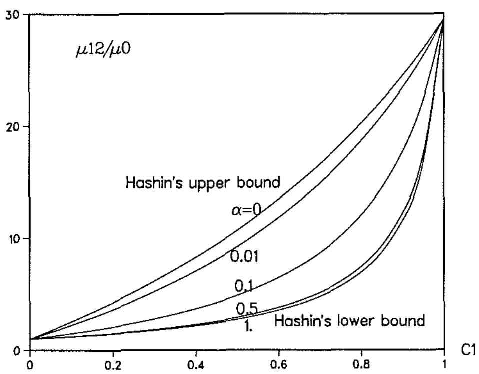

Fig. 6 The variations of the axial shear modulus of the transversely-isotropic composite

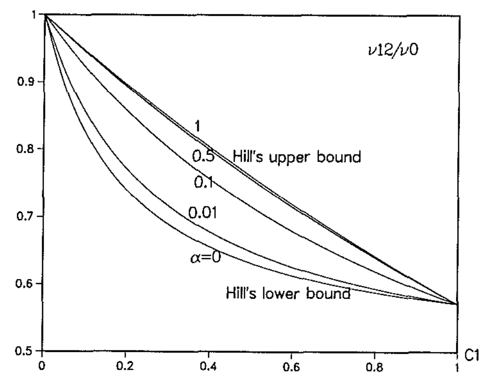

Fig. 9 The variations of the major Poisson's ratio of the transversely-isotropic composite

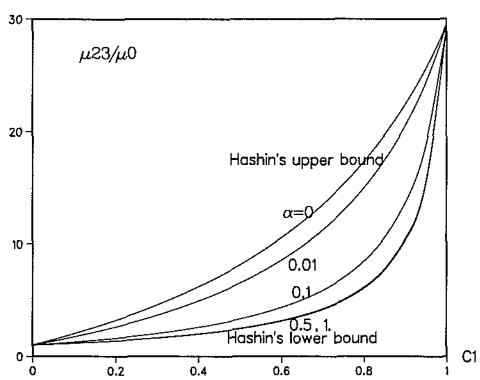

Fig. 7 The variations of the transverse shear modulus of the transversely-isotropic composite

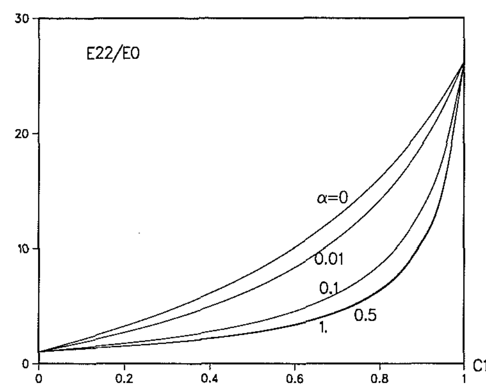

Fig. 10 The variations of the transverse Young's modulus of the transversely-isotropic composite

companied by a decrease in the total number of ribbons in a reciprocal way. Then, due to the reciprocal relation between the ribbon width and the aspect ratio (at a constant t), the influence of ribbon width can be directly deduced from that of the aspect ratio.

Acknowledgment

This work was supported by the National Science Foundation, Solid and Geo-Mechanics Program, under Grant MSM86-14151. The authors are grateful to the reviewer who pointed out the possibility that the results given in (23) to (28) for the monotonically-aligned thin ribbons could be identical to those of a laminated medium. And they are.

References

Chow, T. S., 1978, "Effect of Particle Shape at Finite Concentration on the Elastic Moduli of Filled Polymers," *Journal of Polymer Science: Polymer Physics Edition*, Vol.16, pp. 959–965.

Christensen, R. M., 1979, *Mechanics of Composite Materials*, John Wiley and Sons, New York.

Eshelby, J. D., 1957, "The Determination of the Elastic Field of an Ellipsoidal Inclusion, and Related Problems," *Proceedings of the Royal Society*, London, Vol. A241, pp. 376–396.

Hashin, Z., and Rosen, B. W., 1964, "The Elastic Moduli of Fiber-Reinforced Materials," ASME JOURNAL OF APPLIED MECHANICS, Vol. 31, pp. 223–232.

Hashin, Z., 1965, "On Elastic Behavior of Fibre Reinforced Materials of Arbitrary Transverse Phase Geometry," *Journal of the Mechanics and Physics of Solids*, Vol. 13, pp. 119–134.

Hashin, Z., and Shtrikman, S., 1963, "A Variational Approach to the Theory of the Elastic Behaviour of Multiphase Materials," *Journal of the Mechanics and Physics of Solids*, Vol. 11, pp. 127–140.

Hill, R., 1963, "Elastic Properties of Reinforced Solids: Some Theoretical

Principles," *Journal of the Mechanics and Physics of Solids*, Vol. 11, pp. 357–372.
Hill, R., 1964, "Theory of Mechanical Properties of Fibre-Strengthened Materials: I. Elastic Behaviour," *Journal of the Mechanics and Physics of Solids*, Vol. 12, pp. 199–212.
Mori, T., and Tanaka, K., 1973, "Average Stress in the Matrix and Average Elastic Energy of Materials with Misfitting Inclusions," *Acta Metallurgica*, Vol. 21, pp. 571–574.
Mura, T., 1987, *Micromechanics of Defects in Solids*, 2nd ed., Martinus Nijhoff, Dordrecht, The Netherlands.
Takao, Y., Chou, T.-W., and Taya, M., 1982, "Effective Longitudinal Young's Modulus of Misoriented Short Fiber Composites," ASME JOURNAL OF APPLIED MECHANICS, Vol. 49, pp. 536–540.
Tandon, G. P., 1986, *Micromechanical Determination of Elasticity and Plasticity of Composites*, Ph.D. Thesis, Rutgers University, p. 52.
Tandon, G. P., and Weng, G. J., 1986, "Average Stress in the Matrix and Effective Moduli of Randomly Oriented Composites," *Composites Science and Technology*, Vol. 27, pp. 111–132.
Taya, M., and Chou, T.-W., 1981, "On Two Kinds of Ellipsoidal Inhomogeneities in an Infinite Elastic Body: An Application to a Hybrid Composite," *International Journal of Solids and Structures*, Vol. 17, pp. 553–563.
Taya, M., and Mura, T., 1981, "The Stiffness and Strength of an Aligned Short-Fiber Reinforced Composite Containing Fiber-End Cracks Under Uniaxial Applied Stress," ASME JOURNAL OF APPLIED MECHANICS, Vol. 43, pp. 361–367.
Weng, G. J., 1984, "Some Elastic Properties of Reinforced Solids, With Special Reference to Isotropic Ones Containing Spherical Inclusions," *International Journal of Engineering Science*, Vol. 22, pp. 845–856.
Zhao, Y. H., Tandon, G. P., and Weng, G. J., 1989, "Elastic Moduli for a Class of Porous Materials," *Acta Mechanica*, Vol. 76, pp. 105–130.

APPENDIX

Components of Eshelby's S_{ijkl} Tensor for an Elliptic Cylinder

Taking axis 1 to be infinitely extended, axis 2 along the thickness and axis 3 along the width of the elliptic cylinder, and defining the aspect ratio α to be the ratio of thickness to width ($\alpha = t/w$), one has

$$S_{1111} = S_{1122} = S_{1133} = 0,$$

$$S_{2222} = \frac{1}{2(1-\nu_0)}\left[\frac{1+2\alpha}{(1+\alpha)^2} + \frac{1-2\nu_0}{1+\alpha}\right],$$

$$S_{3333} = \frac{\alpha}{2(1-\nu_0)}\left[\frac{\alpha+2}{(1+\alpha)^2} + \frac{1-2\nu_0}{1+\alpha}\right],$$

$$S_{2211} = \frac{\nu_0}{1-\nu_0}\frac{1}{1+\alpha},$$

$$S_{2233} = \frac{1}{2(1-\nu_0)}\left[\frac{1}{(1+\alpha)^2} - \frac{1-2\nu_0}{1+\alpha}\right],$$

$$S_{3311} = \frac{\nu_0}{1-\nu_0}\frac{\alpha}{1+\alpha},$$

$$S_{3322} = \frac{\alpha}{2(1-\nu_0)}\left[\frac{\alpha}{(1+\alpha)^2} - \frac{1-2\nu_0}{1+\alpha}\right],$$

$$S_{1212} = \frac{1}{2(1+\alpha)},$$

$$S_{1313} = \frac{\alpha}{2(1+\alpha)},$$

$$S_{2323} = \frac{1}{4(1-\nu_0)}\left[\frac{1+\alpha^2}{(1+\alpha)^2} + (1-2\nu_0)\right], \tag{A1}$$

and other $S_{ijkl} = 0$, where ν_0 is the Poisson ratio of the matrix.

When the elliptic cylinders exist in the shape of thin ribbons, so that $\alpha = t/w \rightarrow 0$, the above components can be simplified to

$$S_{1111} = S_{1122} = S_{1133} = S_{3333} = S_{3311} = S_{3322} = S_{1313} = 0,$$

$$S_{2222} = 1,$$

$$S_{2211} = S_{2233} = \frac{\nu_0}{1-\nu_0},$$

$$S_{1212} = S_{2323} = \frac{1}{2},$$

$$\text{other} \quad S_{ijkl} = 0. \tag{A2}$$

A. K. Kaw
Assistant Professor,
Department of Mechanical Engineering,
University of South Florida,
Tampa, FL 33620-5350
Assoc. Mem. ASME

J. G. Goree
Professor,
Department of Mechanical Engineering,
Clemson University,
Clemson, SC 29634-0921
Mem. ASME

Effects of Interleaves on Fracture of Laminated Composites: Part I—Analysis

The influence of placing interleaves between fiber-reinforced plies in multilayered composite laminates is investigated. The geometry of the composite is idealized as a two-dimensional, isotropic, linearly elastic media consisting of a damaged layer bonded between two half-planes and separated by thin interleaves of low extensional and shear moduli. The damage in the layer is taken in the form of a symmetric crack perpendicular to the interface. The case of an H-shaped crack in the form of a broken layer with delamination along the interface is also analyzed. Fourier integral transform techniques are used to develop the solutions in terms of singular integral equations.

1 Introduction

Laminated fiber-reinforced composite materials such as Graphite/Epoxy are being used extensively in aircraft structures and are replacing many metallic components. This is mainly due to their potential for reducing weight and the capacity to be tailored to optimize the structural strength and stiffness. However, due to the fiber and matrix interaction and the multi-ply configuration of such composites, the mechanical behavior is quite complex and has challenged the designer with a new class of problems. One particular area which has received considerable attention in the past decade has been their low tolerance to interfacial damage. This type of damage, frequently caused by impact, is a common and an unavoidable occurrence during manufacturing, maintenance, and service of aircraft structures.

One suggested method, discussed by Masters (1985) and Sun (1985), to improve interfacial damage tolerance is to place thin films of adhesive, called interleaves, between those plies where delamination is more likely to occur. This concept is illustrated schematically by Masters (1985, Fig. 2). An interleaf typically has a large shear failure strain and remains a separate layer between plies after curing, unlike the epoxy matrix used in the prepreg plies. Experimental results reported by Masters (1985) and Sun (1985) do indeed indicate that such adhesive layers are effective in reducing the size of interply delamination as well as in increasing the load required to initiate delamination.

These studies indicate that low velocity impact results in transverse matrix cracks in the 90 deg plies due to the tensile strains caused by bending. When these cracks intersect the 0 deg plies they may initiate delamination at the ply interfaces. If the ply thickness is small compared to the laminate thickness and the damaged ply is away from the midplane, the tensile stress gradient will be small over the ply thickness. The approximation of a uniform tensile strain then should give a good measure of the influence of the crack and the interleaf on delamination. An analytic solution of this problem has, however, not been given adequate treatment. A detailed solution is certainly necessary in order to develop an understanding of the influence of the various material parameters on the behavior of interleafed composites. This is the primary focus of the present study.

A number of related problems have been solved based on various forms of two-dimensional or axisymmetric approximations. Sneddon and Srivastav (1971) solved the problem of a transverse crack in a strip of finite width. Gupta and Erdogan (1974) considered the problem of two symmetric edge cracks in an infinite strip. Hilton and Sih (1971) studied the problem of a strip bonded to two half-planes of different materials with a crack perpendicular to the interface. Bogy (1973) considered the same geometry as Hilton and Sih (1971) and discussed the dependence of the solution on material parameters. Both the solutions by Bogy (1973) and Hilton and Sih (1971) allowed only embedded cracks. Ashbaugh (1973) and Gupta (1973) reconsidered this problem with the added condition that the crack could propagate up to the interface. Erdogan and Backioglu (1977) solved the fracture problem of a composite plate consisting of perfectly-bonded parallel load-carrying laminates and buffer strips. Gecit and Erdogan (1978) relaxed the property of a perfect bond between plies and studied the effect of the thickness and elastic properties of adhesive layers between plies in laminated structures. The problem of two dissimilar elastic bonded half-planes containing a perpendicular crack terminating at the interface was studied by Cook and Erdogan (1972). Goree and Venezia (1977) extended this study to include

Contributed by the Applied Mechanics Division of The American Society of Mechanical Engineers for presentation at the Winter Annual Meeting, San Francisco, Calif., December 10-15, 1989.

Discussion on this paper should be addressed to the Editorial Department, ASME, United Engineering Center, 345 East 47th Street, New York, N.Y. 10017, and will be accepted until two months after final publication of the paper itself in the Journal of Applied Mechanics. Manuscript received and accepted by the ASME Applied Mechanics Division, April 15, 1989.

Paper No. 89-WA/APM-45.

an interface crack that grows along the interface as well as crosses the interface. Lu and Erdogan (1983) looked at a related problem for the geometry of two dissimilar infinitely long but finite width strips.

The intent of this study is to develop a fracture and crack growth model based on the methods used in the above studies, and then investigate the predicted influence of an interleaf on damage growth in a laminated composite. The composite is approximated by two isotropic half-planes separated from a finite width layer by thin interleaves (Fig. 1). This is an idealization of a general laminated composite where one concentrates on a single damaged layer, while the outer layers are approximated by half-planes with average elastic properties. A uniform tensile strain is assumed to be applied to the composite in the y-direction. A typical composite is actually multilayered and orthotropic. The approximation of isotropic, linearly elastic media gives a more tractable formulation and, along with a proper choice of material and geometrical parameters, should assist in understanding the influence of the interleaves on damage growth.

The interleaf is modeled as uncoupled distributed tension and shear springs. Gecit and Erdogan (1978) used this spring model to solve the problem of periodically-arranged dissimilar layers separated by thin adhesive layers with crack perpendicular to the interface. However, this approximation was used only for the case of embedded cracks in the layers. For the case of cracks up to the interface of the layers, the spring model was replaced by an elastic continuum. This made the formulation and the solution cumbersome. Including delamination along the interface, which was not considered in their study, with a continuum model for the adhesive layers, would involve further complexity in algebraic manipulations and analysis. Other mathematical difficulties involved in including delamination would be the classical singular and oscillatory stresses near an interface crack tip. The stresses undergo infinite reversals of sign as the crack tip is approached, and it is also implied that the crack surfaces overlap near the crack tip which is physically inadmissible. A short literature survey of problems, with such singularities, is given by Comninou (1977). Comninou (1977) reconsidered the problem of a traction-free interface crack between two dissimilar half-planes in a tension field in an attempt to explain the oscillatory stresses near the crack tip. She assumed that the crack was not completely open and that the faces were in frictionless contact near the crack tips. She solved the resulting integral equations for the length of the contact zone and obtained crack tip stresses free of oscillatory singularities. Recently, Gautesen and Dundurs (1987) obtained an exact solution for the integral equations developed by Comninou (1977). Knowles and Sternberg (1983) solved the same problem (Comninou, 1977) using the nonlinear theory of elastostatic plane stress. The crack was found to open smoothly near the crack tips, where the stresses were singular but not of oscillatory type. The spring model, on the other hand, removes this behavior and also simplifies the mathematical nature of the model. This simplification is made at the expense of approximating the shear and normal stresses as being constant through the thickness of the interleaf. If an average or point-stress failure criterion is used, then such an approximation is justified. The resulting stresses in the adhesive are finite everywhere, while stresses with logarithmic singularities are shown to occur in the half-planes and the layer at the interface crack tips.

Based on these approximations, a general formulation is developed for plane strain and generalized plane stress. The displacement and stress fields are expressed in terms of Fourier transforms and, by using Fourier inverse transform techniques, the solution is obtained in closed-form in terms of integral equations.

Three cases, depending on the extent of damage, are studied in this work. In the first case the center layer is assumed to have a symmetric, traction-free embedded crack along the x-axis; in the second case the crack is assumed to cross the layer and intersect the interface, and lastly, damage in the form of a broken layer with symmetric delaminations along the interface is examined. The behavior of stresses at critical locations, for example at the crack tips, is studied to understand the influence of the relative material properties and the geometry of the interleaf and the plies. The geometry is shown in Fig. 1.

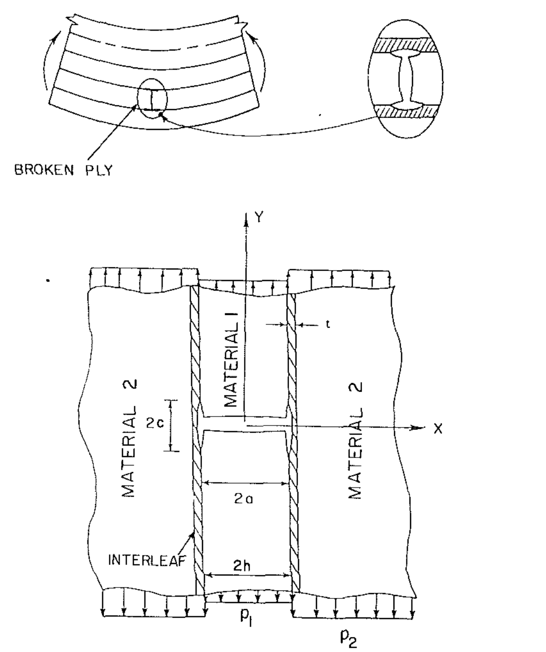

Fig. 1 Laminate with a broken ply under bending and geometry of the problem

The formulation of the integral equations and a discussion of the behavior of the solution in the vicinity of the crack tips will be presented. Some of the very lengthy algebraic expressions and the details of the manipulations have been omitted from this paper to save space. It is hoped that the significant points are covered in sufficient detail though, and that the resulting behavior is clearly described. The complete development, including all intermediate steps, is contained in the first author's Ph.D. dissertation (Kaw, 1987) and in the corresponding NASA report. The authors will gladly supply a copy of this work to any interested reader.

2 Formulation and Singular Behavior of Solution

Consider a laminated composite (Fig. 1) in plane strain or generalized plane stress consisting of a single damaged layer (Material 1) of width "$2h$", Young's modulus E_1 and Poisson's ratio ν_1; half-planes (Material 2) having Young's modulus E_2, and Poisson's ratio ν_2; and thin interleaves of thickness "t", Young's modulus E_3 and Poisson's ratio ν_3.

The composite is assumed to be loaded parallel to the y-axis with uniform remote stresses p_1 and p_2 as shown. The applied stresses are related such as to give uniform remote strains in the y-direction. Hence, $p_1/p_2 = E_1/E_2$ for generalized plane stress; $p_1/p_2 = [(1-\nu_2^2)E_1] / [(1-\nu_1^2)E_2]$ for plane strain. The solution to the problem of a stress-free crack and loads applied far away from the crack can be obtained by superposing the solutions of two problems. Let S_I be the solution to the problem of the composite without cracks and loaded with uniform remote stresses p_1 and p_2. The solution of this problem is simply a uniform tensile strain throughout the composite. Assume S_{II} to be the solution to the problem of the composite with damage and having no remote applied loads but with a uniform compression of magnitude p_1 on the transverse crack surface.

The complete solution of the problem is, hence, given by $S_{\text{total}} = S_{\text{I}} + S_{\text{II}}$. The intent of this study is to find the solution S_{II}.

2.1 Displacement and Stress Field Equation. The displacement field for a cracked layer is derived by adding the Fourier transform solutions for an infinitely long, uncracked strip and an infinitely large body with a crack (Sneddon and Lowengrub, 1969) and is given by

$$u_1(x,y) = -\frac{2}{\pi}\int_0^\infty \left\{\frac{1}{\eta}\left[f_1(\eta)-\frac{\kappa_1-1}{2}g_1(\eta)\right]\sinh(\eta x) + xg_1(\eta)\cosh(\eta x)\right\}\cos(\eta y)d\eta - \frac{2}{\pi}\int_0^\infty \frac{\phi_1(\xi)}{\xi}\left(\frac{\kappa_1-1}{2}-\xi y\right)e^{-\xi y}\sin(\xi x)d\xi,$$

$$v_1(x,y) = \frac{2}{\pi}\int_0^\infty \left\{\frac{1}{\eta}\left[f_1(\eta)+\frac{\kappa_1+1}{2}g_1(\eta)\right]\cosh(\eta x) + xg_1(\eta)\sinh(\eta x)\right\}\sin(\eta y)d\eta + \frac{2}{\pi}\int_0^\infty \frac{\phi_1(\xi)}{\xi}\left(\frac{\kappa_1+1}{2}+\xi y\right)e^{-\xi y}\cos(\xi x)d\xi. \quad (1a,b)$$

The corresponding stress field is given by

$$\frac{\sigma^1_{xx(x,y)}}{2\mu_1} = -\frac{2}{\pi}\int_0^\infty \left[f_1(\eta)\cosh(\eta x) + \eta x g_1(\eta)\sinh(\eta x)\right]\cos(\eta y)d\eta - \frac{2}{\pi}\int_0^\infty \phi_1(\xi)(1-\xi y)e^{-\xi y}\cos(\xi x)d\xi,$$

$$\frac{\sigma^1_{yy(x,y)}}{2\mu_1} = \frac{2}{\pi}\int_0^\infty \{[f_1(\eta)+2g_1(\eta)]\cosh(\eta x) + \eta x g_1(\eta)\sinh(\eta x)\}\cos(\eta y)d\eta - \frac{2}{\pi}\int_0^\infty \phi_1(\xi)(1+\xi y)e^{-\xi y}\cos(\xi x)d\xi,$$

$$\frac{\sigma^1_{xy(x,y)}}{2\mu_1} = \frac{2}{\pi}\int_0^\infty \{[f_1(\eta)+g_1(\eta)]\sinh(\eta x) + \eta x g_1(\eta)\cosh(\eta x)\}\sin(\eta y)d\eta - \frac{2}{\pi}\int_0^\infty \xi y\phi_1(\xi)e^{-\xi y}\sin(\xi x)d\xi. \quad (2a\text{–}c)$$

Similarly, the displacement field for the half-plane is

$$u_2(x,y) = \frac{2}{\pi}\int_0^\infty \left\{\frac{1}{\eta}\left[f_2(\eta)+\frac{\kappa_2-1}{2}g_2(\eta)\right] + xg_2(\eta)\right\}e^{-\eta x}\cos(\eta y)d\eta,$$

$$v_2(x,y) = \frac{2}{\pi}\int_0^\infty \left\{\frac{1}{\eta}\left[f_2(\eta)-\frac{\kappa_2+1}{2}g_2(\eta)\right] + xg_2(\eta)\right\}e^{-\eta x}\sin(\eta y)d\eta. \quad (3a,b)$$

The corresponding stress field equations are given by

$$\frac{\sigma^2_{xx(x,y)}}{2\mu_2} = -\frac{2}{\pi}\int_0^\infty [f_2(\eta)+\eta x g_2(\eta)]e^{-\eta x}\cos(\eta y)d\eta,$$

$$\frac{\sigma^2_{yy(x,y)}}{2\mu_2} = \frac{2}{\pi}\int_0^\infty [f_2(\eta)+(\eta x-2)g_2(\eta)]e^{-\eta x}\cos(\eta y)d\eta,$$

$$\frac{\sigma^2_{xy(x,y)}}{2\mu_2} = -\frac{2}{\pi}\int_0^\infty [f_2(\eta)+(\eta x-1)g_2(\eta)]e^{-\eta x}\sin(\eta y)d\eta. \quad (4a\text{–}c)$$

In equations (2) and (4), μ_i, $(i = 1,2)$ is the shear modulus, $\kappa_i = 3-4\nu_i$, $(i = 1,2)$ for plane strain and $\kappa_i = (3-\nu_i)/(1+\nu_i)$, $(i = 1,2)$ for generalized plane stress and ν_i, $(i = 1,2)$ is the Poisson's ratio.

The unknown functions f_1, g_1, ϕ_1, f_2, and g_2 in the displacement and stress field equations (1)–(4) are determined by applying appropriate boundary and continuity conditions relating to the problem. The solution is obtained in terms of singular integral equations.

2.2 Derivation and Solution of the Integral Equations. Three cases related to the extent of the damage are investigated. The first case deals with a symmetric transverse crack of length "$2a$" ($a < h$) located centrally along the x-axis. In the second case, the crack can extend up to the interface ($a = h$) and represents a broken layer. The last case accounts for a crack up to the interface ($a = h$) along with symmetric splitting of length "$2c$" parallel to the y-axis at the interface ($x = \pm h$) (Fig. 1). This last geometry is commonly called the H-shaped crack. The nature of the damage effects the continuity and boundary conditions of the problem. Hence, each case is studied separately. An asymptotic analysis is carried out to study the singular behavior of stresses and displacement slopes in the vicinity of the crack tips.

2.2.1 Crack Within the Layer (a < h). As discussed in Section 1, the interleaves are modeled as uncoupled distributed tension and shear springs and the stiffness of these springs is given (Gecit and Erdogan, 1978) as

$$K_n = E_o/t, \quad K_s = \mu_3/t, \quad (5a,b)$$

where $E_o = E_3/(1-\nu_3^2)$ for generalized plane stress and $E_o = E_3(1-\nu_3)/[(1+\nu_3)(1-2\nu_3)]$ for plane strain.

By modeling the interleaf as springs, the transverse and shear stresses are constant through the thickness of the interleaf. The continuity conditions along $x = h$ are then written as

$$\sigma^1_{xy}(h,y) = \sigma^2_{xy}(h,y),\ \sigma^1_{xx}(h,y) = \sigma^2_{xx}(h,y), \quad 0 \le |y| \infty, \quad (6a,b)$$

$$\sigma^1_{xx}(h,y) = K_n[u_2(h,y)-u_1(h,y)], \quad 0 < |y| \infty, \quad (7a)$$

$$\sigma^1_{xy}(h,y) = K_s[v_2(h,y)-v_1(h,y)], \quad 0 < |y| \infty. \quad (7b)$$

The homogeneous boundary conditions along $y = 0$ are

$$\sigma^1_{xy}(x,0) = 0, \quad |x| < h, \quad \sigma^2_{xy}(x,0) = 0, \quad |x| > h, \quad (8a,b)$$

$$v_2(x,0) = 0, \quad |x| > h. \quad (8c)$$

The mixed boundary conditions along $y = 0$ are

$$\sigma^1_{yy}(x,0) = -p(x) \quad |x| < a, \quad (9)$$

$$v_1(x,0) = 0, \quad a < |x| < h. \quad (10)$$

The crack surface traction is assumed to be constant for this study and is given by $p(x) = p_1$. However, the problem is formulated here for the general case of a symmetric function of "x," where $p(x) = p_1$ is a special case.

Substituting the stress and displacement field equations (1)–(4) in the continuity conditions (6) and (7), and taking the inverse Fourier transforms in "y" yields the following simultaneous equations:

$$a_{i1}f_1(\eta) + a_{i2}g_1(\eta) + a_{i3}f_2(\eta) + a_{i4}g_2(\eta) = D_i(\eta), \quad (i=1,\ldots,4), \quad (11)$$

where a_{ij}, $(i=1,\ldots,4)$ and D_i, $(i=1,\ldots,4)$ are given by Kaw (1987, Appendix B).

The boundary condition (10) may be expressed as

$$v(x) \equiv v_1(x,0) = \frac{2}{\pi}\int_0^\infty \frac{\phi_1(\xi)}{\xi}\left(\frac{\kappa_1+1}{2}\right)\cos\xi x\, d\xi = 0,\ a < |x| < h. \quad (12)$$

Taking the Fourier cosine transform of equation (12) gives

$$\frac{\phi_1(\xi)}{\xi} = \frac{2}{\kappa_1+1}\int_0^a v(t)\cos\xi t\,dt. \tag{13}$$

By solving the algebraic equations (11) and using equation (13), the stresses and displacements can be written in terms of the unknown displacement function, $v(t)$. The boundary condition (9) can then be written as

$$\int_{-a}^{a}\frac{v(t)}{(t-x)^2}dt + \int_{-a}^{a}K_{11}(t,x)\,v(t)\,dt = -\frac{\pi(1+\kappa_1)p(x)}{4\mu_1}, \quad |x|<a, \tag{14}$$

where $K_{11}(t,x)$ is dependent on the solution of equations (11).

Using integration by parts, the singular integral equation (14) can be expressed in terms of the slope of the crack-opening displacement, defined as

$$G(x) = \frac{dv(x)}{dx}. \tag{15}$$

The integral equation then has the form

$$v(a)F(x) + \int_{-a}^{a}\frac{G(t)}{t-x}dt + \int_{-a}^{a}G(t)\bar{K}_{11}(t,x)\,dt = -\frac{\pi p(x)(1+\kappa_1)}{4\mu_1}, \quad |x| < a, \tag{16}$$

where $F(x)$ and $\bar{K}_{11}$ are functions which depend on the solution of equations (11). A detailed description of these functions can be found in Kaw (1987), where it is also shown that the six material constants can be reduced to four (Dundurs, 1967).

It is now assumed that the slope of the crack-opening displacement function, $G(t)$ is given by

$$G(t) = \frac{H(t)}{(a^2-t^2)^{\gamma}}, \quad |t| < a,\ 0 < \mathrm{Re}\,\gamma < 1, \tag{17}$$

where $H(t)$ satisfies the Holder conditions (Muskhelishvili, 1953). By studying the dominant part of the integral equation (16), (Gupta, 1973; Kaw, 1987) the solution is found to be given by $\gamma = 1/2$. The singular integral equation (16) may then be expressed as

$$\int_{-a}^{a}\frac{H(t)}{\sqrt{a^2-t^2}}\left[\frac{1}{t-x} + \bar{K}_{11}\ (t,x)\right]dt = -\frac{\pi(1+\kappa_1)p(x)}{4\mu_1}. \tag{18}$$

Since the index of the integral equation (16) is $+1$ (Erdogan, Gupta, and Cook, 1972), the solution will contain an arbitrary constant, which is determined by the single-valuedness condition

$$\int_{-a}^{a}G(t)dt = 0. \tag{19}$$

The normal (cleavage) stress, $\sigma^1_{yy}(a+,0)$ at the crack tip, then has the classic square-root singularity (Kaw, 1987, Appendix C). The mode I stress intensity factor, K_{I}, is defined, following Erdogan (1972) as

$$K_{\mathrm{I}} = \lim_{x\to a+}\sqrt{2(x-a)}\ \sigma^1_{yy}\ (x,0). \tag{20}$$

2.2.2 Crack Up to the Interface (a = h). The boundary and continuity conditions for the crack extending up to the interface remain the same as for the case of the crack within the layer as discussed in Section 2.2.1. Hence, the governing singular integral equation (16) is valid for this case too. However, the Fredholm kernel $\bar{K}_{11}(t,x)$ becomes unbounded as $x \to h$ and $t \to +h$ or $x \to h$ and $t \to -h$, simultaneously. The unbounded terms in $\bar{K}_{11}(t,x)$ are due to the asymptotic behavior of the integrand defining $K_{11}(t,x)$. The coefficient $F(x)$ of $v(a)$ $(a = h)$ in equation (16) also becomes unbounded as $x \to h$ or $x \to -h$. The unbounded terms in $F(x)$ are due to the asymptotic behavior of the integrand defining $F(x)$. These functions are examined in detail by Kaw (1987).

The behavior of the slope function, $G(t)$ at the end points can be found by considering the dominant part of the singular integral equation, which can be expressed as

$$v(h)\int_0^{\infty}f^{\infty}(\eta,x)e^{-\eta h}d\eta + \int_{-h}^{h}G(t)\left[\frac{1}{t-x} + \bar{K}^{\infty}_{11}(t,x)\right]dt = B(x), \quad |x| < h, \tag{21}$$

where $B(x)$ is a bounded function, and $f^{\infty}(\eta,x)$ and $\bar{K}^{\infty}_{11}(t,x)$ are given in Kaw (1987).

Assume $G(t)$ has an integrable power singularity at the end points $t = \pm h$ given by $G(t) = H(t)/(h^2-t^2)^{\gamma}$, where $0 < \mathrm{Re}\gamma < 1$ and $H(t)$ satisfies the Holder conditions in $[-h,h]$. Using equation (21), and following Kaw (1987) and Gupta and Erdogan (1974), the characteristic equation obtained is

$$-\cos\pi\gamma + 2\gamma^2 - 4\gamma + 1 = 0. \tag{22}$$

This characteristic equation is independent of the material constants and is identical to the characteristic equation obtained for the solution of an edge crack in an infinite strip (Gupta and Erdogan, 1974). There are no roots of equation (22) in the acceptable range of $0 < \mathrm{Re}\,\gamma < 1$, which implies $G(t)$ does not have a power singularity. Hence, $G(t)$ either has a logarithmic singularity or is bounded at the end points $t = \pm h$.

Assuming $G(t)$ is a bounded function $G(t) = H(t)$, where $H(t)$ satisfies the Holder conditions in $[-h, h]$, and using equation (21), the following equation is obtained.

$$v(h)[B_5e^{B_6(h-x)}\log(h-x) + B_5e^{B_6(h+x)}\log(h+x)] = B(x), \tag{23}$$

where B_5 and B_6 are material constants (Kaw, 1987, Appendix B) and $B(x)$ is a bounded function. This equality is possible only if the displacement at the end points, $v(\pm h)$, is zero. This is not the case because the interleaf is modeled as distributed tension and shear springs, which allows the broken layer to displace at the end points under a uniform pressure, p_1 on the cracked surface. Hence, $G(t)$ cannot be bounded at the end points. This leaves only the possibility of a logarithmic singularity for $G(t)$.

Assume $G(t)$ has an integrable logarithmic singularity at $t = \pm h$ expressed as

$$G(t) = H(t)\log\left(\frac{h+t}{h-t}\right), \quad |t| < h, \tag{24}$$

where $H(t)$ satisfies the Holder condition in the closed interval $[-h,h]$. Note that since $G(t)$ is an odd function, $H(t)$ must be an even function, that is $H(t) = H(-t)$.

Consider the sectionally-holomorphic functions

$$\phi(z) = \int_{-h}^{h}\frac{G(t)}{t-z}dt = \int_{-h}^{h}\frac{H(t)\log\left(\frac{h+t}{h-t}\right)}{t-z}dz = \phi_1(z) - \phi_2(z), \tag{25}$$

where

$$\phi_1(z) = \int_{-h}^{h}\frac{H(t)\log(h+t)}{t-z}dt,$$

$$\phi_2(z) = \int_{-h}^{h}\frac{H(t)\log(h-t)}{t-z}dt. \tag{26a,b}$$

According to (Muskhelishvili, 1953, Chapter 4), near $z = h$,

$$\phi_1(z) = H(h)\log(2h)\log(z-h) + \phi_0(z), \qquad (27)$$

where $\phi_0(z)$ is a bounded function tending to a definite limit at $z = h$. Near $z = -h$,

$$\phi_1(z) = H(h)\int_{-h}^{h}\frac{\log(h+t)}{t-z}\,dt + \text{bounded function.} \qquad (28)$$

Consider the function

$$\Omega(z) = \frac{1}{2\pi i}\int_{-h}^{h}\frac{\log(h+t)}{t-z}\,dt. \qquad (29)$$

Using the Plemelj formulas (Muskhelishvili, 1953),

$$\Omega^+(t_0) - \Omega^-(t_0) = \log(t_0+h) \quad \text{for} \quad t_0 \in [-h,h]. \qquad (30)$$

Also,

$$\omega^+(t_0) - \omega^-(t_0) = -\log(t_0+h) \quad \text{for} \quad t_0 \in [-h,h], \qquad (31)$$

if

$$\omega(z) = \frac{1}{2}\left[\frac{\{\log(z+h)\}^2}{2\pi i} - \log(z+h)\right]. \qquad (32)$$

Adding equations (30) and (31),

$$(\Omega+\omega)^+ - (\Omega+\omega)^- = 0. \qquad (33)$$

Therefore, the function $[\Omega(z) + \omega(z)]$ is holomorphic in the neighborhood of $z = -h$, that is, near $z = -h$,

$$\Omega(z) = -\frac{1}{2}\left[\frac{\{\log(z+h)\}^2}{2\pi i} - \log(z+h)\right] + \text{holomorphic function.} \qquad (34)$$

From equations (27) and (34), the behavior of $\phi_1(z)$ near the end points $z = \pm h$ is written as

$$\phi_1(z) = H(h)\log(2h)\log(z-h) - \frac{H(h)}{2}[\{\log(z+h)\}^2 - 2\pi i\log(z+h)] + \text{holomorphic function.} \qquad (35)$$

Similarly, the behavior of $\phi_2(z)$ near the end points $z = \pm h$ can be expressed as

$$\phi_2(x) = H(h)\log(2h)\log(z+h) + \frac{H(h)}{2}[\log(z-h)]^2 + \text{holomorphic function.} \qquad (36)$$

Applying the Plemelj formulas (Muskhelishvili, 1953) in equations (35) and (36), equation (25) is reduced for $z = x$, $2h + x$, and $2h - x$. Using these results in equation (21), and separating the unbounded terms,

$$[-B_5 e^{B_6(h-x)}\log(h-x) - B_5 e^{B_6(h+x)}\log(h+x)]v(h) - 4H(h)[\log(h-x) + \log(h+x)] = B(x), \qquad (37)$$

where $B(x)$ contains all the bounded terms. For the boundedness of the left-hand side of equation (37), it is required that

$$H(h) = -\frac{B_5}{4}v(h) = -\frac{\kappa_1+1}{4\mu_1}K_s\,v(h). \qquad (38)$$

Noting that

$$\sigma^1_{xy}(h,0+) = \sigma^2_{xy}(h,0+) = -K_s\,v(h), \qquad (39)$$

$$H(h) = \frac{\kappa_1+1}{4\mu_1}\sigma^1_{xy}(h,0+), \qquad (40)$$

then

$$\lim_{x\to\pm h^-} G(x) = \frac{\kappa_1+1}{4\mu_1}\sigma^1_{xy}(h,0+)\lim_{x\to\pm h^-}\log\left(\frac{h+x}{h-x}\right). \qquad (41)$$

This proves the assumption that the slope, $G(x)$ of the crack opening displacement function, $v(x)$, has a logarithmic singularity at the end points is correct. Note that the coefficient of the logarithmic term is dependent on the shear stress at the end point, $(x = \pm h, y = 0+)$.

The present problem of a crack in the layer extending up to the interface can also be viewed as two semi-infinite strips with uniform pressure, p_1, applied on the end $(y=0)$, and unknown finite tractions on the longitudinal edges $(x = \pm h)$. These tractions depend on the elastic properties and geometrical parameters of the strip, interleaf, and the half-planes. This geometry can be compared with the known exact solutions for a semi-infinite strip (obtained from the free-body diagram of the classical half-plane $[y > 0]$ problem with uniform pressure over a finite range, $-h < x < h$), with the following boundary conditions

$$\sigma_{xy}(x,0) = 0, \quad \sigma_{yy}(x,0) = -p_1 \quad |x| < h, \qquad (42a,b)$$

$$\sigma_{xx}(\pm h,y) = -\frac{p_1}{\pi}\left[\frac{\pi}{2} - \tan^{-1}\frac{y}{2h} - \frac{2hy}{4h^2+y^2}\right], \quad 0<y<\infty, \qquad (42c)$$

$$\sigma_{xy}(\pm h,y) = \mp\frac{p_1}{\pi}\frac{4h^2}{4h^2+y^2}, \quad 0<y<\infty. \qquad (42d,e)$$

The solution to equations (42) is given by Timoshenko and Goodier (1970, Chapter 5) by using the Airy stress function method. The slope of the vertical displacement is given by

$$\frac{\partial v(x,0)}{\partial x} = -\frac{(\kappa+1)p_1}{4\mu\pi}\log\left(\frac{h+x}{h-x}\right), \qquad (43)$$

or

$$\frac{\partial v(x,0)}{\partial x} = \frac{\kappa+1}{4\mu}\sigma_{xy}(h,0+)\log\left(\frac{h+x}{h-x}\right), \qquad (44)$$

where μ is the shear modulus, $\kappa = 3-4\nu$ for plane strain and $\kappa = (3-\nu)/(1+\nu)$ for generalized plane stress, and ν is the Poisson's ratio of the strip.

It is interesting to note that both the problems have a logarithmic singularity at the end points $x = \pm h$. In fact, equations (41) and (44) are identical expressions for the slope functions, $G(x)$ at $x = \pm h$. A finite nonzero shear stress at the points $(x = \pm h, y = 0+)$ is the reason for the logarithmically-singular slope functions in the two problems.

Also, the shear stress in the half-plane is discontinuous, nonzero, and finite at $x = h$, $y = 0$. Hence, the axial normal stress, $\sigma^2_{yy}(h^+,0)$, is also logarithmically singular (Timoshenko and Goodier, 1970; Bogy, 1970) in the half-plane and is given by

$$\lim_{x\to h^+}\sigma^2_{yy}(x,0) = \tilde{K}\lim_{x\to h^+}\log(x-h) + \text{Order }(1), \qquad (45)$$

where $\tilde{K}$ is a modified stress intensity factor given by

$$\tilde{K} = \frac{4}{\pi}\sigma^1_{xy}(h,0+) = -\frac{4K_s v(h)}{\pi}. \qquad (46)$$

The same expression is obtained by an asymptotic analysis by Kaw (1987, Appendix D). It is interesting to note that a discontinuity in the normal loads on the half-plane does not produce unbounded stresses, but unsymmetric shear stresses do so at the point of discontinuity.

2.2.3 H-Shaped Crack (a = h, c > 0). The damage considered in this case is a broken layer ($a = h$) with delaminations of length "2c" along the interface (Fig. 1). By including delaminations, only the continuity conditions (7) are different from those given in Section 2.2.1 and are given by

$$\sigma^1_{xx}(h,y) = K_n < |y|-c > [u_2(h,y)-u_1(h,y)], \quad 0 < |y| < \infty, \qquad (47)$$

$$\sigma^1_{xy}(h,y) = K_s < |y|-c > [v_2(h,y)-v_1(h,y)], \quad 0 < |y| < \infty, \qquad (48)$$

where $<a> = 0$ if $z < 0$, $<a> = 1$ if $a > 0$.

Defining two unknown functions, $\phi_2(y)$ and $\phi_3(y)$, by

$$\frac{2\mu_1\phi_2(y)}{\kappa_1+1} = \sigma^1_{xx}(h,y) - K_n[u_2(h,y) - u_1(h,y)], \quad 0 \le |y| < \infty, \tag{49}$$

$$-\frac{2\mu_1\phi_3(y)}{\kappa_1+1} = \sigma^1_{xy}(h,y) - K_s[v_2(h,y) - v_1(h,y)], \quad 0 \le |y| < \infty, \tag{50}$$

the continuity conditions (47) and (48) can be written as

$$\sigma^1_{xx}(h,y) = 0, \quad 0 \le |y| < c \tag{51}$$

$$\frac{2\mu_1\phi_2(y)}{\kappa_1+1} = \langle c - |y| \rangle \{\sigma^1_{xx}(h,y) - K_n[u_2(h,y) - u_1(h,y)]\}, \quad 0 \le |y| < \infty, \tag{52}$$

$$\sigma^1_{xy}(h,y) = 0, \quad 0 \le |y| < c, \tag{53}$$

$$-\frac{2\mu_1\phi_3(y)}{\kappa_1+1} = \langle c - |y| \rangle \{\sigma^1_{xy}(h,y) - K_s[v_2(h,y) - v_1(h,y)]\}, \quad 0 \le |y| < \infty. \tag{54}$$

The homogeneous boundary conditions given by equations (8) are identically satisfied by the stress and displacement field equations (1)–(4).

Following the same procedure given in the Section 2.2.1, the boundary condition (9) can be written in the form of a singular integral equation given by

$$\int_{-h}^{h} \frac{v(t)}{(t-x)^2}dt + \int_{-h}^{h} K_{11}(t,x)v(t)dt + \int_0^c K_{12}(x,z)\phi_2(z)dz + \int_0^c K_{13}(x,z)\phi_3(z)dz = -\frac{\pi p(x)(1+\kappa_1)}{4\mu_1}, \quad |x| < h. \tag{55}$$

Similarly, after separating the dominant part of the kernels, equations (51) and (53) can be written as

$$\int_{-h}^{h} K_{21}(y,t)v(t)dt + \int_0^c K_{22}(y,z)\phi_2(z)dz - \frac{\pi}{2}\phi_2(y) + \int_0^c K_{23}(y,z)\phi_3(z)dz = 0, \quad 0 \le |y| < c, \tag{56}$$

$$\int_{-h}^{h} K_{31}(y,t)v(t)dt + \int_0^c K_{32}(y,z)\phi_2(z)dz + \int_0^c K_{33}(y,z)\phi_3(z)dz - \frac{\pi}{2}\phi_3(y) = 0, \quad 0 \le |y| < c. \tag{57}$$

The values of K_{ij}, $(i=1,3,\ j=1,3)$ are given by Kaw (1987).

Using integration by parts, the singular integral equation (55) can be obtained in terms of the slope of the crack-opening displacement function $G(x) = dv(x)/dx$ as

$$v(h)F(x) + \int_{-h}^{h} \frac{G(t)}{t-x}dt + \int_{-h}^{h} G(t)\bar{K}_{11}(t,x)dt + \int_0^c K_{12}(x,z)\phi_2(z)dz + \int_0^c K_{13}(x,z)\phi_3(z)dz = -\frac{\pi p(x)(1+\kappa_1)}{4\mu_1}, \quad |x| < h. \tag{58}$$

Assume, in this case, that $G(t)$ is a bounded function, then

$$G(t) = H(t), \tag{59}$$

where $H(t)$ satisfies the Holder conditions in the closed interval $[-h, h]$.

For $c = 0$ and $a = h$, equation (58) reduces to equation (16) obtained for the case of the crack up to the interface. Hence, the first three terms in equation (58) contribute the unbounded terms given by the left-hand side of equation (23), and are expressed as

$$U_1(x) = v(h)[B_5 e^{B_6(h-x)}\log(h-x) + B_5 e^{B_6(h+x)}\log(h+x)]. \tag{60}$$

The unbounded terms contributed by the fifth term of the singular integral equation (58) are given by

$$U_2(x) = \int_0^c K^\infty_{13}(x,z)\,\phi_3(z)dz, \tag{61}$$

where $K^\infty_{13}(x,z)$ is the unbounded part of $K_{13}(x,z)$. The unbounded part contributed by the fifth term in the integral equation (58) is found to be (Kaw, 1987)

$$U_2(x) = -\phi_3(0)\log(h-x) - \phi_3(0)\log(h+x) + \text{holomorphic function.} \tag{62}$$

Following the same procedure, the fourth term in equation (58) is found to have no unbounded terms.

Adding equations (60) and (62), and using equations (53) and (54), $[U_1(x) + U_2(x)]$ is found to be a bounded function from which it follows that the sum total of the unbounded terms cancels out. This then proves that the assumption of a bounded slope function, $G(t)$, is correct.

Similar behavior of the slope function was reported by Backioglu and Erdogan (1977) for the problem of a semi-infinite strip of finite width "$2h$" under a self-equilibrating pressure on the end ($y = 0$) and stress-free longitudinal edges ($x = \pm h$).

The axial stress in the half-plane has a logarithmic singularity at $x = h$, $y = \pm c$. This is the well-known logarithmic singularity (Timoshenko and Goodier, 1970; Bogy, 1970) due to the finite discontinuity in the shear load on a half-plane and is given by

$$\lim_{x\to h^+} \sigma^2_{yy}(x,c) = \hat{K} \lim_{x\to h^+} \log(x-h) + \text{Order}(1), \tag{63}$$

where $\hat{K}$ is the modified stress intensity factor and is defined by

$$\hat{K} = \frac{2}{\pi}\sigma^1_{xy}(h,c+) = \frac{2}{\pi}K_s[v_2(h,c) - v_1(h,c)] = \frac{4\mu_1}{\pi(\kappa_1+1)}\phi_3(c-). \tag{64}$$

The axial stress $\sigma^2_{yy}(h^+,0)$ in the half-plane is bounded, as the shear load is continuous and zero at $x = h$, $y = 0$.

The axial stress in the layer is logarithmically singular at the interface crack tip ($x = \pm h$, $y = \pm c$), and is given at $x = h$, $y = c$ by

$$\lim_{x\to h^-} \sigma^1_{yy}(x,c) = -\hat{K} \lim_{x\to h^-} \log(h-x) + \text{Order}(1). \tag{65}$$

Note that for a split length approaching zero, the modified SIF, $\hat{K}$, is exactly half the value of the modified SIF, $\tilde{K}$ given by equation (46) for the case of the broken layer ($a=h$). This is because the discontinuity in the shear load on the half-plane reduces by one-half for an infinitesimal split length.

The solutions to the above developed integral equations and the results are presented and discussed in Part II of this paper to follow.

Acknowledgment

This work was supported by the Fatigue and Fracture Branch of the Materials Division, NASA Langley Research Center, Hampton, Va., under Grant No. NAG-1-629. Dr. T. K. O'Brien was the grant monitor.

References

Ashbaugh, N. E., 1973, "Stresses in Laminated Composites Containing a Broken Layer," ASME Journal of Applied Mechanics, Vol. 40, pp. 533–540.

Backlioglu, M., and Erdogan, F., 1977, "The Crack-Contact and the Free-End Problem for a Strip Under Residual Stress," ASME Journal of Applied Mechanics, Vol. 44, pp. 41–46.

Bogy, D. B., 1973, "The Plane Elastostatic Solution for a Symmetrically Loaded Crack in a Strip Composite," *International Journal of Engineering Science*, Vol. 11, pp. 985–996.

Bogy, D. B., 1970, "On the Problem of Edge-Bonded Elastic Quarter-Planes Loaded at the Boundary," *International Journal of Solids and Structures*, Vol. 6, pp. 1287–1313.

Comninou, M., 1977, "The Interface Crack," ASME Journal of Applied Mechanics, Vol. 44, pp. 631–636.

Cook, T. S., and Erdogan, F., 1972, "Stresses in Bonded Materials with a Crack Perpendicular to the Interface," *International Journal of Engineering Science*, Vol. 10, pp. 677–697.

Dundurs, J., 1967, "Effect of Elastic Constants on Stress in a Composite Under Plane Deformations," *Journal of Composite Materials*, Vol. 1, pp. 310–322.

Erdogan, F., and Bakioglu, M., 1977, "Stress-Free Problems in Layered Materials," *International Journal of Fracture*, Vol. 13, pp. 739–749.

Gautesen, A. K., and Dundurs, J., 1987, "The Interface Crack in a Tension Field," ASME Journal of Applied Mechanics, Vol. 54, pp. 93–98.

Gecit, M. R., and Erdogan, F., 1978, "The Effect of Adhesive Layers on the Fracture of Laminated Structures," *ASME Journal of Engineering Materials and Technology*, Vol. 100, pp. 2–9.

Goree, J. G., and Venezia, W. A., 1977, "Bonded Elastic Half-Planes with an Interface Crack and Perpendicular Intersecting Crack That Extends into the Adjacent Material," *International Journal of Engineering Science*, Vol. 15, Part 1, pp. 1–17; Part 2, pp. 19–27.

Gupta, G. D., and Erdogan, F., 1974, "The Problem of Edge Cracks in an Infinite Strip," ASME Journal of Applied Mechanics, Vol. 41, pp. 1001–1006.

Gupta, G. D., 1973, "A Layered Composite with a Broken Laminate," *International Journal of Solids and Structures*, Vol. 9, pp. 1141–1154.

Hilton, P. D., and Sih, G. C., 1971, "A Laminate Composite with a Crack Normal to the Interfaces," *International Journal of Solids and Structures*, Vol. 7, pp. 913–930.

Kaw, A. K., 1987, "Damage Growth in Composite Laminates with Interleaves," Ph.D. Dissertation, Clemson University, Clemson, S.C.

Knowles, J. K., and Sternberg, E., 1983, "Large Deformation Near a Tip of an Interface Crack Between Two Neo-Hookean Sheets," *Journal of Elasticity*, Vol. 13, pp. 257–293..

Lu, M., and Erdogan, F., 1983, "Stress Intensity Factors in Two Bonded Elastic Layers Containing Cracks Perpendicular to and on the Interface," *Engineering Fracture Mechanics*, Vol. 18, Part 1, pp. 491–506; Part 2, pp. 507–528.

Masters, J. E., 1985, "Characterization of Impact Damage Development in Graphite/Epoxy Laminates," *ASTM Symposium on Fractography of Modern Engineering Materials*, Nashville, Tenn.

Muskhelishvili, N. I., 1953, *Singular Integral Equations*, Noordhoff.

Sneddon, I. N., and Srivastav, R. P., 1971, "The Stress Field in the Vicinity of a Griffith Crack in a Strip of Finite Width," *International Journal of Engineering Sciences*, Vol. 9, pp. 479–488.

Sneddon, I. N., and Lowengrub, M., 1969, "Crack Problems in the Classical Theory of Elasticity," John Wiley and Sons, New York.

Sun, C. T., 1985, "Suppression of Delamination in Composite Laminates Subjected to Impact Loading," *11th Annual Mechanics of Composite Review*, Dayton, OH, pp. 106–113.

Timoshenko, S. P., and Goodier, J. N., 1970, *Theory of Elasticity*, McGraw-Hill, New York.

A. K. Kaw
Assistant Professor,
Department of Mechanical Engineering,
University of South Florida,
Tampa, FL 33620-5350
Assoc. Mem. ASME

J. G. Goree
Professor,
Department of Mechanical Engineering,
Clemson University,
Clemson, SC 29634-0921
Mem. ASME

Effects of Interleaves on Fracture of Laminated Composites: Part II—Solution and Results

The numerical solution of the integral equations derived in Part I of this work is developed and the critical stresses and displacements are calculated. These results indicate that interleaves increase the interfacial damage tolerance and significantly relieve the stresses in the undamaged plies. Interface (H-shaped) cracks have a stable growth with the mode I opening stress becoming compressive after a small longitudinal growth. Additional interface crack extension is due to shear stresses (mode II) only. In order to recommend an interleaf thickness-to-layer width ratio, the influence of relative material properties, structural weight, and stress reduction is studied.

1 Introduction

In Part I of this study, integral equations were developed which represent the influence of interleaves on damage growth in laminated composites. The composite was approximated by linearly elastic, isotropic media made of half-planes separated from a finite width layer by thin interleaves (Part I, Fig. 1). Three cases, depending on the extent of damage, were studied. In the first case the center layer was assumed to have a symmetric central crack along the x-axis, in the second case the crack touching the interface was analyzed, and lastly, damage extending in the form of symmetric delaminations along the interface (H-shaped crack) was examined. Using the Fourier transform expressions for displacement and stresses, and applying inverse Fourier transform techniques, solutions were developed for the three cases of damage.

In this part of the study, numerical solution techniques based on Gaussian integration techniques (Kaya and Erdogan, 1987; Erdogan, Gupta and Cook, 1972) and Hadamard's (1923) concept of differentiation of Cauchy integrals are developed. Critical stresses and displacements are calculated to investigate the influence of relative elastic properties and geometry of the interleafed composite on interface debonding, extent and suppression of delamination, and stress relieving in the undamaged plies. The results provide useful information that can assist the designer in the selection of suitable material and geometrical parameters of the interleaf for a particular baseline laminate.

Certain commercial materials and their manufacturers have been mentioned in this paper for a practical discussion of results. The use of these materials in this paper is not an official endorsement of these materials or manufacturers, either expressed or implied, by the authors or their university affiliations and sponsors.

References made to equations developed in Part I of this study will be prefixed by I. For example, equation (I7*a*) refers to equation (7*a*) of Part I. The numerical solutions for each of the three cases are given first, followed by a discussion of the results in Section 3.

Contributed by the Applied Mechanics Division of The American Society of Mechanical Engineers for presentation at the Winter Annual Meeting, San Francisco, Calif., December 10-15, 1989.

Discussion on this paper should be addressed to the Editorial Department, ASME, United Engineering Center, 345 East 47th Street, New York, N.Y. 10017, and will be accepted until two months after final publication of the paper itself in the Journal of Applied Mechanics. Manuscript received and accepted by the ASME Applied Mechanics Division, April 15, 1989.

Paper No. 89-WA/APM-46.

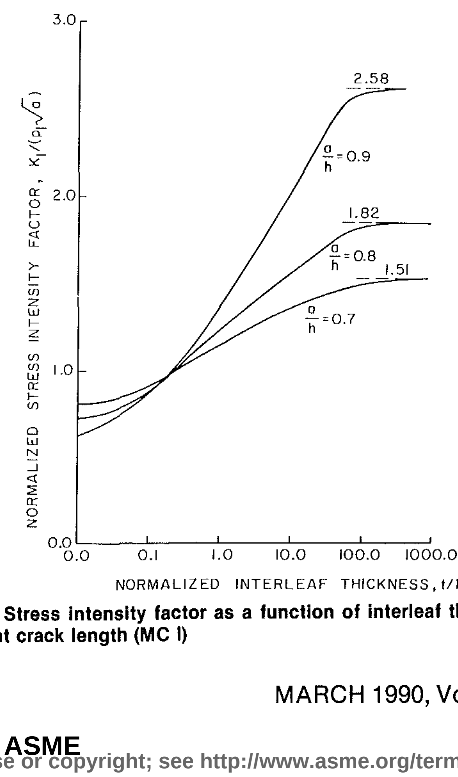

Fig. 1 Stress intensity factor as a function of interleaf thickness for constant crack length (MC I)

2 Solution Techniques

2.1 Crack Within the Layer. Normalizing the variables of equation (I16) and (I18), with respect to the half crack length "a",

$$s=\frac{t}{a},\ r=\frac{x}{a},\ G(t)=G(as)=\phi(s),$$

$$p(x)=p(ar)=S(r),\ H(t)=H(as)=\psi(s), \qquad (1)$$

equation (I18) may then be written as

$$\int_{-1}^{1}\frac{\psi(s)}{a\sqrt{1-s^2}}\left[\frac{1}{s-r}+a\bar{K}_{11}[as,\ ar]\right]ds$$
$$=-\frac{\pi S(r)(1+\kappa_1)}{4\mu_1},\ |r|<1. \qquad (2)$$

The integral equation (2) is approximated by using Gauss-Chebyshev integration formulae and techniques (Erdogan, Gupta, and Cook, 1972) to give

$$\frac{\pi}{N}\sum_{i=1}^{N}\psi(s_i)\left[\frac{1}{a(s_i-r_j)}+\bar{K}_{11}(as_i,\ ar_j)\right]$$
$$=-\frac{\pi S(r_j)(1+\kappa_1)}{4\mu_1},\ (j=1,2,\ .\ .\ .\ ,\ N-1), \qquad (3)$$

where

$$s_i\ =\ \cos\left[\frac{(2i-1)\pi}{2N}\right],\ (i=1,2,\ .\ .\ .\ ,\ N), \qquad (4)$$

$$r_j\ =\ \cos\left[\frac{\pi j}{N}\right],\ (j=1,2,\ .\ .\ .\ ,\ N-1). \qquad (5)$$

The single valuedness condition (I19) can be approximated as

$$\sum_{i=1}^{N}\psi(s_i)=0. \qquad (6)$$

Equations (3) and (6) represent a $N\times N$ system of simultaneous linear equations which gives numerical values for $\psi(s)$ at the discrete points, s_i, given by equation (4).

The normal (cleavage) stress, $\sigma_{yy}(a^+,0)$ at the crack tip, has a square root singularity (Kaw, Appendix C, 1987). A stress intensity factor, K_1, is defined as

$$K_1=\lim_{x\to a^+}\sqrt{2(x-a)}\,\sigma^1_{yy}(x,0). \qquad (7)$$

Equation (7) can be rewritten (Kaw, Appendix C, 1987) in nondimensional terms as

$$K_1=-\frac{4\mu_1}{(1+\kappa_1)}\frac{\psi(1)}{\sqrt{a}}. \qquad (8)$$

2.2 Crack Up to the Interface. The numerical techniques enumerated in (Erdogan, Gupta, and Cook, 1972) to solve singular integral equations with Cauchy kernels are based on the exact Cauchy principal-value integral expression (Abramowitz and Stegun, 1964) of orthogonal Jacobi polynomials, $P_n^{(\alpha,\beta)}(t)$, given by

$$\int_{-1}^{1}\frac{(1-t)^{\alpha}(1+t)^{\beta}P_n^{(\alpha,\beta)}(t)}{t-x}dt$$
$$=\pi\cot(\alpha\pi)(1-x)^{\alpha}(1+x)^{\alpha}P_n{}^{(\alpha,\beta)}(x)-\frac{2^{\alpha+\beta}\Gamma(\alpha)\Gamma(n+\beta+1)}{\Gamma(n+\alpha+\beta+1)}$$
$$\times F\left[n+1;\ -n-\alpha-\beta;\ 1-\alpha;\ \frac{1-x}{2}\right]$$
$$\times[\alpha>-1,\beta>-1,\alpha\neq 0,1,2,\ .\ .\ .\ ],\ |x|<1, \qquad (9)$$

where $\Gamma(\alpha)$ is the Gamma function and $F(\alpha;\ \beta;\ \gamma;\ z)$ is a hypergeometric series. This relationship forms the basis for solving singular integral equations with a simple Cauchy kernel, where the unknown slope function has a power singularity of the order of (α) and (β) at the end points. But in the present case the slope function has a logarithmic singularity at the end points, and a similar numerical technique could not be found in the literature. Hence, solving equation (I14) directly for the unknown displacement function, $v(x)$, is suggested.

Normalizing the following variables with respect to the half-layer width "h",

$$s=\frac{t}{h},\ r=\frac{x}{h},\ V(s)=\frac{v(t)}{h},$$

$$K'_{11}(r,s)=h^2K_{11}(t,x),\ S(r)=p(x), \qquad (10)$$

equation (I14) can be rewritten in the nondimensional form as

$$\int_{-1}^{1}\frac{V(s)}{(s-r)^2}ds+\int_{-1}^{1}h^2V(s)K_{11}(hs,hr)ds$$
$$=-\frac{\pi S(r)(1+\kappa_1)}{4\mu_1},\ |r|<1. \qquad (11)$$

Equation (11) has $1/(s-r)^2$ type integrand and are called to be a strong singularity. Such integrands are classically nonintegrable and cannot be defined even in the principal value sense. A concept used by Hadamard (1923) interprets improper integrals with such singularities in the finite part sense. Kaya and Erdogan (1987) used this concept to solve elastodynamic problems such as the problem of an edge crack perpendicular to the free boundary of an elastic half-plane.

Using the Cauchy principal value integrals (Tricomi, 1957) gives, for use later,

$$⨍_{-1}^{1}\frac{P_n(t)}{t-x}dt=-2Q_n(x),\ |x|<1, \qquad (12)$$

where $P_n(t)$ and $Q_n(t)$ are Legendre polynomials of the first and second kind, respectively.

Hadamard's concept uses direct differentiation on Cauchy integrals to obtain finite part integrals. For example, this procedure gives

$$\frac{d}{dx}\int_{-1}^{1}\frac{f(t)}{t-x}dt=\int_{-1}^{1}\frac{f(t)}{(t-x)^2}dt. \qquad (13)$$

Using equation (13) direct differentiation in equation (12), it follows that

$$⨎_{-1}^{1}\frac{P_n(t)}{(t-x)^2}dt=-\frac{2(n+1)}{(1-x^2)}[xQ_n(x)-Q_{n+1}(x)],\ |x|<1. \qquad (14)$$

Now, assuming in equation (11) that the displacement function can be represented as

$$V(s)\simeq\sum_{n=0}^{N}A_nP_n(s), \qquad (15)$$

equation (11) can then be written as

$$\sum_{n=0}^{N}A_n\left[\frac{-2(n+1)}{1-r^2}\{rQ_n(r)-Q_{n+1}(r)\}\right.$$
$$\left.+\int_{-1}^{1}h^2P_n(s)K_{11}(hs,hr)ds\right]=-\frac{\pi S(r)(1+\kappa_1)}{4\mu_1},\ |r|<1. \qquad (16)$$

A collocation method is used to solve for the unknown coefficients, A_n. The choice of collocation points, symmetrically distributed on the interval $(-1,\ 1)$, is not restricted, but more points concentrated near the end points improves the rate of convergence (Baker, 1977). The roots of the Legendre polynomials are a suitable choice, and this gives

$$\sum_{n=0}^{N} A_n\Big[\frac{-2(n+1)}{1-r_i^2}\{r_i Q_n(r_i)-Q_{n+1}(r_i)\}$$

$$+\int_{-1}^{1} h^2 P_n(s) K_{11}(hs,hr_i)ds\Big] = -\frac{\pi S(r_i)(1+\kappa_1)}{4\mu_1},$$

$$(i=0,1,2,\ \ldots\ ,N-1,N), \qquad (17)$$

where r_i is the ith zero of the Legendre polynomial $P_{N+1}(x)$, and

$$P_N(x)=\frac{1}{2^N N!}\frac{d^N}{dx^N}[x^2-1]^N. \qquad (18)$$

Equation (17) represents a $[(N+1)\times(N\times 1)]$ system of linear equations which can be used to evaluate the coefficients, A_n.

The modified stress intensity factor, $\tilde{K}$ defined by equation (I46), is expressed numerically as

$$\tilde{K}=-\frac{4K_s h}{\pi}\sum_{n=0}^{N} A_n. \qquad (19)$$

2.3 H-Shaped Crack. Normalizing the dimension of equations (I55)–(I57), with respect to the half-layer width "h", and half split length "c",

$$s=\frac{t}{h},\ r=\frac{x}{h},\ w=\frac{z}{c},\ q=\frac{y}{c},$$

$$v(t)=\theta_1(s)h,\ \phi_2(z)=\theta_2(w)c,\ \phi_3(z)=\theta_3(w)c,\ p(x)=S(r), \qquad (20)$$

the following integral equations are obtained in the nondimensional form:

$$\int_{-1}^{1}\frac{\theta_1(s)}{(s-r)^2}ds+\int_{-1}^{1}h^2K_{11}(hr,hs)\theta_1(s)ds$$

$$+\int_0^1 c^2K_{12}(hr,cw)\theta_2(w)dw$$

$$+\int_0^1 c^2K_{13}(hr,cw)\theta_3(w)dw=-\frac{\pi S(r)(1+\kappa_1)}{4\mu_1},\ \ |r|<1, \qquad (21)$$

$$\int_{-1}^{1} h^2K_{21}(cq,hs)\theta_1(s)ds$$

$$+\int_0^1 c^2K_{22}(cq,cw)\theta_2(w)dw-\frac{\pi c}{2}\theta_2(q)$$

$$+\int_0^1 c^2K_{23}(cq,cw)\theta_3(w)dw=0,\quad 0<q<1, \qquad (22)$$

$$\int_{-1}^{1} h^2K_{31}(cq,hs)\theta_1(s)ds+\int_0^1 c^2K_{23}(cq,cw)\theta_2(w)dw$$

$$+\int_0^1 c^2K_{33}(cq,cw)\theta_3(w)dw-\frac{\pi c}{2}\theta_3(q)=0,\quad 0<q<1. \qquad (23)$$

To determine the numerical solution to the three integral equations (21)–(23), the following forms for the unknown functions are assumed

$$\theta_1(s)\simeq\sum_{k=0}^{K}A_kP_k(s), \qquad (24a)$$

$$\theta_2(s)\simeq\sum_{l=0}^{L}B_lT_l(w), \qquad (24b)$$

$$\theta_3(s)\simeq\bar{C}_O+\sum_{m=1}^{M}C_mT_m(w), \qquad (24c)$$

where $P_k(s)$ and $T_l(w)$ are Legendre and Chebyshev polynomials of the first kind, respectively. The normalized crack-opening displacement function $\theta_1(s)$ is approximated by a series of Legendre polynomials because of the availability of a direct relationship (14) for integrands with strong singularities. The other normalized displacement functions, $\theta_2(w)$ and $\theta_3(w)$, are approximated by a series of Chebyshev polynomials. It has been shown (Fox and Parker, 1968) that a series of Chebyshev polynomials converges more rapidly than any other series of Gegenbauer polynomials, and converges much more rapidly than power series.

Using Hadamard's concept expressed mathematically by equation (14) for Legendre polynomials, the series approximations (24) for the unknown functions $\theta_i(s)$, $(i=1,2,3)$, and the even and odd symmetry of $\theta_2(w)$ and $\theta_3(w)$, respectively, equations (21)–(23) can be rewritten as

$$\sum_{k=0}^{K}A_kZ_{11}(k,r)+\sum_{l=0}^{L}B_lZ_{12}(l,r)+\sum_{m=0}^{M}C_mZ_{13}(m,r)$$

$$=-\frac{\pi S(r)(1+\kappa_1)}{4\mu_1},\ \ |r|<1, \qquad (25)$$

$$\sum_{k=0}^{K}A_kZ_{21}(k,q)+\sum_{l=0}^{L}B_lZ_{22}(l,q)$$

$$+\sum_{m=0}^{M}C_mZ_{23}(m,q)=0,\ \ |q|<1, \qquad (26)$$

$$\sum_{k=0}^{K}A_kZ_{31}(k,q)+\sum_{l=0}^{L}B_lZ_{32}(l,q)$$

$$+\sum_{m=0}^{M}C_mZ_{33}(m,q)=0,\ \ |q|<1, \qquad (27)$$

where Z_{ij}, $(i=1,2,3,\ j=1,2,3)$ are given in terms of finite integrals of K_{ij} (Kaw, Appendix B, 1977).

Note that since the displacement function $\theta_3(w)$ is an odd function of "w" and is nonzero at $w=0$, the first term of the series approximation of the function $\theta_3(w)$ is assumed to be of the form

$$\bar{C}_0=C_0\operatorname{sign}(w),$$

where

$$\operatorname{sign}(w)\ =\ +1,\ \text{if } w>0,$$
$$=\ -1,\ \text{if } w<0.$$

The collocation method is again used to solve for the unknowns A_k, B_l, and C_m. The choice of collocation points is distributed symmetrically on the interval $(-1,1)$ for equations (25)–(27). More points are concentrated near the end points to improve the rate of convergence (Baker, 1977). The roots of the Legendre polynomials satisfy such a selection of collocation points.

Equation (25)–(27) hence represents a $[(K+L+M+3)\times(K+L+M+3)]$ system of linear equations which can be simultaneously solved for the unknown coefficients A_k, B_l, C_m. The unknown functions θ_i, $(i=1,2,3)$, can hence be calculated by using equations (24).

The modified stress intensity factor given by equation (I64) can be numerically expressed as

$$\hat{K}=\frac{4\mu_1 c}{\pi(\kappa_1+1)}\sum_{m=0}^{M}C_m. \tag{28}$$

3 Results and Discussion

The results presented here are for the case of plane strain with a constant pressure, p_1, on the crack surface and no loads at infinity. This is the solution denoted by S_{II} in Part I. The complete solution S_{total} can be obtained simply by adding the uniform strain solution, S_I, which is given by constant stresses and no damage as

$$\sigma_{yy}^1=p_1,\ \sigma_{yy}^2=p_1\frac{(1-\nu_1^2)E_2}{(1-\nu_2^2)E_1}. \tag{29a,b}$$

Five material combinations, given in Table 1 are used in the results and are abbreviated as MC I, MC II, MC III, MC IV, and MC V.

The Young's moduli, E_1 and E_2 in the material combination, MC I, are the stiffness properties in the 90 deg and 0 deg directions of a unidirectional T300/5208 Graphite/Epoxy[1] laminate. MC I is the most significant material combination, because a transverse notch is more likely to develop first in a 90 deg ply. This behavior was observed by Masters (1985) in his experimental study of impact loading of laminates. Most of the sample results shall hence be discussed for this material combination. The interleaf properties[2] in Table 1 were communicated by Masters as used in his experimental study (Masters, 1985).

Table 1 Material combinations used

Material Combinations	Layer E_1 (GPA)	Layer ν_1	Half-Plane E_2 (GPA)	Half-Plane ν_2	Interleaf E_3 (GPA)	Interleaf ν_3
MC I	10.35	.28	182.90	.28	3.45	.35
MC II	31.05	.28	10.35	.28	3.45	.35
MC III	10.35	.28	10.35	.28	3.45	.35
MC IV	182.90	.28	182.90	.28	3.45	.35
MC V	182.90	.28	10.35	.28	3.45	.35

3.1 Crack Within the Layer. In this problem, a symmetric transverse crack of length "$2a$" ($a/h<1$)[3] is situated in the layer and is opened by a uniform pressure, p_1. The crack-tip axial stress has a square-root-type singularity and the coefficient of this singularity is defined as the mode I stress intensity factor (SIF), K_I given by equation (I20). When the SIF reaches a critical value $K_I=K_{Ic}$, it is assumed that the crack will propagate. This critical value is called the fracture toughness and is taken to be constant for a particular material. It should be pointed out that the SIF depends on the crack length and the applied load. This criterion can be directly used only for brittle materials and needs modification for ductile materials, where yielding may exist. The simplicity of the criterion, however, makes it a single parameter to predict crack growth and fracture, and is useful even for cracks where yielding is in the form of small plastic zones.

Before presenting the detailed results, the adequacy of modeling the interleaves as distributed shear and tension springs will be discussed. Gecit and Erdogan (1978) solved the problem of embedded cracks in periodic buffer strips separated by adhesive layers and modeled, the latter, both as springs and as a continuum. They found small differences in the results obtained for the two models if the interleaf moduli and thickness were smaller than those of the strips. For example, for a material combination close in properties to MC III and MC IV, and $a/h=0.9$ and ($t/h<0.2$)[4], a difference of less than 3 percent was found in the SIFs. Results from the present study for the normalized SIF, $K_I/(p_1 a)$, are plotted as a function of interleaf thickness in Fig. 1 for MC I. The values of the normalized SIF corresponding to the special cases of an interleaf thickness of zero, as well as that of the thickness approaching infinity, are found to be in excellent agreement with those special cases found in the literature. For the interleaf thickness approaching infinity, which is equivalent to an interleaf moduli of zero, or therefore corresponding to stress-free longitudinal sides of the layer, the normalized SIFs reach asymptotic values identical to those obtained by Sneddon and Srivastav (1971). They solved the problem of a transverse crack in a finite width strip with unloaded longitudinal edges. The normalized SIF, for the other special case of an interleaf thickness of being exactly equal to zero, and found to be identical to those obtained by Hilton and Sih (1971) and Bogy (1973). They solved the problem of a layer, with an internal crack normal to the interface, bonded between two half-planes. These limit cases and the results of Gecit and Erdogan (1978) for thin interleaves give considerable assurance as to the usefulness of the results in predicting the behavior of the interleafed composite laminates with an embedded crack.

Additional significant results may be obtained from Fig. 1, where it is seen that the normalized SIF increases with an increase in the interleaf thickness. This behavior is true for all material combinations. It does not, however, imply that the global strength of the laminate is necessarily decreased by interleafing laminates. For example, if the initial damage is in a 90 deg ply, the presence of the interleaf may result in a complete failure of the ply at a lower load. The subsequent behavior of the laminate when this ply is fully broken, and the influence of the interleaf on delamination, additional ply failure, and ultimate laminate strength may, however, be higher than with no interleaf. This behavior is considered in the next two sections.

Further, from Fig. 1, the SIF (numerator of the normalized SIF) is found to decrease as the crack length is increased for small interleaf thicknesses. Since the SIF is directly related to the load-carrying capacity of a material, a decreasing SIF implies a higher load required to continue the crack. The crack growth is hence considered to be stable. For example, for $a/h=0.9$ and $t/h<0.08$, the crack growth is stable. This behavior of a stable crack for small interleaf thicknesses holds only for MC I, that is, for the case of the crack in a layer which is less stiff than the half-plane.

The maximum cleavage stress, $\sigma_{yy}^2(h,0)/p_1$, in the half-plane occurs in line with the crack tip at the interface and is plotted in Fig. 2 as a function of interleaf thickness for MC I. For small crack lengths ($a/h<0.8$), this stress is an increasing function is the range of small interleaf thicknesses (or large interleaf moduli), but is relieved on further increase in the thickness. This behavior is not found for large crack lengths. For example, for $a/h=0.9$, the stress decreases monotonically with an increase in the interleaf thickness. Interestingly, for material combination MC V, where the crack is in a stiffer material, the increase in the cleaveage stress in the range of small interleaf thicknesses is much more substantial for all crack lengths. In such cases the introduction of a thin interleaf can, in fact, cause higher cleavage stresses and perhaps assist in continuing the crack across the interface.

[1]T300/5208 Graphite/Epoxy composite laminate is made of T300-graphite fibers (manufactured by Union Carbide) in Rigidite 5208-epoxy resin (registered trademark of Narmco Materials).

[2]Private communication of the second author with Dr. John E. Masters, Chemical Research Division, American Cyanamid Company, Stamford, Conn. 06904.

[3]a/h = Crack length to layer width ratio.

[4]t/h = Interleaf thickness to half-layer width ratio.

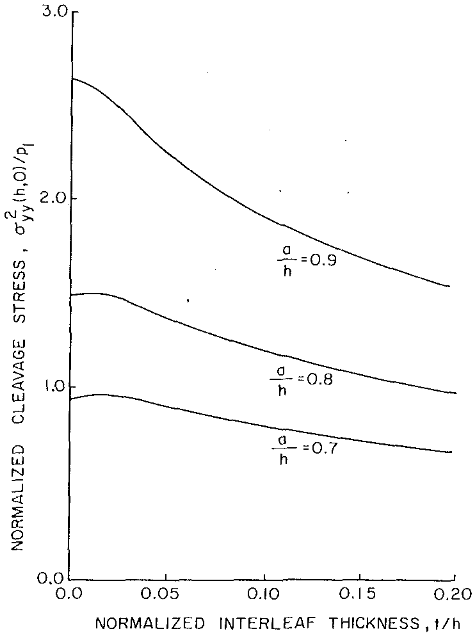

Fig. 2 Maximum cleavage stress in the half-plane as a function of interleaf thickness for constant crack length (MC I)

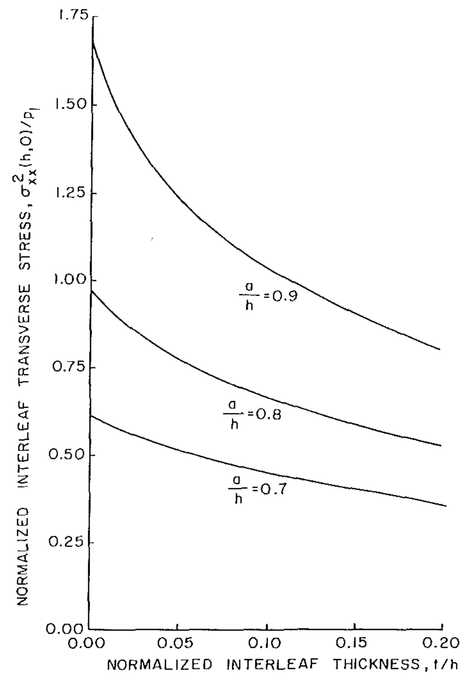

Fig. 3 Maximum interleaf transverse stress as a function of interleaf thickness for constant crack length (MC I)

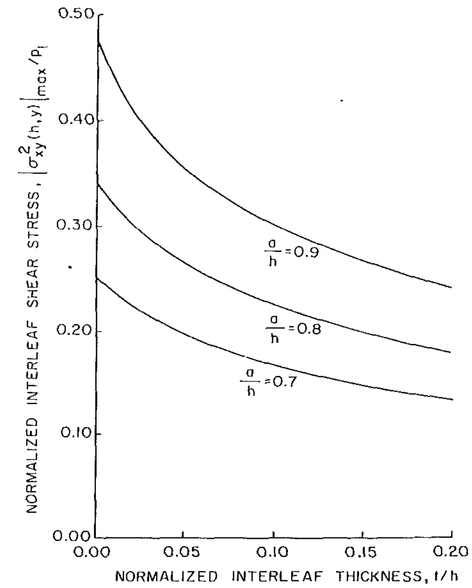

Fig. 4 Maximum interleaf shear stress as a function of interleaf thickness for constant crack length (MC I)

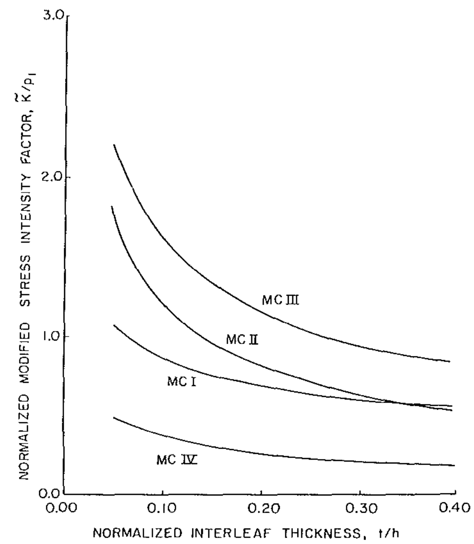

Fig. 5 Modified stress intensity factor as a function of interleaf thickness for different material combinations

The maximum interleaf transverse stress is maximum and tensile at $y=0$, and decreases as the interleaf thickness is increased and is plotted in Fig. 3 for MC I. This behavior is found to be typical and is exhibited for all material combinations. The maximum interleaf shear stress, like the maximum interleaf transverse stress, is a decreasing function of interleaf thickness and is plotted in Fig. 4 for MC I.

3.2 Crack Up to the Interface. The only difference between this and the previous case is that the symmetric crack now extends up to the interface and represents a broken layer. Due to the interleaf being modeled as a spring, the axial stress in the half-plane for this case has a logarithmic singularity at the crack tip. A modified SIF, $\tilde{K}$ is defined by the coefficient of this singularity and is given by equation (I46).

Figure 5 shows that this modified stress intensity factor $\tilde{K}$ decreases as a function of increasing interleaf thickness. This decrease is rapid up to $t/h=0.3$. The modified SIF, $\tilde{K}$, unlike the SIF, K_I, for the crack within the layer does not directly give a measure of the load-carrying capacity from the linear elastic fracture mechanics point of view. It may be recalled that modeling the adhesive as a spring resulted in a logarithmically-singular axial stress in the half-plane at the crack tip. A continuum model would give a power singularity but also not of a square root type (Gecit and Erdogan, 1978). One of the methods to determine the strength of the composite in such cases is to use failure criteria based on average stresses or point stresses and compare them with the ultimate strength of the undamaged material. A measure of the axial stresses at a specific point $x=1.01h$ in the half-plane, as well as the average axial stresses calculated over the interval $x=h$ to $1.01h$ in the half-plane, showed the same behavior of a rapid decrease as the interleaf thickness is increased to $t/h=0.3$. From the above observations, and noting that the interleaves have an insignificant load-carrying capacity but do add to the

Table 2 Length of delamination until closure of crack for different material combinations

Material Combination	Split Length Until Closure of Crack, c/h		
	t/h = 0.1	t/h = 0.2	Results from [12]
MC I	0.35	0.21	0.260
MC II	0.018	0.004	0.096
MC III	0.205	0.13	0.164
MC IV	-----	< 0.002	0.164

weight of the structure, an interleaf thickess of approximately 15 percent of the layer thickness seems suitable. It may be mentioned that graphite, epoxy, and the interleaf material have densities of the same order (1400 kgms/m^3).

3.3 H-Shaped Crack. In this case, a symmetric transverse crack extending up to the interface and symmetric delamination along the interface is considered, as shown, in Fig. 1 (Part I). The axial stresses in the half-plane and the layer are, for this case, logarithmically singular at the interface crack tips and are given by equations (I63) and (I65), respectively. Since the interleaf is modeled as springs, the transverse and shear stresses are finite in the interleaf even at the crack tip.

Figure 6 gives the transverse and shear stresses at the interface crack tip, ($x=h$, $y=c$) as a function of split length for MC I. The transverse stress is tensile for no split and decreases rapidly as the splitting is initiated and grows. This peel (transverse) stress becomes compressive and therefore closes the split for relatively small split lengths. On the other hand, the interleaf shear stress at the interface crack tip shows a very slow continued increase with split length growth. These results indicate that the split tip closes early and that most of the interface crack growth is due to shear alone. It is also found that the split length at which the crack closes decreases as the interleaf thickness is increased. The same behavior is exhibited for all material combinations. However, the order of the split length for the split to close varies considerably for each material combination and is illustrated in Table 2. The results are also compared with those obtained by the authors using the formulation and computer code developed by Goree and Venezia (1977) for the case of the two bonded half-planes with a transverse crack and delamination (T-shaped crack) along the interface. A further discussion on this behavior for longitudinal splitting is presented by Wolla and Goree (1987).

The above results indicate that for a crack (that is, a broken ply adjacent to the interleaf) in the strong plies (MC II, MC IV), delamination (or, at least positive peel stresses) is suppressed very early after initiation. For a crack in the weak plies (MC I, MC III), the extent of delamination is significant and suggests the need for the interleaves as well as that the bond-to-ply interfaces be of high tensile and shear strength. Also, from Fig. 13 for zero split length, the interleaf transverse and shear stresses at the interface crack tip are seen to decrease with an increase in the interleaf thickness. This implies that a thicker interleaf will increase the external load required to initiate delamination. The same behavior is exhibited for all material combinations.

3.4 Comparison With Experimental Studies. Although results from a detailed experimental investigation are not available for direct comparison with the analytical predictions, the preliminary experimental studies done by Masters (1985) and Sun (1985) are helpful in comparing the behavior of composite laminates with interleaves. These results support the analytically predicted behavior. Sun (1985) used a baseline

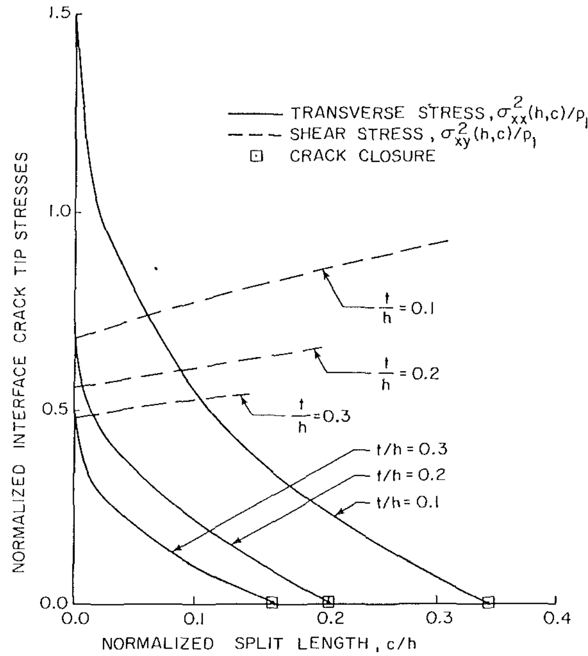

Fig. 6 Transverse and shear stresses at the interface crack tip as a function of split length for constant interleaf thickness (MC I)

laminate specimen AS4/3501-6 Graphite/Epoxy ($0_5/90_5/0_5$) and placed 5 mil adhesive film (FM1000 by American Cyanamid) between the 0 deg and 90 deg plies. The impact velocity required to initate delamination in the adhesive layered (interleaf) laminate was twice as large as that required for the baseline laminate. Similar results were reported by Masters (1985) for the AS4/1808 Graphite/Epoxy laminate $[(\pm 45/0/90/0/90)_2/\pm 45/0/90/\pm 45/]_S$. Figure 14 in Masters (1985), shows the photomicrographs of the transverse cracks developed in the 90 deg plies of a baseline and an interleafed laminate. For the same impact loads, the interleafed laminate showed no delamination, and damage was limited to transverse cracks. Delaminations occurred only for higher loads but were smaller than the ones developed for baseline laminates at comparable energy levels.

4 Conclusions

An analytical study is carried out to assist in the understanding of the influence of interleaves on the damage tolerance of multilayered composite laminates. The geometry of the problem is idealized as a damaged layer bonded to two half-planes and separated by thin interleaves. The interleaves are modeled as distributed tension and shear springs. The damage in the layer is a symmetric transverse crack, which may extend up to the interface. Delamination along the interface is also analyzed. Material combinations assumed to approximate Graphite/Epoxy laminates interlayered with thin thermoplastic film are used to discuss the results. The following conclusions are drawn from the study.

A. For the case of a crack within the layer:
   (1) The stresses at the crack tip are singular and have, as expected, the classical square root singularity.
   (2) The introduction of the low modulus interleaves increases the potential for the crack to extend while it is within the layer but reduces the stresses at the interface, which improves delamination damage tolerance.
   (3) If the crack is in a layer which is stiffer than the half-planes, the use of interleaves results in higher cleavage stresses in the half-plane and may assist in continuing the crack across the interface.

B. For the case of a crack up to the interface:

(4) By modeling the interleaves as distributed tension and shear springs, the axial stress in the half-planes is logarithmically singular at the crack tip.

(5) The stresses in the interleaves and the half-planes reduce with an increase in the interleaf thickness. The rate of this reduction is most rapid for small interleaf thicknesses. For example, for the material combinations of interleafed Graphite/Epoxy used in the results, the optimum thickness is of the order of 15 percent of the layer thickness. Any further increase in the thickness of the interleaf is an unprofitable addition to structural weight.

C. For the case of an H-shaped crack:

(6) The axial stresses in the layer and the half-planes at the interface crack tip are logarithmically singular, whereas the axial stresses in the half-planes at the intersecting points of the interface cracks and the transverse crack are bounded.

(7) The growth of delamination along the interface is stable. The split tip closes as the transverse stresses become compressive for small split lengths and further growth is due to shear alone.

(8) The split length until the split tip closes decreases with an increase in the interleaf thickness (or decrease in interleaf moduli).

Based on the above conclusions, an interleaf thickness of the order of 15 percent of the layer width is recommended for typical Graphite/Epoxy laminates. Since transverse cracks are more likely to occur in weak plies, the weak-stiff ply interfaces are prone to high stresses, which makes interleafing such interfaces a first choice. Similarly, the weak-weak ply interfaces are also prone to higher stresses, but the possibility of a crossover of the transverse crack is also high. This makes interleafing such interfaces a secondary choice.

Acknowledgment

This work was supported by the Fatigue and Fracture Branch, Materials, Division, NASA Langley Research Center, Hampton, Va., under Grant No. NAG-1-629. Dr. T. K. O'Brien was the grant monitor.

References

Abramowitz, M., and Stegun, I. A., 1964, "Handbook of Mathematical Functions," National Bureau of Standards, Applied Mathematics Series, 55.

Baker, C. T. H., 1977, *The Numerical Treatment of Integral Equations*, Claredon Press, Oxford.

Erdogan, F., Gupta, G. D., and Cook, T. S., 1972, "On the Numerical Solution of Singular Integral Equations," *Method of Analysis and Solution to Crack Problems*, G. C. Sih, ed., Noordhoff.

Fox, L., and Parker, I. B., 1968, *Chebyshev Polynomials in Numerical Analysis*, Oxford University Press, London.

Gecit, M. R., and Erdogan, F., 1978, "The Effect of Adhesive Layers on the Fracture of Laminated Structures," *ASME Journal of Engineering Materials and Technology*, Vol. 100, pp. 2-9.

Goree, J. G., and Venezia, W. A., 1977, "Bonded Elastic Half-Planes with an Interface Crack and Perpendicular Intersecting Crack That Extends into the Adjacent Material," *International Journal of Engineering Science*, Vol. 15, Part 1, pp. 1-17; Part 2, pp. 19-27.

Hadamard, J., 1923, *Lectures on Cauchy's Problems in Linear Partial Differential Equations*, Yale University Press.

Kaw, A. K., 1987, "Damage Growth in Composite Laminates with Interleaves," Ph.D. Dissertation, Clemson University, Clemson, S.C.

Kaya, A. C., and Erdogan, F., 1987, "On the Solution of Integral Equations with Strongly Singular Kernels," *Quarterly of Applied Mathematics*, Vol. 45, pp. 105-122.

Masters, J. E., 1985, "Characterization of Impact Damage Development in Graphite/Epoxy Laminates," *ASTM Symposium on Fractography of Modern Engineering Materials*, Nashville, Tenn.

Sneddon, I. N., and Srivastav, R. P., 1971, "The Stress Field in the Vicinity of a Griffith Crack in a Strip of Finite Width," *International Journal of Engineering Sciences*, Vol. 9, pp. 479-488.

Sun, C. T., 1985, "Suppression of Delamination in Composite Laminates Subjected to Impact Loading," *11th Annual Mechanics of Composite Review*, Dayton, OH, pp. 106-113.

Tricomi, F. G., 1957, *Integral Equations*, John Wiley and Sons, New York.

Wolla, J. M., and Goree, J. G., 1987, "Experimental Evaluation of Longitudinal Splitting in Unidirectional Composites," *Journal of Composite Materials*, Vol. 21, pp. 49-67.

Three-Dimensional Solutions for Antisymmetrically Laminated Anisotropic Plates

Ahmed K. Noor
Professor,
Fellow, ASME

W. Scott Burton
Research Scientist,
Assoc. Mem., ASME

George Washington University,
NASA Langley Research Center,
Hampton, VA 23665

Analytic three-dimensional elasticity solutions are presented for the stress and free vibration problems of multilayered anisotropic plates. The plates are assumed to have rectangular geometry and antisymmetric lamination with respect to the middle plane. A mixed formulation is used with the fundamental unknowns consisting of the six stress components and the three displacement components of the plate. Each of the plate variables is decomposed into symmetric and antisymmetric components in the thickness direction, and is expressed in terms of a double Fourier series in the Cartesian surface coordinates. Extensive numerical results are presented showing the effects of variation in the lamination and geometric parameters of composite plates on the importance of the transverse stress and strain components.

1 Introduction

Although a complete three-dimensional elasticity solution for simply-supported homogeneous isotropic plates was presented by Vlasov (1957), recent development of fibrous composites has stimulated interest in the use of the three-dimensional theory of elasticity for obtaining highly accurate predictions of the response characteristics of plates. Srinivas et al. (1969, 1970a, 1970b, 1973), Jones (1970), Lee (1967), Pagano (1969, 1970), and Pagano and Hatfield (1972) presented analytic solutions to the free vibration, bending, and stability problems of laminated plates. Lee and Reismann (1969) studied the dynamic response of rectangular plates. However, all the cited solutions are limited to either the cylindrical bending case, or the case of simply-supported boundary conditions of *orthotropic* (*or cross-ply*) plates.

This paper presents an analytic solution for the stress and free vibration problems of rectangular multilayered *anisotropic* plates. The plates consist of a number of perfectly-bonded layers which have antisymmetric lamination with respect to the middle plane. The solutions are periodic in x_1 and x_2. Extensive numerical results are presented for the effect of the different lamination and geometric parameters of the plate on the significance of the transverse stresses and strains.

2 Mathematical Formulation

Figure 1 shows the geometric characteristics of the plate as follows: L_1 and L_2 are the side lengths in the x_1 and x_2 directions, and h is the total thickness of the plate. The dimensionless coordinates ξ_1, ξ_2, and ζ are introduced, where:

$$\xi_\alpha = \frac{x_\alpha}{L_\alpha} \qquad (\alpha = 1,2 \text{ and } \alpha \text{ is not summed}) \tag{1}$$

$$\zeta = \frac{x_3}{h}. \tag{2}$$

The analytical formulation is based on the linear three-dimensional theory of anisotropic elasticity (see Lekhnitskii, 1981 and Hearmon, 1961). The individual layers are assumed to be homogeneous, *anisotropic*, and are antisymmetrically laminated with respect to the middle plane of the plate. At each point a plane of elastic symmetry exists parallel to the middle plane. The sign convention for the different displacement and stress components is shown in Fig. 1.

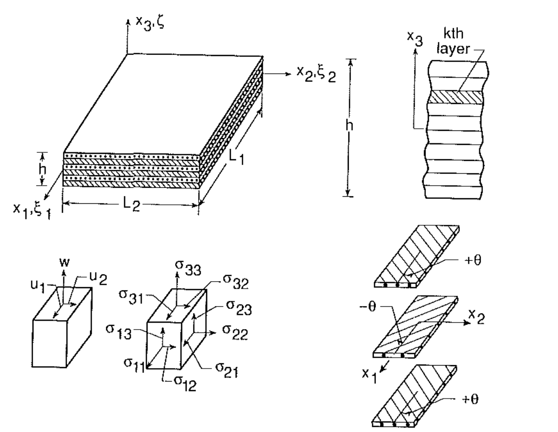

Fig. 1 Laminated anisotropic composite plates and sign convention for stresses and displacements

Contributed by the Applied Mechanics Division of The American Society of Mechanical Engineers for presentation at the Winter Annual Meeting, San Francisco, Calif., December 10-15, 1989.

Discussion on this paper should be addressed to the Editorial Department, ASME, United Engineering Center, 345 East 47th Street, New York, N. Y. 10017, and will be accepted until two months after final publication of the paper itself in the Journal of Applied Mechanics. Manuscript received by the Applied Mechanics Division, November 8, 1988; final revision, May 2, 1989.

Paper No. 89-WA/APM-39.

2.1 Displacement and Stress Expansions. For unsymmetric response, each of the plate variables is decomposed into symmetric and antisymmetric components in the thickness direction, and is expanded in a double Fourier series in the Cartesian surface coordinates. The Fourier series are chosen such that the displacements and stresses are periodic in x_1 and x_2 with periods $2L_1$ and $2L_2$.

The following expansions are used for the displacement and stress components:

$$\begin{Bmatrix} u_1 \\ u_2 \\ w \end{Bmatrix} = \sum_{m=0} \sum_{n=0} \left[\begin{Bmatrix} \bar{u}_{1_{mn}} \sin m\pi\xi_1 \cos n\pi\xi_2 \\ \bar{u}_{2_{mn}} \cos m\pi\xi_1 \sin n\pi\xi_2 \\ \bar{w}_{mn} \sin m\pi\xi_1 \sin n\pi\xi_2 \end{Bmatrix} + \begin{Bmatrix} \tilde{u}_{1_{mn}} \cos m\pi\xi_1 \sin n\pi\xi_2 \\ \tilde{u}_{2_{mn}} \sin m\pi\xi_1 \cos n\pi\xi_2 \\ \tilde{w}_{mn} \cos m\pi\xi_1 \cos n\pi\xi_2 \end{Bmatrix} \right] \tag{3}$$

$$\begin{Bmatrix} \sigma_{11} \\ \sigma_{22} \\ \sigma_{33} \end{Bmatrix} = \sum_{m=0} \sum_{n=0} \left[\begin{Bmatrix} \bar{\sigma}_{11_{mn}} \\ \bar{\sigma}_{22_{mn}} \\ \bar{\sigma}_{33_{mn}} \end{Bmatrix} \cos m\pi\xi_1 \cos n\pi\xi_2 + \begin{Bmatrix} \tilde{\sigma}_{11_{mn}} \\ \tilde{\sigma}_{22_{mn}} \\ \tilde{\sigma}_{33_{mn}} \end{Bmatrix} \sin m\pi\xi_1 \sin n\pi\xi_2 \right] \tag{4}$$

$$\begin{Bmatrix} \sigma_{23} \\ \sigma_{13} \\ \sigma_{12} \end{Bmatrix} = \sum_{m=0} \sum_{n=0} \left[\begin{Bmatrix} \bar{\sigma}_{23_{mn}} \sin m\pi\xi_1 \cos n\pi\xi_2 \\ \bar{\sigma}_{13_{mn}} \cos m\pi\xi_1 \sin n\pi\xi_2 \\ \bar{\sigma}_{12_{mn}} \sin m\pi\xi_1 \sin n\pi\xi_2 \end{Bmatrix} + \begin{Bmatrix} \tilde{\sigma}_{23_{mn}} \cos m\pi\xi_1 \sin n\pi\xi_2 \\ \tilde{\sigma}_{13_{mn}} \sin m\pi\xi_1 \cos n\pi\xi_2 \\ \tilde{\sigma}_{12_{mn}} \cos m\pi\xi_1 \cos n\pi\xi_2 \end{Bmatrix} \right] . \tag{5}$$

In equations (3), (4), and (5) the bar ($\bar{}$) and tilde ($\tilde{}$) refer to symmetric and antisymmetric quantities, with respect to the middle plane. Each of these quantities is a function of the thickness coordinate, ζ. Note that the displacement and stress expansions, equations (3), (4) and (5), are periodic in x_1 and x_2 with periods $2L_1$ and $2L_2$. The following displacement conditions are therefore satisfied on the middle plane ($\zeta = 0$):

$$\text{At } x_1 = 0, L_1 : u_1 = w = 0 \tag{6}$$

$$\text{At } x_2 = 0, L_2 : u_2 = w = 0. \tag{7}$$

The displacement conditions, equations (6) and (7), are satisfied when either m, n, or both, are zero. For $m = n = 0$, only the $\tilde{w}$ term in the displacement expansions, equations (3), survives. For $m = 1$, $n = 0$; $\bar{u}_1$, $\tilde{u}_2$, and $\tilde{w}$ survive, and for $m = 0$, $n = 1$, $\tilde{u}_1$, $\bar{u}_2$ and $\tilde{w}$ survive.

The external surface loads are also periodic and are expanded in double Fourier series similar to the displacement components in their respective directions (see equations (3)). For free vibration problems the right-hand sides of equations (3), (4), and (5) should be multiplied by $e^{i\omega t}$, where ω is the frequency of vibration of the plate and t is time.

2.2 Governing Equations. A mixed formulation is used with the fundamental unknowns consisting of the symmetric and antisymmetric components of the displacements and stresses. The governing equations of the plate consist of the constitutive relations (strain-stress relations, with the strains expressed in terms of displacements), and the equations of motion. For the purpose of simplifying the form of the equations, the material compliance matrix for each layer, $[a]$, is decomposed into the sum of orthotropic and anisotropic (nonorthotropic) parts, $[a_o]$ and $[a_1]$ (see Appendix). Moreover, the stresses and displacements are each divided into two groups as follows:

Nomenclature

$a_{IJ}^{(k)} (I,J = 1,\ldots,6)$ = elastic compliances of the kth layer of the plate
$[a]$ = matrix of compliance coefficients
$[a_o]$, $[a_1]$ = orthotropic and nonorthotropic parts of the matrix $[a]$
E_L, E_T = elastic moduli in the direction of fibers and normal to it
G_{LT}, G_{TT} = shear moduli in plane of fibers and normal to it
$\{H_l\}$ and $\{H_2\}$ = vectors of stress unknowns
h = total plate thickness
L_1, L_2 = side lengths of the plate
m,n = Fourier harmonics in the x_1 and x_2 directions, respectively
NL = number of layers of laminated plate
$p_i (i = 1,\ldots,3)$ = intensities of external surface loading in the coordinate directions
$[S_o]$ = matrix of coefficients
$[S_1]$ = matrix of linear first-order ordinary differential operators
U = total strain energy
U_1, U_2, U_3 = strain energy components associated with $(\sigma_{\alpha\beta}, \epsilon_{\alpha\beta})$, $(\sigma_{\alpha 3}, 2\epsilon_{\alpha 3})$ and $(\sigma_{33}, \epsilon_{33})$, respectively
u_1, u_2, w = displacement components in the coordinate directions
$\{X_1\}$, $\{X_2\}$ = vectors of displacement unknowns
x_1, x_2, x_3 = Cartesian coordinate system
Θ = fiber orientation angle
ξ_1, ξ_2, ζ = dimensionless coordinates in the x_1, x_2, and x_3 directions, respectively
ρ = mass density of the material of the plate
σ_{11}, σ_{22}, σ_{33} = normal stress components
σ_{23}, σ_{13}, σ_{12} = shear stress components
$\Omega = \omega\sqrt{\rho h^2 / E_T}$ = dimensionless frequency
ω = circular frequency of vibration of the plate

Bars and Tildes

A bar ($\bar{}$) and a tilde ($\tilde{}$) refer to the symmetric and antisymmetric components of the response quantities (or external loading) in the thickness direction, respectively

Subscripts

m,n refer to the (m,n) Fourier harmonic
L refers to direction of fibers
T refers to the direction transverse to the fibers

Superscript

t denotes transposition

$$\{H_1\}_{mn} = \begin{Bmatrix} \bar{\sigma}_{11_{mn}} \sin m\pi\xi_1 \sin n\pi\xi_2 \\ \bar{\sigma}_{22_{mn}} \sin m\pi\xi_1 \sin n\pi\xi_2 \\ \bar{\sigma}_{33_{mn}} \sin m\pi\xi_1 \sin n\pi\xi_2 \\ \tilde{\sigma}_{23_{mn}} \sin m\pi\xi_1 \cos n\pi\xi_2 \\ \tilde{\sigma}_{13_{mn}} \cos m\pi\xi_1 \sin n\pi\xi_2 \\ \tilde{\sigma}_{12_{mn}} \cos m\pi\xi_1 \cos n\pi\xi_2 \end{Bmatrix},$$

$$\{H_2\}_{mn} = \begin{Bmatrix} \tilde{\sigma}_{11_{mn}} \cos m\pi\xi_1 \cos n\pi\xi_2 \\ \tilde{\sigma}_{22_{mn}} \cos m\pi\xi_1 \cos n\pi\xi_2 \\ \tilde{\sigma}_{33_{mn}} \cos m\pi\xi_1 \cos n\pi\xi_2 \\ \bar{\sigma}_{23_{mn}} \cos m\pi\xi_1 \sin n\pi\xi_2 \\ \bar{\sigma}_{13_{mn}} \sin m\pi\xi_1 \cos n\pi\xi_2 \\ \bar{\sigma}_{12_{mn}} \sin m\pi\xi_1 \sin n\pi\xi_2 \end{Bmatrix} \qquad (8)$$

$$\{X_1\}_{mn} = \begin{Bmatrix} \tilde{u}_{1_{mn}} \cos m\pi\xi_1 \sin n\pi\xi_2 \\ \tilde{u}_{2_{mn}} \sin m\pi\xi_1 \cos n\pi\xi_2 \\ \bar{w}_{mn} \sin m\pi\xi_1 \sin n\pi\xi_2 \end{Bmatrix},$$

$$\{X_2\}_{mn} = \begin{Bmatrix} \bar{u}_{1_{mn}} \sin m\pi\xi_1 \cos n\pi\xi_2 \\ \bar{u}_{2_{mn}} \cos m\pi\xi_1 \sin n\pi\xi_2 \\ \tilde{w}_{mn} \cos m\pi\xi_1 \cos n\pi\xi_2 \end{Bmatrix}. \qquad (9)$$

For each layer and each pair of harmonics, m and n, the governing equations can be partitioned into two coupled sets of equations associated with $\{H_1\}_{mn}$, $\{X_1\}_{mn}$ and $\{H_2\}_{mn}$, $\{X_2\}_{mn}$ as follows:

$$\left(\begin{bmatrix} -a_o & S_o + S_1 \\ S_o' + S_1' & 0 \end{bmatrix}_{mn} - \rho\omega^2 \begin{bmatrix} 0 & 0 \\ 0 & I \end{bmatrix} \right) \begin{Bmatrix} H_1 \\ X_1 \end{Bmatrix}_{mn} - \begin{bmatrix} a_1 & 0 \\ 0 & 0 \end{bmatrix} \begin{Bmatrix} H_2 \\ X_2 \end{Bmatrix}_{mn} = 0 \qquad (10)$$

and

$$\left(\begin{bmatrix} -a_o & -S_o + S_1 \\ -S_o' + S_1' & 0 \end{bmatrix}_{mn} - \rho\omega^2 \begin{bmatrix} 0 & 0 \\ 0 & I \end{bmatrix} \right) \begin{Bmatrix} H_2 \\ X_2 \end{Bmatrix}_{mn} - \begin{bmatrix} a_1 & 0 \\ 0 & 0 \end{bmatrix} \begin{Bmatrix} H_1 \\ X_1 \end{Bmatrix}_{mn} = 0 \qquad (11)$$

where $[I]$ is the identity matrix, $[S_o]$ is a matrix of coefficients, and $[S_1]$ is a matrix of linear first-order ordinary differential operators. The explicit forms of $[a_o]$, $[a_1]$, $[S_o]$, and $[S_1]$ are given in the Appendix.

The complete description of the plate response requires: (*a*) the governing equations, equations (10) and (11) for each layer, (*b*) the stress equilibrium and displacement continuity conditions at layer interfaces, and (*c*) the conditions at the top and bottom surfaces of the plate.

The equilibrium and continuity conditions at the interfaces between two typical layers κ and $\kappa+1$ can be written in the following compact form:

$$\sigma_{i3}^{(\kappa)} - \sigma_{i3}^{(\kappa+1)} = 0, \qquad i = 1 \text{ to } 3 \qquad (12)$$

$$u_\alpha^{(\kappa)} - u_\alpha^{(\kappa+1)} = 0, \qquad \alpha = 1, 2 \qquad (13)$$

and

$$w^{(\kappa)} - w^{(\kappa+1)} = 0 \qquad (14)$$

where superscripts κ and $\kappa+1$ refer to the layers κ and $\kappa+1$. Equations (13) and (14) imply perfect bonding between the different layers (i.e., no slip). The stress conditions at the top and bottom surfaces are:

$$\sigma_{i3} = p_i, \quad i = 1 \text{ to } 3 \qquad (15)$$

where p_i are the intensities of the external surface loading in the coordinate directions. For free vibration problems, $p_i = 0$. Note that equations (12) to (14) can be replaced by two sets of equations of the same form; one relating the symmetric components (quantities with a bar) and the other relating the antisymmetric components (quantities with a tilde).

2.3 Computational Procedure. The stress and vibrational responses of the plate are obtained by using the procedure described in Srinivas and Rao (1970a), Srinivas et al. (1970b), and Srinivas (1973). The procedure is based on solving the characteristic equation associated with equations (10) and (11) for each layer, and each pair of Fourier harmonics (m,n); finding the twelve roots and twelve eigenvectors; then solving a set of simultaneous equations representing the conditions at the top and bottom surfaces, and at the interfaces between the different layers; equations (12) to (15).

2.4 Comments on the Fourier Expansions and the Governing Equations. The following two comments concerning the Fourier expansions and governing equations are in order:

1 The Fourier expansions for the stresses and displacements used herein were inspired by, and are consistent with, those presented by Bert and Chen (1978) and Bert and Birman (1987), in conjunction with a two-dimensional first-order shear deformation theory. The symmetric and antisymmetric components of the in-plane displacements and in-plane stresses of the three-dimensional theory correspond to the in-plane displacements, rotation components, extensional forces, and bending moments of the two-dimensional theory; respectively.

2 The Fourier expansions for the stresses and displacements, equations (3), (4), and (5), provide an exact representation for the stress and free vibrational responses of rectangular composite plates. Moreover, *the governing equations uncouple in harmonics* provided: (*a*) the lamination is angle-ply antisymmetric with respect to the middle plane, cross-ply symmetric with respect to the middle plane, or a combination of the two (e.g., antisymmetric quasi-isotropic lamination), (*b*) the displacements and stresses are periodic in x_1 and x_2, and (*c*) the external surface loading components are periodic in x_1 and x_2, and can be expanded in Fourier series analogous to those used for the corresponding displacement components, equations (3).

The first condition can be verified by examining the constitutive relations for a pair of layers, κ^+ and κ^-, which are symmetrically situated with respect to the middle plane; and noting that for the stress and displacement expansions to be valid the following relations must be satisfied between the compliance coefficients of the two layers:

$$a_{ij}^{(\kappa^+)} = a_{ij}^{(\kappa^-)} \qquad (16)$$

$$a_{i+3,\,i+3}^{(\kappa^+)} = a_{i+3,\,i+3}^{(\kappa^-)} \qquad (17)$$

$$a_{i6}^{(\kappa^+)} = -a_{i6}^{(\kappa^-)} \qquad (18)$$

$$a_{45}^{(\kappa^+)} = -a_{45}^{(\kappa^-)} \qquad (19)$$

where in equations (16) to (19) $i, j = 1$, 2 and 3. Equations (16) to (19) are satisfied for angle-ply antisymmetric laminates, cross-ply symmetric laminates, and combinations of the two. In the case of cross-ply laminates, $a_{i6}=a_{45}=0$, $[a_1]=0$; and the governing equations, equations (10) and (11), are uncoupled.

3 The displacement and stress expansions satisfy the following inversion symmetry conditions (see Noor and Camin (1976), Noor et al. (1977)):

$$\begin{Bmatrix} u_1 \\ u_2 \\ w \end{Bmatrix}_{(\xi_1,\xi_2,\zeta)} = \begin{Bmatrix} -u_1 \\ -u_2 \\ w \end{Bmatrix}_{(-\xi_1,-\xi_2,\zeta)} \tag{20}$$

$$\begin{Bmatrix} \sigma_{11} \\ \sigma_{22} \\ \sigma_{33} \\ \sigma_{23} \\ \sigma_{13} \\ \sigma_{12} \end{Bmatrix}_{(\xi_1,\xi_2,\zeta)} = \begin{Bmatrix} \sigma_{11} \\ \sigma_{22} \\ \sigma_{33} \\ -\sigma_{23} \\ -\sigma_{13} \\ \sigma_{12} \end{Bmatrix}_{(-\xi_1,-\xi_2,\zeta)}. \tag{21}$$

Numerical Studies

Parametric studies were conducted using the foregoing procedure to assess the effects of variation in the lamination and geometric parameters on the significance of transverse stresses in laminated plates. These studies can help in assessing the reliability of various two-dimensional theories used in predicting the stress and vibrational responses of highly anisotropic plates.

The composite plates considered in this study are square angle-ply and quasi-isotropic laminates with $L_1=L_2=1$ *m*. The plates have antisymmetric laminations with respect to the middle plane. The solutions are periodic in x_1 and x_2 with periods $2L_1$ and $2L_2$. The material characteristics of the individual layers were taken to be those typical of high-modulus fibrous composites, namely:

$$G_{LT}/E_T=0.5,\ G_{TT}/E_T=0.35,\ \upsilon_{LT}=0.3,\ \upsilon_{TT}=0.49$$

where L refers to the direction of fibers and T refers to the transverse direction; and υ_{LT} is the major Poisson's ratio. Note that for transversely isotropic material, $G_{TT}/E_T = 0.3356$, instead of the 0.35 used in the present study. The fiber orientation for the angle-ply and quasi-isotropic laminates was selected to be $[+\theta/-\theta\ \ldots]$ and $[+45/0/90/-45/\ \ldots]$, respectively (starting from the top layer in each case). For static stress analysis problems, the plates were subjected to normal loading on the top and bottom surfaces $p_3 = \bar{p}_3 \sin \pi\xi_1 \sin \pi\xi_2$, and for free vibration problems, only the fundamental frequencies and the associated mode shapes and modal stresses are considered. Typical results are presented in Table 1 and in Figs. 2, 3, and 4.

Four parameters were varied, namely, the fiber orientation angle of the individual layers, θ; the number of layers, NL; the degree of orthotropy of the individual layers, E_L/E_T; and the thickness ratio of the plate, h/L_1. The fiber orientation angle was varied between 0 and 45; NL was varied between 2 and 20; E_L/E_T was varied between 3 and 30; and h/L_1 between 0.01 and 0.3. The effect of variation of the thickness ratio, h/L_1, and the fiber orientation angle, θ, of angle-ply plates on the magnitude of the fundamental vibration frequencies is shown in Table 1.

As a step towards assessing the importance of transverse stresses in composite plates, the total strain energy of the plate was decomposed into three components: U_1 associated with $\sigma_{\alpha\beta}$ and $\epsilon_{\alpha\beta}$; U_2 associated with $\sigma_{\alpha 3}$ and $2\epsilon_{\alpha 3}$; and U_3 associated with σ_{33} and ϵ_{33} ($U_3=1/2\int_V \sigma_{33}\epsilon_{33}dV$), where $\epsilon_{\alpha\beta}$, $2\epsilon_{\alpha 3}$ and ϵ_{33} are the extensional, transverse shear, and

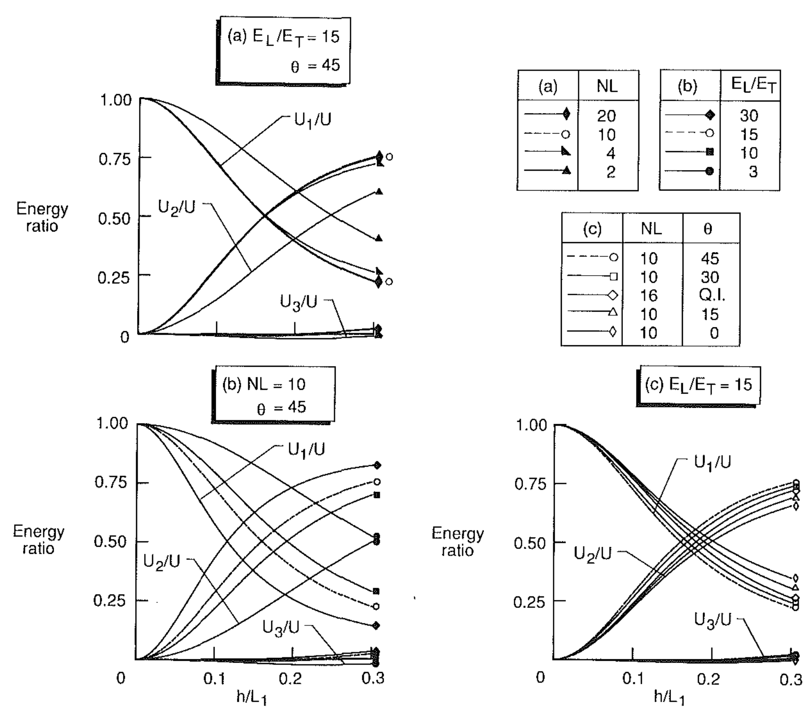

Fig. 2 Variation of strain energy components with geometric and lamination parameters of composite plates. Angle-ply and quasi-isotropic (Q.I.) composite plates subjected to static loading $\bar{p}=p_0 \sin \pi\xi_1 \sin \pi\xi_2$; U_1, U_2, and U_3 are the strain energy components associated with $(\sigma_{\alpha\beta}, \epsilon_{\alpha\beta})$, $(\sigma_{3\alpha}, 2\epsilon_{3\alpha})$, and $(\sigma_{33}, \epsilon_{33})$, respectively.

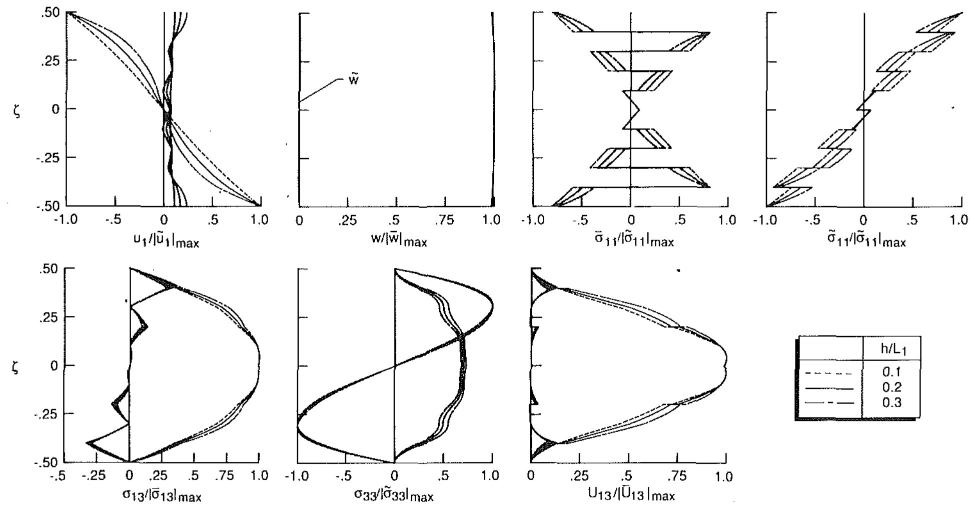

Fig. 3 Effect of the thickness ratio, h/L_1, on the distribution of stresses, displacements, and transverse shear strain energy density in the thickness direction, associated with the lowest vibration mode. Angle-ply composite plates with $E_L/E_T = 15$, $NL = 10$, $\theta = 45$ deg. Plots of $\bar{u}_1$, $\bar{\sigma}_{11}$, $\bar{\sigma}_{13}$, $\bar{\sigma}_{33}$, $\bar{U}_{13}$ are shaded.

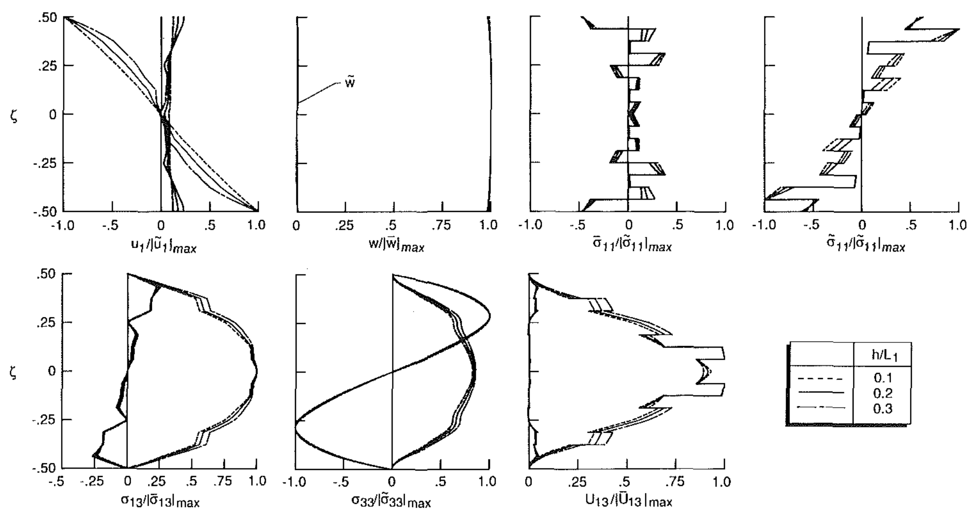

Fig. 4 Effect of thickness ratio, h/L_1, on the distribution of stresses, displacements, and transverse shear strain energy density in the thickness direction associated with the lowest vibration mode. Quasi-isotropic composite plates with $E_L/E_T = 15$, $NL = 16$, $\theta = [45/0/90/-45/45/0/90/-45]_{AS}$. Plots of $\bar{u}_1$, $\bar{\sigma}_{11}$, $\bar{\sigma}_{13}$, $\bar{\sigma}_{33}$, $\bar{U}_{13}$ are shaded.

Table 1 Effect of thickness ratio, h/L_1 and fiber orientation angle, θ, on the fundamental vibration frequencies, $\Omega = \omega\sqrt{\rho h^2/E_T}$, obtained by three-dimensional elasticity theory. Ten-layered angle-ply composite plates with $E_L/E_T = 15$, $NL = 10$. Solutions are periodic in x_1 and x_2 (see equations (3) to (5)).

h/L_1	$\theta = 15$ deg	$\theta = 30$ deg	$\theta = 45$ deg
0.01	$0.1328/10^{-2}$	0.1510×10^{-2}	0.1595×10^{-2}
0.10	0.1162	0.1296	0.1351
0.15	0.2304	0.2532	0.2617
0.20	0.3588	0.3889	0.3993
0.25	0.4934	0.5286	0.5400
0.30	0.6307	0.6692	0.6810

transverse normal strains, respectively. The effect of variation of the four parameters, θ, NL, E_L/E_T and h/L_1 on the strain energy ratios U_1/U, U_2/U, and U_3/U (where $U = U_1 + U_2 + U_3$) was studied. Typical results are presented in Fig. 2 for static loading. Also, Figs. 3 and 4 show the effects of variation of the thickness ratio of the plate, h/L_1, on the distribution of displacements, stresses, and transverse shear strain energy density, $U_{13} = 1/2\sigma_{13} \times 2\epsilon_{13}$, in the thickness direction, associated with the fundamental frequency, for angle-ply and quasi-isotropic plates, respectively. Both the symmetric and antisymmetric parts of the response quantities (with respect to the middle plane) are shown in Figs. 3 and 4. For clarity, the quantities associated with $\{X_2\}$ and $\{H_2\}$; namely, the symmetric $\bar{u}_1$, $\bar{\sigma}_{11}$, $\bar{\sigma}_{33}$, and antisymmetric $\bar{\sigma}_{13}$, are shaded in the figures. The quantity $\bar{U}_{13} = 1/2\bar{\sigma}_{13} \times 2\bar{\epsilon}_{13}$ is also shaded. The antisymmetric $\tilde{w}$ was approximately zero in all cases.

Note that since the symmetric and antisymmetric components of each response quantity are multipled by different trigonometric functions in ξ_1 and ξ_2 (see equations (3) to (5)), the value of the response quantity is a linear combination of the two components. An examination of Figs. 2 through 4 reveals:

1 As to be expected, the transverse shear strain energy ratio, U_2/U, increases with the increase in the fiber orientation angle (from 0 deg to 45 deg), the thickness ratio of the plate, the number of layers, and the degree of orthotropy of the individual layers. For plates with $h/L_1 = 0.1$, U_2/U can exceed 0.40. The increase in U_2/U is associated with a decrease in the ratio of U_1/U.

2 A sharp increase in the ratio U_2/U is observed as NL increases from 2 to 4. This is followed by a less pronounced increase in the range $4 < NL < 10$, and no noticeable change occurs for $NL > 10$.

3 The transverse normal strain energy ratio, U_3/U, is considerably smaller than the transverse shear ratio U_2/U. This is particularly true for the vibrational response. For statically loaded plates, U_3/U approaches 3.5 percent for thick multilayered plates with $h/L_1 = 0.3$ and $NL > 10$.

4 For thin plates ($h/L_1 \leq 0.1$), the variation of the in-plane displacements $\tilde{u}_\alpha$ in the thickness direction is nearly linear, w is nearly uniform, and $\sigma_{\alpha\beta}$ is nearly piecewise linear. As h/L_1 increases, the nonlinearity of the variations of u_α and $\sigma_{\alpha\beta}$ in the x_3 direction becomes more pronounced. The nonlinearity is amplified by increasing the modular ratio, E_L/E_T. On the other hand, the thickness variation of the transverse displacement w, transverse normal stress $\tilde{\sigma}_{33}$, and transverse shear stresses $\tilde{\sigma}_{13}$ is insensitive to variations in h/L_l.

5 For the fundamental vibration modes the maximum values of the components of the response vectors $\{H_1\}$ and $\{X_1\}$ are higher than the corresponding values of $\{H_2\}$ and $\{X_2\}$. This is particularly true for the displacements and the transverse shear stresses (see Figs. 3 and 4).

Concluding Remarks

Analytical three-dimensional elasticity solutions are presented for the stress and free vibration problems of multilayered anisotropic plates with perfectly-bonded layers. The plates are assumed to have rectangular geometry and an antisymmetric lamination with respect to the middle plane. Each of the plate stresses and displacements is decomposed into symmetric and antisymmetric components in the thickness direction, and is expressed in terms of a double Fourier series in the Cartesian surface coordinates.

Extensive numerical results are presented showing the effects of variation in the lamination and geometric parameters of composite plates on the importance of the transverse stress and strain components. The numerical studies show that the transverse shear stresses and strains increase with the increase in the fiber orientation angle, the thickness ratio of the plate, the number of layers, and the degree of orthotropy of the individual layers. Moreover, the transverse shear stresses and strains have a much more pronounced effect on the response of multilayered plates than that of transverse normal stresses and strains. The latter are expected to become noticeable (of the order of 3.5 percent or more) only for deformations with very short wavelengths (thickness-to-wavelength ratio of the order of 0.3), and in the regions of highly localized loadings (or loadings with sharp variation).

Acknowledgment

The present research is partially supported by NASA Grant No. NAG1-788 and by Air Force Office of Scientific Research Grant No. 87-0115. The authors acknowledge useful discussions with Ivo Babuska of the University of Maryland, James H. Starnes, Jr. of NASA, and Anthony K. Amos of AFOSR.

References

Bert, C. W., and Chen, T. L. C., 1978, "Effect of Shear Deformation on Vibration of Antisymmetric Angle-Ply Laminated Rectangular Plates," *Int. J. Solids Struct.*, Vol. 14, pp. 465–473.

Bert, C. W., and Birman, V., 1987, "Dynamic Instability of Shear Deformable Antisymmetric Angle-Ply Plates," *Int. J. Solids Struct.*, Vol. 23, pp. 1053–1061.

Hearmon, R. F. S., 1961, *An Introduction to Applied Anisotropic Elasticity*, Oxford University Press, London.

Jones, A. T., 1970, "Exact Natural Frequencies for Cross-Ply Laminates," *J. Composite Materials*, Vol. 4, pp. 476–491.

Lee, C. W., 1967, "Three-Dimensional Solution for Simply-Supported Thick Rectangular Plates," *Nuclear Engineering and Design*, Vol. 6, pp. 155–162.

Lee, Y. C., and Reismann, H., 1969, "Dynamics of Rectangular Plates," *International Journal of Engineering Science*, Vol. 7, pp. 93–113.

Lekhnitskii, S. G., 1981, *Theory of Elasticity of an Anisotropic Body*, Mir Publishers, Moscow.

Noor, A. K., and Camin, R. A., 1976, "Symmetry Considerations for Anisotropic Shells," *Computer Methods in Applied Mechanics and Engineering*, Vol. 9, pp. 317–335.

Noor, A. K., Mathers, M. D., and Anderson, M. S., 1977, "Exploiting Symmetries for Efficient Postbuckling Analysis of Composite Plates," *AIAA Journal*, Vol. 15, pp. 24–32.

Pagano, N. J., 1969, "Exact Solutions for Composite Laminates in Cylindrical Bending," *Journal of Composite Materials*, Vol. 3, pp. 398–411.

Pagano, N. J., 1970, "Exact Solutions for Rectangular Bidirectional Composites and Sandwich Plates," *Journal of Composite Materials*, Vol. 4, pp. 20–34.

Pagano, N. J., and Hatfield, S. J., 1972, "Elastic Behavior of Multilayered Bidirectional Composites," *AIAA Journal*, Vol. 10, pp. 931–933.

Srinivas, S., Rao, A. K., and Joga Rao, C. V., 1969, "Flexure of Simply Supported Thick Homogeneous and Laminated Rectangular Plates," *Zeitschrift fur Angewandte Mathematik und Mechanik*, Vol. 49, pp. 449–458.

Srinivas, S., and Rao, A. K., 1970a, "Bending, Vibration and Buckling of Simply Supported Thick Orthotropic Rectangular Plates and Laminates," *Int. J. Solids Struct.*, Vol. 6, pp. 1464–1481.

Srinivas, S., Joga Rao, C. V., and Rao, A. K., 1970b, "An Exact Analysis for Vibration of Simply-Supported Homogeneous and Laminated Thick Rectangular Plates," *Journal of Sound and Vibration*, Vol. 12, pp. 187–199.

Srinivas, S., 1973, "A Refined Analysis of Composite Laminates," *Journal of Sound and Vibration*, Vol. 30, pp. 495–507.

Vlasov, B. F., 1957, "On One Case of Bending of Rectangular Thick Plates," *Vestnik Moskovskogo Universitieta*, (in Russian), No. 2, pp. 25–34.

APPENDIX

Explicit Form of the Arrays in the Governing Equations

The explicit form of the arrays $[a_o]$, $[a_1]$, $[S_o]_{m,n}$, and $[S_1]$ in equations (10) and (11), associated with the pair of harmonics (m,n), are given in this appendix.

$$[a_o] = \left[\begin{array}{ccc|ccc} a_{11} & a_{12} & a_{13} & \cdot & \cdot & \cdot \\ & a_{22} & a_{23} & \cdot & \cdot & \cdot \\ & & a_{33} & \cdot & \cdot & \cdot \\ \hline & & & a_{44} & \cdot & \cdot \\ & & & & a_{55} & \cdot \\ \text{Symmetric} & & & & & a_{66} \end{array}\right];$$

$$[a_1] = \left[\begin{array}{ccc|ccc} \cdot & \cdot & \cdot & \cdot & \cdot & a_{16} \\ & \cdot & \cdot & \cdot & \cdot & a_{26} \\ & & \cdot & \cdot & \cdot & a_{36} \\ \hline & & & \cdot & a_{45} & \cdot \\ & & & & \cdot & \cdot \\ \text{Symmetric} & & & & & \cdot \end{array}\right] \qquad (A1)$$

$$
[S_o]_{m,n} = \left[\begin{array}{ccc}
-\frac{m\pi}{L_1} & \cdot & \cdot \\
\cdot & -\frac{n\pi}{L_2} & \cdot \\
\cdot & \cdot & \cdot \\
\hdashline
\cdot & \cdot & \frac{n\pi}{L_2} \\
\cdot & \cdot & \frac{m\pi}{L_1} \\
\frac{n\pi}{L_2} & \frac{m\pi}{L_1} & \cdot
\end{array}\right] ; \; [S_1] = \left[\begin{array}{ccc}
\cdot & \cdot & \cdot \\
\cdot & \cdot & \cdot \\
\cdot & \cdot & 1 \\
\hdashline
\cdot & 1 & \cdot \\
1 & \cdot & \cdot \\
\cdot & \cdot & \cdot
\end{array}\right] \frac{d}{dx_3} \qquad (A2)
$$

where a_{IJ} (I, $J = 1$ to 6) are the compliance coefficients of the material (see Hearmon, 1961; Lekhnitskii, 1981), and a dot $(\cdot)$ refers to a zero term.

G. W. Hunt
Reader in Structural Mechanics,
Civil Engineering Department,
Imperial College,
London, U.K.

L. S. da Silva
Assistant Professor,
Civil Engineering Department,
University of Coimbra,
Coimbra, Portugal

Interactive Bending Behavior of Sandwich Beams

A multi-degree-of-freedom nonlinear Rayleigh-Ritz formulation for a sandwich beam is developed and is used to demonstrate the possible sudden destabilizing effects associated with wrinkling on the compressive face. Through-core stretching and core shearing effects are included. Nonlinear load-deflection curves, for various loading conditions including point loads and uniformly distributed loads, are presented.

1 Introduction

Recent nonlinear buckling studies of compressively loaded sandwich sections, typically as shown in Fig. 1, have revealed the possibility of a sudden secondary destabilization in the early post-buckling regime of overall (Euler) buckling, as the face under maximum compression itself buckles in a manner akin to that of a strut on an elastic foundation. The process may involve considerable shearing in the core, as well as interaction between the faces through the core thickness. Allowing analytically for these complications, a six degree-of-freedom buckling model has been proposed (Hunt et al., 1988; da Silva and Hunt, 1989), which involves a complex nonlinear interaction between three active buckling modes. The bifurcational nature of the response means that numerical solution may be unreliable (Duxbury et al., 1989), but with local buckling typified by a single wavelength, the equilibrium paths can be found by direct solution.

For the same sections loaded so that they bend rather than buckle, a similar destabilization of the compressive face can also occur. This time, however, in contrast to the bifurcation response, the reduction in stiffness develops smoothly out of the linear solution. The process is again amenable to the modal formulation, but crucial new features emerge; most importantly, the altered deflected form means that a large (strictly infinite) number of modes of differing wavelengths should be included. However, without the multiple equilibrium states associated with bifurcations, paths can successfully be traced using numerical procedures such as the Newton-Raphson algorithm. Examples, showing clear-cut destabilizations at moderately large lateral deflection, are presented; these are analyzed on an Apple Macintosh, and include a maximum of 126 degrees-of-freedom representing 31 differing wavelengths.

The present analysis allows for the important effects of through-core straining; thus, in the stressed state, the core thickness varies along the length. The pattern that develops is for a localized thinning of the section, usually toward the ends, as dependent upon the particular loading detail and boundary conditions. This significant feature, of course, remains unexplored by formulations based on or around the assumptions of simple bending theory.

2 Formulation

Following a recent contribution on the interactive buckling of sandwich struts (Hunt et al., 1988), the deflection of a laterally loaded beam is described by two distinct sets of modal configurations, snake and hourglass, defined with reference to Fig. 2. The snake mode is made up to two independent components, shear (q_s) and tilt (q_t),

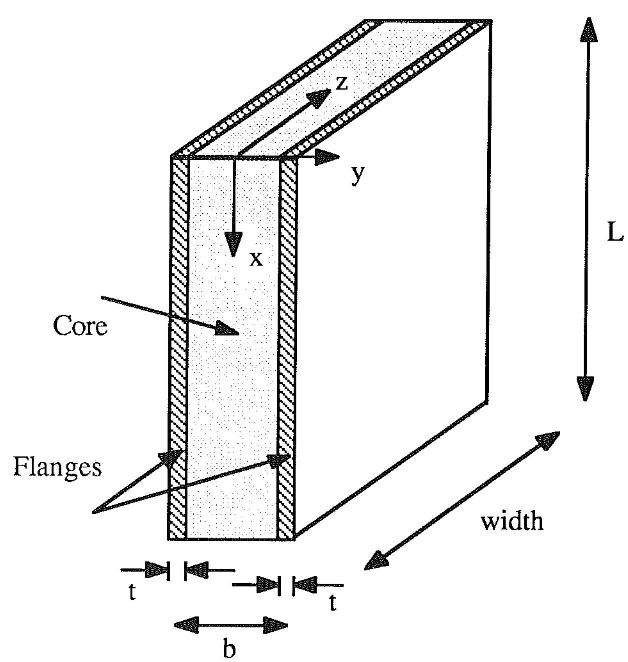

Fig. 1 Sandwich panel

Contributed by the Applied Mechanics Division of THE AMERICAN SOCIETY OF MECHANICAL ENGINEERS for publication in the JOURNAL OF APPLIED MECHANICS.

Discussion on this paper should be addressed to the Technical Editor, Leon M. Keer, The Technological Institute, Northwestern University, Evanston, IL 60208, and will be accepted until two months after final publication of the paper itself in the JOURNAL OF APPLIED MECHANICS. Manuscript received by the ASME Applied Mechanics Division, January 3, 1989; final revision, April 26, 1989.

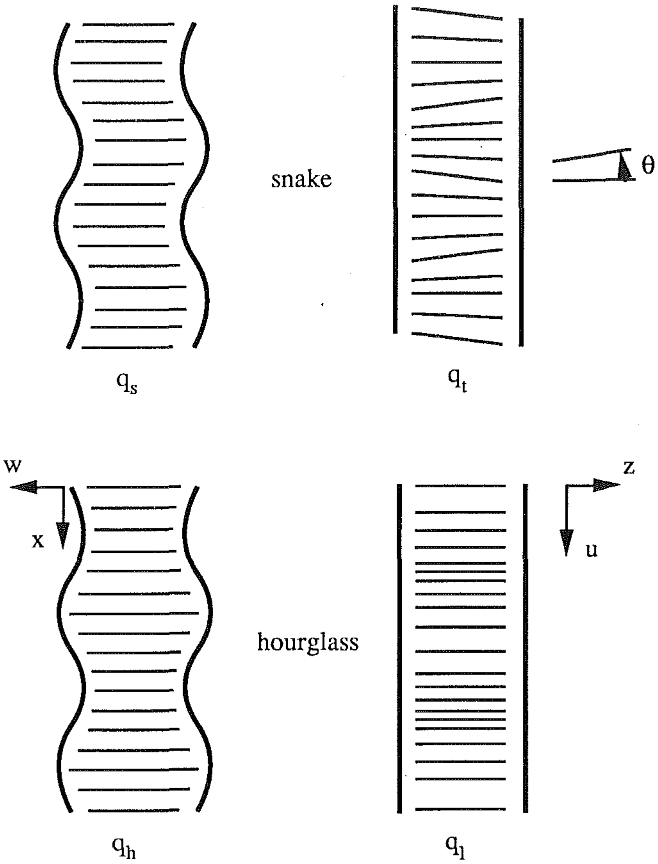

Fig. 2 The two modal contributions for a specific wave number

$$w = q_s \frac{L}{i} \sin\frac{i\pi x}{L}$$

$$\theta = q_t \pi \cos\frac{i\pi x}{L} \tag{1}$$

where L is the length of the strut and i is the wave number (Hunt et al., 1988). The hourglass mode, shown at the bottom, can be seen as two back-to-back struts on elastic foundations, and allows through-thickness strains to develop. In analogy with the snake mode, it involves two components, a sinusoidal out-of-plane deflection (q_h) and a longitudinal compressive wave (q_l), which bears the same relation to q_h as tilt to shear in the snake mode. These are thus defined by

$$w = q_h \frac{2y}{b} \frac{L}{i} \sin\frac{i\pi x}{L}$$

$$u = -\frac{b}{2} q_1 \pi \cos\frac{i\pi x}{L} \tag{2}$$

where b is the core thickness (distance between flanges), and we note that this implies a linear variation in shear strain angle through the core (Hunt et al., 1988). For simplicity, it is assumed that the flanges are thin ($t << b$), as it is the case in most practical applications. To complete the modal description while allowing for a greater flexibility of the sandwich model, we include also the pure compressive mode, shown in Fig. 3. This comprises two degrees-of-freedom, simply defined as

$$u = A_5 x$$

$$w = A_6 y, \tag{3}$$

A_6 corresponding to the Poisson effect and being introduced to overcome the problem of a net change of core thickness in an hourglass mode with odd wave number.

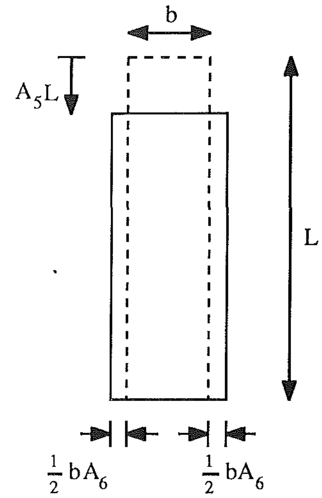

Fig. 3 Total end and transverse shortening

Unlike the buckling problem, where the feature of an optimum wave number for maximum interaction reduced the problem to six major degrees-of-freedom analysis (Hunt et al., 1988), an accurate description of the bending problem requires a large number of interacting wave numbers. A new "double-barreled" notation is thus introduced as follows:

a_{1i} = q_s component of snake mode with wave number i
a_{2i} = q_h component of corresponding hourglass mode with wave number i
a_{3i} = q_t component of snake mode with wave number i
a_{4i} = q_l component of corresponding hourglass mode with wave number i
A_5 = total end shortening
A_6 = total transverse shortening

where the wave number i takes any integer value from 1 to ∞. Note that, with the introduction of the extra modal component q_l, subscripts no longer coincide with those of the earlier publication (Hunt et al., 1988). The displacements can now be written in general form as:

$$w = \sum_{i=1}^{\infty} \left[\left(a_{1i} + a_{2i}\frac{2y}{b} \right) \frac{L}{i} \sin\frac{i\pi x}{L} \right] + A_6 y$$

$$u = -\sum_{i=1}^{\infty} \left[\left(y a_{3i} + \frac{b}{2} a_{4i} \right) \pi \cos\frac{i\pi x}{L} \right] + A_5 x. \tag{4}$$

3 Potential Energy Function

3.1 Strain Energy. Analysis proceeds by determining the potential energy function. The strain energy includes all the terms obtained in the buckling study, together with some new energy contributions, due to the extra degrees-of-freedom (a_{4i} and A_6) and the inclusion of a range of odd wave numbers. Thus, using the same strain-displacement relations and strain energy expressions (Hunt et al., 1988), the strain energy of a sandwich beam is given as the sum of the contributions from the core and flanges (bending and membrane),

$$\text{S.E.} = V_{fb} + V_{fm} + V_c. \tag{5}$$

Specifically, the flanges (bending and membrane) strain energy contributions, V_{fb}, and V_{fm}, respectively, are given by

$$V_f = V_{fb} + V_{fm} = \frac{1}{2} \frac{E_f t^3}{12(1-\nu_f^2)} \int_0^L \left(\frac{\partial^2 w}{\partial x^2} \right)^2 dx$$

$$+ \frac{1}{2} E_f t \int_0^L (\epsilon_x)_m^2 dx \tag{6}$$

summed over both flanges, where the first term represents the contribution from the bending strain, already integrated over the thickness, t, of each flange, and $(\epsilon_x)_m$ represents the longitudinal membrane strain, which includes the linear strain-displacement contribution $(\partial u/\partial x)$ and the (averaged) release in compression caused by the curved as opposed to straight configuration of the flanges (Hunt, 1986). Being in a fully two-dimensional stress state ($\sigma_z=\tau_{xz}=\tau_{yz}=0$), the strain energy of the core, V_c, obtained from the general expression for the strain energy of a two-dimensional solid body expressed in terms of strains, includes longitudinal (ϵ_x), transverse (ϵ_y), and shear (γ) strain contributions. While the first is analogous to the flange membrane strains, the remaining two are directly obtained from the small-displacement strain-displacement relations (da Silva and Hunt, 1990). Thus, V_c is written

$$V_c=\frac{\bar{E}_c}{2}\int_0^L\int_{-b/2}^{+b/2}(\epsilon_x^2+\epsilon_y^2+2\nu_c\epsilon_x\epsilon_y)dxdy+\frac{G_c}{2}\int_0^L\int_{-b/2}^{+b/2}\gamma^2dxdy \tag{7}$$

where E_c, ν_c, and G_c are the elastic properties of the core and we define

$$\bar{E}_c=\frac{E_c}{1-\nu_c^2}. \tag{8}$$

3.2 Work Done by the Load. The work done by the load is quite different from that of the buckling problem, any generic lateral load doing work directly on the active coordinates a_{1i}, a_{2i}, and a_{3i}, associated with lateral displacements and rotations, rather than the (passive) total end shortening A_5. We note that no work is done on a_{4i}, this being a pure longitudinal deformation. Writing the total work done by the load (W.D.L.) as

$$(\text{W.D.L.})=\sum_{\substack{i=1\\ \phi=1,2,3}}^{\infty}(\text{W.D.L.})_{\phi i}=-\mathcal{P}\sum_{\substack{i=1\\ \phi=1,2,3}}^{\infty}(V'_{\phi i}a_{\phi i}) \tag{9}$$

where $\mathcal{P}$ represents a generalized lateral load, it follows that the energy coefficients $V'_{\phi i}$ ($\phi=1,2,3$) can be written

$$V'_{\phi i}=\frac{-(\text{W.D.L.})_{\phi i}}{\mathcal{P}a_{\phi i}} \tag{10}$$

where $(\text{W.D.L.})_{\phi i}$ represents the contribution of the modal deformation associated with $a_{\phi i}(\phi=1,2,3)$. Since the work done by the load is dependent on the specific type (concentrated load, uniformly distributed load, etc.), the algebraic expressions for the $V'_{\phi i}$'s are left unspecified; so that general results can be obtained, particular examples being considered later.

3.3 Potential Function. The potential function is obtained as usual,

$$V=\text{total strain energy}-\text{work done by load}. \tag{11}$$

Differentiation of the total potential energy function (11) with respect to A_5 and A_6 yields two equilibrium equations, linear in A_5 and A_6, which can be used to eliminate these (passive) degrees-of-freedom from further consideration, giving

$$A_5=\frac{1}{4}\pi^2\sum_{i=1}^{\infty}\left(a_{1i}^2+\left(1-\frac{2}{3}\psi\right)a_{2i}^2\right)$$

$$A_6=-\nu_c\left[A_5-\frac{1}{4}\pi^2\sum_{i=1}^{\infty}\left(a_{1i}^2+\frac{1}{3}a_{2i}^2\right)\right]-\frac{2L}{b\pi}\sum_{i=1}^{\infty}\left(\frac{1-(-1)^i}{i^2}a_{2i}\right)-\nu_c\frac{b\pi}{2L}\sum_{i=1}^{\infty}((1-(-1)^i)a_{4i}) \tag{12}$$

where ψ is defined as the ratio of effective core stiffness to total effective stiffness,

$$\psi=\frac{E_cb}{2E_ft+E_cb} \tag{13}$$

so that a reduced energy function is written as

$$\begin{aligned}V=\frac{1}{2}\sum_{i=1}^{\infty}\Bigg[&V_{1i1i}a_{1i}^2+V_{2i2i}a_{2i}^2+V_{3i3i}a_{3i}^2+V_{4i4i}a_{4i}^2\\&+2V_{1i3i}a_{1i}a_{3i}+2V_{2i4i}a_{2i}a_{4i}+\sum_{\substack{j=1\\(i\neq j)}}^{\infty}(V_{2i2j}a_{2i}a_{2j}+V_{4i4j}a_{4i}a_{4j})\Bigg]\\&+\sum_{i=1}^{\infty}\Bigg[V_{1i2i3i}a_{1i}a_{2i}a_{3i}+\sum_{\substack{j=1\\(i\neq j)}}^{\infty}V_{1i2i3j}a_{1i}a_{2i}a_{3j}\Bigg]\\&+\sum_{i=1}^{\infty}\Bigg[\frac{1}{4}V_{1i1i2i2i}a_{1i}^2a_{2i}^2+\frac{1}{24}V_{2i2i2i2i}a_{2i}^4\\&+\sum_{\substack{j=1\\(i\neq j)}}^{\infty}\left(\frac{1}{2}V_{1i1j2i2j}a_{1i}a_{1j}a_{2i}a_{2j}+\frac{1}{2}V_{2i2i2j2j}a_{2i}^2a_{2j}^2\right)\Bigg]\\&+\mathcal{P}\sum_{i=1}^{\infty}(V'_{1i}a_{1i}+V'_{2i}a_{2i}+V'_{3i}a_{3i})\end{aligned} \tag{14}$$

representing a Taylor series about the unloaded state where $\mathcal{P}=a_{\phi i}=0(\phi=1,2,3,4)$. Specifically, the energy coefficients are given by

$$V_{1i1i}=2K^i+\frac{1}{2}\pi^2G_cb$$

$$V_{3i3i}=\frac{1}{4}i^2\pi^4\left(\frac{b}{L}\right)^2\left(E_ft+\frac{1}{6}\bar{E}_cb\right)+\frac{1}{2}\pi^2G_cb$$

$$V_{2i2j}=\begin{cases}2(K^i+\bar{k}^i)+\dfrac{1}{6}\pi^2G_cb-4\bar{E}_cb\left(\dfrac{L}{b\pi}\right)^2\dfrac{(1-(-1)^i)(1-(-1)^j)}{i^2j^2} & \text{if } i=j\\[2ex] -4\bar{E}_cb\left(\dfrac{L}{b\pi}\right)^2\dfrac{(1-(-1)^i)(1-(-1)^j)}{i^2j^2} & \text{if } i\neq j\end{cases}$$

$$V_{4i4j}=\begin{cases}\dfrac{1}{4}i^2\pi^4\left(\dfrac{b}{L}\right)^2\left(E_ft+\dfrac{1}{6}\bar{E}_cb\right)-\dfrac{1}{4}\pi^2\left(\dfrac{b}{L}\right)^2\bar{E}_cb\nu_c^2(1-(-1)^i)^2 & \text{if } i=j\\[2ex] -\dfrac{1}{4}\pi^2\left(\dfrac{b}{L}\right)^2\bar{E}_cb\nu_c^2(1-(-1)^i)(1-(-1)^j) & \text{if } i\neq j\end{cases}$$

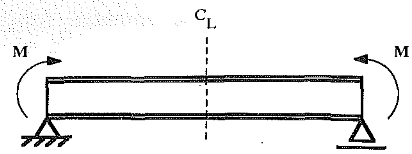

Fig. 4 Sandwich beam loaded by two equal end-moments

$$V_{1i3i} = -\frac{1}{2}\pi^2 G_c b$$

$$V_{1i2i3j} = -\pi^3\left(\frac{b}{L}\right)\left(E_f t + \frac{1}{6}\bar{E}_c b\right)\frac{1-(-1)^j}{2}$$

$$V_{1i8i} = \frac{1}{2}\pi^2 \bar{E}_c c \nu_c^2$$

$$V_{1i1j2i2j} = \begin{cases} \pi^4\left(E_f t + \frac{1}{6}\bar{E}_c b\right) & \text{if } i=j \\ \frac{\pi^4}{2}\left(E_f t + \frac{1}{6}\bar{E}_c b\right) & \text{if } i\neq j \end{cases}$$

$$V_{2i2i2j2j} = \begin{cases} \pi^4 \bar{E}_c b\left[\frac{2}{5} - \frac{1}{3}(\psi - \nu_c^2(1-\psi))\right] & \text{if } i=j \\ \frac{\pi^4}{3}\bar{E}_c b\left[\frac{2}{5} - \frac{1}{3}(\psi - \nu_c^2(1-\psi))\right] & \text{if } i\neq j \end{cases} \quad (15)$$

where K^i and $\bar{k}^i$ are defined as

$$K^i = \frac{i^2\pi^4 E_f t^3}{24(1-\nu_f^2)L^2} \quad (16)$$

$$\bar{k}^i = \frac{\bar{E}_c L^2}{i^2 b}. \quad (17)$$

3.4 Equilibrium Equations and Solution Procedure. Differentiating equation (14), with respect to each of the $a_{\phi i}$s ($\phi = 1, 2, 3, 4,$), in turn gives the equilibrium equations

$$\frac{\partial V}{\partial a_{1i}} = V_{1i1i}a_{1i} + V_{1i3i}a_{3i} + \sum_{j=1}^{\infty} V_{1i2i3j}a_{2i}a_{3j} + \sum_{j=1}^{\infty}\alpha V_{1i1j2i2j}a_{1j}a_{2i}a_{2j} + \mathcal{P}V'_{1i} = 0$$

$$\frac{\partial V}{\partial a_{2i}} = \sum_{j=1}^{\infty} V_{2i2j}a_{2j} + V_{2i4i}a_{4i} + \sum_{j=1}^{\infty} V_{1i2i3j}a_{1i}a_{3j} + \sum_{j=1}^{\infty}\alpha V_{1i1j2i2j}a_{1i}a_{1j}a_{2j} + \sum_{j=1}^{\infty}\beta V_{2i2i2j2j}a_{2i}a_{2j}^2 + \mathcal{P}V'_{2i} = 0$$

$$\frac{\partial V}{\partial a_{3i}} = V_{3i3i}a_{3i} + V_{1i3i}a_{1i} + \sum_{j=1}^{\infty} V_{1j2j3i}a_{1j}a_{2j} + \mathcal{P}V'_{3i} = 0$$

$$\frac{\partial V}{\partial a_{4i}} = \sum_{j=1}^{\infty} V_{4i4j}a_{4j} + V_{2i4i}a_{2i} = 0 \quad (18)$$

where

$$\alpha = \begin{cases} \frac{1}{2} \text{ if } i=j \\ 1 \text{ if } i\neq j \end{cases} \qquad \beta = \begin{cases} \frac{1}{6} \text{ if } i=j \\ \frac{1}{2} \text{ if } i\neq j. \end{cases}$$

The solution of these equations is obtained numerically after the elimination of the passive coordinates a_{3i} and a_{4i} and consequent reduction of the number of simultaneous equations, using a standard Newton-Raphson procedure by incrementing the load. In contrast with the buckling problem, the convergence of the method is good because there is a single smooth-varying solution at zero load, despite the existence of unconnected equilibrium paths at higher load levels.

4 Results and Discussion

To explore the interactive features responsible for the destiffening behavior of the system, we next pick a typical sandwich component from the literature (Brush and Almroth, 1975), adapted to become a more realistic beam (da Silva and Hunt, 1990), and use it to test our general formulation with an infinite number of degrees-of-freedom. Specifically, the sandwich beam is of length $L = 508$ mm, core thickness, $b = 50.8$ mm, flange thickness $t = 0.508$ mm, flange Young's modulus $E_f = 68947.57$ N/mm^2, flange Poisson's ratio $\nu_f = 0.3$, core Young's modulus $E_c = 198.57$ N/mm^2, core shear modulus $G_c = 82.74$ N/mm^2, and core Poisson's ratio $\nu_c = 0.2$, where the unrounded form of these constants results from our choice to express them in metric rather than the original Imperial units.

4.1 Example 1: Equal End-Moments *M*. As a first example, we start by considering a pure bending situation, where the sandwich beam, assumed to be simply supported at the ends, is loaded by two equal and opposite end-moments, M, as illustrated in Fig. 4. Before proceeding with the analysis, it is necessary to evaluate the work done by the load in order to obtain the expressions for the $V'_{\phi i}$, as earlier indicated. The work done by the load is given by the product of load (moment) times the displacement (rotation) in the direction of the load so that we have

$$\text{W.D.L.} = \frac{M}{2t+b}\sum_{i=1}^{\infty}\left\{\left[t(\theta_x)_{\substack{x=0\\y=b/2}} + t(\theta_x)_{\substack{x=0\\y=-b/2}} + \int_{-b/2}^{b/2}(\theta_x)_{x=0}dy\right] - \left[t(\theta_x)_{\substack{x=L\\y=b/2}} + t(\theta_x)_{\substack{x=L\\y=-b/2}} + \int_{-b/2}^{b/2}(\theta_x)_{x=L}dy\right]\right\} \quad (19)$$

giving

$$\text{W.D.L.} = 2\pi M\sum_{i=1}^{\infty}\left[\frac{(1-(-1)^i)}{2}a_{3i}\right] \quad (20)$$

and finally, using equation (10),

$$\begin{cases} V'_{1i} = 0 \\ V'_{2i} = 0 \\ V'_{3i} = -\frac{2\pi}{L}\left[\frac{(1-(-1)^i)}{2}a_{3i}\right] \end{cases} \quad (21)$$

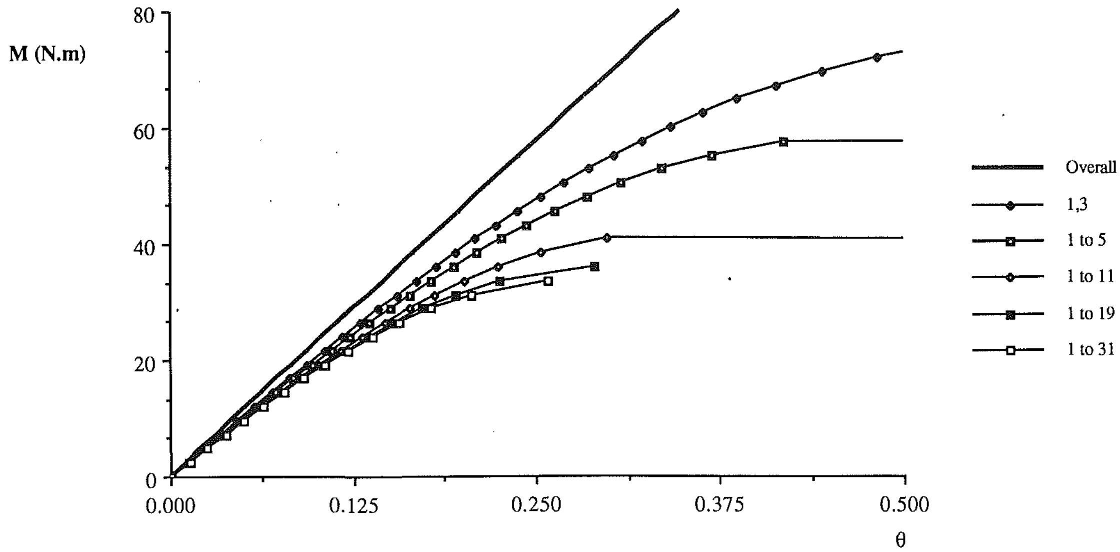

Fig. 5(a)

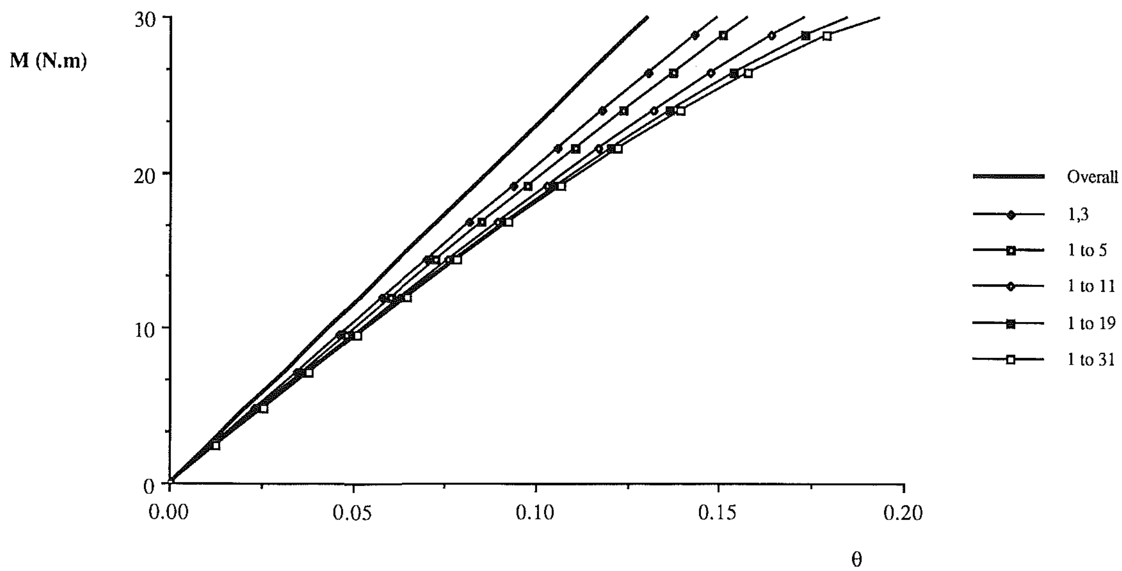

Fig. 5(b)

Fig. 5 Moment-rotation curves for a sandwich beam loaded by two equal end-moments M

nondimensionalized with respect to length to match the strain energy terms.

Solution can now be obtained as previously described. These are plotted in Fig. 5, which shows two views of the various moment-rotation curves, obtained for an increasing number of interacting wave numbers. The linear solution, obtained by considering only the snake mode with wave number 1, is also plotted for comparison. Reflecting the Rayleigh-Ritz nature of the model, solutions represent upper bounds to the true behavior, the accuracy increasing with the number of pairs of modes. Reasonable convergence is apparently achieved for more than 19 interacting wave numbers, as seen in Fig. 5.

The typical nonlinear response of the system clearly identifies two different stages of behavior. The first (linear) stage corresponds to deformation of the beam mostly in one-half sine wave, with little contribution from the other modes, representing a good approximation to the exact solution to the linearized problem, as obtained by Allen (1969). As the response becomes less stiff, the other modes become increasingly more important, reflecting the beam (face) on elastic foundation (core) effect caused by the compressive forces induced in one of the flanges by the bent configuration of the beam, corresponding to flexural wrinkling of the sandwich beam. Because of the symmetry of the loading with respect to the vertical axis of symmetry of the beam, as shown in Fig. 4, deformation modes with an even number of waves do not contribute.

4.2 Example 2: Concentrated Load P at Midspan. To provide an example of a more common loading case, we next consider the same sandwich beam of the previous example, loaded by a concentrated load P (per millimeter width) applied at midspan, acting on the top face of the beam. Following the same procedure of the previous example, we start by evaluating the work done by the point load, P, given by

$$\text{W.D.L.} = P\sum_{i=1}^{\infty} (w)_{\substack{x=L/2\\ y=b/2}} \tag{22}$$

or, replacing for the lateral displacement, w,

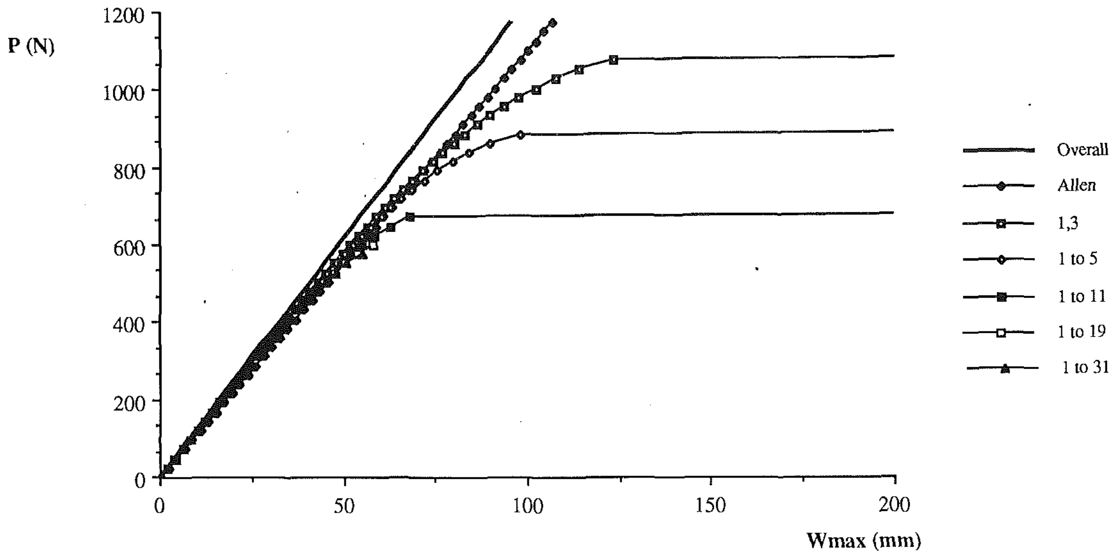

Fig. 6(*a*)

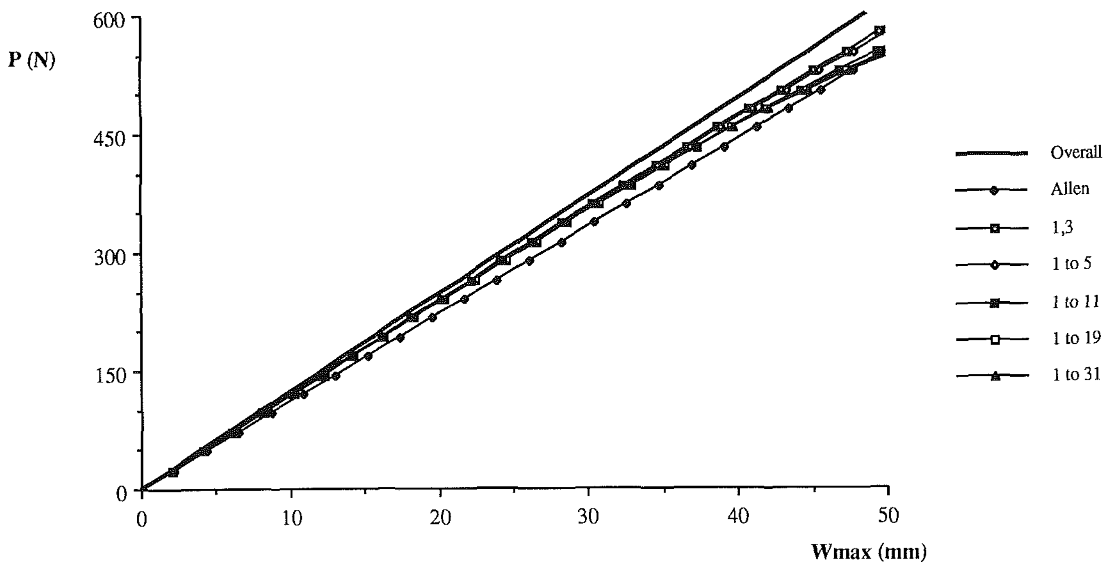

Fig. 6(*b*)

Fig. 6 Load-deflection curves for a sandwich beam loaded by a point load *P* applied at midspan

$$\text{W.D.L.} = P\sum_{i=1}^{\infty}\left\{(a_{2i}-a_{2i})\frac{L}{i}\left[\frac{(-1)^{(i-1)/2}}{2}(1-(-1)^i)\right]\right\} \tag{23}$$

so that the $V'_{\phi i}$ coefficients, again nondimensionalized with respect to L, are given by

$$\begin{cases} V'_{1i} = -\dfrac{1}{i}\left[\dfrac{(-1)^{(i-1)/2}}{2}(1-(-1)^i)\right] \\ V'_{2i} = +\dfrac{1}{i}\left[\dfrac{(-1)^{(i-1)/2}}{2}(1-(-1)^i)\right] \\ V'_{3i} = 0 \end{cases} \quad . \tag{24}$$

Despite the different loading case, results are similar to our previous example, the sandwich beam once again exhibiting a destiffening response triggered by the instability of the compressive face. The load-displacement (deflection at midspan) curves are plotted on Fig. 6, which includes the linear solution obtained by using the overall (snake) mode alone and the corresponding Allen solution for a simply-supported sandwich beam without overhang (Allen, 1969). Reasonable convergence is once again achieved for about 20 interacting wave numbers, the symmetry of the loading ruling out contributions from the even-numbered waves. We note that our overall (linear) solution does not exactly coincide with Allen's results. This is to be expected, the deformation pattern used to model the deflection of the sandwich beam in our linearized case given in equation (4*a*) with $i=1$ being only approximate. Hence, the corresponding load-displacement curve is stiffer than the exact result obtained by Allen for the linear case, given by

$$w = -\frac{Px^2L}{24EI}\left(3-\frac{2x}{L}\right) - \frac{PL}{4AG}\left(1-\frac{I_f}{I}\right)^2\left\{\frac{2x}{L} - \frac{2}{aL}\left[\sinh ax + \beta_1(1-\cosh ax)\right]\right\} \tag{25}$$

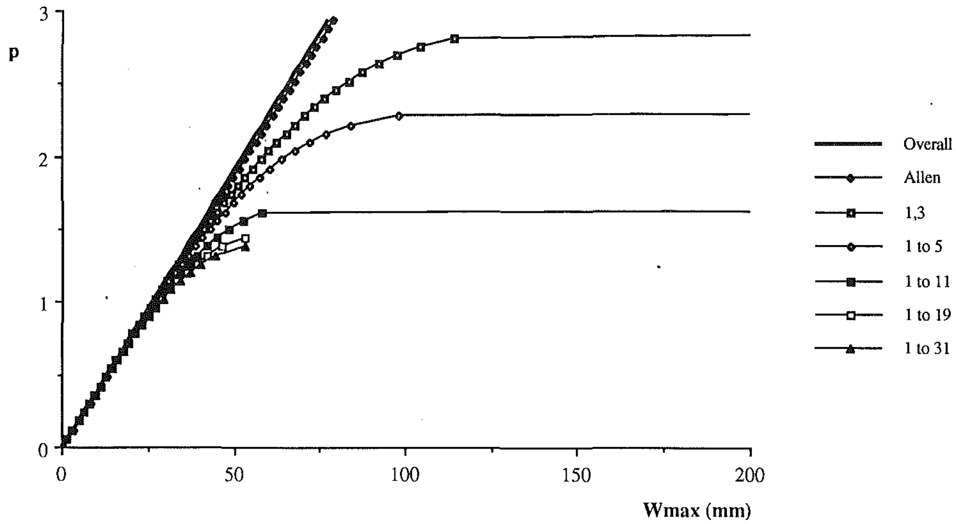

Fig. 7(a)

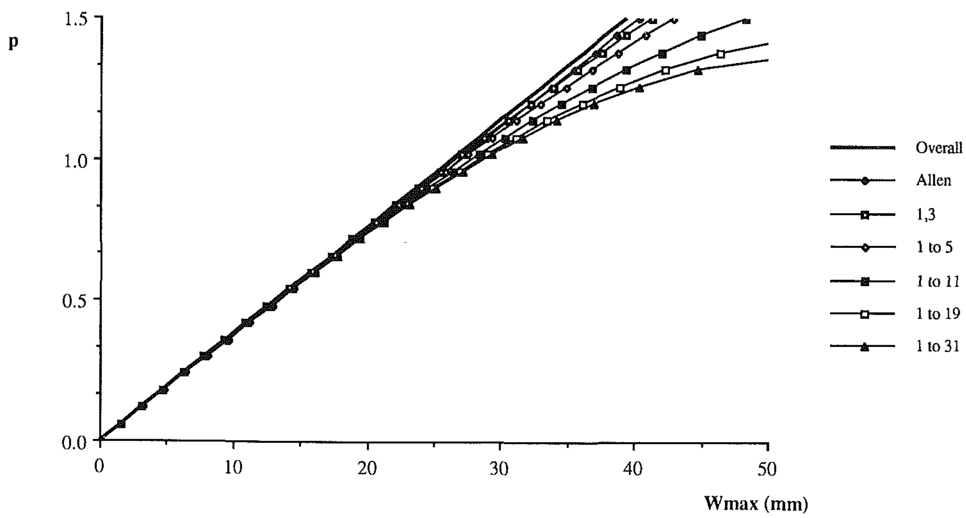

Fig. 7(b)

Fig. 7 Load-deflection curves for a sandwich beam loaded by a uniformly distributed load p

where I is the inertia of the section, I_f the inertia of the faces, A is a modified measure of the area of the cross-section, E is the Young modulus of the faces, G is the shear modulus of the core, the remaining constants being defined as

$$\beta_1 = \tanh\frac{aL}{2}$$

$$a^2 = \frac{AG}{EI_f(1 - I_f/I)}. \tag{26}$$

4.3 Example 3: Uniformly Distributed Load p. Our final example consists of the same sandwich beam loaded by an uniformly distributed load p (per unit length and per millimeter width) spanning the full length of the sandwich beam. The work done by the load p is thus given by

$$\text{W.D.L.} = \frac{p}{2t+b}\sum_{i=1}^{\infty}\left\{\int_0^L \left[t(w)_{y=b/2} + t(w)_{y=-b/2} + \int_{-b/2}^{b/2} w dy\right]\right\} \tag{27}$$

yielding

$$\text{W.D.L.} = p\sum_{i=1}^{\infty}\left[a_{1i}\left(\frac{L}{i}\right)^2 \frac{1-(-1)^i}{\pi}\right] \tag{28}$$

and, using equation (10) and dividing by L,

$$\begin{cases} V'_{1i} = -\left(\frac{L}{\pi}\right)\frac{1-(-1)^i}{i^2} \\ V'_{2i} = 0 \\ V'_{3i} = 0 \end{cases}. \tag{29}$$

Results are shown in Fig. 7, exhibiting the same load-deflection response of our previous examples, with an overall deformation followed by wrinkling of the compressive face. Comparison between our overall solution and results obtained by Allen (1969) for this loading case are also plotted, showing better agreement than the previous case, reflecting the closer approximation to the true deflection pattern. Convergence is achieved as for the former cases, the even-numbered waves not featuring in the response, as before, owing to the symmetry of the loading.

5 Concluding Remarks

This paper features a distinctive form of interacting bending behavior in sandwich beams which is characterized by a nonlinear response arising from the interaction between modes with different wavelengths. The influence of the hourglass mode is crucial, allowing through-core straining to take place and enabling the one-sided wrinkling in combination with the corresponding snake mode. As for the buckling problem, the cubic cross-terms of energy are crucial for the interaction, but here appear largely linking odd-numbered modal contributions.

The flexural wrinkling highlighted by the analysis is closely connected to the instability of the compressive face, in analogy with a strut on an elastic foundation. This analogy has been used to compute a critical wrinkling load, by neglecting the overall bending component of the beam and assuming that both the core and the tensile face are unstrained before buckling (Chong and Hartsock, 1974; Gutierrez and Webber, 1980); the problem is thus treated as a sudden buckle, rather than allowing the wrinkling deformation to develop smoothly out of the linear solution, as in the present work.

It is clear that the thickness of the faces is a crucial parameter, large face-to-core thickness ratios resulting in linear responses with no wrinkling, which match Allen's antiplane solution (Allen, 1969). This is recently verified by O'Connor (1985), using a finite element package for thick-faced sandwich beams.

The introduction of the extra degree-of-freedom in the generalized hourglass mode constitutes an additional new refinement. This has been shown to have a significant quantitative effect, leading to an additional reduction of effective load-carrying capacity of the sandwich beam of the order of seven percent. In combination with the tilt component of the snake mode, it allows for a shift of the neutral axis of the beam, and thus opens the way for the analysis of sandwich beams with faces of different thickness.

Acknowledgment

The authors would like to acknowledge financial support from the Calouste Gulbenkian Foundation for L.S. da Silva.

References

Allen, H. G., 1969, *Analysis and Design of Structural Sandwich Panels*, Pergamon, Oxford, U.K.

Brush, D. O., and Almroth, B. O., 1975, *Buckling of Bars, Plates and Shells*, McGraw-Hill, New York.

Chong, K. P., and Hartsock, J. A., 1974, "Flexural Wrinkling in Foam-filled Sandwich Panels," *J. Eng. Mech Div.*, Vol. 100, pp. 95–110.

da Silva, L. S., and Hunt, G. W., 1989, "Interactive Buckling in Sandwich Structures with Core Orthotropy," *Journal of Mechanics of Structures and Machines*, in press.

Duxbury, P. G., Crisfield, M. A., and Hunt, G. W., 1989, "Benchtests for Geometric Nonlinearity," *Computers and Structures*, Vol. 33, pp. 21–29.

Gutierrez, A. J., and Webber, J. P. H., 1980, "Flexural Wrinkling of Honeycomb Sandwich Beams with Laminated Faces," *Int. J. Solids Structures*, Vol. 16, pp. 645–651.

Hunt, G. W., 1986, "Hidden (a)symmetries of elastic and plastic bifurcation," *Applied Mechanics Reviews*, ASME, New York, Vol. 39, pp. 1165–1186.

Hunt, G. W., da Silva, L. S., and Manzocchi, G. M. E., 1988, "Interactive Buckling in Sandwich Structures," *Proceedings of the Royal Society of London*, Vol. 417A, pp. 155–177.

O'Connor, D. J., 1985, *The Flexural Behavior of Sandwich Beams with Thick Facings and Rigid Plastic Foam Cores*, D. Phil. Thesis, University of Ulster.

Roger Ghanem
Post Doctoral Research Associate,
Department of Civil Engineering.

P. D. Spanos
L. B. Ryon Endowed Chair in Engineering,
Mem. ASME

Rice University,
Houston, TX 77251-1892

Polynomial Chaos in Stochastic Finite Elements

A new method for the solution of problems involving material variability is proposed. The material property is modeled as a stochastic process. The method makes use of a convergent orthogonal expansion of the process. The solution process is viewed as an element in the Hilbert space of random functions, in which a sequence of projection operators is identified as the polynomial chaos of consecutive orders. Thus, the solution process is represented by its projections onto the spaces spanned by these polynomials. The proposed method involves a mathematical formulation which is a natural extension of the deterministic finite element concept to the space of random functions. A beam problem and a plate problem are investigated using the new method. The corresponding results are found in good agreement with those obtained through a Monte-Carlo simulation solution of the problems.

Introduction

In recent years the development of mechanical and structural systems requiring stringent reliability standards has been witnessed. This fact along with the advent of digital computations have intensified the interest in the analysis of systems the properties of which exhibit random fluctuations. Introducing uncertainty in the corresponding mathematical models reflects a more realistic representation, indeed, of engineering systems and of their response to natural loads. The resulting mathematical complications, however, are great and have had a major impact in precluding an effective treatment of the problem. The current ordinary methods for solving the problem are Monte Carlo simulation methods (Shinozuka, 1987), perturbation methods (Nakagiri and Hisada, 1982; Liu, Besterfield, and Belytschko, 1988) and Neumann expansion methods (Adomian and Malakian, 1980; Shinozuka, 1987). Further, Lawrence (1987) has suggested a heuristic Galerkin approach for solving the related class of problems. In all of these methods, the approximations involved must be interpreted with caution from a perspective of convergence and versatility. In a previous publication (Spanos and Ghanem, 1989), the authors have suggested a method that makes use of an orthogonal decomposition of a random process (Masri and Miller, 1982) and a Neumann expansion scheme to achieve a more efficient implementation of the randomness into the solution process. The solution has been found in good agreement with Monte Carlo simulation results over a wide range of random fluctuations. This paper extends the ideas presented previously by the authors. An orthogonal expansion in terms of the polynomial chaos (Wiener, 1938, Kallianpur, 1989) is used to represent the random response by a convergent series. The proposed formulation is construed as a natural extension of the deterministic finite element concept to the space of random functions.

Contributed by the Applied Mechanics Division of The American Society of Mechanical Engineers for presentation at the Winter Annual Meeting, San Francisco, Calif., December 10-15, 1989.

Discussion on this paper should be addressed to the Editorial Department, ASME, United Engineering Center, 345 East 47th Street, New York, N.Y. 10017, and will be accepted until two months after final publication of the paper itself in the Journal of Applied Mechanics. Manuscript received by the ASME Applied Mechanics Division, October 10, 1988; final revision, May 2, 1989.

Paper No. 89-WA/APM-42.

Preliminary Concepts

Denote by $\mathbf{H}$ the Hilbert space of deterministic scalar functions defined by mapping a subset $\mathbf{D}$ of R^n onto the real line R. Further, let Ω denote the space of elementary random events. Then, the Hilbert space of functions defined by mapping Ω onto the real line will be denoted by Θ. Each map $\Omega \rightarrow R$ defines a random variable. Elements of $\mathbf{H}$ and Θ are denoted by roman and greek letters, respectively.

Treat a random process as a collection, $\{\alpha_x(\theta)\}$, of indexed random variables. In what follows, the indexing set is taken to be a subset of the domain $\mathbf{D}$ over which the problem is defined. This subset may represent either spatial or temporal coordinates.

Consider an operator equation defined over $\mathbf{H} \times \Theta$

$$Q(\mathbf{x}_2,\theta)u(\mathbf{x}_2,\theta) = f(\mathbf{x}_1,\theta), \tag{1}$$

where $\mathbf{x}_1$ and $\mathbf{x}_2$ are elements of $\mathbf{D}$ and θ is an element of Ω representing the random component. In general, $Q(\mathbf{x}_2, \theta)$ is a differential or integral operator and $u(\mathbf{x}_2,\theta)$ is the response to an input $f(\mathbf{x}_1,\theta)$. Clearly, both $u(\mathbf{x}_2,\theta)$ and $f(\mathbf{x}_1,\theta)$ are stochastic processes. Given the joint probabilistic information about $Q(\mathbf{x}_2,\theta)$ and $f(\mathbf{x}_1,\theta)$, the solution is completely determined if the joint probabilistic information about $Q(\mathbf{x}_2,\theta)$, $f(\mathbf{x}_1,\theta)$, and $u(\mathbf{x}_1,\theta)$ is obtained. Such information, however, is often difficult to obtain. Thus, a more modest amount of information is usually sought. First, the joint information requirement is replaced by marginal information about the response process $u(\mathbf{x}_1,\theta)$. Secondly, the marginal probability distribution of $u(\mathbf{x}_1,\theta)$ is replaced by a set of moments, from which an estimate of the desired probabilistic information is obtained. Therefore, even before any solution is attempted, several simplifying assumptions are introduced. In the following a systematic and rigorous analysis of problems defined by equation (1) is made. It is shown that some of these assumptions can be relaxed.

Assuming that the dependence of $Q(\mathbf{x}_2,\theta)$ on θ involves a random function $\alpha_x(\theta)$, equation (1) can be rewritten as

$$\left(\mathbf{L}(\mathbf{x}_2) + \mathbf{S}(\mathbf{x}_2,\alpha_{x_2}(\theta))\right) u(\mathbf{x}_2,\theta) = f(\mathbf{x}_1,\theta). \tag{2}$$

In this equation, $\mathbf{L}(\mathbf{x}_2)$ represents an operator obtained from $Q(\mathbf{x}_2,\theta)$ by statistical averaging over θ. The symbol $\mathbf{S}(\mathbf{x}_2,\alpha_{x_2}(\theta))$ denotes the fluctuations of the operator $Q(\mathbf{x}_2,\theta)$ about $\mathbf{L}(\mathbf{x}_2)$. The function $\alpha_x(\theta)$ can be thought of as representing the stochastic fluctuations about the mean of some property of the system that is involved in the operator $Q(\mathbf{x}_2,\theta)$.

The functional dependence on $\mathbf{x}$ of realizations of α_x is not explicitly known. This fact constitutes a major difficulty in attempting a numerical treatment of the problem. The difficulty can be overcome by using the Karhunen-Loeve expansion (Loeve, 1977) which involves a representation of the process in terms of a denumerable set of random variables. Specifically, $\alpha_x(\theta)$ may be expressed as

$$\alpha_x(\theta) = \sum_{i=1}^{\infty} \sqrt{\lambda_i}\, \xi_i\, a_i(x), \tag{3}$$

where $\{\xi_i\}$ is a set of orthonormal random variables, and λ_i and $a_i(x)$ are deterministic quantities signifying the eigenvalues and eigenfunctions of the covariance kernel of α_x, respectively. In equation (3) the terms in the series are arranged in descending order of magnitude of the eigenvalues λ_i. Obviously, the joint distribution of $\{\xi_i\}$ depends on that of α_x. In the case that α_x is a Gaussian process, the set $\xi \equiv \{\xi_i\}$ forms a Gaussian vector. In view of equation (3), equation (2) becomes

$$\left(\mathbf{L}(\mathbf{x}_2) + \mathbf{R}(\mathbf{x}_2,\xi)\right) u(\mathbf{x}_2) = f(\mathbf{x}_1), \tag{4}$$

where the symbol $\mathbf{R}(\mathbf{x}_2,\xi)$ denotes the dependence of the operator $Q(\mathbf{x}_2,\theta)$ on the random variables $\{\xi_i\}$.

Mathematical Formulation

Projection in H: Deterministic Finite Element. In equation (3) the set $\{a_i(\mathbf{x})\}$ forms an orthonormal basis in the Hilbert space $\mathbf{H}$. Introducing a change of basis in $\mathbf{H}$ from $\{a_i(\mathbf{x})\}$ to $\{z_i(\mathbf{x})\}$, the excitation process $f(x)$ can be expanded as

$$f(x) = \sum_{i=1}^{\infty} \phi_i z_i(\mathbf{x}). \tag{5}$$

Clearly, $\{z_i(\mathbf{x})\}$ can be selected to be expeditious for any particular problem under consideration. Similarly, the response process can be expanded as

$$u(\mathbf{x}) = \sum_{i=1}^{\infty} \mu_i z_i(\mathbf{x}), \tag{6}$$

where $\{\mu_i\}$ are appropriate random variables. Truncation of the series in equations (5) and (6) at the Nth term represents the projection of the functions $f(\mathbf{x})$ and $u(\mathbf{x})$, respectively, onto the N-dimensional subspace of $\mathbf{H}$ spanned by $\{z_i(\mathbf{x})\}_{i=1}^{N}$. Substituting for $u(\mathbf{x})$ and $f(\mathbf{x})$ in equation (4) by their respective projections onto R^N results in the following expression for the error

$$\epsilon = \sum_{n=1}^{N} [\mathbf{L}(\mathbf{x}_2) + \mathbf{R}(\mathbf{x}_2,\xi)] z_n(\xi)\mu_n - \phi_n z_n(\mathbf{x}). \tag{7}$$

In equation (7) $\{\phi_n\}$ are known coefficients independent of x, and $\{\mu_n\}$ are the unknowns to be determined. One way of determining these coefficients is to constrain the error to be orthogonal to the space spanned by $\{z_i(\mathbf{x})\}$. In this manner a set of N algebraic equations in the N unknowns μ_n is obtained. The ith equation has the form

$$\sum_{n=1}^{N} \mu_n \int_{R^n} [\mathbf{L}(\mathbf{x}_2) + \mathbf{R}(\mathbf{x}_2,\xi)] z_n(\mathbf{x}_2) z_1(\mathbf{x}_1) d\mathbf{x}_2 - \phi_n \int_{R^n} z_n(\mathbf{x}) z_i(\mathbf{x}) d\mathbf{x} = 0. \tag{8}$$

In general, the set $\{z_i(\mathbf{x})\}$ is of bounded support; it is nonvanishing only over a subset of $\mathbf{D}$. Based on this observation it is seen that a finite element mesh can be obtained by selecting $\{z_i(\mathbf{x})\}$ to be appropriate shape functions. In this case, carrying out the indicated integrations by parts a matrix equation is obtained

$$[\hat{\mathbf{L}} + \hat{\mathbf{R}}(\xi)]\hat{\mu} = \hat{\mathbf{f}}, \tag{9}$$

involving the deterministic $N \times N$ matrix $\hat{\mathbf{L}}$, the random $N \times N$ matrix $\hat{\mathbf{R}}$, and the N-dimensional random vectors $\hat{\mu}$ and $\hat{\mathbf{f}}$ with components μ_i and ϕ_i, respectively. Note that $\hat{\mathbf{L}}$ is a banded, symmetric, and positive definite $N \times N$ matrix. Further, if the set $\{z_i(x)\}$ is chosen to be, as is customary in finite element methods, a set of piecewise polynomials, then $\hat{\mu}$ will be a vector whose elements represent the random nodal responses.

The preceding development conforms with the deterministic Galerkin finite element formulation. The process α_x will subsequently be assumed to be Gaussian. Also, it will be assumed that the process α_x appears as a multiplicative factor in the expression for the random operator $\mathbf{R}(\mathbf{x}_2,\xi)$. Then, equation (9) can be put in the form

$$\left[\sum_{m=0}^{M} \xi_m \mathbf{R}_m\right]\hat{\mu} = \hat{\mathbf{f}}, \tag{10}$$

where $\mathbf{R}_m$ is an $N \times N$ deterministic matrix, $\hat{\mathbf{f}}$ is an N-dimensional deterministic vector and

$$\mathbf{R}_0 \equiv \hat{\mathbf{L}} \quad \text{and} \quad \xi_0 \equiv 1. \tag{11}$$

Expansion of Nodal Random Response Vector $\hat{\mu}$. The Hilbert space Θ is complete. Thus, the random nodal response vector $\hat{\mu}$ can be expanded in a mean-square convergent series

$$\hat{\mu} = \sum_{i=0}^{\infty} \mathbf{c}_i\, \gamma_i, \tag{12}$$

where $\mathbf{c}_i$ is a deterministic vector and $\{\gamma_i\}_{i=1}^{\infty}$ is a basis in Θ. In connection with $\{\gamma_i\}$, the notions of homogeneous chaos and polynomial chaos will be introduced (Wiener, 1938; Kallianpur, 1980). Let $\{\xi_i\}_{i=1}^{\infty}$ be a set of orthonormal Gaussian random variables. Consider the space $\hat{\Gamma}_p$ of all polynomials in $\{\xi_i\}_{i=1}^{\infty}$ of degree not exceeding p. Let Γ_p represent the set of all polynomials in $\hat{\Gamma}_p$ orthogonal to $\hat{\Gamma}_{p-1}$. Finally, let $\bar{\Gamma}_p$ be the space spanned by Γ_p. Then, the subspace $\bar{\Gamma}_p$ of Θ is called the pth homogeneous chaos, and Γ_p is called the pth polynomial chaos. Using this basis, equation (12) can be rewritten as

$$\hat{\mu} = \sum_{p \geq 0} \sum_{n_1 + \ldots + n_r = p} \sum_{1_1, 1_2, \ldots, 1_r} \mathbf{a}_{1_1 1_2 \ldots 1_r}^{n_1 n_2 \ldots n_r} \Gamma_p(\xi_{1_1}, \ldots, \xi_{1_r}), \tag{13}$$

where $\Gamma_p(.)$ is the polynomial chaos of order p and the coefficients $\mathbf{a}$ are deterministic vectors. The superscript n_i over $\mathbf{a}$ refers to the number of occurrences of ξ_{1_i} in the argument list for $\Gamma_p(.)$. It is noted that the above statement is a variation of the Cameron-Martin theorem (Cameron and Martin, 1947). Expanding equation (13), $\hat{\mu}$ can then be expressed as

$$\hat{\mu} = \mathbf{a}_0\Gamma_0 + \sum_{i_1=1}^{\infty} \mathbf{a}_{i_1}\Gamma_1(\xi_{i_1}) + \sum_{i_1=1}^{\infty} \sum_{i_2=1}^{i_1} \mathbf{a}_{i_1,i_2}\Gamma_2(\xi_{i_1}\ \xi_{i_2})$$

$$+ \sum_{i_1=1}^{\infty} \sum_{i_2=1}^{i_1} \sum_{i_3=1}^{i_2} \mathbf{a}_{a_1,i_2,i_3} \Gamma_3(\xi_{i_1}\, \xi_{i_2}\, \xi_{i_3}) + \ldots, \tag{14}$$

where $\Gamma_p(.)$ are successive polynomial chaoses of their argument. The polynomial chaoses of order greater than one have zero-mean and polynomials of different order are orthogonal to each other, so are polynomials of same order but with different arguments. Up to the third order, the polynomial chaoses are

$$\Gamma_0 = 1 \tag{15}$$

$$\Gamma_1(\xi_{i_1}) = \xi_{i_1} \tag{16}$$

$$\Gamma_2(\xi_{i_1},\xi_{i_2}) = \xi_{i_1}\xi_{i_2} - \delta_{i_1 i_2} \tag{17}$$

$$\Gamma_3(\xi_{i_1},\xi_{i_2},\xi_{i_3}) = \xi_{i_1}\xi_{i_2}\xi_{i_3} - \xi_{i_1}\,\delta_{i_2 i_3} - \xi_{i_2}\delta_{i_1 i_3} - \xi_{i_3}\delta_{i_1 i_2} \tag{18}$$

where δ_{ij} is the Kronecker delta. In place of $\{\Gamma_p\}$ in the expansion (14), any set spanning the same subspace could have been used. For example, the set

$$\{\xi_0,\ \xi_{i_1},\ \xi_{i_1}\xi_{i_2},\ \xi_{i_1}\xi_{i_2}\xi_{i_3},\ \ldots\}$$

of nonorthogonal polynomials is readily available. Note that using this latter set results in a representation of the response process that is similar in form to the one obtained by the authors (Spanos and Ghanem, 1989) using a Neumann expansion for the inversion of the random operator in equation (10). An orthogonal basis, however, yields better convergence, as will be demonstrated in the numerical examples. Note also that the first summation in equation (14) represents the Gaussian component of the process μ. Thus, for a Gaussian process, the above expansion reduces to a single summation, the coefficients a_{i_1} being the coefficients in the Karhunen-Loeve expansion of the process. Equation (14) is an expansion in θ. Thus, any other dependence of the function μ is carried over to the expansion coefficients a_i.

Projection in Θ: Stochastic Finite Element. Truncating equation (14) at the pth-order polynomial and substituting for $\hat{\mu}$ into equation (10) yields an expression for the resulting error

$$\epsilon = \hat{\mathbf{f}} - \left[\sum_{m=0}^{M} \mathbf{a}_0 \mathbf{R}_m \Gamma_0 \xi_m + \sum_{m=0}^{M} \mathbf{R}_m \sum_{i_1=1}^{M} \mathbf{a}_{i_1} \Gamma_1(\xi_{i_1}) \xi_m + \ldots \right.$$
$$\left. + \sum_{m=0}^{M} \mathbf{R}_m \sum_{i_1=1}^{M} \ldots \sum_{i_p=1}^{i_{p-1}} \mathbf{a}_{i_1,\ldots,i_p}\, \Gamma_p(\xi_{i_1},\ldots,\xi_{i_p}) \xi_m \right]. \tag{19}$$

This error results from truncating the series in equation (10) after a finite number of terms, as well as from using a finite number of terms in the expansion for the system parameter α_x. The error, as expressed by equation (19), is made orthogonal to the solution space. Mathematically, this condition can be expressed as

$$\langle \epsilon,\ \Gamma_s(\pi_s^M(\xi_{i_1},\ \ldots,\xi_{i_s})) \rangle = 0 \qquad s \le p \tag{20}$$

where $\langle\, . \,\rangle$ denotes the operator of mathematical expectation; $\pi_s^M(\xi_{i_1}\ \ldots,\ \xi_{i_s})$ is a permutation operator that chooses, with renewal, s elements from the family given by its argument, with $0 \le i_k \le M$, $(1 \le k \le p)$, the resulting combinations not being permutations of each others. This orthogonality constraint results in a set of algebraic equations that can be solved for the coefficients $\mathbf{a}_{i_1,\ldots,i_k}$, $(i_1 + \ldots + i_k \le s)$. Once these coefficients are computed, the expansion (14) for the response process is determined. From equation (14) it can be seen that all the probabilistic information concerning the process u is contained in the expansion coefficients. For instance, the average response is equal to $\mathbf{a}_0$. Therefore, once these coefficients have been computed, the probability distribution of the response u can, at least theoretically, be determined.

Numerical Implementation

The numerical implementation of the projection in $\mathbf{H}$ follows the same guidelines as those for the deterministic finite element methods (Akin, 1982). Thus, the treatment in the present section is confined to the implementation of the projection in Θ. The first step in implementing the proposed method consists of expanding the random process α_x representing the randomness of the system parameters. If this process is assumed to have a Gaussian distribution, the expansion in equation (14) reduces to the Karhunen-Loeve expansion of the process. Then, the computations leading to the expansion consist of solving an integral eigenvalue equation for the covariance kernel. For a number of useful covariance models, the solution for such an equation can be obtained analytically. In general, however, a numerical solution procedure may have to be implemented. The next step in the solution procedure consists of implementing the expansion provided by equation (14) for the response process. The size of the resulting system of equations is proportional to the size of the homogeneous chaos used, as defined by the number of its basis functions. It can be seen that for the pth chaos, $\bar{\Gamma}_p$ is spanned by the basis $\{\Gamma_p(\pi_p^M(\xi_{i_1},\ \ldots,\ \xi_{i_p}))\}$. In general, for the pth homogeneous chaos, using M elements from the set $\{\xi_i\}_{i=1}^{\infty}$, there are $\frac{1}{p!}\prod_{k=0}^{p-1}(M+k)$ elements in the set of the basis vector spanning the subspace. The total number of basis vectors, therefore, is

$$L = 1 + \sum_{s=1}^{p} \frac{1}{s!} \prod_{k=0}^{s-1} (M+k). \tag{21}$$

Let the resulting set of L basis vectors be mapped, in a one-to-one mapping, to a set with ordered indices denoted by $\{\gamma_i\}_{i=1}^{L}$. Then, equation (14) may be rewritten as

$$\mu = \sum_{i=0}^{\infty} a_i\, \gamma_i. \tag{22}$$

Repetitive application of the orthogonality condition, given by equation (20) for successive polynomial chaoses, results in the matrix equation

$$\mathbf{K}\,\mathbf{a} = \mathbf{F} \tag{23}$$

where $\mathbf{a}$ is the LN-dimensional vector of coefficients. In equation (23), $\mathbf{K}$ is a $LN \times LN$ deterministic matrix consisting of block submatrices, where the (i, j) block is an $N \times N$ matrix given by the equation

$$\mathbf{K}_{ij} = \sum_{m=0}^{M} \mathbf{R}_m \langle\, \gamma_i\, \gamma_j\, \xi_m \,\rangle. \tag{24}$$

Further, $\mathbf{F}$ is a LN-dimensional deterministic vector given by the equation

$$\mathbf{F}_i = \langle \mathbf{f} \gamma_i \rangle. \tag{25}$$

Clearly, if $\mathbf{f}$ is Gaussian and stastically independent of the random parameters in the operator $Q(\mathbf{x}_2,\theta)$, equation (25) reduces to

$$\mathbf{F}_i = \begin{cases} \langle \mathbf{f}_i \rangle & \text{if } i = 1 \\ 0 & \text{if } i > 1. \end{cases} \tag{26}$$

The right-hand side of equation (24) involves computing the sums of averages of products of independent Gaussian random variables. It is quite straightforward to automate the generation of the $\mathbf{K}_{ij}$ submatrices as well as their assembling into the global matrix $\mathbf{K}$. The order of the resulting system of equations is equal to $L \times N$, where N is the size of the corresponding deterministic system. Note that it has been found in Spanos and Ghanem (1989) that values for M of two or four are enough

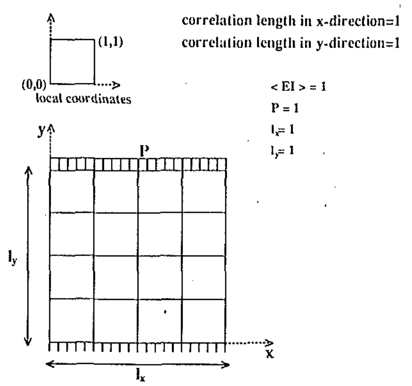

Fig. 1 Plate with random rigidity; exponential covariance model

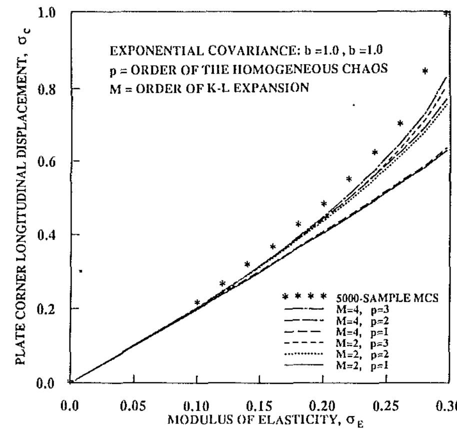

Fig. 2 Standard deviation of longitudinal displacement at the corner of the plate versus standard deviation of the bending rigidity; exponential covariance

for an adequate representation of fairly large levels of random fluctuations in the parameters of the system. Then, the increase in the size of the system for the stochastic problem is not excessive and may be warranted by accuracy and reliability requirements. Further, an approach to solve the extended system of equations is to note that the solution resulting from using any lower-order expansion does, indeed, provide a converging approximation to the true solution. Therefore, the solution from any lower-order expansion can be used as a first approximation in an iterative scheme for finding the coefficients of the higher-order expansion.

Applications

Random Plane Stress. Consider first a problem involving a thin plate, clamped at one side and subjected to a unit uniform in-plane tension applied at the opposite side, as shown in Fig. 1. The modulus of elasticity E of the plate is assumed to be a homogeneous random process with mean $\bar{E}$ and covariance function $C(x_1,y_1;x_2,y_2)$ reflecting the correlation of the process at two positions (x_1,y_1) and (x_2,y_2) on the plate. The covariance function decays exponentially, and is given by the equation

$$C(x_1,\, y_1;\, x_2,\, y_2) \;=\; \sigma_E^2\, e^{-|x_1-x_2|/b_x - |y_1-y_2|/b_y}. \qquad (27)$$

Here, b_x and b_y represent the correlation length of the process in the x-direction and in the y-direction, respectively, and σ_E is the standard deviation of the modulus of elasticity. The plate is assumed to have a rectangular shape with sides of dimensions l_x and l_y, respectively. The projection of the solution process in $\mathbf{H}$ is achieved by choosing a basis set consisting of piecewise bilinear polynomials, yielding a bilinear interpolation of the displacements inside each element in terms of their nodal values. The plate is, thus, subdivided into 16 finite elements.

The next stage in the computations consists of solving the integral eigenvalue problem posed by the equation

$$\lambda_n \psi_n(x_1,y_1) \;=\; \int_{-l_x/2}^{l_x/2} \int_{-l_y/2}^{l_y/2} C(x_1,y_1;x_2,y_2)\psi_n(x_2,y_2)dx_1dy_1. \qquad (28)$$

Substituting equation (27) for the covariance kernel and setting

$$\psi_n(x_1,y_1) \;=\; \psi_i^{(x)}(x_1)\psi_j^{y}\,(y_1) \text{ and } \lambda_n \;=\; \lambda_i^{(x)}\,\lambda_j^{(y)}, \qquad (29)$$

the solution of equation (28) reduces to the product of the solutions of two equations of the form

$$\lambda_i^x\, \psi_i^{(x)}(x_1) \;=\; \int_{-l_x/2}^{l_x/2} e^{-|x_1-x_2|/b_x} \bullet \psi_i^{(x)}\,(x_2)dx_2. \qquad (30)$$

The solution of this equation is well documented in the literature (Van Trees, 1968). In the final expression for the eigenfunctions, it should be noted that two functions of the form given by equation (29) correspond to each eigenvalue. The second function is obtained from the first one by permuting the subscripts. Therefore, the complete normalized eigenfunctions are given by the equation

$$\phi_n(x,y) \;=\; \frac{1}{\sqrt{2}}\left[\psi_i^{(x)}(x)\psi_j^{(y)}\,(y) \;+\; \psi_j^{(x)}(x)\psi_i^{(y)}(y)\right]. \qquad (31)$$

Once the expansion for the system parameters is known, the solution procedure outlined in the previous section is implemented. Specifically, the matrices $\hat{\mathbf{L}}$ and $\mathbf{R}_m$ appearing in equations (10) and (11) are given explicitly by the equations

$$\mathbf{R}_m \;=\; \sum_e \int_{\mathbf{D}} \phi_m(r_1,r_2)B^{e^T}P^eB^e dr_1dr_2 \qquad (32)$$

and

$$\hat{\mathbf{L}} \;=\; \sum_e \int_{\mathbf{D}} B^{e^T}\bar{D}^eB^e dr_1dr_2, \qquad (33)$$

where

$$D^e \;=\; E^eP^e. \qquad (34)$$

Here, D^e is the matrix of constitutive relations relating the stresses to the corresponding strains over a plate element; $\bar{D}^e$ is the mean value of D^e, and B^e is a strain interpolation matrix derived from H^e through the strain-displacement relations. The symbol E^e denotes the modulus of elasticity over element "e", P^e is defined by equation (34), and H^e is the displacement interpolation matrix. In equations (32) and (33), the summations extend over all the finite elements.

Two and four terms, respectively, were used in the Karhunen-Loeve expansion ($M=2$ and $M=4$). Polynomial chaos or order, up to and including three, were implemented in the expansion (14), from which the covariance matrix of the response is obtained. Figure 2 depicts the results for the normalized standard deviation, σ_o, of the longitudinal displacement at the free corner of the plate. The results were obtained from approximations using successive orders of Γ_p. The problem was also solved using the Monte-Carlo simulation method. Records representing realizations of the modulus of elasticity of the plate were obtained by linearly combining the columns of the Cholesky factor of the covariance matrix using Gaussian white noise as weights. The resulting deterministic problem was solved for each realization. The results were then compiled, and the desired statistics of the response were extracted. Note the agreement of the results from the proposed method with those from the Monte Carlo simulation. This agreement is quite encouraging since it involves values of the coefficient of variation of the medium up to 0.3. The range of value encompasses most engineering applications. Figure 3 shows the magnitude of the coefficients a_i of the polynomial chaos in the

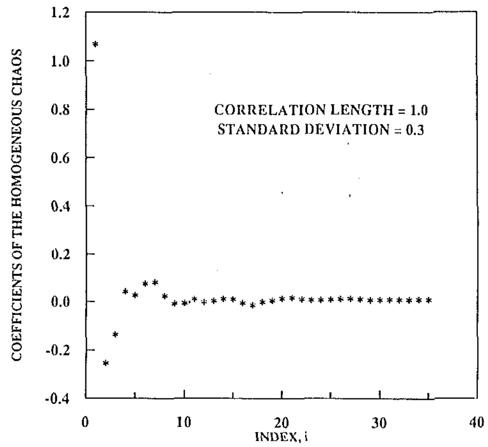

Fig. 3 Coefficients of the homogeneous chaos expansion for the longitudinal displacement at the free end of the plate; equation (12)

expansion given by equation (14) for the response. Note the negligible contribution of the higher-order terms.

Beam on Random Elastic Foundation. The second problem involves an Euler-Bernoulli beam of length L, modulus of elasticity E, mass moment of inertia I, and mass density m. The beam is supported on an elastic foundation having a reaction modulus $k(x)$. It is assumed that $k(x)$ is the realization of a one-dimensional Gaussian random process with mean value $\bar{k}(x)$ and covariance function $C_{kk}(x_1,x_2)$. Further, assume that the beam is subjected to a zero-mean random excitation $f(x,t)$. It is assumed that the cross-spectral density function of $f(x,t)$ is given by the equation

$$S_{ff}(x_1,x_2;\omega) = e^{-|x_1-x_2|/\omega b}, \tag{35}$$

where x_1 and x_2 denote two locations on the beam b is a correlation length of the excitation process, and ω stands for frequency. In the present analysis, the correlation length b is assumed to be a constant.

The differential equation governing the motion of the beam, assuming constant bending rigidity, is

$$\left[m\frac{\partial^2}{\partial t^2} + c\frac{\partial}{\partial t} + EI\frac{\partial^4}{\partial x^4} + k(x)\right] u(x,t) = f(x,t), \tag{36}$$

where c is a coefficient of viscous damping. Following a discretization procedure similar to the one used in the previous example, the beam is divided into $N = 10$ finite elements and a matrix equation is obtained of the form

$$M\ddot{U}(t) + C\dot{U}(t) + KU(t) + K_f U(t) = f(t), \tag{37}$$

where a dot denotes differentiation with respect to time, and all the matrices are $2N \times 2N$. For simplicity, the damping matrix is assumed to be of the form

$$C = c_M M + c_K K, \tag{38}$$

where c_M and c_K are two constants.

Expanding the process $k(x)$ into a Karhunen-Loeve series truncated at the Mth term, and taking the Fourier transform of equation (37), leads to

$$\left[H(\omega) + \sum_{k=1}^{M} \xi_k K_f^{(k)}\right] U(\omega) = F(\omega), \tag{39}$$

where

$$U(\omega) = \int_{-\infty}^{\infty} U(t)e^{-i\omega t}\,dt \quad \text{and}$$

$$F(\omega) = \int_{-\infty}^{\infty} f(t)\, e^{-i\omega t}\,dt, \tag{40}$$

and

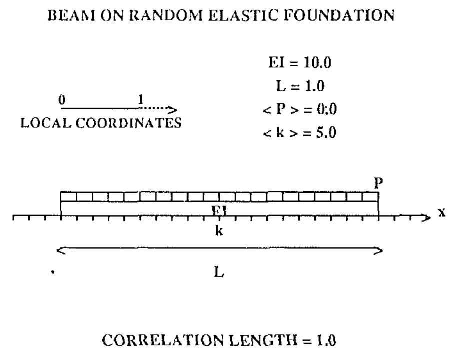

Fig. 4 Beam on random elastic foundation subjected to a random dynamic excitation; exponential covariance model

$$H(\omega) = [-\omega^2 M + i\omega C + K + \bar{K}_f] \tag{41}$$

is a deterministic matrix. Equation (39) can be rewritten as

$$\left[I + \sum_{k=1}^{M} \xi_k Q_f^{(k)}\right] U(\omega) = P(\omega), \tag{42}$$

where

$$Q_f^{(k)} = H(\omega)^{-1} K_f^{(k)} \quad \text{and} \quad P(\omega) = H(\omega)^{-1} F(\omega). \tag{43}$$

The formulation presented in the preceding sections can now be implemented by applying equations (14) and (20) to obtain a set of algebraic equations in the form of equation (23). Alternatively, the inverse of the operator appearing in equation (42) can be expressed via its Neumann expansion (Shinozuka, 1987) in this case the spectral density matrix for the response process becomes

$$S_{UU}(\omega) = \sum_{i=1}^{\infty}\sum_{j=1}^{\infty} (-1)^{i+j}\left[\sum_{k=0}^{M}\xi_k Q_f^{(k)}\right]^i S_{PP}(\omega) \left[\sum_{k=0}^{M}\xi_k Q_f^{(k)}\right]^j. \tag{44}$$

It is numerically more efficient to expand $S_{PP}(\omega)$ in its spectral series and perform the spatial discretization on the eigenfunctions of the expansion. Indeed, this was implemented into the finite element code developed to solve this problem. It was observed that four terms from the spectral expansion of $S_{PP}(\omega)$ were enough to reach convergence in the numerical results. The number of necessary terms depends, of course, on the choice of the parameter b in equation (35), which was taken to be equal to 0.1.

In the numerical implementation of this problem, an exponential covariance kernel was used for the reaction modulus $k(x)$ in the form

$$C_{kk}(x_1,x_2) = \sigma_k^2\, e^{-|x_1-x_2|/b} \tag{45}$$

where b is a correlation length equal to 1 and σ_k is the standard deviation of the process. A unit length for the beam was assumed, and the mean value of the reaction modulus of the foundation was set equal to 1. The mass per unit length was taken to be 0.2, the bending rigidity EI of the beam was set to 2. It was also assumed that the constants c_K and c_M appearing in equation (38) are both equal to 0.1. The correlation coefficient for the supporting foundation was taken equal to 0.06 and two terms were used in the K-L expansion of the corresponding process. The physical set-up is shown in Fig. 4. Figure 5 shows the spectral density $S_{uu}(\omega)$ of the displacement at one end of the beam. The problem was also solved using the Neumann expansion already described (Spanos and Ghanem, 1989). The results are shown in Fig. 7. Note the good agreement for both methods until the damped natural frequency of the beam is approached, causing the norm of the matrix

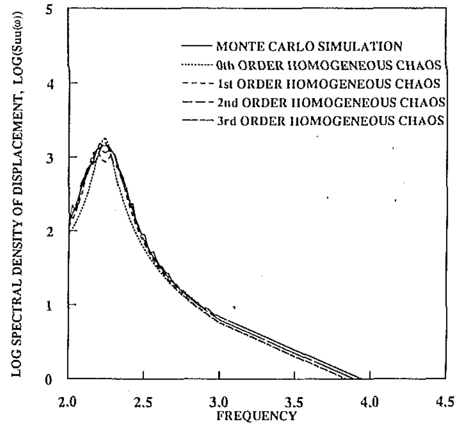

Fig. 5 Spectral density of the displacement at the end of the beam

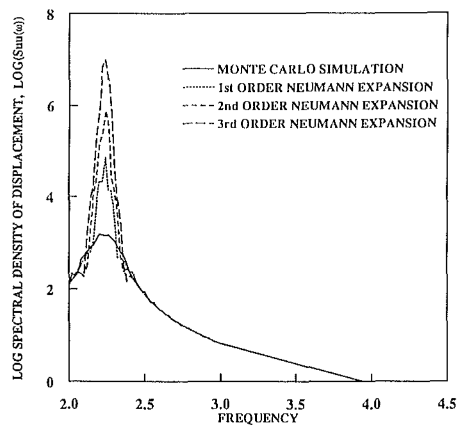

Fig. 6 Spectral density of the displacement at the end of the beam

$$\left[I + \sum_{k=1}^{M} \xi_k \, Q_f^{(k)} \right]$$

to increase beyond the radius of convergence of the Neumann expansion. The Monte Carlo simulation was conducted using the Cholesky decomposition of the covariance matrix as described in the previous example.

Conclusion

A new method has been developed for treating problems involving random media. A complete basis in the Hilbert space Θ of random functions is identified. This basis consists of the polynomial chaoses which are orthogonal polynomials in the white noise. The response is expressed as a convergent series along this basis. The method provides a natural extension for deterministic finite element methods to problems exhibiting random system behavior. The proposed method was applied to a plate problem involving random variability in the material properties and to a problem of a beam on a random elastic foundation subjected to a random dynamic loading. Good agreement between the results of this method and pertinent Monte Carlo simulation results over a wide range of random fluctuation levels was observed.

Acknowledgment

The financial support of this work from a PYI-1984 National Science Foundation award and the NCEER 88-2008 project from the National Research Center for Earthquake Research at the University of New York at Buffalo is gratefully acknowledged.

References

Adomian, G., and Malakian, K., 1980, "Inversion of stochastic partial differential operators—The linear case," *J. Math. Anal. Appl.*, Vol. 77, pp. 309–327.

Akin, J. E., 1982, *Application and Implementation of Finite Element Methods*, Academic Press.

Cameron, R. H., and Martin, W. T., 1947, "The orthogonal development of nonlinear functionals in series of Fourier-Hermite functionals," *Ann. Math.*, Vol. 48, pp. 385–392.

Kallianpur, Gopinath, 1980, *Stochastic Filtering Theory*, Springer-Verlag, New York.

Lawrence, M. A., 1987, "Basis random variables in finite element analysis," *International Journal for Numerical Methods in Engineering*, Vol. 24, pp. 1849–1863.

Liu, W. K., Besterfield, G., and Belytschko, T., 1988, "Transient probabilistic systems," *Computer Methods in Applied Mechanics and Engineering*, Vol. 67, pp. 27–54.

Loeve, M., 1963, *Probability Theory*, 2nd ed., Van Nostrand, Princeton, N.J.

Masri, S., and Miller, R., 1982, "Compact Probabilistic Representation of Random Processes," ASME Journal of Applied Mechanics, Vol. 49, pp. 871–876.

Nakagiri, S., and Hisada, T., 1982, "Stochastic finite element method applied to structural analysis with uncertain parameters," *Proc. Intl. Conference on FEM*, pp. 206–211.

Shinozuka, M., ed., 1987, *Stochastic Mechanics*, Vol. I, Department of Civil Engineering, Columbia University, New York.

Spanos, P. D., and Ghanem, R., 1989, "Stochastic finite element expansion for random media," *Journal of Engineering Mechanics*, Vol. 115, No. EM5, May, ASCE, New York.

Van Trees, H. L., 1968, *Detection, Estimation and Modulation Theory*, Part I, John Wiley and Sons, Inc., New York.

Wiener, N., 1938, "The homogeneous chaos," *Amer. J. Math.*, Vol. 60, pp. 897–936.

J. M. Snyder
Visiting Assistant Professor,
Department of Civil and Environmental Engineering.

J. F. Wilson[1]
Professor,
School of Engineering,
Mem. ASME.

Duke University,
Durham, NC 27706

Dynamics of the Elastica With End Mass and Follower Loading

Orthotropic, polymeric tubes subjected to internal pressure may undergo large deformations while maintaining linear moment-curvature behavior. Such tubes are modeled herein as inertialess, elastic cantilever beams (the elastica) with a payload mass at the tip and with internal pressure as the eccentric tip follower loading that drives the configurations through large deformations. From the nonlinear equations of motion, dynamic beam trajectories are calculated over a range of system parameters for the special case of a point mass at the tip and a terminated ramp pressure loading. The dynamic responses, which are unique because the loading history and the range of motion are fully defined, are presented in nondimensional form and are compared to static responses presented in a companion study. These results are applicable to the dynamic design of high flexure, tube-type, robotic manipulator arms.

Introduction

The statically loaded elastica has been studied for over 200 years, starting with the work by Euler (1744); but studies of the dynamically loaded elastica remain scarce. The literature survey by Schmidt and DaDeppo (1971) lists no solutions of dynamic elastica problems. Keller and Ting (1966) solved the problem of a vibrating beam with finite displacements using perturbation methods, but solutions of this type are not suitable for the larger range of deformations of the present problem. A solution of a physically different, dynamic elastica problem that models the behavior of paper as it exits a copying machine was recently solved by Mansfield and Simmonds (1987). To our knowledge, there are no published studies dealing with our current topic: the dynamic behavior of an inertialess elastica, a cantilever beam with a tip mass and tip follower loadings that drive the system to unique dynamic configurations. We now discuss the physical basis for this elastica.

Our work herein was motivated by the need to understand and then control the motion of high flexure, orthotropic, tube-type manipulator arms driven by internal pressure. An element of such an arm is illustrated in Fig. 1(*a*). Typically , such an element is fabricated from polyurethane, has a thin corrugated bellows section for part of its circumference, and a flat side that contains the neutral axis of bending. The center of pressure on the rigid end caps is offset from the neutral axis by a distance d_d (Fig. 1(*a*)) and the element bends when pressurized (Fig. 1(*b*)), lifting the payload W_d. A laboratory model of a manipulator arm composed of several such elements end-to-end was designed by the second author and is described by Horgan (1987). A general static analysis and adaptive control schemes for such tube-type elements and manipulator arms are presented by Wilson and Mahajan (1989).

To demonstrate that the tube elements of the type described in these last two references and in Fig. 1(*a*) may be modeled as the elastica, we performed a series of static experiments on

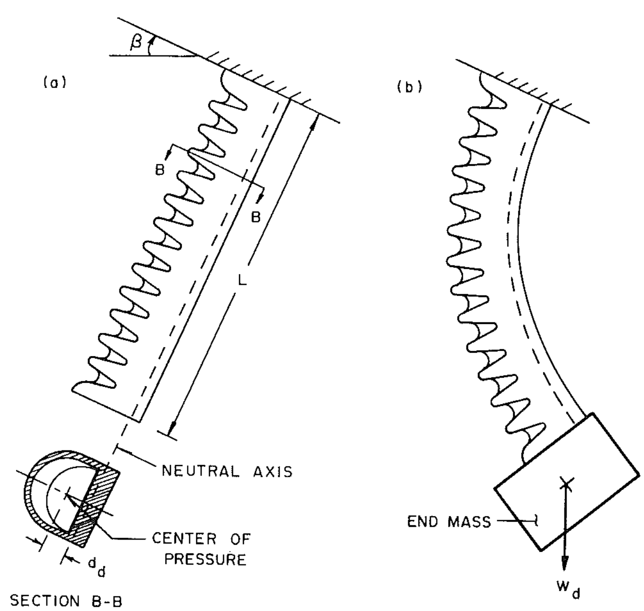

Fig. 1 **(*a*) Unloaded tube element; (*b*) pressurized tube element end mass**

[1]To whom correspondence should be addressed.

Contributed by the Applied Mechanics Division of THE AMERICAN SOCIETY OF MECHANICAL ENGINEERS for publication in the JOURNAL OF APPLIED MECHANICS.

Discussion on this paper should be addressed to the Technical Editor, Leon M. Keer, The Technological Institute, Northwestern University, Evanston, IL 60208, and will be accepted until two months after final publication of the paper itself in the JOURNAL OF APPLIED MECHANICS. Manuscript received by the ASME Applied Mechanics Division, September 9, 1988; final revision, May 19, 1989.

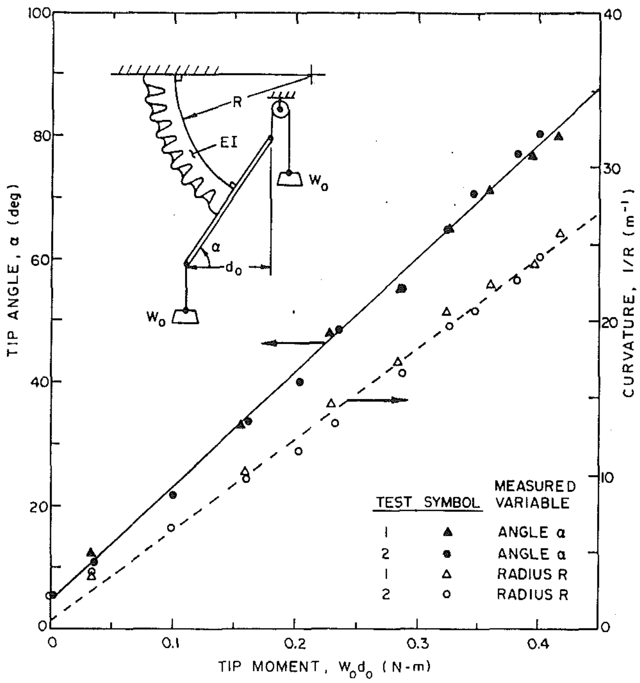

Fig. 2 Elastic behavior of an orthotropic polyurethane tube with a tip moment (pneumatic finger AU-GR1-004, Simrit Corp., Arlington Heights, IL)

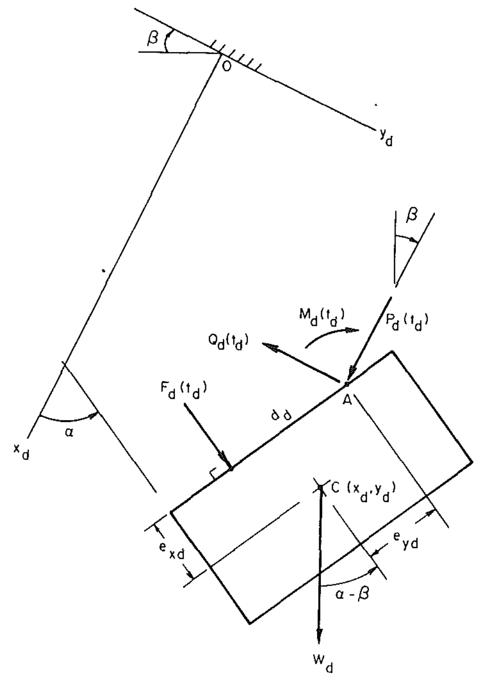

Fig. 4 Free-body sketch of end mass

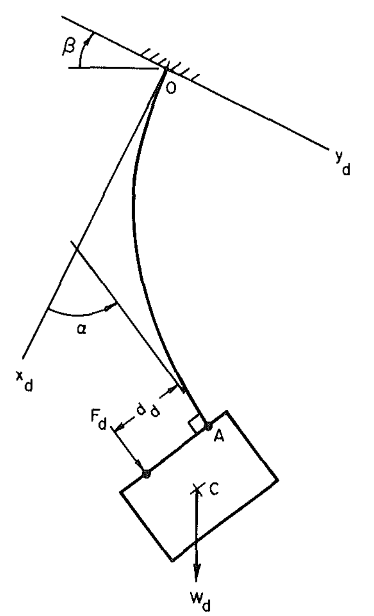

Fig. 3 Beam model with coordinate system and loads

several commercially available tube configurations. A schematic view of our experimental setup is shown in the insert of Fig. 2. In that figure, we present data for one typical tube element for which the model number and manufacturer are given in the figure caption. In the experiment, we used pairs of dead weights, W_1, separated by a distance, d_0, to effect pure moments, $W_0\, d_0$, at the tip of the vertical cantilever tube. For discrete values of tip moment, we traced directly on paper placed behind the tube the orientation of the tip bar and the inner radius of the tube; and from these tracings we measured the tip angle, α, and the radius, R, of the bent tube.

The results of Fig. 2 are for two tests performed 24 hours apart and are typical of the results that we obtained for geometrically similar polyurethane tubes, both larger and smaller in size. Note that our tube had an initial curvature so that neither α nor $1/R$ was zero in the unloaded state. We observed no tube buckling even as α approached 80 deg. The straight lines of Fig. 2 are the least-squares fit to the experimental data: the solid line for moment-tip angle data and the broken line for moment-curvature data, for which the respective correlation coefficients (r-values) were 0.998 and 0.996. From the slope of the moment-curvature line, the tube's bending stiffness, EI, was calculated as 0.0176 N-m^2. These experimental data justify modeling such tubes as the elastica.

In other experiments in which we pressurized the same configuration tested above, we found that the tube could lift a dead-weight tip load that was up to 30 times the tube's self weight. This result serves to justify a further assumption of our analysis: that if the tip mass or payload is very large compared to the tube mass, the inertia effects of the tube may be neglected. In the analysis that follows, this end mass or payload is constant. Deformations of the elastica are achieved by applying a prescribed internal pressure to the tube, which is equivalent to prescribing a time-varying eccentric follower load at the tip. The static behavior of this model of the elastica was presented in a companion study (Wilson and Snyder, 1988).

Mathematical Model

The idealized beam model, the coordinate system, and the tip loads are shown in Fig. 3. The beam is rigidly attached at point A to the end mass, a block with its center of gravity at C. The forces acting on the block are: its self-weight W_d; the prescribed driving pressure force, $F_d(t_d)$, a follower load; and the elastic reaction forces of the beam at point A. A free-body sketch of this block is shown in Fig. 4. Here, $P_d(t_d)$, $Q_d(t_d)$, and $M_d(t_d)$ are the beam's reaction forces on the block where P_d and Q_d are parallel to the fixed coordinate axes, x_d, and y_d, respectively. All damping forces are neglected.

In Figs. 1, 3, and 4 the subscript d on a quantity indicates that the quantity has a physical dimension such as distance or time. The following nondimensional system parameters are defined in terms of these physical quantities.

$$F=\frac{F_dL^2}{EI} \quad P=\frac{P_dL^2}{EI} \quad Q=\frac{Q_dL^2}{EI} \quad W=\frac{W_dL^2}{EI} \tag{1a}$$

$$x=\frac{x_d}{L} \quad y=\frac{y_d}{L} \quad e_x=\frac{e_{xd}}{L} \quad e_y=\frac{e_{yd}}{L} \tag{1b}$$

$$d=\frac{d_d}{L} \quad M=\frac{M_dL}{EI} \quad t=\sqrt{\frac{g}{L}}t_d \quad J=\frac{J_dg}{EI} \tag{1c}$$

Here, J_d is the mass moment of inertia of the block about an axis perpendicular to the plane of motion and passing through point C. L is the length of the beam, EI is the beam's bending stiffness, and g is the acceleration due to gravity.

When Newton's laws are applied to the block in Fig. 4, and equations (1) are used, the equations of motion are expressed as

$$\frac{d^2x}{dt^2} = W\cos\beta + P + F\cos\alpha \tag{2}$$

$$\frac{d^2y}{dt^2} = W\sin\beta - Q + F\sin\alpha \tag{3}$$

$$J\frac{d^2\alpha}{dt^2} = F(d-e_y)-M+ P(e_x\sin\alpha - e_y\cos\alpha)+Q(e_x\cos\alpha+e_y\sin\alpha). \tag{4}$$

For the special case in which the block is a point mass, $J = e_x = e_y = 0$ and equation (4) becomes

$$M = F\,d. \tag{5}$$

In equations (1) and (2), W and d are known constants and $F = F(t)$ is a specified function of time. For the case of a point mass, equation (5) establishes $M = M(t)$ when $F(t)$ is specified.

We now establish the relationships among the reaction loads P, Q, and M and the tip coordinates x, y, and α. To do this, we assume that the beam behaves as follows: It is linear elastic; its transverse shear deformations are negligible; it has a uniform flexural stiffness EI; its neutral axis in bending is inextensible; and it is straight when not loaded. With these assumptions, Wilson and Snyder (1988) showed that the tip coordinates in integral form are

$$x=\int_{\theta+\theta_0}^{\alpha+\theta_0}\frac{\cos(\phi-\theta_0)d\phi}{\sqrt{a+b\cos\phi}} \quad y=\int_{\theta+\theta_0}^{\alpha+\theta_0}\frac{\sin(\phi-\theta_n)d\phi}{\sqrt{a+b\cos\phi}} \tag{6a}$$

and the condition of inextensibility (or constant L) is

$$1 = \int_{\theta_0}^{\alpha+\theta_0}\frac{d\phi}{\sqrt{a+b\cos\phi}} \tag{6b}$$

where

$$a=M^2-b\cos(\alpha+\theta_0) \tag{6c}$$

$$b=2\sqrt{P^2+Q^2} \tag{6d}$$

$$\theta_0 = \arctan\left(\frac{Q}{P}\right), \text{ with } -\pi<\theta_0\leq\pi. \tag{6e}$$

In general, the magnitudes alone of the forces P, Q, and M do not uniquely determine the tip coordinates. For our model, however, the sequence of loading and range of motion are specified so that the elastica has single curvature as shown in Figs. 1 and 3. Thus, the three equations (6a) and (6b) provide the unique relation among the three loads P, Q, and M and the three tip coordinates x, y, and α. Equations (2), (3), (4), and (6), together with the loading and the initial conditions, define our elastica.

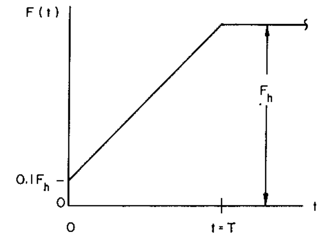

Fig. 5 Terminated ramp loading function

Consider the special case of a point mass at the tip. Equation (4) then reduces to (5), and in integral form equations (2) and (3) may be written as:

$$\int_0^t\int_0^\eta (F(\xi)\cos\alpha(\xi)+P(\xi))\,d\xi\,d\eta+ W\left(\frac{1}{2}t^2\cos\beta+t\frac{dx}{dt}(0) + x(0)-x(t)\right)=0 \tag{7}$$

$$\int_0^t\int_0^\eta (F(\xi)\sin\alpha(\xi)-Q(\xi))\,d\xi\,d\eta+ W\left(\frac{1}{2}t^2\sin\beta+t\frac{dy}{dt}(0) + y(0)-y(t)\right)=0. \tag{8}$$

With the trapezoidal rule, equations (7) and (8) become:

$$\sum_{i=0}^{n} D_i^n\left(\sum_{j=0}^{i} D_j^i\,(F_j\cos\alpha_j + P_j)\right) + W\left(\frac{1}{2}n^2h^2\cos\beta + nh\dot{x}_0+x_0-x_n\right)=0 \tag{9}$$

$$\sum_{i=0}^{n} D_i^n\left(\sum_{j=0}^{i} D_j^i\,(F_j\sin\alpha_j - Q_j)\right) + W\left(\frac{1}{2}n^2h^2\sin\beta + nh\dot{y}_0+y_0-y_n\right)=0. \tag{10}$$

With h as the step size and k and n as integers, the time, tip angle, initial conditions, and loads are, respectively:

$$t=nh \quad \alpha_k=\alpha(kh) \quad D_k^n=\begin{cases}\frac{1}{2}h, & \text{if } k=0 \text{ or } k=n\\ h, & \text{if } 0<k<n\end{cases} \tag{11a}$$

$$x_k=x(kh) \quad \dot{x}_0=\frac{dx}{dt}(0) \quad y_k=y(kh) \quad \dot{y}_0=\frac{dy}{dt}(0) \tag{11b}$$

$$F_k=F(kh) \quad P_k=P(kh) \quad Q_k=Q(kh). \tag{11c}$$

Numerical Results and Discussion

An IBM 3081 computer and IMSL (1987) software were used to obtain numerical results. Program listings are given by Snyder (1988). Here, equations (9) and (10) and subroutine DNEQNF were used to march out discretized solutions to equations (2) and (3). Subroutine DQDAGS and golden section bracketing were used to evaluate the integrals of equations (6).

Numerical results were based on a range of system parameters representative of practical, polyurethane tubes (beams) subjected to air pressure levels available in most laboratories. The terminated ramp function of Fig. 5, with a rise time, t,

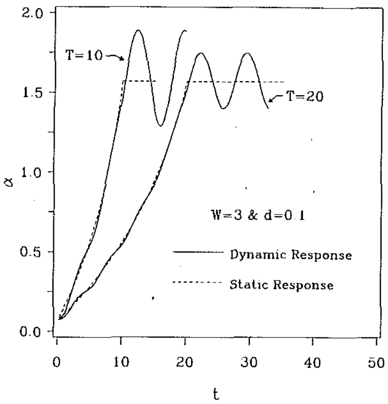

Fig. 6 Variation of end rotation with time when $W = 3$ and $d = 0.1$

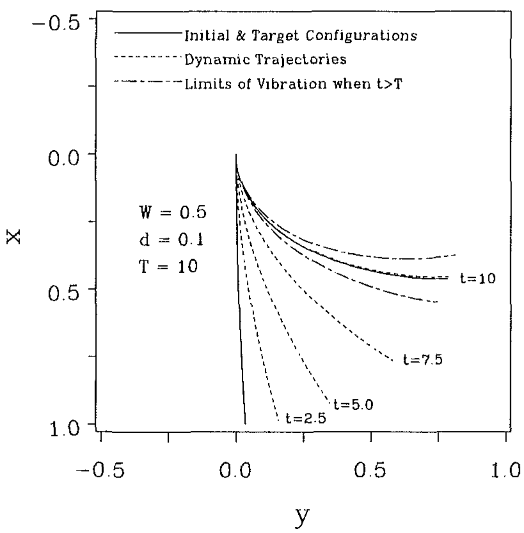

Fig. 7 Trajectories of the elastica with $W = 0.5$, $d = 0.1$, and $T = 10$

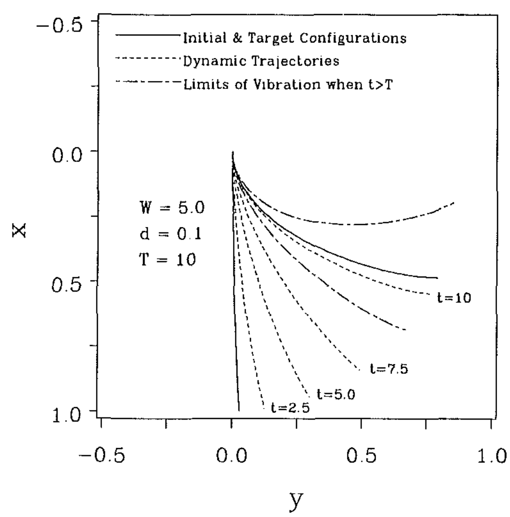

Fig. 8 Trajectories of the elastica with $W = 5$, $d = 0.1$, and $T = 10$

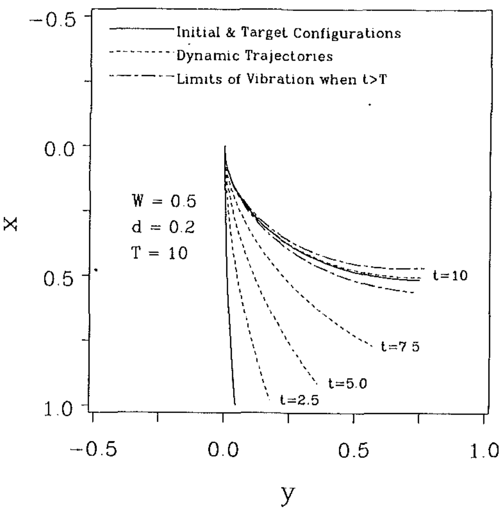

Fig. 9 Trajectories of the elastica with $W = 0.5$, $d = 0.2$, and $T = 10$

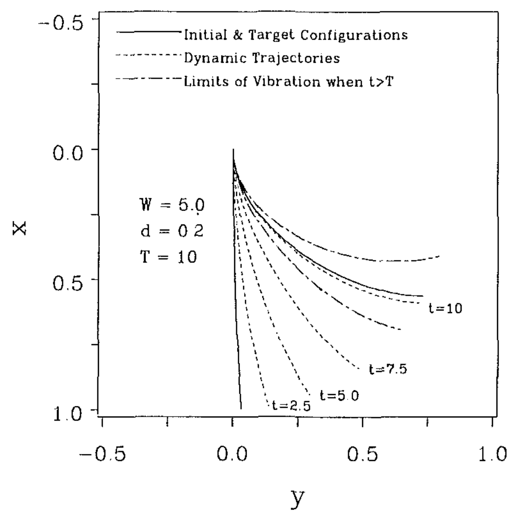

Fig. 10 Trajectories of the elastica with $W = 5$, $d = 0.2$, and $T = 10$

and a terminal force, F_h, was chosen as the driving force, $F(t)$. To avoid beam flipover (Wilson and Snyder, 1988), values of F_h were selected for each combination of W and d such that the target static equilibrium value of α would be $\pi/2$. The beam was initially at rest with a static pressure force, $F = 0.1\, F_h$, and β was chosen as zero. For $W = 0.5$ and 5.0, for $d = 0.1$ and 0.2, and for $T = 10$ and 20, trajectories of the dynamic elastica were calculated using time steps, h, of $T/50$, $T/100$, $T/200$, and $T/400$ ($T/300$ was used for $T = 10$, $d = 0.2$, $W = 5$). In each case, $h = T/200$ gave results that agreed to at least three significant figures with the results for the smaller step size. Thus, $h = T/200$ was used to obtain the results shown in Figs. 6–12.

Figure 6 shows the tip rotation, α, as a function of time for $W=3$, $d=0.1$, and $T=10$ and 20. This behavior, which is analogous to the dynamic response of an undamped linear oscillator, typifies the dynamics of the elastica for the range of parameters studied herein. On the IBM 3081 computer, about 18 minutes of CPU time was required to generate the curve for $T = 10$ and about 13 minutes was required for $T = 20$.

Each of Figs. 7–10 show: solid lines for the statically-loaded elastica at the initial and target positions; uniform dashed lines for the trajectories of the dynamically-driven elastica as time increases; and nonuniform broken lines for the envelopes of oscillation when $t > T$. With a fixed T and d, when the amplitude of the tip oscillations about $\alpha = \pi/2$ are compared for the two extremes of tip mass, the higher W effects the higher amplitude of tip oscillation. These figures also show that the target positions of the tip of the elastica vary with

Table 1 Initial and target tip coordinates based on static computations (Wilson and Snyder, 1988)

		Initial Position, $F_o = 0.1\ F_h$			Target Position : $\alpha_h = \pi/2$		
	W	x_o	y_o	α_o	F_h	x_h	y_h
d = 0.1	0.5	.99914	.036230	.071198	7.44763	.46317	.78598
	1.0	.99920	.034711	.070278	8.32510	.46509	.78734
	2.0	.99928	.032601	.069681	10.0311	.46925	.78941
	3.0	.99933	.031157	.069878	11.6747	.47373	.79077
	4.0	.99937	.030070	.070420	13.2599	.47839	.79158
	5.0	.99940	.029199	.071114	14.7913	.48315	.79194
d = 0.2	0.5	.99866	.044936	.090016	4.87759	.51554	.74912
	1.0	.99879	.042686	.088346	5.41951	.52176	.74713
	2.0	.99893	.039481	.086747	6.46429	.53355	.74307
	3.0	.99903	.037235	.086314	7.46249	.54457	.73894
	4.0	.99909	.035524	.086434	8.41960	.55490	.73478
	5.0	.99915	.034147	.086836	9.34016	.56461	.73061

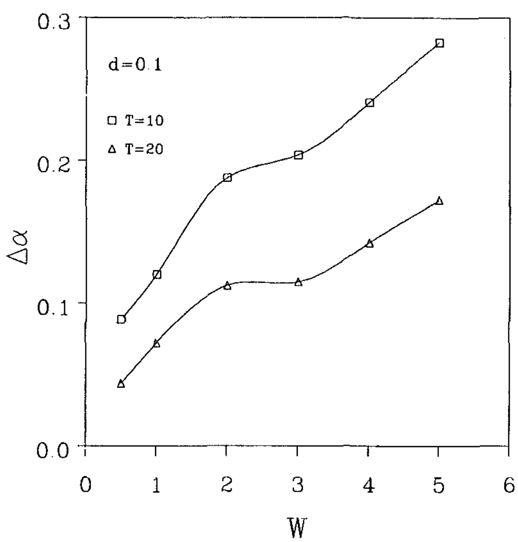

Fig. 11 Variation of overshoot with end mass when d = 0.1

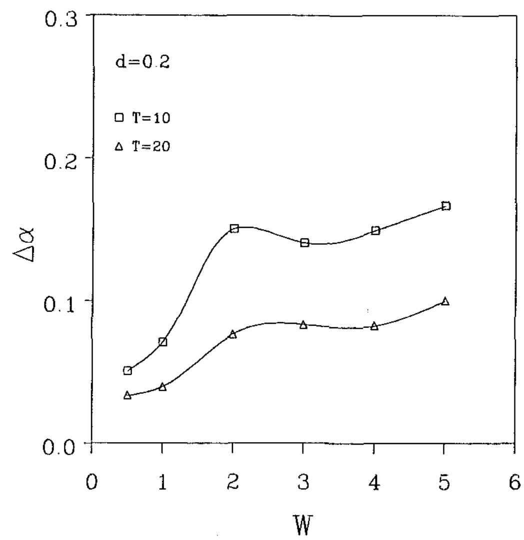

Fig. 12 Variation of overshoot with end mass when d = 0.2

both tip mass and eccentricity; it is not possible to drive the tip of the elastica to identical target positions with two different tip masses. Table 1 lists the static initial and target tip coordinates and the terminal pressure loads for each case evaluated in these studies.

In applications such as the positioning of the payload, it is important to know the amount that the tip overshoots its target position. Define angular overshoot as

$$\Delta\alpha = \frac{\alpha_{\max}}{\pi/2} \tag{14}$$

where $\alpha_{\max}$ is the maximum dynamic tip rotation and $\pi/2$ is the target tip rotation. Figures 11 and 12 summarize the numerical results, and show that for a fixed T and W, the overshoot decreases dramatically when d is increased from 0.1 to 0.2. In these two figures, the symbols denote the points in parameter space chosen for the numerical calculations. The connecting lines are cubic spline fits.

In summary, we have represented a load-carrying, cantilevered, orthotropic tube with high bending deformations as an elastica with a point mass at its tip. The driving force is an eccentric follower load. We calculated the pre-flipover dynamic trajectories and end-point overshoot of this ideal elastica. The results, calculated in terms of nondimensional system parameters, are useful in the design of novel, highly-flexible robotic arm manipulators and may serve as the basis for algorithms employed for active motion control of such arms. Beyond the scope of the present studies, and perhaps of less practical interest, are the topological folds close to and beyond the points in parameter space that lead to static flipover as predicted by Wilson and Snyder (1988).

Acknowledgment

This study was sponsored in part by the U.S. Defense Advanced Research Projects Agency under contract No. MDA903-84-C-0243.

References

Euler, L., 1744, *Methodus Inveniendi Lineas Curvas Maximi Minimive Proprietate Gaudentes* (*Additamentum I, De Curvis Elasticis*), Lausanne and Geneva.

Horgan, John, 1987, "A Polyurethane Proboscus," *Scientific American*, Vol. 256, No. 4, p. 73.

IMSL, 1987, *Math/Library User's Manual*, IMSL, Inc., Houston, Texas.

Keller, J. B., and Ting, L., 1966, "Periodic Vibrations of Systems Covered by Nonlinear Differential Equations," *Comm. Pure Appl. Math.*, Vol. 19, No. 4, pp. 371-420.

Mansfield, L., and Simmonds, J. G., 1987, "The Reverse Spaghetti Problem: Drooping Motion of an Elastica Issuing from a Horizontal Guide," ASME JOURNAL OF APPLIED MECHANICS, Vol. 54, No. 1, pp. 147-150.

Schmidt, R., and DaDeppo, D. A., 1971, "A Survey of Literature on Large Deflections of Nonshallow Arches. Bibliography of Finite Deflections of Straight and Curved Beams, Rings, and Shallow Arches," *The Journal of the Industrial Mathematics Society*, Vol. 21, Part 2, pp. 91-114.

Snyder, J. M., 1988, "Dynamics of Curved, Elastic Structures," Ph.D. dissertation, School of Engineering, Duke University, Durham, N.C.

Wilson, J. F., Snyder, J. M., 1988, "The Elastica with End Load Flipover," ASME JOURNAL OF APPLIED MECHANICS, Vol. 55, No. 4, pp. 845-848.

Wilson, J. F., and Mahajan, U., 1989, "The Mechanics and Positioning of Highly Flexible Manipulator Limbs," ASME *Journal of Mechanisms, Transmissions, and Automation in Design*, Vol. 111, No. 3, pp. 232-237.

Kazuyuki Yagasaki
Assistant Professor,
Department of Mechanical Engineering,
Tamagawa University,
Machida, Tokyo 194, Japan

Masaru Sakata
Professor.

Koji Kimura
Associate Professor.

Department of Mechanical Engineering Science,
Tokyo Institute of Technology,
Meguro-ku, Tokyo 152, Japan

Dynamics of a Weakly Nonlinear System Subjected to Combined Parametric and External Excitation

In this paper we study the dynamics of a weakly nonlinear single-degree-of-freedom system subjected to combined parametric and external excitation. The averaging method is used to establish the existence of invariant tori and analyze their stability. Furthermore, by applying the Melnikov technique to the average system it is shown that there exist transverse homoclinic orbits resulting in chaotic dynamics. Numerical simulation results are also given to demonstrate the theoretical results.

1 Introduction

Recently, there has been increasing interest in the problem of nonlinear dynamics such as chaos and bifurcation behavior. In particular, the existence of chaos in strongly nonlinear systems has been established through experiments and numerical simulation (see, e.g., Moon, 1987). It was also shown, by a perturbation technique originally proposed by Melnikov (1963), that for periodically forced, strongly nonlinear oscillators there exist transverse homoclinic orbits which are responsible for the chaotic dynamics (cf., Holmes, 1979; Salam and Sastry, 1985; see also Guckenheimer and Holmes, 1983). However, strong nonlinearity is not always necessary for chaotic dynamics to exit. In fact, HaQuang et al. (1987) found chaotic motions in numerical simulation of a weakly nonlinear single-degree-of-freedom system, although theoretical evidence is not given.

In this paper we study the dynamics of a weakly nonlinear single-degree-of-freedom system subjected to combined parametric and external excitation:

$$\ddot{x}+\bar{\delta}\dot{x}+(1+\bar{\beta}\cos\bar{\nu}t)x+\bar{\alpha}x^3=\bar{\gamma}\cos\omega t, \tag{1}$$

where damping $\bar{\delta}$, nonlinearity $\bar{\alpha}$, parametric force amplitude $\bar{\beta}$, frequency $\bar{\nu}$, and external force amplitude $\bar{\gamma}$ are small and frequency ω is near unity, so that the primary resonance to the external excitation is assumed. Also, an overdot denotes differentiation with respect to time t.

Equations of type (1) were considered in Ness (1971), and Troger and Hsu (1977), who used the averaging method to obtain the steady-state (periodic) solutions. Also, Plaut and Hsieh (1987), and HaQuang et al. (1987) observed chaotic motions in numerical integrations of the systems similar to (1).

The outline of this paper is as follows: In Section 2 we state the averaging theory in a suitable form and apply it to obtain a nearly integrable system. We describe the integrable structure of the unperturbed system when there exist separatrix loops.

Equation (1) has two frequencies, ω and $\bar{\nu}$ which are generally incommensurate. Hence we have to treat (1) as a nonlinear oscillator with quasi-periodic forcing, so that the most simple steady-state solutions are quasi-periodic and construct invariant tori in the extended phase space. In Section 3, analyzing periodic solutions of the averaged system, we establish the existence of invariant tori and determine their stability.

In Section 4 we first review the Melnikov technique. Then, applying it to the averaged system, we show that there exist homoclinic orbits resulting in chaotic dynamics of (1). The use of the Melnikov method to analyze averaged systems was first proposed by Holmes (1980), but in many applications, the perturbations of the averaged systems have relatively rapid oscillation, so that Melnikov functions become exponentially small and serious technical problems arise (see Sanders, 1982; Guckenheimer and Holmes, 1983, Section 4.7). Holmes (1986), however, could neglect higher-order time-dependent terms and avoid these difficulties in the analysis of a two-degree-of-freedom system. In equation (1) the existence of slowly-varying parametric excitation prevents our analysis from these problems.[1]

In Section 5 we demonstrate the theoretical predictions by numberical simulation using the Runge-Kutta-Gill method. In Section 6 conclusions are given.

2 Equation of Motion and Averaging

2.1 Van der Pol Transformation. We introduce two small

Contributed by the Applied Mechanics Division of THE AMERICAN SOCIETY OF MECHANICAL ENGINEERS for publication in the JOURNAL OF APPLIED MECHANICS.

Discussion on this paper should be addressed to the Technical Editor, Leon M. Keer, The Technological Institute, Northwestern University, Evanston, IL 60201, and will be accepted until two months after final publication of the paper itself in the JOURNAL OF APPLIED MECHANICS. Manuscript received by the Applied Mechanics Division, August 23, 1988; final revision, March 27, 1989.

[1] After our work was finished, we learned of work by Holmes et al. (1987) who overcame many of these difficulties resulting from exponential smallness of the Melnikov function.

parameters ϵ and μ, such that $0<\epsilon<<\mu<<1$. Let $\bar{\alpha}=\epsilon\alpha$, $\bar{\gamma}=\epsilon\gamma$, $\bar{\nu}=\epsilon\gamma$, $\bar{\delta}=\epsilon\mu\delta$, and $\bar{\beta}=\epsilon\mu\beta$. Then equation (1) becomes

$$\ddot{x}+\epsilon\mu\delta\dot{x}+(1+\epsilon\mu\beta\cos\epsilon\nu t)x+\epsilon\alpha x^3=\epsilon\gamma\cos\omega t,$$

or, as a first-order equation,

$$\dot{x}=y$$
$$\dot{y}=-x+\epsilon\{[-\alpha x^3+\gamma\cos\omega t]+\mu[-\delta y-(\beta\cos\epsilon\nu t)x]\}. \tag{2}$$

The system (2) contains a "fast" time t and a "slow" time ϵt. We consider the primary resonance to the external excitation $\omega\approx 1$ and set $\omega^2-1=\epsilon\Omega$.

Using the invertible Van dèr Pol transformation

$$\begin{pmatrix} u \\ v \end{pmatrix} = A \begin{pmatrix} x \\ y \end{pmatrix},$$

$$A=\begin{pmatrix} \cos\omega t & -\omega^{-1}\sin\omega t \\ -\sin\omega t & -\omega^{-1}\cos\omega t \end{pmatrix},$$

$$A^{-1}=\begin{pmatrix} \cos\omega t & \sin\omega t \\ -\omega\sin\omega t & -\omega\cos\omega t \end{pmatrix}, \tag{3}$$

we have

$$\dot{u}=-\epsilon\Big\{\frac{1}{\omega}[\Omega(u\cos\omega t-v\sin\omega t)-\alpha(u\cos\omega t-v\sin\omega t)^3+\gamma\cos\omega t]+\mu\frac{1}{\omega}[\delta\omega(u\sin\omega t+v\cos\omega t)-\beta(u\cos\omega t-v\sin\omega t)\cos\epsilon\nu t]\Big\}\sin\omega t,$$

$$\dot{v}=-\epsilon\Big\{\frac{1}{\omega}[\Omega(u\cos\omega t-v\sin\omega t)-\alpha(u\cos\omega t-v\sin\omega t)^3+\gamma\cos\omega t]+\mu\frac{1}{\omega}[\delta\omega(u\sin\omega t+v\cos\omega t)-\beta(u\cos\omega t-v\sin\omega t)\cos\epsilon\nu t]\Big\}\cos\omega t. \tag{4}$$

The system (4) contains slowly varying terms and is of the form

$$\dot{\mathbf{x}}=\epsilon\{\mathbf{f}(\mathbf{x},\omega t)+\mu\mathbf{g}(\mathbf{x},\epsilon\nu t,\omega t)\}, \tag{5}$$

where

$$\mathbf{x}=\begin{pmatrix} u \\ v \end{pmatrix},\ \mathbf{f}=\begin{pmatrix} f_1 \\ f_2 \end{pmatrix},\ \mathbf{g}=\begin{pmatrix} g_1 \\ g_2 \end{pmatrix}\in\mathbf{R}^2, \tag{6}$$

and $\mathbf{f}(\mathbf{x},\theta)$ is 2π-periodic in θ and $\mathbf{g}(\mathbf{x},\tau,\theta)$ is 2π-periodic in both τ and θ.

2.2 Averaging Theory and Poincaré Map. We now outline the averaging results for the system (5). Consider $\tau=\epsilon\nu t$ as a new state variable. Then, the system (5) can be written in the standard form

$$\dot{x}=\epsilon\{\mathbf{f}(\mathbf{x},\omega t)+\mu\mathbf{g}(\mathbf{x},\tau,\omega t)\},\quad \dot{\tau}=\epsilon\nu. \tag{7}$$

The right-hand sides of (7) are of period $T=2\pi/\omega$ in t. Since $\mathbf{g}$ is 2π-periodic in τ, the $(\mathbf{x},\tau)$ phase space of (7) is the product $\mathbf{R}^2\times S^1$, where $S^1=\mathbf{R}/2\pi$ is the circle of length 2π.

Applying the averaging theorem (see Hale, 1969; Guckenheimer and Holmes, 1983; Sanders and Verhulst, 1985) to (7), we can show that there exists a change of coordinates $\mathbf{x}=\mathbf{y}+\epsilon\mathbf{w}_\mu(\mathbf{y},\epsilon\nu t,\omega t)$ under which (5) becomes

$$\dot{\mathbf{y}}=\epsilon\{\bar{\mathbf{f}}(\mathbf{y})+\mu\bar{\mathbf{g}}(\mathbf{y},\epsilon\nu t)\}+\epsilon^2\mathbf{h}_{\epsilon,\mu}(\mathbf{y},\epsilon\nu t,\omega t), \tag{8}$$

where the subscripts ϵ and μ indicate functions of ϵ and μ, and

$$\bar{\mathbf{f}}(\mathbf{y})=\frac{1}{T}\int_0^T\mathbf{f}(\mathbf{y},\omega t)dt,\ \bar{\mathbf{g}}(\mathbf{y},\tau)=\frac{1}{T}\int_0^T\mathbf{g}(\mathbf{y},\tau,\omega t)dt. \tag{9}$$

It is shown by a straightforward calculation that $\mathbf{w}_\mu(\mathbf{y},\tau,\theta)$ and $\mathbf{h}_{\epsilon,\mu}(\mathbf{y},\tau,\theta)$ are 2π-periodic in τ and θ. Moreover, if $\mathbf{x}(t)$ and $\mathbf{y}(t)$ are, respectively, solutions of the system (5) and the truncated averaged system

$$\dot{\mathbf{y}}=\epsilon\{\bar{\mathbf{f}}(\mathbf{y})+\mu\bar{\mathbf{g}}(\mathbf{y},\epsilon\nu t)\}, \tag{10}$$

with $\mathbf{x}(0)=\mathbf{x}_0$ and $\mathbf{y}(0)=\mathbf{y}_0$, and also $\mathbf{x}_0=\mathbf{y}_0+0(\epsilon)$, then $\mathbf{x}(t)=\mathbf{y}(t)+0(\epsilon)$ on a time scale $t\sim 1/\epsilon$.

We consider Poincaré maps $P_{\epsilon,\mu}$, $\bar{P}_{\epsilon,\mu}$ associated with (5) and (10). The systems (5) and (10) can be rewritten as

$$\dot{\mathbf{x}}=\epsilon\{\mathbf{f}(\mathbf{x},\theta)+\mu\mathbf{g}(\mathbf{x},\tau,\theta)\},\ \dot{\tau}=\epsilon\nu,\ \dot{\theta}=\omega, \tag{11}$$

$$\dot{\mathbf{y}}=\epsilon\{\bar{\mathbf{f}}(\mathbf{y})+\mu\bar{\mathbf{g}}(\mathbf{y},\tau)\},\ \dot{\tau}=\epsilon\nu,\ \dot{\theta}=\omega, \tag{12}$$

where $(\mathbf{x},\tau,\theta)$, $(\mathbf{y},\tau,\theta)\in\mathbf{R}^2\times S^1\times S^1$. We define a global cross-section $\Sigma=\{(\mathbf{x},\tau,\theta)\in\mathbf{R}^2\times S^1\times S^1\ |\theta=0\}$, and obtain the Poincaré maps $P_{\epsilon,\mu}$, $\bar{P}_{\epsilon,\mu}:\Sigma\to\Sigma$, such that

$$P_{\epsilon,\mu}:(\mathbf{x}(0),\tau)\to(\mathbf{x}(T),\tau+\epsilon\nu T), \tag{13}$$

$$\bar{P}_{\epsilon,\tau}:(\mathbf{y}(0),\tau)\to(\mathbf{x}(T),\tau+\epsilon\nu T), \tag{14}$$

where $\mathbf{x}(t)$ and $\mathbf{y}(t)$ are solutions of (5) and (10). By the averaging theorem we find that $P_{\epsilon,\mu}$ is well approximated by $\bar{P}_{\epsilon,\mu}$ as

$$P_{\epsilon,\mu}=\bar{P}_{\epsilon,\mu}+0(\epsilon). \tag{15}$$

Assume that the averaged system (10) has a hyperbolic periodic orbit $\bar{\gamma}_\mu$ (note that the trajectory of $\bar{\gamma}_\mu$ is independent of ϵ). Then the closed curve, $\bar{\gamma}_\mu$, is a normally hyperbolic invariant 1-torus of the averaged Poincaré map, $\bar{P}_{\epsilon,\mu}$. By the invariant manifold theorem (Hirsch et al., 1977) this implies that for sufficiently small ϵ, the Poincaré map $P_{\epsilon,\mu}=\bar{P}_{\epsilon,\mu}+0(\epsilon)$ has a normally hyperbolic invariant 1-torus $\gamma_{\epsilon,\mu}$ near $\bar{\gamma}_\mu$. (See Fig. 1(*a*).) The flow of the suspended system (11) also has a normally-hyperbolic invariant 2-torus near $\bar{\gamma}_\mu\times S^1$. Since the action of $P_{\epsilon,\mu}$ gives rise to the rotation by $\epsilon\nu T$ in the τ-direction, the invariant torus $\gamma_{\epsilon,\mu}$ isn't subjected to phase locking. Thus, if $\bar{\gamma}_\mu$ has period $2\pi/\epsilon\nu$, then quasi-periodic motions occur in (5), as shown in Fig. 1(*b*).

2.3 Nearly Integrable Averaged System. Applying the averaging method to (4), we obtain a nonautonomous equation

$$\dot{u}=\frac{\epsilon}{2\omega}\Big\{\Big[\Omega v-\frac{3}{4}\alpha(u^2+v^2)v\Big]+\mu[-\delta\omega u-\beta v\cos\epsilon\nu t]\Big\},$$

$$\dot{v}=\frac{\epsilon}{2\omega}\Big\{\Big[-\Omega u+\frac{3}{4}\alpha(u^2+v^2)u-\gamma\Big]+\mu[-\delta\omega v+\beta u\cos\epsilon\nu t]\Big\}. \tag{16}$$

Changing time variable $t\to\epsilon t/2\omega$, (16) becomes

$$\dot{u}=\Big[\Omega v-\frac{3}{4}\alpha(u^2+v^2)v\Big]+\mu\Big[-\delta\omega u-\beta v\cos\nu_0 t\Big],$$

$$\dot{v}=\Big[-\Omega u+\frac{3}{4}\alpha(u^2+v^2)u-\gamma\Big]+\mu[-\delta\omega v+\beta u\cos\nu_0 t], \tag{17}$$

where $\nu_0=2\omega\nu$. By the transformation

$$J=\frac{u^2+v^2}{2},\quad \phi=\tan^{-1}(v/u), \tag{18}$$

(17) can be written as

$$\dot{J}=-\gamma\sqrt{2J}\sin\phi-\mu(2\delta\omega J),$$

$$\dot{\phi}=-\Omega+\frac{3}{2}\alpha J-\frac{\gamma\cos\phi}{\sqrt{2J}}+\mu\beta\cos\nu_0 t. \tag{19}$$

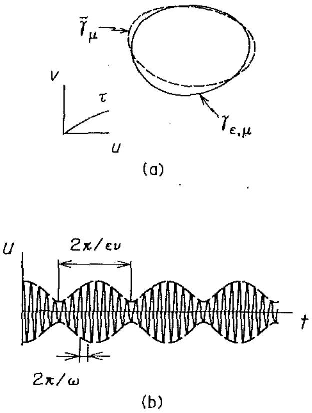

Fig. 1 Relationship between the averaged and the full system; (*a*) invariant tori $\bar{\gamma}_\mu$, $\gamma_{\epsilon,\mu}$, (*b*) quasi-periodic motion

When $\mu=0$, (19) becomes a completely integrable Hamiltonian system

$$\dot{J}=-\gamma\sqrt{2J}\sin\phi,$$
$$\dot{\phi}=-\Omega+\frac{3}{2}\alpha J-\frac{\gamma\cos\phi}{\sqrt{2J}} \tag{20}$$

where the Hamiltonian energy is

$$H(J,\phi)=-\Omega J+\frac{3}{4}\alpha J^2-\gamma\sqrt{2J}\cos\phi. \tag{21}$$

We now describe this integrable structure, which will be used in the following sections. Here we assume that $\alpha>0$, $\Omega>0$, and $0<\gamma<4/9(\Omega^3/\alpha)^{1/2}$. Then there exist centers $(J,\phi)=(j_1,\pi)$, $(j_3,0)$, and a hyperbolic saddle (j_2,π), where $0<j_1<j_2<j_3$ are roots of the cubic equation

$$x^3-2\left(\frac{2\Omega}{3\alpha}\right)x^2+\left(\frac{2\Omega}{3\alpha}\right)^2x-2\left(\frac{\gamma}{3\alpha}\right)^2=0. \tag{22}$$

We denote these fixed points (j_1,π), (j_2,π), $(j_3,0)$ by $\mathbf{p}_i$, $i=1,2,3$. The level set

$$H(J,\phi)=H(J_2,\pi)\equiv H_0 \tag{23}$$

is composed of two homoclinic orbits, Γ_+, Γ_-, and the point $\mathbf{p}_2$. The homoclinic orbits, $(J_\pm(t),\phi_\pm(t))$, are given by

$$J_\pm(t)=\pm\frac{2r_+r_-}{(r_+-r_-)\cosh at\pm(r_++r_-)}+j_2,$$
$$\phi_\pm(t)=\arccos\left[\frac{1}{\gamma\sqrt{2J_\pm(t)}}\left(-\Omega J_\pm(t)+\frac{3}{4}\alpha J_\pm^2(t)-H_0\right)\right], \tag{24}$$

where $a=3\alpha\sqrt{-r_+r_-}/4$, $r_\pm=2(\kappa\pm\sqrt{2\kappa j_2})$, and $\kappa=2\Omega/3\alpha-j_2$. The phase portraits are shown in Fig. 2. Note that we consider the phase space (J,ϕ) as $\mathbf{R}\times S^1$. Also, the level set $H=0$ contains the line $J=0$ on which the vector field is singular, and thus the orbits with $H=0$ have discontinuities at $J=0$, $\phi=\pi/2$, and $J=0$, $\phi=3\pi/2$.

3 Invariant Tori

For small $\mu>0$, the averaged system (19) has hyperbolic periodic orbits $(J_i(t),\phi_i(t))$ near fixed points $\mathbf{p}_i$, $i=1,2,3$, of (20). Similarly to (13) we define a Poincaré map $F_{\epsilon,\mu}:\Sigma\to\Sigma$ for the suspended flow of (2) (see also (11)). By the transformations (3) and (18), and the averaging theorem (cf., section 2), these hyperbolic periodic orbits of (19) correspond to normally hyperbolic invariant tori T_i, $i=1,2,3$, of the Poincaré map $F_{\epsilon,\mu}$, and equivalently to normally hyperbolic invariant 2-tori for the suspended flow of (2). The orbits on the invariant tori indicate quasi-periodic motions. In this section we obtain approximate expressions for T_i, $i=1,2,3$, and determine their stability using perturbation techniques.

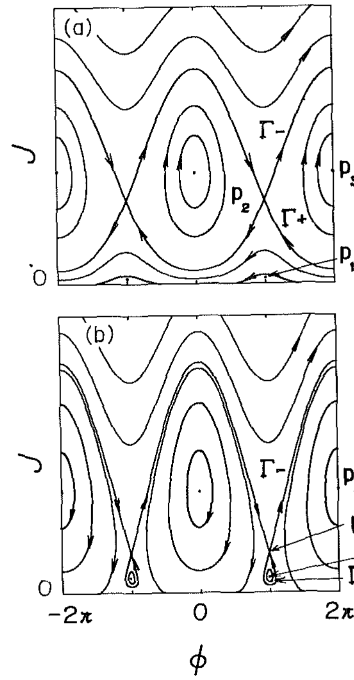

Fig. 2 Phase portraits of (20); (*a*) $0<\gamma<\frac{2}{9}\sqrt{\frac{2\Omega^3}{\alpha}}$, (*b*) $\frac{2}{9}\sqrt{\frac{2\Omega^3}{\alpha}}<\gamma<\frac{4}{9}\sqrt{\frac{\Omega^3}{\alpha}}$

3.1 Periodic Orbits of the Averaged System. We assume the periodic solutions $(J_i(t),\phi_i(t))$, $i=1,2,3$, of (19) to be of the form

$$J_i(t)=j_i+\mu\xi_i(t),\ i=1,2,3,$$
$$\phi_i(t)=\pi+\mu\eta_i(t),\ i=1,2,\ \phi_3(t)=\mu\eta_3(t). \tag{25}$$

Substitution of (25) into (19) yields, to 0(1),

$$\dot{\xi}_i=\pm\gamma\sqrt{2j_i}\eta_i-2\delta\omega j_i,$$
$$\dot{\eta}_i=\left[\frac{3}{2}\alpha\mp\gamma(2j_i)^{-3/2}\right]\xi_i+\beta\cos\nu_0t,\ i=1,2,3, \tag{26}$$

where the upper choice of sign refers to the cases $i=1,2$ and the lower choice to the case $i=3$. Since the systems (26) are linear, we can solve them directly to obtain periodic solutions

$$\xi_i=A_i\cos\nu_0t,$$
$$\eta_i=\mp\frac{\nu_0A_i}{\gamma\sqrt{2j_i}}\sin\nu_0t\pm\frac{\delta\omega}{\gamma}\sqrt{2j_i},\ i=1,2,3, \tag{27}$$

where

$$A_i=\pm\frac{\beta\gamma\sqrt{2j}}{\lambda_i^2-\nu_0^2},\ i=1,2,3, \tag{28}$$

$$\lambda_i^2=\frac{\gamma^2}{2j_i}\mp\frac{3}{2}\alpha\gamma\sqrt{2j_i},\ i=1,2,3. \tag{29}$$

Here we assumed

$$\nu_0\neq\lambda_i,\quad i=1,2,3. \tag{30}$$

Obviously, for small $\mu>0$, the periodic orbit $(J_2(t),\phi_2(t))$ is unstable. We now calculate the stability of the orbit $(J_1(t),\phi_1(t))$. Consider small perturbations of $(J_1(t),\phi_1(t))$ and let

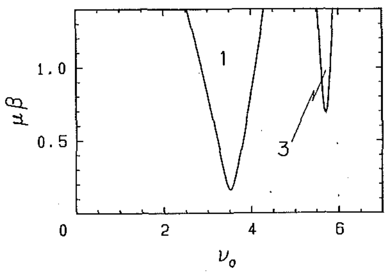

Fig. 3 Instability regions in the $\nu_0-\mu\beta$ plane; $\alpha=2$, $\gamma=1.5$, $\Omega=3$, $\mu\delta\omega=0.05$. Numbers 1 and 3 represent the periodic orbits $(J_i(t),\ \phi_i(t))$, $i=1,\ 3$.

$$J=J_1(t)+\Delta J, \quad \phi=\phi_1(t)+\Delta\phi, \tag{31}$$

where ΔJ and $\Delta\phi$ are small. Substituting (31) into (19) and using (25) and (27), we obtain, to $0(\mu,\Delta J,\Delta\phi)$,

$$\Delta\dot{J}=-\mu\left(\frac{\nu_0 A_1}{2j_1}\sin\nu_0 t+\delta\omega\right)\Delta J + \left(\gamma\sqrt{2j_1}+\mu\frac{\gamma A_1}{\sqrt{2j_1}}\cos\nu_0 t\right)\Delta\phi,$$

$$\Delta\dot{\phi}=\left[\left(\frac{3}{2}\alpha-\frac{\gamma}{(2j_1)^{3/2}}\right)+\mu\frac{3\gamma A_1}{(2j_1)^{5/2}}\cos\nu_0 t\right]\Delta J + \mu\left(\frac{\nu_0 A_1}{2j_1}\sin\nu_0 t-\delta\omega\right)\Delta\phi. \tag{32}$$

When $\mu=0$, (32) becomes

$$\Delta\dot{J}=\gamma\sqrt{2j_1}\Delta\phi,$$
$$\Delta\dot{\phi}=\left(\frac{3}{2}\alpha-\frac{\gamma}{(2j_1)^{3/2}}\right)\Delta J, \tag{33}$$

and solutions are given by

$$\Delta J=K\cos\lambda_1 t+L\sin\lambda_1 t,$$
$$\Delta\phi=\frac{\lambda_1}{\gamma\sqrt{2j_1}}(-K\sin\lambda_1 t+L\cos\lambda_1 t), \tag{34}$$

where K and L are constants. For small $\mu>0$ the trivial solution $(\Delta J,\ \Delta\phi)=(0,\ 0)$ of (32) is unstable only if $\nu_0\approx 2\lambda_1$, as in the Mathieu equation with small damping. We assume $\nu_0^2=(2\lambda_1)^2+0(\mu)$ and set

$$\mu\sigma_1=(\nu_0/2)^2-\lambda_1^2. \tag{35}$$

Using the transformation

$$\Delta J=z_1\cos\frac{1}{2}\nu_0 t-z_2\sin\frac{1}{2}\nu_0 t,$$

$$\Delta\phi=\frac{1}{\gamma\sqrt{2j_1}}\frac{1}{2}\nu_0\left(-z_1\sin\frac{1}{2}\nu_0 t-z_2\cos\frac{1}{2}\nu_0 t\right), \tag{36}$$

in (32), and applying the averaging method, we have

$$\dot{z}_1=\mu\left\{-\delta\omega z_1+\left(\frac{3\nu_0 A_1}{16j_1}-\frac{3\gamma^2 A_1}{8\nu_0 j_1{}^2}+\frac{\sigma_1}{\nu_0}\right)z_2\right\},$$

$$\dot{z}_2=\mu\left\{\left(\frac{3\nu_0 A_1}{16j_1}-\frac{3\gamma^2 A_1}{8\nu_0 j_1{}^2}-\frac{\sigma_1}{\nu_0}\right)z_1-\delta\omega z_2\right\}. \tag{37}$$

The trivial solution of (37) is unstable if

$$(\delta\omega)^2-\left(\frac{3\nu_0 A_1}{16j_1}-\frac{3\gamma^2 A_1}{8\nu_0 j_1{}^2}+\frac{\sigma_1}{\nu_0}\right)\left(\frac{3\nu_0 A_1}{16j_1}-\frac{3\gamma^2 A_1}{8\nu_0 j_1{}^2}-\frac{\sigma_1}{\nu_0}\right)<0, \tag{38}$$

or, to $0(\mu)$,

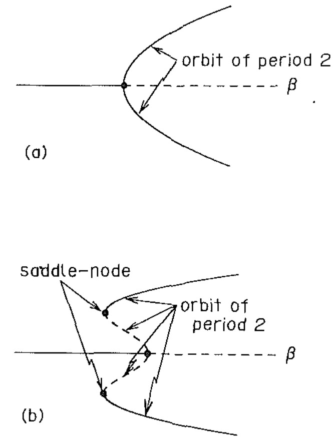

Fig. 4 Period doubling bifurcations, ——— stable orbits; ····· unstable orbits: (*a*) supercritical and (*b*) subcritical, following saddle bifurcation of orbits of period 2

$$(\mu\beta)^2>\left\{\frac{4\lambda_1^3(2j_1)^{3/2}}{\gamma[\lambda_1^2(2j_1)-\gamma^2]}\right\}^2\left\{\frac{1}{4\lambda_1^2}\left[\left(\frac{\nu_0}{2}\right)^2-\lambda_1^2\right]^2+(\mu\delta\omega)^2\right\}, \tag{39}$$

where we used (28) and (35). The condition (39) represents the instability region for the orbit $(J_1(t),\ \phi_1(t))$ of (19). Analogously, we obtain the instability region for $(J_3(t),\ \phi_3(t))$, to $0(\mu)$, as follows:

$$(\mu\beta)^2>\left\{\frac{4\lambda_3^3(2j_3)^{3/2}}{\gamma[\lambda_3^2(2j_3)-\gamma^2]}\right\}^2\left\{\frac{1}{4\lambda_3^2}\left[\left(\frac{\nu_0}{2}\right)^2-\lambda_3^2\right]^2+(\mu\delta\omega)^2\right\}. \tag{40}$$

Figure 3 shows these unstable regions of $(J_i(t),\ \phi_i(t))$, $i=1,\ 3$, with $\alpha=2$, $\gamma=1.5$, $\Omega=3$ and $\mu\delta\omega=0.05$. In the figure both regions are labeled by $i=1,\ 3$.

It also follows from this analysis that in the unstable regions (39) and (40), the harmonic components of frequency $\nu_0/2$ grow and, consequently, 1/2 subharmonic orbits of (19) exist. This suggests that a period doubling bifurcation occurs when β is increased while ν_0 is fixed near $2\lambda_i$, $i=1$ or 3. The period doubling bifurcation, however, is not necessarily supercritical as in Fig. 4(*a*); it may be subcritical, following saddle-node bifurcations at which stable and unstable orbits of period-2 are created, as in Fig. 4(*b*).

3.2 Invariant Tori. We now turn to the Poincaré map $F_{\epsilon,\mu}$ associated with (2). Using the transformations (3) and (18), invariant tori of $F_{\epsilon,\mu}$ are obtained as follows:

$$T_i=\{(x_i(\tau),\ y_i(\tau),\ \tau)\,|\,\tau\in S^1)\}+0(\epsilon),\ i=1,\ 2,\ 3, \tag{41}$$

where

$$x_i(\tau)=\sqrt{2J_i(\tau/\nu_0)}\cos\phi_i(\tau/\nu_0),$$
$$y_i(\tau)=-\omega\sqrt{2J_i(\tau/\nu_0)}\sin\phi_i(\tau/\nu_0),\ i=1,\ 2,\ 3. \tag{42}$$

Stability types of invariant tori T_i are the same as $(J_i(t),\ \phi_i(t))$, $i=1,\ 2,\ 3$. We also note that, corresponding to a period doubling bifurcation in the averaged system (19), a doubling of torus (cf., Kaneko, 1986) occurs when T_1 or T_3 becomes unstable.

4 Chaotic Motions

4.1 Melnikov's Method. For two-dimensional periodic systems, Melnikov (1963) has developed a global perturbation technique which provides a criterion for the existence of chaotic orbits in specific systems. We first review the

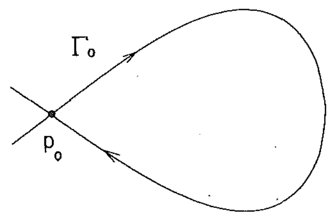

Fig. 5 Unperturbed structure

Melnikov technique. For details see Greenspan and Holmes (1983), and Guckenheimer and Holmes (1983).

Consider the systems of the form

$$\dot{\mathbf{x}} = \mathbf{f}(\mathbf{x}) + \epsilon \mathbf{g}(\mathbf{x}, t), \ \mathbf{x} = \begin{pmatrix} u \\ v \end{pmatrix} \in \mathbf{R}^2, \ 0 < \epsilon \ll 1, \tag{43}$$

where $\mathbf{f}: \mathbf{R}^2 \rightarrow \mathbf{R}^2$, $\mathbf{g}: \mathbf{R}^3 \rightarrow \mathbf{R}^2$ are sufficiently smooth and $\mathbf{g}(\mathbf{x}, t)$ is $\tilde{T}$-periodic in t. We make the following assumptions:

(A1) For $\epsilon = 0$, (43) reduces to a planar Hamiltonian system with Hamiltonian $H(u, v)$:

$$\dot{u} = f_1(u, v) = \frac{\partial H}{\partial v}, \ \dot{v} = f_2(u, v) = -\frac{\partial H}{\partial u}. \tag{44}$$

(A2) The Hamiltonian system (44) possesses a homoclinic orbit $\mathbf{q}_0(t)$ to a hyperbolic saddle point $\mathbf{p}_0$. We set $\Gamma_0 = \{\mathbf{q}_0(t) \mid t \in \mathbf{R}\} \cup \{\mathbf{p}_0\}$. (See Fig. 5).

Since $\mathbf{g}$ is 2π-periodic, we suspend the system (43) over the space $\mathbf{R}^2 \times \tilde{S}^1$:

$$\dot{x} = \mathbf{f}(\mathbf{x}) + \epsilon \mathbf{g}(\mathbf{x}, \theta), \ \dot{\theta} = 1, \ (\mathbf{x}, \theta) \in \mathbf{R}^2 \times \tilde{S}^1, \tag{45}$$

where $\tilde{S}^1 = \mathbf{R}/\tilde{T}$ is the circle of length $\tilde{T}$. Then we have a Poincaré map $\tilde{P}_\epsilon^{t_0}$ defined on a global cross-section $\tilde{\Sigma}^{t_0} = \{(\mathbf{x}, \theta) \mid \theta = t_0\} \subset \mathbf{R}^2 \times \tilde{S}^1$. Specifically, $\tilde{P}_\epsilon^{t_0}$ is obtained by

$$\tilde{P}_\epsilon^{t_0}: \mathbf{x}(t_0) \rightarrow \mathbf{x}(t_0 + \tilde{T}). \tag{46}$$

It follows from assumption (A2) that the unperturbed Poincaré map $\tilde{P}_0^{t_0}$ has a hyperbolic fixed point $\mathbf{p}_0$ and that there exist stable and unstable manifolds $W^s(\mathbf{p}_0)$ and $W^u(\mathbf{p}_0)$ of $\mathbf{p}_0$, respectively, defined as

$$W^s(\mathbf{p}_0) = \{\mathbf{x} \in \tilde{\Sigma}^{t_0} \mid (P_0^{t_0})^n \mathbf{x} \rightarrow \mathbf{p}_0 \ \text{as} \ n \rightarrow +\infty\},$$
$$W^u(\mathbf{p}_0) = \{\mathbf{x} \in \tilde{\Sigma}^{t_0} \mid (P_0^{t_0})^n \mathbf{x} \rightarrow \mathbf{p}_0 \ \text{as} \ n \rightarrow -\infty\}, \tag{47}$$

such that $W^s(\mathbf{p}_0) \cap W^u(\mathbf{p}_0) = \Gamma_0$.

For $\epsilon > 0$ sufficiently small, $\tilde{P}_\epsilon^{t_0}$ still has a hyperbolic fixed point $\mathbf{p}_\epsilon^{t_0} = \mathbf{p}_0 + 0(\epsilon)$ with stable and unstable manifolds $W^s(\mathbf{p}_\epsilon^{t_0})$, $W^u(\mathbf{p}_\epsilon^{t_0})$ which are close to the stable and unstable manifolds $W^s(\mathbf{p}_0)$, $W^u(\mathbf{p}_0)$ of $\mathbf{p}_0$. As described in Greenspan and Holmes (1983) and Guckenheimer and Holmes (1983), the distance $d(t_0)$ between the manifold $W^s(\mathbf{p}_\epsilon^{t_0})$ and $W^u(\mathbf{p}_\epsilon^{t_0})$ (cf., Fig. 6) is measured by

$$d(t_0) = \frac{\epsilon M(t_0)}{|\mathbf{f}(\mathbf{q}_0(0))|} + 0(\epsilon^2). \tag{48}$$

Here $M(t_0)$ is called the Melnikov function and given by the simple formula

$$M(t_0) = \int_{-\infty}^{\infty} \mathbf{f}(\mathbf{q}_0(t)) \wedge \mathbf{g}(\mathbf{q}_0(t), t + t_0) dt, \tag{49}$$

where the wedge product is defined by $\mathbf{a} \wedge \mathbf{b} = a_1 b_2 - a_2 b_1$.

From (48) we see that if $M(t_0)$ has a simple zero at s, i.e.,

$$M(s) = 0, \ \frac{\partial M}{\partial t_0}(s) \neq 0, \tag{50}$$

then by the implicit function theorem, $d(t_0)$ also has a simple zero near s and hence there exist transverse intersections of $W^s(\mathbf{p}_\epsilon^{t_0})$ and $W^u(\mathbf{p}_\epsilon^{t_0})$ which yield transverse homoclinic orbits. The existence of such orbits implies that $\tilde{P}_\epsilon^{t_0}$ has an invariant Cantor set Λ; the dynamics of $\tilde{P}_\epsilon^{t_0}$ restricted to Λ is conjugate to that of Smale's horseshoe, so that Λ contains a countable set of periodic orbits of arbitrarily long periods, an uncountable set of bounded nonperiodic ("chaotic") orbits and a dense orbit (cf., Guckenheimer and Holmes, 1983).

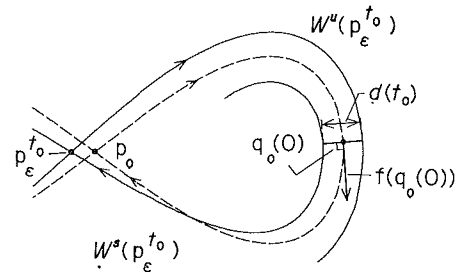

Fig. 6 Perturbed manifolds and the distance function

4.2 Chaos in the Averaged System. We apply the Melnikov method to the averaged equation (19) in which μ plays a role of ϵ. The Melnikov functions for $\Gamma_\pm$ become

$$M_\pm(t_0) = \int_{-\infty}^{\infty} \Big\{ [-\gamma\sqrt{2J_\pm(t)} \sin\phi_\pm(t)] \cdot \beta \cos\nu_0(t + t_0)$$
$$- \Big[-\Omega + \frac{3}{2}\alpha J_\pm^2(t) - \frac{\gamma\cos\phi_\pm(t)}{\sqrt{2J_\pm(t)}} \Big] [-2\delta\omega J_\pm(t)] \Big\} dt. \tag{51}$$

Substituting (24) into (51) and evaluating the integral by the method of residues, we have

$$M_+(t_0) = -\frac{8\pi\beta\nu_0 \sinh(4\nu_0\theta_0/3\rho\alpha)}{3\alpha\sinh(4\nu_0/3\rho\alpha)} \sin\nu_0 t_0$$
$$- \frac{16\delta\omega}{3\alpha}\Big(\Omega\theta_0 - \frac{9}{8}\rho\alpha\Big), \tag{52a}$$

$$M_-(t_0) = -\frac{8\pi\beta\nu_0 \sinh(4\nu_0\theta_0/3\rho\alpha)}{3\alpha\sinh(4\nu_0/3\rho\alpha)} \sin\nu_0 t_0$$
$$+ \frac{16\delta\omega}{3\alpha}\Big(\Omega[\pi - \theta_0] + \frac{9}{8}\rho\alpha\Big), \tag{52b}$$

where $\theta_0 = \arccos\ [(r_+ + r_-)/(r_+ - r_-)]$ and $\rho = \sqrt{-r_+ r_-}$. Note that θ_0 and ρ depend only on α, γ, and Ω.

We define

$$R_+(\alpha, \gamma, \Omega, \nu_0) = \frac{|8\Omega\theta_0 - 9\rho\alpha|}{4\pi\nu_0} \frac{\sinh(4\pi\nu_0/3\rho\alpha)}{\sinh(4\theta_0\nu_0/3\rho\alpha)}, \tag{53a}$$

$$R_-(\alpha, \gamma, \Omega, \nu_0) = \frac{|8\Omega(\pi - \theta_0) + 9\rho\alpha|}{4\pi\nu_0}$$
$$\times \frac{\sinh(4\pi\nu_0/3\rho\alpha)}{\sinh(4(\pi - \theta_0)\nu_0/3\rho\alpha)}, \tag{53b}$$

It follows from the Melnikov theory that if

$$\frac{\beta}{\delta\omega} > R_+(\alpha, \gamma, \Omega, \nu_0), \tag{54a}$$

or

$$\frac{\beta}{\delta\omega} > R_-(\alpha, \gamma, \Omega, \nu_0), \tag{54b}$$

then the averaged system (19) has transverse homoclinic orbits resulting in chaotic dynamics.

In Fig. 7 we show the homoclinic bifurcation curves $\beta/\delta\omega = R_\pm(\alpha, \gamma, \Omega, \nu_0)$ with $\alpha = 2$, $\gamma = 1.5$, and $\Omega = 3$. In this case three types of chaotic motions are expected. In the region $\beta/\delta\omega > R_+$, there exist motions which swing back and forth through $\phi = \pi$ toward $\phi > \pi$ and $\phi < \pi$ in an irregular manner. In the region $\beta/\delta\omega > R_-$, there exist motions which erratically rotate in the ϕ-direction, roughly along Γ_-. In the region

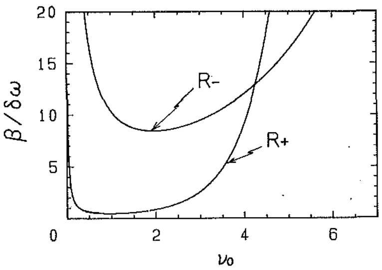

Fig. 7 Homoclinic bifurcation curves, $\alpha=2$, $\gamma=1.5$, $\Omega=3$

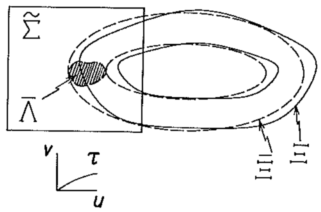

Fig. 8 Normally hyperbolic invariant sets

where $\beta/\delta\omega > R_+$ and $\beta/\delta\omega > R_-$, besides these two types of chaotic motions, there exist motions which swing through $\phi=\pi$ and rotate approximately by 2π in the ϕ-direction in arbitrary orders.

4.3 Chaos in the Weakly Nonlinear Oscillator. We next describe the behavior of the original system (2) by using arguments given in Section 5 of Holmes (1986).

Changing time variable $t \to \epsilon\nu t$, the averaged system (10) is written as

$$\dot{\mathbf{x}} = \bar{\mathbf{f}}(\mathbf{x}) + \mu\bar{\mathbf{g}}(\mathbf{x}, \tau), \quad \dot{\tau} = 1. \tag{55}$$

We define a Poincaré map $\tilde{P}_\mu : \tilde{\Sigma} \to \tilde{\Sigma}$, where $\tilde{\Sigma} = \{(\mathbf{x}, \tau) \mid \tau = 0\} \in \mathbf{R}^2 \times S^1$, such as (46). Suppose that $\tilde{P}_\mu$ has transverse homoclinic orbits. Then there exists an invariant Cantor set $\bar{\Lambda}$ on which $\tilde{P}_\mu$ is topologically equivalent to a Smale horseshoe map. This implies that the flow of (55) contains a bundle of solutions $\bar{\Xi}$ whose cross-section is the Cantor set $\bar{\Lambda}$.

As in Section 2.2, we consider the Poincaré maps $P_{\epsilon,\mu}$, $\bar{P}_{\epsilon,\mu}$ associated with (5) and (10). Recall $P_{\epsilon,\mu} = \bar{P}_{\epsilon,\mu} + 0(\epsilon)$ (see (15)). Since the Cantor set $\bar{\Xi}$ is also a normally hyperbolic invariant set of $\bar{P}_{\epsilon,\mu}$, it follows from the invariant manifold theorem (Hirsch et al., 1977) that $P_{\mu,\epsilon}$ has a normally hyperbolic invariant set Ξ near $\bar{\Xi}$ (see Fig. 8). Hence, for $0 < \epsilon \ll \mu \ll 1$, if either (54*a*) or (54*b*) is satisfied, then the Poincaré map $F_{\epsilon,\mu}$ of (2) has an invariant set with Cantor-type structure. Using a technique similar to Wiggins (1988b), we can show that the dynamics of $F_{\epsilon,\mu}$ normal to the τ-direction in such an invariant set is "Smale-horseshoe-like" and chaotic.[2]

In closing this section we remark that the chaotic orbits of Smale horseshoe type are essentially unstable. Therefore, only transient chaotic motions are expected and almost all orbits may converge to stable periodic or quasi-periodic orbits. Thus Melnikov analysis doesn't necessarily provide a criterion for "observable" chaos. However, as shown by numerical simulation in the next section, we can observe chaotic motions of Smale horseshoe type if there exists no other attractor (see also Greenspan and Holmes, 1983, Section 10.6).

5 Numerical Simulation

Numerical integrations of the averaged system (19) and the

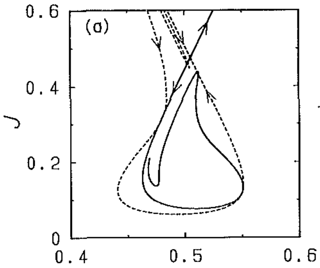

Fig. 9(*a*)

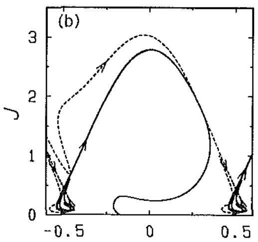

Fig. 9(*b*)

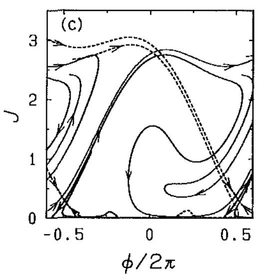

Fig. 9(*c*)

Fig. 9 Numerically computed Poincaré map $\tilde{P}_\mu$ of (19), $\alpha=2$, $\gamma=1.5$, $\Omega=3$, $\mu\delta\omega=0.05$, $\nu_0=3.5$: (*a*) $\mu\beta=0.25$, (*b*) $\mu\beta=0.53$, (*c*) $\mu\beta=2.7$. Stable manifolds are shown by solid lines, unstable manifolds by broken lines.

original system (1) have been performed using the Runge-Kutta-Gill method.

5.1 Averaged System. We first show the numerical simulation results for the averaged system (19) for fixed $\alpha=2$, $\gamma=1.5$, $\Omega=3$, $\mu\delta\omega=0.05$, $\nu_0=3.5$ ($\lambda_1 \approx 1.75$, $\lambda_3 \approx 2.85$) and $\mu\beta$ varying.[3] These cases correspond to the primary resonance $\nu_0 \approx 2\lambda_1$ in equation (32).

In Fig. 9, we show plots of the stable and unstable manifolds $W^s(\mathbf{p}_{2,\mu})$, $W^u(\mathbf{p}_{2,\mu})$ obtained from computations of Poincaré map $\tilde{P}_\mu$ of (19).[4] The lower stable and unstable manifolds first intersect at $\mu\beta \approx 0.25$ and the upper manifolds about $\mu\beta \approx 0.53$. These value are compared with the theoretical values of 0.242 and 0.530 from (53), respectively.

As $\mu\beta$ increases, transverse intersection between $W^s(\mathbf{p}_{2,\mu})$ and $W^u(\mathbf{p}_{2,\mu})$ occurs and, consequently, a horseshoe map is constructed. However, there exist stable periodic points to which almost all orbits converge and chaotic motions aren't observed until $\mu\beta$ takes a much higher value.

Figure 10 shows a bifurcation diagram for the Poincaré map $\tilde{P}_\mu$. For small $\mu\beta$, there exist two stable fixed points $\mathbf{p}_{i,\mu}$, $i=1, 3$. As $\mu\beta$ increases, a pair of period-two points are created near $\mathbf{p}_{1,\mu}$ at $\mu\beta \approx 0.160$, and then $\mathbf{p}_{1,\mu}$ becomes unstable at $\mu\beta \approx 0.167$, while the theoretical value from (39) is about

[2]Recently Wiggins (1988a, 1988b) generalized the Melnikov method to quasi-periodically forced systems. This technique has been applied to quasi-periodically forced single-degree-of-freedom systems by Wiggins (1987, 1988a, 1988b) and Ide and Wiggins (1989). We could have utilized this version of Melnikov's method to obtain our results.

[3]Sometimes we couldn't integrate equation (19) numerically because of the singular property about $J=0$. In such cases we solved (17) numerically and changed coordinates from (u, v) to (J, ϕ) in order to obtain numerical solutions of (19).

[4]Here we set $t_0=0$ and abbreviate the superscript t_0 of $\tilde{P}_\mu^{t_0}$. We also used the index theory of Poincaré (cf., Coddington and Levinson, 1955, Chapter 16) to obtain the unstable fixed point $\mathbf{p}_{2,\mu}$, as in Hsu (1980).

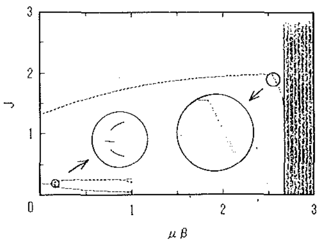

Fig. 10 Bifurcation diagram for the Poincaré map $\tilde{P}_\mu$, $\alpha=2$, $\gamma=1.5$, $\Omega=3$, $\mu\delta\omega=0.05$, $\nu_0=3.5$

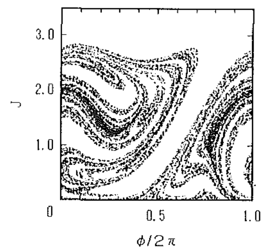

Fig. 11 Numerically computed orbits of the Poincaré map $\tilde{P}_\mu$, $\alpha=2$, $\gamma=1.5$, $\Omega=3$, $\mu\delta\omega=0.05$, $\nu_0=3.5$, $\mu\beta=2.7$

0.168. This suggests that saddle node and period doubling bifurcations occur at these values of $\mu\beta$, as in Fig. 4(b). As $\mu\beta$ continues to increase, a sequence of period doubling bifurcations occurs and accumulates to chaos at $\mu\beta\approx 0.9970$ (orbits of periods 2^n, $n\leq 6$, were observed). At $\mu\beta\approx 0.9972$ the chaotic attractor suddenly disappears, and almost all orbits seem to the asymptotic to $\mathbf{p}_{3,\mu}$. The fixed point $\mathbf{p}_{3,\mu}$, which is stable for a wide range of $\mu\beta$ value, undergoes a period doubling bifurcation at $\mu\beta\approx 2.543$. Further period doublings, however, cannot be observed and chaotic motions suddenly appear at $\mu\beta\approx 2.66$. Such interruption of period doubling cascades in plane maps was indicated in Holmes and Whitley (1984). Grebogi et al. (1983) also described phenomena of sudden changes in chaotic states, which they called "crises."

The "strange attractor" of Poincaré map $\tilde{P}_\mu$ at $\mu\beta=2.7$ is shown in Fig. 11, which should be compared with Fig. 9(c). We observed that this chaotic orbit erratically swings through $\phi=\pi$ and rotations in ϕ-direction.

5.2 Weakly Nonlinear Oscillator. We next show the results for equation (1) with fixed $\bar{\alpha}=0.2$, $\bar{\gamma}=0.15$, $\omega=1.14$, $\bar{\nu}=0.1535$, $\bar{\delta}=0.004386$, and $\bar{\beta}$ varying. These results correspond to the above results for the averaged system (19) if we set $\epsilon=0.1$.

Figure 12 shows projections of the computed orbits of the Poincaré map F associated with (1) onto (x, y)-plane. For small $\bar{\beta}$, there exist two stable invariant tori T_i, $i=1$, 3, as shown in Fig. 12(a), (b), in which the theoretical results given in Section 3.2 are also plotted as the dashed lines for the purpose of comparison. When $\bar{\beta}$ increases, an invariant torus, such as shown in Fig. 12(c), appears near the torus T_1 at $\bar{\beta}\approx 0.0119$ and then T_1 becomes unstable at $\bar{\beta}\approx 0.0169$; a doubling of torus occurs as predicted in Section 3.2.

Although it follows from the analysis in Section 4 that chaotic orbits appear at $\bar{\beta}=0.0242$ or $\bar{\beta}=0.0530$, chaotic motions cannot be observed near these parameter values. When $\bar{\beta}$ increases past about 0.0617, the doubling cascade of torus occurs (three doublings of torus were observed, see also Fig. 12(d)), and chaotic motions appear at $\bar{\beta}\approx 0.06707$ while the chaotic attractor vanishes at $\bar{\beta}\approx 0.06713$. T_3 seems to be the only attractor for $0.06713\lesssim\bar{\beta}\lesssim 0.3308$ and undergoes a doubling of torus at $\bar{\beta}\approx 0.3308$. (See Fig. 12($e$).) The new invariant torus becomes unstable at $\bar{\beta}\approx 0.3315$ and chaotic motions appear suddenly. The chaotic attractor at $\bar{\beta}=0.34$ is shown in Fig. 12(f).

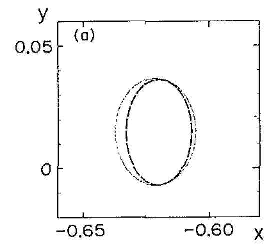

Fig. 12(a)

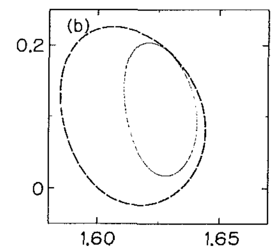

Fig. 12(b)

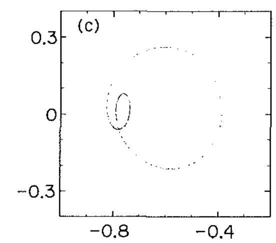

Fig. 12(c)

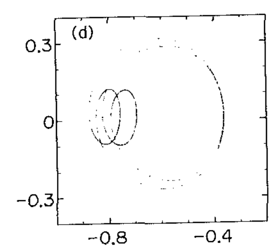

Fig. 12(d)

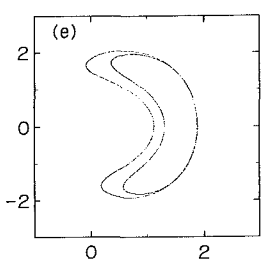

Fig. 12(e)

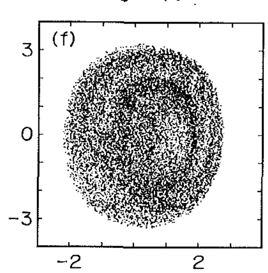

Fig. 12(f)

Fig. 12 Numerically computed orbits of the Poincaré map of (1) onto (x, y)-plane, $\bar{\alpha}=0.2$, $\bar{\gamma}=0.15$, $\omega=1.14$, $\bar{\nu}=0.1535$, $\bar{\delta}=0.004386$: (a), (b) $\bar{\beta}=0.008$; (c) $\bar{\beta}=0.05$; (d) $\bar{\beta}=0.065$; (e) $\bar{\beta}=0.331$; (f) $\bar{\beta}=0.34$. In (a) and (b) the theoretical results are also plotted as dashed lines.

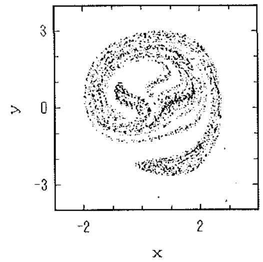

Fig. 13 Double Poincaré section, $\bar{\alpha}=0.2$, $\bar{\gamma}=0.15$, $\omega=1.14$, $\bar{\beta}=0.34$, $\bar{\nu}=0.1535$, $\bar{\delta}=0.004386$

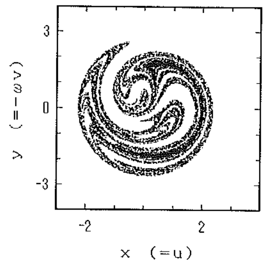

Fig. 14 Strange attractor in the averaged system (17), $\alpha=2$, $\gamma=1.5$, $\Omega=3$, $\mu\delta\omega=0.05$, $\nu_0=3.5$, $\mu\beta=2.7$ ($\omega=1.14$)

Figure 13 shows the double Poincaré section (Moon and Holmes, 1985; Moon, 1987) for the chaotic attractor in Fig. 12(f). In order to draw this figure, we took the thin section $0<\tau<0.02\pi$ and projected points falling in this slice onto x-y plane. Thus, the chaotic attractor in Fig. 12(f) has a fractal structure similar to that for the averaged system in Fig. 14, which is produced by changing coordinates from (J, ϕ) to (u, v) and applying the transformation (3) at $t=0$ ($y=u$, $y=-\omega v$) in Fig. 9(c). This observation indicates that the existence of transverse homoclinic orbits in the averaged system is responsible for chaotic dynamics of the original system, as described in Section 4.3.

In Fig. 15 we show numerical solutions $x(t)$. Figure 15(a) and (b) display the quasi-periodic orbits corresponding to two invariant tori of Poincaré map F at $\bar{\beta}=0.05$; one is T_3 and the other shown in Fig. 12(c). After a doubling of torus, the new beating motions have twice as long beating periods as the previous one, see Fig. 15(b). The chaotic orbit at $\bar{\beta}=0.34$ is also shown in Fig. 15(c).

6 Conclusions

In this paper we have studied the dynamics of a weakly nonlinear single-degree-of-freedom system subjected to combined parametric and external excitation. By using the averaging method, the invariant tori and their stability were analyzed. The orbits on these invariant tori indicate quasi-periodic motions. Furthermore, we applied the Melnikov technique to the averaged equation and utilized the invariant manifold theory to predict the regions in parameter space where chaotic orbits may exist.

In numerical simulation the existence of invariant tori and chaos was confirmed. We also observed doublings of torus, which correspond to period-doubling bifurcations in the averaged system. In some cases such bifurcations seem to succeed infinitely and accumulate to chaos, and in other cases chaotic attractors appear after a finite number of doublings.

Our results demonstrate the validity of the averaging method combined with the Melnikov technique to prove the existence of chaos in weakly nonlinear systems, together with the work of Holmes (1986) who analyzed a two-degree-of-freedom system subjected to periodic excitation. The approach used here is also applicable to a wide class of quasi-periodically forced weakly nonlinear oscillators. In the subsequent work we will pursue the chaotic dynamics of such systems.

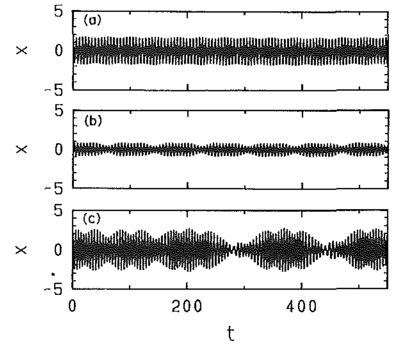

Fig. 15 Numerical solutions of (1), $\bar{\alpha}=0.2$, $\bar{\gamma}=0.15$, $\omega=1.14$, $\bar{\nu}=0.1535$, $\bar{\delta}=0.004386$: (a), (b) $\bar{\beta}=0.05$, (c) $\bar{\beta}=0.34$

Acknowledgments

The authors would like to thank Prof. Naoki Asano of Ibaraki University for helpful discussions. They also acknowledge the reviewers for useful comments and constructive suggestions, which have improved this work.

References

Coddington, E. A., and Levinson, N., 1955, *Theory of Ordinary Differential Equations*, McGraw-Hill, New York.

Grebogi, C., Ott, E., and Yorke, J. A., 1983, "Crises, Sudden Changes in Chaotic Attractors, and Transient Chaos," *Physica D*, Vol. 7, pp. 181–200.

Greenspan, B. D., and Holmes, P. J., 1983, "Homoclinic Orbits, Subharmonics and Global Bifurcations in Forced Oscillations," *Nonlinear Dynamics and Turbulence*, G. Barenblatt, G. Iooss, and D. D. Joseph, eds., Pitman, London, pp. 172–214.

Guckenheimer, J., and Holmes, P., 1983, *Nonlinear Oscillations, Dynamical Systems and Bifurcations of Vector Feilds*, Springer-Verlag, New York.

Hale, J. K., 1969, *Ordinary Differential Equations*, John Wiley and Sons, New York.

HaQuang, N., Mook, D. T., and Plaut, R. H., 1987, "A Nonlinear Analysis of the Interactions Between Parametric and External Excitations," *Journal of Sound and Vibration*, Vol. 118, pp. 425–439.

Hirsch, M. W., Pugh, C. C., and Shub, M., 1977, *Invariant Manifolds*, Lecture Notes in Mathematics, No. 583, Springer-Verlag, New York.

Holmes, P., 1979, "A Nonlinear Oscillator With a Strange Attractor," *Philosophical Transactions of the Royal Society of London*, Ser. A, Vol. 292, pp. 419–448.

Holmes, P. J., 1980, "Averaging and Chaotic Motions in Forced Oscillations," *SIAM Journal on Applied Mathematics*, Vol. 38, pp. 65–80; Errata and addenda, Vol. 40, pp. 167–168.

Holmes, P., 1986, "Chaotic Motions in a Weakly Nonlinear Model for Surface Waves," *Journal of Fluid Mechanics*, Vol. 162, pp. 365–388.

Holmes, P., Marsden, J., and Scheurle, J., 1987, "Exponentially Small Spilitting of Separatrices," *Proceedings of the National Academy of Sciences of the United States of America*, to be published.

Holmes, P., and Whitley, D., 1984, "Bifurcations of One- and Two-dimensional Maps," *Philosophical Transactions of the Royal Society of London*, Series A, Vol. 311, pp. 43–102.

Hsu, C. S., 1980, "A Theory of Index for Point Mapping Dynamical Systems," ASME Journal of Applied Mechanics, Vol. 47, pp. 185–190.

Ide, K., and Wiggins, S., 1989, "The Bifurcation to Homoclinic Tori in the Quasiperiodically Forced Duffing Oscillator," *Physica D*, Vol. 34, pp. 169–182.

Kaneko, K., 1986, *Collapse of Tori and Genesis of Chaos in Dissipative Systems*, World Scientific, Singapore.

Melnikov, V. K., 1963, "On the Stability of the Center for Time Periodic Perturbations," *Transactions of the Moscow Mathematical Society*, Vol. 12, pp. 1–56.

Moon, F. C., 1987, *Chaotic Vibrations, an Introduction for Applied Scientists and Engineers*, John Wiley and Sons, New York.

Moon, F., and Holmes, W. T., 1985, "Double Poincaré Sections of a Quasiperiodically Forced, Chaotic Attractor," *Physics Letters A*, Vol. 111, pp. 157–160.

Ness, D. J., 1971, "Resonance Classification in a Cubic System," ASME Journal of Applied Mechanics, Vol. 38, pp. 585–590.

Plaut, R. H., and Hsieh, J.-C., 1987, "Chaos in a Mechanism With Delays Under Parametric and External Excitation," *Journal of Sound and Vibration*, Vol. 114, pp. 73–90.

Salam, F. M. A., and Sastry, S. S., 1985, "Dynamics of the Forced Josephson Junction Circuit: the Regions of Chaos," *IEEE Transactions on Circuits and Systems*, Vol. 32, pp. 784–796.

Sanders, J. A., 1982, "Melnikov's Method and Averaging," *Celestial Mechanics*, Vol. 28, pp. 171–181.

Sanders, J. A., and Verhulst, F., 1985, *Averaging Methods in Nonlinear Dynamical Systems*, Springer-Verlag, New York.

Troger, H., and Hsu, C. S., 1977, "Response of a Nonlinear System Under Combined Parametric and Forcing Excitation," ASME Journal of Applied Mechanics, Vol. 44, pp. 179–181.

Wiggins, S., 1987, "Chaos in the Quasiperiodically Forced Duffing Oscillator," *Physics Letters A*, Vol. 124, pp. 138–142.

Wiggins, S., 1988a, "On the Detection and Dynamical Consequences of Orbits Homoclinic to Hyperbolic Periodic Orbits and Normally Hyperbolic Invariant Tori in a Class of Ordinary Differential Equations," *SIAM Journal on Applied Mathematics*, Vol. 48, pp. 262–285.

Wiggins, S., 1988b, *Global Bifurcations and Chaos—Analytical Methods*, Springer-Verlag, New York.

Mario Di Paola
Professor.
Dipartimento di Ingegneria Strutturale e Geotecnica,

Giovanni Petrucci
Consulting Engineer.
Istituto di Costruzione di Macchine

Universita di Palermo,
Viale delle Scienze,
90128 Palermo, Italy

Spectral Moments and Pre-Envelope Covariances of Nonseparable Processes

A critical review of the definition of the spectral moments of a stochastic process in the nonstationary case is presented. An adequate time-domain representation of the spectral moments in the stationary case is first established, showing that the spectral moments are related to the variances of the stationary analytical pre-envelope processes. The extension to the nonstationary case is made in the time domain evaluating the covariances of the nonstationary pre-envelope showing the differences between the proposed definition and the classical one made introducing the evolutionary power.

1 Introduction

Many time-varying loadings to structures are modeled as stochastic processes and the response analysis can be established in a probabilistic sense. The stochastic processes of input and response may often be nonstationary for frequency content and amplitude, as in the case of a strong motion phase during an earthquake (Kameda, 1975) and can be adequately represented as nonseparable processes (Priestley, 1965).

For Gaussian inputs and linear systems, the first and the second-order moments completely define the statistics of the response. However, in many cases such as prediction of the first excursion failure, fatigue failure, etc., we are concerned with the statistics of the envelope process. The above, following Dugundji (1958) and Yang (1972), and Krenk et al. (1983), for stationary and nonstationary processes, respectively, can be seen as the modulus of the pre-envelope (Arens, 1957; Dugundji, 1958); i.e., a complex process, the real part of which is the given process while its imaginary part is related to the real one in such a way that the complex process exhibits power only in the positive frequency range. It follows that the statistics of the envelope are related to the covariances of the pre-envelope.

It has been shown (Di Paola, 1985) that the covariances of the pre-envelope are, in the stationary cases, strictly related to the so-called spectral moments SM (hereafter referred to as SM) (Vanmarcke, 1972). In particular, the SM, defined as the moments of the one-sided power spectral density function have, in time domain, the meaning of variances of the pre-envelope (Di Paola, 1985).

The extension of the SM to the nonstationary case is usually made in the frequency domain as the moments of the one-sided evolutionary power spectral density (Priestley, 1965; Hammond 1968; Shinozuka, 1970). However, such definition, with exception of the zeroth one SM, has no physical meaning in the time domain and enjoyment of unsatisfactory properties, for example, in the transient case of an oscillator subjected to white noise input (see Corotis, 1972).

Here a comparison between the SM in the nonstationary case and the pre-envelope covariances (PEC) is presented. In particular, it is shown that only the area of the evolutionary power coincides with the PEC, while all other moments differ from the variances of the various derivatives of the pre-envelope and, as a consequence, the moments of the evolutionary power do not give any information on the statistics of the envelope.

The PEC for a multi-degree-of-freedom linear system subjected to nonstationary, nonseparable processes is also presented, and the numerical aspect on their evaluation is discussed in the application.

For clarity's sake, in the next two sections the complex representation of pre-envelope processes is first discussed.

2 Stationary Pre-Envelope Process

Let $\mathbf{F}(t)$ be an n-dimensional real stationary stochastic process vector given in the Priestley (1965) representation as follows:

$$\mathbf{F}(t)=\int_{-\infty}^{\infty} e^{-i\omega t}d\mathbf{Z}(\omega)=\int_{-\infty}^{\infty} e^{i\omega t}d\mathbf{Z}^*(\omega). \tag{1}$$

i is the imaginary unit ($i=\sqrt{-1}$), while the asterisk indicates the complex conjugate and $d\mathbf{Z}(\omega)$ is a stochastic vector process having orthogonal increments, i.e.,

$$E[d\mathbf{Z}(\omega_1)d\mathbf{Z}^{*T}(\omega_2)]=\delta(\omega_2-\omega_1)d\psi(\omega_1) \tag{2}$$

where $E[\,\cdot\,]$ means stochastic average, $\delta(t)$ is the Dirac's delta, the superimposed T means transpose, and $d\psi(\omega)$ is a deterministic Hermitian positive-definite matrix. It is worth noting

Contributed by the Applied Mechanics Division of THE AMERICAN SOCIETY OF MECHANICAL ENGINEERS for publication in the JOURNAL OF APPLIED MECHANICS.

Discussion on this paper should be addressed to the Editorial Department, ASME, United Engineering Center, 345 East 47th Street, New York, N.Y. 10017, and will be accepted until two months after final publication of the paper itself in the JOURNAL OF APPLIED MECHANICS. Manuscript received by the ASME Applied Mechanics Division, November 10, 1987; final revision, January 6, 1989.

that in order for equation (1) to be fulfilled, it is necessary that the process vector $d\mathbf{Z}(\omega)$ be complex, such that its real and imaginary parts are even and odd functions of ω, respectively.

Without loss of generality we consider that $\mathbf{F}(t)$ is a zero-mean process and $\psi(\omega)$ is a differentiable matrix, and hence, the following relationship

$$d\psi(\omega)=\mathbf{G}(\omega)d\omega \tag{3}$$

holds, $\mathbf{G}(\omega)$ being the Hermitian power spectral density function matrix defined in both the positive and negative frequency ranges.

Let us consider a new process vector $\tilde{\mathbf{F}}(t)$, derived from $\mathbf{F}(t)$, such that the corresponding power spectral density function matrix $\tilde{\mathbf{G}}(\omega)$ is one-sided, i.e.,

$$\tilde{\mathbf{G}}(\omega)=2U(\omega)\mathbf{G}(\omega)=\mathbf{S}(\omega), \tag{4}$$

$U(\omega)$ being the unit step function. Equation (4) is verified if the vector $d\tilde{\mathbf{Z}}(\omega)$, corresponding to $\tilde{\mathbf{F}}(\omega)$, takes on the following form:

$$d\tilde{\mathbf{Z}}(\omega)=\frac{1}{\sqrt{2}}(1+\operatorname{sgn}(\omega))d\mathbf{Z}(\omega)=\frac{2}{\sqrt{2}}U(\omega)d\mathbf{Z}(\omega) \tag{5}$$

$\operatorname{sgn}(\omega)$ being the signum function. Equation (2), rewritten for the stochastic process vector $\tilde{\mathbf{Z}}(\omega)$, now gives:

$$\begin{aligned}E[d\tilde{\mathbf{Z}}(\omega_1)d\tilde{\mathbf{Z}}^{*T}(\omega_2)]&=2U(\omega_1)d\psi(\omega_1)\delta(\omega_2-\omega_1)\\&=\mathbf{S}(\omega_1)d\omega_1\delta(\omega_2-\omega_1).\end{aligned} \tag{6}$$

Using equation (5), the appropriate description of the vector $\tilde{\mathbf{F}}(t)$ takes on the form:

$$\tilde{\mathbf{F}}(t)=\int_{-\infty}^{\infty}e^{-i\omega t}d\tilde{\mathbf{Z}}(\omega)=\frac{2}{\sqrt{2}}\int_0^{\infty}e^{-i\omega t}d\mathbf{Z}(\omega). \tag{7}$$

This equation shows that $\tilde{\mathbf{F}}(t)$ is a complex vector having frequency content only in the positive frequency range, and it can easily be seen that its real part is proportional to the real process $\mathbf{F}(t)$ defined in equation (1), while its imaginary part is the signumless Hilbert Transform of the real one, i.e., $\tilde{\mathbf{F}}(t)$ constitute an analytic process (Papoulis 1965, Nigam 1982), and is the so-called "pre-envelope" (Arens, 1957; Dugundji, 1958).

$$\tilde{\mathbf{F}}(t)=\frac{1}{\sqrt{2}}(\mathbf{F}(t)-i\hat{\mathbf{F}}(t)) \tag{8}$$

where the accent ˆ means Hilbert Transform:

$$\hat{\mathbf{F}}(t)=\frac{1}{\pi}\int_{-\infty}^{\infty}\frac{\mathbf{F}(\rho)}{t-\rho}d\rho. \tag{9}$$

In the stationary case the vector $\hat{\mathbf{F}}(t)$ can be written in the form

$$\hat{\mathbf{F}}(t)=i\int_{-\infty}^{\infty}e^{-i\omega t}\operatorname{sgn}(\omega)d\mathbf{Z}(\omega). \tag{10}$$

It is worth noting that the modulus of the jth entry of the complex process vector defined in equation (8) is proportional to the "envelope" of $F_j(t)$.

The cross-correlation function matrix of the complex vector $\tilde{\mathbf{F}}(t)$ is given in the form:

$$\mathbf{R}_{\tilde{\mathbf{F}}\tilde{\mathbf{F}}}(\tau)=E[\tilde{\mathbf{F}}(t)\tilde{\mathbf{F}}^{*T}(t+\tau)]=\int_0^{\infty}e^{i\omega\tau}\mathbf{S}(\omega)d\omega. \tag{11}$$

From this equation it can easily be shown that the cross-correlation matrix of the vector $\tilde{\mathbf{F}}(t)$ is complex and such that its real part is the cross-correlation function of the real vector $\mathbf{F}(t)$ while its imaginary part is the Hilbert Transform of the real one, i.e.,

$$\mathbf{R}_{\tilde{\mathbf{F}}\tilde{\mathbf{F}}}(\tau)=\mathbf{R}_{\mathbf{FF}}(\tau)+i\hat{\mathbf{R}}_{\mathbf{FF}}(\tau). \tag{12}$$

The real and the imaginary parts of the cross-correlation function matrix can be rewritten in equivalent forms as follows:

$$\mathbf{R}_{\mathbf{FF}}(\tau)=\mathbf{R}_{\hat{\mathbf{F}}\hat{\mathbf{F}}}(\tau)=-\hat{\hat{\mathbf{R}}}_{\mathbf{FF}}(\tau)=\int_{-\infty}^{\infty}e^{i\omega t}\mathbf{G}(\omega)d\omega \tag{13}$$

$$\hat{\mathbf{R}}_{\mathbf{FF}}(\tau)=\mathbf{R}_{\mathbf{F}\hat{\mathbf{F}}}(\tau)=-\mathbf{R}_{\hat{\mathbf{F}}\mathbf{F}}(\tau)=-i\int_{-\infty}^{\infty}e^{i\omega t}\operatorname{sgn}(\omega)\mathbf{G}(\omega)d\omega. \tag{14}$$

As a conclusion the process vector $\tilde{\mathbf{F}}(t)$ having the representation given in equation (8) exhibits power only in the positive frequency range and has the complex cross-correlation function defined in equation (12).

3 Nonstationary Pre-Envelope Process

Let $\mathbf{F}(t)$ be a real nonstationary nonseparable stochastic process vector. Following Priestley, its representation is given in the form:

$$\mathbf{F}(t)=\int_{-\infty}^{\infty}e^{-i\omega t}\mathbf{A}(\omega,\ t)d\mathbf{Z}(\omega)=\int_{-\infty}^{\infty}e^{i\omega t}\mathbf{A}^*(\omega,\ t)d\mathbf{Z}^*(\omega) \tag{15}$$

where $\mathbf{A}(\omega,\ t)$ is a slowly time-varying deterministic function matrix and $d\mathbf{Z}(\omega)$ is the stochastic process vector already defined in equation (2). As for the stationary case, due to the fact that the process $\mathbf{F}(t)$ is real, the real and the imaginary parts of the vector $\mathbf{A}(\omega,\ t)\ d\mathbf{Z}(\omega)$ must be even and odd functions of ω, respectively.

The complex representation of the nonstationary process vector can be obtained by inserting the process vector $d\tilde{\mathbf{Z}}(\omega)$ defined in equation (5) into equation (15), thus obtaining:

$$\tilde{\mathbf{F}}(t)=\int_{-\infty}^{\infty}e^{-i\omega t}\mathbf{A}(\omega,\ t)d\tilde{\mathbf{Z}}(\omega)=\frac{2}{\sqrt{2}}\int_0^{\infty}e^{-i\omega t}\mathbf{A}(\omega,\ t)d\mathbf{Z}(\omega). \tag{16}$$

This equation shows that the nonstationary vector process $\tilde{\mathbf{F}}(t)$ is a complex vector having frequency content only in the positive frequency range, and it can easily be seen that its real part is proportional to the real vector process $\mathbf{F}(t)$ defined in equation (15), while its imaginary part will be denoted as $-\bar{\mathbf{F}}(t)$. Hence, we can write:

$$\tilde{\mathbf{F}}(t)=\frac{1}{\sqrt{2}}(\mathbf{F}(t)-i\bar{\mathbf{F}}(t)) \tag{17}$$

It is to be emphasized that $\bar{\mathbf{F}}(t)$ coincides with $\hat{\mathbf{F}}(t)$ only in the stationary case, while in the nonstationary case it is given as

$$\bar{\mathbf{F}}(t)=i\int_{-\infty}^{\infty}e^{-i\omega t}\operatorname{sgn}(\omega)\mathbf{A}(\omega,\ t)d\mathbf{Z}(\omega). \tag{18}$$

The modulus of the jth entry of the vector $\tilde{\mathbf{F}}(t)$ in equation (17) is proportional to the envelope function of $F_j(t)$ defined by Yang (1972). The complex cross-correlation function matrix of the complex vector $\tilde{\mathbf{F}}(t)$ can be written as follows:

$$\begin{aligned}\mathbf{R}_{\tilde{\mathbf{F}}\tilde{\mathbf{F}}}(t_1,\ t_2)&=E[\tilde{\mathbf{F}}(t_1)\tilde{\mathbf{F}}^{*T}(t_2)]\\&=\int_0^{\infty}e^{i\omega\tau}\mathbf{A}(\omega,\ t_1)\mathbf{S}(\omega)\mathbf{A}^{*T}(\omega,\ t_2)d\omega\end{aligned} \tag{19}$$

in which $\tau=t_2-t_1$.

The real and the imaginary parts of the correlation matrix $\mathbf{R}_{\tilde{\mathbf{F}}\tilde{\mathbf{F}}}(t_1,\ t_2)$ can be rewritten in equivalent forms as follows:

$$\mathbf{R}_{\mathbf{FF}}(t_1,\ t_2)=\mathbf{R}_{\bar{\mathbf{F}}\bar{\mathbf{F}}}(t_1,\ t_2)=\int_{-\infty}^{\infty}e^{i\omega\tau}\mathbf{A}(\omega,\ t_1)\mathbf{G}(\omega)\mathbf{A}^{*T}(\omega,\ t_2)d\omega \tag{20}$$

$$\mathbf{R}_{\mathbf{F}\hat{\mathbf{F}}}(t_1, t_2) = -\mathbf{R}_{\hat{\mathbf{F}}\mathbf{F}}(t_1, t_2)$$

$$= -i\int_0^\infty \mathrm{sgn}(\omega)e^{i\omega\tau}\mathbf{A}(\omega, t_1)\mathbf{G}(\omega)\mathbf{A}^{*T}(\omega, t_2)d\omega. \tag{21}$$

Using equations (20) and (21), the correlation function matrix $\mathbf{R}_{\tilde{\mathbf{F}}\tilde{\mathbf{F}}}(t_1, t_2)$ can be rewritten in the form:

$$\mathbf{R}_{\tilde{\mathbf{F}}\tilde{\mathbf{F}}}(t_1, t_2) = \mathbf{R}_{\mathbf{F}\mathbf{F}}(t_1, t_2) + i\mathbf{R}_{\mathbf{F}\hat{\mathbf{F}}}(t_1, t_2). \tag{22}$$

In the next section it will be shown that the complex representation of the vector $\tilde{\mathbf{F}}(t)$ given in equations (7) and (16) for the stationary and nonstationary case, respectively, are essential not only for the definition of the envelopes, but also for the correct definition of the spectral moments (Vanmarcke 1972) in both stationary and nonstationary cases. (See also Di Paola 1985.)

4 Spectral Moments and Pre-Envelope Covariances, Stationary Case

In this section the covariances of the stationary process defined in equation (8) are presented. In order to do this, let $\tilde{\mathbf{P}}(t)$ the $2n$ dimensional vector of the state variables, be introduced as follows:

$$\tilde{\mathbf{P}}^T(t) = [\tilde{\mathbf{F}}^T(t)\dot{\tilde{\mathbf{F}}}^T(t)] \tag{23}$$

where the upper dot means time differentiation and $\tilde{\mathbf{F}}(t)$ is the stationary process vector given in equation (8). Using the main properties of the correlation function given in equations (13) and (14) evaluated for $\tau = 0$, the time-independent Hermitian cross-covariance matrix of the complex vector $\tilde{\mathbf{P}}(t)$, i.e., the PEC matrix, is given as:

$$\mathbf{\Sigma}_{\tilde{\mathbf{P}}\tilde{\mathbf{P}}} = E[\tilde{\mathbf{P}}(t)\tilde{\mathbf{P}}^{*T}(t)] = E[\mathbf{P}(t)\mathbf{P}^T(t)] + iE[\mathbf{P}(t)\hat{\mathbf{P}}^T(t)] \tag{24}$$

where $\mathbf{P}(t)$ is the real vector of state variables

$$\mathbf{P}^T(t) = [\mathbf{F}^T(t)\dot{\mathbf{F}}^T(t)]. \tag{25}$$

Equation (24) shows that the real part of the matrix $\mathbf{\Sigma}_{\tilde{\mathbf{P}}\tilde{\mathbf{P}}}$ is the traditional covariance matrix of the real process vector $\mathbf{P}(t)$, while the imaginary part is the cross-covariance between the real vector $\mathbf{P}(t)$ and its Hilbert Transform.

The matrix $\mathbf{\Sigma}_{\tilde{\mathbf{P}}\tilde{\mathbf{P}}}$ can be rewritten in an extended form as follows

$$\mathbf{\Sigma}_{\tilde{\mathbf{P}}\tilde{\mathbf{P}}} = \begin{vmatrix} E[\tilde{\mathbf{F}}(t)\tilde{\mathbf{F}}^{*T}(t)] & E[\tilde{\mathbf{F}}(t)\dot{\tilde{\mathbf{F}}}^{*T}(t)] \\ E[\dot{\tilde{\mathbf{F}}}(t)\tilde{\mathbf{F}}^{*T}(t)] & E[\dot{\tilde{\mathbf{F}}}(t)\dot{\tilde{\mathbf{F}}}^{*T}(t)] \end{vmatrix}. \tag{26}$$

In previous papers (Borino et al., 1988; Muscolino, 1988), this matrix has been called, in a less appropriate manner, cross-covariance spectral matrix (CCS matrix).

Using equation (7) to represent the stochastic vector $\tilde{\mathbf{F}}(t)$, after some simple algebra it can easily be seen that the various block matrices of the matrix $\tilde{\mathbf{\Sigma}}_{\tilde{\mathbf{p}}\tilde{\mathbf{p}}}$ take on the form:

$$E[\tilde{\mathbf{F}}(t)\tilde{\mathbf{F}}^{*T}(t)] = \int_0^\infty \mathbf{S}(\omega)d\omega = \mathbf{\Lambda}_{0,\,\mathbf{FF}} \tag{27}$$

$$E[\tilde{\mathbf{F}}(t)\dot{\tilde{\mathbf{F}}}^{*T}(t)] = i\int_0^\infty \omega\mathbf{S}(\omega)d\omega = i\mathbf{\Lambda}_{1,\,\mathbf{FF}} \tag{28}$$

$$E[\dot{\tilde{\mathbf{F}}}(t)\dot{\tilde{\mathbf{F}}}^{*T}(t)] = \int_0^\infty \omega^2\mathbf{S}(\omega)d\omega = \mathbf{\Lambda}_{2,\,\mathbf{FF}}. \tag{29}$$

Equations (27)–(29) show that the PEC matrix is related to the moments of the one-sided power spectral matrix $\mathbf{S}(\omega)$, i.e., to the so-called SM (Vanmarcke, 1972).

Inserting equation (27)–(29) in (26), the frequency domain representation of the PEC matrix is given as:

$$\mathbf{\Sigma}_{\tilde{\mathbf{P}}\tilde{\mathbf{P}}} = \begin{vmatrix} \int_0^\infty \mathbf{S}(\omega)d\omega & i\int_0^\infty \omega\mathbf{S}(\omega)d\omega \\ -i\int_0^\infty \omega\mathbf{S}^*(\omega)d\omega & \int_0^\infty \omega^2\mathbf{S}(\omega)d\omega \end{vmatrix}. \tag{30}$$

Comparing equations (24) and (30), the important connection between the SM and the PEC is evidenced.

The presence of the imaginary unit in the out-of-diagonal block matrices in equation (30) inverts the roles of the real and imaginary parts of the first spectral moment, with respect to the cross-covariance $E[\tilde{\mathbf{F}}(t)\ \dot{\tilde{\mathbf{F}}}(t)]$.

It is interesting to note that the PEC matrix particularized for the vector $\mathbf{F}(t)$, having only one component, is such that its determinant is related to the bandwidth parameter (Vanmarcke, 1972).

5 Spectral Moments and Pre-Envelope Covariances, Nonstationary Case

The SM in the nonstationary case are defined in the literature as the moments of the so-called one-sided evolutionary spectral density (Shinozuka, 1970):

$$\mathbf{S}(\omega, t) = \mathbf{A}(\omega, t)\mathbf{S}(\omega)\mathbf{A}^{*T}(\omega, t) \tag{31}$$

and the extension of the time-dependent SM is usually made in the form (Corotis et al., 1972):

$$\mathbf{\Lambda}_{j,\,\mathbf{FF}}(t) = \int_0^\infty \omega^j\mathbf{S}(\omega, t)d\omega \qquad j \geqq 0. \tag{32}$$

Using the main properties of the correlation function given in equations (21) and (22), particularized for $t_1 = t_2 = t$, it can easily be seen that for $j = 0$, equation (32) gives:

$$\mathbf{\Lambda}_{0,\,\mathbf{FF}}(t) = \int_0^\infty \mathbf{S}(\omega, t)d\omega = E[\tilde{\mathbf{F}}(t)\tilde{\mathbf{F}}^{*T}(t)]$$

$$= E[\mathbf{F}(t)\mathbf{F}^T(t)] + iE[\mathbf{F}(t)\hat{\mathbf{F}}^T(t)]. \tag{33}$$

This equation shows that the zeroth coincides with the covariance of the complex process defined in equation (17), while for j greater than zero, the moments of the one-sided evolutionary power spectral density function matrix has no analogous correspondence in the time domain of the variance of the pre-envelope processes, as in the stationary case.

The time-dependent PEC matrix is given in the form:

$$\mathbf{\Sigma}_{\tilde{\mathbf{p}}\tilde{\mathbf{p}}}(t) = E[\tilde{\mathbf{P}}(t)\tilde{\mathbf{P}}^{*T}(t)]. \tag{34}$$

where $\tilde{\mathbf{P}}(t)$ is defined in equation (23) and while $\tilde{\mathbf{F}}(t)$ is defined in equation (17). The block matrices of $\mathbf{\Sigma}_{\tilde{\mathbf{p}}\tilde{\mathbf{p}}}(t)$ are given in equation (26), the first block matrix has already been defined in equation (33), while the other blocks can be written in the form:

$$E[\tilde{\mathbf{F}}(t)\dot{\tilde{\mathbf{F}}}^{*T}(t)] = E[\mathbf{F}(t)\dot{\mathbf{F}}^T(t)] + iE[\mathbf{F}(t)\dot{\hat{\mathbf{F}}}^T(t)] \tag{35}$$

$$E[\dot{\tilde{\mathbf{F}}}(t)\dot{\tilde{\mathbf{F}}}^{*T}(t)] = E[\dot{\mathbf{F}}(t)\dot{\mathbf{F}}^T(t)] + iE[\dot{\mathbf{F}}(t)\dot{\hat{\mathbf{F}}}^T(t)]. \tag{36}$$

Using equation (16) to represent the nonstationary vector $\tilde{\mathbf{F}}(t)$, and writing its time differentiation in the form

$$\dot{\tilde{\mathbf{F}}}(t) = \frac{2}{\sqrt{2}}\int_0^\infty e^{-i\omega t}\mathbf{A}_1(\omega, t)d\mathbf{Z}(\omega) \tag{37}$$

where

$$\mathbf{A}_1(\omega, t) = -i\omega\mathbf{A}(\omega, t) + \dot{\mathbf{A}}(\omega, t), \tag{38}$$

equations (37) and (38) can be rewritten as

$$E[\tilde{\mathbf{F}}(t)\dot{\tilde{\mathbf{F}}}^{*T}(t)] = \int_0^\infty \mathbf{A}(\omega, t)\mathbf{S}(\omega)\mathbf{A}_1^{*T}(\omega, t)d\omega \tag{39}$$

$$E[\dot{\tilde{\mathbf{F}}}(t)\dot{\tilde{\mathbf{F}}}^{*T}(t)] = \int_0^\infty \mathbf{A}_1(\omega, t)\mathbf{S}(\omega)\mathbf{A}_1^{*T}(\omega, t)d\omega \tag{40}$$

or, in an explicit form

$$E[\tilde{\mathbf{F}}(t)\dot{\tilde{\mathbf{F}}}^{*T}(t)] = i\int_0^\infty \omega\mathbf{S}(\omega, t)d\omega + \int_0^\infty \mathbf{S}_1(\omega, t)d\omega \tag{41}$$

$$E[\dot{\tilde{\mathbf{F}}}(t)\dot{\tilde{\mathbf{F}}}^{*T}(t)] = \int_0^\infty \omega^2\mathbf{S}(\omega, t)d\omega$$

$$-i\int_0^\infty [\omega\mathbf{S}_1(\omega, t) - \mathbf{S}_1^*(\omega, t)]d\omega + \int_0^\infty \mathbf{S}_2(\omega, t)d\omega \tag{42}$$

where

$$\mathbf{S}_1(\omega, t) = \mathbf{A}(\omega, t)\mathbf{S}(\omega)\dot{\mathbf{A}}^{*T}(\omega, t);$$
$$\mathbf{S}_2(\omega, t) = \dot{\mathbf{A}}(\omega, t)\mathbf{S}(\omega)\dot{\mathbf{A}}^{*T}(\omega, t). \tag{43}$$

Equations (41) and (42) show that the variances of the nonstationary pre-envelope processes $\tilde{\mathbf{F}}(t)$ and $\dot{\tilde{\mathbf{F}}}(t)$ can be constructed adding to the moments of the one-sided evolutionary spectrum other quantities involving the time derivatives of the function matrix $\mathbf{A}(\omega, t)$. Only when $\mathbf{A}(\omega, t)$ is a smooth function matrix varying very slowly in t, $\dot{\mathbf{A}}(\omega, t)$ is approximately equal to zero, is the cross-covariances of the pre-envelope processes proportional to the time-dependent spectral moments defined in equation (32). (See also To, 1986.) On the other hand, when comparing equation (27)-(29) with equations (33), (41), and (42), it seems to be more reasonable to evaluate the covariances of the pre-envelope in the nonstationary case, in the time domain, i.e., defining the time-dependent PEC as the covariances of the nonstationary complex processes $\tilde{\mathbf{F}}(t)$ and $\dot{\tilde{\mathbf{F}}}(t)$

$$\Lambda_{0,\mathbf{FF}}(t) = E[\tilde{\mathbf{F}}(t)\tilde{\mathbf{F}}^{*T}(t)] \tag{44}$$
$$i\tilde{\Lambda}_{1,\mathbf{FF}}(t) = E[\tilde{\mathbf{F}}(t)\dot{\tilde{\mathbf{F}}}^{*T}(t)] \tag{45}$$
$$\tilde{\Lambda}_{2,\mathbf{FF}}(t) = E[\dot{\tilde{\mathbf{F}}}(t)\dot{\tilde{\mathbf{F}}}^{*T}(t)]. \tag{46}$$

Using these quantities instead of the moments of the evolutionary power, some quantities of engineering interest, such as the probability density function of the envelope and the mean-rate threshold crossing of the given barrier, can be computed in an exact manner (Di Paola and Muscolino, 1987; Muscolino, 1988), while only approximate expression can be obtained using covariances of the real processes or the moments of the evolutionary power.

6 Input-Output Relationships

The equation of motion of an n-degree-of-freedom linear structural system is governed by the following equation:

$$\mathbf{M}\ddot{\mathbf{X}} + \mathbf{C}\dot{\mathbf{X}} + \mathbf{K}\mathbf{X} = \mathbf{F}(t) \tag{47}$$

where, $\mathbf{M}$, $\mathbf{C}$, and $\mathbf{K}$ are the inertia damping and stiffness matrices, respectively, $\mathbf{X}(t)$ is the vector of displacements. $\mathbf{F}(t)$ is the forcing function vector. The vector solution $\mathbf{X}(t)$ can be obtained in the form:

$$\mathbf{X}(t) = \int_0^t \mathbf{H}(t-\tau)\mathbf{F}(\tau)d\tau + \mathbf{G}(t)\mathbf{K}\mathbf{U}_0 + \mathbf{H}(t)\mathbf{M}\dot{\mathbf{X}}_0 \tag{48}$$

$\mathbf{H}(t)$ being the impulse response function matrix, $\mathbf{G}(t)$ is related to the matrix $\mathbf{H}(t)$ in the form:

$$\dot{\mathbf{G}}(t) = \mathbf{H}(t), \tag{49}$$

and $\mathbf{X}_0$, $\dot{\mathbf{X}}_0$ are the vectors of initial conditions.

For greater convenience, let the state vector

$$\mathbf{U}^T(t) = [\mathbf{X}^T(t)\dot{\mathbf{X}}^T(t)] \tag{50}$$

be introduced, then the vector solution $\mathbf{X}(t)$ is written in the form

$$\mathbf{U}(t) = \mathbf{W}(t)\,\mathbf{U}_0 + \int_0^t \mathbf{L}(t-\tau)\mathbf{F}(\tau)d\tau \tag{51}$$

in which we have set

$$\theta(t) = \begin{vmatrix} -\mathbf{G}(t)\mathbf{K} & \mathbf{H}(t)\mathbf{M} \\ -\dot{\mathbf{G}}(t)\mathbf{K} & \dot{\mathbf{H}}(t)\mathbf{M} \end{vmatrix}; \quad \mathbf{L}(t)\begin{vmatrix} \mathbf{H}(t) \\ \dot{\mathbf{H}}(t) \end{vmatrix}; \quad \mathbf{U}_0 = \begin{vmatrix} \mathbf{X}_0 \\ \dot{\mathbf{X}}_0 \end{vmatrix} \tag{52}$$

Equation (51) is able to give the state vector solution, $\mathbf{U}(t)$, in the deterministic case. The vector $\mathbf{U}(t)$ is either real or complex depending on whether the forcing vector is real or complex. In order to evaluate the PEC of the vector solution $\mathbf{U}(t)$, the forcing vector $\mathbf{F}(t)$ must be defined as in equation (8) or (17) in the stationary or nonstationary case, respectively.

6.1 P.E.C. Matrix of the Output-Stationary Case. Particularizing the equation (51) for stationary condition and complex forcing function defined as in equation (8), we obtain the stationary response of the state vector in the form

$$\tilde{\mathbf{U}}(t) = \int_{-\infty}^t \mathbf{L}(t-\tau)\tilde{\mathbf{F}}(\tau)d\tau$$

$$= \frac{2}{\sqrt{2}}\int_0^\infty \left[\int_{-\infty}^t \mathbf{L}(t-\tau)e^{-i\omega\tau}d\tau\right]d\mathbf{Z}(\omega). \tag{53}$$

After some easy manipulations, the latter can be rewritten in the form

$$\tilde{\mathbf{U}}(t) = \frac{2}{\sqrt{2}}\int_0^\infty e^{-i\omega t}\mathbf{L}^*(\omega)d\mathbf{Z}(\omega) \tag{54}$$

in which $\mathbf{L}(\omega)$ is the Fourier Transform of $\mathbf{L}(t)$. From this equation it can easily be seen that $\mathbf{U}(t)$ is a complex process such that its imaginary part is the (signumless) Hilbert transform of the corresponding real one, i.e.,

$$\tilde{\mathbf{U}}(t) = \frac{2}{\sqrt{2}}[\mathbf{U}(t) - i\hat{\mathbf{U}}(t)]. \tag{55}$$

The PEC matrix of the vector $\mathbf{X}$, according to equation (24), is given in the form:

$$\Sigma_{\tilde{\mathbf{U}}\tilde{\mathbf{U}}} = E[\tilde{\mathbf{U}}(t)\tilde{\mathbf{U}}^{*T}(t)] = \begin{vmatrix} \Lambda_{0,\mathbf{XX}} & i\Lambda_{1,\mathbf{XX}} \\ -i\Lambda_{1,\mathbf{XX}}^* & \Lambda_{2,\mathbf{XX}} \end{vmatrix} \tag{56}$$

in which the various block matrices can be written as

$$\Lambda_{0,\mathbf{XX}} = E[\tilde{\mathbf{X}}(t)\tilde{\mathbf{X}}^{*T}(t)] = \int_0^\infty \mathbf{H}^*(\omega)\mathbf{S}(\omega)\mathbf{H}^T(\omega)d\omega \tag{57}$$

$$i\Lambda_{1,\mathbf{XX}} = E[\tilde{\mathbf{X}}(t)\dot{\tilde{\mathbf{X}}}^{*T}(t)] = -i\int_0^\infty \omega\mathbf{H}^*(\omega)\mathbf{S}(\omega)\mathbf{H}^T(\omega)d\omega \tag{58}$$

$$\Lambda_{2,\mathbf{XX}} = E[\dot{\tilde{\mathbf{X}}}(t)\dot{\tilde{\mathbf{X}}}^{*T}(t)] = \int_0^\infty \omega^2\mathbf{H}^*(\omega)\mathbf{S}(\omega)\mathbf{H}^T(\omega)d\omega. \tag{59}$$

The latter equations give, in compact form, all the envelope covariances of the nodal response in the stationary case, show-

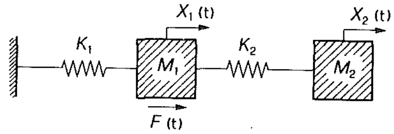

Fig. 1 The two-degrees-of-freedom system

ing the perfect correspondence with the pe-envelope covariances of the response process.

6.2 P.E.C. Matrix of the Output-Nonstationary Case. In order to obtain the PEC matrix of the output in the nonstationary case, the forcing function vector in equation (51) must be defined as in equation (17), it follows that the vector solution is given in the form

$$\tilde{\mathbf{U}}(t)=\theta(t)\tilde{\mathbf{U}}_0+\int_0^t \mathbf{L}(t-\tau)\tilde{\mathbf{F}}(\tau)d\tau=$$

$$=\theta(t)\mathbf{U}_0+\frac{2}{\sqrt{2}}\int_0^\infty e^{-i\omega t}\mathbf{N}^*(\omega,\ t)d\mathbf{Z}(\omega) \tag{60}$$

in which we have set

$$\mathbf{N}(\omega,\ t)=\int_0^t \mathbf{L}(t-\tau)\mathbf{A}(\omega,\ t)e^{-i\omega t(t-\tau)}d\tau \tag{61}$$

and $\tilde{\mathbf{U}}_0$ is the complex vector of initial conditions given as

$$\mathbf{U}_0=\frac{2}{\sqrt{2}}(\mathbf{U}_0-i\bar{\mathbf{U}}_0) \tag{62}$$

in which $\bar{\mathbf{U}}_0$ has the same probability distribution as $\mathbf{U}_0$.

The time-dependent PEC matrix of the vector $\tilde{\mathbf{U}}(t)$ is given in the form

$$\Sigma_{\tilde{U}\tilde{U}}(t)=\int_0^\infty \mathbf{N}^*(\omega,\ t)\mathbf{S}(\omega)\mathbf{N}^T(\omega,\ t)d\omega$$

$$+\theta(t)\Sigma_{\tilde{U}\tilde{U}}(0)\theta^T(t)+\mathbf{Q}(t)+\mathbf{Q}^{*T}(t) \tag{63}$$

in which $\Sigma_{\tilde{U}\tilde{U}}(0)$ is the PEC matrix evaluated at time $t=0$, and $\mathbf{Q}(t)$ is the complex matrix given in the form

$$\mathbf{Q}(t)=\theta(t)\int_0^t E[\tilde{\mathbf{U}}_0\tilde{\mathbf{F}}^T(\tau)]\mathbf{L}^T(t-\tau)d\tau. \tag{64}$$

For deterministic zero-start conditions, the PEC matrix is given in the simpler form

$$\Sigma_{\tilde{U}\tilde{U}}(t)=\int_0^\infty \mathbf{N}^*(\omega,\ t)\mathbf{S}(\omega)\mathbf{N}^T(\omega,\ t)d\omega \tag{65}$$

in which the various block matrices are given as

$$\Lambda_{0,\mathbf{XX}}(t)=\int_0^\infty \mathbf{R}_0^*(\omega,\ t)\mathbf{S}(\omega)\mathbf{R}_0^T(\omega,\ t)d\omega \tag{66}$$

$$i\tilde{\Lambda}_{1,\mathbf{XX}}(t)=\int_0^\infty \mathbf{R}_0^*(\omega,\ t)\mathbf{S}(\omega)\mathbf{R}_1^T(\omega,\ t)d\omega \tag{67}$$

$$\tilde{\Lambda}_{2,\mathbf{XX}}(t)=\int_0^\infty \mathbf{R}_1^*(\omega,\ t)\mathbf{S}(\omega)\mathbf{R}_1^T(\omega,\ t)d\omega \tag{68}$$

and

$$\mathbf{R}_0(\omega,\ t)=\int_0^t \mathbf{H}(t-\tau)\mathbf{A}(\omega,\ t)e^{-i\omega\tau}d\tau \tag{69}$$

$$\mathbf{R}_1(\omega,\ t)=\int_0^t \dot{\mathbf{H}}(t-\tau)\mathbf{A}(\omega,\ t)e^{-i\omega\tau}d\tau. \tag{70}$$

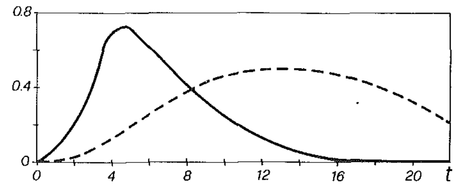

Fig. 2(a)

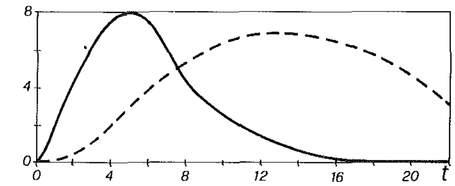

Fig. 2(b)

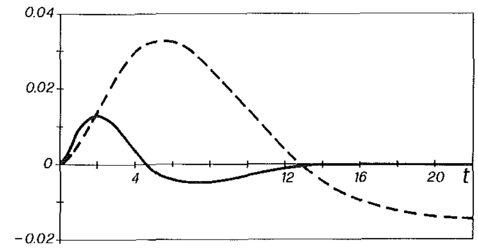

Fig. 2(c)

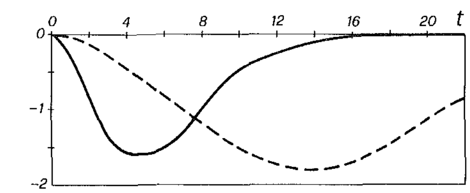

Fig. 2(d)

Fig. 2 Modal pre-envelope covariances: (a) dashed line $E[\tilde{Y}_1\ \tilde{Y}_1^*]$ full line 40 $E[\tilde{Y}_2\ \tilde{Y}_2^*]$, (b) dashed line $E[\dot{\tilde{Y}}_1\ \dot{\tilde{Y}}_1^*]$, full line $4E[\dot{\tilde{Y}}_2\ \dot{\tilde{Y}}_2^*]$, (c) dashed line Re $E(E[\tilde{Y}_1\ \dot{\tilde{Y}}_1^*])$, full line 4 Re$(E[\tilde{Y}_2\ \tilde{Y}_2])$, (d) dashed line Im$(E[\tilde{Y}_1\ \dot{\tilde{Y}}_2^*])$

Evaluating for each frequency the integrals in equations (69) and (70) and substituting the latter in equations (66)–(68), the various block matrices of $\Sigma_{\tilde{U}\tilde{U}}(t)$ can be computed.

7 Numerical Example

As an application, a two-degree-of-freedom, classically damped system depicted in Fig. 1 has been analyzed. In this case the vector solution $\mathbf{X}$ can be evaluated by means of the mode superposition as follows:

$$\mathbf{X}=\phi\mathbf{Y} \tag{71}$$

where ϕ is the modal matrix normalized with respect to $\mathbf{M}$, and $\mathbf{Y}$ is the vector solution of the decoupled modal differential equations. The examinated system is characterized by the following data

$M_1=M_2=1$ kg; $K_1=50$ New/cm; $K_2=33$ New/cm.

The modal analysis provided the following results:
Natural radian frequencies: $\omega_1=3.76$ rad/s; $\omega_2=10.93$ rad/s

Modal Matrix: $\phi=\begin{vmatrix} 0.811 & 0.585 \\ 0.585 & -0.811 \end{vmatrix}$

the damping ratio, here assumed equal for both modes, is $\xi=0.05$. The input process is defined as in equation (16), in which $A(\omega,\ t)$ is given in the form (Spanos, 1983):

$$A(\omega,\ t)=\sqrt{8}\exp\left(-\frac{1}{2}bt\right)t\exp\left(-\frac{1}{2}\beta(\omega)t\right);\ 0\leqq\omega<\infty. \tag{72}$$

The process $d\tilde{Z}(\omega)$ is such that

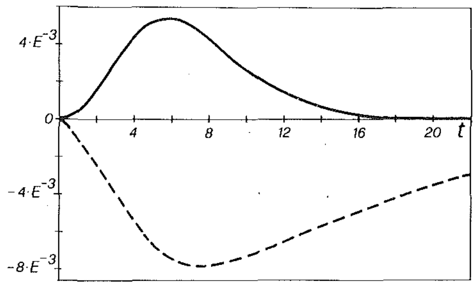

· Fig. 3(a)

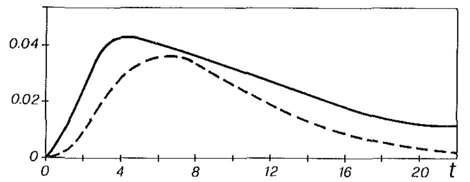

Fig. 3(b)

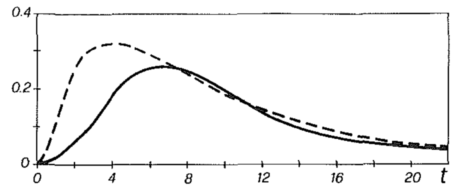

Fig. 3(c)

Fig. 3 Modal pre-envelope covariances: (a) dashed line Im($E[\tilde{Y}_1\tilde{Y}_2^*]$), full line Re($E[\tilde{Y}_1\tilde{Y}_2^*]$), (b) dashed line Im($E[\tilde{Y}_1\tilde{Y}_2^*]$), full line Re($E[\tilde{Y}_1\tilde{Y}_2^*]$), (c) dashed line Im($E[\tilde{Y}_1\tilde{Y}_2^*]$), full line Re($E[\tilde{Y}_1\tilde{Y}_2^*]$)

$$E[d\tilde{Z}(\omega_1)d\tilde{Z}(\omega_2)^*]=\alpha(\omega_1)\delta(\omega_2-\omega_1)d\omega_1 \quad (\omega>0). \tag{73}$$

The parameters chosen for the analysis are

$$b=.15\mathrm{s}^{-1};\ \beta(\omega)=\alpha(\omega)=(\omega/5\pi)^2\mathrm{s}^{-1}. \tag{74}$$

The spectrum of the input is characterized by a dominant frequency decreasing with time from about 5π rad/sec to 2π rad/sec, and by the fact that its total power initially increases with time and then gradually decreases.

In Fig. 2 the modal covariances of pre-envelope complex processes $\tilde{Y}_i(i=1, 2)$ are plotted. In these figures it can be seen that the peaks of the curves of the different modes are located at different instants, according to the behavior of the input process. It is to be emphasized that if the function $A(\omega, t)$ and the power spectral density function had been chosen as real functions, all the moments of the evolutionary power would be real functions, while in the new representation, $E[\tilde{Y}_i\dot{\tilde{Y}}_i]$, $i=1, 2$ are complex functions.

In Fig. 3 the various modal cross-covariances are plotted, while in Fig. 4 the (nodal) covariances of the pre-envelope complex process $\tilde{X}_2(t)$ (displacements of the second mass) are plotted.

From a practical point of view, the numerical evaluation of the nonstationary PEC needs to be conducted in the following way: First of all, in a suitable time interval, depending on the behavior of the input process, an adequate number of instants must be selected. For each instant, the $R_0(\omega, t)$, $R_1(\omega, t)$ complex coefficients given in equation (69), (70) have to be evaluated, and an integration over the instantaneous frequency range of the input process for every covariance must be effected according to equations (66)–(68).

These integrals are difficult to solve analytically, but are not affected by particular computational problems, so that the most delicate aspect of the numerical problem is the evaluation of the $R_0(\omega, t)$ and $R_1(\omega, t)$ coefficients. If no analytical solution of such integrals can be found, for each instant considered and for each coefficient, a different numerical integration from 0 to the current instant must be effected. Such integrals depend essentially on the form of the $\mathbf{A}(\omega, t)$ input function.

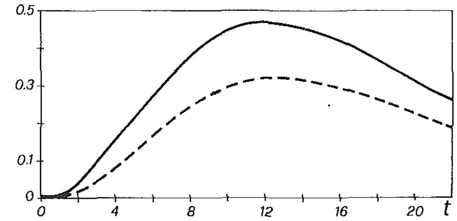

Fig. 4(a)

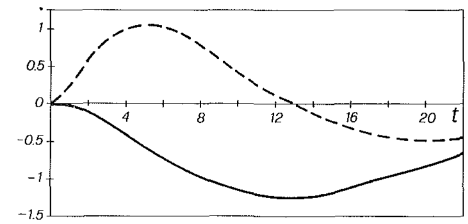

Fig. 4(b)

Fig. 4 Nodal pre-envelope covariances: (a) dashed line $E[\tilde{X}_2\tilde{X}_2^*]$, full line $E[\dot{\tilde{X}}_2\tilde{X}_2]/10$, (b) dashed line 50 Re($E[\tilde{X}_2\tilde{X}_2^*]$), full time Im($E[\tilde{X}_2\tilde{X}_2^*]$)

In the present application a closed-form solution was easily found, but it is not reported for brevity's sake.

8 Conclusions and Discussion

The probabilistic structures of a real Gaussian process is fully determined by the first two moments (mean and covariance). In some cases of engineering interest, however, we are concerned with the statistics of the so-called envelope, that is, for narrow band process, a smooth curve joining the peaks of the process. Following Dugundji (1958) in the stationary case, and Yang (1972) in the nonstationary case, the envelope is defined as the modulus of the pre-envelope, i.e., a complex process, the real part of which is the given process, while the imaginary part is related to the real ones in such a way that the resulting complex process exhibits power only in the positive frequency range. In order to obtain the statistics of the envelope, the variances of the pre-envelope need to be evaluated, rather than the variances of the given real process.

Here the covariances of such complex process have been evaluated, and it is shown that in the stationary case these covariances are strictly related to the so-called spectral moments. In particular, PEC matrix has been defined, the real part of which is the well-known covariance matrix of the real process, while its imaginary part contains the lowest imaginary part of the even SM, and the real part contains the first odd SM.

Because the statistical characterization of the envelope requires both the real and the imaginary parts of the complex process, both the real and the imaginary parts of the PEC matrix are essential for the evaluation of the peak statistics of the real process.

In order to extend the previous concepts to the nonstationary case, the complex representation of the nonstationary processes (introduced by Yang) has been adopted and extended to the vector processes, and the covariances of the pre-envelope process has been evaluated. The pre-envelope covariance coincides with the zeroth-order moment of the evolutionary power, while no analogous correspondence can be obtained between the higher moments of the evolutionary power and the covariances of the derivatives of the pre-envelope.

On other hand, remembering that the SM are useful quantities for the evaluation of the statistic of the peaks, and the latter are related to the moduli of the complex processes, it seems to be more appropriate to evaluate the higher-order time-dependent pre-envelope covariances of the various derivatives of the nonstationary complex processes, instead of the moments of the evolutionary power.

It is shown that the pre-envelope covariances are given as the sum of the traditional higher-order SM obtained as the moments of the evolutionary power and other similar quantities involving the derivatives of the modulating functions.

The pre-envelope covariance of a multi-degree-of-freedom linear system excited by a nonstationary, nonseparable process has been also discussed and the numerical aspects have been evidenced by means of a numerical example.

References

Arens, R., 1957, "Complex processes for envelopes of normal noise," *IRE Trans. on Information Theory*, Vol. 3, pp. 204-207.

Borino, G., Di Paola, M., and Muscolino, G., 1988, "Non-stationary spectral moments of base excited MDOF systems," *Earth. Engng. and Struct. Dyn.*, Vol. 16, pp. 745-756.

Corotis, R. S., Vanmarcke, E. H., and Cornell, C. A., 1972, "First Passage of Non-Stationary Random Processes," *Journal of Engng. Mech. Div.*, Vol. 98, No. EM2, pp. 401-414.

Di Paola, M., 1985, "Transient Spectral Moments of Linear Systems," *S. M. Archives*, Vol. 10, pp. 225-243.

Di Paola, M., and Muscolino, G., 1987, "Spectral Moments and Envelope for Non-Stationary Non-Separable Processes," *Proc. of the Int. Conf. ICASP 5*, Vol. 1, pp. 55-62.

Dugundji, J., 1958, "Envelope and Pre-Envelope of Real Waveforms," *IRE Transaction on Information Theory*, Vol. 4, pp. 53-57.

Hammond, J. K., 1968, "On the Response of Single and Multidegree of Freedom Systems to Non-Stationary Random Excitation," *Journal of Sound and Vibration*, Vol. 7, pp 393-416.

Kameda, A., 1975, "Evolutionary Spectra of Seismogram by Multifilter," *Journal of The Engng. Mech. Div.*, Vol. 101, No. EM6, pp. 787-801.

Krenk, S., Madsen, H. O., and Madsen, P. H., 1983, "Stationary and Transient Response Envelopes," *Journal of Engng. Mech. Div.*, Vol. 109, No. EM1, pp. 263-277.

Muscolino, G., 1988, "Non-Stationary Envelope in Random Vibration Theory," *Journal of Engng. Mech. Div.*, Vol. 114, No. 8, pp. 1396-1413.

Nigam, N. C., 1982, "Phase Properties of a Class of Random Processes," *Earthquake Engineering and Structural Dynamics*, Vol. 10, pp. 711-717.

Papoulis, A., 1965, "Probability Random Variables and Stochastic Processes," McGraw-Hill, Kogakusha, Tokyo.

Priestley, M. B., 1965, "Evolutionary Spectra and Non-Stationary Processes," *Journal of the Royal Statistical Society*, Vol. 27, pp. 204-228.

Shinozuka, M., 1970, "Random Processes with Evolutionary Power," *Journal of Eng. Mech. Div.*, Vol. 96, pp. 543-545.

Spanos, P. T. D., and Solomos, G. P., 1983, "Markov Approximation to Transient Vibration," *Journal of Eng. Mech. Div.*, Vol. 1, pp. 1134-1149.

To, C. W. S., 1986, "Response Statistic of Discretized Structures to Non-Stationary Vibration," *Journal of Sound and Vibration*, Vol. 105, pp. 217-231.

Vanmarcke, E. H., 1972, "Properties of Special Moments with Application to Random Vibration," *Journal of Eng. Mech. Div.*, Vol. 98, pp. 425-446.

Yang, J. N., 1972, "Non-Stationary Envelope Process and First Excursion Probability," *Journal of Structural Mechanics*, Vol. 1, pp. 231-248.

H. C. M. Chan [1]
Research Assistant,
Department of Civil Engineering,
Massachusetts Institute of Technology,
Cambridge, MA

The Principle of Asymptotic Proportionality

The Principle of Asymptotic Proportionality, which is based on the Green's function method for equilibrium problems, is proposed. Using this principle, the induced far-field variable due to any distribution of applied physical quantities can be approximated. This principle has been verified by considering the induced stresses due to applied tractions and dislocations in two-dimensional linear elastic media, and has been shown to be applicable to other physical phenomena such as electrostatics, gravitation, and electromagnetism.

Introduction

The Green's function method has been widely used to solve equilibrium problems (for example, see Hildebrand, 1976). For a physical system under equilibrium with given boundary conditions, the induced field variable (such as stress, temperature, and electrostatic potential), due to a unit concentrated "charge" (such as traction, heat source, and electrostatic charge), is given by a Green's function (or influence function). Using the Green's function, the resultant induced field due to any applied distribution of charges can be found. Capitalizing on this method of solution and postulating a specific property of the Green's function, the induced field at large distances from the location of the applied charges can be approximated.

Starting with the analysis of stress fields induced in a two-dimensional linear elastic medium by a certain applied traction distribution, the Principle of Asymptotic Proportionality (PAP) is introduced. Then it will be shown that PAP can also be applied to other applied charges, including semi-infinite dislocations, electrostatic charges, and heat and fluid flows.

The Principle of Asymptotic Proportionality

Consider a two-dimensional linear elastic medium with given boundary conditions (Fig. 1). The medium is at equilibrium with an arbitrary applied traction distribution (in the y-direction), $\rho(x)$, on a segment of length h on the x-axis. The stresses at a certain point P in the medium induced by the applied traction, $\rho(x)$, can be found by using the suitable Green's function for the given boundary conditions:

$$F=\int_0^h G(x,\overline{OP})\rho(x)dx \tag{1}$$

where F is a certain stress component and $G(x,\overline{OP})$ is the corresponding Green's function.

Using integration by parts, we have

$$F=\left[G(x,\overline{OP})\int_o^x \rho(x)dx\right]_{x=0}^{h} - \int_o^h\left(\int_o^x \rho(x)dx\right)\frac{dG(x,\overline{OP})}{dx}dx$$

$$=G(h,\overline{OP})\int_o^h \rho(x)dx-\int_o^h \rho^{(-1)}(x)G^{(1)}(x,\overline{OP})dx, \tag{2}$$

where

$$\rho^{(-1)}(x)=\int_o^x \rho(x)dx \tag{3}$$

and

$$G^{(1)}(x,\overline{OP})=\frac{dG(x,\overline{OP})}{dx}. \tag{4}$$

Hence,

$$F=G(h,\overline{OP})\rho^{(-1)}(h)-\int_o^h G^{(1)}(x,\overline{OP})\phi^{(-1)}(x)dx. \tag{5}$$

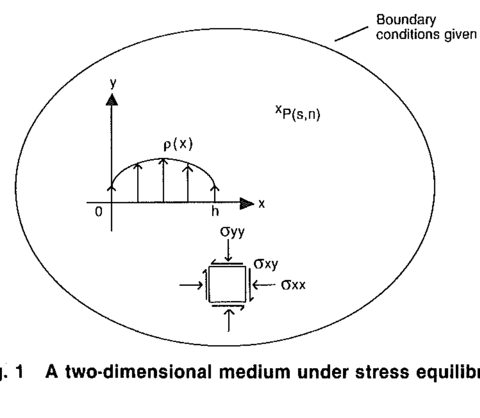

Fig. 1 A two-dimensional medium under stress equilibrium

[1] Presently at British Petroleum Research Centre, Sunbury-on-Thames, Middlesex TW16 7LN, U.K.

Contributed by the Applied Mechanics Division of THE AMERICAN SOCIETY OF MECHANICAL ENGINEERS for publication in the JOURNAL OF APPLIED MECHANICS.

Discussion on this paper should be addressed to the Technical Editor, Leon M. Keer, The Technological Institute, Northwestern University, Evanston, IL 60208, and will be accepted until two months after final publication of the paper itself in the JOURNAL OF APPLIED MECHANICS. Manuscript received and accepted by the ASME Applied Mechanics Division, April 12, 1988.

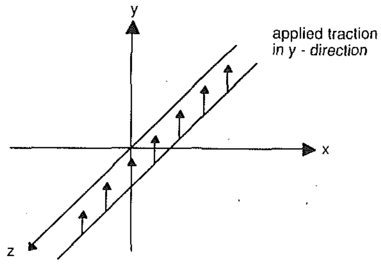

Fig. 2 Kelvin's problem for plane strain

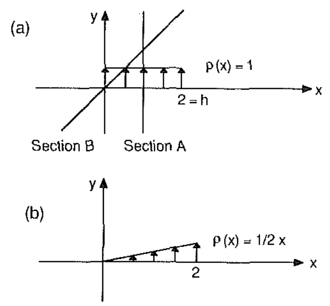

Fig. 3 Two different applied traction distributions

By applying integration by parts repeatedly to (5), we have

$$
\begin{aligned}
F = {} & G(h, \overline{OP})\rho^{(-1)}(h) - G^{(1)}(h, \overline{OP})\rho^{(-2)}(h) \\
& + G^{(2)}(h, \overline{OP})\rho^{(-3)}(h) - \ldots \\
& + (-1)^m G^{(m)}(h, \overline{OP})\rho^{(-m-1)}(h) \\
& + (-1)^{m+1}\int_o^h G^{(m+1)}(x, \overline{OP})\rho^{(-m-1)}(x)dx \qquad (6) \\
& (m = 0, 1, 2, \ldots),
\end{aligned}
$$

where

$$\rho^{(-i-1)}(x) = \int_o^x \rho^{(-i)}(x)dx$$

$$G^{(i+1)}(x, \overline{OP}) = \frac{d}{dx}G^{(i)}(x, \overline{OP}) \quad (i = 0, 1, 2, \ldots)$$

$$\rho^{(0)}(x) = \rho(x),\ G^{(0)}(x, \overline{OP}) = G(x, \overline{OP}).$$

Now if

$$
\begin{aligned}
& \rho^{(-1)}(h) = \rho^{(-2)}(h) = \ldots = \rho^{(-k)}(h) = 0, \\
& \qquad \rho^{(-k-1)}(h) \neq 0,\ (k = 1, 2, 3, \ldots), \qquad (7)
\end{aligned}
$$

then

$$
\begin{aligned}
F = {} & (-1)^k G^{(k)}(h, \overline{OP})\rho^{(-k-1)}(h) \\
& + (-1)^{k+1}\int_o^h G^{(k+1)}(x, \overline{OP})\rho^{(-k-1)}(x)dx. \qquad (8)
\end{aligned}
$$

(It has been implicitly assumed that $G(x, \overline{OP})$ is differentiable and $\rho(x)$ is integrable with respect to x $(k+1)$ times.) Let $r = |\overline{OP}|$. It is postulated that, with minor exceptions, $G^{(k+1)}(x, \overline{OP})$ (with $0 \leq x \leq h$) has a lower order of magnitude than $G^{(k)}(h, \overline{OP})$, when r/h is large. Assume (reasonably) that $\rho^{(-k-1)}(x)$ is finite and bounded. Thus, for large r/h,

$$F \cong (-1)^k G^{(k)}(h, \overline{OP})\rho^{(-k-1)}(h). \qquad (9)$$

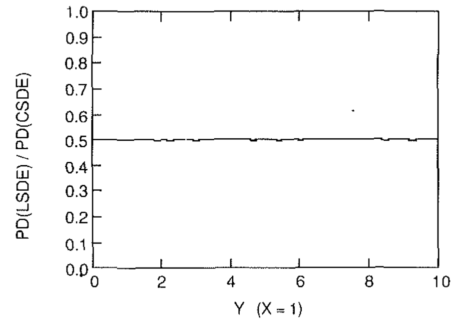

Fig. 4 Ratio of induced σ_{yy} along Section A

Equation (7) can be considered to be a set of conditions specifying that kth $(k = 1, 2, 3, \ldots)$ order equilibrium exists over the applied traction distribution. When (7) is not satisfied, zeroth-order equilibrium $(k = 0)$ is considered to exist.

The Principle of Asymptotic Proportionality (PAP) is thus stated as follows:

When the applied traction distribution is under the kth-order equilibrium, with minor exceptions, the induced stresses F at a point P far from the region of the applied tractions are approximately proportional to the $(k+1)$th integral of the applied distribution:

$$F \cong (-1)^k G^{(k)}(h, \overline{OP})\rho^{(-k-1)}(h). \qquad \text{(9 repeated)}$$

(The minor exceptions will be considered later.)

It should be noted that the aforementioned formulation for PAP can be applied to other physical quantities as long as linear superposition, as exemplified by (1), holds. Thus PAP can be applied to many physical phenomena such as electrostatic and magnetic fields, and heat and fluid flows.

Kelvin's Problem For Plane Strain

An example application of PAP is made using Kelvin's problem for plane strain in which a line force (with dimension force/length) is applied in the y-direction in an infinite linear elastic solid (Fig. 2). The Green's function for the induced stress σ_{yy} at point $P(s, n)$ is given by Crouch et al., 1983:

$$G(x, \overline{OP}) = 2(1-\nu)g_n - ng_{nn} \qquad (10)$$

where ν = Poisson's ratio

$$g(s, n) = \frac{1}{4\pi(1-\nu)} \ \ln[(s-x)^2 + n^2]^{1/2}$$

$$g_n = \partial g/\partial n = \frac{1}{4\pi(1-\nu)} \frac{n}{(s-x)^2 + n^2}$$

$$g_{nn} = \partial^2 g/\partial n^2 = \frac{1}{4\pi(1-\nu)} \frac{(s-x)^2 - n^2}{[(s-x)^2 + n^2]^2}. \qquad (11)$$

For a certain distribution of line forces, $\rho(x)$, as shown in Fig. 1, the induced stress, σ_{yy} at P, is given as F in equation (1). Now suppose that zeroth-order equilibrium exists $(k = 0)$. It is to be shown, as an example, that (9) holds for two specific traction distributions.

The first distribution is a constant distribution of applied traction along the x-axis and the second a linear distribution (Fig. 3). The induced stress, σ_{yy}, by each of the two distributions has been found in closed form (Chan, 1986) and the stresses are compared along Section A (Fig. 3(a)). The ratio of σ_{yy} due to the linear distribution (denoted by PD (LSDE)) to that due to the constant distribution (PD(CSDE)) is plotted in Fig. 4 against y. It can be seen that the ratio remains at around

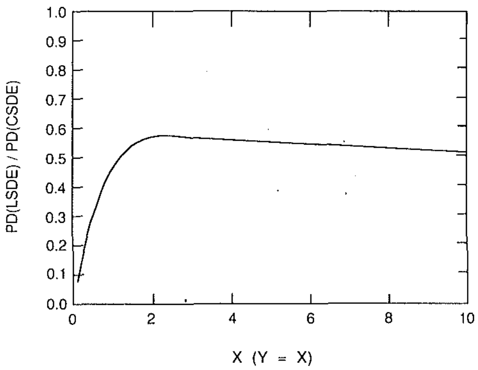

Fig. 5 Ratio of induced σ_{yy} along section B

0.5. This is because, as according to (9), σ_{yy} is approximately proportional to $\rho^{(-1)}(h)$, which is the total applied force (see (3)). The total applied force for the linear distribution is half of that for the constant distribution. The same ratio along Section B (Fig. 3(a)) is also plotted against x (Fig. 5). It can be seen that the ratio approaches 0.5 as x becomes large, i.e., r/h is large.

For self-equilibrating applied traction distributions, Saint-Venant's Principle holds which states that the induced stresses at points far from the origin are negligible (for example, see Sternberg, 1954; Horgan and Knowles, 1983). When viewed under the framework of PAP, we can see that the same conclusion can be reached. For self-equilibrating traction $\rho(x)$,

$$\rho^{(-1)}(h)=0 \qquad \text{(force equilibrium)}$$

$$\begin{aligned}\rho^{(-2)}(h) &= \int_o^h \rho^{(-1)}(x)dx \\ &= \Big[x\rho^{(-1)}(x)\Big]_o^h - \int_o^h x\rho(x)dx \\ &= \Big[h\rho^{(-1)}(h)-0\Big]-0 \qquad \text{(moment equilibrium)} \\ &=0.\end{aligned}$$

Thus, second or higher-order equilibrium exists ($k\geq 2$). From (9) and an inspection of (10) and (11), it can be concluded that the induced stress σ_{yy} approaches zero as r/h increases. Thus, in this example, PAP includes Saint-Venant's Principle and actually tells us how the induced stresses decay through (9).

Extended Concept of "Equilibrium"

The previous discussion shows that second-order equilibrium is static equilibrium under the conventional viewpoint. Applied distributions at higher-order equilibria and the resulting far-field stresses are examined in this section. Consider applied tractions on a straight line segment (Fig. 6) with example cases (b) to (f). Suppose we are interested in induced σ_{yy} at point P, denoted by σ, due to the applied tractions. At first we must determine the order of equilibrium of $\rho(x)$. For $\rho(x)$ given in Figs. 6(b) and 6(c), zeroth-order equilibrium ($k=0$) exists because

$$\rho^{(-1)}(1)=\int_o^1 \rho(x)dx\neq 0.$$

In these cases, σ is approximately proportional to $\rho^{(-k-1)}(1)=\rho^{(-1)}(1)$.

In case (b)

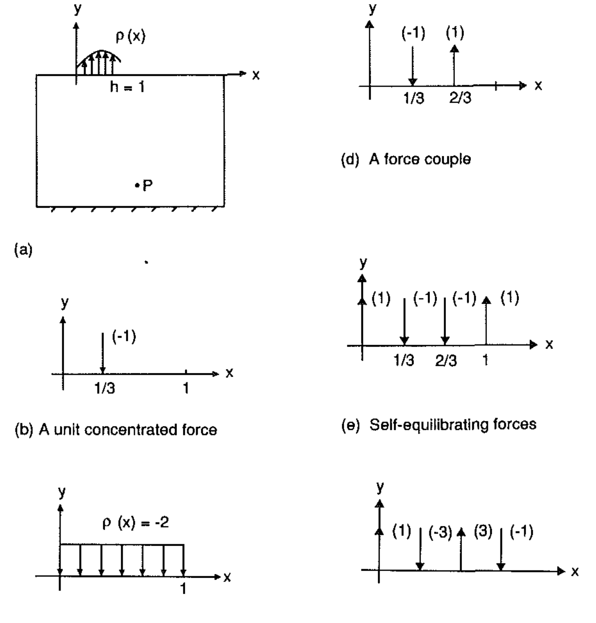

Fig. 6 Two-dimensional linear elastic medium under applied tractions

$$\rho(x)=-\delta\left(x-\frac{1}{3}\right),$$

where $\delta(x)$ is the Direc-Delta distribution. Therefore,

$$\rho^{(-1)}(1)=\int_o^1 -\delta\left(x-\frac{1}{3}\right)dx=-1.$$

In case (c),

$$\rho(x)=-2.$$

Therefore,

$$\rho^{(-1)}(1)=\int_o^1(-2)dx=-2.$$

Thus, σ in (c) is approximately twice that in (b), which agrees with intuition because the total applied force in (c) is twice that in (b). Here, Saint-Venant's principle cannot be applied directly because the applied tractions in (b) and (c) are not statically equivalent.

For case (d),

$$\rho(x)=-\delta\left(x-\frac{1}{3}\right)+\delta\left(x-\frac{2}{3}\right)$$

$$\begin{aligned}\therefore\ \rho^{(-1)}(x) &= \int_o^x \rho(x)dx \\ &= -u\left(x-\frac{1}{3}\right)+u\left(x-\frac{2}{3}\right),\end{aligned}$$

where $u(x)$ is the unit step function.

$$\begin{aligned}\rho^{(-2)}(x) &= \int_o^x \rho^{(-1)}(x)dx \\ &= -\left(x-\frac{1}{3}\right)u\left(x-\frac{1}{3}\right)+\left(x-\frac{2}{3}\right)u\left(x-\frac{2}{3}\right).\end{aligned}$$

Thus,

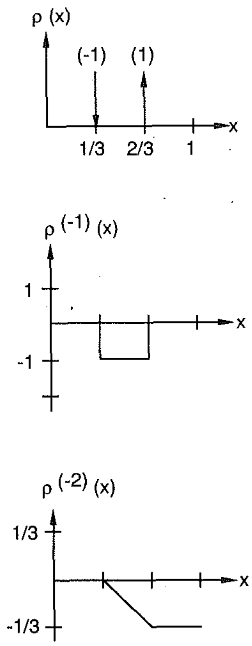

Fig. 7 Applied distribution at first-order equilibrium ($k=1$)

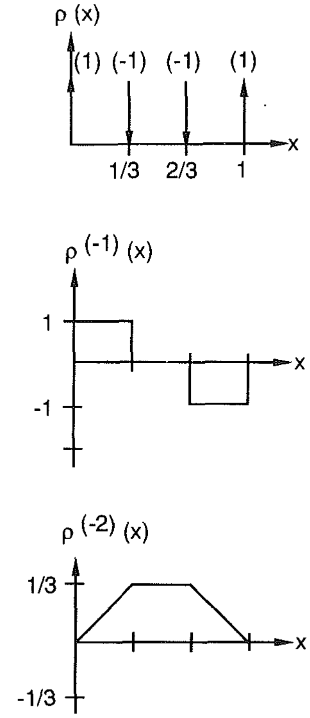

Fig. 8 Applied distribution at second-order equilibirum ($k=2$)

$$\rho^{(-1)}(1) = -1+1=0$$

$$\rho^{(-2)}(1) = -\left(1-\frac{1}{3}\right)+\left(1-\frac{2}{3}\right) = -\frac{1}{3}\neq 0.$$

Therefore, first-order equilibrium ($k=1$) occurs. This result can also be obtained by integrating $\rho(x)$ graphically as shown in Fig. 7.

Since $k=1$ in (*d*), σ in (*d*) is of a lower order of magnitude than that in (*b*) and (*c*).

For cases (*e*) and (*f*), static equilibrium exists, and by Saint-Venant's principle σ is small. However, by using PAP we can see further that σ in (*f*) is actually of a lower order than σ in (*e*). The integrations required to obtain the orders of equilibrium are carried out graphically in Figs. 8 and 9.

In Fig. 8, after obtaining $\rho^{(-2)}(x)$, it is clear that $\rho^{(-3)}(x)\neq 0$. Thus, $k=2$. In Fig. 9, $k=3$. Thus, one is tempted to say that the applied tractions in Fig. 9 is "more at equilibrium" than those in Fig. 8.

Theorem of Equivalent Expansions

Fracture opening and slip displacements can be modeled by semi-infinite dislocations (Chan, 1986). A semi-infinite dislocation occurs when there is a displacement discontinuity across the two surfaces of a slit which begins inside an infinite medium and extends to the boundary at infinity. Figure 10 shows a normal and a shear semi-infinite dislocation at the origin (D_d and D_b, respectively). Only the opening mode is considered in the following discussion.

Let $d_n(s)$ be the negative of the opening displacement along the fracture axis (Fig. 11). Within the infinitesimal element of length ds at s, the opening increases by an infinitesimal amount $dd_n(s)$, i.e., the applied infinitesimal dislocation at s is $dd_n(s)$. The applied dislocation distribution is then given by

$$\rho(s) = \frac{dd_n(s)}{ds}.$$

For an embedded fracture the closure condition demands that

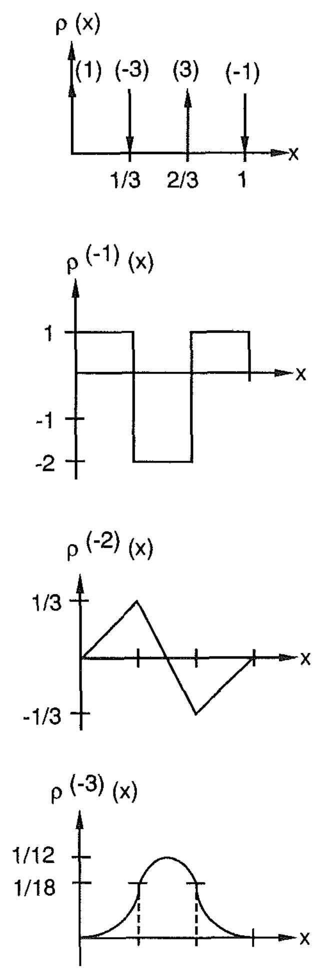

Fig. 9 Applied distribution at third-order equilibrium ($k=3$)

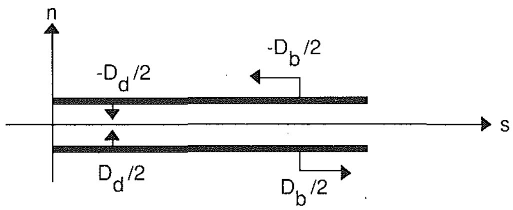

Fig. 10 Normal and shear semi-infinite dislocations

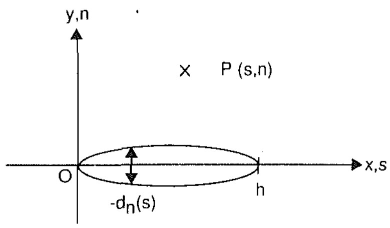

Fig. 11 Fracture opening modeled by normal dislocations

$$\int_o^h \frac{dd_n(s)}{ds} = 0$$

$$\text{i.e.,}\quad \rho^{(-1)}(h) = 0.$$

Thus, at least first-order equilibrium exists. When first-order equilibrium does exist, according to PAP the induced stresses/displacements at distances far from the crack are approximately proportional to $\rho^{(-2)}(h)$ and

$$\rho^{(-2)}(h) = \int_o^h \rho^{(-1)}(s)ds = \int_o^h d_n(s)ds.$$

The volume of expansion E of the fracture is defined as

$$E = -\int_0^h d_n(s)ds = -\rho^{(-2)}(h).$$

Thus, the Theorem of Equivalent Expansions, as a corollary of PAP, is formulated as follows:

Each induced stress or displacement component at large distances from a crack due to its opening, with minor exceptions, is approximately proportional to the expansion and is independent of the opening shape.

A numerical experiment was carried out to verify the Theorem of Equivalent Expansions in Chan (1986). The induced displacements and stresses due to the collapse of an underground fracture were modeled using a computer program called FROCK (acronym for Fractured ROCK). FROCK is based on a hybridized Displacement Discontinuity Element and Fictitious Stress Element scheme (Chan et al., 1988), in which exact, closed-form influence functions for the elements were used.

Fig. 12 shows a square medium with an embedded fracture under plain strain. If the fracture closes uniformly by 1 unit, the expansion is $-1\times 200 = -200$ square units. The induced displacements and stresses (as calculated using FROCK) along Section A (Fig. 12) are, respectively, shown in Figs. 13 and 14 in solid curves. When the expansion takes another shape in which the central half of the fracture closes uniformly by 2 units, the induced displacements and stresses are shown in Figs. 13 and 14 in dotted curves. One can see that the corresponding solid and dotted curves are very close to each other. This example shows that the induced displacements and stresses at locations far from the fracture mainly depend on the expansion of the fracture and not on the opening shape.

The Theorem of Equivalent Expansions for each of the induced stress components in an infinite medium has been proved in Chan (1986). There is an exception for induced σ_{xy} at points P near the vertical axis (i.e., $n \gg s$). However, in this case, the induced σ_{xy} is small compared with the two other induced stress components and, hence, the exception is considered to be minor.

Similarly, by considering shear dislocation, the Theorem of Equivalent Distortions has also been established (Chan, 1986). These two theorems have important applications in fracture mechanics including monitoring of underground fracture expansion using only surface measurements, indirect measurement of the expansion of a crack in a plate, and derivation of the equivalent moduli for fractured media.

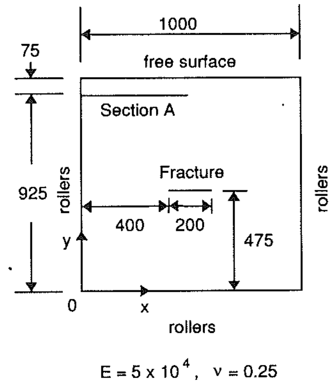

Fig. 12 Collapse of underground fracture

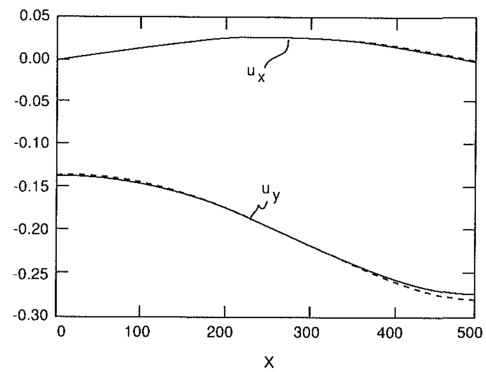

Fig. 13 Induced displacements along Section A due to closure of embedded fracture

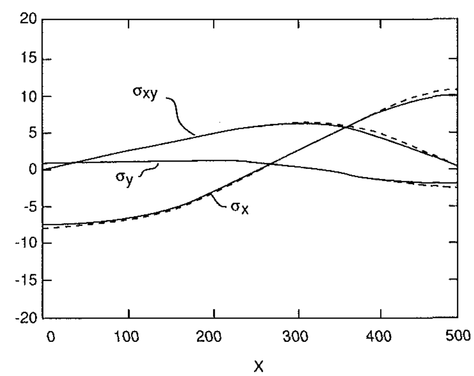

Fig. 14 Induced stresses along Section A due to closure of embedded fracture

Electrostatic Fields

The electric field strength (or electric intensity), E, in an infinite free medium with permittivity, ϵ, at a point P due to a point charge q is

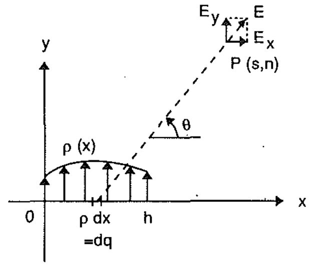

Fig. 15 Electric field due to applied charge distribution $\rho(x)$

$$\mathrm{E}=\frac{1}{4\pi\epsilon}\frac{q}{d^2}$$

where d is the distance between q and P. For an applied charge distribution $\rho(x)$ on the x-axis (Fig. 15), the Green's function of the x-component of the electric field E_x is then

$$G_x(x,\overline{OP})=\frac{\cos\theta}{4\pi\epsilon d^2}=\frac{1}{4\pi\epsilon}\frac{s-x}{[(s-x)^2+n^2]^{3/2}}.$$

($n=0$) far from the applied charges. In this case,

$$G_x(x,\overline{OP})=\frac{1}{4\pi\epsilon}\frac{1}{(s-x)^2}.$$

The postulate that (recall $r=|\overline{OP}|$)

$$G_x^{(k+1)}(x,\overline{OP})\ll G_x^{(k)}(h,\overline{OP}),\ 0\leq x\leq h,\ r/h \text{ is large,} \tag{12}$$

is clearly satisfied and PAP applies. If the point P is on the vertical axis, postulate (12) may not be satisfied. However, in this case E_x is small compared with E_y, and it can be shown that PAP applies to E_y whose Green's function is

$$G_y(x,\overline{OP})=\frac{\sin\theta}{4\pi\epsilon d^2}=\frac{1}{4\pi\epsilon}\frac{n}{[(s-x)^2+n^2]^{3/2}}.$$

Similar arguments can be used to show that PAP also applies to E_y with minor exceptions.

Other Potential Fields

After PAP has been shown to be applicable to electrostatics, generalization to other fields covered by potential theory is immediate. At first we examine how PAP can be applied in electrostatic potential theory:

The governing equation of the electrostatic potential $\Phi(s, n)$ is the Laplace's equation

$$\nabla^2\Phi=\frac{\partial^2\Phi}{\partial s^2}+\frac{\partial\Phi}{\partial n^2}=0. \tag{13}$$

The electric field (E_x, E_y) is given by

$$\mathrm{E}_x=-\frac{\partial\Phi}{\partial s},\ \mathrm{E}_y=-\frac{\partial\Phi}{\partial n}. \tag{14}$$

An applied concentrated charge q at the point $(x, 0)$ of an infinite medium with permittivity, ϵ, induces the potential

$$\Phi_q(s,n)=\frac{1}{4\pi\epsilon}\frac{q}{\sqrt{(s-x)^2+n^2}}.$$

The electrostatic potential Φ is then

$$\Phi=\Phi_q+\Phi_{\mathrm{ref}}$$

where Φ_{ref} is the reference potential, which is the potential existing before q is applied. It is assumed that Φ_{ref} is not affected by the application of q. For free space $\Phi_{\mathrm{ref}}=0$, and the equation for the electric field in the previous section can be obtained by (14). When $\Phi_{\mathrm{ref}}\neq 0$, both Φ_q and Φ_{ref} have to be considered in (14).

In the previous section it has been shown that PAP is applied to the partial derivative (E_x and E_y) of Φ_q, here it can also be shown that PAP applies to Φ_q itself since its Green's function is

$$G_q(x,\overline{OP})=\frac{1}{4\pi\epsilon}\frac{1}{\sqrt{(s-x)^2+n^2}}$$

which satisfies postulate (12) with some exceptions.

Note that PAP may not apply to Φ because its Green's function, if any, depends on Φ_{ref}.

At this point it is interesting to notice that the asymptotic behavior of the far-field potential has been widely examined (for example, see Owen, 1963, II.J). Usually isolated concentrated charges are considered and Taylor's series expansion is used on $G_q(x,\overline{OP})$ to arrive at an infinite series. PAP differs from this usual approach because repeated integration by parts, instead of the Taylor's series, is used to arrive at the infinite series in equation (6).

Since now that PAP has been shown to be applicable to electrostatic fields, PAP can also be applied to other potential fields such as gravitation, magnetism, temperature, and fluid velocity potential because they can all be represented by potential functions satisfying Laplace's equation. However, in the case of gravitation negative masses (if any) are required to create first and higher-order equilibria.

Magnetic Field of a Current-Carrying Wire

Consider a long straight wire in an infinite space carrying a current I pointing perpendicularly out of the $x-y$ plane. The current I can be regarded as a concentrated charge applied at the position of the wire. If the current is applied according to the distribution $\rho(x)$ on the $x-$axis, the Green's function for the x and $y-$ components of the induced magnetic field at P are, respectively,

$$G_x=\frac{-\mu}{2\pi}\frac{n}{(s-x)^2+n^2}$$

$$G_y=\frac{\mu}{2\pi}\frac{s-x}{(s-x)^2+n^2}$$

where μ is the permeability of the infinite space.

It can be shown that PAP applies to the magnetic field induced by the current-carrying wire, with minor exceptions. One application (which may not be economical at present) is that the induced magnetic field of current-carrying wires can be greatly reduced by arranging the wires so that a high-order equilibrium exists. For examples of higher-order equilibria, see Figs. 7 to 9. It is quite commonly known that a higher-order equilibrium distribution can be obtained by subtracting the shifted distribution from a given distribution: If $\rho(x)$ is at kth-order equilibrium, $\rho(x)-\rho(x-c)$ is at $(k+1)$-order equilibrium, where c is a nonzero constant.

Conclusion and Further Comments

A general physical principle (PAP) has been established which uses the Green's function method to approximate the induced far field due to any applied charge distribution. For most physical problems (especially for problems with finite boundaries), the corresponding Green's functions have not been found. However, even for those problems, PAP is useful because (9) gives at least an approximate proportional relationship.

This paper has dealt specifically with an applied charge distribution on a straight line segment. For two and three-dimensional geometries of applied charge distribution, similar formulations can be established.

Acknowledgments

Most of the present research results were obtained while the author was a research assistant in the Department of Civil Engineering, the Massachusetts Institute of Technology, under the supervision of Drs. V. Li and H. H. Einstein.

The research at the Massachusetts Institute of Technology was sponsored by the U.S. Army Research Office under grant No. DAAG24-83-K-0016 and was later continued at the California State University at Fullerton.

The author also appreciates the discussions with his colleagues at California State University, Fullerton, including Dr. G. Cohn on the topic of electrostatics.

References

Chan, H. C. M., 1986, "Automatic two-dimensional multi-fracture propagation modelling of brittle solids with particular application to rock," Sc.D. dissertation, Department of Civil Engineering, Massachusetts Institute of Technology, Cambridge, Mass.

Chan, H. C. M., Li, V., and Einstein, H. H., 1988, "A hybridized displacement discontinuity and indirect boundary element method to model fracture propagation," submitted to *International Journal of Fracture*, accepted for publication.

Crouch, S. L., and Starfield, A. M., 1983, *Boundary Element Methods in Solids Mechanics*, G. Allen and Unwin, pp. 46–47.

Hildebrand, F. B., 1976, *Advanced Calculus for Applications*, Prentice-Hall, Englewood Cliffs, N.J., pp. 652–658.

Horgan, C. O., and Knowles, J. K., 1983, "Recent developments concerning Saint-Verant's principle," *Advances in Applied Mechanics*, Vol. 23, pp. 179–269.

Owen, G. E., 1963, *Introduction to electromagnetic theory*, Allyn and Bacon.

Sternberg, E., 1954, "On Saint-Verant's principle," *Quarterly Appl. Math.*, Vol. 11, pp. 393–402.

Dynamics and Stability of a Flexible Cylinder in a Narrow Coaxial Cylindrical Duct Subjected to Annular Flow

M. P. Paidoussis
Fellow, ASME

D. Mateescu

W.-G. Sim

Department of Mechanical Engineering,
McGill University,
Montreal, Quebec, H3A 2K6 Canada

This paper considers analytically the dynamics of a flexible cylinder in a narrow coaxial cylindrical duct, subjected to annular flow. In the present analysis, in contrast to existing theory, the viscous forces are not derived by an adaptation of Taylor's unconfined-flow relationships, but by a systematic, albeit approximate, solution of the Navier-Stokes equations, which accounts for the unsteady viscous effects much more fully than heretofore; it is found that, for very narrow annuli, the contribution of these unsteady viscous forces to the overall unsteady forces on the cylinder can be much larger than that of the steady skin friction and pressure-drop effects alone. The present analysis also differs from existing theory in that the inviscid forces are not derived via the slender-body approximation, and hence the analysis is also applicable to bodies of relatively small length-to-radius ratio.

The dynamics and stability of typical systems with fixed ends is investigated, concentrating mainly on viscous effects and comparing the results with those of previous work. It is found that, as the annular gap becomes narrower, the system loses stability by divergence at smaller flow velocities, provided the gap size is such that inviscid fluid effects are dominant. For very narrow annuli, however, where viscous forces predominate, this trend is reversed, and further narrowing of the annular gap has a stabilizing effect on the system; furthermore, in some cases the system loses stability by flutter *rather than divergence.*

1 Introduction

The dynamics of cylindrical beams in axial flow was first studied theoretically and experimentally in the 1960s by Paidoussis (1966a,b) for systems in unconfined flow. In the theory, the inviscid forces were formulated by means of slender-body theory, and viscous forces were adapted from formulations developed earlier for unconfined flows by Taylor (1952). It was found, both theoretically and experimentally, that cylinders with both ends supported lose stability by divergence, followed at higher flow by coupled-mode flutter; in contrast, cantilevered cylinders lose stability by one-degree-of-freedom flutter (Hopf bifurcation), and this only if the free end is streamlined (i.e., it is terminated by an ogival end). Similar work was conducted for towed cylinders, displaying a more intricate dynamical behavior (Hawthorne, 1961; Paidoussis, 1968).

The theory was extended later (Paidoussis, 1973), removing an inconsistency in the formulation of the viscous forces (which did not change the predicted dynamical behavior substantially) and considering the effect of confinement of the flow by a duct. Both inviscid and viscous forces were developed from the earlier formulations. It was found that, as the flow is confined, the unsteady inviscid forces associated with lateral motions of the system become larger (effectively, the virtual mass of the fluid is increased) and the system loses stability much earlier.

The theory was further refined (Paidoussis and Ostoja-Starzewski, 1981) by (*i*) deriving the inviscid forces for confined flow by the full (linear) potential-flow theory, rather than the slender-body approximation, so that the analysis be applicable to nonslender cylinders also, and (*ii*) considering compressibility effects. The inviscid forces in this case were formulated by means of the generalized force Fourier-transform method. It was found that the potential flow refinement effectively raised the critical flow velocities for instability, since slender-body theory overestimates the fluid-dynamic forces on cylinders of relatively small length-to-radius ratio, L/a. Compressibility effects were found to be secondary, unless L/a were small. Nevertheless, in this otherwise sophisticated analysis of the problem, the viscous force formulation based on an adaptation of Taylor's expressions for unconfined flow was retained.

Contributed by the Applied Mechanics Division of The American Society of Mechanical Engineers for publication in the Journal of Applied Mechanics.

Discussion on this paper should be addressed to the Technical Editor, Prof. Leon M. Keer, The Technological Institute, Northwestern University, Evanston, IL 60201, and will be accepted until two months after final publication of the paper itself in the Journal of Applied Mechanics. Manuscript received by the ASME Applied Mechanics Division, April 5, 1988; final revision, March 28, 1989.

In parallel to the foregoing, similar and notable research on the dynamics and flow-induced vibration of cylinders in axial flow was conducted by Chen and co-workers (Chen and Wambsganss, 1971; Chen, 1977; Yeh and Chen, 1978), where the references cited are examples of an extensive set of publications.

This paper presents a new formulation of the equations of motion, with the following principal differences to existing theory. First, the inviscid forces are obtained by potential flow theory, not using the slender-body approximation, so the theory is applicable also to cylinders of small length-to-radius ratio—but utilizing the simplifying assumption of a small annular gap with respect to the cylinder radius (Mateescu and Paidoussis, 1984), corresponding to the technologically most important geometry (Hobson, 1982; Mateescu and Paidoussis, 1985, 1987). Second, and this is the principal contribution of the present work, the unsteady viscous forces were not formulated by an adaptation of Taylor's expressions but by a systematic, albeit approximate, application of the Navier-Stokes equations (Mateescu and Paidoussis, 1985). The need for this new formulation becomes obvious when it is realized that the earlier one based on Taylor's expressions gives rise to viscous forces which are associated with skin friction and pressure-drop effects and are therefore passive, in the sense that they do not influence the *unsteady flow* around the oscillating cylinder. Although this is quite reasonable for unconfined or slightly confined flow, it is clearly not realistic for highly confined annular flows. In this paper, these unsteady coupled viscous effects, i.e., the viscosity-related modification of the unsteady pressure, are taken into account, albeit approximately, and will be seen to exert considerable influence on the dynamics of the system.

The motivation for this study is both academic and practical. Rigid or flexible cylindrical elements in narrow annular flows are widely used in engineering and have been known to be subject to instabilities and large vibrations; e.g., control rods in guide tubes of PWR-type nuclear reactors, fuel-cluster stringers in AGR-type reactors, feedwater spargers in BWR-type reactors, tubes in the baffle regions of some kinds of heat exchangers, and certain types of valves and pistons (Mateescu and Paidoussis, 1985, 1987). The interested reader is also referred to Hobson's (1982) and Mulcahy's (1980, 1983, 1988) work on flow-induced instabilities in narrow annuli, sometimes referred to as leakage-flow-induced vibrations or instabilities.

2 The Equation of Cylinder Motions

The cylinder under consideration has radius a (diameter $D=2a$), cross-sectional area A_s, length L, density ρ_s, and flexural rigidity EI. The annular gap is H, hence the radius of the confining duct is $a_d=a+H$, and the undisturbed flow velocity in the annulus is U (Fig. 1).

Let $e_o(x,t)$ be the lateral displacement of the cylinder, which is assumed to be small. The equation of motions may be written in the form (Paidoussis, 1973)

$$EI\frac{\partial^4 e_o}{\partial x^4}-\left[-\frac{\partial P_m}{\partial x}A_s(L-x)+\int_x^L F_l dx\right]\frac{\partial^2 e_o}{\partial x^2}$$
$$-\frac{\partial P_m}{\partial x}A_s\frac{\partial e_o}{\partial x}+\rho_s A_s\frac{\partial^2 e_o}{\partial t^2}=F_p+F_v, \quad (1)$$

where $P_m(x)$ is the mean pressure in the duct, $F_p(x,t)$ is the unsteady potential (inviscid) fluid force acting on the oscillating cylinder per unit length, $F_v(x,t)$ is the unsteady lateral viscous fluid force, and $F_l(x)$ is the longitudinal steady viscous force per unit length due to the longitudinal component of skin friction on the cylinder. This form of the equation of motion applies to the case where the cylinder, although clamped at both ends in terms of lateral motion, can slide axially at the downstream end, so that terms due to pressurization (Paidoussis, 1973) are absent here, but will be discussed later. It is thus obvious that equation (1) is that for an Euler-Bernoulli beam, subjected to variable tension arising from surface traction due to skin friction, which is related to the pressure drop in the annular flow, as well as to coupled inviscid and viscous lateral forces.

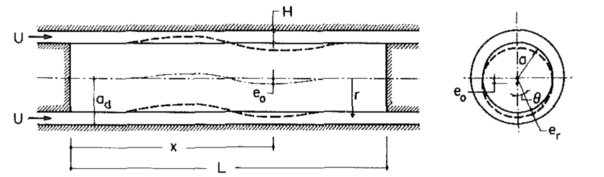

Fig. 1 Geometry of the cylinder oscillating in a duct with annular flow

The task ahead is the determination of the inviscid force, F_p, in Section 3, and the viscous forces F_l, F_v, and $(\partial P_m/\partial x)\times A_s$ in Section 4.

3 Derivation of the Inviscid Forces

These forces will be derived by potential flow theory. The velocity potential, $\Phi(x, r, \theta, t)$, must satisfy the Laplace equation

$$\nabla^2\Phi=\frac{\partial^2\Phi}{\partial x^2}+\frac{\partial^2\Phi}{\partial r^2}+\frac{1}{r}\frac{\partial\Phi}{\partial r}+\frac{1}{r^2}\frac{\partial^2\Phi}{\partial\theta^2}=0, \quad (2)$$

subjected to the boundary conditions

$$\left.\frac{\partial\Phi}{\partial r}\right|_{r=a_d}=0,$$
$$\left.\frac{\partial\Phi}{\partial r}\right|_{r=a}=\frac{\partial e_r}{\partial t}+\left[\frac{\partial\Phi}{\partial x}\frac{\partial e_r}{\partial x}+\frac{1}{r}\frac{\partial\Phi}{\partial\theta}\frac{1}{r}\frac{\partial e_r}{\partial\theta}\right]_{r=a},$$
$$\left.\frac{\partial\Phi}{\partial x}\right|_{x\to-\infty}=U, \quad (3)$$

where e_r is the radial displacement at the azimuthal direction θ,

$$e_r(x,\theta,t)=e_o(x,t)\cos\theta=E(x)\cos\theta\, e^{i\Omega t}. \quad (4)$$

The velocity potential may be written as

$$\Phi=\phi_s+\phi, \quad (5)$$

the sum of steady and unsteady components. Because of cylindrical symmetry, the steady-state component simply gives $\partial\phi_s/\partial x=U$. Hence, assuming small motions, the boundary conditions may be linearized and simplified to

$$\left.\frac{\partial\phi}{\partial r}\right|_{r=a_d}=0,\quad \left.\frac{\partial\phi}{\partial x}\right|_{x\to-\infty}=0, \quad (6)$$

$$\left.\frac{\partial\phi}{\partial r}\right|_{r=a}=\frac{\partial e_r}{\partial t}+U\frac{\partial e_r}{\partial x}=[i\Omega\, E(x)+U\, E'(x)]\cos\theta\, e^{i\Omega t}, \quad (7)$$

where the prime denotes differentiation with respect to x.

Now, $E(x)$ could be clearly expressed in terms of eigenfunctions $\psi_k(x)$ of a beam with the same boundary conditions as the cylinder under consideration (clamped-clamped). However, as will be seen shortly, it is more convenient to separate these eigenfunctions into two components, one trigonometric, $\psi_{1k}(x)$, and the other hyperbolic, $\psi_{2k}(x)$; thus,

$$E(x)=\sum_k a_k\psi_k(x)=\sum_k a_k[\psi_{1k}(x)+\psi_{2k}(x)], \quad (8)$$

where

$$\psi_{1k}(x) = -\cos\beta_k x + \sigma_k \sin\beta_k x,$$
$$\psi_{2k}(x) = \cosh\,\beta_k x - \sigma_k \sinh\,\beta_k x \tag{9}$$

and $\sigma_k = (\cosh\,\beta_k L - \cos\,\beta_k L)/(\sinh\,\beta_k L - \sin\,\beta_k L)$, the $\beta_k L$ being the corresponding eigenvalues.

In view of equations (4) and (8), reduced potentials $\hat{\phi}_k(x,r)$ may be introduced as follows:

$$\phi(x,r,\theta,t) = \sum_k a_k \hat{\phi}_k(x,r)\,\cos\theta\, e^{i\Omega t}. \tag{10}$$

Furthermore, changing variable r to z, defined by

$$z = r - a, \tag{11}$$

and restricting the analysis to very narrow annuli, where $r - a \ll a$, so that $1/r \simeq 1/a$, one obtains

$$\frac{\partial^2 \hat{\phi}_k}{\partial x^2} + \frac{\partial^2 \hat{\phi}_k}{\partial z^2} + \frac{1}{a}\frac{\partial \hat{\phi}_k}{\partial z} - \frac{1}{a^2}\hat{\phi}_k = 0, \tag{12}$$

with the boundary conditions

$$\left.\frac{\partial \hat{\phi}_k}{\partial z}\right|_{z=ha} = 0, \quad \left.\frac{\partial \hat{\phi}_k}{\partial z}\right|_{z=0} = i\Omega\,\psi_k(x) + U\,\psi_k'(x), \tag{13}$$

where $h = (a_d - a)/a = H/a$.

The solution of (12) may be effected by separation of variables. Thus, defining

$$\hat{\phi}_k(x,z) = f_k(x)\,F_k(z) \tag{14}$$

and substituting into (12) gives

$$d^2 f_k/dx^2 \pm \beta_k^2 f_k(x) = 0, \tag{15a}$$

$$a^2\, d^2F_k/dz^2 + a\, dF_k/dz - (1 \pm \beta_k^2\, a^2)\,F_k(z) = 0, \tag{15b}$$

where, in view of equations (9), the separation variable is equal to β_k^2. Clearly the two sets of solutions arising for $+\beta_k^2$ and $-\beta_k^2$ can each be associated with either ψ_{1k} or ψ_{2k} defined by (9), which a posteriori justifies the introduction of these two components of ψ_k.

Considering the $+\beta_k^2$ case, it is found that

$$f_{1k}(x) = A_1\,\cos\,\beta_k x + A_2\,\sin\,\beta_k x,$$
$$F_{1k}(z) = [\cosh\,(q_k z/a) + R_1\,\sinh\,(q_k z/a)]e^{-\frac{1}{2}z/a}, \tag{16}$$

where

$$q_k = \left[\frac{5}{4} + \beta_k^2\,a^2\right]^{1/2}. \tag{17}$$

Substituting into boundary conditions (13) leads to

$$f_{1k}(x)[dF_{1k}/dz]_{z=0} = i\,\Omega\,\psi_{1k}(x) + U\,\psi_{1k}'(x),$$
$$f_{1k}(x)[dF_{1k}/dz]_{z=ha} = 0, \tag{18}$$

through which the constants A_1, A_2, R_1, may be determined, and thus also $\hat{\phi}_{1k}$. Proceeding similarly, the solution associated with $-\beta_k^2$ in equations (15), $\hat{\phi}_{2k}$, may also be determined. Hence, $\hat{\phi}_k = \hat{\phi}_{1k} + \hat{\phi}_{2k}$, evaluated on the surface of the cylinder $(z=0)$, is found to be

$$\hat{\phi}_k(x,0) = a\sum_{j=1}^{2} G_{jk}[i\Omega\,\psi_{jk}(x) + U\,\psi_{jk}'(x)], \tag{19}$$

where

$$G_{1k} = \frac{-q_k + \dfrac{1}{2}\tanh\,(q_k h)}{\left(q_k^2 - \dfrac{1}{4}\right)\tanh\,(q_k h)},$$

$$G_{2k} = \begin{cases} \dfrac{c_k^* - \dfrac{1}{2}\tan\,(c_k^* h)}{\left(c_k^{*2} + \dfrac{1}{4}\right)\tan(c_k^* h)}, & \text{for } \beta_k^2 a^2 > \dfrac{5}{4}, \\[2ex] \dfrac{-c_k + \dfrac{1}{2}\tanh\,(c_k h)}{\left(c_k^2 - \dfrac{1}{4}\right)\tanh\,(c_k h)}, & \text{for } \beta_k^2 a^2 < \dfrac{5}{4}; \end{cases}$$

the q_k are given by (17) and

$$c_k^* = \left[\beta_k^2 a^2 - \frac{5}{4}\right]^{1/2}, \quad c_k = \left[\frac{5}{4} - \beta_k^2 a^2\right]^{1/2}. \tag{21}$$

It ought to be noted that the restriction of the analysis to narrow annuli results in a closed-form solution; otherwise, a solution would still have been possible, but would involve Bessel functions.

Having determined ϕ, and hence Φ, the pressure on the surface of the cylinder may be found, after suitable linearization, through the unsteady Bernoulli equation,

$$P - P_\infty = \frac{1}{2}\rho\,U^2 - \frac{1}{2}\rho\,|\nabla\Phi|^2 - \rho\frac{\partial\Phi}{\partial t} \tag{22}$$

where ρ is the fluid density. Hence, the force on the cylinder may be obtained by integration,

$$F_p(x,\,t) = -\int_0^{2\pi} a[P - P_\infty]\Big|_{r=a}\cos\theta\,d\theta. \tag{23}$$

Utilizing equations (5) and (19) and $d\phi_s/dx = U$ in (22), F_p is found from equation (23) to be

$$F_p(x,\,t) = -\rho\,a^2\,\pi\,e^{i\Omega t}\sum_k a_k(-\Omega^2 P_{k2} + i\Omega\,P_{k1} + P_{k0}), \tag{24}$$

where each of the P_{kj} is associated with the jth time derivative. Hence, P_{k2} is the component associated with inertial effects, P_{k1} with damping effects, and P_{k0} with stiffness effects; they are given by

$$P_{k2} = -\sum_{j=1}^{2} G_{jk}\psi_{jk}, \quad P_{k1} = -2U\sum_{j=1}^{2} G_{jk}\psi_{jk}',$$

$$P_{k0} = -U^2\,\beta_k^2\sum_{j=1}^{2}(-1)^j G_{jk}\psi_{jk}. \tag{25}$$

4 Determination of the Viscous Forces

It is most convenient to develop this work in nondimensional terms, and to this end

$$X = \frac{x}{L},\ R = \frac{r}{a},\ h = \frac{H}{a},\ l = \frac{L}{a},$$

$$T = \frac{Ut}{a},\ p = \frac{P - P_\infty}{\rho\,U^2} = p_v + p_p, \tag{26}$$

are defined, where the subscripts p and v stand for potential and viscous components, respectively. Hence, for fully developed laminar flows the continuity and the first of the three Navier-Stokes equations may be written as

$$\frac{1}{l}\frac{\partial u}{\partial x} + \frac{1}{R}\frac{\partial}{\partial R}(Rv) + \frac{1}{R}\frac{\partial w}{\partial\theta} = 0, \tag{27}$$

$$\frac{\partial u}{\partial T} + \frac{u}{l}\frac{\partial u}{\partial X} + v\frac{\partial u}{\partial R} + \frac{w}{R}\frac{\partial u}{\partial\theta}$$
$$= \frac{2h}{\mathrm{Re}}\left[\frac{1}{l^2}\frac{\partial^2 u}{\partial X^2} + \frac{1}{R}\frac{\partial}{\partial R}\left(R\frac{\partial u}{\partial R}\right)\right.$$

$$+ \frac{1}{R^2} \frac{\partial^2 u}{\partial \theta^2} \Big] - \frac{1}{l} \frac{\partial p}{\partial X}, \tag{28}$$

while the other two Navier-Stokes equations are not given here for brevity; u, v, w are the components of the dimensionless flow velocity, nondimensionalized with respect to the mean flow velocity U, and Re is the Reynolds number based on the hydraulic diameter of the annulus; $D_H = 2H = 2ah$.

The velocity vector associated with potential flow may be written as $U[(1+u_p)i_x + v_p i_r + w_p i_\theta]$, where $u_p = (\partial\phi/\partial x)/U$, $v_p = (\partial\phi/\partial r)/U$, $w_p = (\partial\phi/\partial\theta)/Ur$, and the associated perturbation pressures as $p_p = (P_p - P_\infty)/(\rho\ U^2)$. Then, one may write

$$u(x,r,\theta,t) = u_v(x,r;\theta,t) + u_p(x,r,\theta,t) \tag{29}$$

and similarly, for v, w, and p, where u_v, v_v, w_v, and p_v, the components associated with viscous effects are considered to depend only slightly on θ and t.

Now, for potential flow, equations (27), (28) may be reduced to Euler's equations of motion, which subtracted from (27), (28) yield

$$\frac{1}{l} \frac{\partial u_v}{\partial X} + \frac{1}{R} \frac{\partial}{\partial R} (R\ v_v) + \frac{1}{R} \frac{\partial w_v}{\partial \theta} = 0, \tag{30}$$

$$\begin{aligned} &\frac{\partial u_v}{\partial T} + \frac{u}{l} \frac{\partial u_v}{\partial X} + v \frac{\partial u_v}{\partial R} + \frac{w}{R} \frac{\partial u_v}{\partial \theta} \\ &\quad + \frac{u_v - 1}{l} \frac{\partial u_p}{\partial X} + v_v \frac{\partial u_p}{\partial R} + \frac{w_v}{R} \frac{\partial u_p}{\partial \theta} \\ &\quad = \frac{2h}{\mathrm{Re}} \Big[\frac{1}{l^2} \frac{\partial^2 u}{\partial X^2} + \frac{1}{R} \frac{\partial}{\partial R} \Big(R \frac{\partial u}{\partial R} \Big) \\ &\quad + \frac{1}{R^2} \frac{\partial^2 u}{\partial \theta^2} \Big] - \frac{1}{l} \frac{\partial p_v}{\partial X} = 0, \end{aligned} \tag{31}$$

and, similarly, for the other two Navier-Stokes equations.

These equations are then simplified drastically by invoking once more that $h \ll 1$ for narrow annuli and by introducing the following assumptions which are similar to those utilized by boundary layer theory, and which may be justified for not very high oscillation frequencies and Reynolds numbers: (i) the radial component of viscous motion v_v is negligible and (ii) the circumferential and axial variations in u and w are negligible as compared to radial variations of the same components. A fuller account of the foregoing may be found in Mateescu and Paidoussis (1987), where it is shown that on the basis of these assumptions equations (30), (31) reduce to

$$\frac{\partial^2 u}{\partial Z^2} = \frac{\mathrm{Re}}{2h} \frac{1}{l} \frac{\partial p_v}{\partial X}, \quad \frac{\partial^2 w}{\partial Z^2} = \frac{\mathrm{Re}}{2h} \frac{1}{R} \frac{\partial p_v}{\partial \theta},$$

$$0 \simeq \frac{\partial p_v}{\partial Z}, \tag{32}$$

where Z is defined as $Z = z/a = R - 1$.

With the aid of Fig. 2, the total *mean* (over the gap height) dimensionless velocity may be approximated by

$$\bar{V}(X,\theta,t) = \bar{u}\cos\beta + \bar{w}\sin\beta, \tag{33}$$

where β may be expressed as

$$\sin\beta = \bar{w}/\bar{V} \simeq \bar{w}(X,\theta,t), \tag{34}$$

since the dimensionless total mean velocity is approximately equal to unity. This is the key to this simplified treatment of unsteady viscous effects: The total mean flow velocity remains approximately constant in magnitude, but its direction fluctuates circumferentially through a small angle β, associated with cylinder motions.

For the purposes of this simplifed analysis, $\bar{w}$ will be calculated from the potential flow as obtained in Section 3;

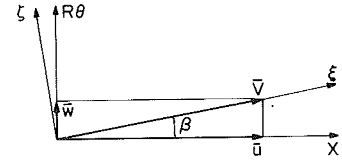

Fig. 2 Diagram showing transformation of coordinates and definition of the angle β

from the potential ϕ and the relationship $w = (\partial\phi/\partial\theta)/(UaR)$, one obtains by integrating across the gap

$$\bar{w} = \sum_k \frac{a_k}{Uh} \Big[\sum_{j=1}^{2} f_{jk}\ W_{jk} \Big] \sin\theta\ e^{i\Omega t}, \tag{35}$$

where

$$f_{jk} = G_{jk}[i\ \Omega\ \psi_{jk} + U\ \psi'_{jk}],$$

$$W_{1k} = \int_0^h \frac{-1}{1+Z} [\cosh(q_k Z) + R_1 \sinh(q_k Z)] e^{1/2Z} dZ, \tag{36}$$

$$W_{2k} = \begin{cases} \displaystyle\int_0^h \frac{-1}{1+Z} [\cos(c_k^* Z) + R_2^* \sin(c_k^* Z)] e^{1/2Z} dZ, & \text{for } (\beta_k a)^2 > \dfrac{5}{4}, \\ \displaystyle\int_0^h \frac{-1}{1+Z} [\cosh(c_k Z) + R_1 \sinh(c_k Z)] e^{1/2Z} dZ, & \text{for } (\beta_k a)^2 < \dfrac{5}{4}, \end{cases}$$

the q_k, c_k, and c_k^* have been given in (17) and (21) and

$$R_1 = \frac{q_k \sinh(q_k h) - \frac{1}{2}\cosh(q_k h)}{-q_k \cosh(q_k h) + \frac{1}{2}\sinh(q_k h)},$$

$$R_2^* = \frac{c_k^* \sin(c_k^* h) + \frac{1}{2}\cos(c_k^* h)}{c_k^* \cos(c_k^* h) - \frac{1}{2}\sin(c_k^* h)},$$

$$R_2 = \frac{-c_k \sinh(c_k h) + \frac{1}{2}\cosh(c_k h)}{c_k \cosh(c_k h) - \frac{1}{2}\sinh(c_k h)}. \tag{37}$$

Using the chain rule of differentiation, the first two of equations (32) may be combined in terms of the new set of coordinates (ξ, ζ) (see Fig. 2) leading to

$$\frac{\partial^2 V}{\partial Z^2} = \frac{\mathrm{Re}}{2h} \frac{\partial p_v}{\partial \xi}, \tag{38}$$

where $V = V(Z)$. Applying equation (38) to the usual no-slip boundary condition gives

$$V(Z) = -\frac{\mathrm{Re}}{2h} \frac{\partial p_v}{\partial \xi} \Big[\frac{1}{2} Z(h-Z) \Big]. \tag{39}$$

By integrating over the narrow annulus, the total mean nondimensional flow velocity, which is equal to 1, of course, is expressed in terms of the viscous perturbation pressure gradient. Thus,

$$\int_0^h \int_0^{2\pi} (1+Z)\,V(Z)\,\cos\beta\, dZ\, d\theta = \pi[(1+h)^2 - 1]. \tag{40}$$

Then, substituting (39) into (40) and recalling that $h \ll 1$, the integral in the latter is evaluated yielding

$$\frac{\partial p_v}{\partial \xi} = -\frac{24}{h}\frac{1}{\mathrm{Re}}. \tag{41}$$

Hence, the (dimensional) shear stress on the surface of the cylinder is given by

$$\tau = \mu\, \frac{U}{a}\, \frac{\partial V}{\partial Z}\Big|_{Z=0} = \rho\, U^2\, \frac{12}{\mathrm{Re}}\,; \tag{42}$$

it is noted that the magnitude of τ is practically independent of time.

The shear stress on the cylinder may be separated into two components: an axial and a circumferential one,

$$\tau_x = \tau \cos\beta \simeq \tau,\ \ \tau_\theta = \tau \sin\beta, \tag{43}$$

respectively.

The analysis has now progressed sufficiently to be able to evaluate the steady longitudinal force F_l and the unsteady lateral viscous force, F_v, of equation (1), which is given by

$$F_l = \int_0^{2\pi} \tau_x\, a\, d\theta,$$

$$F_v = -\int_0^{2\pi} [\tau_\theta \sin\theta + \rho U^2\, p_v \cos\theta] a\, d\theta. \tag{44}$$

Utilizing (43) it is found directly that

$$F_l = \frac{24}{\mathrm{Re}}\, \pi\, a\, \rho\, U^2. \tag{45}$$

The evaluation of F_v is more involved, but by reference to Mateescu and Paidoussis' (1987) work and some perseverence, the reader should be able to reproduce the following result:

$$F_v = -\rho a^2 \pi\, e^{i\Omega t} \sum_k a_k\, (i\Omega\, \bar{P}_{k1} + \bar{P}_{k0}), \tag{46}$$

where

$$\bar{P}_{k1} = U\, \frac{12}{\mathrm{Re}}\, \frac{2+h}{ah^2} \sum_{j=1}^{2} G_{jk}\ W_{jk}\ \psi_{jk},$$

$$\bar{P}_{k0} = U^2\, \frac{12}{\mathrm{Re}}\, \frac{2+h}{ah^2} \sum_{j=1}^{2} G_{jk}\ W_{jk}\ \psi'_{jk}. \tag{47}$$

Finally, $(\partial P_m/\partial x) A_s$ in equation (1) may be obtained via (41), i.e.,

$$\frac{\partial P_m}{\partial x} A_s \simeq \frac{\partial p_v}{\partial \xi}\, \frac{\rho U^2}{a} A_s = -\frac{24}{\mathrm{Re}}\, \frac{\rho U^2}{ah} A_s. \tag{48}$$

In this paper, the viscous forces have been formulated by an approximate solution of the Navier-Stokes equations for the unsteady annular flow field, accounting for the unsteady viscous effects much more fully than the semi-empirical formulation utilized heretofore. Furthermore, although the foregoing analysis applies to laminar flow, its extension to turbulent flow, e.g., using an eddy-viscosity model, is quite feasible.

5 Nondimensionalization and Stability Analysis

All unknown terms in equation (1) have now been determined and the equation of small motions (1) may be written as

$$EI\frac{\partial^4 e_o}{\partial x^4} - \left[\frac{24}{\mathrm{Re}}\, \pi\, a\, \rho\, U^2 \left(1+\frac{1}{h}\right)(L-x)\right] \frac{\partial^2 e_o}{\partial x^2}$$
$$+ \frac{24}{\mathrm{Re}}\, \frac{1}{h}\, \pi\, a\, \rho\, U^2\, \frac{\partial e_o}{\partial x} + \rho_s A_s\, \frac{\partial^2 e_o}{\partial t^2} = F_p + F_v. \tag{49}$$

Considering also the case where the axial sliding is at the upstream end, so that the axial tension distribution is reversed, and the case where no sliding at all is permitted, where compression may arise also through external pressurization (Paidoussis, 1973), this equation may be generalized to

$$EI\, \frac{\partial^4 e_o}{\partial x^4} - \frac{24}{\mathrm{Re}}\, \pi\, a\, \rho\, U^2 \left(1+\frac{1}{h}\right)$$
$$\times \left[\left(1-\frac{1}{2}\,\delta\right)L - x\right] \frac{\partial^2 e_o}{\partial x^2}$$
$$-(1-2\nu)\delta(2-\delta)\bar{P}\, A_s\, \frac{\partial^2 e_o}{\partial x^2} + \frac{24}{\mathrm{Re}}\, \frac{1}{h}\, \pi\, a\, \rho\, U^2\, \frac{\partial e_o}{\partial x}$$
$$+\rho_s A_s\, \frac{\partial^2 e_o}{\partial t^2} = F_p + F_v, \tag{50}$$

where $\delta = 0$ corresponds to the case of an axially-sliding downstream end, $\delta = 2$ to a sliding upstream end, and $\delta = 1$ to no axial sliding at either end; ν is Poisson's ratio and $\bar{P}$ is the overpressure at the midpoint of the cylinder, $1/2L$.

Introducing now the nondimensional parameters

$$\eta = \frac{e_o}{a},\ \ \bar{T} = \left(\frac{EI}{\rho_s A_s}\right)^{1/2} \frac{t}{L^2},\ \ \omega = \left(\frac{\rho_s A_s}{EI}\right)^{1/2} \Omega\, L^2,$$

$$\sigma = \frac{\rho \pi L^2}{\rho_s A_s},\ \ \Pi = \frac{\bar{P}\, A_s L^2}{EI},\ \ \bar{U} = \left(\frac{\rho\, \pi\, a^2 L^2}{EI}\right)^{1/2} U, \tag{51}$$

and together with equations (26) substituting into (50), the dimensionless equation of motion is obtained

$$\eta^{iv} - \frac{24}{\mathrm{Re}}\, \bar{U}^2 l \left(1+\frac{1}{h}\right) \left[\left(1-\frac{1}{2}\,\delta\right) - X\right] \eta''$$
$$-(1-2\nu)\delta(2-\delta)\Pi\eta''$$
$$+ \frac{24}{\mathrm{Re}}\, \bar{U}^2\, \frac{l}{h}\, \eta' + \ddot{\eta} = \left(\frac{L}{aEI}\right)^4 (F_p + F_v), \tag{52}$$

where F_p and F_v are given by (24) and (46), respectively, and the primes and dots denote differentiation by X and $\bar{T}$, respectively.

This equation was discretized by Galerkin's method, utilizing the ψ_k (equation (9)) as comparison functions, and transformed into a standard eigenvalue problem, from which the dimensionless eigenfrequencies of the system, ω_n, may be obtained and stability assessed. Some examples of results obtained in this manner are presented next.

6 Dynamics and Stability: Results and Discussion

6.1 Results for Not-Too-Narrow Annuli. The dynamical behavior of the system is illustrated in Figs. 3 and 4, where $l = L/a = 20$, $h = 0.1$, $\sigma = 323.7$, $[EI/\rho\pi a^2 L^2)]^{1/2} = 1.33$ m/s, and $\mu = 0.007$ Pa s; μ is relatively large here (typical for oil) to highlight the effects of viscous flow.[1] In Fig. 3 are presented the real and imaginary components of the lowest three eigenfrequencies as functions of $\bar{U}$, calculated according to *(i)* entirely inviscid (potential) theory, $\mu = 0$, and *(ii)* unsteady viscous theory, but excluding the steady viscous effects (i.e., pressurization effects, surface traction and related pressure drop, which are time-independent). In Fig. 4, on the other hand, the complete analytical model is utilized, including all potential and unsteady and steady viscous forces. It is recalled

[1]To give the reader a physical appreciation of this system, it should be stated that in this case the ratio of added mass to structural mass-per-unit length is 8.09, whilst the first-mode natural frequency at zero flow is 2.92 and 2.74 Hz, respectively, according to inviscid and (full) viscous theory. For other cases of h and for other fluids, the reader may scale these quantities appropriately (the density of water is approximately 7 percent higher than that of the oil used in these calculations).

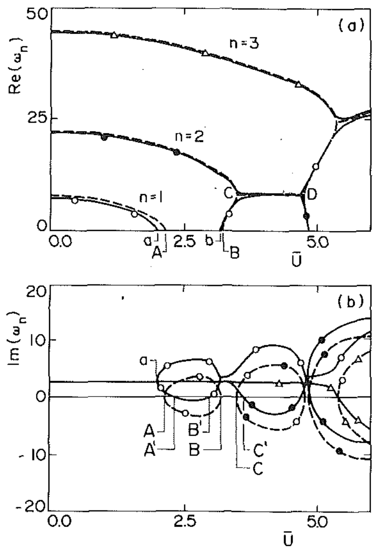

Fig. 3 The (a) real and (b) imaginary components of the nondimensional eigenfrequencies of the lowest three modes as functions of the nondimensional fluid velocity, $\bar{U}$, for potential flow (— — —) and viscous flow (———) considering potential and unsteady viscous effects ($L/a=20$, $H/a=0.1$, $\sigma=323.74$, $[EI/(\rho\pi a^2L^2)]^{1/2}=1.33$ m/s, and $\mu=0$ and 0.007 Pa s, respectively: ○, first mode; ●, second mode; △, third mode

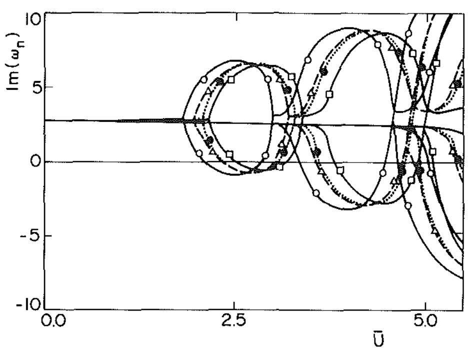

Fig. 4 The imaginary components of the nondimensional eigenfrequencies of the lowest three modes as functions of the nondimensional fluid velocity, $\bar{U}$, for viscous flow considering potential and steady and unsteady viscous effects for the system of Fig. 3: ——□——, C-CS ends; ——○——, CS-C ends; — — △ — —, C-C ends ($\Pi=10$); · · · ● · · ·, C-C ends ($\Pi=50$)

that the system loses stability if $\mathrm{Im}(\omega_n)<0$, by divergence when $\mathrm{Re}(\omega_n)=0$ and by flutter otherwise.

According to potential flow theory for $h=0.1$, the system loses stability at $\bar{U}=2.13$ (point A in Fig. 3) in its first mode by divergence. At high flow this mode is restabilized at $\bar{U}=3.21$ (point B, Fig. 3) and then first and second mode loci coalesce and the system losses stability by coupled-mode flutter at point C($\bar{U}=3.50$). At higher $\bar{U}$ the system is subject to a succession of coupled-mode flutter and divergence instabilities, as may be seen in Fig. 3.

The presence of unsteady viscous forces has the following effects on the dynamics of the system. The eigenfrequencies, in the stable regime, are complex, rather than purely real as in the potential flow case; i.e., the system is subject to damping due to the presence of fluid in the annulus (sometimes referred to as squeeze-film damping). As a result, it takes a higher flow to precipitate divergence; the system loses stability at point A′ (*not* at point *a*) for $\bar{U}=2.29$. Similarly, coupled-mode flutter occurs at a higher flow, $\bar{U}=3.56$. Nevertheless, the fundamental dynamical behavior of the system remains the same as for potential flow. In this respect it is significant that almost up to the point of loss of stability, the $\mathrm{Im}(\omega_n)$ remain essentially constant with $\bar{U}$.

Table 1 The critical points for divergence and coupled-mode flutter for the system of Figs. 3 and 4 ($h=0.1$)

Theory	Critical values of $\bar{U}$	
	Divergence $\bar{U}_{cd}$	Coupled-mode flutter, $\bar{U}_{cf}$
Potential	2.13	3.50
With unsteady viscous forces	2.29	3.56
Complete theory		
(C-CS ends)	2.49	3.80
(CS-C ends)	2.10	3.33
(C-C, $\Pi=10$)	2.30	3.57
(C-C, $\Pi=50$)	2.37	3.62

Table 2 Comparison of $\bar{U}_{cd}$ obtained with the potential-flow versions of the present and earlier theory

l	h	Values of $\bar{U}_{cd}$ Present theory	Paidoussis (1973)	Percent discrepancy Based on last column
20	0.05	1.49	1.39	7.2
	0.10	2.13	1.94	9.8
	0.15	2.64	2.34	12.8
100	0.01	0.631	0.627	0.7
	0.05	1.425	1.387	2.7

Introducing now the results of the full theory, it is noted that $\mathrm{Re}(\omega_n)$ varies with $\bar{U}$ more or less the same as before, and hence only the $\mathrm{Im}(\omega_n)$ are given in Fig. 4, for various cases depending on whether one of the clamped ends allows axial sliding (defined as a CS end) or not (C end); so, we have cases of C-CS, CS-C, or C-C support, where the first, for example, denotes a clamped end at $X=0$ and a clamped-sliding end at $X=1$. For a C-C system, pressurization effects come into play and in Fig. 4 are shown two different cases: $\Pi=10$ and $\Pi=50$. The results are summarized in Table 1.

Hence, in this particular example it is clear that the steady viscous effects are generally as important as the unsteady ones (Table 1), being stabilizing when the downstream end can slide axially and destabilizing when the upstream end can do so; indeed in the latter case, the values of $\bar{U}_{cd}$ and $\bar{U}_{cf}$ are lower than those of pure potential flow. For wholly fixed ends (and relatively small Π), the end of steady forces is smaller, and as seen in Table 1, the unsteady viscous effects are much more important. Also seen in Table 1 is that pressurization (Π) in that case has a stabilizing influence, as expected (Paidoussis, 1973).

Before presenting results for narrower annuli, $h<0.1$, where as will be seen in Section 6.3 the dynamical behavior is more interesting and unexpected, comparison will be made with previous theory.

6.2 Comparison With Previous Theory. Here the critical flow velocities, as predicted by the present and previous theories, will be compared for situations where both should be applicable.

It is well known that the critical flow velocity for divergence, U_{cd}, may be found directly by Euler's method, where all time-dependent terms in the equation of motions are neglected, including the unsteady viscous effects. It is instructive to do just that and to compare the results with those of Paidoussis' (1973). This is done for the simplest possible situation, where all viscous terms are neglected. The results are shown in Table 2. It is noted that U_{cd} for Paidoussis' theory was calculated from

$$\bar{U}_{cd}=2\pi/\chi^{1/2}, \quad \chi=\frac{(1+h)^2+1}{(1+h)^2-1}, \tag{53}$$

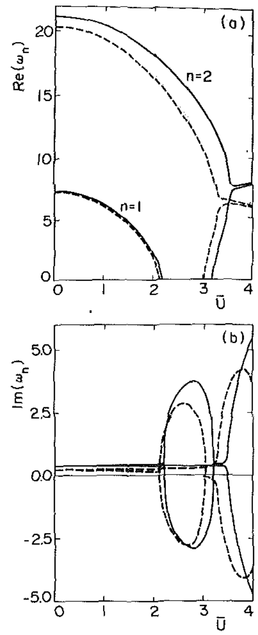

Fig. 5 The present theory (———) compared with that of Paidoussis (1973) (— — —), for the case of $l=20$, $h=0.10$, $[EI/(\rho\pi a^2L^2)]^{1/2}=1.3$ m/s and $\mu=0.00115$ Pa s

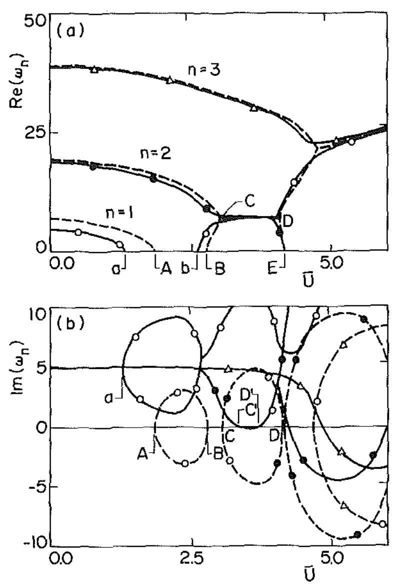

Fig. 6 The (a) real and (b) imaginary components of the nondimensional eigenfrequencies of the lowest three modes as functions of the nondimensional fluid velocity, $\bar{U}$, for potential flow (— — —) and viscous flow (———) considering potential and unsteady viscous effects for the system as Fig. 3, but $h=0.075$; ○, first mode; ●, second mode; △, third mode.

easily obtainable in such simple form, because of the simplicity of the slender-body formulation.

It is seen that best agreement is for a very slender body ($l=L/a=100$), where slender-body theory (Paidoussis, 1973) applies best, and for a very narrow annulus ($h=0.01$), where the narrow-annulus simplification of the present theory (see equation (12)) also applies best. In any event, from the results of $l=100$, $h=0.05$, it is seen that the latter simplification is quite justified for very narrow annuli. Also seen from the results for $h=0.05$, comparing $\bar{U}_{cd}$ for $l=100$ to that $l=20$, is that slender-body theory overestimates the inviscid forces considerably, even for such relatively slender cylinders as $l=20$ (refer also to Paidoussis and Ostoja-Starzewski (1981)).

Next, the results obtained with the full theory are compared with those of Paidoussis' (1973) in Fig. 5, for a case $l=20$, $h=0.10$, $[EI/\rho\pi a^2L^2)]^{1/2}=1.3$ m/s and $\mu=0.00115$ Pa s, corresponding to water flow; in Paidoussis' (1973) theory the following parameters were used: $\beta=0.5$, $\epsilon c_f=0.25$, $c=1.0$. It is noted that in this case the $\mathrm{Re}(\omega_n)$ obtained by the two theories are similar; the results of the older theory are slightly smaller, which reflects the overestimation of fluid effects by the slender-body theory. The discrepancy is larger for $\mathrm{Im}(\omega_n)$, where the older theory (Paidoussis, 1973) gives somewhat smaller values, supporting the supposition made at the outset that the estimation of viscous effects by an adaptation of Taylor's relationships is not particularly appropriate for the study at hand. In Paidoussis' (1966a, 1973) theory, unsteady viscous forces are taken into account by an adaptation of Taylor's relationships, presuming that the mean flow field is approximately the inviscid one, which is not particularly true for narrow annular flows; moreover, the friction coefficients, c_f and c are entirely empirical. The strength of the present theory is that the unsteady viscous forces are predicted analytically via an approximate solution of the Navier-Stokes equations for the viscous flow in the annulus and are, therefore, expected to be closer to reality—especially for very narrow annuli, to be discussed next.

6.3 Results for Very Narrow Annuli. For narrower annular configurations, $h<0.1$, which represent the most interesting situations for engineering applications, the unsteady viscous effects become the most important factor in stabilizing the system. An example is shown in Fig. 6 for $h=0.075$. In this case, the system loses stability, not by divergence but by coupled-mode flutter (point C′ in Fig. 6, where $\mathrm{Re}(\omega)\neq 0$), due to unsteady viscous effects, which is a fundamentally important result to be discussed later. The effect of steady viscous forces in this case is relatively less important, as may be seen in Table 3 (the equivalent of Fig. 4 for this case of $h=0.075$ has not been presented for brevity).

Table 3 The critical points for loss of stability for the systems of Figs. 3, 4, and 6 compared, showing the effect of the annular gap, *h*

Theory	Critical values of $\bar{U}$	
	$h=0.1$	$h=0.075$
Potential	2.13*	1.84*
With unsteady viscous forces	2.29*	3.34**
Complete theory		
(C-CS ends)	2.49*	4.54*
(CS-C ends)	2.10*	2.97**
(C-C, Π=10)	2.30*	3.35**
(C-C, Π=50)	2.37*	3.41**

*Divergence; **Coupled-mode flutter

Table 4 Critical flow velocities for systems with different dimensionless annular gaps, *h* (full theory); in the case of C-C, Π=50

End conditions	h	$\bar{U}$	Type of instability and mode, n
C-CS	0.15	2.78	Divergence, $n=1$
C-CS	0.10	2.49	Divergence, $n=1$
C-CS	0.075	4.54	Divergence, $n=2$
C-CS	0.05	6.80	Flutter, $n=3$
CS-C	0.15	2.54	Divergence, $n=1$
CS-C	0.10	2.10	Divergence, $n=1$
CS-C	0.075	2.97	Flutter, $n=2$
CS-C	0.05	5.15	Flutter, $n=3$
C-C	0.15	2.76	Divergence, $n=1$
C-C	0.10	2.37	Divergence, $n=1$
C-C	0.075	3.41	Flutter, $n=2$
C-C	0.05	5.97	Flutter, $n=3$

Of course, in the last analysis, what is most significant is the overall effect of annular flow on stability, including all terms in the equation of motion: inviscid and viscous, unsteady and steady. The most important results for various annular gaps are summarized in Table 4.

A number of significant observations may be made from the results of Table 4. First, for each of the three cases of end conditions, it is seen that the system is destabilized as h is reduced from 0.15 to 0.10. However, as h is further reduced to 0.075 or 0.05, there is a significant *stabilizing* effect, and the critical flow velocities become higher (see also Table 3). This physically reasonable dynamical behavior, associated with the viscous effects eventually becoming more important than inviscid ones for narrow enough annuli, is demonstrated analytically for the first time in this paper. The second point of interest is that the mode and type of instability change with h. In terms of Figs. 3 and 6, for $h=0.075$ the viscous effects, steady and unsteady, become stronger and the $\mathrm{Im}(\omega_n)$ for small values of $\bar{U}$ are much larger. Thus, the first "loop" in the locus of the first-mode $\mathrm{Im}(\omega_n)$ has no segment with $\mathrm{Im}(\omega_n)<0$; the second-mode loop, which is normally larger (Fig. 6), eventually does lead to instability—by divergence if the system is under tension by the steady viscous forces (C-CS system), and by coupled-mode flutter otherwise.

The loss of stability, in some cases (Table 4) by flutter, is an entirely new result obtained by this theory and calls for some discussion. It may appear surprising that a system with both ends supported, i.e., an "inherently conservative" system, can lose stability by flutter and not by divergence (Paidoussis, 1980, 1987). Howver, of course, the system is truly conservative only so long as unsteady viscous forces are totally absent; indeed, from the results for potential flow theory (not shown here for brevity), the system loses stability by divergence no matter how small h is. Once the unsteady viscous forces are included, however, the system becomes nonconservative in the proper sense, and hence different routes to instability are possible. The dynamics of the system for relatively wide annuli follows the pattern of the potential-flow conservative system; for very narrow annuli, however, where damping forces are stronger, the dynamical behavior is quite different.

Similar observations have been made by varying μ, but will not be discussed here for the sake of brevity.

7 Conclusions

A new and improved analytical model has been developed for the dynamics and stability of flexible cylinders in a narrow duct with annular flow. This theory is capable, for the first time, of taking fully into account unsteady viscous effects and of predicting the viscous forces analytically, rather than empirically.

A number of significant new results were obtained with the aid of the new theory. The most important one is that there are two opposing effects on the dynamics of the system as the annular gap is reduced: (*i*) the destabilizing effect of the inviscid forces and (*ii*) the stabilizing one associated with the unsteady viscous forces. The result of these opposing influences is that, as the annular gap is reduced, the system is initially destabilized (i.e., it becomes unstable at lower flow velocities); however, for sufficiently narrow annuli, further reduction of the gap produces a stabilizing effect on the system. This, in fact, is what intuition would also suggest: The monotonic destabilizing effect of the inviscid forces, eventually predicting instability at infinitesimally small flow velocities for very narrow annuli, cannot be physically correct; indeed, it is counteracted by the increasing importance of the unsteady viscous forces, caused mainly by the viscosity-related changes in the unsteady pressure field, which are accounted for in the present analysis for the first time.

The second item of interest is connected to the mode via which the system loses stability. It is shown that unless the fluid is very viscous or the annular gap very narrow, the system loses stability by divergence, generally in the first (lowest) mode. However, for a sufficiently narrow annulus or high fluid viscosity, the system may lose stability in a higher mode, either by divergence or by flutter. This last possibility is the most interesting one from the fundamental point of view. Something similar to this has been reported by Grotberg and Reiss (1982) for a biological system, where the inclusion of fluid frictional effects could alter the mode of loss of stability from divergence to flutter; however, the physical system involved was quite different.

It should be remarked that the dynamics of the system beyond the first loss of stability are not only of academic interest. As shown by Paidoussis and Pettigrew (1979), the higher instabilities do materialize sequentially in some cases, since none of the instabilities is truly catastrophic in terms of amplitude. Evidently, nonlinear effects limit the amplitude of both divergence and flutter and, for sufficiently narrow annuli, the presence of the duct itself has the same effect.

Comparison of this theory with the closest previous theory available (Paidoussis, 1973) validated all aspects that could be compared. However, as expected, the key element which is unique to this theory, i.e., the prediction of unsteady viscous forces, is different and superior to that of previous theory, by taking into account the viscosity-related changes in the unsteady flow field. In the present theory, instead of obtaining these unsteady viscous forces by an adaptation of formulations applicable to unconfined axial flow, they are derived analytically by means of an approximate solution of the Navier-Stokes equations, which is one of the main contributions of this paper. Hence, for the dynamics and stability of flexible cylinders in narrow annular flow, this theory is superior to previously available ones, although the overall effect is rather small. Of course, exactly how good the theory is will have to await experimental verification, which is currently being planned. However, it should be mentioned that for hinged rigid cylinders oscillating in annular flow, the unsteady viscous theory of Mateescu and Paidoussis (1987) has been validated experimentally (Mateescu et al., 1988 a,b), theory and experiment being in remarkably good agreement.

References

Chen, S. S., and Wambsganss, M. W., 1971, "Parallel-flow-induced Vibration of Fuel Rods," *Nuclear Engineering and Design*, Vol. 18, pp. 253–278.

Chen, S. S., 1977, "Flow Induced Vibrations of Circular Cylindrical Structures. Part I: Stationary Fluids and Parallel Flow," *The Shock and Vibration Digest*, Vol. 9, pp. 25–38.

Grotberg, J. B., and Reiss, E. L., 1982, "A Subsonic Flutter Anomaly," *Journal of Sound and Vibration*, Vol. 80, pp. 444–446.

Hawthorne, W. R., 1961, "The Early Development of the Dracone Flexible Barge," *Proceedings of the Institution of Mechanical Engineers*, Vol. 175, pp. 52–83.

Hobson, D. E., 1982, "Fluid-Elastic Instabilities Caused by Flow in an Annulus," *Proceedings of the BNES Third International Conference on Vibration in Nuclear Plant*, Keswick, U.K., pp. 440–463.

Mateescu, D., and Paidoussis, M. P., 1984, "Annular-Flow-Induced Vibrations of an Axially Variable Body of Revolution in a Duct of Variable Cross-Section," *Proceedings of the ASME Symposium on Flow-Induced Vibrations 1984*, Vol. 4, pp. 53–69.

Mateescu, D., and Paidoussis, M. P., 1985, "The Unsteady Potential Flow in an Axially Variable Annulus and its Effect on the Dynamics of the Oscillating Rigid Center-Body," *ASME Journal of Fluids Engineering*, Vol. 107, pp. 421–427.

Mateescu, D., and Paidoussis, M. P., 1987, "Unsteady Viscous Effects on the Annular-Flow-Induced Instabilities of a Rigid Cylindrical Body in a Narrow Duct," *Journal of Fluids and Structures*, Vol. 1, pp. 197–215.

Mateescu, D., Paidoussis, M. P., and Bélanger, F., 1988a, "Experiments on the Unsteady Annular Flow Around an Oscillating Cylinder," *AIAA 15th Aerodynamic Testing Conference*, San Diego, CA, May 1988, AIAA Paper No. 88-2031.

Mateescu, D., Paidoussis, M. P., and Bélanger, F., 1988b, "Unsteady Pressure Measurements on an Oscillating Cylinder in Narrow Annular Flow," *Journal of Fluids and Structures*, Vol. 2, pp. 615–628.

Mulcahy, T. M., 1980, "Fluid Forces on Rods Vibrating in Finite Length Annular Regions," ASME JOURNAL OF APPLIED MECHANICS, Vol. 47, pp. 234–240.

Mulcahy, T. M., 1983, "Leakage Flow-Induced Vibrations of Reactor Components," *The Shock and Vibration Digest*, Vol. 15, pp. 11–18.

Mulcahy, T. M., 1988, "One-Dimensional Leakage-Flow Vibration Instabilities," *Journal of Fluids and Structures*, Vol. 2, pp. 383–403.

Paidoussis, M. P., 1966a, "Dynamics of Flexible Slender Cylinders in Axial Flow. Part I: Theory," *Journal of Fluid Mechanics*, Vol. 26, pp. 717–736.

Paidoussis, M. P., 1966b, "Dynamics of Flexible Slender Cylinders in Axial Flow. Part II: Experiments," *Journal of Fluid Mechanics*, Vol. 26, pp. 737–751.

Paidoussis, M. P., 1968, "Stability of Towed, Totally Submerged Flexible Cylinders," *Journal of Fluid Mechanics*, Vol. 34, pp. 273–297.

Paidoussis, M. P., 1973, "Dynamics of Cylindrical Structures Subjected to Axial Flow," *Journal of Sound and Vibration*, Vol. 29, pp. 365–385.

Paidoussis, M. P., 1980, "Flow-Induced Vibrations in Nuclear Reactors and Heat Exchangers: Practical Experiences and State of Knowledge," *Practical Experiences with Flow-Induced Vibrations*, E. Naudascher and D. Rockwell eds., Springer-Verlag, Berlin, pp. 1–81.

Paidoussis, M. P., 1987, "Flow-Induced Instabilities of Cylindrical Structures," *Applied Mechanics Reviews*, Vol. 40, ASME, New York, pp. 163–175.

Paidoussis, M. P., and Ostoja-Starzewski, M., 1981, "Dynamics of a Flexible Cylinder in Subsonic Axial Flow, *AIAA Journal*, Vol. 19, pp. 1467–1475.

Paidoussis, M. P., and Pettigrew, M. J., 1979, "Dynamics of Flexible Cylinders in Axisymmetrically Confined Axial Flow," ASME JOURNAL OF APPLIED MECHANICS, Vol. 46, pp. 37–44.

Taylor, G. I., 1952, "Analysis of the Swimming of Long and Narrow Animals," *Proceedings of the Royal Society*, (London), Vol. A214, pp. 158–183.

Yeh, T. T., and Chen, S. S., 1978, "The Effects of Fluid Viscosity on Coupled Tube/Fluid Vibrations," *Journal of Sound and Vibration*, Vol. 59, pp. 453–467.

The Self-Noise From Ordered Structures in a Low Mach Number Jet

R. R. Mankbadi
Cairo University,
Cairo, Egypt
Mem. ASME

This article is concerned with examining the self-noise produced by instability waves in a round jet. The self-noise is defined here as the noise attributed to the nonlinear sources in Lighthill's stress tensor. The calculated self-noise is found to be proportional to the fourth order of the velocity amplitude saturation. The self-interaction of the instability waves results in a "super-directivity." The dependency of the sound intensity on the Strauhal number and on the Mach number is in accordance with observations.

Introduction

Motivated by understanding the mechanism of sound generation at low Mach numbers, Laufer and Yen (1983) examined experimentally the relationship between vortex pairing as an acoustic source and its far-field characteristics. In their experiment, a circular jet was excited at the most unstable frequency. The excitation phase locked the fluctuations into the fundamental and the subharmonic instability waves. The amplitude of the fundamental instability wave was seen to first increase exponentially as it was convected downstream, then it saturated and decreased. The saturation of the fundamental is associated with the periodic vortex formation in which the subsequent subharmonic amplifies. The first and second subharmonic behaved in a similar manner. The flow fluctuations were found to be dominated by those of the fundamental and the first and second subharmonics. A surprising result of their far-field investigations was that although the near-field pressure fluctuations vary linearly with the velocity amplitude fluctuations, the far-field pressure fluctutations are best correlated with the square of the velocity amplitude fluctuations. No explanation was given for this puzzling result. It was concluded that the resulting radiation intensity is proportional to the fourth, rather than the second power of the maximum source amplitude fluctuations. This conclusion suggests a nonlinear sound generation mechanism.

If one splits each velocity component into a mean and a fluctuating one, Lighthill's stress tensor $T_{ij}=\rho_o u_i u_j$ can in turn be decomposed into contributions from the first-order fluctuations and from the second-order fluctuations. The first-order term in Lighthill's stress tensor is conventionally termed the "shear noise" while the second-order term is termed the "self noise." Lighthill's (1952) formulation thus suggests that the shear noise is more important than the self-noise since the former in only linear in the fluctuating velocities while the latter is quadratic in the fluctuating velocities. Based on this assumption, Huerre and Crighton (1983) attemped to explain the observed far-field sound of Laufer and Yen (1983) by calculating the shear noise generated by instability waves in a low Mach number jet. Their theory suggested that the directional variation of intensity should be strongly influenced by certain quadropole factors which were not observed in the experiment. Also, the theory gives a weaker antenna variation than measured. Furthermore, the calculated far-field pressure is linear in the velocity fluctuations while in the experiment, the relation is definitely nonlinear. Huerre and Crighton (1983) made clear that although application of Lighhill's theory predicts some observed features of the far-field sound, it predicts just as clearly features which are not seen in the experiment.

A clue to the interpretation of discrepancy between the theory and observations was given by Laufer and Yen (1983). They pointed out that the measured radiation at a fixed frequency is not necessarily generated by the instability wave of the same frequency, but could be generated through the interaction of waves of different frequencies. For instance, the far-field sound measured at a frequency corresponding to the first subharmonic's frequency is not produced by only the first subharmonic, but can also be a result of the interaction between the fundamental and the first subharmonic, or as a result of the self-interaction of the second subharmonic. If this is the case, then the far-field sound could be interpreted as a result of the second-order self-noise rather than the first-order shear noise. If one considers the self-noise to be important, the far-field sound pressure will be dependent quadratically on the fluctuating velocity as in the experiment. The purpose of this work is therefore to examine the far-field self-noise by calculating the radiation field resulting from the interaction of several instability waves. The analysis essentially follows formulation developed in earlier investigations by Crow (1972), Crighton (1975), Ffowcs-Williams and Kempton (1978) and Huerre and Crighton (1983), among others.

Contributed by the Applied Mechanics Division of THE AMERICAN SOCIETY OF MECHANICAL ENGINEERS for publication in the JOURNAL OF APPLIED MECHANICS.

Discussion on this paper should be addressed to the Technical Editor, Leon M. Keer, The Technology Institute, Northwestern University, Evanston, IL 60208, and will be accepted until two months after final publication of the paper itself in the JOURNAL OF APPLIED MECHANICS. Manuscript received by the ASME Applied Mechanics Division, April 5, 1988; final revision, January 6, 1989.

The Near-Field

The problem considered here is that of a round jet issuing from a nozzle of a given diameter, D, at low speeds. As in Laufer and Yen's (1983) observations, the sound sources are taken here to be dominated by the velocity fluctuations of the instability waves. Considering m instability waves, then the fluctuating velocity components $\tilde{u}$ and $\tilde{v}$ can be put in the following form following Laufer and Yen (1983):

$$[\tilde{u}, \tilde{v}] = \sum_{k=1}^{m} Q_k(x)\, u_{\max,\,k}[\hat{u}_k(r),\ \hat{v}_k(r)]\exp\,(i\alpha_k x - i\omega_k t) + \text{c.c.},$$
$$k = 0, 1, 2, \ldots, m \tag{1}$$

where c.c. denotes a complex conjugate, $u_{\max,k}$ is the maximum fluctuating velocity component, $\hat{u}_k(r)$ and $\hat{v}_k(r)$ are the radial distribution of the velocity fluctuations given as the eigenfunctions of the linear instability equation. α_k is the eigenvalue corresponding to the frequency ω_k. $Q_k(x)$ is the amplitude of the fluctutations which Laufer and Yen (1983) found to be approximately given by:

$$Q_k(x) = \exp[-(x - x_k)^2/\lambda_k{}^2] \tag{2}$$

where λ_k is the wavelength of the k instability wave of frequency $f_k = f_o/(2)^k$, and f_o is the frequency of the fundamental. x_k is the pairing location where the amplitude of the velocity fluctuation of the k wave saturates. This location is governed by a feedback mechanism and is given according to Laufer and Yen (1983) by:

$$x_k/\lambda_k = 2/(1 + M_c) \tag{3}$$

where M_c is the convection Mach number which is about half of the jet exit Mach number. The near-field velocity fluctuations are thus taken here to be given by a wave packet form at each frequency with a Gaussian envelope of width λ_k.

The Far Field

Following Lighthill's (1952) acoustic analogy, the far-field sound pressure, P_s, is given in the polar coordinate system as:

$$P_s(\underline{x}, t) = \frac{1}{4\pi R a_o^2}\iiint\left[\frac{\partial^2}{\partial t^2}(\rho C_r^2)\right] r\,dr\,dx\,d\Delta. \tag{4}$$

a_o is the sound speed in the undisturbed field. R is the distance between the observation point and the exit of the jet. ρ is the undisturbed density and C_r is the total velocity component in the observer's direction given for an axisymmetric flow as

$$C_r = u\cos\theta + v\sin\theta\cos\Delta \tag{5}$$

where u and v are the velocity components in the axial and radial directions, respectively. θ is the angle between the jet centerline and the line connecting the jet exit to the observation point. Δ is the azimuthal angle at the jet centerline that the direction of the source point makes with the direction of the observation point. Square brackets denote that the terms within are calculated at the retarded time, t_r, where

$$t_r = t - |\underline{x} - \underline{y}|/a_o$$

t is the time and $\underline{x}$, $\underline{y}$ are the observer's and source's location, respectively. We use the usual retarded time approximations:

$$t_r = t - R/a_o + (x\cos\theta + r\sin\theta\cos\Delta)/a_o \tag{6}$$

where $R = |\underline{x}|$.

Each flow component is decomposed into a steady term, $\bar{C}_r$, and a fluctuating term, $\tilde{c}_r$. Thus,

$$C_r = \bar{C}_r + \tilde{c}_r.$$

Consequently, for an incompressible flow, Lighthill's stress tensor can be written as

$$T_{ij} = \rho_o[\bar{C}_r{}^2 + 2\bar{C}_r\tilde{c}_r + \tilde{c}_r{}^2]. \tag{7}$$

The steady term in T_{ij} produces no sound, the second term is the shear noise and the last term is the self-noise. The far-field sound produced by the first-order term in T_{ij} has been investigated by Huerre and Crighton (1983) and Mankbadi and Liu (1984). Our attention is focused here on the far field produced by the second-order self-noise term. Thus, the self-noise, far-field is given by:

$$P_s = \frac{\rho_o}{4\pi R a_o{}^2}\int\frac{\partial^2}{\partial t^2}[\tilde{u}^2\cos^2\theta + \tilde{u}\tilde{v}\sin2\theta\cos\Delta$$
$$+ \tilde{v}^2\sin^2\theta\cos^2\Delta]\, r\,dr\,dx\,d\Delta. \tag{8}$$

Taking the velocity fluctuations to be composed of several instability waves as given by equation (1), the far-field, self-noise is obtained in the form

$$P_s = \frac{-\rho_o}{4\pi R a_o{}^2}\sum_k^m\sum_l^m(\omega_k \pm \omega_l)^2 u_{\max,k}u_{\max,l}$$
$$\iiint dx\,r\,dr\,d\Delta\, Q_k Q_l \exp[i(\alpha_k + \alpha_l)x - i(\omega_k + \omega_l)\times\cos\theta/a_o)].$$
$$\exp[-i(\omega_k \pm \omega_l)(t - R/a_o)]\sum_{j=0}^{2} A_j\cos j\Delta + \text{c.c.} \tag{9}$$

where

$$A_0 = \hat{u}_k\hat{u}_l\cos\theta + \hat{v}_k v_l\sin^2\theta/2$$
$$A_1 = (\hat{u}_k + \hat{v}_l)(\hat{v}_k + \hat{v}_l)\sin2\theta$$
$$A_2 = \hat{v}_k\hat{v}_l\sin^2\theta/2.$$

Performing the azimuthal integration, one obtains the self-noise far-field at a frequency of $(\omega_k \pm \omega_l)$ as:

$$P_s(\omega_k \pm \omega_l) = \frac{-\rho_o}{2Ra_o^2}u_{\max,k}u_{\max,l}\exp - i(\omega_k$$
$$\pm\omega_l)(t - R/a_o)]\,(\omega_k \pm \omega_l)^2\iint Q_k Q_l z(\sigma)$$
$$\exp[i(\alpha_k \pm \alpha_l)x]\,dx\,r\,dr + \text{c.c.} \tag{10}$$

where

$$z(\sigma) = A_o J_o(\sigma) - iA_1 J_1(\sigma) - A_2 J_2(\sigma) \tag{11}$$

and J_n, $n = 0, 1, 2$ is the Bessel function of order n and of argument σ given by

$$\sigma = (\omega_k \pm \omega_l)r\sin\theta/a_o. \tag{12}$$

It was shown by Laufer and Yen (1983) that the sound pressure level is concentrated in the first diameter of the jet where the shear layer is compact in the transverse direction. Hence, the integral of equation (10) can be separated into axial and radial integrals as in Huerre and Crighton (1983). Thus, the sound pressure level is given by:

$$p^2(\omega_k \pm \omega_l) = 2(\rho_o/2Ra_o{}^2)^2 u^2_{\max,k}u^2_{\max,l}(\omega_k \pm \omega_l)^2\,|I_x|^2\,|I_r|^2 \tag{13}$$

where

$$I_x = \int_{-\infty}^{\infty} Q_k Q_l \exp[i(\alpha_k \pm \alpha_l)x - i(\omega_k \pm \omega_l)\times\cos\theta/a_o]$$

and

$$I_r = \int_0^{\infty} z(\sigma)\,r\,dr. \tag{15}$$

With $Q_k(x)$ and $Q_l(x)$ given according to equation (2), the integral I_x can be performed to obtain:

$$I_x = \lambda_k\lambda_l[\pi/(\lambda_k^2 + \lambda_l^2)]^{1/2}\exp[-(x_k - x_l)^2/(\lambda_k^2 + \lambda_l^2)].$$
$$\exp[-\pi^2(\lambda_k \pm \lambda_l)^2(1 - M_c\cos\theta)^2/(\lambda_k{}^2 + \lambda_l{}^2)] \tag{16}$$

where $M_c = (\omega_k \pm \omega_l)/[(\alpha_k \pm \alpha_l)a_o]$.

The eigenfuctions $\hat{u}_i$ and $\hat{v}_i$ involved in calculating the radial integral are approximated by the eigenfuctions of the neutral point where $\hat{v} = i\,\mathrm{sech}(\eta)$. For a hyperbolic tangent mean flow profile, $\eta = y/\delta_o$ and δ_o is the initial half width of the shear layer. The integration is further restricted to the thin shear layer. With these assumptions, I_r can be evaluated to obtain:

$$I_r = D\delta_o\,[I_1 J_o \cos^2\theta + I_2(J_o - J_1/\sigma_o)\sin^2\theta - (2\delta_o/D) I_3 \sigma_o J_o \sin 2\theta], \tag{17}$$

$$I_1 = \int_{-\infty}^{\infty} \mathrm{sech}^2\eta \tanh^2\eta\, d\eta$$

$$I_2 = \int_{-\infty}^{\infty} \mathrm{sech}^2\eta\, d\eta$$

$$I_3 = \int_{-\infty}^{\infty} \mathrm{sech}^2\eta \tanh\eta\, d\eta$$

and

$$\sigma_o = \pi(D/\delta_{mo}) MS \sin\theta \tag{18}$$

where S is the radiation Strouhal number under consideration defined as $S = f\delta_{mo}/U_j$. δ_{mo} is the initial momentum thickness of the shear layer, U_j is the jet exit velocity, and $f = \omega/2\pi$.

Considering now the self-noise resulting from the self-interaction of the $(S/2)$ instability component, the far-field radiation intensity can be written as:

$$p^2 = 16\pi^6 \rho_o^2 u_{\max}^4 M_j^4 (D^2/R^2) S^2 (C/U_j)^2 (\delta_o/\delta_{mo})^2\, |I_x|^2\, |I_r|^2 \tag{19}$$

where C is the convection velocity with I_x now given by

$$|I_x|^2 = \exp[-4\pi^2(1 - M_c\cos\theta)^2]. \tag{20}$$

Results and Discussions

Nature of the Sound Sources. Figure 1 shows $|I_r|^2$ as a function of the emission angle θ for various jet velocities at Strouhal numbers $S = \mathrm{St}_n/4$, $\mathrm{St}_n/2$, and St_n where St_n is the Strouhal number of the most amplified natural frequency having a value of 0.017. The first term in I_r is proportional to $\cos^2\theta$ and therefore is a longitudinal quadropole responsible for the sound emission at low angles to the jet axis. The second term in I_r is proportional to $\sin^2\theta$ and therefore is a lateral quadropole responsible for the sound emission at angles perpendicular to the jet axis. Figures 1(*a*), (*b*), and (*c*) show that these two quadropóles are of the same order for the Strouhal numbers considered. At $\theta \approx 0$, $J_o = 1.0$ and therefore, at small angles to the jet axis I_r is independent of the jet velocity. On the other hand, the lateral quadropole in I_r is dependent on the jet velocity through the dependency of $(J_o - J_1/\sigma_o)$ on the Mach number (equation (17)). Therefore, this quadropole can vanish, for a given jet velocity, at a certain angle where $J_o - J_1/\sigma_o = 0$. At low Strouhal numbers corresponding to the second subharmonic, Fig. 1(*a*) shows that within these jet velocities, the lateral quadropole is significant and it decreases with increasing the jet velocity.

Figure 1(*b*) shows that at a Strouhal number corresponding to the first subharmonic, $\mathrm{St}_n/2$, the lateral quadropole also decreases with increasing the jet velocity and vanishes for $\theta = 90$ deg at jet velocity of 70 m/sec. At Strouhal number corresponding to St_n, Fig. 1(*c*) shows that at 90 deg, the lateral quadropole first decreases with increasing the jet velocity then increases again. At higher velocities, the angle at which I_r approaches zero shifts from 90 deg to about 45 deg. The first nonzero root of $J_o - J_1/\sigma_o$ occurs at $\sigma_o = 1.84$. Thus, the lateral quadropole vanishes at an angle given by:

$$\sin\theta_o = 1.84\delta_{mo}/(\pi DMS).$$

For $\delta_{no}/D \approx 0.003$, θ_o is given by $\sin\theta_o = 1.8 \times 10^{-3}/\mathrm{MS}$. This shows that for Strouhal numbers less than $1.8 \times 10^{-3}/\mathrm{M}$, the lateral quadropole does not vanish. For higher Strouhal numbers, the lateral quadropole vanishes at an angle that decreases with increasing the Mach number.

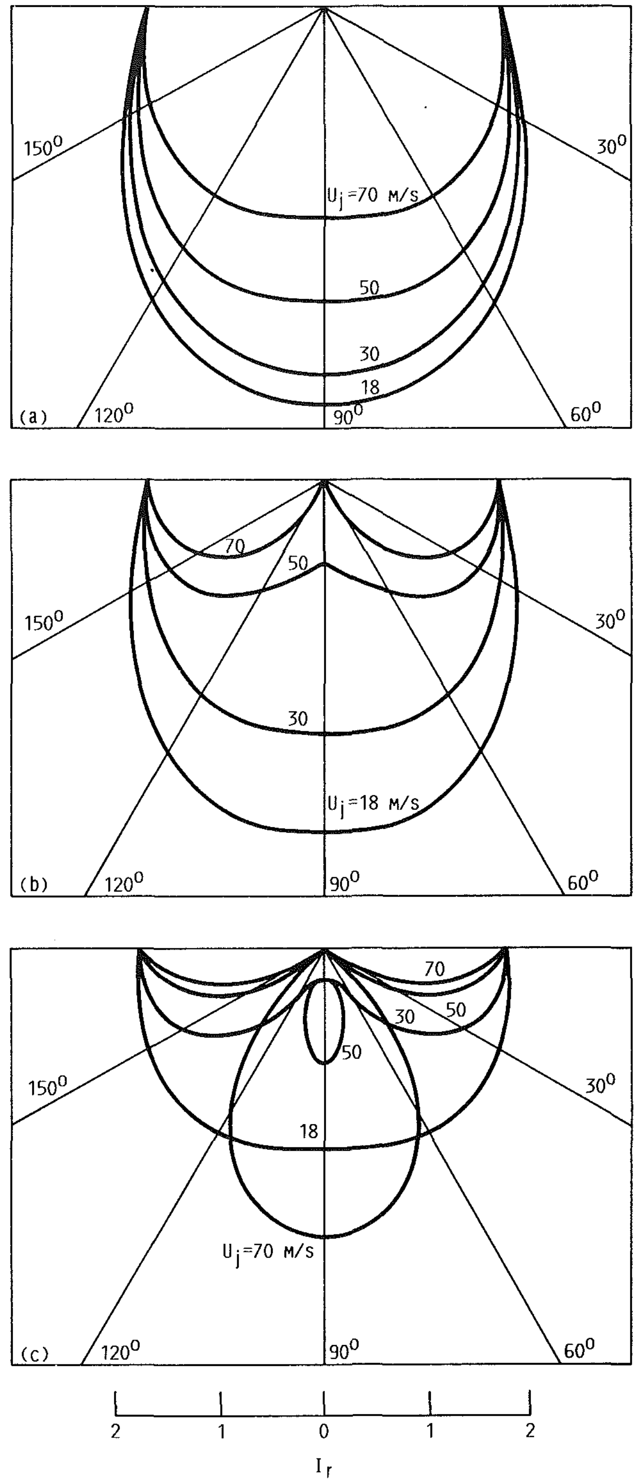

Fig. 1 Effect of jet velocity and Strouhal number on the angular variation of the radial integral I_r; (*a*) $S = \mathrm{St}_n/4$, (*b*) $S = \mathrm{St}_n/2$, (*c*) $S = \mathrm{St}_n$

Directivity

Figures 2 and 3 show a comparison between the calculated directivity of the first and second subharmonics at jet velocities of 30 m/s and 50 m/s, respectively, in comparison with the corresponding measurements. In each case, the theoretical curve is displaced vertically to match the ex-

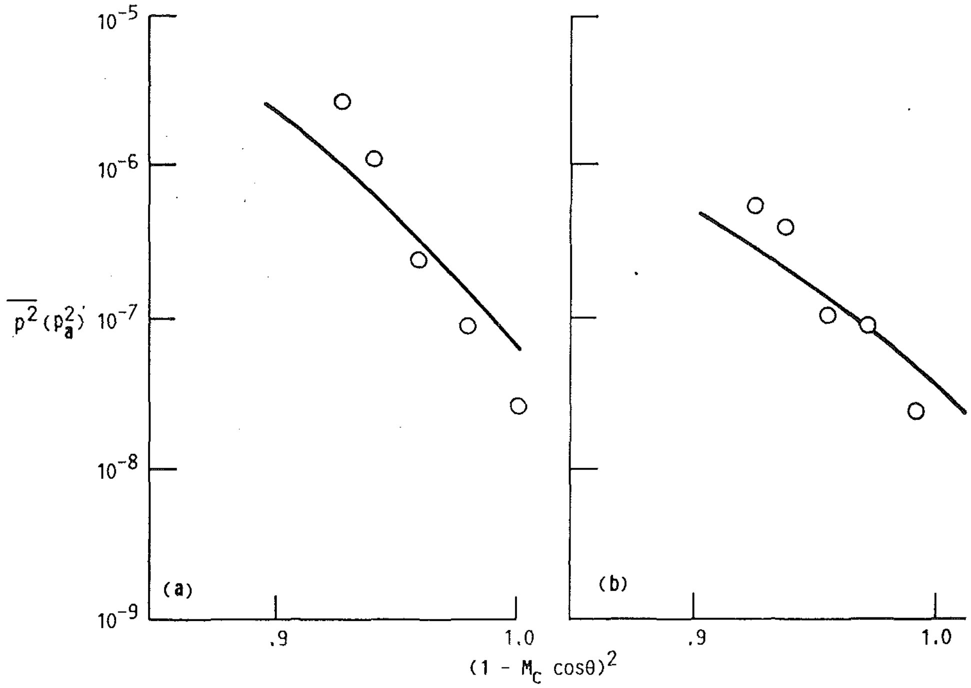

Fig. 2 Directivity of the first and second subharmonic at $U_j = 30$ m/s, excitation level: $\bar{u}^2_{mo}/U^2_j = 4 \times 10^{-3}$; (a) first subharmonic, (b) second subharmonic; 0: experiment (Laufer and Yen 1983)—theory

perimental data around $(1-M_c\cos\theta)^2 = 0.95$. The directivity in the present analysis is a result of the dependency of both I_x and I_r on θ. However, I_r is less dependent on θ than is I_x. Therefore, *the directivity here is basically dependent on* $(I_x)^2$. Thus, in the present analysis, the sound intensity is proportional to exp $(8\pi^2 M_c\cos\theta)$. This is in close agreement with the experimental results of Laufer and Yen (1983) which showed that the directivity is proportional to exp $(90\ M_c\ \cos\theta)$. However, since $8\pi^2 < 90$, the predicted dependency on θ is less than that of the observations as Figs. 2 and 3 indicate. In the case of Huerre and Crighton (1983) where the shear noise was considered to be the dominant sound sources, the directivity of the calculated shear noise was found to behave as exp $(52\ M_c\ \cos\theta)$ which is much less than that of the self-noise and that of the measurements. Therefore, the observed superdirectivity cannot be explained by the shear noise, but can be attributed to the self-noise.

Because $|I_x|^2 \sim \exp(8\pi^2 M_c\ \cos\theta)$, the directivity is dependent on Mach number. As the Mach number is increased, the directivity becomes more pronounced. This can be seen by comparing Fig. 2(*a*) to Fig. 3(*a*) and Fig. 2(*b*) to Fig. 3(*b*) which shows that both theory and observations idicate the directivity to increase with increasing the jet velocity.

Spectra

Figure 4(*a*) shows the spectra of the self-noise at $\theta = 30$ deg radiated at Strouhal number corresponding to $S = 2\mathrm{St}_n$, St_n, $\mathrm{St}_n/2$ and $\mathrm{St}_n/4$, where the vertical scale of Fig. 4(*a*) is a relative one. The radiated noise at given Strouhal S is here a result of the self interaction of the $S/2$ frequency component. According to equation (19), the variation of the intensity with the Strouhal number is a result of the dependency of I_x and I_r, on S. The maximum amplitude saturation, $u_{\max}$, is weakly dependent on the Strouhal number and its relative values were obtained from Laufer and Yen's (1983) data. The corresponding measurements of Laufer and Yen (1983) is shown here as Fig. 4(*b*). Figure 4 shows qualitative agreement between theory and observations. However, one should keep in mind that the noise measured at Strouhal number S is not only a result of the self-interaction of the $S/2$ instability component, but is also due to the shear noise of the S instability component as well as due to the interaction of the $3S/2$ and the $S/2$ frequencies components, or that of the $2S$ and S components. These secondary interactions between $2S$ and S and the interactions between $3S/2$ and S were not considered here. The radiation of the fine-grained random turbulence is responsible for filling the gaps between the observed spikes in the spectra.

Scaling Parameters

In the present formulation, equation (19) shows the $p^2 \sim u^4_{\max}$. This is in good agreement with the observation of Laufer and Yen (1983) as Fig. 5 indicates. Huerre and Crighton's (1983) calculation of the shear noise indicate that $p^2 \sim u^2_{\max}$ which contradicts the observations. Thus, the self-noise can explain the nonlinear nature of the observed far-field sound. Further, Laufer and Yen (1983) have shown that the experimental data for the far-field sound intensity can be scaled according to the form:

$$P = (\bar{p}^2/\rho_o^2 u^2_{\max})(M_j^{-2} S_{tn}^{-2})(R^2/D^2) = (F(1-M_c\cos\theta) \tag{21a}$$

The corresponding theoretical result for the self-noise is

$$P = (\bar{p}^2/\rho_o^2 u^2_{\max})(M_j^{-2} S_{tn}^{-2})(R^2/D^2)$$
$$= (\delta_o/\delta_{mo})^2 (C/U_j)^2 (S/S_{tn})^2\ |I_r|^2\ |I_x|^2. \tag{21b}$$

C is the convection velocity $= 0.5\ U_j$ and $\delta_o \approx 2\delta_{mo}$ and S/S_{tn} is a fraction that depends on the frequency considered. I_r is less dependent on θ than I_x is. Since I_x is a function of $(1-M_c\cos\theta)$ as equation (20) indicates, then the right-hand side of equation (21*b*) can be written as:

$$F(|I_x|^2) = F(1-M_c\cos\theta)$$

which is the same as the experimental results (equation (21*a*)).

The variation of the normalized far-field radiation intensity, as given by equation (21*b*), with the Doppler factor at $S = \mathrm{St}_n/2$, $\mathrm{St}_n/4$ is shown in Fig. 6 in comparison with the experimental data. The figure shows that the calculated nor-

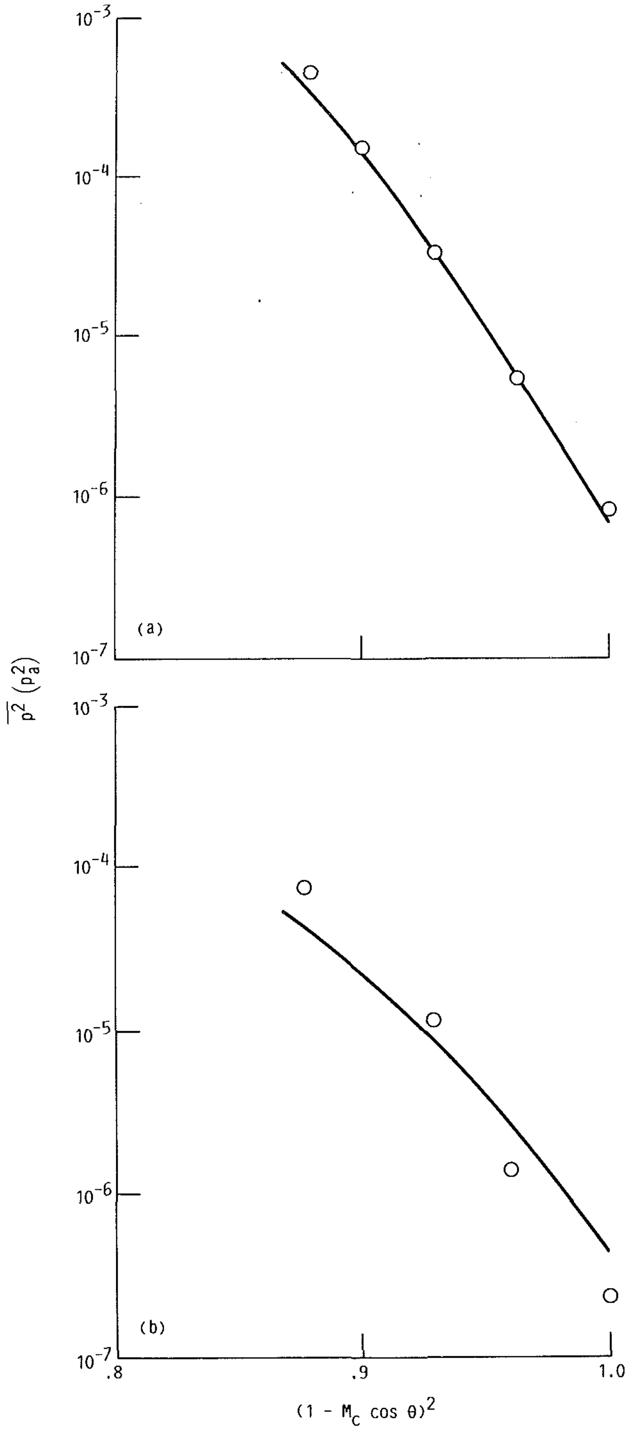

Fig. 3 Directivity of the first and second subharmonics at $U_j = 50$ m/s; (*a*) first subharmonic at excitation level $\bar{u}^2_{mo}/U_j^2 = 4 \times 10^{-3}$, (*b*) second subharmonic at excitation level $\bar{u}^2_{mo}/U_j^2 = 5.8 \times 10^{-3}$; 0: Experiment (Laufer and Yen 1983)—theory

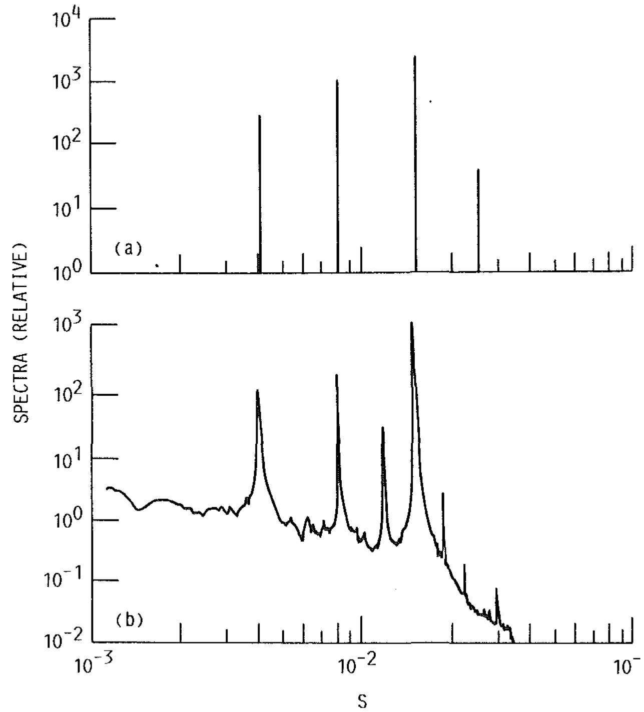

Fig. 4 Far-field spectra: $U_j = 50$ m/s, excitation level $\bar{u}^2_{mo}/U_j^2 = 1 \times 10^{-2}$, $\theta = 30$ deg; (*a*) theory, (*b*) experiment (Laufer and Yen 1983)

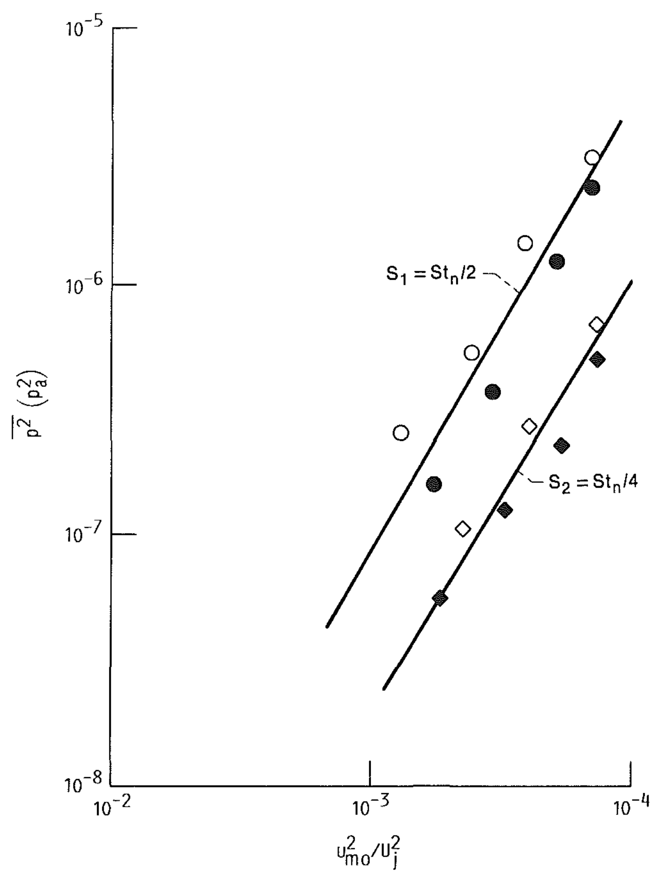

Fig. 5 Variation of the far-field radiation intensity with the saturation amplitude of the eigenmodes, $U_j = 30$ m/sec, $\theta = 30$ deg, ○, ◇, S_1; S_2; ●, ◆, S_1, S_2 (repeat);—theory

malized intensity is weakly dependent on the frequency which is in accordance with observation.

The normalized intensity is dependent on the Mach number through the dependency of I_x on$(1 - M_c\cos\theta)$. Therefore, if one plots the normalized intensity against the Doppler factor for several Mach numbers, the slope of the curve should be almost the same. Figure 7 shows the calculated normalized far-field radiation intensity as a function of the Doppler factor in comparison with the experimental measurements. The figure shows that changing the jet velocity from 30 m/s to 70

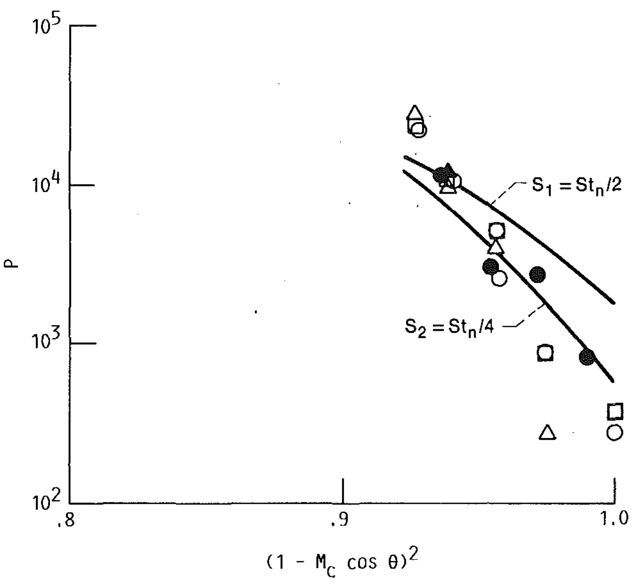

Fig. 6 Normalized far-field radiation intensity variation with the Doppler factor at various forcing levels and frequencies $U_j = 30$ m/s; experiments f_1: $\bar{u}_{mo}^2/U_j^2$:0, $= 4 \times 10^{-3}$, Δ, 2.9×10^{-3}; $\square$ 1.7×10^{-3}; s_2: $\bullet$ $\bar{u}_{mo}^2/U_j^2 = 4 \times 10^{-3}$;—present theory, (equation (21*b*))

m/s has little effect on the slope of the curve as the observations indicate.

Conclusions

Lighthill's theory is used to predict the far-field sound resulting from the self-interactions of instability waves in a round jet. The self noise-intensity was found to be proportional to the fourth order of the velocity amplitude saturation which can explain the nonlinear behavior of the sound intensity observed by Laufer and Yen (1983). The dependency of the sound intensity on Strouhal number and Mach number are in accordance with the observations. This self-interaction of the instability waves results in a "superdirectivity" as in the observations. These agreements between the calculated characteristics of the self-noise and the observations suggest that the noise resulting from the self-interaction of instability

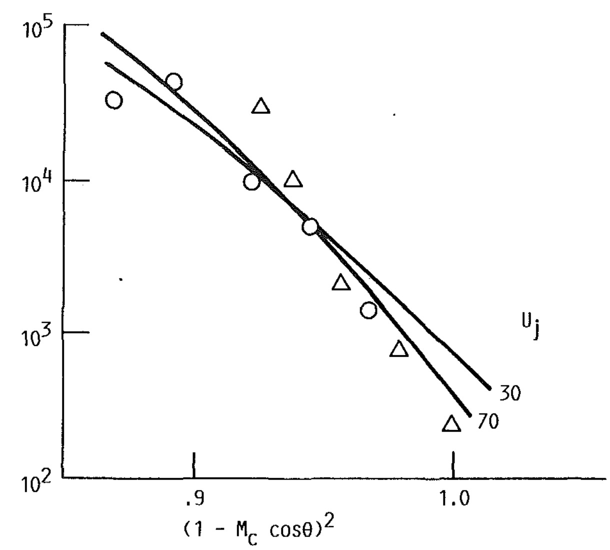

Fig. 7 Normalized far-field radiation intensity variation with the Doppler factor at various jet velocities: 0, $U_j = 70$ m/s; Δ, $U_j = 30$ m/s—theory

waves is a significant noise mechanism that cannot be neglected with respect to the shear noise.

References

Crighton, D. G., 1975, "Basic Principles of Aerodynamic Noise Generation," *Prog. Aerospace Sci.*, Vol. 16, pp. 31–96.

Crow, S. C., 1972, "Acoustic Gain of a Turbulent Jet," *Bull Am. Phys. Soc.*, Paper IE.6.

Ffowcs-Williams, J. E., and Kempton, A. J., 1978, "The Noise from the Large Scale Structure of a Jet," *J. Fluid Mech.*, Vol. 84, pp. 673–694.

Huerre, P., and Crighton, D. C., 1983, "Sound Generation by Instability Waves in a Low Mach Number Jet," AIAA Paper No. 83-o661.

Laufer, J., and Yen, T.-C. 1983, "Noise generation by a low Mach number jet," *J. Fluid Mech.* Vol. 134, pp. 1–31.

Lighthill, M. J., 1952, "On sound generated aerodynamically I. General Theory," *Proc. R. Soc. London*, Vol. A211, pp. 564–587.

Lilley, G. M., 1974, "On the noise from jets," *Noise Mechanisms*, pp. 13.1–13.12; AGARD CP-131.

Mankbadi, R. R., and Liu, J. T. C., 1984, "Sound Generated Aerodynamically Revisited-Large Scale Coherent Structure in a Turbulent Jet as a Source of Sound," *Phil. Tran. Roy. Soc. London*, Vol. A311, pp. 183–217.

Journal of Applied Mechanics

Brief Notes

A Brief Note is a short paper that presents a specific solution of technical interest in mechanics but which does not necessarily contain new general methods or results. A Brief Note should not exceed 1500 words *or equivalent* (a typical one-column figure or table is equivalent to 250 words; a one line equation to 30 words). Brief Notes will be subject to the usual review procedures prior to publication. After approval such Notes will be published as soon as possible. The Notes should be submitted to the Technical Editor of the JOURNAL OF APPLIED MECHANICS. Discussions on the Brief Notes should be addressed to the Editorial Department, ASME, United Engineering Center, 345 East 47th Street, New York, N. Y. 10017, or to the Technical Editor of the JOURNAL OF APPLIED MECHANICS. Discussions on Brief Notes appearing in this issue will be accepted until two months after publication. Readers who need more time to prepare a Discussion should request an extension of the deadline from the Editorial Department.

Stress Fields of Interface Dislocations

Chung-Yuen Hui[1] and Dimitris C. Lagoudas[2]

The procedure of computing the stress field due to an edge dislocation on the interface between two semi-infinite linearly elastic materials under plane-strain has been developed by Dundurs and Sendeckyj (1965), Braekhus and Lothe (1971), and Nakahara and Willis (1973). Dundurs and Sendeckyj used the Airy stress function approach, assuming both materials to be isotropic. The displacement approach used in Braekhus and Lothe (1971) and Nakahara and Willis (1973) is more general and works for the case when both materials are anisotropic and in three dimensions as well. Comninou (1977) obtained the stress field on the interface of the above problem when both materials are isotropic using the stress functions given in (1965), but the stress field elsewhere is not given. It should be noted that a considerable amount of algebra is involved in applying the methods described in Dundurs and Sendeckyj (1965), Braekhus and Lothe (1971), and Nakahara and Willis (1973). In applications (e.g., to find the interaction of a crack with a dislocation on the interface) it is necessary to know the stress field everywhere. The purpose of this note is to derive the stress field of an edge dislocation on the interface between two dissimilar but isotropic linearly elastic half-spaces under plane-strain loading conditions. The analytic function method of Muskhelishvili (1953) is used in our derivation, which leads to a significant reduction of algebra.

Material 1, with shear modulus, G_1, and Poisson's ratio, ν_1, occupies the region $x > 0$ (a Cartesian frame xy is used), while material 2, with shear modulus, G_2, and Poisson's ratio, ν_2, occupies the region $x < 0$. The edge dislocation with Burgers vector (b_x, b_y) is located at the origin, while the interface is the y-axis. All functions and material constants with subscripts 1, 2 correspond to material 1 and 2, respectively. From Muskhelishvili (1953), the displacements and stresses in each region are given by the analytic functions φ_i and ψ_i, i.e.,

$$2G_i(u_i+iv_i) = \kappa_i\,\varphi_i(z)-z\,\overline{\varphi_i'(z)} - \overline{\psi_i(z)}\,. \tag{1}$$

$$(\sigma_{xx})_i + (\sigma_{yy})_i = 2[\varphi_i'(z) + \overline{\varphi_i'(z)}\,], \tag{2}$$

$$(\sigma_{yy})_i - i(\sigma_{xy})_i = \varphi_i'(z)+\overline{\varphi_i'(z)}+z\overline{\varphi_i''(z)}+\overline{\psi_i'(z)}. \tag{3}$$

Let

$$\varphi_i(z) = A_i\ln(z) + C_i, \tag{4}$$

$$\psi_i(z) = B_i\ln(z), \tag{5}$$

where the constants A_i, B_i, C_i are unknown and $\kappa_i = 3-4\nu_i$. The choice of φ_i and ψ_i produces the same displacement field as given by Nakahara and Willis (1973). These constants are determined by imposing (1) continuity of traction across the interface $x = 0, y \neq 0$, (2) global equilibrium so that the total force acting on any circuit enclosing the dislocation is zero, and (3) the displacement jumps $u_1+iv_1-u_2-iv_2$ across the interface to be $(b_x+ib_y)H(y)$. A_i, B_i, and C_i are found to be

$$A_i = \alpha_i(b_y-i\,b_x), \tag{6}$$

$$B_1 = \bar{A}_2,\quad B_2 = \bar{A}_1, \tag{7}$$

$$\kappa_1 C_1 = \frac{i\pi}{2}(\kappa_1 A_1 + A_2)-\bar{A}_1$$

$$\kappa_2 C_2 = \frac{i\pi}{2}(\kappa_2 A_2 + A_1) - \bar{A}_2, \tag{8}$$

where

$$\alpha_1 = \frac{G_1 G_2}{\pi(\kappa_1 G_2 + G_1)},\quad \alpha_2 = \frac{G_1 G_2}{\pi(\kappa_2 G_1 + G_2)}. \tag{9}$$

The constants C_i are determined by fixing u_i+iv_i along the negative y-axis to be $\beta\ln(-y)$, where $\beta = (\kappa_1A_1-\bar{B}_1)/2G_1 = (\kappa_2A_2-\bar{B}_2)/2G_2$.

Using equations (2) and (3), the stress field in material 1 is

$$(\sigma_{xx})_1 = \alpha_1\frac{b_x(y^3-3x^2y)-b_y(-x^3+3xy^2)}{(x^2+y^2)^2} + 2\alpha_1\frac{-b_xy+b_yx}{(x^2+y^2)} - \alpha_2\frac{b_x y+b_yx}{(x^2+y^2)} \tag{10}$$

$$(\sigma_{xy})_1 = \alpha_1\frac{b_x(x^3-3xy^2)+b_y(-y^3+3x^2y)}{(x^2+y^2)^2} + \alpha_2\frac{b_x x-b_y y}{(x^2+y^2)}, \tag{11}$$

$$(\sigma_{yy})_1 = \alpha_1\frac{b_x(-y^3+3x^2y)+b_y(-x^3+3xy^2)}{(x^2+y^2)^2} + 2\alpha_1\frac{-b_xy+b_yx}{(x^2+y^2)} + \alpha_2\frac{b_xy+b_yx}{(x^2+y^2)}. \tag{12}$$

The stress field in material 2 is obtained from the above formulae by interchanging α_1 and α_2. On the interface $x = 0$, the tractions are

[1]Associate Professor, Theoretical and Applied Mechanics Department, Cornell University, Ithaca, NY 14853.

[2]Assistant Professor, Civil Engineering Department, Rensselaer Polytechnic Institute, Troy, NY 12180. Mem. ASME.

Manuscript received by the ASME Applied Mechanics Division, May 10, 1988; final revision, May 14, 1989.

$$(\sigma_{xx})_1 = (\sigma_{xx})_2$$
$$= -b_x(\alpha_1+\alpha_2)\frac{1}{y} + \pi b_y(\alpha_1-\alpha_2)\delta(y), \qquad (13)$$
$$(\sigma_{xy})_1 = (\sigma_{xy})_2$$
$$= -b_y(\alpha_1+\alpha_2)\frac{1}{y} - \pi b_x(\alpha_1-\alpha_2)\delta(y), \qquad (14)$$

which agrees with Comninou's result (Comninou, 1977). σ_{yy} is discontinuous across the interface, i.e.,

$$(\sigma_{yy})_1(0^+,y)$$
$$= b_x(-3\alpha_1+\alpha_2)\frac{1}{y} + \pi b_y(3\alpha_1+\alpha_2)\delta(y), \qquad (15a)$$
$$(\sigma_{yy})_2(0^-,y)$$
$$= b_x(-3\alpha_2+\alpha_1)\frac{1}{y} - \pi b_y(3\alpha_2+\alpha_1)\delta(y). \qquad (15b)$$

Acknowledgment

The authors acknowledge the support of the Army Research Office through the Mathematical Sciences Institute of Cornell University. C.-Y. Hui acknowledges also the support of the Materials Science Center at Cornell, which is funded by the National Science Foundation (DMR-MRL program).

References

Braekhus, J., and Lothe, J., 1971, "Dislocation at and Near Planar Interfaces," *Phys. Stat. Solidi* (*b*), Vol. 43, p. 651.

Comninou, M., 1977, "A Property of Interface Dislocations," *Phil. Mag.*, Vol. 36, p. 1281.

Dundurs, J., and Sendeckyj, G. P., "Behavior of an Edge Dislocation Near a Bimetallic Interface," *J. Appl. Phys.*, Vol. 36, p. 3353.

Muskhhelishvili, N. I., 1953, *Some Basic Problems in the Mathematical Theory of Elasticity* (translated from the Russian by J. R. M. Radok), Noordhoff, Groningen, Holland.

Nakahara, S., and Willis, J. R., 1973, "Some Remarks on Interfacial Dislocations," *J. Phys.*, Vol. F3, p. L249.

Testing Numerical Integrations of Equations of Motion

T. R. Kane[3] and D. A. Levinson[4]

Introduction

After certain defects in step (4) of Kane and Levinson (1988) had been brought to our attention, we discovered that the range of applicability of the method there set forth for testing numerical integrations of equations of motion of mechanical systems could be extended, and the procedure simplified substantially, by replacing step (4) with:

In step (4) let Z denote a function of t that satisfies the differential equation

$$\dot{Z} = -\sum_{r=1}^{p} G_r u_r + \Sigma \qquad (1)$$

where Σ is the following sum over the ν particles forming the system S under consideration:

$$\Sigma = \sum_{i=1}^{\nu} m_i \mathbf{v}^{P_i} \cdot \dot{\tilde{\mathbf{v}}}_t^{P_i}. \qquad (2)$$

Here, m_i is the mass of P_i, a generic particle of S; $\mathbf{v}^{P_i}$ is the velocity of P_i in a Newtonian reference frame N; and $\dot{\tilde{\mathbf{v}}}_t^{P_i}$ is the time-derivative, in N, of the vector $\tilde{\mathbf{v}}_t^{P_i}$ $(i=1, \ldots, \nu)$ which can be identified by inspection when the velocity $\mathbf{v}^{P_i}$ of P_i in N is expressed as a linear function of the generalized speeds u_r $(r=1, \ldots, p)$, that is, as

$$\mathbf{v}^{P_i} = \sum_{r=1}^{p} \tilde{\mathbf{v}}_r^{P_i} u_r + \tilde{\mathbf{v}}_t^{P_i} \quad (i=1, \ldots, \nu). \qquad (3)$$

What makes it easy to carry out this new step (4) is that, in order to form Σ, one need not actually perform a summation over the individual particles of any rigid body that belongs to S. Instead, one can take advantage of the fact that Σ_B, the contribution to Σ of the particles of a rigid body B, is given by

$$\Sigma_B = m\mathbf{v} \cdot \dot{\tilde{\mathbf{v}}}_t + \boldsymbol{\omega} \cdot \mathbf{I} \cdot \dot{\tilde{\boldsymbol{\omega}}}_t \qquad (4)$$

where m is the mass of B; $\mathbf{v}$ is the velocity of the mass center of B in N; $\dot{\tilde{\mathbf{v}}}_t$ is the time-derivative, in N, of the vector $\tilde{\mathbf{v}}_t$ which can be identified by inspection when $\mathbf{v}$ has been expressed as a linear function of the generalized speeds u_r $(r=1, \ldots, p)$, that is, as

$$\mathbf{v} = \sum_{r=1}^{p} \tilde{\mathbf{v}}_r u_r + \tilde{\mathbf{v}}_t. \qquad (5)$$

$\boldsymbol{\omega}$ is the angular velocity of B in N; $\mathbf{I}$ is the central inertia dyadic of B; and $\dot{\tilde{\boldsymbol{\omega}}}_t$ is the time-derivative, in N, of the vector $\tilde{\boldsymbol{\omega}}_t$ which can be identified by inspection when $\boldsymbol{\omega}$ has been expressed as a linear function of the generalized speeds u_r $(r=1, \ldots, p)$, that is, as

$$\boldsymbol{\omega} = \sum_{r=1}^{p} \tilde{\boldsymbol{\omega}}_r u_r + \tilde{\boldsymbol{\omega}}_t. \qquad (6)$$

The line of reasoning that leads to the new step (4) begins with the observation that equation (2) of this Note and equation (5.6.15) of Kane and Levinson (1985) permit one to write

$$-\sum_{r=1}^{p} \tilde{F}_r^* u_r = \dot{K}_2 - \dot{K}_0 + \Sigma. \qquad (7)$$

Adding this equation and equation (22) of Kane and Levinson (1988), and making use of equation (6.1.1) of Kane and Levinson (1985), one finds that, if Z is required to satisfy equation (1), then

$$\dot{V} + \dot{Z} + \dot{K}_2 - \dot{K}_0 = 0 \qquad (8)$$

from which it follows immediately that C defined as in equation (13) of Kane and Levinson (1988) is a constant.

Example

Referring to the system shown in Fig. 5 of Kane and Levinson (1988), one can express ${}^N\mathbf{v}^{B^*}$, the velocity of B^* in N, and ${}^N\boldsymbol{\omega}^B$, the angular velocity of B in N, as

$${}^N\mathbf{v}^{B^*} = \Omega(L+q_4)\mathbf{a}_2 - ru_2\mathbf{a}_3 \qquad (9)$$

and

$${}^N\boldsymbol{\omega}^B = u_1\mathbf{a}_1 + u_2\mathbf{a}_2 + [(L+q_4)\Omega/r]\mathbf{a}_3. \qquad (10)$$

Inspection of equations (9) and (10) reveals that

$${}^N\tilde{\mathbf{v}}_t^{B^*} = \Omega(L+q_4)\mathbf{a}_2 \qquad (11)$$

and

$${}^N\tilde{\boldsymbol{\omega}}_t^B = [(L+q_4)\Omega/r]\mathbf{a}_3. \qquad (12)$$

Differentiation of equations (11) and (12) with respect to t in N, and substitution into equation (4), with

[3] Professor of Applied Mechanics, Stanford University, Stanford, CA. Fellow ASME.

[4] Staff Scientist, Lockheed Palo Alto Research Laboratory, Palo Alto, CA. Mem. ASME.

Manuscript received and accepted by the ASME Applied Mechanics Division, April 17, 1989.

$$(\sigma_{xx})_1 = (\sigma_{xx})_2$$
$$= -b_x(\alpha_1+\alpha_2)\frac{1}{y} + \pi\, b_y(\alpha_1-\alpha_2)\delta(y), \quad (13)$$
$$(\sigma_{xy})_1 = (\sigma_{xy})_2$$
$$= -b_y(\alpha_1+\alpha_2)\frac{1}{y} - \pi\, b_x(\alpha_1-\alpha_2)\,\delta(y), \quad (14)$$

which agrees with Comninou's result (Comninou, 1977). σ_{yy} is discontinuous across the interface, i.e.,

$$(\sigma_{yy})_1(0^+,y)$$
$$= b_x(-3\alpha_1+\alpha_2)\frac{1}{y} + \pi\, b_y(3\alpha_1+\alpha_2)\,\delta(y), \quad (15a)$$
$$(\sigma_{yy})_2(0^-,y)$$
$$= b_x(-3\alpha_2+\alpha_1)\frac{1}{y} - \pi\, b_y\,(3\alpha_2+\alpha_1)\delta(y). \quad (15b)$$

Acknowledgment

The authors acknowledge the support of the Army Research Office through the Mathematical Sciences Institute of Cornell University. C.-Y. Hui acknowledges also the support of the Materials Science Center at Cornell, which is funded by the National Science Foundation (DMR-MRL program).

References

Braekhus, J., and Lothe, J., 1971, "Dislocation at and Near Planar Interfaces," *Phys. Stat. Solidi* (*b*), Vol. 43, p. 651.

Comninou, M., 1977, "A Property of Interface Dislocations," *Phil. Mag.*, Vol. 36, p. 1281.

Dundurs, J., and Sendeckyj, G. P., "Behavior of an Edge Dislocation Near a Bimetallic Interface," *J. Appl. Phys.*, Vol. 36, p. 3353.

Muskhhelishvili, N. I., 1953, *Some Basic Problems in the Mathematical Theory of Elasticity* (translated from the Russian by J. R. M. Radok), Noordhoff, Groningen, Holland.

Nakahara, S., and Willis, J. R., 1973, "Some Remarks on Interfacial Dislocations," *J. Phys.*, Vol. F3, p. L249.

Testing Numerical Integrations of Equations of Motion

T. R. Kane[3] and D. A. Levinson[4]

Introduction

After certain defects in step (4) of Kane and Levinson (1988) had been brought to our attention, we discovered that the range of applicability of the method there set forth for testing numerical integrations of equations of motion of mechanical systems could be extended, and the procedure simplified substantially, by replacing step (4) with:

In step (4) let Z denote a function of t that satisfies the differential equation

$$\dot{Z} = -\sum_{r=1}^{p} G_r u_r + \Sigma \quad (1)$$

where Σ is the following sum over the ν particles forming the system S under consideration:

[3] Professor of Applied Mechanics, Stanford University, Stanford, CA. Fellow ASME.

[4] Staff Scientist, Lockheed Palo Alto Research Laboratory, Palo Alto, CA. Mem. ASME.

Manuscript received and accepted by the ASME Applied Mechanics Division, April 17, 1989.

$$\Sigma = \sum_{i=1}^{\nu} m_i \mathbf{v}^{P_i} \cdot \dot{\tilde{\mathbf{v}}}_t^{P_i}. \quad (2)$$

Here, m_i is the mass of P_i, a generic particle of S; $\mathbf{v}^{P_i}$ is the velocity of P_i in a Newtonian reference frame N; and $\dot{\tilde{\mathbf{v}}}_t^{P_i}$ is the time-derivative, in N, of the vector $\tilde{\mathbf{v}}_t^{P_i}$ $(i=1, \ldots, \nu)$ which can be identified by inspection when the velocity $\mathbf{v}^{P_i}$ of P_i in N is expressed as a linear function of the generalized speeds u_r $(r=1, \ldots, p)$, that is, as

$$\mathbf{v}^{P_i} = \sum_{r=1}^{p} \tilde{\mathbf{v}}_r^{P_i} u_r + \tilde{\mathbf{v}}_t^{P_i} \quad (i=1, \ldots, \nu). \quad (3)$$

What makes it easy to carry out this new step (4) is that, in order to form Σ, one need not actually perform a summation over the individual particles of any rigid body that belongs to S. Instead, one can take advantage of the fact that Σ_B, the contribution to Σ of the particles of a rigid body B, is given by

$$\Sigma_B = m\mathbf{v} \cdot \dot{\tilde{\mathbf{v}}}_t + \boldsymbol{\omega} \cdot \mathbf{I} \cdot \dot{\tilde{\boldsymbol{\omega}}}_t \quad (4)$$

where m is the mass of B; $\mathbf{v}$ is the velocity of the mass center of B in N; $\dot{\tilde{\mathbf{v}}}_t$ is the time-derivative, in N, of the vector $\tilde{\mathbf{v}}_t$ which can be identified by inspection when $\mathbf{v}$ has been expressed as a linear function of the generalized speeds u_r $(r=1, \ldots, p)$, that is, as

$$\mathbf{v} = \sum_{r=1}^{p} \tilde{\mathbf{v}}_r u_r + \tilde{\mathbf{v}}_t. \quad (5)$$

$\boldsymbol{\omega}$ is the angular velocity of B in N; $\mathbf{I}$ is the central inertia dyadic of B; and $\dot{\tilde{\boldsymbol{\omega}}}_t$ is the time-derivative, in N, of the vector $\tilde{\boldsymbol{\omega}}_t$ which can be identified by inspection when $\boldsymbol{\omega}$ has been expressed as a linear function of the generalized speeds u_r $(r=1, \ldots, p)$, that is, as

$$\boldsymbol{\omega} = \sum_{r=1}^{p} \tilde{\boldsymbol{\omega}}_r u_r + \tilde{\boldsymbol{\omega}}_t. \quad (6)$$

The line of reasoning that leads to the new step (4) begins with the observation that equation (2) of this Note and equation (5.6.15) of Kane and Levinson (1985) permit one to write

$$-\sum_{r=1}^{p} \tilde{F}_r^* u_r = \dot{K}_2 - \dot{K}_0 + \Sigma. \quad (7)$$

Adding this equation and equation (22) of Kane and Levinson (1988), and making use of equation (6.1.1) of Kane and Levinson (1985), one finds that, if Z is required to satisfy equation (1), then

$$\dot{V} + \dot{Z} + \dot{K}_2 - \dot{K}_0 = 0 \quad (8)$$

from which it follows immediately that C defined as in equation (13) of Kane and Levinson (1988) is a constant.

Example

Referring to the system shown in Fig. 5 of Kane and Levinson (1988), one can express ${}^N\mathbf{v}^{B^*}$, the velocity of B^* in N, and ${}^N\boldsymbol{\omega}^B$, the angular velocity of B in N, as

$${}^N\mathbf{v}^{B^*} = \Omega(L+q_4)\mathbf{a}_2 - ru_2\mathbf{a}_3 \quad (9)$$

and

$${}^N\boldsymbol{\omega}^B = u_1\mathbf{a}_1 + u_2\mathbf{a}_2 + [(L+q_4)\Omega/r]\mathbf{a}_3. \quad (10)$$

Inspection of equations (9) and (10) reveals that

$${}^N\tilde{\mathbf{v}}_t^{B^*} = \Omega(L+q_4)\mathbf{a}_2 \quad (11)$$

and

$${}^N\tilde{\boldsymbol{\omega}}_t^B = [(L+q_4)\Omega/r]\mathbf{a}_3. \quad (12)$$

Differentiation of equations (11) and (12) with respect to t in N, and substitution into equation (4), with

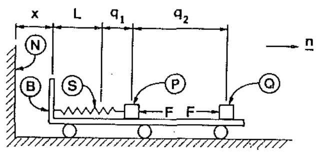

Fig. 1 Two particles on a moving base

$$\mathbf{I} = \frac{2}{5} Mr^2(\mathbf{a}_1\mathbf{a}_1 + \mathbf{a}_2\mathbf{a}_2 + \mathbf{a}_3\mathbf{a}_3), \tag{13}$$

leads to

$$\Sigma_B = \frac{7}{5} M\Omega\dot{\Omega}(L + q_4)^2. \tag{14}$$

Substitution from this equation and equations (55) of Kane and Levinson (1988) into equation (1) gives

$$\dot{Z} = \delta[(u_1 - \Omega)u_1 + u_2^2] + \frac{7}{5} M\Omega\dot{\Omega}(L + q_4)^2, \tag{15}$$

which is precisely equation (59) of Kane and Levinson (1988), but has been obtained with far less labor than the old step (4) required.

A situation in which the new step (4) can be applied, whereas the old step (4) could not, arises in connection with the system depicted in Fig. 1, which consists of a movable base B, and two particles P and Q, each of mass m. B moves horizontally relative to an inertially fixed wall N, in such a way that the distance x between N and B is a specified function of time t. P is connected to B by a linear spring S of modulus k, and P is connected to Q by an actvator (not shown), which exerts oppositely directed forces of magnitude F on each of P and Q. L is the natural length of S, and q_1 and q_2 are generalized coordinates, with q_1 the extension of S, and q_2 the distance from P to Q.

Defining generalized speeds u_1 and u_2 as

$$u_1 = \dot{q}_1, \qquad u_2 = \dot{q}_2, \tag{16}$$

one can write the velocities $\mathbf{v}^P$ and $\mathbf{v}^Q$ of P and Q as

$$\mathbf{v}^P = (\dot{x} + u_1)\mathbf{n} \tag{17}$$

$$\mathbf{v}^Q = (\dot{x} + u_1 + u_2)\mathbf{n}, \tag{18}$$

where $\mathbf{n}$ is a unit vector directed as shown in Fig. 1; and, if F is such that u_2 is related to u_1 in accordance with the relation

$$u_2 = \gamma u_1, \tag{19}$$

where γ is a specified function of t, then equation (18) can be rewritten as

$$\mathbf{v}^Q = [\dot{x} + (1 + \gamma)u_1]\mathbf{n}. \tag{20}$$

Comparison of equations (17) and (20) with equations (3) shows that

$$\tilde{\mathbf{v}}_1^P = \mathbf{n} \tag{21}$$

$$\tilde{\mathbf{v}}_1^Q = (1 + \gamma)\mathbf{n} \tag{22}$$

$$\tilde{\mathbf{v}}_t^P = \dot{x}\mathbf{n} \tag{23}$$

$$\tilde{\mathbf{v}}_t^Q = \dot{x}\mathbf{n}, \tag{24}$$

so that the generalized active force, $\tilde{F}_1$, is given by

$$\tilde{F}_1 = \tilde{\mathbf{v}}_1^P \cdot [(-kq_1 - F)\mathbf{n}] + \tilde{\mathbf{v}}_1^Q \cdot (F\mathbf{n}) = -kq_1 + \gamma F, \tag{25}$$

and substitution from equations (17), (18), (23), and (24) into equation (2) yields

$$\Sigma = m\ddot{x}[2\dot{x} + (2 + \gamma)u_1]. \tag{26}$$

Comparing equations (7) and (8) of Kane and Levinson (1988) with equations (16) and (19) of the present Note, one finds that

$$W_{11} = 1,\ W_{12} = 0,\ W_{21} = 0,\ W_{22} = 1,\ A_{21} = \gamma,\ B_2 = 0 \tag{27}$$

and with

$$V = \frac{1}{2} kq_1^2, \tag{28}$$

and

$$G_1 = \gamma F, \tag{29}$$

it can be verified that equations (9) and (10) of Kane and Levinson (1988) are satisfied. Thus, substitution from equations (29) and (26) into equation (1) yields

$$\dot{Z} = -\gamma F u_1 + m\ddot{x}[2\dot{x} + (2 + \gamma)u_1]. \tag{30}$$

The system's kinetic energy, K, is

$$K = \frac{1}{2} m\{(\dot{x} + u_1)^2 + [\dot{x} + (1 + \gamma)u_1]^2\}, \tag{31}$$

which shows that

$$K_0 = m\dot{x}^2,\ K_2 = \frac{1}{2} m[1 + (1 + \gamma)^2]u_1^2. \tag{32}$$

This, together with equation (28) and equations (13) of Kane and Levinson (1988), leads to the checking function

$$C = \frac{1}{2} kq_1^2 + Z + \frac{1}{2} m[1 + (1 + \gamma)^2]u_1 - m\dot{x}^2. \tag{33}$$

The old step (4), instead of producing equation (30), yields

$$\dot{Z} = -\gamma F u_1 + m\{\ddot{x}[2\dot{x} + (2 + \gamma)u_1] + \dot{\gamma}u_1[\dot{x} + (1 + \gamma)u_1]\}, \tag{34}$$

which contains an extraneous term and would thus give rise to an incorrect checking function.

References

Kane, T. R., and Levinson, D. A., 1985, *Dynamics: Theory and Applications*, McGraw-Hill, New York, p. 154.

Kane, T. R., and Levinson, D. A., 1988, "A Method for Testing Numerical Integrations of Equations of Motion of Mechanical Systems," ASME Journal of Applied Mechanics, Vol. 55, pp. 711–715.

Journal of Applied Mechanics

Discussions

On Immobile Kinematic Chains and a Fallacious Matrix Analysis[1]

S. Pellegrino[2] and C. R. Calladine.[2] A substantial portion of this Brief Note consists of an attack on a paper of ours: Pellegrino and Calladine, 1986. We are familiar with this attack, since it is almost the same as one which the *International Journal of Solids and Structures* had agreed to publish last year, together with a closure by ourselves. At the last minute, however (certainly after we had corrected the proofs of our closure), Kuznetsov decided to withdraw his discussion. In these circumstances we decided to submit a short paper about the matters under discussion to the *International Journal of Solids and Structures*; and this has now been accepted for publication.

We do not wish here to repeat all of our detailed comments on Kuznetsov's opinions; but it is desirable for us to make brief remarks about three of his statements, as follows.

1 Kuznetsov quotes from us: "When we allow the assembly to distort in its inextensional modes, it will be able, after all, to support a completely *arbitrary* set of loads . . . if the matrix $\mathbf{A}'$ is of full rank." He then states: "The premise is devoid of any notion of stability thus emasculating the proposed matrix test."

In fact, a large part of Section 9 of our paper is devoted to a discussion of this point. Our paper was first presented at the I.U.T.A.M. Congress at Lyngby in 1984. As a result of discussions with several participants there, and in consequence of comments provided by referees (as described under *Acknowledgements* in our paper), the version published in 1986 was an improvement of the earlier work. In particular, it included as Fig. 10 the example of Kuznetsov's Fig. 1(c), which had been provided as a destructive counter-example by a referee, but which in fact furnished a nice illustration of our point about the importance of making a sign-check.

2 Kuznetsov states that our method: "fails to recognize the system in Fig. 1(c) as a finite mechanism."

This is not true, provided our method is applied correctly. The method may well appear to fail to detect a finite mechanism if one examines only two particular independent mechanisms; but it succeeds when one considers all linear combinations of these, as indeed Kuznetsov acknowledges. However, whereas he appears to believe that this step involves "an infinite number of operations," in fact the calculation can be done either by hand on a small piece of paper or on a small computer very quickly. We give full details of this in our forthcoming paper. We also emphasize there that our matrix method does not, strictly, detect *finite* mechanisms, but actually those which are "of higher than first order."

3 Kuznetsov dismisses lightly the connection which Tarnai has made between *mirror symmetry* and a *finite mechanism* in his ring example. It seems to us that Tarnai provides a clear insight into a rather complicated three-dimensional assembly. The crucial role of symmetry in this case is completely absent from Kuznetsov's proposed "equivalent" system, shown in his Fig. 3.

References

Pellegrino, S., and Calladine, C. R., 1986, "Matrix Analysis of Statically and Kinematically Indeterminate Frameworks," *International Journal of Solids and Structures*, Vol. 22, pp. 409–428.

Author's Closure

The following is a response to the three remarks of Discussion.

1 The "sign-check" is the crux of the problem. If the authors fully appreciated its crucial role in the problem under consideration they would

(i) employ the perceived "supplemental" check as a basis for their analysis, and find out that a meaningful check calls for the construction and investigation of a certain quadratic form;

(ii) recognize this form as a classic found in works of Levi-Civita and a few others, and used for detection of infinitesimal mechanisms since the early 1900s; and, finally,

(iii) discard their matrix analysis, upon realizing that *it is useless whether or not "supplemented" by the sign-check.* "Unsupplemented," the analysis fails to achieve its stated goal of detecting infinitesimal mechanisms; "supplemented," the matrix analysis is superfluous since the sign-check by itself solves the problem: It yields the quadratic form whose definiteness alone is known to be *both* necessary *and* sufficient for kinematic immobility.

2 This one is a manner of nuance. The "destructive counterexample" could not "furnish a nice illustration of our point about the importance of a sign-check," since the very sign-check, absent in all prior renditions of the paper, was just a late and inadequate *reaction* to the counterexample. When elaborating on it, Pellegrino and Calladine consistently discuss *two* internal mechanisms or (extrapolating their conclusion to a general system) *all* mechanisms. They mention neither the term "linear combination," nor its immediate and unavoidable consequence, "quadratic form," apparently being unaware of both. While the present Discussion refers to linear combination, the persistent absence of any notion of quadratic form is puzzling, especially since this classical form has been reproduced in the subject note. What is this mysterious new sign-check requiring a finite number of opera-

[1] By E. N. Kuznetsov and published in the Mar. 1989 issue of the ASME Journal of Applied Mechanics, Vol. 56, pp. 222–224.

[2] Department of Engineering, University of Cambridge, Cambridge, U.K. CB2 1PZ.

tions "done very quickly"? Can it be that the authors have managed to do away with the old faithful quadratic form and found a simpler alternative sign-check? This certainly would be a significant advance in the state of the art. However, short of this miraculous cure, the proposed matrix method is beyond salvation, as shown in the above (i)–(iii).

3 The absence of symmetry is exactly the point: even the two spans in the "equivalent" system were made unequal. This has been done in order to demonstrate that symmetry *is not* a factor in Maxwell's conceptualization, and that prestress is impossible in *any* finite mechanism. Although Tarnai's ring (a space truss with bars arranged along the edges of Archimedes' antiprism) indeed possesses an interesting symmetry, this has no relation to its inability to hold a self-stress. In the authors' notation (Reference), both of the systems are characterized identically: $s=m=1$, where s is the degree of statical indeterminacy and m is the number of mechanisms. Since both systems are finite mechanisms, neither can be prestressed.

An Alternating Frequency/Time Domain Method for Calculating the Steady-State Response of Nonlinear Dynamic Systems[3]

F. H. Ling.[4] Periodic response of nonlinear dynamic systems are calculated by expanding the response into the Fourier series and using the Fast Fourier Transform (FFT) technique in this paper. This paper is written in an easily understood manner and contains some useful material towards engineering applications. As the authors of the paper pointed out, there are fundamental similarities in the concepts underlying their method (AFT) and the Fast Galerkin method (FG) described in an earlier work of ours (Ling and Wu, 1987). Moreover, the authors listed three differences between these two methods, two of which will be discussed as follows.

The first difference concerns the form of the equations to be solved. It is emphasized that the AFT permits the equations to be of any order, but the FG does not. In fact, there are two subsections (4.4 Treatment of a Second-Order Equation and 4.7 Equations in Implicit Form) in Ling and Wu (1987), in which the possibilities of treating higher-order equations not only in explicit form but also in implicit form are discussed.

The second point is about the form of nonlinearities handled. Although we did not give an example containing a nonanalytical nonlinearity, there is no problem in treating it. Since the nonlinear function $\mathbf{f}[x_m^{(k)}(t),\ t]$ in our notation is calculated numerically at discrete nodes t_i, $i=1, 2, \ldots, 2m_e$, so the nonanalytical nonlinearity can be equally handled.

Besides, a comparison with the Runge-Kutta method and two-point boundary value formulation are touched in this paper. Two remarks will be made as follows. First, a fixed steplength Runge-Kutta method mentioned in the paper is now usually replaced by an adaptive steplength one, especially if there is an abrupt change or even a discontinuity in the nonlinearities (cf., Stoer and Bulirsch, 1982 and also the IMSL subroutine IVPRK and DIVPRK). Second, there are intensive studies on using the shooting method to solve two-point boundary value problems with the aim of calculating periodic solutions (cf., e.g., Ling, 1981, 1982, 1983). To quote from Ling and Wu (1987), "The advantages of the Fast Galerkin Method are the completeness in the theory, the clearness in physical meaning and the directness in error estimation. Especially for simpler problems or problems requiring only low accuracy, the amount of computation by the Fast Galerkin method is less than that of the direct numerical method." Since AFT and FG are in essence the same, so this conclusion may also be applied to AFT.

[3]By T. M. Cameron and J. H. Griffin and published in the March 1989 issue of the ASME Journal of Applied Mechanics, Vol. 154, pp. 149–154.

[4]Visiting Professor, Department of Physics and Engineering Physics, Stevens Institute of Technology, Hoboken, NJ 07030. (On leave from Department of Engineering Mechanics, Shanghai Jiao Tong University, Shanghai 200 030, People's Republic of China.)

References

Ling, F. H., 1981, "Numerische Berechnung periodischer Lösungen einiger nichtlinearer Schwingungssysteme," Dissertation, Uni. Stuttgart.

Ling, F. H., 1982, "Numerische Berechnung periodischer Lösungen nichtlinearer Schwingungssysteme," *Zeitschrift für angewandte Mathematik und Mechanik*, Vol. 62, pp. T55-58.

Ling, F. H., 1983, "A Numerical Treatment of the Periodic Solutions of Non-Linear Vibration Systems," *Applied Mathematics and Mechanics*, Vol. 4, pp. 525–546.

Ling, F. H., and Wu, X. X., 1987, "Fast Galerkin Method and its Application to Determine Periodic Solutions of Non-Linear Oscillators," *International Journal of Non-Linear Mechanics*, Vol. 22, No. 2, pp. 89–98.

Stoer, J., and Bulirsch, R., 1980, *Introduction to Numerical Analysis*, Springer-Verlag, New York, Chapter 6.

Authors' Closure

We thank Professor Ling for his thoughtful and instructive comments on our paper. We especially appreciate the note from his own research that the Fast Galerkin (FG) method offers computational and theoretical advantages over shooting methods in many instances, and that this would also apply to our Alternating Frequency/Time (AFT) domain method.

Several of Professor Ling's comments are replies to our discussion of his work (Ling and Wu, 1987). We agree that the FG and AFT methods are fundamentally similar in balancing multiple harmonic terms in an equation, and using a fast Fourier transform (FFT) to obtain the harmonic content of the nonlinear terms. Consequently, the comments here and in our paper focus on how to view and implement the solution of a nonlinear dynamics problem, rather than on theoretical differences.

Professor Ling is correct in stating that Ling and Wu do mention the possibility of treating higher than first-order equations. However, since they formulate the FG method for systems of first-order ODE's, and do not show how higher-order equations are handled, the reader can be left with the impression that higher-order equations should be decomposed into first-order equations involving the state variables. The point we made is that this adds unnecessary computation since the velocity function is derivable from the displacement function and need not be calculated independently.

Professor Ling is also correct in stating that there is nothing to prevent the FG method from handling nonanalytic nonlinearities. Our work with a discontinuous nonlinearity (Coulomb friction) should be seen as an extension applicable to FG as well as AFT, and not as a limitation in the FG method.

The principal advantage in the AFT implementation is this: The unknowns are the complex components of the discrete Fourier transform of the dependent function, rather than the real coefficients of its Fourier series, as in FG. This simple difference in perspective—for periodic functions they are mathematically equivalent—can provide substantial computational advantages. The advantage is not immediately apparent since the AFT formulation results in a system of complex linear equations rather than the real linear equations obtained from the FG implementation. However, AFT has half as many equations, the bandwidth is smaller, and most methods for solving linear equations apply to complex as well as real systems. Since the number of operations in solving a linear system tends to go in proportion to the square of the number of equations, and there are tricks for achieving special efficiency in complex multiplication, the AFT formulation appears to be more advantageous. Furthermore, if an FFT is used to compute the harmonic components of a function, the AFT method can use the complex components of the FFT directly, saving the overhead of converting to Fourier series coefficients and separating the real and imaginary equations.

We also provide another extension, in addition to treating nonanalytic functions, which can be applied to either AFT or FG. This extension removes insignificant harmonic components from the system of equations in order to achieve even greater computational savings. This also allows us to look at widely disparate harmonic components, due perhaps to multiple forcing frequencies, without creating an equation for each harmonic component below or between the principal harmonics.

In regard to direct integration techniques: we did use an adaptive step-size Runge-Kutta method. In the case of a nonanalytic nonlinearity, such as Coulomb friction, it is essential that a time step not cross over a nonanalytic point. Time steps must end and begin on these points for the Taylor series to be valid. However, to compare the error between AFT and direct integration, we needed a fixed Δt to get a fixed number of sample points per period of oscillation. So the adaptation we made was to use a fixed Δt except around a point of discontinuity where we split the fixed time step into two pieces in order to end and begin on the discontinuity.

This is not the type of adaptive step to which Professor Ling is referring, so it is worth adding that we did try a canned, adaptive step-size algorithm (Press, et al., 1986) for time benchmarks, with poor results. Generic adaptive step-size algorithms can have difficulty with a discontinuous function because the error estimate governing the choice of step size is based on a Taylor series that may not exist. Adaptive step-size Runge-Kutta is still the method of choice with a discontinuous function, but the adaptive step algorithm should be written by the user to incorporate knowledge of the function.

We did not try shooting to converge directly on a steady-state result so we appreciate Professor Ling's comments in this area. We doubt, however, that shooting would ever be computationally advantageous with nonlinearities such as Coulomb friction, since each degree-of-freedom requires three state variables—velocity, displacement, and the position of the friction element. And the typical approach for correcting the initial values of the state variables can have unpredictable results with sharply discontinuous nonlinearities like friction. Also, the error comparison we made with Runge-Kutta would apply to an equivalent shooting method, so we doubt that shooting could offer increased accuracy—at least in the case of a discontinous nonlinearity.

Reference

Press, W. H., Flannery, B. P., Teukolsky, S. A., and Vetterling, W. T., 1986, *Numerical Recipes*, Cambridge University Press, New York.

Maximal Crack Tip Shielding by Microcracking[5]

C. H. Wu.[6] The authors presented a very concise and explicit calculation and showed that normal microcracking maximizes shielding. The starting point is the complementary energy

$$X(\sigma) = X_o(\sigma) + f(\sigma_1, \sigma_2) \tag{1}$$

where

$$\frac{\partial^2 f}{\partial \sigma_\alpha \partial \sigma_\beta} = \begin{cases} 0 & |\sigma| \to 0 \\ C_{\alpha\beta} & |\sigma| \to \infty \end{cases} \tag{2}$$

and $C_{\alpha\beta}$ are explicit expressions derived from a dilute crack concentration assumption. The crack tip J-integral, denoted by J_t, may be written as

$$J_t = F(P) K_t^2 \tag{3}$$

where P is the author's distribution density. The explicit calculation performed by the authors showed that normal microcracking maximizes $F(P)$. The proof is beautifully done.

The meaning of the equality

$$J_t = J_\infty, \tag{4}$$

however, is not clear. It was deduced from the assumption that one of the f's satisfying (2) described "the response of the material under proportional and monotonic stress paths." The exact connection between the statement and the desired crack-tip solution is not clear. On the other hand, the same equation (4) must hold for all f's satisfying (2). The implication is that K_t is not affected by f as long as it satisfies (2).

If the saturated zone and transition zone were actually experimentally determined, then the desired K_t would be determined from a well-defined problem. Let $W(\epsilon, \mathbf{x})$ denote the inhomogeneous strain energy density. Then

$$\frac{\partial p_{\beta\alpha}}{\partial X_\beta} = \frac{\partial W}{\partial x_\alpha} \Big|_{\text{explicit}} \tag{5}$$

where

$$p_{\beta\alpha} = W\delta_{\beta\alpha} - \tau_{\beta\gamma} u_{\gamma,\alpha} \tag{6}$$

is the Eshelby tensor. The result of integrating (5) over the semi-infinitely cracked region is (Wu, 1988)

$$J_t = J_\infty + \int_{\text{Transition}} (\partial W / \partial x_1)_{\text{explicit}}\, dA. \tag{7}$$

It is seen from (4) and (7) that (4) bypasses the difficult task of solving an inhomogeneous inhomogeneity problem. The question is what are the connections, if any, among the infinitely many cases implied by (4) and (7).

References

Wu, C. H., "A semi-infinite crack penetrating an inclusion," ASME Journal of Applied Mechanics, 1988, Vol. 55, pp. 736–738.

[5]By M. Ortiz, and A. E. Giannakopoulos and published in the June 1989 issue of the ASME Journal of Applied Mechanics, Vol. 56, pp. 279–283.

[6]Department of Civil Engineering, Mechanics and Metallurgy, University of Illinois at Chicago, Chicago, IL 60680.

Journal of Applied Mechanics

Book Reviews

Mechanics of Machining: An Analytical Approach to Assessing Machinability, by P. L. B. Oxley, Ellis Horwood Ltd., Chichester, U.K. division of John Wiley and Sons, N.Y., 1989, 242 pages.

REVIEWED BY MILTON C. SHAW[1]

This well written and organized monograph presents a very thorough continuum mechanics approach to steady-state metal cutting where the chips produced are in the form of continuous ribbons. The initial method employed is to determine the flow lines experimentally by measuring the distortion of an internal photoresist grid in front of a tool after cutting has been abruptly interrupted by an explosively-activated quick-stop device. These flow lines are used to obtain strains over the deformation zone extending from the tool tip to the free surface.

A plane-strain slip line field approach was first applied assuming a constant shear flow stress (k). At low cutting speeds and for soft annealed materials showing a large tendency to strain harden, the shear zone was relatively extensive and strain rate and temperature effects were negligible. The variation of k due to strain hardening was included in the analysis. At higher, more practical cutting speeds, the shear zone became more concentrated and approximated a shear plane. A parallel-sided shear zone of width ΔS_2 was then adopted and it became advisable to include the influence of strain rate and temperature on k as well as strain hardening.

The effects of strain hardening and strain rate were included by obtaining experimental material constants from a few points of metal-cutting data. The strain rate pertaining was obtained by approximating ΔS_2 from quick-stop photographs and extending the measured values to other values of feed by using what the author refers to as a scaling factor.

This assumes that ΔS_2 is inversely proportional to the length of the shear zone and, hence, to the feed for a given shear angle. Temperature effects are combined with strain rate effects by use of the velocity modified temperature concept.

A useful discussion of the problem of determining the direction of chip flow for cutting tools having an inclination angle, side cutting-edge angle, and nose radius is given in Chapters 8, 9, and 10.

Not included in the analysis is the fact that the resistance to shear flow for a given material depends not only on strain, strain rate, and temperature, but also on the homogeneity of strain pertaining. The latter quantity is related to structure (defect structure due to second phase particles, inclusions, grain boundaries, voids, etc.). These defects can cause the strain along a chip to be very inhomogeneous frequently giving rise to sawtooth chips or even discontinuous chips that involve cylic behavior. Since the width of the deformation zone in metal cutting is usually the same order of magnitude as the defect spacing, a size effect results. That is, the probability of finding a defect of a given intensity in the concentrated deformation zone decreases as the undeformed chip thickness decreases. This is an important reason why the deformation in metal cutting is usually inhomogeneous and why the specific cutting energy increases exponentially with a decrease in feed rate. The author suggests that the increase in specific energy with decrease in feed can be explained completely by an increase in strain rate. However, it should be kept in mind that metal cutting data has been used to evaluate the material constants ignoring the size effect and that the thickness of the deformation zone has been assumed to vary inversely as the shear plane length (feed). These two effects tend to mask the cause of the size effect and could tend to attribute too much of the increase in specific energy with decrease in feed to strain rate and temperature than is actually the case. However, as long as the analysis is used to interpolate and extend experimental metal cutting data and not to ascertain the basic cause of the observed behavior, this is satisfactory. It is somewhat akin to the velocity modified temperature concept but for strain inhomogeneity.

This book provides about the best treatment possible of the metal-cutting process for the case of homogeneous steady-state strain from the continuum mechanics point of view. It should be studied by all serious researchers in this field for the insight it provides into the intricacies of the process. It should be noted that the author clearly indicates in the preface that the material science (structural) aspects of material behavior are not considered in his treatment. As long as this limitation is recognized and kept in mind, this is a useful contribution. However, to ensure that this important point not be overlooked, it is unfortunate that the title did not read "Continuum Mechanics of Metal Cutting."

[1] Arizona State University, Tempe, AZ. Honorary Mem. ASME.